

BULGARIAN CHEMICAL COMMUNICATIONS

2017 Volume 49 / Special Issue K1

*Journal of the Chemical Institutes
of the Bulgarian Academy of Sciences
and of the Union of Chemists in Bulgaria*

BULGARIAN CHEMICAL COMMUNICATIONS

A quarterly published by

THE BULGARIAN ACADEMY OF SCIENCES

and

THE UNION OF CHEMISTS IN BULGARIA

Volume 49, Special issue K1

ИЗВЕСТИЯ ПО ХИМИЯ

Тримесечно издание на

БЪЛГАРСКА АКАДЕМИЯ НА НАУКИТЕ

и

СЪЮЗ НА ХИМИЦИТЕ В БЪЛГАРИЯ

Том 49, Книга K1

2017

Editor-in-Chief:

V. Beschkov

Visiting editor:

Abdol Ghaffar Ebadi

EDITORIAL BOARD

Ch. Bonev, L. Boyadzhiev, I. Gutzow, I. Havezov, E. Ivanova, K. Petkov, K. Petrov, L. Petrov, I. Pojarlieff, S. Rakovsky, D. Stoychev, P. Petrov, D. Tsalev, D. Vladikova, D. Yankov, V. Kurteva

Members from abroad:

J. M. Albella (Spain), S. Berger (Germany), J. C. Breakman (Belgium), J. Etourneau (France), M. Farina (Italy), K. Friedrich (Germany), J. Gyenis (Hungary), A. J. Kirby (United Kingdom), T. Kowalska (Poland), K. Kutchitsu (Japan), A. Lasia (Canada), O. V. Mazurin (Russia), B. Mutaftshiev (France), E. Peter Kündig (Switzerland), S. De Rosa (Italy), T. F. Tadros (United Kingdom), K. Valko (Hungary)

The annual subscription (for 4 issues) for vol. 48 (2017) is € 160. – including postage, handling and packaging charge.

Payments should be delivered to:

*Editorial Board of Bulgarian Chemical Communications, Institute of Chemical Engineering,
UniCredit Bulbank, IBAN: BG65 UNCR 7630 3400 0017 48; SWIFT/BIC - UNCRBGSF (for Euro €).*

UniCredit Bulbank, IBAN: BG18 UNCR 9660 3119 9033 12; SWIFT/BIC - UNCRBGSF (for local currency BGN).

Chirality- and size-dependent elastic properties of a single-layered graphene sheet

Zh. Wang, Zh. Yu, X. Sun*, Y. Wang, L.Xu

¹ College of Aerospace and Civil Engineering, Harbin Engineering University, Harbin 150001, China

Received, August 1, 2017; Accepted, November 21, 2017

This article mainly uses a structural mechanics approach to analyze the elastic properties of a single-layered graphene sheet (SLGS). Besides, the space frame structure is also adopted to model the interatomic forces of the carbon–carbon bonds. By means of the finite element method, the elastic properties of SLGS on the basis of different chirality and size are measured. According to the results, the elastic properties of SLGS are size- and chirality-dependent, which is in consensus with the literature.

Key words: Single-layered graphene sheet, Elastic properties, Chirality

INTRODUCTION

Based on its one atomic layer thickness, graphene is considered as a two-dimensional (2D) material which consists of carbon atoms set in a honeycomb lattice structure. After it was primarily isolated in 2004 [1], it has received significant attention due to its interesting physical properties like high levels of thermal conductivity [2], stiffness, strength [3], etc. Besides, multilayer graphene also possesses attractive physical characteristics [4-5].

By using experimental and theoretical methods, numerous studies have been carried out on the elastic properties of SLGS. Frank *et al.* proved the Young's modulus of graphene nearly 0.5 TPa with a nanoindentation experiment using atomic force microscope (AFM) [10]. In a similar approach, Lee *et al.* obtained the Young's modulus of graphene approximately equal to 1TPa [3]. By tip-induced deformation experiments Cristina found that the Young's modulus of free monolayer graphene reaches 0.25TPa [6]. From the perspective of theories, the molecular dynamics method was applied to study the Young's modulus of different chirality graphenes by Q.X.Pei *et al.*, they also found that the armchair graphene is 0.89TPa and the zigzag graphene is 0.83TPa [7]. In addition, Hao Bu *et al.* also applied a molecular dynamics method (empirical Tersoff potential) to calculate the Young's modulus of graphene up to 1.24TPa [8]. *AB initio* DFT method was resorted by Fang Liu *et al.* to compute the Young's modulus and Poisson's ratio showing that the values are 1.05TPa and 0.186, respectively [9]. In addition,

Reddy adopted a continuum mechanics

approach to figure the Young's modulus of non-equilibrium and equilibrium, showing that the values are 1.0 TPa and 0.7 TPa, respectively [11]. Li explored a structural mechanics approach that uses space frame structures to model the carbon nanotubes, therefore he expected that the Young's modulus of monolayer graphene was 1.0 TPa [12].

On the basis of molecular structural mechanics, Young's modulus and Poisson's ratio of SLGS was analysed by atomic simulation approach in this work. For this purpose, an equal structural beam was used to imitate the interatomic forces of the carbon–carbon bonds. The equal beam mode with different chirality and size will be used to study the Young's modulus and Poisson's ratio of SLGS.

MODEL

Theoretical foundation molecular mechanics and structural mechanics

Graphene can be considered as a large molecule made up of lots of carbon atoms arranged regularly, each of them being in a force field from the standpoint of molecular mechanics [12]. The force field, created by nucleus-nucleus and electron-nucleus interactions, controls the motions of atoms. As usual, the force field, expressed as a means of steric potential energy, only replies on the comparative position of the nucleus. In Fig. 1, diverse kinds of potential energy are shown. For the system, its whole potential energy under consideration can be calculated as [13]:

$$U_{Total} = \sum U_r + \sum U_\theta + \sum U_\phi + \sum U_\omega + \sum U_{vd\omega} \quad (1)$$

where $U_{vd\omega}$, U_ω , U_ϕ , U_θ and U_r are energies, relative to van der Waals nonbonding

*To whom all correspondence should be sent:
E-mail: sunxiaoyu520634@163.com

interaction, bond torsion, inversion, angle variation and bond stretching, respectively. Generally, the first term is of very little importance compared with the other four terms, which primarily contribute to the whole steric energy. Compared with other terms, the torsion and inversion energies have great importance for graphene which is subjected to in-plane tension loading. Consequently, the sum of angle variation and bond stretching, further represented by harmonic functions under small deformations of linear elasticity, can be used to fairly accurately calculate a monolayer graphene's whole potential energy [14-15]:

$$U_r = \frac{1}{2}k_r(r-r_0)^2 = \frac{1}{2}k_r(\Delta r)^2 \quad (2)$$

$$U_\theta = \frac{1}{2}k_\theta(\theta-\theta_0)^2 = \frac{1}{2}k_\theta(\Delta\theta)^2 \quad (3)$$

where k_θ and k_r stand for the force constants, separately relative to angle variation and bond stretching; θ and r stand for bond-angle and inter-atomic distance after deformation, respectively; θ_0 and r_0 refer to bond angle and distance before deformation, respectively.

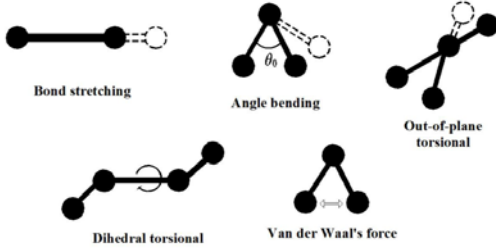


Fig. 1. Potential energy of carbon-carbon bonds

Structural mechanics

Twisting and stretching make up a whole beam's potential energy on the basis of structural mechanics. In Fig. 2, diverse loadings are shown which are used in a uniform beam generating potential energy. Under axial load, a uniform beam's strain energy, N , can be computed as:

$$U_A = \frac{1}{2} \int_0^L \frac{N^2}{EA} dl = \frac{1}{2} \frac{N^2 L}{EA} = \frac{1}{2} \frac{EA}{L} (\Delta L)^2 \quad (4)$$

where E is the Young's modulus of the uniform beam, U_A the tensile energy, A the beam's cross section, ΔL the length variation, and L the length of beam. In the beam, M produces strain energy in the application of pure bending load. U_M , the bending potential energy is given by

$$U_M = \frac{1}{2} \int_0^L \frac{M^2}{EI} dl = \frac{2EI}{L} \alpha^2 = \frac{1}{2} \frac{EI}{L} (2\alpha)^2 \quad (5)$$

where α stands for the rotation angle of the end of the beam and I stands for its moment of inertia.

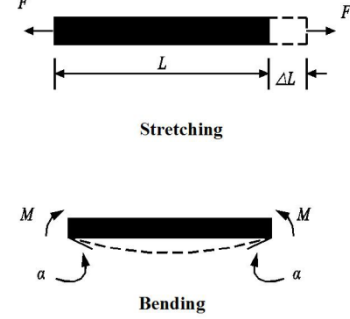


Fig. 2. Stretching and bending of a uniform beam

Equivalent continuum space frame structures model

That is to say, the equivalencies of the relevant terms between molecular and structural mechanic systems are imposed because of the independency of the potential energy terms in those systems. The equivalency of energy between diverse term states an equivalent structural beam. To model interatomic forces of the covalently bonded carbon atoms, an equivalent structural beam is used. Attributions of the beam according to force field constants, covalent stiffnesses, are as:

$$\frac{EA}{L} = k_r, \quad \frac{EI}{L} = k_\theta \quad (6)$$

$\frac{EA}{L}$ and $\frac{EI}{L}$ stand for bending and stretching of the equivalent beams.

There is a possibility that the stiffnesses, which are defined in constants of force field terms, use the structural beam by the stiffness matrix method. Another method using the structural beam suggested the atomistic finite element [16]. It is pointed out that specified diameter and elastic modulus of the beam fulfill the probabilities of using the beam with the atomistic limited approach compared with the stiffness matrix method. Via replacing $A = \frac{\pi d^2}{4}$, $I = \frac{\pi d^4}{64}$ in Eq. (6) according to the force field constants, the beam features are deduced as:

$$d = 4 \sqrt{\frac{k_\theta}{k_r}}, \quad E = \frac{k_r^2 L}{4\pi k_\theta} \quad (7)$$

where E is the modulus of elasticity and d is cross section diameter. L is the length of beam

which is regarded to be equal to the carbon atoms' distance in a covalent bond.

k_θ and k_r are equal to 8.76×10^{-10} Nnm/rad² and 6.52×10^{-7} N/nm, respectively, by employing the AMBER force field of molecular dynamics simulation [15-16]. 0.1412 nm is the distance between two contiguous carbon atoms [21]. We can get $E = 5.488 \times 10^{-6}$ N/nm² and $d = 0.146618$ nm through solving the Eq. (7). Additionally, the ratio of Poisson is reasonably supposed to be 0.3.

To simulate the monolayer graphene nanofilms, the space frame structures, which are made up of beam elements, are shown in terms of the theoretical analysis in the part above. It is forecasted that the mechanical features of the SLGSs are size- and chirality-dependent [17-20]; so, the elastic properties are computed for the armchair sheets and zigzag in diverse sizes. Two geometric parameters, b and a , are described to specify every SLGS. b and a stand for side width and length of the SLGS, respectively. In Fig. 3, the diagram of the SLGSs studied in this research is shown.

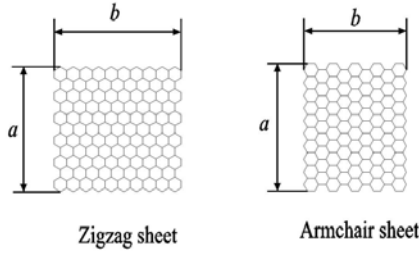


Fig. 3. Zigzag SLGS and armchair SLGS.

To study the elastic properties of SLGS, a space frame structure model is described. Normal stress to the atomistic model's free edge is used for the exploration of the elastic properties of the SLGS under tension. As a result, the continuum sheet's normal stress is presented as:

$$\sigma = \frac{nf}{bt} \quad (8)$$

where n is the number of nodes exposed to the external forces, f is the magnitude of the tensile forces, t and b are the thickness and width of the SLGS, respectively. According to the strain and tensile stress, the Poisson's ratio and Young's modulus are calculated as:

$$E = \frac{\sigma}{\varepsilon_a} = \frac{bt}{\Delta a} \quad \nu = \frac{\varepsilon_b}{\varepsilon_a} = \frac{b}{a} \quad (9)$$

where ε_a and ε_b stand for the tensile strain of SLGS, which are equal to the elongation ratios Δa and Δb to the original side length, a and b .

RESULTS AND DISCUSSION

Through the finite element method, we can determine the SLGS elastic properties. In Figs. 4-7, there are explanations of the Young's modulus and Poisson's ratio of SLGS with diverse size and chirality. The armchair graphene has 0.672 TPa and 0.435, and the zigzag graphene has 0.615 TPa and 0.388, respectively, on the condition that the SLGS width and length are 1.989 nm and 2.215 nm, respectively. This corresponds to the results in the references [11,21]. From the figures it can be perceived that with the gradually increasing size, the Poisson's ratio and Young's modulus increase or decrease. So we can prove that the SLGS elastic property is dependent on size. From Figs. 4 and 6 it is perceived that the Young's modulus of armchair graphene is constant (about 0.665 TPa) and that of zigzag graphene increases from 0.615 TPa to 0.700 TPa, on the condition that the length varies and the width is constant. In the other case, the Young's modulus of armchair graphene increases from 0.672 TPa to 0.708 TPa, and that of zigzag graphene is constant (about 0.613 TPa), on the condition that the width varies and the length is constant. From Figs. 5 and 7, we can see that there is a similar trend of the Poisson's ratio for both armchair and zigzag graphene. In this way we can prove that the SLGS elastic property is dependent on chirality.

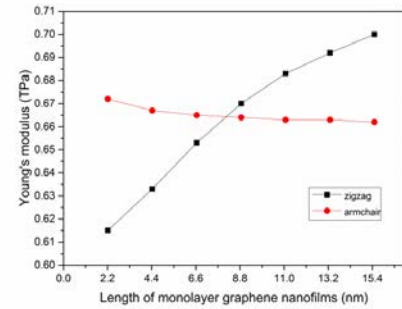


Fig. 4. Young's modulus of SLGS with the variation of length at constant width (1.989 nm).

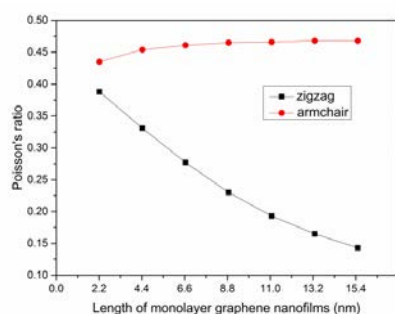


Fig. 5. Poisson's ratio of SLGS with the variation of length at constant width (1.989 nm).

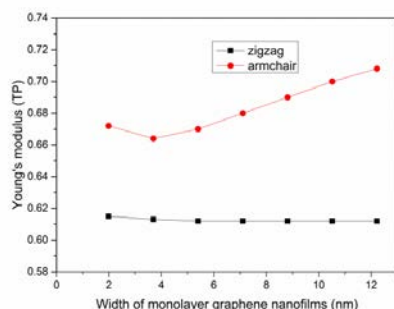


Fig. 6. Young's modulus of SLGS with the variation of width at constant length (2.215 nm).

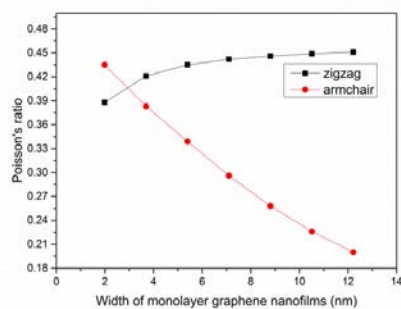


Fig. 7. Poisson's ratio of SLGS with the variation of width at constant length (2.215 nm).

CONCLUSIONS

The finite element model of equal continuum for the SLGS under exterior loads is presented. To this end, based on a SLGS action's atomistic analysis, the Poisson's ratio and Young's modulus of the continuum model are computed. The armchair graphene is 0.672TPa and 0.435, and the zigzag graphene is 0.615TPa and 0.388, on the condition that the SLGS width and length are 1.989 nm and 2.215 nm, respectively. This corresponds to the results in the literature. So the method used in this paper is reasonable. On this basis, the elastic properties of SLGS with different chirality and size are calculated and it is found that with the size gradually increasing, the Poisson's ratio and Young's modulus increase or decrease, so we found that the SLGS elastic property is size-dependent. We also found that the SLGS elastic property is chirality-dependent.

Acknowledgements: This work was supported by the National Natural Science Foundation of China (No. 11602066, No.11472086 and 11532013) and the China Postdoctoral Science Foundation On the 56th bath of surface founds the project (2014M561327) and the National Science Foundation of Heilongjiang Province of China (QC2015058 and 42400621-1-15047), the Foundation Research Funds for the Central Universities.

REFERENCES

1. K.S. Novoselov, A.K. Geim, S.V. Morozov, D. Jiang, Y. Zhang, S.V. Dubonos, I.V. Grigorieva, A.A. Firsov, *Science.*, **306**, 5696 (2004).
2. A.P. Yu, M.E. Itkis, E. Bekyarova, R.C. Haddon, *J. Phys. Chem. C.*, **21**, 111 (2007).
3. C. Lee, X.D. Wei, J.W. Kkysar, J. Hone, *Science*, **321**, 5887 (2008).
4. Y.F. Guo, W.L. Guo, *J. Phys. D.*, **7**, 36 (2003).
5. K.S. Novoselov, E. Mccann, S.V. Morozov, V.I. Fal'ko, M.I. Katsnelson, U. Zeitler, D. Jiang, F. Schedin, A.K. Geim, *Nat. Phys.*, **2**, 2 (2006).
6. G.-N. Cristina, B. Marko, K. Klaus, *Nano lett.*, **8**, 7 (2008).
7. Q.X. Pei, Y.W. Zhang, V.B. Shenoy, *Carbon*, **3**, 48 (2010).
8. H. Bu, Y.F. Chen, M. Zou, H. Yi, K.D. Bi, Z.H. Ni, *Phys. Lett. A.*, **37**, 373 (2009).
9. F. Liu, P.B. Ming, J. Li, *Phys. Rev. B.*, **11**, 22 (2003).
10. I.W. Frank, D.M. Tanenbaum, A.M. Van Der Zande, P.L. Mceuen, *J. Vac. Sci. Technol. B.*, **6**, 25 (2007).
11. C.D. Reddy, S. Rajendran, K.M. Liew, *Nanotechnology*, **3**, 17 (2006).
12. C. Li, T.W. Chou, *Int. J. Solids Struct.*, **10**, 40 (2003).
13. A.K. Rappe, C.J. Casewit, K.S. Colwell, W.A. Goddard, W.M. Skiff, *JACS*, **25**, 114 (1992).
14. W.D. Cornell, P. Cieplak, I.B. Christopher, C.I. Bayly, I.R. Gould, M.M. Kenneth, M.F. David, C.S. David, F. Thomas, W.C. James, A.K. Peter, *J. Am. Chem. Soc.*, **19**, 117 (1995).
15. W.L. Jorgensen, D.L. Severance, *J. Am. Chem. Soc.*, **12**, 112 (1990).
16. G.M. Odegard, T.S. Gates, K.E. Wise, C. Park, E.J. Siochi, *Compos. Sci. Technol.*, **11**, 62 (2002).
17. A. Sakhaee-pour, M.T. Ahmadian, R. Naghdabadi, *Nanotechnology*, **8**, 19 (2008).
18. A. Sakhaee-pour, M.T. Ahmadian, A. Vafai, *Solid State Commun.*, **4**, 145 (2007).
19. A. Sakhaee-pour, *Solid State Commun.*, **1**, 149 (2009).
20. S.P. Wang, J.G. Guo, Y. Jiang, *J. Comput. Theor. Nanosci.*, **1**, 10 (2013).
21. M.S. Dresselhaus, G. Dresselhaus, R. Saito, *Carbon*, **7**, 33 (1996).

Application of a MEE-rock debris separation technique in deep hole bench blasting

M. Zhao¹, J. Zhang², Zh. Lei³, Q. Kang¹

¹Guizhou Xinlian Blasting Engineering Group Co. Ltd. Guiyang, Guizhou 550002, China

²Wuhan University of Technology, Wuhan, Hubei 430070, China

³Guizhou Institute of Technology, Guiyang, Guizhou, 550003, China

Received August 1, 2017, Accepted September 13, 2017

In order to solve the problem of water in boreholes which influences the blasting effect in open pit deep hole bench blasting, an isolator was designed for separating the mixed emulsion explosive (MEE) from rock debris, based on the principle of fluid dynamics. The finite element software ANSYS/LS-DYNA was applied to simulate the posture adjustment of the isolator in the process of falling. The result showed that the designed isolator could meet the purpose of separating MEE from rock debris. Simulation experiments in dry and wet borehole models with and without isolator were performed, and the results showed that the isolator can avoid the explosive misfire caused by mixing of MEE and rock debris, increase the utilization rate of MEE, improve the blasting effect, and meet the purpose of lowering the blasting cost.

Key words: Bench blasting, MEE-rock debris isolator, Numerical simulation, Blasting effect

INTRODUCTION

In open pit deep hole bench blasting, it is common that the borehole is filled with water. Since rock debris are with finer grain size and they are easy to form mixtures at the hole bottom when the slurry emulsion explosive is pumped in, the bottom part of the slurry emulsion explosive would get mixed with rock debris because of the effect of pumping and the weight of the explosive, which would lead to the loss of explosion power and cause the waste of explosives, directly influencing the blasting effect. Lots of studies on enhancing blasting effect and reducing blasting cost have been made home and abroad. Wang [1] studied the application of the emulsion explosives mixing and charging truck in water conservancy projects like the Three Gorges Dam, and stated the advantages and disadvantages of using MEE in boreholes full of water and its technology. Liu Lei *et al.* [2] found that under the water pressure of 0.2 Mpa, the detonation velocity of emulsion explosives sensitized by ordinary chemical could decrease by 74.81% and its shattering brisance could decrease by 49%, and when the pressure is up to 0.3 Mpa, most of the emulsion explosives would be half or all misfired. Adhikary *et al.* [3] studied the influence of water level, charging speed and borehole size on the charging effect of emulsion explosives in boreholes filled with water, and the results showed that when the depth of water was larger than the largest effective range of the jet flow, the explosives would fail to reach the bottom and a water column would be formed, so that the distance from the top of the charging tube to the bottom of the borehole

should be reduced and the charging speed should be increased. Ye Haiwang *et al.* [4] studied the influence of the mixing situation of emulsion explosives, water and rock debris on the blasting effect through experiments and numerical simulations, analyzed the effect of different ways of charging on mixing, and put forward a control method increasing the charging speed and putting the charging tube to the borehole bottom. Pete *et al.* [5] made experiments on the critical diameter and the critical depth of several emulsion explosives, found the critical size of different explosives and discussed the main mechanism of efficacy loss by the geometric dimensions of emulsion explosives. Former studies have revealed the mixing process and action mechanism of explosives, water and rock debris during the charging process of site-mixed emulsion explosives, and found that the mixture would lead to negative effects like degradation of explosives, detonation performance or loss of efficacy, and suggested some techniques to control the negative effects. In order to prevent the efficacy loss caused by the mixing of site-mixed emulsion explosives and rock debris, this paper studied the ways of separating emulsion explosives from rock debris to increase explosive utilization rate.

DESIGN AND MANUFACTURE OF MEE-ROCK DEBRIS ISOLATOR

Based on the principle of fluid dynamics and the space characteristics of boreholes filled with water, the isolator was designed like a plate. Its density must be larger than that of water, so it can sink by its gravity in water and adjust to the level condition with its bottom down under the effect of the uplift and

*To whom all correspondence should be sent:
E-mail: 99113294@qq.com

resistance force of water or air till sinking to the borehole bottom, so as to achieve the goal of separation. Using this isolator in the charging process could effectively separate the explosives and rock debris at the borehole bottom and prevent explosive efficacy loss caused by the mixing at the middle and bottom parts of the borehole.

The isolator was used in a borehole 250 mm in diameter to check its separation effect. Its material was ordinary rubber with density of 1.4 g/cm^3 and thickness of 5 mm. Its structure and size are shown in Fig. 1.

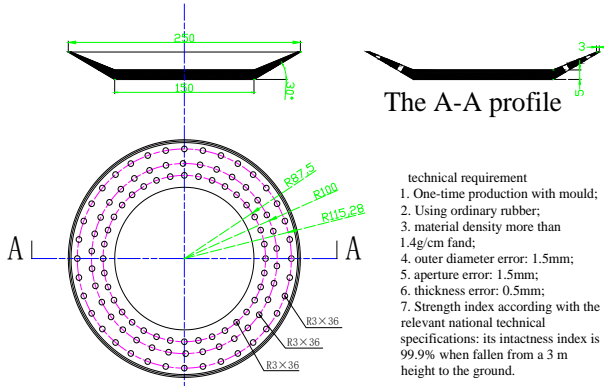


Fig. 1. Plate-shaped MEE-rock debris isolator

Calculation models and parameters

Based on the site experiments, the calculation models were constructed (see Fig. 2). The outside of the model is a steel tube, whose outside diameter is 250 mm. The upper part is filled with air, and the lower part is water. The isolator is in the air at its initial state. According to the site experiments, the isolator can quickly adjust its posture after being put in the water. Therefore, in order to reduce the calculation work, the length of the air column was considered as 1 m, the length of the water column was taken as 3 m, and the distance from the isolator to the water face was 0.3 m.

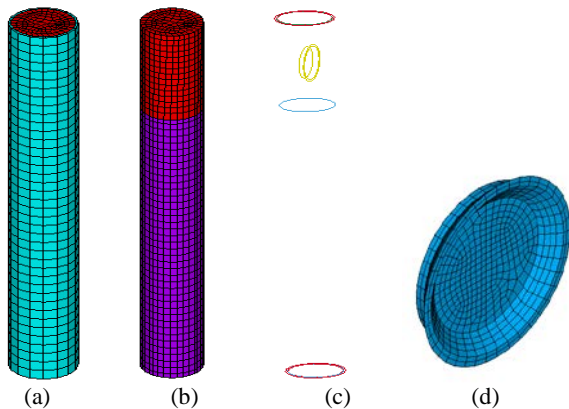


Fig. 2. Calculation models and finite element grids

Fig. 2 shows the calculation models of the numerical simulation of the adjusting process of the isolator and their finite element division, in which Fig. 2 (a) is the finite element grid of the whole calculation model, Fig. 2 (b) is the finite element grids of air (upper part) and water (lower part) in the tube, Fig. 2 (c) is the initial calculation state of the isolator, and Fig. 2 (d) is the finite element grid of the rubber plate at the bottom of the borehole.

The parameters of the materials are as follow: a flexible model is applied to simulate the outside steel tube, and the parameters of its material are shown in Table 1:

Table 1. Material parameters of the steel tube

Density / kg.m^{-3}	Elasticity modulus /GPa	Poisson's ratio
7810	190	0.25

Since air and water in the calculation model are fluid materials, their deformations are distinct under the disturbance of external force, so a state equation should be set during the calculation. In this part, Grüneisen state equation was used for air and water.

The material parameters of air are shown in Table 2:

Table 2. Material parameter of air

Density / kg.m^{-3}	Viscosity factor	C	γ_0
1.252	17.456E-6	343.7	1.4

The material parameters of water are shown in Table 3:

Table 3. Material parameters of water

Density / kg.m^{-3}	Viscosity factor	C	γ_0	S ₁	S ₂
1000	1.202E-3	$\frac{1.647E-3}{3}$	1.4	1.921	0.096

The material parameters of the isolator are shown in Table 4:

Table 4. Material parameters of the isolator

Density / kg.m^{-3}	Elasticity modulus /MPa	Poisson's ratio
1340	7.84	0.3

Simulation result of the process of the isolator falling into water

The process of the isolator falling into water was reproduced by numerical simulation. It theoretically reveals the feasibility of the isolator. Fig. 3 shows the isolator states at different times.

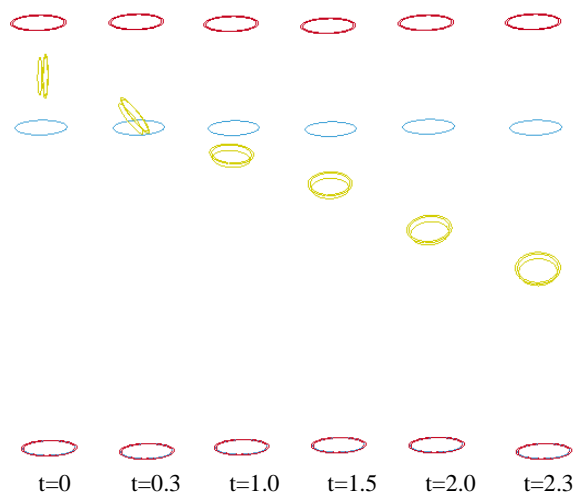


Fig. 3. Simulation results of the falling process of the isolator

Analysis of the simulation results

According to the numerical simulation, when the isolator meets water, it can quickly adjust its posture during the falling process, from vertical to the water level to face up, and there would be slight adjustment in the subsequent falling process, keeping face up. The numerical simulation reproduces the posture adjustment process of the site selection experiments, which shows that the designed MEE-rock debris isolator could adjust its posture automatically during falling, and it can keep face up when it meets water, so as to separate the emulsion explosives and rock debris.

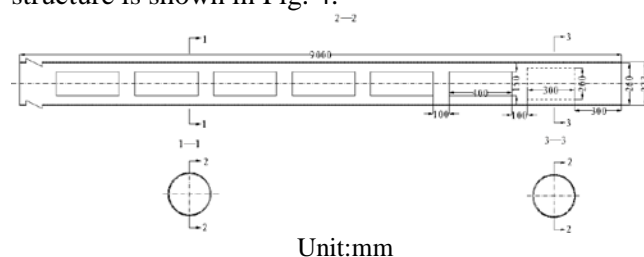
SIMULATION EXPERIMENTS OF THE MIXING OF EMULSION EXPLOSIVES AND ROCK DEBRIS AND PERFORMANCE EXPERIMENT OF THE ISOLATOR

Since rock debris and water would be left in the borehole while drilling, emulsion explosives would get mixed with them, which would seriously influence the explosive's blasting performance, and lead to incomplete bursting of the explosives at the bench bottom and on top of the charge, causing boulders and bootlegs. In case of the appearance of these phenomena and for increasing the utilization factor of explosive energy, this section explores the mixing of MEE, rock debris and water in boreholes by simulation experiments, and experimentally studies the separation performance of the isolator.

Design of the simulation experiment set

The 1:1 model uses a steel tube with 260 mm inner diameter and 9 m length to simulate the borehole. For the convenience of observation, 7 observation windows, 40 cm long and 15 cm wide each, are opened in a line on the tube, and for the

integrity of the "borehole", 2 layers of 3 mm thick high-strength transparent polyethylene sheets are wrapped outside the windows by iron wire. The steel tube is fixed on the ground with falseworks. Its structure is shown in Fig. 4.



Unit:mm

Fig. 4. 1:1 borehole model structure



Fig. 5. On-site charging experiment set

Mixing mode experiments of the emulsion explosive and rock debris

Mixing mode experiments of the emulsion explosive and rock debris in the dry borehole

Put a certain amount of rock debris in the borehole model. Then pump the mixed emulsion explosive into it until continuous mixed emulsion explosive is seen. Plug the borehole model with rock debris. According to the on-site experiments, the mixture amount of the emulsion explosive and rock debris at the borehole bottom is quite large. The highest mixed column reaches 80 cm, and the shortest 18 cm. There is a certain amount of mixture of the emulsion explosive and the plugged rock debris on top of the charge. The length of the mixed column is 5 to 10 cm. Details are shown in Figs. 6 and 7.



Fig. 6. Typical mixture formed on top of the charge and at the bottom of the dry borehole model

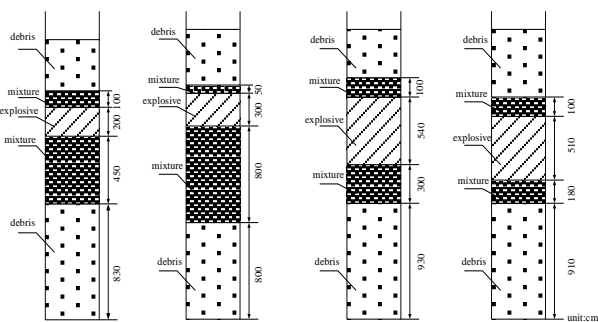


Fig. 7. Charging results in the dry borehole

Based on the experiments, the main reasons in the dry borehole that lead to the mixing of rock debris and the emulsion explosive are: (i) the stickiness of the on-site mixed emulsion explosive: the thinner the explosive, the more mixture there would be; and (ii) the distance between the pumping tube and the rock debris at the borehole bottom: the longer the distance, the more rock debris would be aroused up, and the larger amount of the mixture would be produced.

Mixing of the emulsion explosive and the plugged rock debris in the dry borehole is mainly caused by the impact of rock debris on the column charge while plugging.

Mixing mode experiments of the emulsion explosive and rock debris in the water borehole

Put a certain amount of rock debris in the borehole model, and then pour a certain amount of water into it. When the water gets clear, pump the mixed emulsion explosive in until continuous emulsion explosive is seen. Plug it with rock debris. According to the on-site experiments, the mixed amount of emulsion explosive, rock debris and water at the borehole bottom is quite large. The highest mixed column reaches 100 cm, and the shortest 12 cm. The gaps in the mixed column charge are filled with water in varying degrees (in an experiment, the emulsion explosive was not mixed with rock debris, but it was mixed with water). There is a certain mixture of the emulsion explosive with the plugged rock debris on top of the charge. The length of the mixed column is 9 to 15 cm. Details are shown in Figs. 8, 9 and 10.

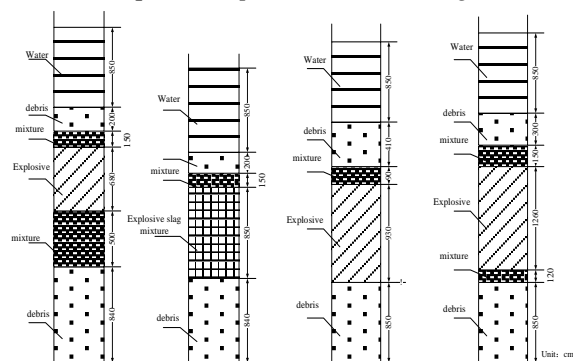


Fig. 8. Charging results in the water borehole



Fig. 9. Charging result of the water borehole model



Fig. 10. Typical mixtures in a borehole with water formed at the top and bottom

Based on the experiments, there would be a certain degree of mixing of the emulsion explosive, rock debris and water at the bottom of the water borehole.

When the distance between the charging tube and the borehole is shorter, most is the mixture of explosives and water, and less is the mixture of explosives and rock debris. When the distance is larger, the mixture is mainly made of explosives, rock debris and water, and the percentage of rock debris in the mixture is higher than that in the first circumstance.

When the pumping tube is plugged into the slurry at the borehole bottom while pumping, because of the disturbance of the pumping, there would be a turbulence flow. Since the slurry has a larger specific gravity than the explosive, the explosive, rock debris and water would quickly get mixed. In this circumstance, the mixing is most thorough, and part of the explosive fails to explode.

Table 5. Performance experiment result of the plate rubber isolator

Type	Experimental condition	Experimental time	Time of sinking to the bottom in the tilting posture	Time of sinking to the bottom in the level posture	Sinking speed, m/min
Plate rubber isolator	In the water-filled borehole	1000	0	100%	2~2.5
	In the dry borehole	1000	89	91.1%	-

Performance experiments of the isolator

The performance experiments of the isolator were conducted in a simulating experiment set. The posture adjustment performances, the sinking speeds of the plate-shaped rubber isolator and the bowl-shaped plastic isolator were simulated in both dry borehole and water-filled borehole. The design parameters were revised based on the experiments. Part of the experimental results of the finalized design of the plate rubber isolator are shown in Table 5

According to the experimental result above, the percentage of the plate rubber isolator sinking to the bottom in the level posture in the water borehole is 100%. Its posture adjusts slowly in the dry borehole, and it is easy to be crushed by the wall while sinking.

Separation experiments of the isolator

According to the experiments of different mixing modes of emulsion explosives and rock debris, with or without water or not, on the bottom of the borehole or on top of the charge, there would be a certain extent of mixing between mixed emulsion explosives, rock debris and water, especially at the borehole bottom, which would influence explosive's blasting performance at that part and causing explosive misfire. That would seriously influence rock fragmentation results at the borehole bottom, and produce boulders and serious bootlegs, slowing down the subsequent exploitation and loading speed. In order to reduce or avoid the above circumstances, isolators are arranged at the bottom of boreholes before pumping and on top of the charge after pumping to prevent mixing between MEEs, rock debris and water, making sure the explosive's utilization ratio. Related experiments are studied.

2.4.1. Mixed emulsion explosive charging experiments with isolators in dry boreholes

Put a certain amount of rock debris in the borehole model. Arrange an isolator before charging, and then pump the explosive until continuous mixed emulsion explosive is seen in the model. Arrange another isolator on top of the charge and plug the model with rock debris. The experiments show that, after the isolators are arranged in the model, there is nearly no mixing both at the bottom of the borehole and on top of the charge. Details are shown in Fig. 11.

Mixed emulsion explosive charging experiments with isolators in water boreholes

Put a certain amount of rock debris in the borehole model, and then pour a certain amount of

water. When the water gets clean, arrange an isolator in the borehole, and then pump a certain amount of the mixed emulsion explosive in it. Arrange another isolator on top of the charge, and plug the borehole with rock debris. The experiments show that, after isolators are arranged in boreholes, there is nearly no mixing between the mixed emulsion explosive and rock debris both at the bottom of the borehole and on top of the charge, but there is a certain mixing between the mixed emulsion explosive and water at the bottom of the boreholes. Details are shown in Figs. 12 and 13.

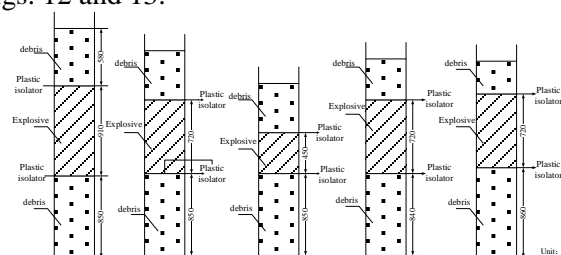


Fig. 11. Structures of charging experiments in dry borehole models

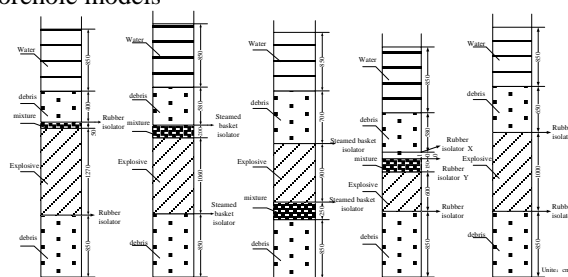


Fig. 12. Structures of charging experiments in water-filled borehole models



Fig. 13. Charging experiments of the mixed emulsion explosive in water-filled borehole models with isolators

All experiments showed that as long as the isolators are arranged, both in the dry borehole and in the water-filled borehole, there is barely mixing between the mixed emulsion explosive and rock debris, which testifies that the function of the isolator is notable.

However, there is still a certain mixing between the mixed emulsion explosive and water. The main reason is the distance between the pumping tube and the borehole bottom. The falling of the mixed emulsion explosive is slow in water. This would be easy to cause that some water is unable to seep up and stays in the boreholes, which would form a

mixture of the MEE and water. The experiments also revealed that if the pumping tube is inserted to the borehole bottom and then pumps the mixed emulsion explosive, the charging result would be noticeably improved and the water at the borehole bottom could be basically squeezed out by the explosive.

CONCLUSION

The plate rubber isolator, designed on the basis of the principle of fluid dynamics, can automatically fall along the borehole under the its gravity, and adjust its posture under the effect of uplift and resistance force of water or air to the level condition with its bottom down before it reached the bottom, which would lead to the separation result.

The large-scale explicit dynamic finite element software, ANSYS/LS-DYNA, was applied to simulate the isolator posture adjustment during falling, and the result shows that the designed isolator could make a self-adjustment while falling, and could cover the water face when it meets water, which would achieve the separation result of the mixed emulsion explosive and rock debris.

The plate-shaped rubber isolator could effectively separate the mixed emulsion explosive and rock debris at the bottom of the borehole, avoiding mixing and the misfire. The isolator has many advantages. Its material is easy to get. Its production process is simple. It is easy to operate, of low cost, and takes little length of the borehole. There is no need to deliberately pay attention to the posture of the isolator.

The on-site mixing experiments showed that the amount of the mixture of MEE, rock debris and water at the borehole bottom is rather large. The highest mixed column reaches 100 cm, and the shortest 12 cm. The gaps in the mixed column charge are filled with water in varying degrees. There is a certain amount of mixture of the emulsion explosive with the plugged rock debris on top of the charge. The length of the mixed column is 9 to 15 cm.

The separation experiments of the isolator showed that the falling posture of the isolator is specific and stable. The percentage of the plate rubber isolator sinking to the bottom in the level posture in the water borehole is 100%. In the dry borehole, its posture adjusts slowly, falls with a quicker speed than the bowl-shaped plastic isolator does, and it is easy to be crushed by the wall while sinking.

The isolator could effectively separate the emulsion explosive from the rock debris at the

borehole bottom or that for plugging, avoiding explosion waste caused by the mixing, thus increasing the utilization ratio of the mixed emulsion explosive. The isolator just takes up 5 mm of the borehole length. Comparing with other types of isolators, this one could improve the utilization ratio of the borehole, achieving the goal of lowering the blasting cost.

Acknowledgements: This work was supported by the high level creative talents training in Guizhou Province(20164030), the National Natural Science Foundation of China (51664007). All these are gratefully appreciated.

REFERENCES

1. Q. Wang, The Advantage of Emulsion Explosive of Mixed Loading Truck in Water-filled-hole Blasting. *Explosive Materials*, 2002.
2. L. Liu, X. Wang, Yang Yi, Y. Wang, *Blasting*, **27**(2), 10 (2010).
3. D P. Adhikary, Numerical simulation of mine water inflow. ISRM International Symposium - EUROCK. 2012.
4. H. Ye, D. Nong, T. Li, J.Ye, *Advanced Materials Research*, , **634-638**(1), 3563 (2013).
5. O.E. Petel, D. Mack, A.J. Higgins, R. Turcotte, S.K. Chan, *Journal of Loss Prevention in the Process Industries*, **20**(4),578 (2007).
6. D. Liu, Two Phase Fluid Dynamic Model. Higher Education Press, 1993.
7. X. Shang, J. Su, H. Wang. ANSYS/LS-DYNA Dynamic Analysis Method and Engineering Projects - 2nd edition. Chian WaterPower Press, 2008.
8. T. Wang, Sh. Song, *Computational Physics*, **24**(3), 361 (2007).
9. L. Wang, N. Wang, L. Zhang, *Propellants Explosives Pyrotechnics*, **37**(1), 83 (2012).
10. C.S. Ho, K. Katsuhiko, *Materials Transactions*, **45**(5), 1722 (2004).
11. S. Cudzilo, P. Kohlicek, V.A. Trzcinski, S. Zeman, *Combustion Explosion & Shock Waves*, **38**(4), 463 (2002).
12. X. Zhang, Analysis on the Effect of Shock-absorption in Pre-splitting Blasting and Its Application in the Slope Excavation. *Coal Mine Blasting*, 2008.
13. Y. Wang, X. Chen, T. Peng, *Chinese Journal of Rock Mechanical and Engineering*, **23**(8), 1385 (2004).
14. F. Sumiya, Y. Hirosaki, Y. Kato, K. Katsuyama, *Science & Technology of Energetic Materials*, **67**, 147 (2006).
15. Y. Zhang, M. Lei, Zh. Ning, Zh. Ma, *China Coal*, **42**(9), 41 (2016).

Evaluation of motor function based on self-correction analytical hierarchy process

X. Li ^{1*}, X. Wang ¹

¹ State Key Laboratory of Synthetical Automation for Process Industries, Northeastern University, Shenyang, Liaoning 110819, China

Received August 1, 2017; Revised November 21, 2017

In the evaluation of clinical rehabilitation functions, different experts will have different views. In order to be able to consider the expert opinions, in this paper the contents and methods of upper limb motor function evaluation were studied, and the evaluation index system was established. Quantitative evaluation of the evaluation index of motor function was carried out, and different evaluation criteria were provided for different evaluation indexes. The method of SFAHP (Self-correction Fuzzy Analytical Hierarchy Process) based on elemental classification was used to evaluate the rehabilitation process of hemiplegia upper limbs. The hierarchical model and evaluation system of evaluation index were established, and the evaluation model of hemiplegia upper limb motor function was established. Systematic analysis method was used to evaluate the feasibility and effectiveness of SFAHP method in the evaluation of upper limb rehabilitation. The evaluation results were consistent with the results of clinical motor function evaluation.

Key words: Motor function evaluation, Self-correction AHP, Evaluation system, Evaluation model.

INTRODUCTION

The clinical results show that the motor function is the main index to reflect the effectiveness of rehabilitation [1, 2]. Therefore, the motor function is important for the hemiplegic treatment and is also crucial for rehabilitation evaluation. In the rehabilitation of the stroke, the training of motor function will be influenced by the personal factors of different therapists and the treatment effect mainly depends on physicians' experience and qualifications [3-5]. Moreover, the rehabilitation level is mainly judged by physicians' clinical experience. Currently, no rehabilitation system can completely replace the therapists in evaluating the rehabilitation level.

This paper reviews and compares all aspects (physical activities and daily activities, etc.) involved in the dyskinesia of hemiplegic upper-limb patients, as well as the current status and potentials of the motor function. Given the differences of experts' evaluation towards rehabilitation, this paper first combines the analytical hierarchy process (frequently used in the decision-making analysis) with the fuzzy analysis method. Then this paper proposed a systematic evaluation method, which is qualitative-and-quantitative and is used for SFAHP (Self-correction Fuzzy Analytical Hierarchy Process) based on element demarcation.

In this paper, an upper-limb rehabilitation robot system was used to determine the index system of

the motor function evaluation and formulate the evaluation standards of all evaluation indexes. Finally, this paper establishes a comprehensive model for evaluating the motor functions of the hemiplegic upper-limbs to test and evaluate the rehabilitation effects of the affected limbs and the grades of the motor functions.

SFAHP-BASED EVALUATION OF THE HEMIPLEGIC UPPER-LIMB MOTOR FUNCTIONS

Main contents in the evaluation of clinical motor function

The dyskinesia is the typical external pathological sign in the stroke. After stroke the dyskinesia symptoms of the hemiplegic patients are mainly dystonia, coordination disorders between muscle groups, and abnormal reflex activities, namely, the motion forms of associated movement, associative reaction and spinal level of tonus reflex [6-7]. The goal of the motor function rehabilitation is to change the abnormal motor patterns of patients, reduce cramp symptoms and guide patients in improving the muscular tension and effectively controlling the movement. In the clinical treatment, four aspects are mainly used to evaluate the motor functions: muscle strength, joint motion degree, equilibrium function, and coordination function [8-11].

Upper-limb rehabilitation robot

The upper-limb rehabilitation robot (Figure (1), Rehabilitation robot structure) has a mechanical arm, an arm holder, and a base. As an executing agency, the robot receives and performs the tasks and guides patient's affected limbs in conducting

To whom all correspondence should be sent:
E-mail: lixing8245@163.com

the training practices of different modes or different intensity. According to the evaluation results of the hemiplegic patients or their affected limbs, the rehabilitation training mode is selected for the following stage to remodel the brain functions and accelerate the rehabilitation.



Fig. 1. Rehabilitation robot structure.

SFAHP (Self-correction Fuzzy Analytical Hierarchy Process)

In this process, the testing functions of the upper-limb rehabilitation robot system can be used to measure the muscle strength and the ranges of joint motions. First, the test motions are set up, and then, the equilibrium function is evaluated in two aspects: the time and the direction for patients to complete the specified test actions. Regarding the coordination function, the same procedures are conducted to test the trajectory smoothness and consistency. The relationships between indexes used for evaluating the motor functions of hemiplegic upper-limbs are shown in Figure (2). SFAHP combines the quantitiveness and

objectivity of AHP with the inclusiveness of the fuzzy comprehensive evaluation method [15-16]. Also, self-correction and circular comparison are adopted in the evaluation to remove extreme values and opinions of expert grading and revise the element scale of the judgment matrix. In this way, personal errors can be reduced in the evaluation.

EVALUATION MODEL OF THE MOTOR FUNCTIONS

Hierarchical structure of evaluation indexes

Layered decomposition and tree ordering are used to process the evaluation indexes of the motor functions and determine the factor set U of the rehabilitation evaluation index system:

$$U = \{ u_1, u_2, u_3 \}$$

where, u_1 is the evaluation of muscle strength and joint motion range in $u_1 = \{u_{11}, u_{12}\}$, u_{11} is the level of muscle strength, and u_{12} is joint motion range.

u_2 is the equilibrium function evaluation in $u_2 = \{u_{21}, u_{22}\}$, u_{21} is motion degree in the correct direction, u_{22} is specified motion time; u_3 is coordination function evaluation in $u_3 = \{u_{31}, u_{32}\}$, u_{31} is smoothness of the motion trajectory, and u_{32} is the consistency of the motion trajectory. The hierarchical structure of the index system for evaluating the hemiplegic upper-limb motor functions is shown in Figure 3.

Index evaluation standards [17]

Different from the methods used for evaluating clinical motor functions, this method uses the data collection of the upper-limb rehabilitation robot, quantifies the evaluation method of the hemiplegic upper-limb motor function indices, and provides the standards of all evaluation indices. The evaluation standards of all indices are as given in ref. [17].

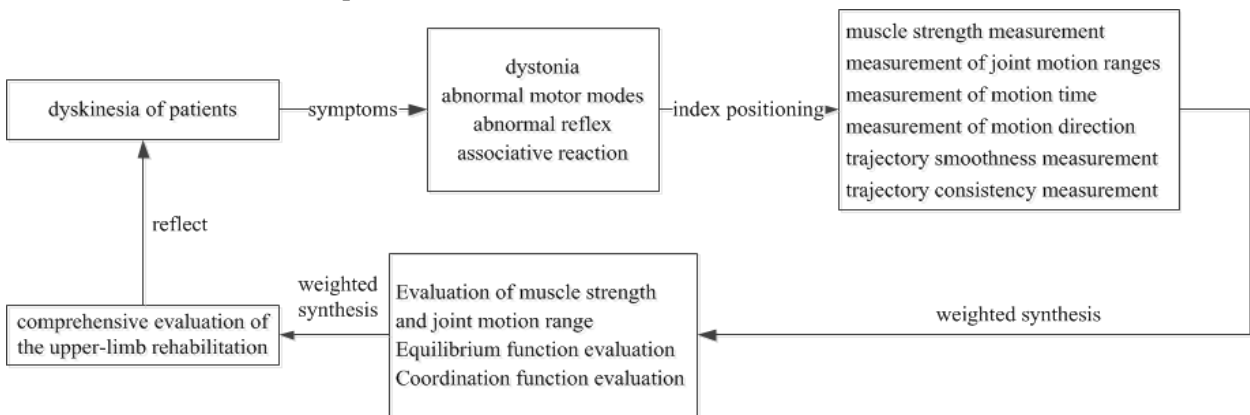


Fig. 2. Diagram of upper limb rehabilitation robot rehabilitation evaluation index.

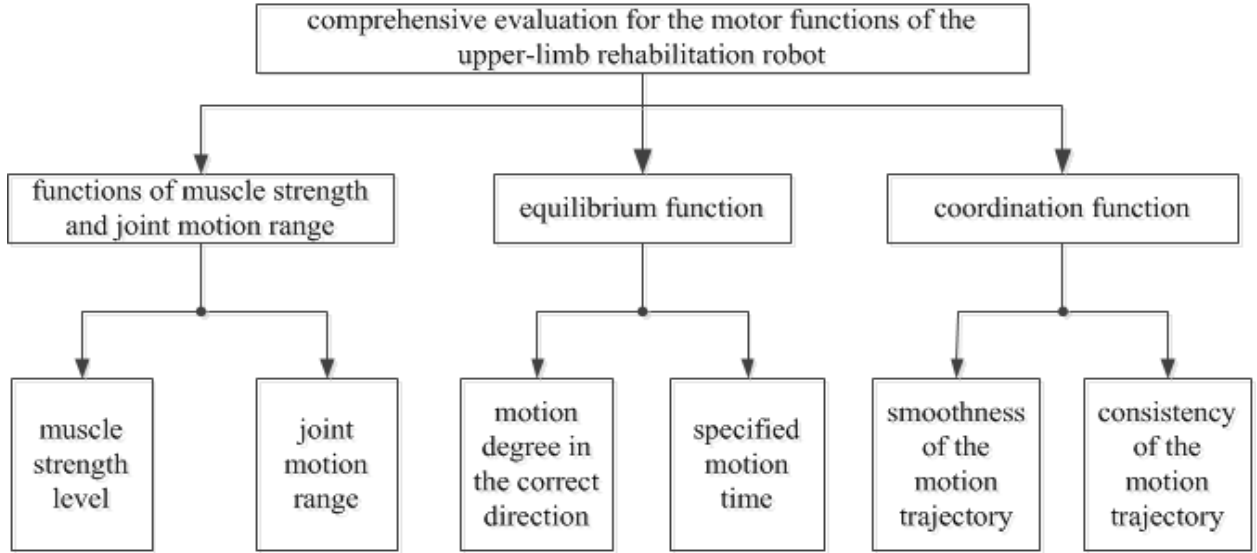


Fig. 3. Hierarchical structure of the motor function index for the upper-limb rehabilitation robot

Construct the commented system

Five comments are established to evaluate the motor function of the hemiplegic upper limbs: excellent, good, moderate, acceptable, and poor. These comments are used to represent the rehabilitation effects of the hemiplegic upper-limb motor functions and the comment set of the motor function evaluation is

$$V = \{v_1, v_2, v_3, v_4, v_5\}$$

Among these comments, v_1 is excellent with scores between 90 and 100; v_2 is good with scores between 80 and 89; v_3 is moderate with scores between 70 and 79; v_4 is pass with scores between 60 and 69; v_5 is pass with scores between 50 and 59.

Determination of the weight coefficient

Scale evaluation: Three clinical rehabilitation physicians were invited to form the expert group and then all layers of elements were through the scale evaluation in the form of questionnaires, designed on the basis of AHP. The importance of influence factors was pairwise compared and the measurement scales were divided into five grades: important, very important, fairly important, slightly important, and equally important, which respectively correspond to the values of 9, 7, 5, 3, and 1. The measurement scale near the left means that the factors in the left column are more important than those in the right column, while the measurement scale near the right means that the factors in the right column are more important than those in the left column.

Establishing the subordinating degree function

Suppose the comment set v has five grades: v_1 means excellent with scores ranging from 90 to 100; v_2 means good with scores ranging from 80 to 89; v_3 means moderate with scores ranging from 70 to 79; v_4 means pass with scores ranging from 60 to 69; v_5 means pass with scores ranging from 50 to 59. This helps to determine the subordinating degree function for evaluating the motor functions of the upper-limb rehabilitation robot. In the equations $i=1,2,3$, $j=1,2$.

$$\mu_{v_1}(u_{ij}) = \begin{cases} 1 & u_{ij} \geq 90 \\ \frac{(u_{ij} - 80)}{10} & 80 \leq u_{ij} < 90 \\ 0 & u_{ij} < 80 \end{cases} \quad (1)$$

$$\mu_{v_2}(u_{ij}) = \begin{cases} \frac{(u_{ij} - 70)}{10} & 70 \leq u_{ij} < 80 \\ \frac{(90 - u_{ij})}{10} & 80 \leq u_{ij} < 90 \\ 0 & u_{ij} < 70, \text{ or } u_{ij} \geq 90 \end{cases} \quad (2)$$

$$\mu_{v_3}(u_{ij}) = \begin{cases} \frac{(u_{ij} - 60)}{10} & 60 \leq u_{ij} < 70 \\ \frac{(80 - u_{ij})}{10} & 70 \leq u_{ij} < 80 \\ 0 & u_{ij} < 60, \text{ or } u_{ij} \geq 80 \end{cases} \quad (3)$$

$$\mu_{v_4}(u_{ij}) = \begin{cases} \frac{(u_{ij} - 50)}{10} & 50 \leq u_{ij} < 60 \\ \frac{(70 - u_{ij})}{10} & 60 \leq u_{ij} < 70 \\ 0 & u_{ij} < 50, \text{ or } u_{ij} \geq 70 \end{cases} \quad (4)$$

$$\mu_{v5}(u_{ij}) = \begin{cases} 0 & u_{ij} \geq 60 \\ \frac{(60-u_{ij})}{10} & 50 \leq u_{ij} < 60 \\ 1 & u_{ij} < 50 \end{cases} \quad (5)$$

Establishing the model of comprehensive evaluation

According to the subordinating degree function listed above, all factors of the data are quantified. Through evaluating single factors, the single factor evaluation vector was established to construct the vague evaluation matrix.

The fuzzy comprehensive evaluation matrix of the motor functions for the upper-limb rehabilitation robot is

$$R_U = (B_{u_1} \ B_{u_2} \ B_{u_3})^T = (W_{u_1} \circ R_{u_1} \ W_{u_2} \circ R_{u_2} \ W_{u_3} \circ R_{u_3})^T \\ = [r_{ij}]_{3 \times 5} = \begin{bmatrix} r_{11} & r_{12} & r_{13} & r_{14} & r_{15} \\ r_{21} & r_{22} & r_{23} & r_{24} & r_{25} \\ r_{31} & r_{32} & r_{33} & r_{34} & r_{35} \end{bmatrix} \quad (6)$$

In the equations, the following condition is satisfied:

$$r_{ij} = \bigvee_{j=1}^5 [W_{u_i} \wedge \mu_{v_j}(u_{ij})] \quad (i=1,2,3; j=1,2,3,4,5)$$

ALGORITHM VERIFICATION

The upper-limb rehabilitation robot was used to evaluate the motor functions of three patients with hemiplegic upper-limbs. In the evaluation, these patients wear mechanical arms and the body electrode patches of the surface electro-myogram signal collector are attached to different parts of the muscles. To ensure the accuracy of the evaluation, the patient performs three tests and the testing results are shown in Table 1.

In terms of muscle strength, the scores of the patient were 85, 85, and 83 in the three tests, respectively. According to equations (9)-(14), the following is obtained.

$$\mu_{v1}(u_{11}) = [\mu_{v1}(85) + \mu_{v1}(85) + \mu_{v1}(83)]/3 = 0.43$$

$$\mu_{v2}(u_{11}) = [\mu_{v2}(85) + \mu_{v2}(85) + \mu_{v2}(83)]/3 = 0.57$$

Table 1. Basic physical properties of high liquid limit soil.

	Muscle strength level	Joint motion range	Motion degree in the correct direction	Motion time of prescript actions	Motion trajectory smoothness	Motion trajectory consistency
1 st test	85	84	83	80	81	80
2 nd test	85	82	82	81	82	80
3 rd test	83	84	82	80	80	81

$$\mu_{v3}(u_{11}) = [\mu_{v3}(85) + \mu_{v3}(85) + \mu_{v3}(83)]/3 = 0$$

$$\mu_{v4}(u_{11}) = [\mu_{v4}(85) + \mu_{v4}(85) + \mu_{v4}(83)]/3 = 0$$

$$\mu_{v5}(u_{11}) = [\mu_{v5}(85) + \mu_{v5}(85) + \mu_{v5}(83)]/3 = 0$$

The following equation can be obtained from equation (6)

$$B_{u_1} = W_{u_1} \circ R_{u_1} = (0.5000, 0.5000) \circ \begin{bmatrix} 0.43 & 0.57 & 0 & 0 & 0 \\ 0.33 & 0.67 & 0 & 0 & 0 \end{bmatrix} \\ = (0.43, 0.5, 0, 0, 0)$$

$$\text{Similarly, } B_{u_2} = W_{u_2} \circ R_{u_2} = (0.23, 0.75, 0, 0, 0)$$

$$B_{u_3} = W_{u_3} \circ R_{u_3} = (0.1, 0.75, 0, 0, 0)$$

The comprehensive evaluation result of the patient's motor functions is:

$$B_U = W_U \circ R_U = (0.1429, 0.4286, 0.4286) \circ \begin{bmatrix} 0.43 & 0.5 & 0 & 0 & 0 \\ 0.23 & 0.75 & 0 & 0 & 0 \\ 0.1 & 0.75 & 0 & 0 & 0 \end{bmatrix} \\ = (0.23, 0.43, 0, 0, 0)$$

The equation can be obtained through normalization.

$$B_U = (0.35, 0.65, 0, 0, 0)$$

CONCLUSION

From this, the overall evaluation result from the upper-limb rehabilitation robot can be obtained for judging the motor functions of hemiplegic patients. According to the principle of the maximum subordination degree, the patient is in good state of motor functions. Thus, it can be understood that the affected limbs of the patient have approximated the normal level. It can be seen that the curve for the SFAHP-based evaluation result of the motor functions is consistent with that of the clinical rehabilitation. It means that the evaluation result is correct and the method can be applied to evaluate the motor functions of hemiplegic upper-limb rehabilitation.

Acknowledgements: This work is supported by “Fundamental Research Funds for the Central Universities” (N1508040), 2015 Liaoning province Doctoral Fund (201501142) and National Natural Science Foundation of China (61503070).

REFERENCES

1. W. Ma, *Chinese Journal of Clinical Rehabilitation*, **6**(7), 10 (2002).
2. Y. Huang, N. Wang, *Chinese Journal of Rehabilitation Medicine*, **11**(4), 185 (1996).
3. H. Miao, *Chinese Rehabilitation Theory and Practice*, **26**(3), 78 (1997).
4. Q. Yin, B. Sheng, F. Wang, *Chinese Rehabilitation Medicine Magazine*, **19**(3), 232 (2004).
5. J. Gu, H. Huang, H. Yu, *Journal of Chongqing Medicine*, **38**(8), 69 (2009).
6. Y. Zhu. Science of Neurological Rehabilitation. Beijing: People’s Publishing House of Military Surgeons, **1**, 335 (2001).
7. A. Wang. Science of Rehabilitation Function Evaluation. Fudan University Press, 2009.
8. M. Mihelj, D. Novak, J. Zihelr, A.Olensek, M. Munih, *Assistive Technology*, **16**(1), 54 (2004).
9. L. Zhou, J. Shao. Stroke rehabilitation treatment: Evaluation of combined application of SGT-700 apparatus and fluoxetine, Proceedings of the 2011 International Conference on Human Health and Biomedical Engineering (HHBE), 343, 2011
10. K.Kubo , T.Miyoshi , A. Kanai, K.Terashima, *Journal of Robotics*, 348207 (14 pp.), (2011).
11. Z. Q. Sun. Medical Comprehensive Evaluation Method. China Science and Technology Press. 2014
12. Q.L. Li, T.M. Ye, Z.J. Du, *Journal of Harbin Engineering University*, **30**(2), 166 (2009).
13. X. J. Chen, L. Liang. Systematic Evaluation Methods and Applications. Press of Chinese Science and Technology University, 1993.
14. Y. Ye, L. Ke, D. Huang. Systematic Comprehensive Evaluation Technology and Applications. Metallurgical Industry Press, 2006.
15. F. Z. Li. Introduction to Dynamic Fuzzy Logic. Yunan Science and Technology Press, 2005.
16. Z. Cao, Dynamic Fuzzy Evaluation and Empirical Analysis of Libraries. Beijing Library Press, 2007.
17. X, Li, J. Wang, *Information-An International Interdisciplinary Journal*, **15**, 11A, 469 (2011)

Biological conversion of H₂ and CO₂ into CH₄ at room temperature and atmospheric pressure: a promising approach for reducing CO₂ emissions and increasing biomethane production

B. Yang, Q. Wang, X. Zhao, Ch. Wang, J. Liu, H. Yang, Sh. Liu, F. Yin*, W. Zhang*

Yunnan Normal University, Kunming, China

Received August 1, 2017, Accepted November 21, 2017

An inoculum of methane-fermented active sludge was used to enrich hydrogenotrophic methanogens, by culturing using a gas mixture of H₂, CO₂ and N₂ as the substrate. Culturing was performed at room temperature and atmospheric pressure and the types and changes of methanogenic archaea in the active sludge before and after the tests were characterized. The results showed that the highest yield of CH₄ obtained was 258 mL from 3L of gas mixture, representing 51.6% of the theoretical maximum. The archaeal population present in the inoculum at the start of the experiment was dominated (84%) by the obligate acetotrophic *Methanosaeta*, which was reduced to 64% at the end of the experiment. In contrast, *Methanosarcina*, which is capable of using H₂ and CO₂, doubled from 8% in the original inoculum to 16% at the end. These experiments demonstrate that cultivation by gas cycling can realize bioconversion of H₂ and CO₂ into CH₄.

Key words: Hydrogenotrophic methanogenic archaea, H₂, CO₂, CH₄, Bioconversion, Gas cycle

INTRODUCTION

During the production of biogas, the gases H₂ and CO₂ can be used by hydrogenotrophic methanogenic archaea to form methane (CH₄) [1]. This metabolic pathway contributes up to 28% of the CH₄ generation in a biogas fermentation system [2]. A large amount of research has been conducted on the bioconversion of CO₂ into CH₄ with the aim of reducing CO₂ emissions [3-7]. For instance, the study of Koide *et al.* indicated that CH₄ may be produced while injecting CO₂ into the ground through artificial simulation of the natural carbon cycle, which would partially solve the problem of greenhouse gas emissions by means of carbon capture and storage [8].

Biogas contains approximately 60% of CH₄ and 35% of CO₂ [9]; the relatively high content of the latter lowers the efficiency of the biogas as energy carrier and is a considerable waste of the carbon source that could, at least potentially, be used by the microorganisms to produce methane. The efficiency of the bioconversion of CO₂ into CH₄ *via* the net reaction $4\text{H}_2 + \text{CO}_2 \rightarrow \text{CH}_4 + 2\text{H}_2\text{O}$ [10, 11] could be greatly enhanced if the remaining CO₂ could also be converted.

Methanogenic prokaryotes can be classified into acetotrophic species that metabolize acetate as a substrate [12], hydrogenotrophic species that use the substrates H₂ and CO₂ [13], and methylotrophic species using methanoic acid, methanol and methylamine as substrates [14]. Tracer tests have indicated that acetotrophic methanogenic archaea

account for more than 70% of the methanogenic archaea typically present in a biogas fermentation system [15]. With the necessary measures taken, growth of hydrogenotrophic methanogens can be promoted, resulting in higher efficiency performance. To this purpose, a biogas fermentation system was designed for operation at normal temperature and pressure, to promote the metabolism and growth of hydrogenotrophic methanogens by addition of excess H₂ and CO₂. The efficiency of methane production was studied and the microbial populations at play were characterized.

EXPERIMENTAL

Inoculum and metabolic substrates

A mixture of anaerogenic and anaerobic active sludge was used as the inoculum for the described experiments, which has been cultivated for a long time in our laboratory. The sludge parameters are 6.83% total solid (TS) content and 59.97% volatile solid (VS) content, with a pH of 7.5. The metabolic substrates used were high purity H₂ and CO₂, while high purity N₂ was provided as the nitrogen source for the microorganisms. No other carbon source than CO₂ was added.

Test setup

Figure 1 shows a schematic drawing of the test setup, which consisted of a fermentation reactor made of plexiglass (dimensions: content 3.18 L, height-to-diameter ratio 5:1), a wet-seal gas holder made of plexiglass (effective volume 4.08 L), a gas circulation pump (YZ2515X, Chuangrui Pump, Co., Ltd., China) with a flow rate ranging from 0 to 250

*To whom all correspondence should be sent:

E-mail: yf6709@sina.com

mL/min, PVC gas circulating tubes and gas input cylinders for H_2 , CO_2 and N_2 .

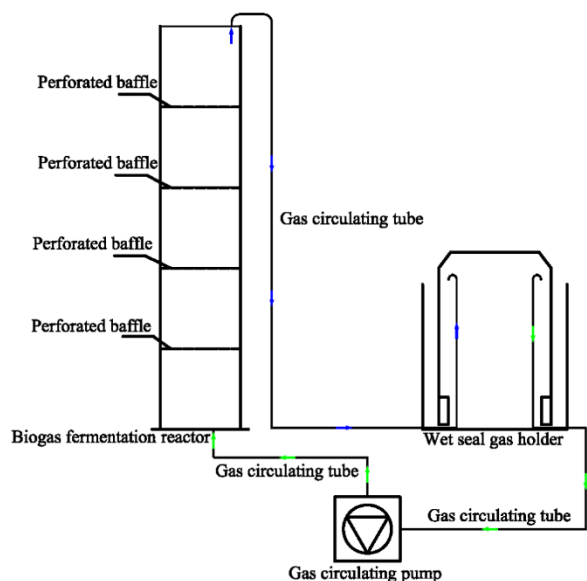


Fig. 1. Schematic diagram of the test setup for enrichment and cultivation of hydrogenotrophic methanogenic archaea

Test method

At the start of the experiment, the fermentation reactor was filled with 1.5 L of inoculum (approximately half of the reactor volume) and then filled up with liquid bioslurry from our laboratory. A gas mixture with volume ratio $H_2:CO_2:N_2=4:1:1$ was used in accordance with the stoichiometry of the reaction equation ($4H_2+CO_2 \rightarrow CH_4+2H_2O$). Approximately 3 L of gas (containing 2 L of H_2 , 0.5L of CO_2 and 0.5 L of N_2) was added through the wet-seal gas holder till the floating bell raised into the lock position. The gas mixture was then pumped into the biogas fermentation reactor by the circulating pump at a flow rate of 12.5 mL/min and returned to the gas holder after passage through the sludge bed. Gas was continuously recirculated at room temperature and normal pressure, while the floating bell continuously sank during the reaction process. When the floating bell reached final position, the test series was considered completed. After composition analysis of the gas left inside the floating bell, the gas holder was emptied and cleaned for the next set of experiments. The inoculum was not replaced for each novel test. The tests included two stages: experimental start-up stage and test operation stage.

Test method

The pH of the sludge was monitored with a digital pH meter (PHS-3C, Hongyi Instruments China) [16]. The gas composition was determined by gas chromatography (GC-6890A, Lunan Apparatus, China) [17]. TS and VS contents were determined

using a gravimetric method after drying at 110 °C and 560 °C, respectively [18]. The types and variations in methanogenic archaea were monitored by 16S rDNA sequencing, for which a DNA extraction kit (MO BIO Laboratories, USA) [19] was used to extract the total DNA of samples while the 16S rDNA amplification (515F and 806R primers) [20, 21] and sequencing was outsourced.

RESULTS AND DISCUSSION

Test start-up stage

The test start-up stage was needed to eliminate any disturbing factors for the subsequent analysis. For instance, water inside the reactor may initially absorb CO_2 (1L water has the capacity to absorb 1L CO_2 at normal temperature and pressure [22]) or any residual CH_4 present in the inoculum could be at first released. The start-up stage lasted 10 days, during which CO_2 continuously entered the reactor, until the gas volume was stabilized and the floating bell remained in position indicating that water and CO_2 in the reactor were saturated and at equilibrium. During this period, the gas composition was analyzed which showed that during the start-up stage 2.2 mL of CH_4 were produced, while it was obvious that this CH_4 has not been liberated from the inoculum since the inoculum did not contain any metabolic substrates for biogas fermenting microorganisms. Thus, it was concluded that after 10 days the system was stable and ready for further tests.

Test operation stage

During the test operation stage, five subsequent tests were performed (each test lasted 5 days) to cultivate hydrogenotrophic methanogenic archaea, while the CH_4 yields were recorded. The results are shown in Figure 2.

As can be seen, CH_4 was produced in all 5 tests, proving that methane can be produced from CO_2 and H_2 by microorganisms as a result of adding external H_2 and CO_2 into the system. During the second, best-performing test, 258 mL of CH_4 was produced, which is 51.6% of the theoretical maximum. The efficiencies of the other tests varied from 27.7% to 37.0%.

Methanogenic archaea community and change analysis

The methane produced in the test setup was most likely produced by hydrogenotrophic methanogenic archaea, while variation in the yield could have been

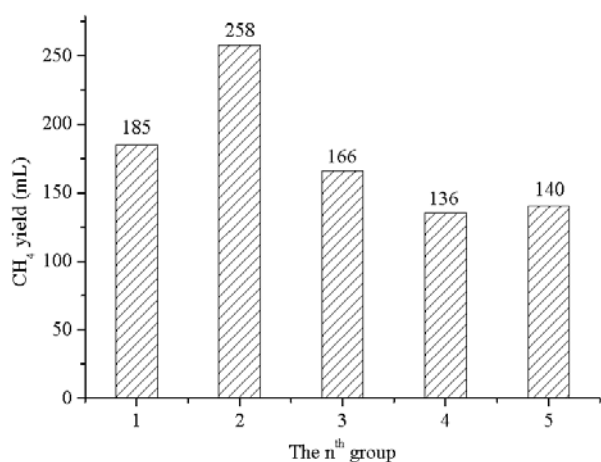


Fig. 1. CH₄ final yield during the test operation stage

result of shifts in the populations. In order to characterize the key players, total DNA was extracted from the inoculated sludge prior to the start of the experiment, and again from the active sludge after completion of the last test. This DNA was used for 16S rDNA amplification and sequencing to analyze the archaeal populations. The results are summarized in Table 1.

As can be seen from Table 1 the obligate acetotrophic *Methanosaeta* [23] comprised a large fraction of the initial inoculum (as determined by 16S sequencing) but their number was significantly reduced during the tests, probably because no acetic substrates were provided. Nevertheless, this genus still represented 64% of all genera detected at the end of the experiment.

Table 1. Contents and changes in methanogenic archaea in populations

Methanogenic archaea	Percentage present	
	At start	After tests
<i>Methanosaeta</i>	84	64
<i>Methanosarcina</i>	8	16
<i>Methanocorpusculum</i>	0.6	0.7
<i>Methanoculleus</i>	0.5	0.9
<i>Methanospirillum</i>	0.4	1
<i>Methanolinea</i>	ND	0.7
<i>Methanoplanus</i>	ND	0.1
<i>Methanofollis</i>	ND	0.2
<i>Methanobacterium</i>	0.9	1

Notes: ND means no DNA detected.

Methanosarcina was the next most abundant species, which can utilize both acetic substrates, as well as H₂ and CO₂ [24]. The latter capacity allowed their increase during the experiment, resulting in a doubling of their number. The hydrogenotrophic *Methanocorpusculum* [25], *Methanoculleus* [26], *Methanospirillum* [27] and *Methanobacterium* [28] species significantly increased during the tests, though their number was relatively low in comparison to *Methanosarcina*. It is worth noting

that other hydrogenotrophic methanogens such as *Methanolinea* [29], *Methanoplanus* [30] and *Methanofollis* [31] species could not be detected in the inoculum due to their originally low abundance, though after the test they were present in detectable numbers.

The results reported here can be advantageous for initiatives to reduce CO₂ emission, produce a renewable energy carrier (biological synthesis of CH₄), and increase potential economic benefits of such initiatives by improved efficiency. The biological conversion of H₂ into the relatively safer energy carrier CH₄ may be carried out using CO₂ which is typically present at levels of 35% in biogas. This would increase the CH₄ content of the biogas, leading to an improved energy content of the biogas.

CONCLUSIONS

(1) Methane was produced from circulating gas in all tests performed, with the highest yield reaching 51.6% of the theoretical maximum. (2) During the experiment, the microbial composition of the sludge changed, from an initial dominance of obligate acetic *Methanosaeta* to a doubling of *Methanosarcina* and an increase of other hydrogenotrophic and methylotrophic species. Thus, cultivation by gas circulation (H₂ and CO₂) may increase the proportion of hydrogenotrophic methanogenic archaea, which would improve the subsequent efficiency of biofermentation.

Acknowledgements: This work was supported by the National Natural Science Foundation of China [grant number 51366015]; the Specialized Research Fund for Doctoral Program of Universities [grant number 20135303110001]; Yunnan Province Key Fund of Applied Basic Research [grant number 2014FA030]; Open Fund from Yunnan Key Laboratory of Rural Energy Engineering [grant number 2015KF07]; the Yunnan Provincial Sciences and Technology Platform Promotion Plan [grant number 2013DH041]; and Collaborative Innovation Center of Research and Development of Renewable Energy in the Southwest Area [grant number 05300205020516009].

REFERENCES

1. H.J. Alves, C.B. Junior, R.R. Niklevicz, E.P. Frigo, M.S. Frigo, C.H. Coimbra-Araújo, *Int J Hydrogen Energy*, **38**, 5215 (2013).
2. S.K. Khanal, *Anaerobic biotechnology for bioenergy production: principles and applications*. 1st ed. New Jersey: John Wiley & Sons, 2011.
3. F.H. Chapelle, K. O'Neill, P.M. Bradley, B.A. Methé, S.A. Ciuffo, L.L. Knobel, D.R. Lovley, *Nature*, **415**, 312 (2002).

4. D.R. Lovley, F.H. Chapelle, *Science*, **272**, 896b (1996).
5. I.S. Kim, M.H. Hwang, N.J. Jang, S.H. Hyun, S.T. Lee, *Int J Hydrogen Energy*, **29**, 1133 (2004).
6. K. Kocha, B. Huber, Y.B. Fernández, J.E. Drewes, *Waste Manage.*, **49**, 36 (2016).
7. J.F. Liu, S.M. Mbadanga, X.B. Sun, G.C. Yang, S. Z. Yang, J.D. Gu, B.Z. Mu, *Biogeosciences Discuss.*, **12**, 1875 (2015).
8. H. Koide., K. Yamazaki, *Environ Geosci.*, **8**, 218 (2001).
9. K. Dahlquist, Technologies for converting biomass to useful energy, combustion, gasification, pyrolysis, torrefaction and fermentation. 1st ed. London: CRC Press, 2013.
10. N.H.M. Yasin, T. Maeda, A. Hu, C. P. Yu, T.K. Wood, *Appl. Energy*, **142**, 426 (2015).
11. M.R. Martin, J.J. Fornero, R. Stark, L. Mets, L.T. Angenent, *Archaea*, article ID 157529 (2013).
12. L. André, M. Ndiaye, M. Pernier, O. Lespinard, A. Pauss, E. Lamy, T. Ribeiro, *Bioresource Technol.*, **207**, 353 (2016).
13. C. Keating, J. P. Chin, D. Hughes, P. Manesiotis, D. Cysneiros, T. Mahony, C.J. Smith, J. W. McGrath, V. O'Flaherty, *Front. Microbiol.*, **7**, 226 (2016).
14. M.A. Lever, *Trends Microbiol.*, **24**, 84 (2016).
15. T. Narihirom, T. Terada, A. Ohashi, J. H. Wu, W. T. Liu, N. Araki, Y. Kamagata, K. Nakamura, Y. Sekiguchi, *ISME J*, **3**, 522 (2009).
16. C. Gou, J. Guo, J. Lian, Y. Guo, Z. Jiang, L. Yue, J. Yang, *Int J Hydrogen Energy*, **40**, 161 (2015).
17. Y. S. Zhu, L. Li, L. J. Fu, Y.P. Wu, *Int. J. Hydrogen Energy*, **40**, 14290 (2015).
18. M. Oleszek, A. Król, J. Tys, M. Matyka, M. Kulik, *Bioresource Technol.* **156**, 303 (2014).
19. L. Guo, M. Lu, Q. Li, J. Zhang, Z. She, *Int. J. Hydrogen Energy*; **40**, 197 (2015).
20. B. Si, Z. Liu, Y. Zhang, J. Li, X.-H. Xing, B. Li, N. Duan, H. Duan, *Int. J. Hydrogen Energy*. **40**. 3191 (2015).
21. L. Zhang, L. Zhang, D. Li, *Int. J. Hydrogen Energy*. **40**, 12201 (2015).
22. W. Lu, H. Guo, I.M. Chou, R.C. Burruss, L. Li, *Geochim. Cosmochim. Acta*, **115**, 183 (2013).
23. W. Liu, W. Cai, Z. Guo, L. Wang, C. Yang, C. Varrone, A. Wang, *Renew. Energy*, **91**, 334 (2016).
24. S. Jabłoński, P. Rodowicz, M. Łukaszewicz, *Int. J. Syst. Evol. Microbiol.* **65**, 1360 (2015).
25. Y. Maspolim, Y. Zhou, C. Guo, K. Xiao, W.J. Ng, *Bioresource Technol*; **190** 289 (2015).
26. J. Rui, J. Li, S. Zhang, X. Yan, Y. Wang, X. Li, *Biotechnol. Biofuels*, **8**, 158 (2015).
27. A.R. Rowe, C.B. Mansfeldt, G.L. Heavner, R.E. Richardson, *Appl. Microb Cell Physiol.* **99**, 2313 (2015).
28. Walter, M. Probst, S. Hinterberger, H. Müller, H. Insam, *Waste Manage.* **49**, 26 (2016).
29. Y. Maspolim, Y. Zhou, C. Guo, K. Xiao, Ng KW. *J. Environ. Sci.*, **36**, 121 (2015).
30. M.A. Lever, A.P. Teske, *Appl. Environ. Microbiol*, **81**, 1426 (2015).
31. T. Narihiro, H. Kusada, Y. Yoneda, H. Tamaki, *Genome Announc.*, **4**, e00199 (2016).

Theoretical and experimental study on the safety chemistry of separation of oil/water transition layer by oxidation of chlorine dioxide

J. Dong, L. Zhu, D. Gu, H. Sheng, Ch. Yan, B. Wang*

College of Chemistry & Chemical Engineering, Northeast Petroleum University, Daqing, China

Received October 28, 2016, Accepted November 22, 2017

The safety chemistry of ClO₂ oxidative treatment of an oil/water transition layer was studied and evaluated by theoretical calculation and experiments. The theoretical analysis indicated that the unsafe factors were recognized as the difference of overpressure during the oxidation process, which originates from the decomposition of ClO₂ and the release of gas from the oxidation of the reduced substances in the layer. The experimental results showed that the process pressure increased to a quite high value with the highly concentrated ClO₂, and the overpressure caused an increase in the reactive temperature. Based on these data, some suggestions were presented for the safe production. The latter should ensure that the decomposed gas from chlorine dioxide leaves the atmosphere smoothly if the reaction process is an open system. ClO₂ should be used at temperatures as low as possible, and the pressure control should be as stable as possible. This study provides safety control of the oxidation performance of chlorine dioxide, and efficient resolution of the settling tank oil/water transition layer with thickening, low-quality crude oil and high water quality.

Key words: Chlorine dioxide, Transition layer, Safety, Oxidation, Overpressure.

INTRODUCTION

The existence of oil/water transition layer in the middle and late stages of crude oil exploitation leads to a significant reduction of dehydration efficiency of crude oil, which seriously affects its quality. In order to solve the problem of separation of oil/water transition layer in a settling tank, the oil/water layer was treated by initial chlorine dioxide oxidation and consequent demulsification. The pilot operation of the ClO₂ oxidative treatment was applied to the oil/water transition layer in oil fields. As the gas chlorine dioxide itself has flammable and explosive characteristics, both production and application of chlorine dioxide bring a lot of danger and inconvenience. At present, the safety of chlorine dioxide oxidation treatment of oil/water transition layer is a relatively new topic. The specifically related to it literature is scarce [1-3]. The oil/water transition layer has a large thickness, and seriously bumps the oil and water separation in the settling tank, overflow tank, electric dehydrator and so on. The layer holds an emulsion of oil and water with black particles which deteriorates the dehydration equipment and downstream water treatment equipment [4-6]. The smooth operation is one of the important issues in the oil field. In order to solve the problem of separation of oil/water transition layer in the settling tank, the layer has been treated by initial chlorine dioxide oxidation and consequent demulsification [4]. The pilot operation of the ClO₂ oxidative treatment has been applied to the oil/water

transition layer in oil fields [4]. However, due to the flammable and explosive characteristics of chlorine dioxide, the production and application of the solution encounter a lot of dangers and safety issues which are essential for the safe and stable production of oil fields [7, 8]. In this paper, theoretical and experimental studies on the safety chemistry of separation of the oil/water transition layer by oxidation of chlorine dioxide were performed, which offer supporting data for safe operation.

EXPERIMENTAL

Analytical methods

The experimental setup of the safety chemistry of the ClO₂ oxidation of the oil/water transition layer is illustrated in Fig. 1.



Fig. 1. Experimental setup of the safety chemistry of the ClO₂ oxidation of the oil/water transition layer

The closed cylinder is equipped with a pressure meter. The samples, from the Daqing oil fields (China), were mixed with ClO₂ and acid, and then

*To whom all correspondence should be sent:
E-mail wangbh@nepu.edu.cn

injected to the cylinder. On heating the system to the given temperatures, the pressure was recorded.

The experimental conditions were set as follows: adding chlorine dioxide of max. 40% to the oil/water emulsions from the transition layer, heating the cylinder to a temperature in the range of 50-90 °C, and recording the changing pressure with temperature after 30 min reaction duration.

RESULTS AND DISCUSSION

Theoretical study of process analysis and safety chemistry

The principle and operation of ClO₂ oxidative demulsification and separation of oil/water transition layer was described in our previous paper [4].

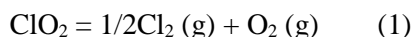
ClO₂ is a powerful oxidizing reagent that is widely applied in water treatment [9]. It has a potential of 1.511V, higher than that of some oxidizing agents such as KMnO₄ (1.51V), Cl₂ (1.36V), OCl⁻ (0.89V) and ClO²⁻ (0.77V). The data indicate that many reducing substances, such as colloid particles, polymers and natural surface active agents in the oil/water transition layer, which dominate the demulsification process, can be oxidized by ClO₂. As a strong oxidizing reagent, ClO₂ is capable of oxidizing the emulsifying materials, as illustrated in Fig. 2.

According to the process of ClO₂-oxidation treatment, the safety chemistry was focused on the reactive change of the process pressure, which originates from the decomposition of ClO₂ and the release of gas from the oxidation of the reduced substances in the layer.

For determination of the limit release, the amount of the released gas can be calculated, that is, assuming that the consumed part of chlorine dioxide contributed to the oxidation of the reduced substances in the layer such as ferrous sulfide, all the gas was released by the decomposition of the residual of ClO₂ plus the evolution of CO₂ and H₂S products of the oxidative process. If the tank keeps chlorine dioxide concentration in the remaining gas space below the explosion limit of 10%, the system safety could be ensured [10-13].

The safety chemistry is displayed by two chemical factors, which lead to an increase in the pressure.

For the decomposition of ClO₂, the chemistry follows:



For the oxidation of the interfacial reduced substances in the transition layer with ClO₂, the chemical scheme is illustrated in Scheme 1.

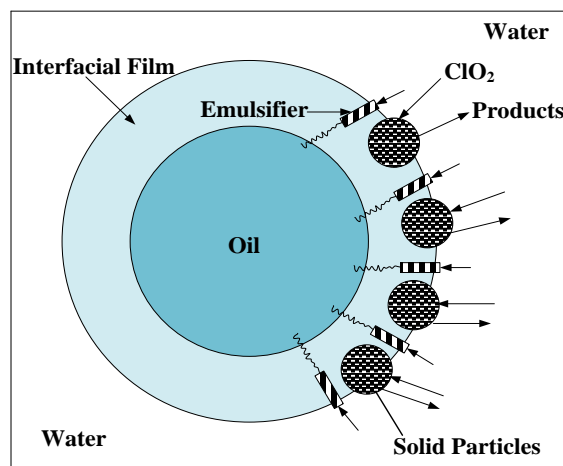
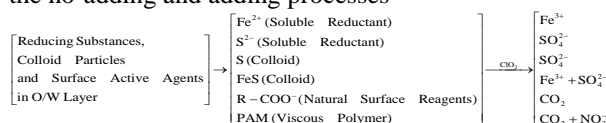


Fig. 2. Dependence of the pressure on temperature for the no-adding and adding processes

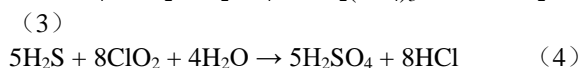
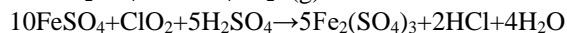
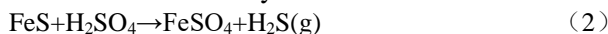


Scheme. 1. Safety chemistry of the oxidation of interfacial reduced substances in the transition layer with ClO₂

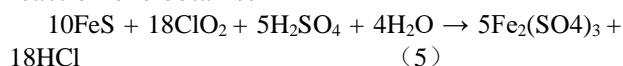
It is seen that the gas is released in the chemical process, which results in a pressure change.

Acidic media such as H₂SO₄ and HCl were added to the system. The safety chemistry was varied in different modes by taking the reaction of an oil/water transition layer as an example.

(1) Safety chemistry of ClO₂-H₂SO₄ treated to the oil/water transition layer:



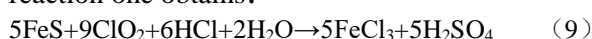
Combining (2), (3) and (4) to the overall reaction one obtains:



(2) Safety chemistry of ClO₂-HCl treated to the oil/water transition layer:



Combining (6), (7) and (8) to the overall reaction one obtains:



In general, the safety of the chlorine dioxide treatment needs the following three points to be taken into account in the practical application. Firstly, chlorine dioxide itself has a heat instability, easy to produce chlorine and oxygen, leading to an explosion in a closed tank; secondly, the mixture of chlorine dioxide with a high concentration of reduced organic substances produces more than 40

KPa of pressure, which is prone to explode; thirdly, chlorine dioxide in water exists in the form of dissolved gas with a low stable concentration. The after-reaction residue of chlorine dioxide is easily volatilized into the air to increase the instantaneous concentration. An explosion will happen when the concentration of chlorine dioxide in the air is higher than 10% (wt/v). Therefore, in the practical application, attention should be paid to choose a reasonable reaction process and to control conditions in order to avoid overpressure or operational errors caused by the loss of the safety.

The safety evaluation of the treatment process was carried out on the basis of the limit of volatilization and comparative standard. The amounts of chlorine dioxide in the gas phase and the liquid phase were calculated by assuming that all the gas was released by decomposition of the residue of ClO₂ and the oxidation of the reduced substances in the layer. It is considered to be a safe limit by controlling that it remains below the 10% safe standard.

Chlorine dioxide is a highly explosive oxidizing gas. When chlorine dioxide in the steam reaches ≥ 40 KPa, it will explode. At a concentration of chlorine dioxide solution higher than 10% (w/v) or 10% (v/v) in the air, it is prone to a low level of explosion. If there is organic steam present, the explosion may become strong. Because of its explosion, chlorine dioxide must be manufactured at the point of use. Chlorine dioxide gas is soluble in water with a balance of 23 times higher concentration in the liquid phase than in the gas phase at 25 °C. If stored in a cool place, strictly sealed and dark, the aqueous solution is very stable. Chlorine dioxide solution is slightly acidic (pH=6), which can enhance its stability due to its disproportionation. So, these points the safe application should be known.

In the case of ClO₂-H₂SO₄ treated oil/water transition layer, the analytical data show that a FeS content of 1.97 mg was determined in 1 m³ transition layer, and 2.73 g of chlorine dioxide was added for the full oxidation. If 0.33 m³ of a 15% (wt/v) chlorine dioxide solution is injected into the transition layer per m³, the system contains 49.5 g of chlorine dioxide. The remaining chlorine dioxide was 46.8 g and the concentration was 3.52% (wt/v), which was less than 10% of the explosion limit. If the remaining chlorine dioxide is fully released, and the gas space is less than 0.155 m³, its concentration in the air is higher than 10%, prone to explosion, with the volume liquid phase : volume gas phase = 1.33: 0.155 \approx 8.57: 1.

In the case of ClO₂-HCl treated oil/water transition layer, both the determined FeS content and consumed ClO₂ amount are the same as the above data. If 0.33 m³ of a 4% (wt/v) chlorine dioxide solution was injected into the transition layer per m³, the system contains 13.2 g of chlorine dioxide. The remaining chlorine dioxide was 10.5 g, and the concentration was 0.79% (wt/v), which was less than 10% of the explosion limit. If the remaining chlorine dioxide is fully released, and the gas space is less than 0.035 m³, the concentration in the air is higher than 10%, prone to explosion, with the volume liquid phase : volume gas phase = 1.33: 0.035 \approx 38.26:1.

Temperature effect on process pressure variation

The temperature-dependent pressure data and curves are shown in Table 1 and Fig. 3.

Table 1. Variation of the pressure on temperature for the no-adding and adding processes

Temperature (°C)	No adding of ClO ₂ (MPa)	Adding of 40% ClO ₂ (MPa)	Pressure difference (MPa)
50	0.010	0.020	0.010
60	0.029	0.046	0.017
70	0.040	0.059	0.019
90	0.073	0.100	0.027

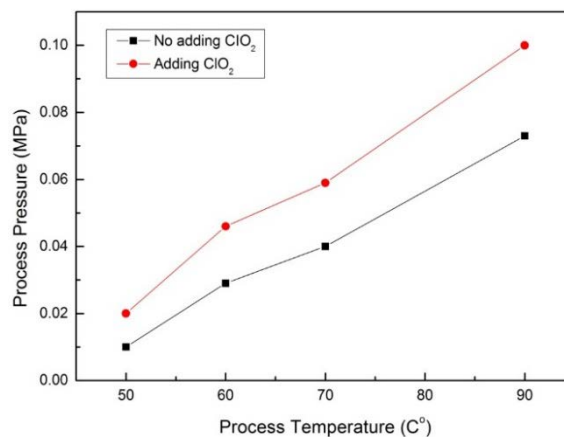


Fig. 3. Dependence of the pressure on the temperature for the no-adding and adding processes

From Table 1 and Fig. 3, it can be seen that the pressure increases with the increase in reaction temperature. When the reaction temperature rises to 90 °C, the pressure reaches 0.1 MPa and 0.073 MPa for no-adding or adding process, respectively. The pressure difference is 0.010 - 0.027 MP in the range between 50 - 90 °C. Compared with the no-adding process, the addition of chlorine dioxide significantly increases the pressure, which indicates that the addition of chlorine dioxide more easily causes overpressure, but as regards the explosion limit, the results could indicate that the pressure after adding chlorine dioxide is far from the explosion

point, indicating that in practice a certain amount of chlorine dioxide can be present with a small risk. When the temperature was 50 °C, the results of the pressure changed with time as shown in Table 2 and Fig. 4.

Table 2. Variation of the pressure on temperatures for the no-adding and adding processes

Reaction time (min)	Process pressure (MPa)
0	0
10	0.022
20	0.024
40	0.026
50	0.026
60	0.026
80	0.026
120	0.026

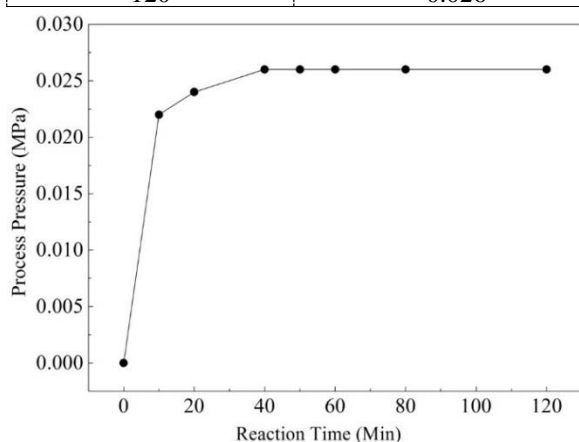


Fig. 4. Dependence of the pressure on temperatures for the no-adding and adding processes

Effect of reaction time on process pressure variation

It can be seen from Table 2 and Fig. 3 that the pressure increases with the reaction time. When the reaction time is 40 min, the pressure reaches the maximum value of 0.026MPa with no further increase. It is demonstrated that the pressure in the reaction tank increases during the initial period after the addition of the appropriate concentration of chlorine dioxide in the actual operation, but the pressure value will not change after a period of time.

Therefore, it will keep a constant value by one measured concentration of chlorine dioxide, in which, the appropriate pressure will eliminate possible explosion hazard.

From the theoretical and experimental study, the following safety suggestions are proposed: (1) in an open reaction system, the decomposed gas of chlorine dioxide should smoothly release the atmosphere; (2) the system should be operated at temperatures as low as possible; (3) the pressure control should be as stable as possible.

CONCLUSIONS

A theoretical and experimental study of the safety chemistry of separation of oil/water transition layer by oxidation using chlorine dioxide was carried out. In summary, chlorine dioxide has flammable and explosive characteristics leading to a lot of danger and inconvenience issues during its production and application. The theoretical analysis indicates that the unsafe factors were recognized as the difference in overpressure during the oxidation process.

The chemistry of the ClO₂ oxidative treatment reveals that the safety is dominated by the released gas which originates from the decomposition of ClO₂ and the evolved gas from the oxidation of the reduced substances in the layer. The experimental results showed that the process pressure increased to a quite high value with the highly concentrated ClO₂, and the overpressure increased at higher reaction temperatures. In the light of the related standards, the change is compliant and adaptive to PetroChina and in-service status of the equipment for the application. For the open reaction system, the decomposed gas of chlorine dioxide is ensured to smoothly release the atmosphere; the system is operated at temperatures as low as possible; the pressure control is kept as stable as possible. This study can provide a safety control of the oxidation performance of chlorine dioxide, and efficient resolution of the settling tank oil/water transition layer with thickening, low-quality crude oil and high water quality and other problems.

REFERENCES

- 1.L.I. Bo, P. Fang and R. H. Shao, *Safety & Environmental Engineering*, **4**, 74 (2011)
- 2.J. Romaine, T. Strawser and M. Knippers, *SPE Production & Facilities*, **11**, 18 (1996).
- 3.Z. Zhang, C. McCann, J. E. Stout, S. Piesczynski, R. Hawks, R. Vidic and L. Y. Victor, *Infection Control & Hospital Epidemiology*, **28**, 1009 (2007).
- 4.D. Yuan, L. Tian, X. Shen, X. Sui and B. Wang, *Journal of Advanced Oxidation Technologies*, **20**, (2017).
- 5.D. D. Yuan, B. H. Wang, H. X. Sheng, H. J. Wu, X. Sui, J. Dong and G. Q. Feng, *Applied Mechanics and Materials*, **295**, 3196 (2013).
- 6.D. D. Yuan, H. J. Wu, H. X. Sheng, X. Sui and B. H. Wang, *Advanced Materials Research*, **652**, 749 (2013).
- 7.Z. Haiqin, L. Ping, Y. Jinping, L. Weidong and Q. Mu, *Natural Gas Industry*, **26**, 152 (2006).
- 8.A. O'Dea and R. Flin, *Safety Science*, **37**, 39 (2001).
9. A. Al-Kdasi, A. Idris, K. Saed and C. T. Guan, *Global Nest: the Int. J.*, **6**, 222 (2004).
- 10.V. Trinetta, R. H. Linton and M. Morgan, *Food Microbiology*, **34**, 296 (2013).
- 11.S. Sorlini, F. Gialdini, M. Biasibetti and C. Collivignarelli, *Water research*, **54**, 44 (2014).

12. W. Yu, T. Reitberger, T. Hjertberg, J. Oderkerk, F. Costa, V. Englund and U. W. Gedde, *Polymer Degradation and Stability*, **111**, 1 (2015).
13. S. D. Hicks, S. Xiong, C. J. Bougher, G. A. Medvedev, J. Caruthers and M. M. Abu-Omar, *Journal of Porphyrins and Phthalocyanines*, **19**, 492 (2015).

Study of the mechanism of magnetron sputtering of hybrid bonded diamond as carbon film coating for the surface of cavity structures

D. Wang *, B. Hu

School of Mechanical and Electric Engineering, Soochow University, Suzhou 215131, People's Republic of China

Received, August 1, 2017; Accepted, November 21, 2017

The carbon film bonding method is an sp³ and sp² hybrid key combination. Compared with common diamond-like carbon (DLC) films for multi-contour cavity structures, magnetron sputtering has many advantages in coating DLC films, such as high hardness, low friction coefficient, corrosion resistance, good optical transmission, etc. However, there are some problems, e.g., non-uniform film thickness and low attraction force between film and substrate. In this research paper, some strategies were developed to solve the above problems: (1) multiple rotating cylindrical magnetron sputtering targets were installed to improve the efficiency and uniformity of films; (2) gradient composite membrane structure was used to improve the poor adhesion between film and substrate and to solve the problem of easy peeling of the single film from the substrate. Based on the above strategies, a uniform DLC film of compact thickness and excellent chemical performance was coated on the complex inner cavity wall of the multi-contour cavity structured product.

Keywords: Diamond-like carbon film; Hybrid bond; Chemical stability; Multi-contour cavity; Magnetron sputtering coating.

INTRODUCTION

In recent years, diamond like-carbon (DLC) films received extensive attentions as a film material with high hardness, low coefficient of friction, corrosion resistance and good optical transmission properties. In addition, the carbon film bonding method is mainly an sp³ and sp² hybrid key combination and its chemical stability is good. It has been widely used for surface modification and micro electromechanical systems of molds [1-3]. The internal structure of the multi outlined cavity is complex, generally composed of cavity, plane, groove, hole and so on. Compared with the ordinary cavity plane, the DLC film for the multi contour cavity structure has the following two main problems [4,5]: firstly, there is a large internal stress in the DLC film, which puts a certain limit to the ultimate film thickness - when the elastic energy in the unit volume exceeds the fracture energy of the unit volume, the film will fall off due to excessive stress; secondly, in the process of DLC film deposition by magnetron sputtering on the complex cavity wall of the multi contour cavity structure as the cathode target for planar sputtering, the latter creates a strong local inhomogeneous magnetic field component of the club and non-uniform target consumption, which leads to concave erosion and poor uniformity of the DLC film.

According to the above two problems based on the characteristics of the complex cavity structure product, this paper aimed at improving the uniformity, compactness and chemical stability of DLC films deposited by a magnetron sputtering coating process.

METHODOLOGY

Adhesion mechanism of DLC film on the substrate

Adhesion is a phenomenon in which the film is attached to the substrate by interaction between the film and the substrate surface. The film quality is an important indicator of the durability and wear resistance of the film on the substrate. Its mechanism can be divided into two kinds: 1) chemical adsorption, 2) physical adsorption [6-8].

1) Chemical adsorption is the creation of chemical bonds between the substrate and the film, including covalent bond, ionic bond, metal bond and so on, which is a kind of adsorption, generally larger than Van De Waals;

2) Physical adsorption is mainly derived from static electricity and van der Waals force, mainly by dispersion force, directional force and induced force composition.

3) The film can be firmly attached to the substrate only when the substrate and the film have a chemical bond. However, this kind of chemical bond is not common, a chemical bond is only generated at the interface and forms the compound.

Growth mechanism of DLC film

The process of DLC film formation is extremely complex, and its growth mechanism is still not fully understood. The sub-implantation model presented by Lifshitz *et al.* is generally accepted in recent years [9]. Particle energy is an important condition in the physical vapor deposition of DLC films. Lifshitz proposed the sub-implantation model (shown in Fig. 1) by considering the effect of the injection on the deposition of the charged particles. The model shows

*To whom all correspondence should be sent:
E-mail: wangwangdeshan@163.com

that, with certain energy, the energetic particles, injected into the substrate beneath the surface, occupy the target location or the target becomes embedded in the interstitial atoms, causing internal pressure, resulting in the density of the film sp³ bonded components. When the energy of the charged particles is lower than a certain value, the ions cannot be injected into the surface of the substrate, and can only stay on the surface. Stress could not be formed in the film to promote the formation of graphite. When the energy of the particle exceeds a certain value, the injected atoms will escape from the original position because of the high energy, which will lower the local stress and inhibit the growth of sp³ components. When the ion energy reaches 20 keV, the local heating of the target is very serious, which makes the film complete.

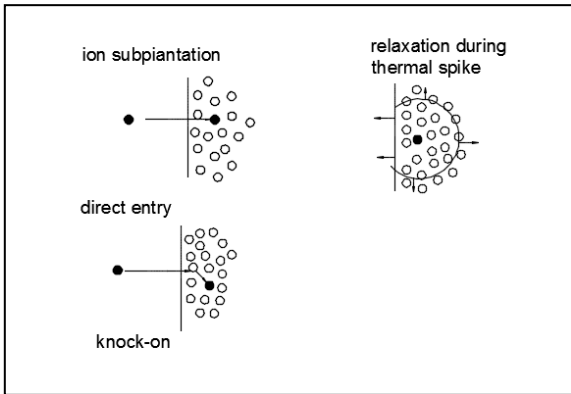


Fig. 1. Sub-implantation model [9]

Principle of DLC film deposition by magnetron sputtering

Magnetron sputtering is a common method for depositing DLC films. The method is characterized by low deposition temperature, large deposition area and high deposition rate. The basic process for manufacturing DLC films consists of: selection of high-purity graphite as the target, selection of inert gas (Ne, Ar) or carbon gas into the inert gas as working gas. Glow discharge in vacuum environment by gas ion bombardment of the target is accelerated under the action of the additional bias; the sputtered carbon ions move onto the substrate to form a thin film (shown in Fig. 2). The selection of technological parameters of magnetron sputtering has an influence on the structure and properties of DLC films: (1) sputtering power, (2) sputtering pressure, (3) sputtering bias, (4) sputtering temperature. This technology has the advantages of stable process, strong controllability, uniform thickness, high adhesion and low internal stress of the DLC thin film, and can produce films of large area [10,11].

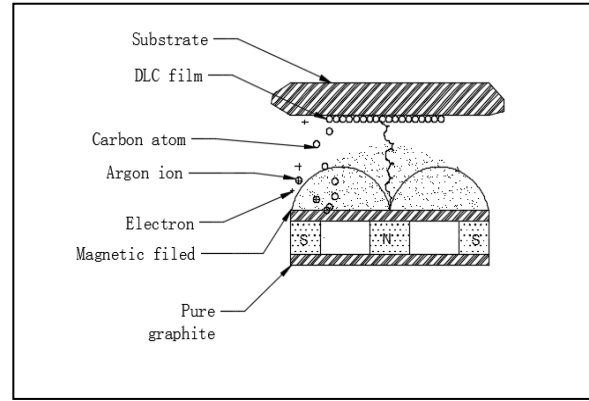


Fig. 2. Principle of DLC film formation

EXPERIMENTAL

For the multi contour cavity structure, the uniformity of the thickness of the DLC film and the quality of the adhesion will directly affect the stability and reliability of the devices. So the key technology of complex cavity structure sputtering DLC film is how to ensure uniformity and density of the DLC film and adhesion between DLC film and substrate.

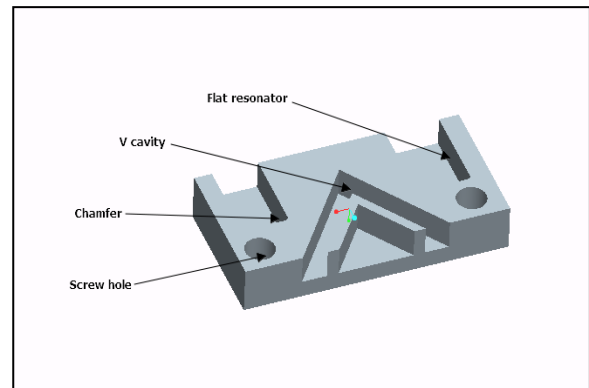


Fig. 3. The multi contour cavity structure

Setting up a number of magnetron sputtering targets and auxiliary magnetic field to improve the uniformity and density of the DLC film

The structure of the unbalanced magnetron sputtering cathode target is improved, and the plasma density of the vacuum coating chamber is enhanced by using a plurality of magnetron sputtering targets and an auxiliary magnetic field. Under the action of magnetic field, a guide pole shoe is introduced to ensure uniformity of the magnetic field intensity level, thereby improving the uniformity of the film layer and the sputtering rate. Meanwhile, by changing the distribution of the magnetic field, internal stress of the complex structure can be generated in the process of sputtering on the substrate, and the uniformity and compactness of the DLC film can be improved.

Adding metal or non-metallic elements to increase the binding force of the DLC film

By using a composite gas, composite target or co-deposition technology the binding force of DLC films substrate material is enhanced, the internal stress of the DLC film is regulated, and the thermal stability of the film is enhanced. Metals including Cr, W, Ti, Ni, etc., and non-metallic elements including Si, O, N, P, etc., can be added.

Adopting transition layer structure to reduce the internal stress of the film layer

By adding a transition layer structure, the bonding strength between the film and the substrate, as well as the thermal stress and the internal stress between the film and the substrate can be increased. For DLC thin films, soft Ti, Cr and other metal layers can be used as transition layer to reduce the internal stress. The addition of transition metals to the DLC films enhances the bonding strength of Ti, Cr transition layer to the DLC film forming DLC thin films with gradient metal component.

Increasing the stability and adhesion strength of the DLC film

The selected appropriate process parameters, including substrate temperature, gas pressure deposition rate, etc., and the improved equipment construction effectively improved the adhesion strength between the film and the substrate interface.

RESULTS AND DISCUSSION

Laboratory equipment

The experimental equipment mainly includes: six-station magnetron sputtering equipment, Fu Liye transform infrared spectrometer, scanning electron microscope, micro hardness tester, coating adhesion automatic scratch tester, ball mill, etc. (Fig. 4).



Fig. 4. Experimental equipment

Experimental process

Table 1. Experimental process

Experimental steps	Contents	Aims
Step 1	A closed magnetic field is formed by using a plurality of magnetron sputtering targets and an auxiliary magnetic field in the coating chamber. Then, the interaction between the targets proceeds by setting the auxiliary magnetic field The plasma density increases and the bias increase to achieve the purpose of deposition for the contour cavity structure.	Making the contour cavity structure deposition coating
Step 2	Vacuum degree is 6.6×10^{-3} Pa, heating temperature is 300°C. Through the argon, the vacuum degree is 8×10^{-1} Pa, duty cycle 80%, voltage of the bias power supply is 800V ~ 1200V, cleaning time is 10 ~ 20 min.	Forming vacuum coating environment
Step 3	Through the Ar gas, vacuum pumping to 5×10^{-1} Pa, bias current is set to 30A, duty cycle is 55%, voltage is 350V ~ 500V; for power supply current of 30A, voltage is 600V, time is 20 min.	Coating Ti layer
Step 4	Through the Ar, the vacuum degree is 5×10^{-1} Pa, the bias power supply current is 35A, the voltage is 350V ~ 500V, the duty cycle is 60%, the plating time is about 20 min.	Coating TiN (1-5) layer
Step 5	Vacuum degree is 6.67×10^{-3} Pa, the heating temperature reached 200°C ~ 300°C. Through the Ar in the coating chamber, the vacuum degree is 2Pa, the voltage of the bias power supply is 800V, duty cycle is 30%, time is about 25min.	Coating TiAlN layer
Step 6	Power supply voltage is set to 250V ~ 300V, through Ar gas, duty cycle is 30%, vacuum degree is 5×10^{-1} Pa, DC supply current is 20A, voltage is 400V ~ 480V, time is about 30min.	Coating Ti layer
Step 7	Through N ₂ , the vacuum degree is 5×10^{-1} Pa, duty cycle is 80%, power supply voltage is 150V ~ 250V, Ti Al target current is 20A, voltage is 450V, time is 240-350 min.	Deposition of TiAlN layer

Results: the film has good structure, compactness and smoothness, the thickness of the film is about 1 ~ 13μm, the uniformity is better than ± 5%, the hardness reaches 1800 HV, the bonding strength is high, the wear resistance and the stability are good, and the isotropic stress is small.

CONCLUSIONS

In this study, DLC films were coated on a multi-profile cavity workpiece substrate by magnetron sputtering based on the combination of sp³ and sp² hybrid bonds. A multi-target rotating column magnetron sputtering target and a gradient composite film structure were adopted. DLC films were coated by Ti, TiN and TiAlN of different intermediate transition layers. Finally, the DLC film was coated on the inner wall of the complex contour cavity structures. The film is continuous and compact with good interface between coating and substrate, uniform and dense, with good strength, hardness, thickness, and excellent chemical stability.

Acknowledgements: This work is supported by Jiangsu Province basic research project (Natural Science Foundation) of China under Grant No. BK20151220. Project name: Study on the adhesion mechanism of the multi contour cavity structure in diamond-like carbon films by magnetron sputtering.

REFERENCES

- W. Huang, Z. Yu, Y. Zhang, L. Liu, T. Huang, *Chinese Journal of Materials Research*, **26**, 1 (2012).
- Y.L. Guo, Y.W. Sun, S.W. Wang, X.B. Wang, Y. Chen, *Advances in Laser and Optoelectronics*, **46**, 4 (2009).
- M.J. Dai, S.S. Lin, H. J. Hou, H.W. Li, *Journal of Die & Mould Manufacture*, **9**, 54 (2005).
- G.H. Song, W. Du, C.L. He, Structure, Properties, Preparation and Characterization of Hard and Superhard Coatings. Beijing, Chemical Industry Press, 2007.
- C.Y. Nie, C.C. Lu, B. Liao, *Journal of Functional Materials*, **40**, 2 (2009)
- Y.Q. Li, H.Q. Wang, W.Y. Wang, Z.N. Yu, H.S. Liu, G. Jin, *Acta Mechanica Sinica*, **28**, 5 (2012).
- Y. Mabuchi, T. Higuchi, Weihnacht V, *Tribology International*, **62**, 6(2013).
- L.H. Li, L.F. Xia, H.Q. Zhang, Y.H. Zhang, Z.M. Zhou, *Journal of Tribology*, **21**, 1 (2001).
- S. Miyagawa, S. Nakao, K. Saitoh, K. Baba, Y. Miyagawa, *Surf. Coat. Tech.*, **41**, 128 (2000).
- Z.Z. Wu, X.B. Tian, F. Pan, K. Ricky, Y. Fu, F. Pan, *Journal of Metal Research*, **50**, 10 (2014).
- Q.F. Zeng, G.N. Dong, F. Yu, G. Liu, *Journal of Vacuum Science and Technology*, **34**, 11(2014).

Research on the moisture content of adjacent soil layer affecting the failure behavior of soil and the uplift bearing capacity of the MEEP pile

Y. Qian^{1,2*}, D. Teng², T. Lu³, R. Wang¹

¹Jilin Jianzhu University, Changchun, China

²Jilin Structure and Earthquake Resistance Technology Innovation Center, Changchun, China

³Northeast Electric Power Design Institute Co. LTD of China Power Engineering Consulting Group, Changchun, China

Received, August 1, 2017; Accepted, November 21, 2017

Using ANSYS software, an analysis model is established for a Multi-Extruded-Expanded-Plates pile (MEEP pile) in different soil layers under vertical tension. The effect of the moisture content of the adjacent soil layer (sandy soil) below and above the bearing plate on the failure behavior of soil surrounding the piles and the uplift bearing capacity of the single pile at the same time is studied. The model improved the calculation mode of uplift bearing capacity of the single pile, which provides a theoretical basis for engineering design of a MEEP pile.

Keywords: Adjacent soil layer, Moisture content, Failure behavior, Uplift bearing capacity, Multi-Extruded-Expanded-Plates pile (MEEP pile)

INTRODUCTION

Under vertical tension, the uplift bearing capacity of a MEEP pile is closely related to the thickness and character of the soil above the bearing plate. Especially for a sandy soil layer, it is a very important mechanical performance index, whose change will affect important physical indices of soil, such as soil adhesion stress, angle of internal friction, density, etc. [1]. So, when the upper soil of the buried MEEP pile is sandy soil, the change in moisture content will have a significant influence on the failure behavior and bearing capacity of the soil. In this paper, the effect of different moisture contents affecting the failure mechanism and bearing capacity of the soil surrounding the MEEP pile was studied through the finite element method and the calculating mode of uplift bearing capacity of the MEEP pile was improved. Due to the too weak shear strength of sandy soil under drying and saturation regime the adhesion stress, angle of internal friction and other parameters are almost zero, thus it makes no sense to study the moisture contents under two conditions - high or low [2-3]. So the present research focuses on the common moisture content of 10%, 15%, 20%, 25%, and 30%, which affects the failure behavior and bearing capacity of the soil surrounding the pile.

ANSYS ANALYSIS

The paper establishes a half-circle section pile model by ANSYS software. The effect of different moisture contents on the bearing capacity of the MEEP pile and the failure mechanism of the soil

surrounding the pile was studied [3]. To establish a MEEP pile model buried in a multilayer soil, different models were formed by changing the moisture content of the model. The results of the comparative analysis were obtained by loading step by step in the course of calculating [4-5].

Determination of material properties

In order to conform to the engineering practice, the physical and mechanical performance index in every soil layer is provided mainly according to practical engineering survey reports. The physical and mechanical performance indices of the concrete pile and every soil layer in the ANSYS modeling, are shown in Table 1.

The MEEP pile is buried in soil with three layers, the top-layer is sandy soil, the middle-layer is silty clay, the sub-layer is clay, the thickness of the three soil layers is 2000 mm, 2500 mm and 3000 mm, respectively.

In order to ensure that the model pile is buried in three layers of soil, the top of the pile is at same level with the surface of the top-layer soil, the bearing plate is set at the middle level of the silty clay layer, the end of pile stretches into the sub-layer soil for 1500 mm, which maintains a certain distance from the end of the pile to the bottom of the sub-layer soil, so the total length of the pile is 6000 mm, the reserved distance of soil surrounding the pile is 3000 mm, which meets the influence range of the soil when the pile and the bearing plate are under load. The size diagram of the model is shown in Figure 1 [6-7]. The five model specifications of the changed moisture content of the sandy soil are shown in Table 2.

*To whom all correspondence should be sent:
E-mail: 654675316@qq.com

Table 1. Physical and mechanical performance indices of pile and soil-layer

Soil layer	Density (g/cm ³)	Elasticity modulus (Mpa)	Poisson Ratio	Cohesion (Kpa)	Friction Angle (°)	Dilation Angle (°)	Coefficient of Friction of Piles
Sandy Soil	1.85E-009	2.0e4	0.25	10.5	38.0	38.0	0.35
Silty Clay	1.9E-009	2.5E4	0.35	17.4	18.29	18.29	0.45
Clay	2.1E-009	3.7E4	0.42	27.8	17.33	17.33	0.5
Concrete Pile	2.5E-009	2.5e7	0.20	-	-	-	-

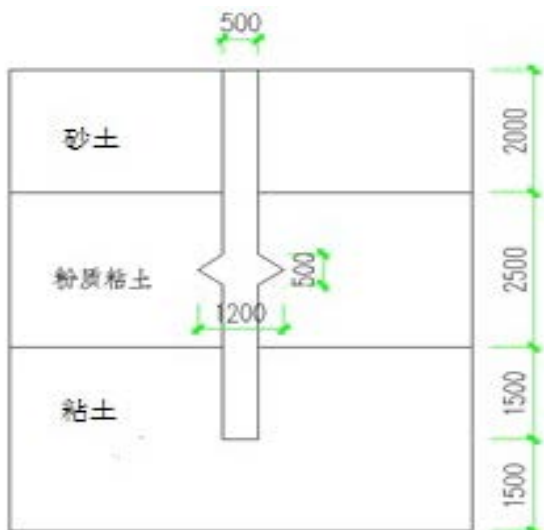


Fig. 1. The model diagram

Table 2. Specification and name of model

Model name	Moisture content (%)
STS1	10
STS2	15
STS3	20
STS4	25
STS5	30

In order to observe the changes in the soil surrounding the pile, a half-circle section pile was designed, the ANSYS model was divided into element grids according to the needs of analysis, and considering the demand of calculating, refinement of the grids was done for the buried plate of pile, pile body and soil cross-section. To consider the actual load situation, a gap of 1 mm is set between the soil model and the pile below the bearing plate, to ensure that the soil is separated from the pile after the pile is loaded. The specific model diagram and grid division are shown in Figures 2 and 3.

ANALYSIS OF THE SIMULATION CALCULATION RESULTS

Analysis of displacement

In the ANSYS analysis, the load is added by an area which is evenly added at the top surface of the half-circle section pile. The load is added from 100KN (which is converted to surface load and

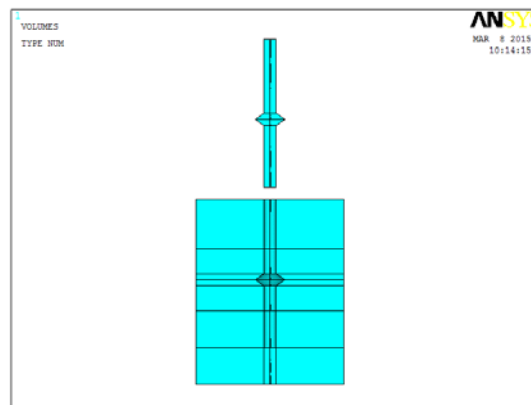


Fig. 2. Model diagram

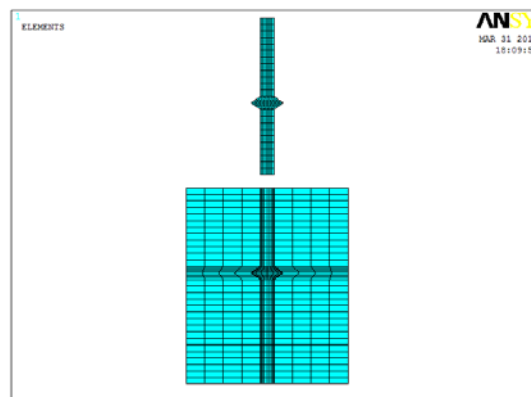


Fig. 3. Grid division of model

load of 500KN/m²) [8-9]; the load is added step by step according to the 100KN. When the results are analyzed, the displacement nephogram of the 7th step (up to 700KN load) of each model is taken, as shown in Figure 4.

From Figure 4 it can be seen that the vertical displacement from STS1 to STS4 is generally the same, and it is obvious that the displacement of STS5 is much larger, the change in soil failure behavior is larger, so the bearing capacity will be lower when the moisture content of soil exceeds 30%.

From the ANSYS analysis, the vertical displacement data extracted of a fixed point on the pile under different load are shown in Table 3. According to these data, a curve of displacement vs load can be drawn, as shown in Figure 5.

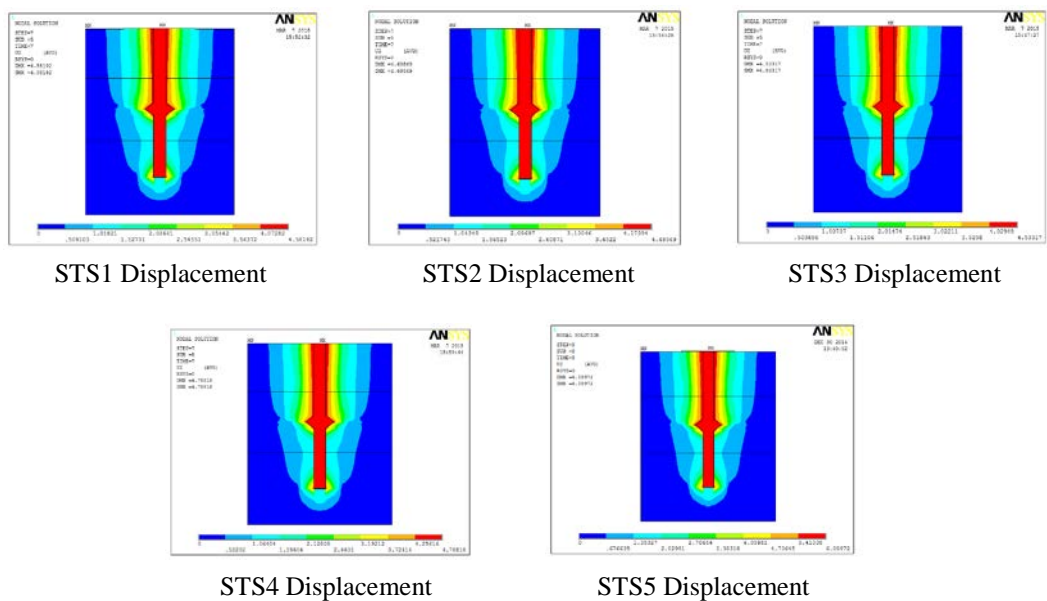


Fig. 4. Displacement nephograms of direction Z

Table 3. The vertical displacement data of a fixed point on the pile under different load

	100KN	200KN	300KN	400KN	500KN	600KN	700KN
STS1 Pile	5.23E-15	0.51539	1.0308	1.5905	2.3495	3.2686	4.4876
STS2 Pile	5.23E-15	0.51539	1.0308	1.5906	2.3598	3.2895	4.5325
STS3 Pile	5.23E-15	0.51539	1.0308	1.591	2.3723	3.3133	4.5812
STS4 Pile	5.23E-15	0.51539	1.0308	1.5922	2.4006	3.3612	4.695
STS5 Pile	5.23E-15	0.51539	1.0308	1.594	2.4238	3.4228	5.0874

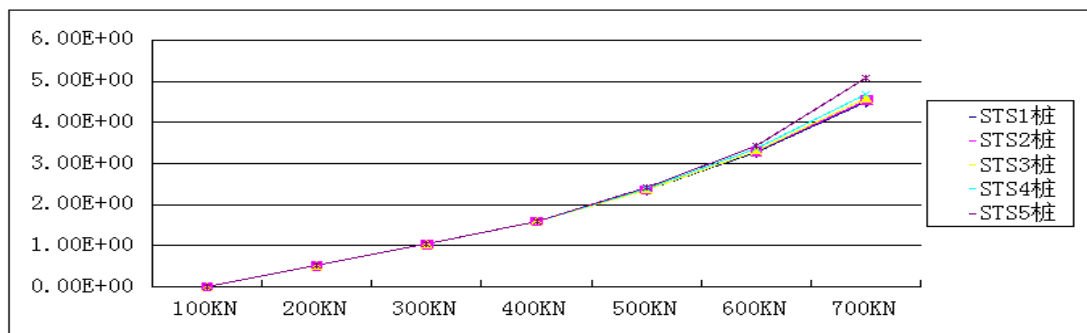


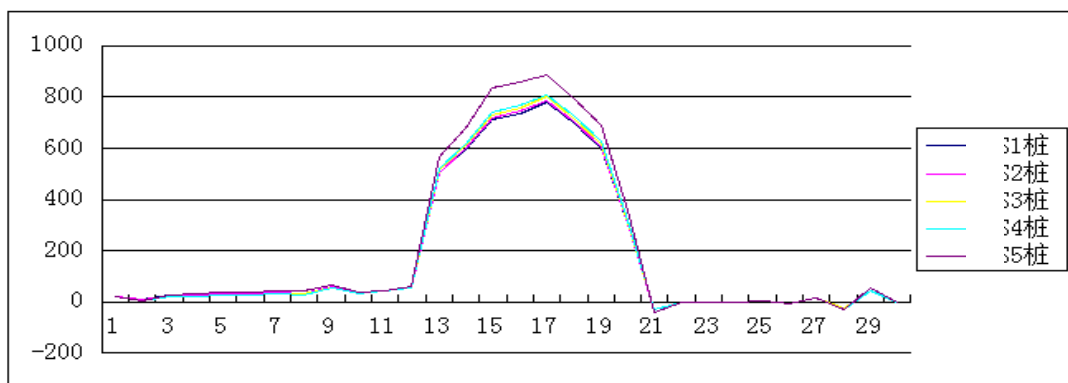
Fig. 5. The displacement-load curve of pile in different moisture content

From figure 5 it can be seen that the displacement changes of the pile with the increase in moisture content from STS1-STS4 are basically the same, the displacement steadily increases with the increase in moisture content. The displacement of STS5 has an obvious twist when load is added to step 6 and step 7, and when load is up to the 8th step (800KN), the bearing capacity cannot meet the requirements and the curve does not converge, so it can be considered

that the failure behavior change and the bearing capacity will be lower when the moisture content exceeds 30%.

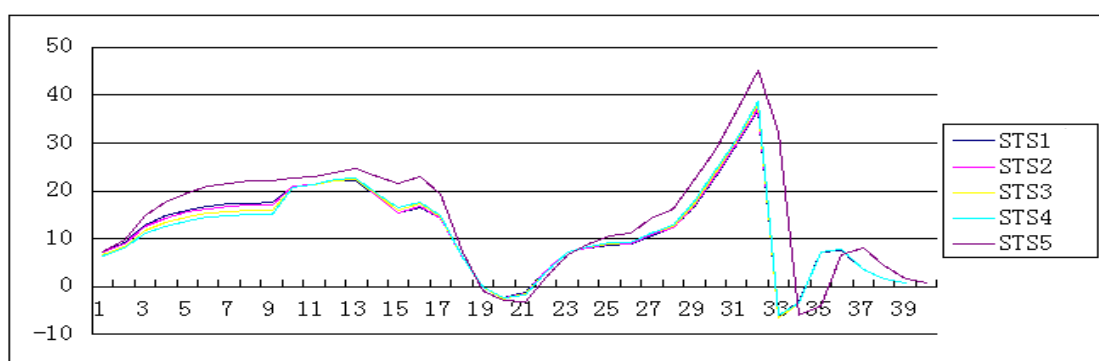
Analysis of stress and strain results

The variation curves of shear stress extracted from the ANSYS results calculated for all kinds of piles and soil surrounding the pile under the same load, are shown in Figures 6 and 7 [10].



Note: The mutated position in curve is the position of the bearing plate

Fig. 6. The curve of shear stress of pile in model with different moisture content



Note: Points 15-21-27 is the position of the bearing plate, points 31-33 is the location of bottom of pile

Fig. 7. The curve of shear stress of soil surrounding pile in model with different moisture content

From Figure 6 it can be seen that the shear stress of the pile body in the different models is the largest at positions of the bearing plate from STS1 to STS4. With the increase in the moisture content of sandy soil, the variations of shear stress at the plate of pile are basically the same. The maximum shear stress of STS5 has a larger variation, which illustrates that when the moisture content of the soil is 30%, the bearing capacity is far less than for the four moisture contents of the sandy soil, so the shear afforded by the bearing plate is the biggest. So it is considered that under vertical tension, if the adjacent layer above the plate of the MEEP pile is sandy soil with moisture content is below 30%, the failure behavior of the soil surrounding the pile is relatively stable and the bearing capacity is relatively better.

From Figure 7 it can be seen that under the same load, the shear stress of the soil surrounding the pile from model STS1 to STS5 creates mutation at the position of the bearing plate, and the same is at the

end of the pile. The shear stress of soil surrounding the pile is minimal at the bearing plate in the different models, but the end of the pile is rarely affected by the shear force under vertical tension, thus the shear stress of the soil at the end of pile is insignificant too. It is the same increase in the shear stress at the upper bearing plate from STS1 to STS4. For the model STS5 whose moisture content is 30%, the shear stress of the soil surrounding the pile at the bearing plate is obviously bigger than for the other piles, that is to say, the cohesive force of sandy soil with moisture content 30% is less than for other moisture contents, which has a significant influence on the uplift bearing capacity. Thus, if the adjacent soil layer above the plate of pile is sandy soil with moisture content below 30%, the bearing capacity is basically stable.

In addition, the elastic strain nephograms of direction Z obtained through the model analysis are shown in Figure 8:

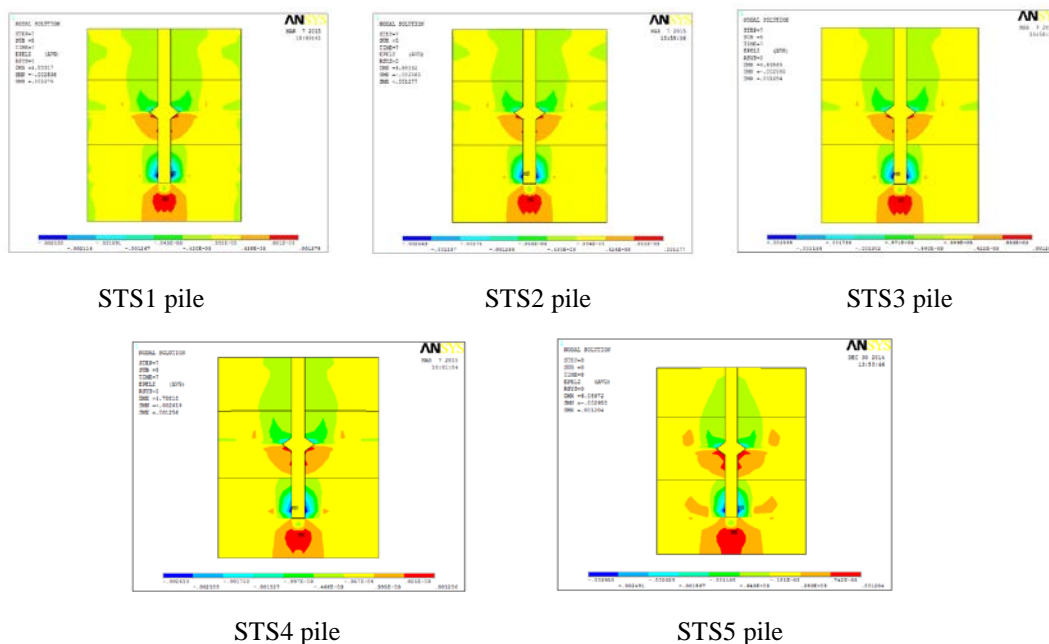


Fig. 8. The elastic strain graph of direction Z in different model

From Figure 8 it can be seen that if the moisture content of sandy soil is different, the maximum elastic strain of direction Z arises near the plate and the end of the pile for models STS1 to STS5 while the value of elastic strain gradually increases for models STS1 to STS3 and decreases for STS3 to STS5. The value distributes symmetry along the pile axis, the maximum of STS1 to STS4 is basically the same, the reduction rate of maximum value of STS5 is accelerated.

By other nephograms and data extracted from simulation calculations [4], relevant conclusions can be drawn: it can be seen from the stress diagram of direction Z that the stress of direction Z is largest at the top of the pile in models STS1 to STS5, and it reduces gradually along the pile body. The stress of the pile body above the bearing plate changes obviously, it is basically the same as below the bearing plate; the stress changes of direction Z are basically equal for STS1 to STS4 and significantly bigger for STS5.

It can be seen from the first principal stress diagram that with the increase in moisture content, the changes of the first principal stress are basically the same for STS1 to STS5. It decreases along the pile body downward the first principal stress, which changes obviously above the bearing plate, but does not change below the plate. The maximum of STS1 to STS4 is basically the same and bigger for STS5.

It can be seen from the total strain figure of direction Z that as the moisture content increases the change of the maximum total strain of direction Z is

basically the same for STS1 and STS2, slightly bigger for STS3. The maximum of total strain of direction Z changes distinctly from STS4 to STS5, the maximum of STS5 is much larger than STS4.

CONCLUSION

It can be concluded that under vertical tension, the moisture content of the adjacent soil layer above the plate of the MEEP pile affects the failure behavior and the bearing capacity of the soil surrounding the pile. From the results of ANSYS analysis, including the displacement nephogram, the curve of displacement vs load, the shear stress of the pile body and soil surrounding the pile, the stress of direction Z, the first principal stress, and the total strain figure of direction Z, and so on, the same conclusion can be drawn: if the adjacent soil layer above the plate is sandy soil with a moisture content between 10% and 30%, the failure behavior of the soil surrounding the pile is basically stable, the bearing capacity is relatively better. By the model the bearing capacity can be calculated when the moisture content is equal to or greater than 30%, and different data such as displacement, stress and strain will undergo great changes, and the bearing capacity will decrease. The formula for calculating the bearing capacity should be adjusted before using.

Acknowledgements: This work is financially supported by National Natural Science Foundation of China (51278224 and 51678275).

REFERENCES

1. H. Chen, F. Ban, X. Liu, *Journal of Hefei University of Technology* (natural science edition), **29**(6), 736 (2006).
2. H. Ling, Z. Yin, Zh. Cai, *Rock and Soil Mechanics*, **29**(3), 651 (2008).
3. X. Liu. The study of the influence of adjacent soil layer on the collapse state of soil and the bearing capacity of the Multi-Extruded- Expanded-Plates pile [M]. Jilin Jianzhu University (2015)
4. Y. Qian, X.Yin, R. Wang, *Geotechnical Engineering World*, **12**(9), 67 (2009):
5. X. Xie. The failure state and bearing capacity study of the Multi-Extruded-Expanded- Plates pile influenced by soil properties [M]. (2015)
6. Ch. Shen, X. Fang, H. Wang S.G. Sun, J.F. Guo, . *The Geotechnical Mechanic*, **30**(5), 1347 (2009).
7. D. Qian, *Journal of geotechnical engineering*, **24**(3): 371(2002).
8. X. Gao. Bearing characteristics test and numerical simulation analysis of the squeezed branch and plate pile [D]. (2007)
9. Ch. Lu, *Journal of engineering survey*, **6**, 12 (2001).
10. Y. Zhang, H. Yuan, *Journal of Beijing university of technology*, **32**(10), 879 (2006).

Photo-induced toxicity in the rotifer *Branchionus plicatilis* by anthracene (ANT) in absence and presence of UV irradiation and mechanisms underlying observed effects

C. Gao, X. Zhang, N. Xu, X. Tang*

College of Marine Life Science, Ocean University of China, Qingdao 266003, China.

Anthracene, a polycyclic aromatic hydrocarbon (PAH), undergoes a series of chemical reactions by absorbing ultra-violet (UV) light, and is potentially phototoxic to aquatic organisms. The aim of this study was to investigate the effects of photo-induced toxicity of anthracene (ANT) alone or in combination with UV radiation on *Branchionus plicatilis* physiological and metabolic functions such as fecundity, reproductive cycle, age-specific survival rate, spawning rate and reproduction rate. The mechanisms underlying ANT-induced phototoxicity were examined by measuring oxidative stress parameters including reactive oxygen species (ROS) and malondialdehyde (MDA) content, activity of antioxidant enzymes superoxide dismutase (SOD), glutathione peroxidase (GPx), catalase (CAT), glutathione S-transferase (GST) and levels of glutathione (GSH). The results showed the following: (1) Compared with single UV-treated and single anthracene-treated groups, the two examined concentrations of anthracene (0.4 µg/L and 4 µg/L) under UV radiation significantly inhibited individual fecundity, shortened the reproductive cycle, and delayed or suspended the arrival of reproduction peak, life cycle parameters of *B. plicatilis* such as net reproduction rate (R0), life expectancy (E0), generation time (T), and intrinsic growth rate (rm). The reproductive capacity of the rotifers was lowered. (2) Under UV radiation, ANT significantly increased ROS and MDA content, leading to changes in activity of antioxidant enzymes. The activity of SOD and GPx decreased within the first 24 h while the activities of SOD, CAT, GPx, GST and GSH were reduced. GSH content was lowered after 48 h. Hence, ANT produced photo-induced toxicity on the reproductive capacity of *B. plicatilis*. Under UV radiation, ANT was more potent in disturbing antioxidant mechanisms resulting in diminished survival rate, reproduction and growth of *B. plicatilis*.

Keywords: Anthracene; *Branchionus plicatilis*; UV light; Life table; Antioxidant enzymes

INTRODUCTION

Polycyclic aromatic hydrocarbons (PAH) are resistant to degradation, persistent and display long-range transport to remote global areas. Currently, PAH are not restricted to areas with human activities, but are also found in remote ecosystems such as the Arctic and the deep sea [1-4]. Due to their high lipo-solubility and octanol-water partition coefficient, PAH are readily absorbed by organisms, bioaccumulate and are enriched along the food chain, eventually imposing threats to human health [5-6].

Photosensitization is one of the important mechanisms underlying PAHs' photo-induced toxicity. Several studies demonstrated that after PAH absorb light, reactive oxygen species (ROS) are generated as a result of photosensitization yielding reactive singlet oxygen which produces lipid peroxidation membrane denaturation and breakdown of macromolecules, eventually inducing damage and death to the organisms [7-9]. In addition, several PAH act similar to natural hormones, disturb normal hormone metabolism and produce endocrine disorders in organisms, adversely affecting the nervous, immune and reproductive systems, and even resulting in malignant neoplasms [10-12].

Anthracene (ANT) is optically active and

undergoes a series of chemical reactions by absorbing UV, such that this chemical is potentially phototoxic to aquatic organisms [13]. Studies examining photo-induced toxicity of PAH on organisms which investigated the antioxidant response and damage of ANT on biological by absorbing UV were conducted by several investigators [14].

Photosensitization causes mass production of reactive oxygen species (ROS). When the ROS production rate exceeds the removal rate by the antioxidant system of an organism, antioxidant reactions occur and biofilms can be damaged. Several studies demonstrated that ROS can also interact with other biological macromolecules such as proteins and nucleotides, resulting in damage or death of cells.

B. plicatilis are widely distributed, short-lived, fast-breeding, easy to cultivate, sensitive to exogenous toxicants, and play a key role in material circulation and energy transfer in marine ecosystems. Nevertheless, there are few studies on the photo-induced toxicity of PAHs on *B. plicatilis*. This paper used anthracene, which is the most optically active compound under UV light, as the stress factor and *B. plicatilis* as the subject, aiming at investigating the photo-induced toxicity of anthracene under exogenous UV radiation conditions on *B. plicatilis*. The possible mechanisms based on photosensitization theories were discussed. This paper filled the research gap

*To whom all correspondence should be sent:
E-mail: : tangxx@ouc.edu.cn

in the photo-induced toxicity of anthracene on *B. plicatilis* and the toxicity mechanisms based on photosensitization theories, providing theoretical basis for future comprehensive evaluation on the photo-induced toxicity of anthracene on marine zooplankton.

RESEARCH METHOD

Lively and strong female *B. plicatilis* cultivated by the Faculty of Fishery, Ocean University of China were used in this study. They were cultivated in 1.5-L glass beakers and then placed in intelligent lighting incubators (GXZ-3008), with a temperature of $20\pm 1^\circ\text{C}$. The light intensity was $1313.8\pm 54.8 \mu\text{W}/(\text{cm}^2\cdot\text{s}^{-1})$ and the photoperiod was 12 h: 12 h. Before the start of formal experiments, the rotifers were tamed for three months under the experimental conditions.

Light Source Setting and Experimental Set-up

The acute toxicity experiment was carried out in lighting incubators at a constant temperature. The UV radiation system mainly consists of two UV-A fluorescent tubes and one UV-B fluorescent tubes. The visible light, UV-A and UV-B intensity is $1313.8\pm 54.8 \mu\text{W}/\text{cm}^2$, $1869.1\pm 25.7 \mu\text{W}/\text{cm}^2$ and $136.1\pm 5.2 \mu\text{W}/\text{cm}^2$, respectively. This can effectively simulate natural sunlight.

Experimental Design

Photo-induced Toxicity Effects of Anthracene on Life Table Parameters and Reproductive Value of B. plicatilis.

Totally 420 healthy and energetic larvae just born for less than three hours were selected from previously cultivated *B. plicatilis*. During the experiment, 80% of the water in each experimental group was replaced every day in order to keep the system stable. Chlorella was given each time during water replacement to maintain the concentration of 1.0×10^6 cell/L. During the first 24 to 72 h, the survival condition of *B. plicatilis* was observed at 4-h intervals with dissecting mirrors. The first spawning time and the first birth time were recorded. After that, observations were made at 8-h intervals to record the maternal spawning number and the number of survivals. At the same time, the dead rotifers were removed and the newly born larvae were moved to another 24-well plate for cultivation. The experiment ended when the last parent died.

Photo-induced Toxicity Mechanisms of Anthracene on B. plicatilis based on Photosensitization Theories

Two different concentrations of anthracene (0.4 $\mu\text{g}/\text{L}$ and 4 $\mu\text{g}/\text{L}$) were used in the

experiment. After concentration accumulation, the rotifers were transferred to new culture media, further divided into groups with/without UV radiation treatment. After the pre-cultured larvae were exposed to UV and UV-free (control) radiation, anthracene concentration in each group was quantified, and there were three subgroups in parallel for each group treated with certain concentration of anthracene. The rotifer density was 100 individuals/mL. There was no feeding during the experiment. There were 10000 rotifers (about 0.2 g) for each parallel sub-group. The rotifers were collected at the 24th h and 48th h. With the addition of 0.86% saline solution, these rotifers were disintegrated in an ice bath with an ultrasonic cell crusher, and the operation lasted for five seconds at 10-sec intervals. They were completely fragmented after five sessions of crushing and underwent centrifugation at 2500 r/min for 10 minutes at 0°C . The supernatant was used to measure the activity of different antioxidant enzymes in the crude extraction, the total suspended particulate (TSP), ROS, MDA content, and the activity of SOD, POD, CAT, GPX, GR, GST, GSH, in the crude enzyme solution.

RESULTS AND DISCUSSION

Effect of UV radiation and Anthracene Concentrations on Life Table Parameters of B. Plicatilis

Under UV radiation, anthracene greatly affects life table parameters of *Branchionus plicatilis*, specifically illustrated as follows: (1) Life expectancy is shortened very remarkably in the anthracene-treated group under UV radiation ($P<0.01$). The suppression is notably dose-dependent. (2) The net reproduction rate in the 4 $\mu\text{g}/\text{L}$ anthracene-treated group without UV radiation is greatly elevated to 7.22, but drops notably to 1.51 when the counterpart is exposed to UV radiation. (3) Compared with the control group, the generation time in the 4 $\mu\text{g}/\text{L}$ anthracene-treated group under UV radiation is inhibited significantly ($P<0.01$), and the resulting generation time is just 87.5% of that in the control. (4) Compared to the control, the intrinsic growth rate in the 4 $\mu\text{g}/\text{L}$ anthracene-treated group without UV radiation considerably increases ($P<0.01$). The two anthracene-treated groups under UV radiation (0.4 $\mu\text{g}/\text{L}$ and 4 $\mu\text{g}/\text{L}$) show remarkably lower intrinsic growth rates ($P<0.01$). The rate decreases obviously with the increasing anthracene concentration, reaching to the minimum of 0.12/h in the 4 $\mu\text{g}/\text{L}$ anthracene-treated group under UV radiation.

Table 1. Toxic effects of ANT on the life table of *B. plicatilis* under UV radiation

Condition	Expectancy e_x (h)	Net reproductive rate / R_0 (ind)	Generation Time/ T (h)	Intrinsic increasing rate / r_m (h^{-1})
TROL	272.40±3.56	6.04±0.42	93.91±2.25	0.46±0.07
UV	280.20±8.43	6.53±0.33	87.60±2.94	0.51±0.08
LANT	256.02±6.33	6.34±0.54	91.76±2.56	0.49±0.11
0.4µg/LANT	273.20±4.73	5.65±0.35	91.86±4.04	0.45±0.09
4µg/LANT	278.02±5.14	7.22±0.56 ^c	87.62±1.78	0.63±0.08 ^{**}
0.4µg/L ANT vs UV	210.48±3.14 ^{**}	3.09±0.24 ^{**}	91.65±4.50	0.29±0.05 ^{**}
4µg/L ANT vs UV	175.81±4.23 ^{**}	1.51±0.13 ^{**}	82.09±1.78 [*]	0.12±0.04 ^{**}

Note: Data are shown as means ± SE (n=3). Asterisks indicate statistically significant differences with respect to the values of control cultures ($P < 0.05$).

The significant changes in the rotifers' life table parameters in anthracene-treated groups under UV radiation reveal noteworthy photo-induced toxicity of anthracene on *Branchionus plicatilis*. Meanwhile, the net production rate and intrinsic growth rate are sensitive indicators of evaluating the photo-induced toxicity in *Branchionus plicatilis*. Anthracene is strongly phototoxic to *Branchionus plicatilis* and can lead to a continuous increase in ROS by photosensitization.

(1) Production of ROS causes the MDA content in *Branchionus plicatilis* to rise with time. The photo-induced effects of anthracene can significantly increase the MDA level and thus further exacerbate the degree of lipid peroxidation in the rotifers.

(2) The activity of enzymes sensitive to ROS, such as POD, SOD and GPx was affected within the first 24 h of the experiment. The activity of POD, CAT, GPx and GST and the GSH content were hindered after 48 h whereas the activity of glutathione reductase (GR) was enhanced. The effects of anthracene on the antioxidant enzymes in *Branchionus plicatilis* were much stronger when exposed to UV radiation.

CONCLUSION

This paper used anthracene as the stress factor and *Branchionus plicatilis*, critical zooplankton in marine ecosystems, as the experimental subject. The effect of photo-induced toxicity of anthracene on *Branchionus plicatilis* was investigated at physiological and biochemical, individual, and population levels and the preliminary discussion was conducted on the underlying mechanisms based on photosensitization theories.

Rise in the net reproduction rate and intrinsic growth rate was observed in the 4 µg/L anthracene-treated group compared with the control, which is probably related to excitatory effect caused by toxicity. This phenomenon is commonly noted in studies using *B. plicatilis* as an experimental subject, proving that it is normal for these rotifers to respond to stimulation under low toxicity. In our study, when the rotifers were treated with anthracene under UV radiation, the

individual spawning number was reduced and the reproduction peak was delayed or suspended; the age-specific survival rate, the longest life span, the net reproduction rate and the intrinsic growth rate were also considerably lowered. Besides, the generation time was remarkably shortened and the life expectancy dropped, greatly reducing the reproductive value. These results showed serious negative impacts on the rotifers' potential growth. This is likely because the rotifers' reproductive system was damaged by anthracene under UV radiation. These changes in parameters illustrate that anthracene not only possesses strong photo-induced reproductive toxicity on *B. plicatilis*, but also has photo-induced toxicity on these rotifers at the population level. Among all reproduction and life table parameters, the net reproduction rate and the intrinsic growth rate can be used as sensitive indicators for photo-induced toxicity evaluation.

Previous research has suggested that toxicity mechanisms of PAHs are mainly based on photosensitization; In particular, ROS resulting from photosensitization can cause oxidative damages to a variety of aquatic organisms. The degree of membrane lipid peroxidation in *B. plicatilis* was notably intensified due to anthracene under irradiation conditions. This severely disturbed the ROS balance in the rotifers, leading to more remarkable changes in the antioxidant system and ultimately adverse effects on the reproduction. Hence, the photo-induced toxicity mechanisms of anthracene on *B. plicatilis* might be explained by the photosensitizing activity of anthracene and the oxidative stress induced by ROS in these rotifers.

The anthracene concentration used in the study was slightly higher than its actual concentration in the sea. The UV and visible light intensity value was adopted based on the annual average sunlight UV and visible light intensity at 12:00 noon in Zhengzhou, China. The experiments were conducted in laboratories within a short period of time such that the causal relationship can be established from the data obtained, enabling us to determine and estimate the effects of pollutants in the actual environment.

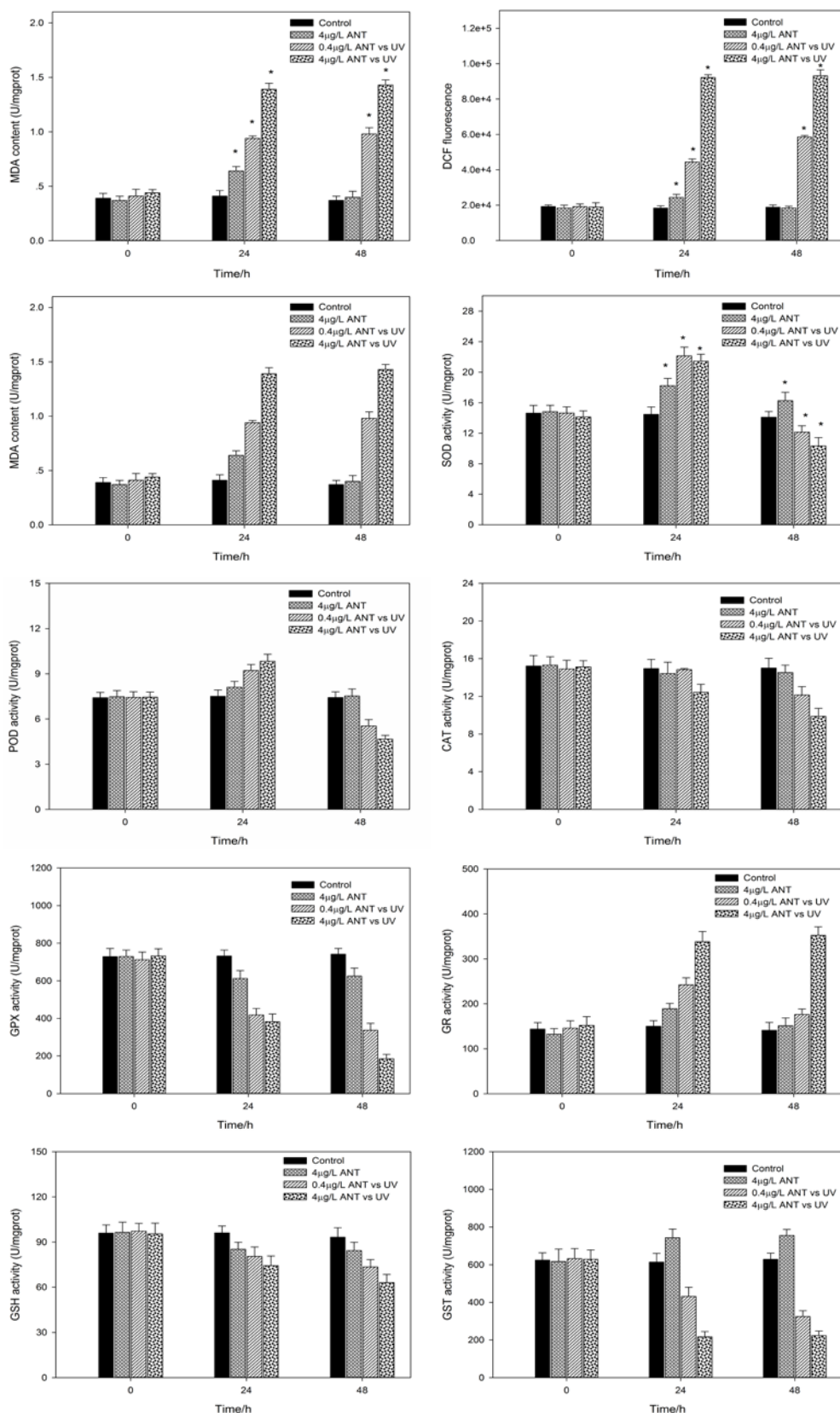


Fig. 1. Effect of different concentrations of ANT on TSP, ROS, MDA, SOD, POD, CAT, GPx, GST, GSH, GR activities in *B. plicatilis* with or without UV radiation exposure.

Note: * represents statistically significant differences between control and treatments at the $P < 0.05$ level.

REFERENCES

1. C. J. Halsall, L. A. Barrie, P. Fellin, D. C. G. Muir, B. N. Billeck, L. Lockhart, F. Ya. Rovinsky, E. Ya. Kononov, B. Pastukhov, *Environ. Sci. Technol.*, **31**(12), 3593 (2015).
2. K. Hylland, *J. Toxicol. Env. Heal. A.*, **69**(1-2), 109 (2006).
3. D.M. Pampanin, J. Le Goff, K. Skogland, C. R. Marcucci, M. Lorentzen, *J. Toxicol. Env. Heal.*, **79**, 633 (2016).
4. V. Berg, M. Kraugerud, R. Nourizadeh-Lillabadi. *J. Toxicol. Env. Heal. A.*, **79**(13-15), 538 (2016).
5. Y. Liang, M. F. Tse, L. Young, M. H. Wong, *Water Res.*, **41**(6), 1303 (2007).
6. A. Jansen, J. L. Lyche, A. Polder, J. Aaseth, *J. Toxicol. Env. Heal. B.*, **20**(1), 1 (2017).
7. J. Choi, J. T. Oris, *Environ. Toxicol. Chem.*, **19**(11), 2699 (2000).
8. C. A. Rodriguez, H. I. Browman, J. A. Runge, J. F. St-Pierre, Impact of solar ultraviolet radiation on hatching of a marine copepod, *Calanus finmarchicus*. *Mar. Ecol. Prog. Ser.*, 2000, 85-93.
9. S. Dong, P. P. Fu, R. N. Shirsat, J. Leszczynski. *Chem. Res. Toxicol.*, **15**(3), 400 (2002).
10. S. M. Billiard, M. E. Hahn, D. G. Franks, R. E. Peterson, P. V. Hodson, *Comp. biochem. Phys. B., biochemistry and molecular biology*, **133**(1), 55 (2002).
11. M. Gesto, J. L. Soengas, J. M. Míguez, *Aquat. Toxicol.*, **86**(3), 341 (2008).
12. K. Yoon, S. J. Kwack, H. S. Kim, B. M. Lee, *J. Toxicol. Environ. Heal. B.*, **17**(3), 127 (2014).
13. R. E. Thomas, M. Lindeberg, P. M. Harris, S. D. Rice, *Mar. Pollut. Bull.*, **54**, 726 (2007).
14. Y. S. El-Alawi, B. J. McConkey, D. G. Dixon, B. M. Greenberg, *Ecotox. Environ. Safe.*, **51**, 12 (2002).

Analysis of seepage characteristics of mine fractures based on geothermal utilization

P. Huang¹, Y. Zhang^{2*}

¹College of Environment and Resources, Fuzhou University, Fuzhou, Fujian, China

²Department of safety science and engineering, Qingdao University of Technology, Qingdao, Shandong, China

Received September 27, 2017; Accepted November 23, 2017

This paper discusses the feasibility of using the fluid seepage characteristics to develop the underground thermal energy of the mine so as to combine the thermal hazards treatment of underground mine with the utilization of thermal energy. This paper puts forward the idea of using a high-pressure water pump to make cracks, and scouring the underground hot rock with cold water to get the heat energy. The main factor of the natural gushing water in the mine is found out. The causes and characteristics of the rock fracture deformation are analyzed. The data show that the rock fracture deformation and seepage relationship model can be established in the equivalent continuous medium state. In this paper, the relationship between fracture and seepage of rock mass is established, and the relationship between the flow of mine groundwater in rock mass and fracture deformation is obtained.

Key words: Rock mass fracture, Seepage, Heat energy, Storage effect

INTRODUCTION

Various adverse micro-climates may happen in the mine production, which are mainly high temperature and high humidity in the mine. The so-called high temperature refers to the underground temperature of more than 300C; the so-called high humidity refers to the relative humidity of more than 80%. The micro-climate with high temperature and high humidity indicates thermal hazards [1]. To solve the problem of high temperature and high humidity in underground mine can ensure the health of underground workers, satisfy ergonomics requirements and improve working efficiency. In the mining process, a large number of hot water was poured out, which directly led to underground thermal hazards, while these hot water contains massive, exploitable energy. The realization of integrating thermal hazards treatment of underground mine with the utilization of geothermal energy will bring a qualitative leap of China's energy-saving and emission reduction project.

DEVELOPING GEOTHERMAL ENERGY BY SEEPAGE

Exploiting geothermal energy by taking advantage of water seepage was first proposed by the United States in the 1960's. Japan and European countries developed high-temperature rock technology since that time [2]. The United States performed experiments at Fenton Hill between 1978 and 1986; the Britain did experiments at Cornwall Rosemanowes Quarry; Japan carried out

some tests in the elbow area in 1984. And they all achieved some results.

These fractures are usually saturated with water or steam in the thermal rock geothermal reservoir when rock fractures are suitable. After drilling, water and steam can be used as working fluid for the extraction of heat and can be used to generate electricity. There is no water in the dry thermal rock geothermal reservoir, so the geothermal reservoir must be injected with water. In order to keep the permeability high and the flow resistance low, it is necessary to press the rock with water to connect the wells and make the joints open. And then rinse a large area of dry and hot rock with flowing water to obtain high-temperature liquid in the long term. Experiments at Fenton Hill confirmed the feasibility of this approach, and nine months' experiments from 1978 to 1980, 3 ~ 5MW of geothermal energy was produced. Stratum Due to the low flow resistance, the water is injected into the stratum until it is produced from another well, and the energy used is less than 2% of the heat produced.

The biggest difficulty with the geothermal utilization methods above is how to carry out underground thermal energy surveys and the expensive drilling costs. If the natural underground heat energy can be used when mining is carried out, the problems and costs of surveying technology are completely solved. Therefore, with very little input, inexhaustible and clean energy can be obtained. The mine thermal rock is fractured by the high-pressure water pump so that it has fractures with good seepage effects. Those fractures eventually converge in the designed roadway. A hot water recycling bin was built near the fracture, into which the surface cold water was poured, and then hot

*To whom all correspondence should be sent:
E-mail: zhyoliang@163.com

water was drawn to the ground to use by the pump. That is a viable way.

If the extracted hot water is used in the air conditioning system to cool and heat, it will save about 67% more electricity than electricity by a preliminary economic analysis.

SOURCE OF MINE SPRING

For the development and utilization of geothermal energy, expensive exploration and drilling cost has been plaguing engineering technologists in geothermal development, but in the mining activities, the natural formation of the mine, after the completion of mining tasks, even when mining, the permeability of water can be used as a hot water well.

Water filling source

Mine water disaster refers to the mine in the construction and development process, different forms, different sources of water, through a certain way into the pit, and then cause adverse and harmful effect on mine construction and production. There are three problems that must be considered in the discussion of the source of mine water: 1. Does the water supply exist? 2. Does the water filling pathway exist? 3. What is the water filling strength? Since most mining activities are below the surface of the earth, therefore, groundwater has become the most important water source for underground water supply. As a water filling source, groundwater can be divided into indirect water filling source, direct water filling source and self-filling water source, these 3 basic forms. For most mineral deposits in the north, indirect water filling is the most common. The indirect water filling water source refers to the water source which is mainly distributed around the ore body [3].

Water filling pathway

The mine water filling pathway means the water passage between the filling water source and the mine. In structural water guiding channel, most common type are faults, fractures etc. Rock mass is the composed of rock and structural plane, in the process of the rock formation, the material foundation and macroscopic structure and heterogeneity of the rock mass and the original structural plane of the rock mass are formed, and then a large number of structural planes and secondary structural planes have been developed after the late structural, unloading and weathering processes [4]. The structural plane is also called fracture, so it is also called fracture rock mass. The underground water of rock slope can be called mine

slope, fracture rock ground water. After the mine is excavated, along with the downward extension of the stope, it changes the hydrogeological environment nearby, and the groundwater enters the stope and tunnel along the rock fracture, which brings inconvenience to the underground operation. In order to study the water filling strength, it is necessary to understand the seepage of fluid in the rock mass fracture. This paper will focus on the influence of rock mass fracture and deformation on water seepage.

ROCK MASS FRACTURE ANALYSIS

Cause of fracture

Fractures are one of the most common features in rock formations, including nature fracture and man-made fracture according to the rigorous geomechanics. There are many methods of man-made fracture, which are not described in detail here. The reason for the nature fracture is that the increase of stress exceeds the rupture strength of formation rock. It is attributed to various geomechanics factors. Such as the formation of folds and faults when the operation of the crust; the overburden erosion will form a difference, stress, etc. through each weak surface.

Characteristics of rock mass fracture

A large number of primary fractures formed during the diagenetic process of the rock mass. Ore bodies occurred in structural fracture zone, during the long process of mineralization, rock masses have experienced many severe tectonic changes, after many tectonic actions, unloading and weathering, a large number of structural fractures and secondary fractures have been developed.

Typical rock mass joint fracture simulation next work [5], see Figure 1. Typical mine slope joint fracture statistical results [6], see Table 1. From which we can see that the development of fracture of rock mass is dense, and the fracture distribution is obvious. In most mines, rock fractures are intensive, the maximum fracture spacing or average fracture spacing is almost negligible compare with the size of rock mass or surface area, the flow field volume is far greater than the typical characterization of unit volume of REV, so in the establishment of fluid rock deformation crack and seepage relationship model can be assumed to be in the equivalent continuum condition, which can objectively reflect the groundwater seepage characteristics.

ESTABLISHMENT OF RELATION MODEL BETWEEN ROCK MASS FRACTURE DEFORMATION AND SEEPAGE

Fluid Storage Effect Model

Fluid storage effect means when a fluid flows through the pores of a porous medium, The mutual influence of fluid flow and rock deformation, resulting in expansion of rock and compression of pore volume, As a result, the fluid appears to be trapped by the pores of the rock and stored in pores. The storage effect of fluid is the direct manifestation of the influence of rock deformation on seepage flow under fluid-structure interaction, which is very different from the conventional linear seepage.

When the porosity of rock mass reaches a certain extent, the rock mass can be considered as a porous medium, under one-dimensional flow condition, the continuity equation of rock mass with fluid storage effect can be expressed in the lower equation [7-9]:

$$\frac{1}{V_b} \frac{\partial}{\partial t} (\rho_f V_b \phi) + \frac{\partial}{\partial x_i} (\rho_f v_{fi}) = 0 \quad (1)$$

where V_b is the rock mass, ϕ - the porosity, ρ_f - the ensity of rhw fluid, v_{fi} - the seepage velocity of the fluid.

On the premise of equivalent continuum which is stated in 3.2 in this paper, we make the following assumptions about Eq. (1).

The deformation of fluid and solid particles is elastic deformation.

The strain of porous medium is small strain and satisfies Eq. (2).

$$\begin{cases} \frac{V_b}{V_{bo}} = 1 - \varepsilon_v \\ \frac{V_{bo}}{V_b} = 1 + \varepsilon_v \end{cases} \quad (2)$$

Derive by deduction,

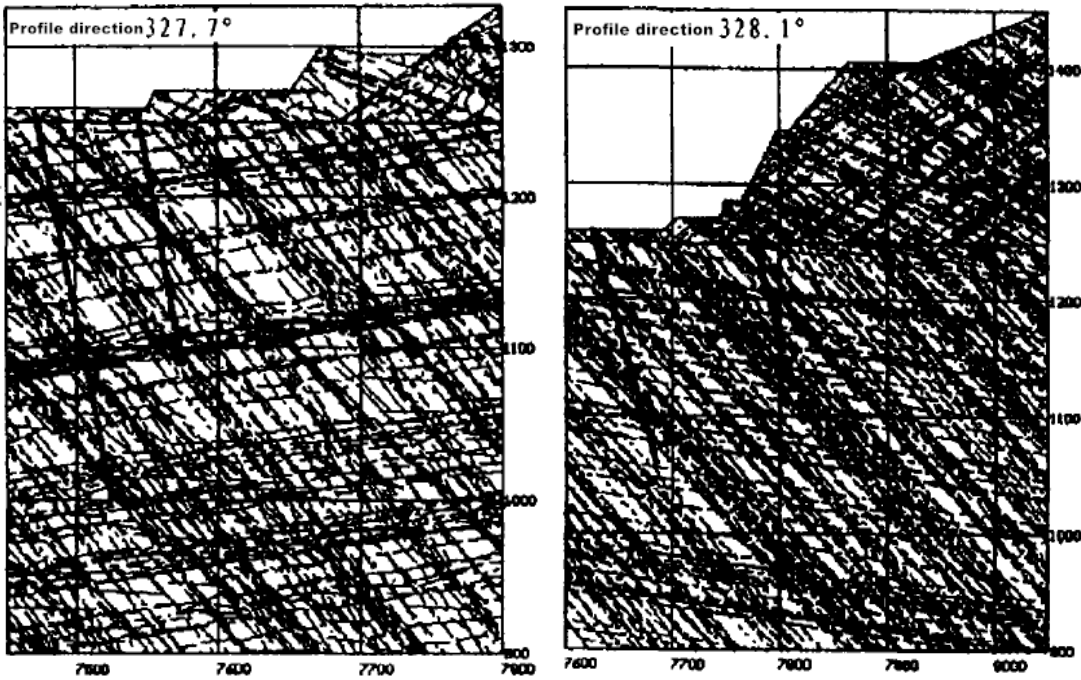


Fig. 1. Pan Gang Zhu jia bao iron mine Nanbang slope edge joints network simulation diagram

Table 1 Jianshan iron mine statistical analysis of slope crack spacing

Measuring point	Lithology	Sample capacity	Mean value (cm)	Standard deviation (cm)	Exponential distribution
1	Amphibolite	66	11.662	7.929	Yes
2	Quartzite	22	16.864	11.576	Yes
3	Chlorite schist	30	19.391	19.322	Yes
4	Grunerite-schist	32	8.933	3.268	Yes

$$\frac{1}{V_b} \frac{\partial}{\partial t} (\rho_f V_b \phi) = \rho_{fo} \frac{\partial}{\partial t} \left\{ - \underbrace{\varepsilon_v}_{\text{骨架}} + (1 - \phi_0) \underbrace{\left[\frac{\sigma_m - p_p}{K_s (1 - \phi_0)} + \frac{p_p}{K_s} \right]}_{\text{固相颗粒}} + \phi_0 \underbrace{\left(\frac{p_p}{K_f} \right)}_{\text{流体}} \right\} \dots (3)$$

where ϕ_0 is the initial porosity, ρ_{fo} - the initial fluid density, V_{bo} - the initial volume of porous medium, σ_m - the mean stress.

It can be found in Eq. (3), the fluid storage effect is a complex function of skeleton deformation, solid particle deformation and fluid deformation in porous medium.

The elastic deformation of a porous medium (3) can be expressed as,

$$\varepsilon_v = \frac{1}{K} (\sigma_m - a p_p) \quad (4)$$

Another form of expression of Eq. (3) can be derived:

$$\frac{1}{V_b} \frac{\partial}{\partial t} (\rho_f V_b \phi) = \rho_{fo} \left(\frac{a}{K_b} \right) \frac{\partial}{\partial t} \left(-\sigma_m + \frac{p_p}{B} \right) \quad (5)$$

Where

$$B = \frac{\frac{1}{K_b} - \frac{1}{K_s}}{\frac{1}{K_b} - \frac{1}{K_s} + \phi_0 \left(\frac{1}{K_f} - \frac{1}{K_s} \right)} \quad (6)$$

In the formula, K_b —Bulk modulus of rock, K_s —Bulk modulus of mineral particle, K_f —Bulk modulus of fluid.

Additional stress model induced by fracture

In porous medium, pore pressure changes cause volume changes, this induced deformation will also cause an additional stress acting on the stratum. The variation of stress induced by pore pressure changes can be expressed by the stress coefficient as,

$$\eta = \frac{a(1 - 2\nu)}{2(1 - \nu)} \quad (7)$$

where, η is the stress coefficient, a - the Biot coefficient; ν - the Poisson ratio of the porous medium.

The change of stress caused by the change of pore elasticity can be calculated by the following formula,

$$\Delta\sigma = \Omega \cdot \eta \cdot \Delta p_p \cdot f(t) \quad (8)$$

where, Ω is the quantization of boundary and

other nonideal conditions, namely, the influence of different boundary conditions, $f(t)$ - typical time spread function, the value is 1 when steady, the initial value is 0, Δp_p - change in mineral pressure.

The stress coefficient η is not affected by the characteristics of the pore fluid.

The influence of boundary conditions on the elastic stress of holes

A large number of studies abroad show that the variation of pore elastic stress and pore pressure satisfy the following relation formula,

$$\Delta\sigma_x + \Delta\sigma_y + \Delta\sigma_z = 4\eta\Delta p_p \quad (9)$$

In the formula, $\Delta\sigma_x, \Delta\sigma_y, \Delta\sigma_z$ —Pore stress increment in the x, y, z direction,

Δp_p —Variation of pore pressure.

The single stress component in the three directions of x, y, z is greatly affected by boundary conditions, for one dimensional boundary problems with free moving top / bottom boundaries, On the basis of Eq. (9), it is concluded that $\Delta\sigma_x, \Delta\sigma_y, \Delta\sigma_z$ satisfies the following relationships,

$$\begin{cases} \Delta\sigma_x = 2\eta\Delta p_p \\ \Delta\sigma_y = 0 \\ \Delta\sigma_z = 2\eta\Delta p_p \end{cases} \quad (10)$$

Similarly for two-dimensional plane strain boundary problems, $\Delta\sigma_x, \Delta\sigma_y, \Delta\sigma_z$ satisfies the following relationships,

$$\begin{cases} \Delta\sigma_x = \Delta\sigma_y = \eta\Delta p_p \\ \Delta\sigma_z = 2\eta\Delta p_p \end{cases} \quad (11)$$

Similarly, for three-dimensional plane strain boundary problems, $\Delta\sigma_x, \Delta\sigma_y, \Delta\sigma_z$ satisfies the following relationships,

$$\Delta\sigma_x = \Delta\sigma_y = \Delta\sigma_z = \left(\frac{4\eta}{3} \right) \Delta p_p \quad (12)$$

CONCLUSIONS

Based on the analysis above, we can draw the following conclusions:

(1) For the mines containing massive geothermal energy, certain techniques can be employed to fully

utilize the hot rock and the naturally gushing hot water. The flow of mine groundwater in the rock interacts with the rock fracture deformation.

(2) There is a lot of difference between the flow pattern of groundwater in the fractured rock mass and the conventional linear seepage. The deformation of the rock mass will produce a stress on the stratum, whose value is independent of the nature of the water, but merely related with the external force that leads to rock fracture deformation.

Acknowledgements: Financial support is provided by the National Science Foundation of China (51604082, 51204100), China Postdoctoral Fund (2016M602170 and 2017T100508), Key research and development plan of Shandong province (2017GSF20113).

REFERENCES

1. S. Zhang, Mineral resources development engineering. Wuhan Industrial University Press, 4, 485 (2000).
2. Y. Zhao, Rock fluid mechanics in mine. Beijing: China Coal Industry Publishing House. 1991.
3. H.U. Weiyue. Mine flood control theory and method. Beijing, China, Coal Industry Publishing House, 2005.6.8~29.
4. N.P. Walte, P.D. Bonsb, C.W. Passchier, *Journal of Structural Geology*, **27**, 1666 (2005).
5. Panzihua Steel Research Institute, mine branch, A comprehensive study on the mining area of the South support mine and the mining area of Juran mine in advance, 1998, 10.
6. Maanshan Institute of Mining Research, "Seven. Five" national key scientific and technological research project, 1st, Taiyuan, Steel Corp, Jianshan iron ore open-pit slope optimization design method area. 1990, 12.
7. X. Liu, P. Luo. Rock mechanics and petroleum engineering. Beijing: Petroleum Industry Press, 2004.10.84~92.
8. Y. Zhang, Sh. Lu, *Electronic Journal of Geotechnical Engineering*, **21**(12), 10317 (2016).
9. R. Wang, Y. Zhang. *Electronic Journal of Geotechnical Engineering*, **21**(12), 10393 (2016).

Supercritical CO₂ extraction of organic matter from coal based on CO₂ sequestration in deep coal seams

H. Yu*, R. Jiang, L. Chen

School of Chemical and Environmental Engineering, Shandong University of Science and Technology, 266590 Qingdao, China.

Received, August 17, 2017; Accepted November 23, 2017

To evaluate the potential for mobilizing organic matter in coal during CO₂ sequestration into deep coal beds, three coal samples of different rank were extracted with supercritical CO₂ (Sc-CO₂) using a self-assembled experimental device. The results showed that the extract yields decrease with the increase in coal rank, extraction temperature or coal particle size. Sc-CO₂ extraction yields of lignite, bituminous and anthracite coal sample with a size less than 0.2 mm were 749, 218 and 201 mg/kg on a dry, ash-free basis at 40 °C, respectively. Most of the small molecular organics in coal could be extracted at 40 °C with Sc-CO₂, especially for low-rank lignite and high-rank anthracite. Although Sc-CO₂ has a strong dissolution effect on small coal molecules, medium and high pressure (> 7 MPa) did not favor the diffusion of the extract from coal into the CO₂-free phase. The main control factors in Sc-CO₂ extraction of different rank coals may be different, e.g., the dissolved-organics quantity for lignite, the extraction temperature for bituminous coal, and the pore structure of coal for anthracite. These results demonstrate that Sc-CO₂ dissolved small organic molecules trapped within coal will be mobilized with CO₂, which is important to evaluate CO₂ sequestration into deep coal seams.

Key words: Supercritical, CO₂, Extraction, Coal, Sequestration.

INTRODUCTION

The injection of CO₂ into deep coal seams can not only enhance the recovery of coal bed methane, but also sequester CO₂ [1-3]. However, there are many unknowns and gaps in our knowledge to understand sequestration process [4]. This gap of knowledge is due in part to an incomplete understanding of the physical and chemical interactions between CO₂ and coal [5,6]. The possible effect of CO₂ sequestration on environmental quality is not known due to the interactions. For example, CO₂ injected into coal seams may mobilize organic matter from the coal matrix. In the event of CO₂ leakage from the coal bed, this organic matter may be transported into adjacent aquifer units and compromise water quality [7-9].

Solvent extraction of coal has been used to obtain valuable information about coal structure and organic matter in coal [10,11]. Supercritical CO₂ (Sc-CO₂) can extract some valuable compounds from plant matter to replace conventional organic solvents [12-14]. Sc-CO₂ can dissolve small organic molecules and their presence in the coal makes it necessary for researchers to consider Sc-CO₂ extraction of coal [8, 15]. Soluble small molecules from coal not only affect the migration of CO₂ in coal seams [16], but also pollute groundwater [17], causing serious environmental safety and health (ES&H) problems [1].

There have been some works on Sc-CO₂ extraction of coal. Reucroft *et al.* [18] and Larsen [19] reported that CO₂ storage in coal is not a simple adsorption, but is dissolution. Kolak and Robert [8] reported that the total measured alkane concentrations extracted from the coal samples ranged from 3.0 mg/kg (anthracite) to 64 mg/kg (lignite) of dry coal. Karacan [20] reported that some organic matter in coal can be dissolved in CO₂ at long-term contact of coal with CO₂.

In this paper, Sc-CO₂ extraction of coal samples with different rank was carried out with a self-assembled extraction device at a given pressure and temperature. The dissolution by Sc-CO₂ of small organic molecules involved in CO₂ injection in coal seams was discussed. The results can lay the foundation for studying CO₂ migration in coal reservoirs, prediction of reservoir pressure change, coal seam permeability and ES&H problems.

EXPERIMENTAL

Experimental apparatus and materials

Experimental apparatus

The basic configuration of the self-assembled device for Sc-CO₂ extraction, built on the basis of the classical Sc-CO₂ extraction system, is shown in Fig. 1 [21-25].

The essential parts of the experimental device mainly include pressurization for CO₂ injection, coal extraction, collection and enrichment of extracts, and extraction yield measurement. (1) The part of Sc-CO₂ pressurization and injection provides clean Sc-

*To whom all correspondence should be sent:
E-mail: yuhongguan65@163.com

CO₂. This part includes a CO₂-cylinder, a booster pump for CO₂ pressurization, a needle valve to open/cut off CO₂ access to the extraction cell, a CO₂ storage tank to remove organic matter from CO₂, and an air-compressor for driving the booster pump. (2) The extraction part can be used to extract organic molecules from coal with Sc-CO₂, including an extraction cell (using a dust filter paper), a manometer for determination of CO₂ pressure in the extraction cell, a needle valve to control CO₂ flow yield, and a water bath for constant extract temperature. (3) Extracts collection part mainly includes a needle valve, two collection vessels, a restrictor to keep the flow-rate constant, an anti-volatilization conduit to avoid extracts volatilization with CO₂, a solvent for trapping extracts, and an ice bath for keeping extracts at low temperature. (4) In the Extracts measurement part the extracts are separated from the solvents and their quantity is determined using a nitrogen blowing system to remove the solvent and an analytical balance to obtain the extract mass.

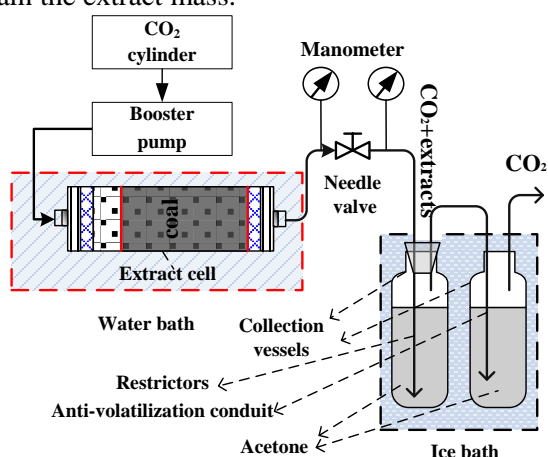


Fig. 1. Simplified diagram of the experimental apparatus

Materials

To investigate the effect of coal rank on Sc-CO₂ extraction, the extraction experiments were carried out using Neimeng bituminous coal, Shanxi anthracite and Yinni lignite. The quality indices of the three coals are shown in Table 1.

The main experimental procedures are shown in Fig. 2, including sample preparation, CO₂ injection and its leak detection, extraction of coal, collection of extract, solvent removal and determination of extraction yield.

Experimental procedure

About 100 g of air-dry coal sample was put into an extraction cell. The temperature of the water bath was set to the adopted value, the pressure in the gas

storage tank was increased to about 20 MPa by the booster pump.

Table 1. Coal quality indices of coal samples

Coal sample	Proximate analysis (wt %)			
	Moisture M_{ad}	Ash A_{ad}	Volatile matter V_{ad}	Fixed carbon FC_{ad}
Yinni	6.89	9.06	42.09	41.96
Neimeng	3.87	7.51	32.65	55.97
Shanxi	2.87	10.51	8.29	78.33

After about 10 min, CO₂ was injected into the extraction cell. The pressurized CO₂ injection operation was completed when the pressure in the extraction cell was stabilized to a set value (10 MPa) for 2 h with repeatedly pressurized CO₂, which means 2 h of static extraction.

Two 5 mL portions of acetone were added to the two collection vessels, respectively, the restrictor was inserted into the first solvent vessel, and the anti-volatilization conduit was inserted into the second vessel.

The extraction program consisted of a 2-h static (no-flow) step followed by a dynamic (flow) step at a flow rate of approximately 5 mL/min. After the extraction, the solvent was transferred into a weighing vial, and was evaporated under a gentle stream of nitrogen. The extract in the vial was weighed and Sc-CO₂ extraction yield of coal was calculated by Eq. (1).

$$\eta_{daf} = \frac{100m_E}{m_C(100 - M_{ad} - A_{ad})} \times 10^6 \quad (1)$$

where η_{daf} is the extraction yield of coal expressed on a dry, ash-free basis, mg/kg; m_E is the mass of the extract, g; m_C is the mass of experimental coal sample, g; M_{ad} and A_{ad} are the moisture and ash content on an air-dry basis in coal, respectively (Table 1), %.

The process of Sc-CO₂ extraction included extraction of raw coal and re-extraction of the extracted coal. Sc-CO₂ extraction of raw coal was carried out at 40, 60 and 80°C. The extracted raw-coal residue at 40°C (EC40) was re-extracted with Sc-CO₂ at 60°C and the extracted EC40 residue at 60°C (EC60) was re-extracted with Sc-CO₂ at 80 °C.

The collection of extracts includes one-stage extraction and multi-stage extraction. The one-stage extraction means that the extracts are continuously collected without replacement of the solvent during the whole extraction process, and multi-stage extraction means replacement of the solvent at different pressure drop stages.

RESULTS AND DISCUSSION

Single-stage extraction of Raw Coal

In order to comprehensively understand the effect of coal rank and temperature on CO₂ extraction, the extraction was carried out under static conditions at 10 MPa for 2 h, followed by dynamic extraction of raw coal at 40, 60 and 80 °C. To ensure that the Sc-CO₂ extract can be completely removed from the coal voids by CO₂, the CO₂ pressure in the extraction cell was continuously reduced from 10 MPa to atmospheric pressure with a flow rate of 5 mL/min. The ratio of extraction yield to CO₂ density (η_{daf}/D) was used to explain the effect of CO₂ density (D) on the extraction. CO₂ density (D) at 40, 60 and 80 °C at 10 MPa was 628.61, 289.95 and 221.60 kg/m³, respectively, calculated by the SW equation [26].

Extraction yields of coal and ratio of yield to CO₂ density (η_{daf}/D) for Yinni, Neimeng and Shanxi coals are shown in Table 2. It can be seen from Table 2 that under the same temperature conditions, the yield decreases with the increase in coal rank, e.g., at 40 °C the η_{daf} value of Yinni lignite is nearly 3.5 times that of Neimeng bituminous coal, and 3.7 times that of Shanxi anthracite. Lignite contains a large number of small organic molecules and a larger pore size while anthracite has a lower number of free small molecules and smaller pore size structures [27].

Table 2. Sc-CO₂ extraction yield and ratio of the yield to CO₂ density (η_{daf}/D) for raw coal

T (°C)	Extraction yield η_{daf} (mg·kg ⁻¹)			η_{daf}/D (kg·mg·kg ⁻¹ ·m ⁻³)		
	Yinni	Neimeng	Shanxi	Yinni	Neimeng	Shanxi
40	749	218	201	1.19	0.35	0.32
60	648	191	172	2.23	0.66	0.59
80	528	154	150	2.38	0.69	0.68

It can be seen from Table 2 that the extraction yield of all coals decreases and the η_{daf}/D value increases with the increase in temperature. This is consistent with the inversely proportional solubility of small molecules to the CO₂ density [28]. The acting force between small organic molecules in coal and the coal matrix decreases when the temperature is raised, which helps extracts to dissociate from coal and be extracted by CO₂. On the other hand, elevated temperature favors the expansion of coal pores and the diffusion of small organic molecules into the free phase of the coal matrix. The decrease in extraction yield with the increase in temperature indicates that the dissolution of small organic molecules in coal is an important factor to control Sc-CO₂ extraction of coal, rather than the interaction of CO₂ with the coal matrix and the pore structure of coal.

Single-stage re-extraction of extracted coal

In order to assess the remaining extracts in Sc-CO₂ extracted coal, the extracted coal from raw coal at 40 °C (EC40) and the residual coal of EC40 at 60 °C (EC60) were re-extracted with Sc-CO₂ at 60 and 80 °C, respectively. Just like the raw coal, EC40 and EC60 were extracted at 10 MPa, and the extracts were continuously collected at a flow rate of 5 mL/min until depressurized to 0 MPa. Table 3 shows the extraction yield of raw coal, EC40 and EC60 and their distribution for Yinni, Neimeng and Shanxi coal.

Table 3. Sc-CO₂ extraction yields of extracted coals and their proportion at different temperatures

T (°C)	Coal	η_{daf} (mg·kg ⁻¹)			Proportion (%)		
		Yini	Neimeng	Shanxi	Yinni	Neimeng	Shanxi
40	Raw coal	749	218	201	83.61	48.14	71.86
60	EC40	36	179	66	3.99	39.51	23.53
80	EC60	111	56	13	12.4	12.35	4.61
Total	-	896	453	280	100	100	100

It can be seen from Table 3 that the Yinni coal has the highest total-extraction yield (896 mg/kg), Neimeng coal takes the second place (453 mg/kg), and Shanxi has the lowest extraction yield (280 mg/kg). The total extraction yield of Yinni coal is nearly 2 times that of Neimeng bituminous coal and 3.2 times that of Shanxi anthracite.

The extraction yield of raw coal at 40 °C is higher than that of re-extraction for EC40 at 60 °C and EC60 at 80 °C, and the percentage of the extraction yield of raw coal in Yinni, Neimeng and Shanxi coal is 83.61%, 48.14% and 71.86% at 40 °C, respectively. Comparing the extraction yields of raw coal and extracted coal (EC40 and EC60), it can be found that most of the small organic molecules dissolved in Sc-CO₂ can be extracted, especially for Yinni lignite.

For the extraction yield of extracted coal (EC40) at 60 °C, Neimeng coal has the highest re-extraction yield (179 mg/kg), Shanxi coal takes the second place (66 mg/kg), and Yinni lignite has the lowest extraction yield (36 mg/kg). The percentage of the extraction yield of EC40 in Neimeng, Shanxi and Yinni coal is 39.51%, 23.53% and 3.99 % at 60 °C, respectively. The re-extraction yields of EC60 at 80 °C are 111, 56 and 13 mg/kg for Yinni lignite, Neimeng coal and Shanxi anthracite at 80 °C, accounting for 12.40%, 12.35% and 4.61% of the total extraction yield, respectively.

Sc-CO₂ extraction depends not only on temperature, pressure [29] and nature of the extract [30], but also on the pore characteristics of coal [31,32], the existing forms of extracts and the force between the extracts and the coal matrix [33,34].

Less than 50% of the Sc-CO₂ extract is extracted from Neimeng raw-coal at 40°C. So, small molecules in Neimeng coal are difficult to extract from coal. The vapor pressure of small molecules in the coal matrix and the pore size in coal increase with temperature increase, the elevated temperature is favorable for the extraction of small molecules in bituminous coal with medium pore size. The elevated temperature is favorable for extraction of Neimeng bituminous coal.

Up to 83.61% of the Sc-CO₂ extract is extracted from Yinni lignite at 40 °C and only 3.69% and 12.40% of the extractable extract from the coal is extracted from the EC40 and EC60 at 60 and 80 °C, respectively. The small organic molecules of Yinni lignite are easily extracted by Sc-CO₂ at 40 °C and the molecules being not easily extracted in the EC60, are extracted by Sc-CO₂ at 80 °C due to the increased vapor pressure of the small organic molecules. The effect of elevated temperature on Yinni lignite is not significant, and most of the extracts can be extracted at 40 °C.

With increasing coalification (progressing from lignite to bituminous coal to anthracite), the amount of lower-molecular-weight species (guest molecules) in coal and the quantity of micropores both increase, but the quantity of macropores and functional groups decreases. The increase in rank is accompanied by a conversion of alicyclic structures to aromatic layer. So, Shanxi anthracite displays the lowest extraction yield and is at the second place as regards extraction difficulty.

Small organic molecules in lignite are easily extracted at 40 °C, the main controlling factor being the quantity of such molecules in coal. Raw coal and extracted coal (EC40 and EC60) for Neimeng coal both have certain amounts of extracts at all extraction temperatures, which indicates that the temperature is the main controlling factor for bituminous coal. Anthracite is also easily extracted at 40 °C, but the main controlling factors of the extraction are the coal pore structure and the force between CO₂ and coal for anthracite.

Multiple extraction with single-stage

Single-stage extraction yield of Yinni lignite is the highest, so this coal was used to investigate the residual extracts obtained by multiple extraction. The raw coal with size less than 0.2 mm was extracted 3 times at 40 °C; the extracted coal at 40 °C (EC40) was re-extracted 2 times at 60 °C, and the extracted coal at 60 °C (EC60) was re-extracted 2 times at 80 °C. The extracts were continuously collected at a flow rate of 5 mL/min until depressurized to 0 MPa, just like the single-stage above. Table 4 shows the yield

of multiple extraction with single-stage and its distribution.

Table 4. Extraction yield of multiple-stage extractions with single-stage and their proportion of raw-coal and extracted-coal samples for Yinni coal

T (°C)	Coal	No.	η_{daf} (mg.kg ⁻¹)			Proportion (%)	
			Each	Subtotal	Total	Each	Subtotal
40	Raw coal	1	753			94.01	
		2	20	801		2.50	81.82
		3	28		979	3.49	
60	EC40	1	35	55		63.64	5.62
		2	20			36.36	
80	EC60	1	84	123		68.29	12.56
		2	39			31.71	

Multi-stage extraction

The main aim of this part was to investigate whether the extract exists at pressures below CO₂ critical pressure of 7.38 MPa. In order to dynamically understand the change in extraction yield, coal extraction experiments were carried out by collecting extracts at different pressure stages, called multi-stage extraction in the following text. Neimeng and Shanxi coals were selected for multi-stage extraction because Neimeng coal only has 48.14% extraction yield (Table 3) at 40 °C and Shanxi coal is anthracite with smaller pore size.

Neimeng coal

Table 5 shows the extraction yield of Neimeng coal at different pressure drop stages. 3 depressurization stages of extraction (10-9 MPa, 9-7 MPa and 7-0 MPa) were carried out for raw coal at 40 °C. The extraction yield of raw coal with a depressurization stage of 7-0 MPa was the highest, and that at 9-7 MPa the lowest. Although CO₂ at a pressure below 7 MPa is in non-supercritical state, the extraction yield was the highest in the depressurization stage at 7-0 MPa. This indicates that there are extracts in the non-supercritical CO₂, which are easy to diffuse into free phase of CO₂ at a lower pressure. In addition, the total extraction yield, 197 mg/kg with the pressure drop of 3 times (solvent removal), is lower than the 218 mg/kg (Table 2) with the single-stage extraction (one solvent-removal). This may be caused by the loss of extracts during nitrogen blowing and natural solvent removal.

EC40 was extracted with CO₂ two times at 60 °C, the first extraction being carried out with 3 depressurization stages (10-8 MPa, 8-6.5 MPa and 6.5-0 MPa), and the second with 2 stages (10-6.5 MPa and 6.5-0 MPa). The re-extraction yield at high pressure (10~8 MPa for the first time and 10-6.5 MPa for the second time) was zero, and the second extraction yield (20 mg/kg) of EC40 was

significantly lower than the first one (161 mg/kg). This means that most of the extracts in EC40 can be extracted with one extraction.

To investigate whether CO₂ has a high extraction yield of Neimeng coal at a lower pressure, CO₂ extraction of Neimeng coal was carried out at a pressure below 7 MPa at 40 °C. The extraction yield was about 3 mg/kg, which indicates that CO₂ in non-supercritical state has a very low extraction capacity for Neimeng coal.

Table 5. Sc-CO₂ extraction yields of raw coal and extracted coal for Neimeng coal under different depressurization stages

T (°C)	Coal	No.	Pressure (MPa)	η _{daf} (mg.kg ⁻¹)		
				Each	Subtotal	Total
40	Raw coal	1	10~9	25	197	
			9~7	20		
			7~0	152		
60	EC40	1	10~8	0	161	423
			8~6.5	25		
		6.5~0	136	20		
		2	10~6.5		0	
80	EC60	1	6.5~0	20	45	
			10~7	10		
			7~5.5	25		
			5.5~0	10		

The re-extraction of EC60 is divided into three depressurization stages (10-7 MPa, 7-5.5 MPa and 5.5-0 MPa) at 80 °C. It can be seen from Table 5 that the extraction yield of EC60 at 80 °C is lower. The extraction yield of Neimeng coal is 423 mg/kg with 4-fold extraction and 11 depressurization stages, which is lower than that of the three-fold extraction (453 mg/kg). This may be due to the loss of extracts during solvent removal mentioned above.

Shanxi coal

The extraction yield with a 10-7.5 MPa depressurization stage was the highest and that at 7.5-5.5 MPa the lowest.

The extraction of EC40 was carried out at 60 °C with 2-fold depressurization (10-7.5 MPa and 7.5-0 MPa). It can be seen from Table 6 that the extraction yield at a depressurization of 10-7.5 MPa is obviously higher than that at depressurization stage of 7.5-0 MPa.

Just like EC40 extraction, the extraction of EC60 was carried out at 80 °C with 2-fold depressurization (10-7.5 MPa and 7.5-0 MPa). No extracts were detected at depressurization stage of 10-7.5 MPa, and the extraction yield of EC60 was very low at a depressurization stage of 7.5-0 MPa.

The extraction yield of Shanxi coal is 264 mg/kg with 7-fold depressurization, which is lower than that of the 3-fold extraction (280 mg/kg). Similar to that of Neimeng coal, the loss of extract during solvent removal will result in a lower extraction yield for the multi-stage extraction.

Table 6. Sc-CO₂ extraction yields of raw coal and extracted coal for Shanxi coal under different depressurization stages

T (°C)	Coal sample	Pressure (MPa)	η _{daf} (mg.kg ⁻¹)		
			Each	Subtotal	Total
40	Raw coal	10-7.5	95	190	264
		7.5-5.5	27		
		5.5-0	68		
60	EC40	10-7.5	50	62	
		7.5-0	12		
80	EC60	10-7.5	0	12	
		7.5-0	12		

Effect of coal size on extraction

In order to investigate the effect of coal size on the extraction, Neimeng raw coal with coal size less than 6 mm was extracted 3 times at 40 °C, EC40 and EC60 were extracted 2 times at 60 °C and 80 °C, respectively. Table 7 shows the extraction yield of Neimeng coal with coal size less than 6 mm.

Table 7. Sc-CO₂ extraction yields of raw coal and extracted coal samples of Neimeng coal (<6mm)

T (°C)	Coal	No.	η _{daf} (mg/kg)		
			Each	Subtotal	Total
40	Raw coal	1	22	53	152
		2	13		
		3	18		
60	EC40	1	11	24	
		2	13		
80	EC60	1	40	75	
		2	35		

As can be seen from Table 7, Sc-CO₂ extraction yield of Neimeng coal with size less than 6 mm is much lower than that sized below 0.2 mm. The coal particle size significantly affects the extraction yield and the latter decreases when the coal particle size increases. Coal with a lower particle size is favorable for the diffusion of CO₂ into the coal pores, but also will favor the diffusion of small organic molecules dissolved in CO₂ into CO₂-free phase.

The extraction yield of EC60 at 80 °C (75 mg/kg) is higher than that of EC40 at 60 °C (24 mg/kg). The increase in temperature could effectively expand the micropores of coal and increase the vapor pressure of small organic molecules. Elevated temperature results in that CO₂ more easily diffuses into the micropores of coal, dissolves the small molecules in coal, and extracts are more favorable for entering CO₂ free phase.

CONCLUSIONS

Sc-CO₂ extraction yield of coal decreases with the increase in coal rank. The extraction yield of Yinni lignite, Neimeng bituminous and Shanxi anthracite coal samples with particle size less than 0.2 mm is 749, 218 and 201 mg/kg on a dry, ash-free basis at 40 °C, respectively. With the increase in extraction temperature, the extraction yield of coal decreases. The main small molecular organics in coal could be extracted at 40 °C with Sc-CO₂, especially for low-rank lignite and high-rank anthracite. The extract yield of coal with non-supercritical CO₂ was very low, but the highest quantity of Sc-CO₂ extracts was collected at a pressure below 7 MPa. The shrinkage of the coal matrix facilitates the diffusion of the extracts into CO₂ free phase and a higher yield of extract will be obtained at a lower pressure (<7 MPa). The extraction yield increases with the decrease in coal size. The main controlling factors of Sc-CO₂ extraction of coal rank are different. Under the present experimental conditions, the main controlling factor for Inni lignite is the amount of small organic molecules, for Neimeng bituminous coal - the extraction temperature and for Shanxi anthracite - the micropore structure in coal.

Acknowledgements: This research was supported by the National Natural Science Foundation of China (Grant Nos. 51174127 and 21176145) and Shandong Province Natural Science Foundation (No. ZR2011DM005).

REFERENCES

1. C. M. White, D. H. Smith, K. L. Jones, A. L. Goodman, S. A. Jikich, R. B. LaCount, S. B. DuBose, E. Ozdemir, B. I. Morsi, K. T. Schroeder, *Energy Fuels*, **19**, 659 (2005).
2. H. Yu, G. Zhou, W. Fan, J. Ye, *Int. J. Coal Geol.*, **71**, 345 (2007).
3. H. Yu, L. Zhou, W. Guo, J. Cheng, Q. Hu, *Int. J. Coal Geol.*, **73**, 115 (2008).
4. R. Jiang, H. Yu, L. Wang, *Bulg. Chem. Commun.*, **49**, 509 (2017).
5. B. B. Gathitu, W. Chen, M. McClure, *Ind. Eng. Chem. Res.*, **48**, 5024 (2009).
6. D. Zhang, L. Gu, S. Li, P. Lian, J. Tao, *Energy Fuels*, **27**, 387 (2013).
7. A. Scherf, C. Zetzl, I. Smirnova, M. Zettlitzer, A. Vieth-Hillebrand, *Energy Procedia*, **4**, 4524 (2011).
8. J. J. Kolak, R. C. Burruss, *Energy Fuels*, **20**, 566 (2006).
9. R. Jiang, H. Yu, L. Wang, *J. China Coal Soc.*, **41**, 680 (2016).
10. B. Tian, Y. Y. Qiao, Y. Y. Tian, K. C. Xie, Q. Liu, H. F. Zhou, *Fuel Process. Technol.*, **154**, 210 (2016).
11. G. Zhou, C. Xu, W. Cheng, Q. Zhang, W. Nie, *J. Anal. Methods Chem.*, **2015**, 467242 (2015).
12. Y. Chen, Q. Han, Y. Wang, Q. Zhang, X. Qiao, *J. Appl. Polym. Sci.*, **132**, 41723 (2015).
13. S. Diankov, P. Subra-Paternault, I. Hinkov, I. Pentchev, *Bulg. Chem. Commun.*, **44**, 399 (2012).
14. X. Zhao, C. Wei, J. Zhong, J. Li, *Bulg. Chem. Commun.*, **48**, 153 (2016).
15. S. Atashrouz, H. Mirshekar, *Bulg. Chem. Commun.*, **46**, 104 (2014).
16. L. Zhong, K. Cantrell, A. Mitroshkov, J. Shewell, *Environ. Earth Sci.*, **71**, 4261 (2013).
17. S. W. Hedges, Y. Soong, J. R. McCarthy Jones, D. K. Harrison, G. Irđi, E. Frommell, R. Dilmore, C. White, *Int. J. Environ. Pollut.*, **29**, 457 (2007).
18. P. J. Reucroft, A. R. Sethuraman, *Energy Fuels*, **1**, 72 (1987).
19. J. W. Larsen, *Int. J. Coal Geol.*, **57**, 63 (2004).
20. C. Ö. Karacan, *Energy Fuels*, **17**, 1595 (2003).
21. H. Sovová, *J. Supercrit. Fluids*, **66**, 73 (2012).
22. S. Milosevic, Z. Lepojevic, Z. Zekovic, S. Vidovic, *Hem. Ind.*, **65**, 147 (2011).
23. G. W. Jung, M. S. Uddin, K. T. Kwon, B. S. Chun, *Am J. Biotechnol.*, **9**, 7702 (2010).
24. M. Skerget, M. Bezjak, K. Makovsek, Z. Knez, *Acta Chim. Slov.*, **57**, 60 (2010).
25. S. H. Page, Jr. Bruce A. Benner, J. A. Small, S. J. Choquette, *J. Supercrit. Fluids*, **14**, 257 (1999).
26. R. Span, W. Wagner, *J. Phys. Chem. Ref. Data*, **25**, 1509 (1996).
27. S. Yao, K. Zhang, K. Jiao, W. Hu, *Energ. Explor. Exploit.*, **29**, 1 (2011).
28. T. Sasaki, H. Takeishi, Z. Yoshida, *J. Supercrit. Fluids*, **15**, 23 (1999).
29. Y. C. Sharma, B. Singh, J. Korstad, *Green Chem.*, **13**, 2993 (2011).
30. S. M. Pourmortazavi, S. S. Hajimirsadeghi, *J. Chromatogr. A*, **1163**, 2 (2007).
31. K. Zhang, Y. Cheng, W. Li, D. Wu, Z. Liu, *J. Nat. Gas Sci. Eng.*, **40**, 288 (2017).
32. K. Zhang, Y. Cheng, K. Jin, H. Guo, Q. Liu, J. Dong, W. Li, *Energy Fuels*, **31**, 4731 (2017).
33. K. Araus, E. Uquiche, J. M. Del Valle, *J. Food Eng.*, **92**, 438 (2009).
34. B. Tian, Y. Qiao, Q. Liu, D. Li, Y. Tian, *J. Anal. Appl. Pyrol.*, **124**, 266 (2017).
35. H. Yu, W. Guo, J. Cheng, Q. Hu, *Int. J. Coal Geol.*, **74**, 250 (2008).
36. H. Yu, J. Yuan, W. Guo, J. Cheng, Q. Hu, *Int. J. Coal Geol.*, **73**, 156 (2008).
37. W. Bratek, K. Bratek, I. Gerus-Piasecka, S. Jasieńko, P. Wilk, *Fuel*, **81**, 97 (2002).

Evaluation of regional innovation ability based on green and low-carbon perspective

H. Wang*, L. An, X. Zhang

School of Economics & Management, Northwest University, 710127, Shaanxi xi'an. China

Received September 15, 2017; Accepted November 23, 2017

The aim of this paper is to evaluate the green innovation ability in China. The paper attempted to construct an index system from the three aspects of green innovation and used FAHP to evaluate the innovation ability. The evaluation result of the innovation input and output ability is "general", but the result of innovation environment is "poor". Thus, countries and regions should pay more attention to the environment and energy factors in innovation in future.

Key words: Green innovation, Innovation ability, Evaluation, Innovation input, Innovation output, Innovation environment

INTRODUCTION

Global climate change is becoming increasingly serious, coupled with the global financial crisis. Since 2008, the world began to seek for green and low-carbon economic development mode, to actively change the traditional mode of economic growth, and make a transition from extensive to intensive and green. In 1999, the World Watch Institute pointed out that both industrialized countries and developing countries must take a long-term development strategy to take an ecological road and promote eco-technological innovation. In recent years, China experienced sustained and rapid economic growth partly at the expense of resource and environment. Air pollution in the Beijing Tianjin Hebei region, the Pearl River Delta and Yangtze River Delta have aroused great concern. The phenomenon of atmospheric haze is prominent and the main pollutant emissions exceed the environment capacity. Environmental problems have become some of the most important threats to human health, public safety and social stability. Economic growth means environment damage. Facing the double pressure of resource waste and environment pollution, Chinese government made a "12th Five-Year plan" putting forward the development concept of energy conservation, emissions reduction, green, low-carbon, promoted resource-saving and environment friendly way of production and consumption and encouraged innovation development strategy and green technology to change the ecological environment and promote China economy towards a healthy and sustainable development road.

Recently, scientific and technologic innovation and environmental crisis consciousness of Chinese government constantly increased resources investment in science and technology innovation. We hope to keep growing the scientific and technologic innovation output, at the same time focussing the

attention to environmental protection in order to promote energy conservation and emissions reduction. Some ways such as electric cars, shared cycling, single and double restrictions, etc., have been implemented. Green innovation activity has certain achievements, but there is disparity in comparison with the developed countries's green innovation ability. Trying to find the main factors which influence the innovation ability and measuring region innovation ability have become the major concern in China. According to the main factors that affect the innovation ability, recent research hopes to find a path to promote China's innovation ability, improve the ecological environment, and promote the development of a green innovation process. The evaluation of China region innovation ability and the factors which influence it is practical as a guideline.

REVIEW

The combination of environment and innovation has become a new hot research spot. So green innovation, also known as ecological environment innovation and sustainable innovation has gradually aroused the attention of scholars. Kemp *et al.* defined green innovation as a new technology or new products to avoid or reduce the damage to the environment [1]. Based on the concept of green innovation, Brunnermeier *et al.* found through analysis of factors influencing environment innovation with econometric models that increasing pollution expenditures affected green innovation [2]. An empirical study of the SEM model used by Chiou *et al.* pointed out that green innovation has a significant effect on environment performance and competitive advantage [3]. Because China is on an upswing of economic and social development based on the traditional innovation theory, introducing green ecological concepts, promoting technology innovation activities can lead to a low-carbon economy, green ecological road, and then enhance China's innovation ability, and reduce environment load.

Research on the evaluation of the innovation

To whom all correspondence should be sent:
E-mail: 165253617@qq.com

ability from green low-carbon perspective is still scarce, the majority concentrated on construction of an evaluation index system of innovation ability. Tang and Jiang summarized the research results of the innovation ability evaluation of the final results from three aspects such as evaluation principles, evaluation index system and evaluation index system method [4]. Wei and Han defined the concept and structure of innovation ability, put forward the relevant elements of innovation ability, analyzed the role and impact of different elements of innovation, and pointed out that combining all kinds of elements can achieve sustainable technology innovation [5].

Many attempts have been made to design an evaluation method of innovation ability. Xu *et al.* used a mathematical model of fuzzy comprehensive evaluation to discuss the general program evaluation of innovation ability. The method was scientific, standardized and quantified [6]. Cao and Wang discussed the innovation ability from seven aspects, designed a corresponding index system to correspond to each ability, and gave an explanation to each sub-index connotation [7]. Dong and Fu believed that we must analyze the connotation of innovation ability, follow the design principle of innovation ability evaluation index system, and construct a corresponding evaluation index system. On this basis, Delphy method and multilevel fuzzy comprehensive evaluation method were used to establish a specific evaluation model, so as to provide an operable management analysis tool for the research of innovation ability[8]. Han and Pang searched for a method through all input, output and process features to directly measure the innovation ability. They designed a set of precise evaluation index systems using a fuzzy mathematic method. At last, that research got good results by empirical calculation [9].

Based on previous research, the evaluation of innovation ability on green and low-carbon perspective, needs to develop a set of index systems including input/output of general innovative activities, energy and environment. The evaluation index system can measure the innovation ability based on the green and low-carbon perspective in line with the actual needs of economic and social development.

EVALUATION METHOD

Evaluation index

From the green and low-carbon point of view, the innovation ability index system should include innovation input, innovation output and innovation environment considering energy and environment conditions[10,11]. According to the observability and comparability of the evaluation index system [12], this paper will cover green innovation input, green innovation output and green innovation

environment to construct a regional innovation ability evaluation index system for a certain period of time.

Innovation input is the basic prerequisite for enterprises to carry out technological innovation activities, including resource input and personnel input innovation. R&D personnel and innovation team as the key carrier of tacit knowledge transfer, is an important force to carry out technology innovation [13]. The continuous introduction and cultivation of innovative talents requires adequate financial support. Advanced instruments and equipment provide a guarantee for continuous development of technological innovation activities, and can effectively promote the output of innovative achievements.

Innovation output includes new invention, new technology and new product produced by an area, which can effectively promote social progress, improve work efficiency, or make people's life more convenient [14]. Some potential scientific and technological achievements are also included. Of course, the emergence of technical service undertaking for scientific, technological research is the prerequisite for new products, new technologies and new inventions.

Innovation environment provides an effective guarantee for the cultivation and promotion of regional innovation capability [15]. At the same time, innovation also has a profound impact on the environment and resources. Green innovation advocates the creation of new products, new technologies which do not destroy the natural resources and environment. Specific indicators are embodied in the following.

Fuzzy AHP comprehensive evaluation

X indicates the first level index, and X_i is used as evaluation index i . The evaluation indices are set $X=\{X_1, X_2, X_3\}$. Innovation input is X_1 , innovation output X_2 , innovation environment X_3 . $X_{ij}=\{X_{i1}, X_{i2}, \dots, X_{ik}\}$, $i=1, 2, 3, j=1, 2, \dots, K$. The second-level indicators belong to first-level index.

Use V to denote the hierarchy collection, $V=\{V_1, V_2, \dots, V_p\}$, each level corresponds to a fuzzy subset. If p is too large, it is difficult to describe the attribution of the class. If p is too small, the evaluation is rough and it is difficult to guarantee the quality of evaluation. This article uses 5 levels of evaluation, that is, $p=5$, the corresponding rating for {very good, good, general, poor, very poor}.

Generally speaking, each index in an evaluation index system is not equally important, and their effects on the evaluation results are different. Therefore, before synthesizing, the weights of each index should be determined, and the weight is the variable of a certain index in the total evaluation index system, which represents the contribution

degree of the index to the overall evaluation system. Here, the weight is the weight vector, expressed by ω .

A fuzzy judgment matrix is established to determine the relative importance of the elements. According to the fuzzy judgment scale, the fuzzy judgment matrix is judged by the expert as shown in Table 1.

Table 1 Fuzzy judgment matrix

X	X ₁	X ₂	X ₃
X ₁	0.5	0.4	0.7
X ₂	0.6	0.5	0.6
X ₃	0.3	0.4	0.5

The fuzzy judgment matrix then is transformed into fuzzy consistent matrix. The fuzzy consistent matrices of X₁, X₂ and X₃ are obtained. Then continue to calculate the relative weight as shown in Tables 2 and 3.

Table 2. Weight of first-level indicators

First-level indicators	Weight
Innovation input (X ₁)	0.32
Innovation output (X ₂)	0.31
Innovation environment(X ₃)	0.37

According to the calculation method described in the preceding section, the membership degree of qualitative and quantitative indexes is calculated respectively.

Table 3. Weight of second-level indicators

Second-level indicators	Weight
Number of professional and technical personnel per 10000 persons (X ₁₁)	0.23
Total number of R&D personnel (X ₁₂)	0.19
Technology developers accounted for the proportion of employees (X ₁₃)	0.24
Funding for scientific and technological activities (X ₁₄)	0.19
Proportion of technological development funds in product sales revenue (X ₁₅)	0.16
Patent grant (X ₂₁)	0.23
Proportion of added value of scientific research and comprehensive technical services (X ₂₂)	0.18
Technology market turnover (X ₂₃)	0.19
Proportion of output value of new products in total industrial output value (X ₂₄)	0.24
Collected papers (X ₂₅)	0.16
Environment pollution index (X ₃₁)	0.35
Comprehensive energy consumption output rate (X ₃₂)	0.37
Government policy, innovation, support (X ₃₃)	0.28

Membership degree of the evaluation index

Taking the index of "government policy innovation support strength" as an example, the membership degree of qualitative index is calculated. Because of the fuzziness of qualitative indices, 10 experts were invited to participate in the evaluation of the survey. Take the quantitative indicators of "the amount of funding for science and technology activities" as an example. The average amount of funding value is 317, the highest is 446, and the lowest is 106. The difference will be divided into 5 regions: (106, 174) (174, 242) (242, 310) (310, 378) (378, 446). This index's membership degree "very good" is 0, "good" is 0.11, "general" is 0.89, "poor" and "very poor" is 0. Other statistics are shown in Table 4.

Table 4 Membership degree

Indicators	Grade				
	Very good	Good	General	Poor	Very poor
X ₁₁	0	0	0.48	0.52	0
X ₁₂	0	0	0.16	0.84	0
X ₁₃	0	0.19	0.81	0	0
X ₁₄	0	0.11	0.89	0	0
X ₁₅	0	0.25	0.75	0	0
X ₂₁	0	0.43	0.57	0	0
X ₂₂	0	0.32	0.68	0	0
X ₂₃	0	0	0.67	0.33	0
X ₂₄	0	0.46	0.54	0	0
X ₂₅	0	0	0.64	0.36	0
X ₃₁	0	0	0	0.48	0.52
X ₃₂	0	0	0	0.57	0.43
X ₃₃	0.2	0.6	0.2	0	0

Thus, the membership matrix of the first-level index can be obtained.

$$PX1 = \begin{pmatrix} 0 & 0 & 0.48 & 0.52 & 0 \\ 0 & 0 & 0.16 & 0.84 & 0 \\ 0 & 0.19 & 0.81 & 0 & 0 \\ 0 & 0.11 & 0.89 & 0 & 0 \\ 0 & 0.25 & 0.75 & 0 & 0 \end{pmatrix}$$

The other first-level index subordinate degree matrix can also be obtained. As a result, the comprehensive evaluation result vector of innovation input: $Z_{X1} = \omega_{X1} \times P_{X1} = (0, 0.10, 0.62, 0.28, 0)$; the comprehensive evaluation result vector of innovation output: $Z_{X2} = \omega_{X2} \times P_{X2} = (0, 0.27, 0.61, 0.12, 0)$; the comprehensive evaluation result vector of innovation environment: $Z_{X3} = \omega_{X3} \times P_{X3} = (0.055, 0.17, 0.055, 0.38, 0.34)$.

Corresponding to the maximum membership degree of the evaluation results, the grade of the maximum membership degree is the tendency grade of the evaluation result. The maximum membership degree is valid in principle through the validity test.

RESULTS AND DISCUSSION

This paper used FAHP to evaluate the regional green innovation ability in China. The final result is that innovation input ability and innovation output ability are “general”, while innovation environment is “poor”. This conclusion is basically consistent with the reality of China's innovation. In the past, the whole society had been pursuing economic growth excessively, while ignoring the environment. In recent years, people have been fully aware that innovation cannot be achieved at the expense of environment and waste of energy. Sustainable economic and social development can be achieved only by making full use of green resources and creating new technologies to conserve energy.

CONCLUSION

Research on innovation capability, especially green innovation ability, is designed with many different research indicators and research methods. In this paper, the selection of indicators and methods should be further studied to be more scientific and practical. With regard to future research, The authors hope that there will be more research on green innovation, and also hope to make a breakthrough in the construction of a green innovation ability index system and methods.

Acknowledgements: *The authors thank Shaanxi Social Science Foundation Project "Research on innovation driven development of Shaanxi based on value chain upgrading" for financial and instrumental supports.*

REFERENCES

1. R. Kemp, A. Arundel, K. Smith, Survey Indicators for Environmental Innovation, *R. IDEA Paper*, (1998).
2. S.B. Brunnermeier, M.A. Cohen, *Journal of Environmental Economics and Management*, **45** (2), 278 (2003).
3. T.Y. Chiou, H.K. Chan, F. Lettice, *J. Transportation Research Part E: Logistics and Transportation Review*, **47** (6), 822 (2011).
4. W. Tang, R.F. Jiang. *J. Scientific and Technological Progress and Countermeasures*, (5), 195 (2007).
5. J. Wei, W. Han, *J. Scientific Research Management*, **6**(12-18), (1998).
6. Z.J. Xu, H. Ling, F.Z. Song. A Fuzzy Comprehensive Evaluation of Technological Innovation Ability, *J. Scientific Study*, **15** (1), 105 (1997).
7. C.Y. Cao, H. Xu, *J. Prediction.*, **2**, 66 (1998).
8. G. Dong, Q.S. Fu, *J. Business Model Research.*, **9**, 33 (2004).
9. J.Y. Han, G.X. Pang, *Journal of Hebei University of Science and Technology*, **3**, 90 (2002).
10. N. Qin, *J. Operations Research and Management Science*, **21** (5), 193 (2012).
11. P. Lanoie, M. Patry, R. Lajeunesse, *Journal of Productivity Analysis*, **30** (2), 121 (2008).
12. F. Zong, *J. Operations Research and Management Science*, **20**(6), 226 (2001).
13. J.C. Guan, K.H. Chen, *J. Technoinnovation*, **30** (5-6), 348 (2010).
14. W. Nasierowski, F.J. Arcelus, *J. Socioeconomic Planning Sciences*, **37** (3), 215 (2003).
15. H. Fogelberg, S. Thorpenberg, *J. Science and Public Policy*, **39** (3), 347 (2012).

Nitrogen transformation and biodiversity characteristics of fluvo-aquic soil from Hebei plain, China

Y. Liu, H. Pang, X. Li, T. Gao*, W. Zhao

Key Laboratory of Biological Technology for Containment Prevention in Hebei Province, School of Environmental Science and Engineering, Hebei University of Science and Technology, Shijiazhuang 050018 China

Received August 17, 2017, Accepted November 23, 2017

To reveal the nitrogen transformations and the microbial community in the upper (0-20 cm) and low (20-40cm) layer of fluvo-aquic soil, the effects of microorganisms were investigated through drip irrigations by Chinese cabbage culture experiments. Three treatments of drip irrigation: groundwater (CK), groundwater with five types of bacteria (I#) and groundwater with one type of bacteria (A#) were conducted. 16S rDNA was used to detect the microbial community. Results suggested that drip irrigation with different bacteria significantly affected the nitrogen transformations in the upper soil layer. The total nitrogen (TN) concentration was the lowest ($483.94 \text{ mg}\cdot\text{kg}^{-1}$) in soils using I# water compared with the other two treatments, suggesting that bacteria in I# water enhanced nitrogen transformation. The highest levels of nitrate in the 6th week of $17.45 \text{ mg}\cdot\text{kg}^{-1}$, $23.98 \text{ mg}\cdot\text{kg}^{-1}$ and $18.14 \text{ mg}\cdot\text{kg}^{-1}$ were found for I#, CK and A# water, respectively. The changes in ammonium concentrations were stable ($0.19\text{-}0.34 \text{ mg}\cdot\text{kg}^{-1}$) in both soil layers treated with different drip irrigations in week 2-9. The TN, nitrate and ammonium concentrations in the lower layer soil showed the same trend but small variation changes compared with that in the upper soil layer. The *phylum* proteobacterium was most prominent among the bacterial phyla in soil, followed by actinobacteria, whereas thaumarchaeota and phyla proteobacteria were dominant among archaea and ammonia oxidizing bacteria, respectively. *Nitrososphaera*, *cenarchaeum* and *candidatus* were the most abundance genera across all soil samples for archaea community and *nitrosomonas* species were dominant as $\text{NH}_4^+\text{-N}$ oxidizers in the soil.

Key words: Fluvo-aquic soil, Nitrogen transformation, Biodiversity, PCR-DGGE

INTRODUCTION

Microorganisms play important roles in the biogeochemical cycling of major nutrients, especially nitrogen (N) in fluvo-aquic soil. Due to microbial activity, soil is the most active area of the N cycle. A large amount of organic nitrogenous compounds are easily transformed by microorganisms into ammonium ($\text{NH}_4^+\text{-N}$) and then can be oxidized to nitrate ($\text{NO}_3^-\text{-N}$) through nitrification. $\text{NO}_3^-\text{-N}$ is converted to N_2 which is released into the atmosphere through de-nitrification process [1]. $\text{NH}_4^+\text{-N}$ oxidation is a key step in the N cycle because $\text{NO}_3^-\text{-N}$ as a final product of nitrification benefits plant growth [2].

Traditionally, nitrification is mainly carried out by ammonia-oxidizing bacteria (AOB) [3], and AOB occurring in soils are known to belong to β -proteobacteria represented by the genera *Nitrospira* and *Nitrosomonas* [4]. It was also found that ammonia-oxidizing archaea (AOA) may be another group of ammonia oxidizers [5]. The AOA are wide-spread in diverse environments, including soils [6], wastewater treatment bioreactors [7], marine sediments [8] and open ocean water [9]. Several studies indicated that AOA even outnumbered AOB in soils [10, 11], however, it is

still not clear which group of ammonia-oxidizing microorganisms plays a more important role in the fluvo-aquic soils.

Previous studies indicated that many factors such as nitrogen fertilization, pH, ammonia/ammonium, soil moisture, organic carbon, irrigation water quality, temperature, and salinity can affect the abundance and community structure of AOA and AOB [5]. Among them, irrigation water qualities are considered as an important factor affecting soil microbial community composition and activity. The impacts of irrigation with different water qualities on the soil microbial community have been partially evaluated and show contrasting results [12]. Therefore, it is important to determine the microbial structure of the AOB and AOA community in response to different irrigation water quality to understand the microorganism responsible for ammonia oxidation pathway occurring in fluvo-aquic soils. On the other hand, changes in microbial structure and activity in turn have important implications for the N transformation in soil. The analysis of gene abundance of these functional groups of microbes could provide a good estimation of soil N transformations [13]. To date, only a few studies have examined the effects of water quality on soil microbes [14-16]. To the best of our knowledge, the effects of drip irrigation with different bacteria on soil microorganisms and soil nitrogen transformations have not been evaluated.

To whom all correspondence should be sent:
E-mail: taizhonggao@hebust.edu.cn

Thus, the aim of this research was: 1) to understand the effect of water quality on the abundance and community compositions of soil microbial communities; 2) to determine the effect of water on soil N transformations and contributions of AOA and AOB in soils. Considering the high complexity and biodiversity of soil microbial communities, a 70-day experiment using typical fluvo-aquic soil in China was designed and the change in $\text{NH}_4^+\text{-N}$ and $\text{NO}_3^-\text{-N}$ concentrations and gene abundance of total bacteria was analyzed. Special attention was paid to functional microbes (N-fixation bacteria, AOA, and AOB) using real-time quantitative PCR.

MATERIALS AND METHODS

Soil samples

Fluvo-aquic soils (0-40 cm) were collected from Wuqiang County. The field site was located in the eastern part of China ($38^\circ18'32''$ N, $115^\circ58'41''$ E), comprising a total area of approximately 67 987 km^2 of the Hebei plain, with a population of about 50 million people. The site lies between the west of the Bohai Bay and the east of the Taihang Mountain.

Soils were collected from soil cores (20 cm diam \times 40 cm deep) with a split soil corer (AMS, Inc., American Falls, ID, USA) and pooled by split-plot. Cores were arranged in a randomized complete block design with 3 replications. The samples were sieved through a $<2\text{mm}$ sieve to remove plant tissue and divided into upper layer (0-20cm) and lower layer (20-40cm) according to the depth of site. All soil samples were kept cool with ice in the field and maintained at 4°C in the lab until processed. Chemical and physical properties of the soil are shown in Table 1.

Experimental design and treatment

Experiments were carried out on soil culture-potted Chinese cabbage from Aug. 7 to Oct. 5, 2015.

They consisted of three treatments of drip irrigation: groundwater (CK), groundwater with five types of bacteria (I#, 100:1, v/v), groundwater with one type of bacteria (A#, 100:1, v/v), each with three replicates. The amount of bacteria in the liquid was $10^6\text{CFU}\cdot\text{mL}^{-1}$. The five types of bacteria in I# were all gram-positive (G^+) bacteria, including *arthrobacter* species, *ensifer* species, *empedobacter*

species, *chryseobacterium* species, and *zobellella* species. These five species show high N transformation quality [17-20]. The bacterium in A# was a strain of *bacillus subtilis*. It is a Gram-positive bacterium commonly found in soil and is an excellent model organism for the study of basic cell processes. The application of *Bacillus subtilis* to the soil or *via* seed may provide disease control [21].

All bacteria used in this study were purchased from the Chinese Academy of Sciences, Institute of Life Science, Beijing. The Chinese cabbage was dripped once a day using an irrigation system after budding, and the amount was 50 ml at a time. The Chinese cabbages were protected from heavy rainfall and strong light and removed after incubation of 5 weeks. Soil was regularly loosened. During the study period, soil samples were collected once every 7 days from the upper and lower layers. The samples were dried naturally, sieved, and then analyzed.

Genomic DNA extraction and PCR

Bacterial genomic DNA was isolated from 0.3g soil samples according to the CTAB/SDS method. DNA was diluted to $1\text{ ng}\cdot\mu\text{l}^{-1}$ using sterile water. Its concentration and purity were quantified using a NanoDrop ND-1000 spectrophotometer (NanoDrop Technologies, USA) by running it on 1% agarose gel with 0.5 M tris-borate-EDTA buffer. The samples were then transported to Novogene Bioinformatics Technology Co. Ltd. (Beijing, China) for PCR optimization and pyrosequencing analysis.

PCR was performed with 16S/18S rRNA gene primers. All PCR reactions were carried out on $30\ \mu\text{l}$ PCR mixtures with $15\ \mu\text{l}$ Phusion[®] High-Fidelity PCR Master Mix (New England Biolabs, Ipswich, USA), $0.2\ \mu\text{M}$ forward and reverse primers, and about 10 ng template DNA. Thermal cycling procedure consisted of initial denaturation at 98°C for 1 min, followed by 30 cycles of denaturation at 98°C for 10 s, annealing at 50°C for 30 s, extension at 72°C for 30 s, and a final extension at 72°C for 5 min. The PCR products were examined by 2% agarose gel electrophoresis and were purified with the GeneJET Gel Extraction Kit (Thermo Fisher Scientific, MA, USA). Samples with a band between 400-450bp in gel electrophoresis were chosen for further experiments.

Table 1. Physicochemical characteristics and nitrogen concentration of the fluvo-aquic soil samples.

Sampling location (depth)	pH	Organic matter (g/kg)	TN (g/kg)	$\text{NO}_3^-\text{-N}$ (mg/kg)	$\text{NH}_4^+\text{-N}$ (mg/kg)	$\text{NO}_2^-\text{-N}$ (mg/kg)	Bacterial concentration (CFU/g)
Wuqiang(0-20 cm)	7.8	28.6	1.6	139.2	2.86	0.2	2.6×10^6
Wuqiang(20-40cm)	7.8	17.8	1.0	35.9	0.68	0.3	3.4×10^6

Illumina sequencing and data analysis

Sequencing libraries were generated using NEBNext® Ultra™ DNA Library Prep Kit for Illumina® (New England Biolabs), following the manufacturer's protocol, and index codes were added to them. The library quality was assessed on the Qubit® 2.0 fluorometer (Thermo Fisher Scientific) and Agilent 2100 bioanalyzer. Finally, the library was sequenced in an IlluminaHiSeq platform, and 250 bp paired-end readings were generated.

The relative abundance of major phyla and genera were used to describe the microbial community composition. To compute the alpha diversity, Shannon diversity index was calculated at 97% operational taxonomic unit level.

Chemical analysis

Soil samples were thoroughly mixed in the lab and analysis of chemical and physical properties of soils was done by standard procedures. TN, NO₃⁻-N, NH₄⁺-N and NO₂⁻-N were analyzed according to Chinese SEPAS standard Methods[22]. Soil pH was measured by a single function pH electrode (R-27012-06, Cole-Parmer Inc.) using a soil-to-water ratio of 1:2.5.

RESULTS AND DISCUSSION

Effect of bacteria on soil N concentration

Effect of bacteria on TN concentration

The effect of bacteria on soil TN concentration is shown in Figure 1. TN concentration shows similar trends in the upper soil layers after drip irrigation with different bacteria, showing an initial decrease from weeks 1–5, when the Chinese cabbage absorbed soil nutrients during its growth stage and then the variations became smooth. The minimum TN concentration in the upper soil layer was shown in week 5 when Chinese cabbage was grown up. It was 483.94 mg·kg⁻¹ using I# water drip-irrigated treatment, which is lower than CK water drip-irrigated (528.45 mg·kg⁻¹) and A# water drip-irrigated (699.99 mg·kg⁻¹) treatment in upper the soil layer. Reasonable interpretation is that the bacteria in I# water enhanced N transformation, result in higher NO₃⁻-N and NH₄⁺-N release, which were easily absorbed by Chinese cabbage. Therefore the TN in the upper soil layer using I# water was the lowest as N was transferred from soil to the Chinese cabbage. The N in the Chinese cabbage should be further detected.

After the Chinese cabbage was harvested, the TN in the upper layer tended to significantly increase to 932.66 mg·kg⁻¹, 1042.92 mg·kg⁻¹, 1073.59 mg·kg⁻¹ for I#, CK and A# water in week 10, respectively. Same trend was reported by other studies when conifer species were harvested in forest soil[23].

The TN concentration in the lower layer soil showed the same trend with that in the upper layer soil. However, the changes cope was small. It was observed during the experiments that the soil was drier than the upper layer soil, indicating that the water with different bacteria did not or little reached the lower layer soil because of the depth.

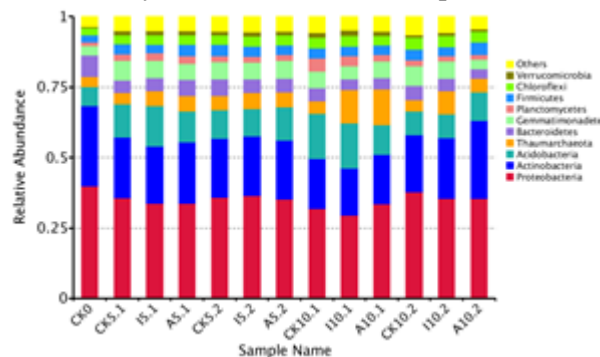


Fig. 1. Effect of bacteria on soil TN change.

Effect of bacteria on NO₃⁻-N concentration

Changes in NO₃⁻-N concentration were similar to those in TN concentration in the upper soil layer after different water drip irrigations (Figure 2). It decreases with the time in week 1-5 from 17.4 mg·kg⁻¹ (before water drip irrigation) to 6.31 mg·kg⁻¹, 7.22 mg·kg⁻¹ and 8.77 mg·kg⁻¹ for I#, CK and A# water in week 5, respectively. The NO₃⁻-N concentration from week 5 to week 6 in the upper soil layer shows a rapid lifting for three different bacteria treatment. This causes the highest levels of NO₃⁻-N in the soil in the 6th week of 17.45 mg·kg⁻¹, 23.98 mg·kg⁻¹ and 18.14 mg·kg⁻¹ for I#, CK and A# water, respectively. This relates to the harvest of Chinese cabbage and the effect of the bacteria. However, there was a slightly decrease in NO₃⁻-N concentration in the upper soil layer since week 7 for these three different treatments. NO₃⁻-N level at I# water treatment did not differ from the treatment of others despite its level of NO₃⁻-N is the lowest one (from 17.45 mg·kg⁻¹ to 14.43 mg·kg⁻¹).

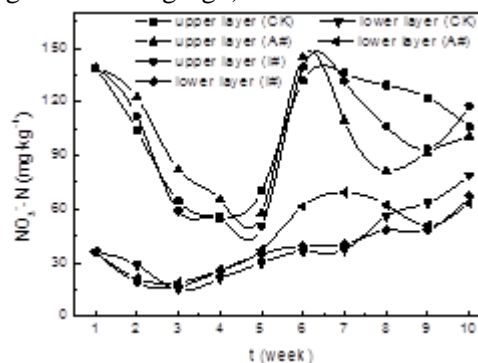


Fig. 2. Effect of bacteria on soil NO₃⁻-N change.

It is likely that bacteria in I# water stimulate the growth of soil nitrifying bacteria so NO₃⁻-N is the highest in soil by I# water treatment. Decrease of NO₃⁻-N by I# water treatment is also the slowest when compared to the other two treatments. As the

experiment continued, the diversity and quantity of microbes, especially bacteria in I# water, increased because of reproduction and organic N was continuously converted to NO₃⁻-N through nitrification, leading to an increase in NO₃⁻-N concentration[24].

Effect of bacteria on NH₄⁺-N concentration

The effect of different bacteria on NH₄⁺-N concentration in the soil is shown in Figure 3.

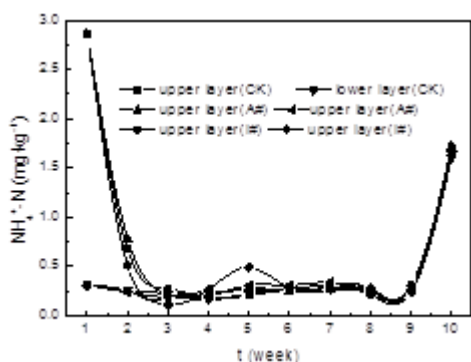
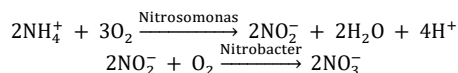


Fig. 3. Effects of bacteria on soil NH₄⁺-N change.

The changes in NH₄⁺-N concentration were stable (0.19-0.34 mg·kg⁻¹) in the lower soil layers related with different drip irrigations during weeks 2–9. The values did not change overall, probably due to the decrease in nutrient requirements of Chinese cabbage, low diversity and quantity of aerobic microbes, and weakening of the biochemical action of the N cycle[25]. Interestingly, during weeks 9–10, NH₄⁺-N concentration greatly fluctuated and the values sharply increased higher than the initial values. Further research should be done to find a reasonable explanation. The changes in NH₄⁺-N concentration in the upper soil layer were also similar after treatment with different drip irrigations. There was no significant difference between the upper and lower soil layer.

The changes in NH₄⁺-N lever during the experiments maybe due to the nitrification process in the aerobic surface soil [7]. The reaction is:



The reprocesses probably also affect the content of TN in the soil as shown in Figure 1.

Analysis of the whole microbial community

The relative abundance of the 10 most abundant phyla is shown in Figure 4. No significant differences in bacterial abundance were observed among the different drip irrigations and incubation times. The bacterial distribution showed that *Proteobacteria* was the most dominant phylum with mean relative abundance of 35.0%, followed by *Actinobacteria* (21.3%) and *Acidobacteria* (11.1%). The same predominant groups have been previously observed in other studies on other soil

samples[26].The remaining phyla including *Thaumarchaeota*, *Bacteroidetes*, *lanctomycetes*, *Gemmatimonadetes*, *Firmicutes*, *Chloroflexi*, and *Verrucomicrobia*, accounted for <34% of the relative abundance observed, and were designated as minor. In addition, 5.1% of the clones could not be assigned to any particular phylum, after comparison with RDP and/or GenBank databases, or else had a sequence length too short to be conclusive.

Shannon diversity index (H) was calculated by the formula $H = -\sum p_i \ln p_i$, where p_i is the ratio of

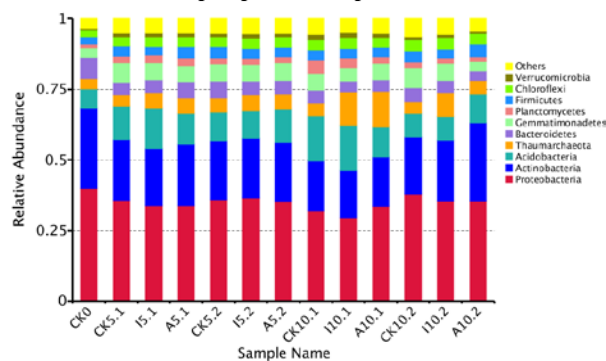


Fig. 4. Relative abundance of 10 most abundant phyla in the bacteria under drip irrigation with CK, I# and A# water.('5' represents the incubation after 5 weeks, '10' represents the incubation after 10 weeks, '1' represents the upper layer, '2' represents the lower layer).

The relative intensity of band i and the relative intensity of the lane, used to estimate the species diversity in the soil are listed in Table 2. Shannon diversity indices of bacteria indicated that different drip irrigations and incubation times affected the soil bacterial community diversity. After 10 weeks of incubation, the values of H for soils with different drip irrigations slightly decreased (e.g., from 9.6 to 9.4 for I5.1 and I10.1, respectively), except the soil irrigated with only CK water, which slightly increased (e.g., from 9.6 to 9.7 for CK5.1 and CK10.1, respectively). However, all H values were higher than that of soil sample CK0, suggesting a high level of species diversity in the soil after irrigation with different bacterial water.

Table 2. Soil microbial functional diversity indices based on the Shannon diversity index

Samples	Bacteria	AOA	AOB
CK0	8.485	4.322	0.36
CK5.1	9.641	4.698	0.196
I5.1	9.635	5.199	0.161
A5.1	9.64	3.5	0.407
CK5.2	9.672	4.312	0.699
I5.2	9.595	4.174	0.183
A5.2	9.635	4.62	0.278
CK10.1	9.743	3.996	0.181
I10.1	9.439	4.063	0.225
A10.1	9.348	5.255	0.242
CK10.2	9.748	4.86	0.666
I10.2	9.543	5.195	0.444
A10.2	9.37	4.038	0.231

The species diversity of AOA had a vastly different trend compared to that of the bacterial community (Table 2). Mean value of H (4.5) was consistently higher in soil samples irrigated with water than in the sample without any treatment (CK0, 4.3), whereas it was lower or higher for each sample in the control treatment as compared to the sample CK0, with no consistent trend.

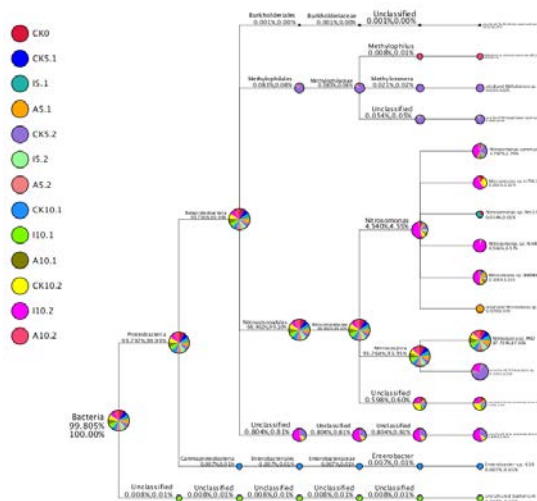


Fig. 5. Species classification tree of 20 predominant AOB in soil samples. the former percentage was of all species and the latter accounts for the percentage of the selected species in the sample.

Previous findings have shown that *Nitrosospira*-like species are the dominant species of AOB in paddy soil [27]. Our phylogenetic analysis results provided further evidence that *Nitrosomonas* species were dominant and might be the main ammonia oxidizers in the soil (Figure 5).

CONCLUSIONS

In the upper layer soil, the lowest TN level was 528.45 mg·kg⁻¹, 483.94 mg·kg⁻¹, and 699.99 mg·kg⁻¹ for CK, I# and A# water soils in the 5th week, respectively, and the lowest NO₃⁻-N level was 23.98 mg·kg⁻¹, 17.45 mg·kg⁻¹ and 18.14 mg·kg⁻¹. NH₄⁺-N concentrations were stable during the incubation time except a tremendous decrease from the 1st to the 2nd week and increase from 9th to 10th week. The changes of TN, NH₄⁺-N, and NO₃⁻-N in the lower layer soil showed the same trends as the upper layer soil with low level and smooth changes.

Phylum *proteobacteria* was the most dominant phylum with mean relative abundance of 35.0%, followed by *Actinobacteria* (21.3%) and *Acidobacteria* (11.1%). The AOA community was composed mainly of *Thaumarchaeota* in all samples. *Nitrososphaera*, *Cenarchaeum* and *Candidatus* were the most abundant genera, as for AOB community. *Nitrosomonas* species were dominant and might be the main ammonia oxidizers in the soil.

Acknowledgement: This work was supported by the National Natural Science Foundation of China (grant No. 41373096). Hebei Natural Science Foundation (grant No. E2016208144).

REFERENCES

1. C.A. Francis, J.M. Beman, M.M.M. Kuypers, *The ISME Journal*, **1**, 1 (2007).
2. Y. Yu, G.M. Zeng, Y.N. Chen, J.C. Zhang, Z. Yu, Z.F. Liu, C.X. Hu, *Environmental Science*, **32**, 10 (2011).
3. X. Chen, L.-M. Zhang, J.-P. Shen, W.-X. Wei, J.-Z. He, *Biology and Fertility of Soils*, **47**, 3 (2011).
4. U. Purkhold, A. Pommereningröser, S. Juretschko, M.C. Schmid, H.P. Koops, M. Wagner, *Environ Microbiol*, **66**, 5368 (2000)
5. L. Yan, Z. Li, G. Wang, Y. Gao, Y. Wang, J.-D. Gu, W. Wang, *Ecological Engineering*, **93**, 24 (2016).
6. M. Tourna, M. Stieglmeier, A. Spang, M. Könneke, A. Schintlmeister, T. Urich, A. Richter, *Proceedings of the National Academy of Sciences of the United States of America*, **108**, 20 (2011).
7. T. Zhang, L. Ye, A.H.Y. Tong, M.-F. Shao, S. Lok, *Applied Microbiology and Biotechnology*, **91**, 4 (2011).
8. P. Wang, Y. Wei, T. Li, F. Li, J. Meng, C.L. Zhang, *Geomicrobiology Journal*, **31**, 1 (2014).
9. H. Luo, B.B. Tolar, B.K. Swan, C.L. Zhang, R. Stepanauskas, M. Ann Moran, J.T. Hollibaugh, *ISME Journal*, **8**, 3 (2014).
10. L. Huang, H. Dong, S. Wang, Q. Huang, H. Jiang, *Geomicrobiology Journal*, **31**, 1 (2014).
11. Y. Sher, Z. Ronen, A. Nejidat, *Journal of basic microbiology*, **56**, 8 (2016).
12. C. Becerra-Castro, A.R. Lopes, I. Vaz-Moreira, E.F. Silva, C.M. Manaia, O.C. Nunes, *Environment International*, **75**, 117 (2015).
13. C. Ju, J. Xu, X. Wu, F. Dong, X. Liu, Y. Zheng, *Environmental Pollution*, **208**, Part B, 811 (2016).
14. E. Orlofsky, N. Bernstein, M. Sacks, A. Vonshak, M. Benami, A. Kundu, K. Shapiro, *Agriculture Ecosystems & Environment*, **215**, 140 (2016).
15. W. Tian, Y. Zhao, H. Sun, J. Bai, Y. Wang, C. Wu, *Ecological Engineering*, **70**, 3 (2014).
16. Z. Jin, J. Lei, S. Li, X. Xu., *European Journal of Soil Science*, **66**, 3 (2015).
17. Y. Lei, Y. Wang, H. Liu, C. Xi, L. Song, *Applied Microbiology and Biotechnology*, **100**, 9 (2016).
18. W. Guo, J. Li, M. Shi, K. Yuan, N. Li, G. Wang, *International Journal of Systematic & Evolutionary Microbiology*, **66**, 10 (2016).
19. A.L. Quéré, N. Tak, H.S. Gehlot, C. Lavire, T. Meyer, D. Chapulliot, M. Rohmer, *BMC Genomics*, **18**, 1 (2017).
20. M. Dsouza, *BMC Genomics*, **16**, 1 (2015).
21. N. Ashwini, S. Srividya, *3 Biotech.*, **4**, 2 (2014).
22. Ministry of Environmental Protection of the People's Republic of China. *Environmental Protection*, **7**, 3 (2003).

23. J.A. Foote, T.W. Boutton, D.A. Scott, *Forest Ecology & Management*, **355**, 48 (2015).
24. R. Suntari, R. Retnowati, Soemarno, M. Munir, *International Journal of Agriculture & Forestry*, **3**, 6 (2013).
25. C. Fujii, T. Nakagawa, Y. Onodera, N. Matsutani, K. Sasada, R. Takahashi, T. Tokuyama, *Soil Science and Plant Nutrition*, **56**, 2 (2010).
26. T. Yamada, S. Araki, W. Ikeda-Ohtsubo, K. Okamura, A. Hiraishi, H. Ueda, G. Endo. *Systematic & Applied Microbiology*, **36**, 5 (2013).
27. S. Lu, X. Liu, Z. Ma, Q. Liu, Z. Wu, X. Zeng, Z. Gu, *Frontiers in Microbiology*, **6**, 326 (2016).

Slicing filling principle and repeated mining key technology for extra-thick coal seams in small coal pit destroyed areas

Ch. Li¹, X.-K. Sun², J.-H. Xu³, Q.-L. Chang^{1,2*}

¹ School of Mines, Key Laboratory of Deep Coal Resource Mining of Ministry of Education of China, China University of Mining and Technology, Xuzhou 221116, China

² ShanDong Energy Zibo Mining Group CO.,LTD, Zibo, Shandong 255120, China

³ State Key Laboratory of Coal Resources and Safe Mining, China University of Mining & Technology, Xuzhou 221116, China

Received September 15, 2017; Accepted December 11, 2017

Aiming to solve the problems of the efficiency of repeated mining technique in small coal pit destroyed areas, the principle of slicing filling and repeated mining was applied, and techniques were proposed for slicing grouting filling in small coal pit destroyed areas and reconstruction of cutting layers, spacer layers and support layers. Grouting filling eliminates potential safety hazards in small coal pit destroyed areas. Simultaneously, a complete area which is best for normal mining was built; the thickness and intensity of each layer were determined, and the filling materials and ratio of each layer were also provided. Field application proved that slicing filling and repeated mining achieves good results in safely recycled coal seams in small coal pit destroyed areas with high efficiency. Although the cost of coal is increased by 1.21 CNY (Chinese Yuan) per ton, the approach provides an innovative method for the safe and efficient backfill mining of coal resources in small coal pit destroyed areas and waste utilization in a mining area.

Keywords: Extra-thick coal seam, Small coal pit destroyed area, Slicing filling, Backfill mining technology.

INTRODUCTION

Driven by market interests, some small coal pits conduct predatory coal mining operations which destroy the integrity of the entire coalfield [1-3]. According to the second coalfield predication in our country, the coal resources in Xinjiang, Inner Mongolia, Shanxi and Shaanxi account for 81.3% of the total volume across the country. However, in most mining areas in the northwest regions, small coal pit mining is damaging mining fields especially in Shanxi and Inner Mongolia which have abundant coal resources of high quality [4-6]. As is well known, the areas in the whole coal field destroyed by small coal pit mining activities are called destroyed areas in small coal pit mining, including both mined-out areas and residual coal layer.

Restricted by regional economies and less advanced techniques, the mining technique used in small coal pits is not well developed, including room and pillar mining and alley mining with a recovery rate of less than 20% [7,8]. Accidents such as water inrush, fires, gas explosions and roof collapses are major potential hazards threatening coal mine safety production. In recent years, injuries caused by permeable small coal pits are often seen, especially in mined-out areas [9-12].

Integral coal fields are badly damaged locally by small coal pit mining which also seriously affects the normal layout of large-scale mines working face. Small coal pit destroyed areas are high-risk and inefficient in recycling coal resources and the backfill mining in small coal pit destroyed areas is still in the exploration stage without reliable mining technology and theory.

Therefore, it is necessary to study the technique of restoring small coal pit destroyed areas by grouting filling, and then employing normal mining methods that are taking conventional mining methods to exploit in the working face. Although there has been a lot of research conducted by experts from home and abroad on filling methods and materials in mined-out areas, there are few studies on the key technology of slicing filling thickness and intensity, filling materials and ratios and repeated mining technology [13-17]. The repeated mining technology is mining technology that assigns the working face in the destroyed areas of small coal pit after grouting filling the mined-out areas. This paper studies the slicing filling principle and key repeated mining technology of extra-thick coal seams in small coal pit destroyed areas, providing an innovative theory and technique for the safe and efficient backfill mining of coal resources in small coal pit destroyed areas and waste utilization in mining areas.

To whom all correspondence should be sent:

E-mail: zkdcql@163.com

EXPERIMENTAL

Engineering situation in a small coal pit destroyed area

China Coal Pingshuo Group Co., Ltd., 2# is a modernized extensive mine with an annual production capability of ten million tons. However, it has been badly damaged by small coal pit mining activity. Recoverable reserves in the second mining area 9# are 45.19 million tons, among which the fully mechanized working face B909 covers small coal pit mined-out area of 30,000 m². The length of the working face B909 is 300 m with an advance length of 1600 m and the thickness of the coal seam is 14.5 m with a dip of 1°-3°. There are 7 destroyed areas in the working face, the volume amounting to 20260 m³. There are no poisonous gases or burning zones in these 7 mined-out areas, but a small amount of seepage as shown in Fig. 1. The goaf A, which is close to the open-off cut (“open-off cut” is the roadway of working face formed during the initial mining), is shown in Fig. 2. Under such geological and mining conditions, it is a challenging technical problem to operate a fully mechanized working face of ten million tons and achieve mining with safety and high efficiency.

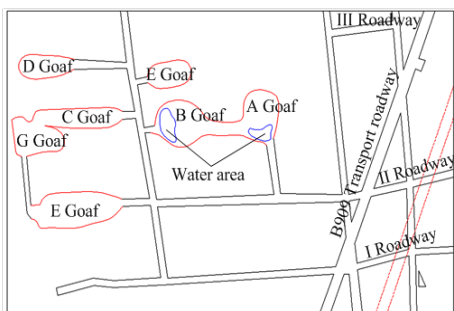


Fig. 1. Working face distribution of mined-out area in a small coal pit

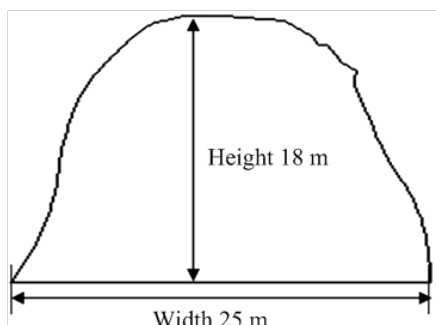


Fig. 2. Space form of small coal pit mined-out area A (length 25 m)

Slicing grouting filling principle and key technology

As shown in Fig. 1, the working face B909 is in a small coal pit which is randomly distributed with a large area of influence. Small face mining will cause a great loss of coal resources and will not ensure

stable production of a ten million tons working face and thus companies will lose economic benefits. Security cannot be guaranteed if the working face is directly pushed through the destroyed area and therefore it is proposed to adopt the slicing grouting filling method in mined-out areas in the small coal pit, then build the coal seam and roof, restore the integral mining area, assign ten million tons fully-mechanized face and conduct normal mining.

Slicing grouting filling principle of small coal pit destroyed area

This technique provides guarantees for assigning working faces of repeated mining to fill small coal pit destroyed areas by grouting which eliminates potential hazards in mined-out areas and, at the same time, is one of the key technologies ensuring safe and high-efficient backfill mining in small coal pit destroyed area. Due to the large space in small coal pit mined-out areas, filling the area with some material will not only increase the cost of filling, but is also against safe and high-efficiency mining. Therefore, a slicing grouting filling technology is proposed that fills the destroyed area by grouting and then builds cutting layers, spacer layers and support layers, as shown in Fig. 3. The cutting layer is at the bottom of the mined-out area in a small coal pit. Above the cutting layer is a spacer layer, constructed by grouting filling and then the support layer, protected by the spacer layer, also ensures that filling material in the support layer and that in the cutting layer automatically separate when a shearer is passing through the cutting layer. The support layer is used to combat the impact of collapsed coal and to protect the working face to safely pass the destroyed area.

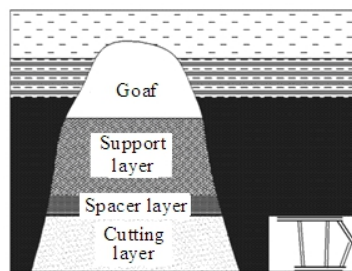


Fig. 3. Filling mined-out area A in a small coal pit

Key technology of slicing grouting filling

The key technology of ensuring that the working face safely passes the destroyed area and thereby realizing high-efficient backfill mining of the coal seam in a small coal pit destroyed area with the lowest cost is to rationally construct a cutting layer, spacer layer and support layer, develop relevant filling materials and find out their appropriate ratio.

(1) Determination of the thickness of cutting layer, spacer layer and support layer. When normal mining commences at the working face in the complete coal seam, it can be seen that the thickness

of the cutting layer is the same as the mining height. The spacer layer protects the support layer from being damaged when the coal feeder is working and ensures that the filling material in the support layer and that in the cutting layer automatically separate. The thickness of the spacer layer is usually less than 10 cm.

The mined-out area in a small coal pit is filled by slicing grouting filling, constructing a support layer, spacer layer and cutting layer to form a comparatively complete mining area and then assigning a working face for normal repeated mining. Figs. 4 and 5 show that when the mining working face is pushed into the filling area in a small coal pit and affected by mining pressure, the roof of the mined-out area in a small coal pit may become unstable and collapse. Coal waste caused by roof collapse would impact the support layer, thus affecting safe repeated mining of the working face. Therefore, the support layer is the crucial factor ensuring safe working at the face and its thickness and intensity are strictly restricted to combat the impact and have a great loading capacity. The height and span of the unfilled space in the mined-out area in a small coal pit, the thickness of the cutting layer and the physical and mechanical parameters determine the weight of the collapsed coal seam and its impact on the support layer. The equation describing the support layer thickness is derived by establishing the mechanical model.

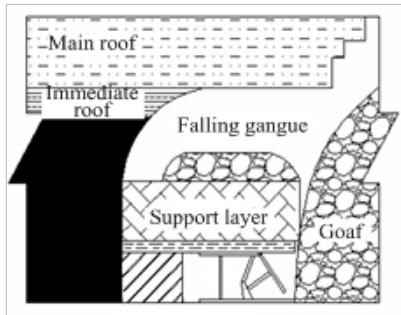


Fig. 4. Profile of filling area working face

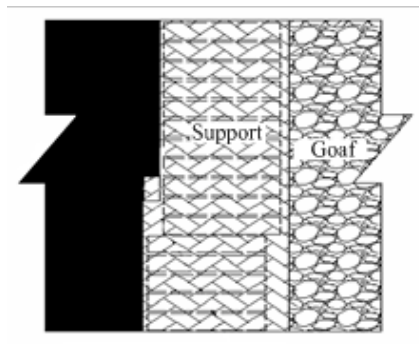


Fig.5. Structure of working face and roof of filling area

Impact force F of caving rock in old workings is as follows:

$$F = P(1 + \sqrt{1 + \frac{2H}{P} \frac{E}{M}}) \quad (1)$$

$$\begin{aligned} \varepsilon_x &= \frac{1}{E}[\sigma_x - \mu(\sigma_y + \sigma_z)] \\ \varepsilon_y &= \frac{1}{E}[\sigma_y - \mu(\sigma_x + \sigma_z)] \\ \varepsilon_z &= \frac{1}{E}[\sigma_z - \mu(\sigma_x + \sigma_y)] \end{aligned} \quad (2)$$

According to the generalized laws of Hooke based on the elasticity theory given in Eq. (2), combining boundary conditions and Mohr Coulomb failure criteria, we get:

$$\frac{F}{2M(l+b)} = c + \frac{\mu F}{(1-\mu)lb} \tan \varphi \quad (3)$$

If the distance between the end face andro of is not destroyed, the thickness of the sup-por t layer M should be:

$$M \geq \frac{K_d P \quad l \quad b}{2(l \quad b + \frac{\mu}{1-\mu} K_d P \quad \varphi) \quad l \quad b} \quad (4)$$

where P is the height of collapsed rock; K_d is the dynamic load coefficient (“dynamic load coefficient” means the impacting coefficient of roof caving rock in small coal pit mined-out areas under the influence of mining); H represents the distance between roof and support layer in the small coal pit mined-out area; E , M and F are the elastic modulus, the thickness of the support layer and the impact force of collapsed rock on the support layer, respectively; l indicates the distance between hydraulic support and coal wall; b is the hydraulic support width of not advancing support in time; the internal friction angle, the cohesion force and the Poisson’s ratio are indicated by φ , c and μ , respectively.

According to B909 geomechanic parameters, combining with space conditions of each mined-out area and Eq. (4), it can be seen that the thickness of the support layer in the B909 mined-out area is more than 5 m, the cutting layer thickness is 3.8 m which is equal to the mining height and the spacer layer thickness is 10 cm.

(2) Performance requirements of filling materials in cutting layer, spacer layer and support layer. In order to ensure safe and high-efficient repeated mining of small coal mine destroyed areas, based on slicing grouting filling repeated mining theory and the function of the cutting layer, spacer layer and support layer, the performance requirements of the cutting layer, spacer layer and support layer are as follows:

Cutting layer: this has the characteristics of a brittle material with a compressive strength of 1-2 MPa, and is convenient for washing.

Spacer layer: this has the characteristics of loose

Table 1. Input parameters for the filling materials

Performance parameters	Performance index		
	Filling material I	Filling material II	Filling material III
Water-cement ratio (by weight)	1:2	2:1	2.5:1
Density (kg/cm ³)	1.250-1.280	0.6-0.65	0.28-0.30
Unilateral filling material (kg)	400-430	300-330	80-100
Hardening time (min)	3-5 (Adjustable)	3-5 (Adjustable)	3-5 (Adjustable)
Final hardening uniaxial compressive strength (MPa)	4.0-5.0	1.5-2.0	0.1-0.4

rock with a compressive strength less than 0.5 MPa, weak tensile and shear strengths.

Support layer: this has the characteristics of plastic materials with a compressive strength greater than 4 MPa.

(3) Performance and ratio of filling materials.

Performance requirements of filling materials: good fluidity, strong permeability, environmental friendliness and low cost.

Ratio of filling materials: basic materials are Remy filling material, fly ash and foaming agent with the ratio of 2:1:0.003 (by weight), an appropriate excipient is added together with water.

By studying material ratios, three filling materials of different performance were developed: filling material I (used to fill reconstructed support layer), filling material II (used to fill reconstructed cutting layer) and filling material III (used to fill reconstructed spacer layer). Relevant parameters of the filling materials are shown in Table 1. Repeated mining key technology of restored small coal mine destroyed area

Parameter design of fully mechanized working face of repeated mining

The mined-out area in a small coal pit is restored with filling technology. Parameter design of fully mechanized working face of repeated mining is the same as with a normal working face with an annual mining production capacity of ten million tons and daily production capacity of more than 30 thousand tons. Fig. 6 shows that the length of working face is 300 m with an advance length of 1600 m.

Repeated mining technology and process of fully mechanized working face

Taking advantage of a roadway to fill a small coal mine destroyed area by grouting, there is no need to supplement roadway support nor to alter the system after the mined-out area is filled. The original support, coal feeder and conveyor need not be changed against the filling area. After filling the mined-out areas in small coal pit destroyed areas, the working face is assigned to mining.

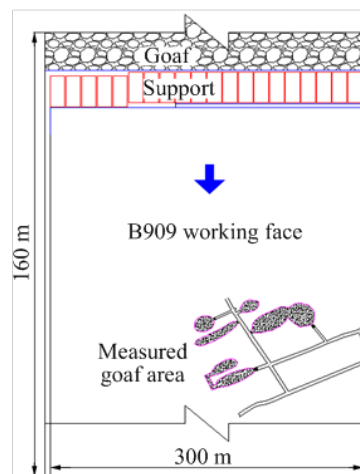


Fig. 6. Arrangement plan of B909 fully mechanized working face

The mining method is a fully mechanized top caving mining method, except for the filling areas. The height of the bottom slicing mining is 3.8 m and the thickness of the caving coal is 10.7 m. The mining technology remains unchanged, however, when the working face is approaching the filling area. However, the advance speed should be reduced in order to fully release the sinking deformation energy of the roof, which is the released energy caused by deformation. When the working face is passing through the filling area, advance speed should be increased in order to avoid the maximum sinking pressure of the roof. The screw type grouting pump and surface grout experiment are shown in Fig. 7, the backfilling technical system is shown in Fig. 8, and the underground construction site is shown in Fig. 9.

Strata-pressure behavior of a fully mechanized working face when passing small coal pit destroyed area

According to the actual measurements of strata-pressure behavior, when a fully mechanized working face is passing through the filling area in a small coal pit, the working resistance of the supports is usually lower. For example, when working face B909 is passing through a mined-out area, the resistance force of the filling section is obviously lower than the caving coal section (Fig. 10).



Fig. 7. Grouting pump and surface grout experiment

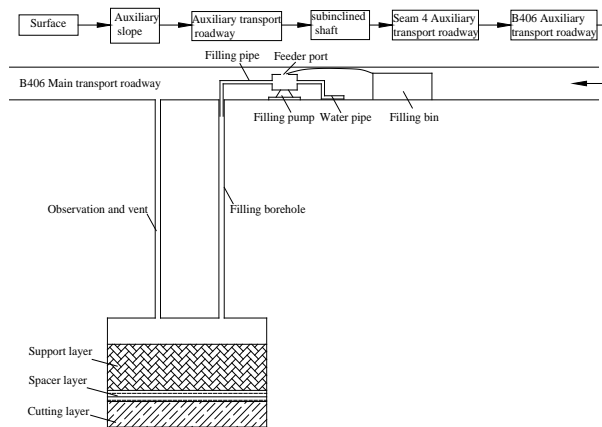


Fig. 8. Backfilling technical system

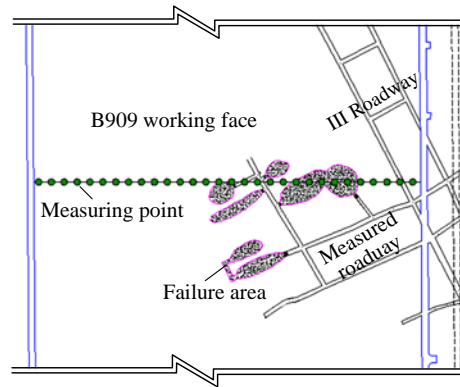


Fig. 9. Underground construction site

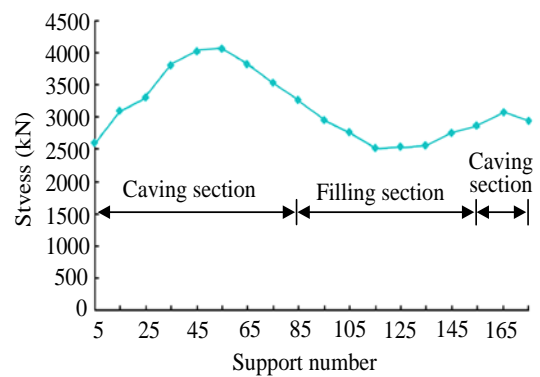
RESULTS AND DISCUSSION

As shown in Fig. 11, the filling and cementation effects are very good and the shearer cuts normally in repeated mining. Coal production of B909 working face reaches 9.1 million tons with a mining rate of more than 87%, which is calculated by subtracting the amount of coal due to mining loss. The volume of these 7 mined-out areas in small coal pits amounts to 20260 m³ using 5329 tons of filling materials which increases the cost of a ton of coal by 1.21 Yuan. The working face passes small coal mine destroyed areas at a fast speed, achieving

safe and highly-efficient mining of a fully mechanized working face in an environmentally friendly manner.



(a) Measuring points arrangement of working face



(b) Stress curve of working face support

Fig. 10. Monitoring and stress curve of B909 fully mechanized working face support



(a) Section of working face passing through cutting layer



(b) Cementation effect of cutting layer

Fig. 11. Effect drawing of small coal mine destroyed area repeated mining

CONCLUSIONS

1. This study fundamentally eliminates the major potential safety hazards of water inrush, fires and gas explosion in mined-out areas and achieves large-scale, continuous, safe and highly-efficient repeated mining of tens of millions of tons from working faces in small coal pit destroyed areas by slicing grouting filling, constructing a cutting layer, spacer layer and support layer, and then assigning the working face for repeated mining.

2. This paper provides the thickness and mechanical performance requirements of the cutting layer, spacer layer and support layer, establishes a mechanical model and derives an equation for support layer thickness. The thickness and mining height of the cutting layer are the same and the compressive strength of the cutting layer is less than 0.5 MPa. The spacer layer is 10 cm thick with a compressive strength of 1-2 MPa. The support layer is more than 5 m thick with a compressive strength of more than 4 MPa.

3. Appropriate filling materials and ratios were developed and the cutting layer, spacer layer and support layer were reconstructed in small coal mine destroyed areas to restore a ten million tons fully mechanized working face. Repeated mining by filling achieved good results with the cost of a ton of coal increasing by 1.21 Yuan and the recovery rate of coal resources increased which ensured regular production of mine and improved its safe production.

Acknowledgements: Financial support for this research was provided by the National Natural Science Foundation of China (No.51304200); Chinese Postdoctoral Science Fund Special Fund Project (No.2014T70560); the China Postdoctoral Science Foundation Project (No.2013M540477); A Project Funded by the Priority Academic Program

Development of Jiangsu Higher Education Institutions; Top-notch Academic Programs Project of Jiangsu Higher Education Institutions; the Special Funds of Taishan Scholar Construction Project of China (201309)

REFERENCES

1. W.G. Huang, Z.T. Wang, Y. Xu, *China Min. M.*, **24**, 4 (2015).
2. Q.Y. Wang, *I Coal*, **12**, 21 (2009).
3. Z.H. Xu, Y.S. Zhao, H.B. Gao, P.L. Gong, *J. China Coal Soc.*, **40**, 33 (2015).
4. X.M. Nie, *Resources Env. Eng.*, **9**, 60 (2009).
5. B.P. Deng, China University of Mining and Technology (Beijing) PhD thesis, Beijing, 2013.
6. B.J. Zhou, J.H. Xu, R. Wu, Z.S. Man, *J. Min. Saf. Eng.*, **3**, 317 (2012).
7. Z.X. Liu, W.G. Dang, Q.L. Liu, G.H. Chen, K. Peng, *J. Min. Science and Technol.*, **23**, 337 (2013).
8. J.M. Zhu, Z.W. Ma, J.H. Xu, J.A. Wu, *Metal M.*, **3**, 10 (2012).
9. X. Wang, M.Y. Weng, *Coal Sci. and Technol.*, **10**, 41 (2012).
10. K.F. Zhang, B.G. Yang, H.G. Yang, W.M. Yuan, Y.N. Zhang, *Coal Sci. and Technol.*, **8**, 60 (2013).
11. Q.X. Huang, L. Li, *Coal Min. Technol.*, **3**, 38 (2011).
12. Q.W. Sun, H. Zhu, Z.L. Cui, *J. China Saf. Sci.*, **11**, 74 (2011).
13. S.W. Wang, Master's thesis of Xi'an University of Science and Technology, Xi'an, 2012.
14. B.S. Choudhary, S. Bhanwar, S. Kumar, *J. Min. Sci. and Technol.*, **23**, 893 (2013).
15. B.P. Deng, H.W. Wang, Y.D. Jiang, S. Liu, C. Wang, *Eng.*, **7**, 72 (2013).
16. Z.G. Ma, J.Q. Fan, K. Sun, G.Z. Zhao, Y.G. Pan, *J. Min. Saf. Eng.*, **28**, 499 (2011).
17. H.Q. Zhang, G.S. Meng, *Coal Sci. and Technol.*, **7**, 8 (2013).

Pyrolysis characteristics and kinetic analysis of waste cooking oil

B. Li^{1*}, J. Li², H. Zhou², Y. Wei¹, H. Wang¹, J. Hu²

¹State Key Laboratory of Complex Nonferrous Metal Resources Clean Utilization, Kunming University of Science and Technology, Kunming 650093, China

²Faculty of Metallurgical and Energy Engineering, Kunming University of Science and Technology, Kunming 650093, China.

Received August 30, 2017; Accepted December 11, 2017

The pyrolysis characteristics of waste cooking oil, pretreated by removing impurities and water, were studied by a thermal analysis technology at heating rates of 5°C, 10 °C and 20 °C /min. The pyrolysis mechanism function $f(\alpha)$ and kinetic parameters of waste cooking oil pyrolysis were determined by the Coats-Redfern method through TG curves. The results showed that the pyrolysis of waste cooking oil could be divided into three stages: volatilization of light components, pyrolysis of heavy components and crack and polymerization of the residue. A three-dimensional diffusion model of the Jander function $3D(n=2)$ was conformed to the pyrolysis process of waste cooking oil with the mechanism function $f(\alpha)=6(1-\alpha)^{2/3}[1-(1-\alpha)^{1/3}]^{1/2}$. The activation energy for the main pyrolysis stage of waste cooking oil pyrolysis increased with the increase in heating rate. The triglycerides in waste cooking oil firstly cracked into fatty acids, acroleins and fatty aldehydes. Then, at a temperature about 400-500 °C, the products of the first step decomposed to small molecules.

Key words: Waste cooking oil; Kinetic analysis; Activation energy; Triglycerides; Coats-Redfern method

INTRODUCTION

In the past several hundred years, fossil fuel has been an important source of energy relied on for survival and development of human society. With the increase in global energy demand and the growing concern of the environment, it is extremely urgent to look for alternative low-carbon, clean and renewable energy resources. The utilization of wastes is an important way to reduce greenhouse gas emissions. According to the Chinese waste cooking oil analysis report, there were above 4.5 million tons waste cooking oil generated in China, but only 8 wt. % of them were used in industrial production. Therefore, a reasonable treatment of waste cooking oil is of great significance to realize the goal of low-carbon and clean utilization of energy resources.

Waste cooking oil is mainly derived from animal fat and vegetable oil which are commonly used in food and beverage industry. It contains toxins. Once it flows to rivers, it will cause pollution of water bodies, which will lead to environmental pollution; if you consume waste cooking oil, it will destroy the white blood cells and digestive tract mucosa, causing food poisoning, and even cancer. But because of its high viscosity and high acid value, it is difficult to be directly used [1]. Waste cooking oil is a kind of biomass oil; it cannot be ignored that waste cooking oil, as a new type of energy, gives similar products as do pyrolysis of fossil fuels. Biomass oil as a substitute for fossil fuels has a certain research foundation, so waste cooking oil has a great

application prospect.

The methods of utilizing waste cooking oil are as follows: soap and detergent production by saponification reaction, feed grade mixed oil after processing, biodiesel production by transesterification with alcohols, as well as biofuels and biogas production by pyrolysis [1, 2]. A lot of studies have been focused on the pyrolysis of waste oil or co-pyrolysis of waste oil and other biomass to produce biodiesel and biogas. The factors of influence include temperature, retention time, heating rate etc. [3-7]. Techniques of thermal and kinetic analysis have been widely applied to reveal the pyrolysis mechanism of biomass [8-10]. Thermal cracking, despite its shortcomings (such as special distillation equipment, various reaction plans and products), is one of the best technologies compared to others. Therefore, this paper proposed waste oil research by pyrolysis. The common methods used for kinetic analysis of biomass pyrolysis include integral methods, differential methods, distributed activation energy method, etc. [11]. The Coats-Redfern method, that is a kind of integral method, has been extensively used to determine the kinetic parameters for biomass pyrolysis due to its simplicity and accuracy.

In this work, the characteristics of waste cooking oil pyrolysis were studied by thermogravimetry (TG) coupled with Fourier transform infrared spectroscopy (FTIR). The pyrolysis kinetic parameters of waste cooking oil were calculated by the Coats-Redfern method through TG curves at heating rates of 5°C, 10°C and 20°C/min,

To whom all correspondence should be sent:

E-mail: libokmust@163.com

respectively. The gasification mechanism of waste oil was determined by analysis.

EXPERIMENTAL

Materials and methods

The waste cooking oil used in this study was obtained from the sewer of the city Kunming, China and pretreated for removing impurities and water. Elemental analysis and proximate analysis were carried out on a Euro-EA 3000. The fatty acid composition of waste cooking oil was analyzed by gas chromatography coupled with mass spectrometry (GC-MS).

The pyrolysis characteristics of waste cooking oil were studied using a TG apparatus (NETZSCH STA 449F3) at the heating rates of 5 °C, 10 °C and 20 °C/min, respectively. Approximately 10 mg of a sample were put into the crucible and heated from ambient temperature to 800 °C with different heating rates in a high-purity nitrogen (99.999%) flow of 50 mL/min. The sample was naturally cooled to ambient temperature after the experiment.

The Perkin Elmer Frontier Fourier transform infrared spectrometer was used to analyze the gas products. The import/export of FTIR was connected with the thermal analyzer. The temperature of the gas pool was 280 °C. The range of infrared spectrum wave numbers was 4000-450 cm⁻¹, and heating rate was 20 °C/min.

Kinetic analysis

The experimental data for kinetic analysis of waste cooking oil pyrolysis were obtained by TG at different heating rates. The degree of conversion for the waste cooking oil pyrolysis is defined as:

$$\alpha = \frac{1 - f_t}{1 - f_0} \quad (1)$$

where f_t is the residual rate at time t , f_0 is the final residual rate.

The reaction rate can be described by a kinetic equation under non-isothermal conditions with a linear regime of temperature increase in time [12] as follows:

$$\frac{d\alpha}{dT} = \frac{A}{\beta} \exp\left(-\frac{E}{RT}\right) f(\alpha) \quad (2)$$

Where α is the degree of conversion, β is the heating rate, E is the activation energy of the reaction, R is the universal gas constant with a value of 8.314 J•mol⁻¹•K⁻¹, $f(\alpha)$ is differential mechanism

function.

Integral for the equation (2) is expressed as:

$$G(\alpha) = \frac{A}{\beta} \int_{T_0}^T \exp\left(-\frac{E}{RT}\right) dT \quad (3)$$

$G(\alpha)$ is defined as:

$$G(\alpha) = \int_0^\alpha \frac{1}{f(\alpha)} d\alpha \quad (4)$$

Combining equations (6) and (7), equation (3) can be presented as equation (5).

$$\frac{A}{\beta} \int_{T_0}^T \exp\left(-\frac{E}{RT}\right) dT = \frac{AE}{\beta R} P(u) \quad (5)$$

$$P(u) = \int_0^u \frac{-e^{-u}}{u^2} du = \frac{e^{-u}}{u^2} \left(1 - \frac{2!}{u} + \frac{3!}{u^2} - \frac{4!}{u^3} + \dots\right) \quad (6)$$

$$u = -\frac{E}{RT} \quad (7)$$

Then make the first approximation to equation (6) and simultaneous equations (3), (5) and (6). The approximate formula of Coats-Redfern can be obtained as:

$$G(\alpha) = \frac{A}{\beta} \frac{RT^2}{E} \left(1 - \frac{2RT}{E}\right) \exp\left(-\frac{E}{RT}\right) \quad (8)$$

From the logarithms of both sides of equation (8), equation (9) is obtained:

$$\ln\left[\frac{G(\alpha)}{T^2}\right] = \ln\left[\frac{AR}{\beta E} \left(1 - \frac{2RT}{E}\right)\right] - \frac{E}{RT} \quad (9)$$

For most reactions, the activation energy $E \gg RT$. The equation (9) can be simplified as

$$\ln\left[\frac{G(\alpha)}{T^2}\right] = \ln\left(\frac{AR}{\beta E}\right) - \frac{E}{RT} \quad (10)$$

So for a constant heating rate, the linear relationship between $\ln(G(\alpha)/T^2)$ and $1/T$ can be obtained. The E can be determined from the slope while A can be calculated from the intercept.

RESULTS AND DISCUSSION

Analysis of the characteristics of waste oil

The results of the ultimate analysis of waste cooking oil are listed in Table 1, showing that the main elements of waste cooking oil are carbon (C), hydrogen (H) and oxygen (O). The fatty acid composition of waste cooking oil was analyzed by GC-MS (see Table 2), showing that the carbon chain length of the fatty acids of waste cooking oil in the range of C16~C18, is consistent with the literature data [13].

Table 1. Ultimate analysis of waste cooking oil

Sample	C	H	O ^a	N	S	M
Waste cooking oil (wt. %)	77.81	12.33	8.93	0.86	0.07	0.54

M: Moisture content; ^a: The oxygen (O) content is determined by difference.

Table 2. GC-MS composition of waste cooking oil.

Composition	C16:0	C18:0	C18:1	C18:2	Others ^a
Content (wt. %)	16.89	7.55	37.45	25.53	12.58

^a: Calculated by difference.

TG analysis of waste cooking oil pyrolysis

The TG curves of waste cooking oil pyrolysis at different heating rates are shown in Fig. 1. There were three weight loss stages for the process of waste cooking oil pyrolysis. The first stage was the volatilization of components with low boiling points, such as moisture, aldehydes, ketones, glycerin and lower fatty acid produced by the decay of oil and fat within the temperature range from ambient temperature to about 200°C [14]. The weight loss rate of the first stage was about 1.6 wt. %. The pyrolysis of heavy components (second stage) took place from about 200°C to 507°C with a weight loss rate above 95 wt. %. The third stage was the crack and polymerization of the residue over 507°C with a weight loss rate of <1wt. %. As shown in Fig. 2, the main weight loss stage for waste cooking oil pyrolysis moved to high temperature zone on rising the temperature. The reason was that the sample was heated more uniformly at the low heating rate, which was conducive to the diffusion of pyrolysis gas, so that the weight loss was more likely to be detected by the balance. The residual rate decreased on rising the temperature, because the heating time of the sample was longer at low heating rate, which promoted the polymerization of macromolecules.

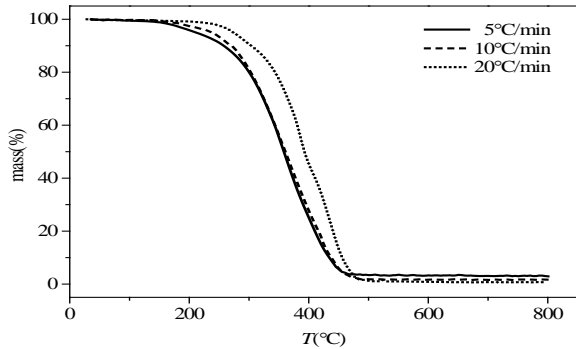


Fig. 1. TG curves of waste cooking oil pyrolysis at different heating rates.

Kinetic calculation of waste cooking oil pyrolysis

The degrees of conversion as a function of temperature for waste cooking oil pyrolysis at different heating rates are shown in Fig. 2. On rising the temperature, the degree of conversion increased and reached a plateau. Similarly to the TG curves,

the α - T curves moved to the high temperature zone with the increase in heating rate.

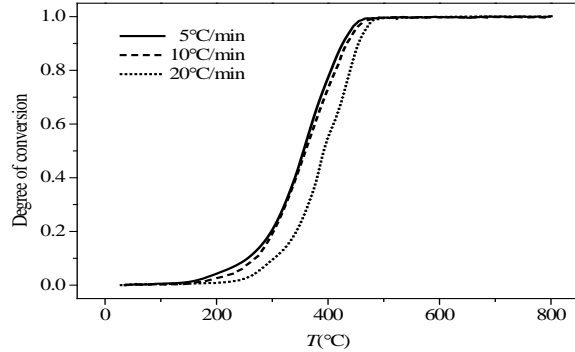


Fig. 2. Degree of conversion as a function of temperature for waste cooking oil pyrolysis.

According to the TG and α - T curves, the second stage of waste cooking oil pyrolysis for different heating rates was chosen for calculation of kinetics because of the significant weight loss rate. Based on the maximum correlation coefficient of $\ln[G(\alpha)/T^2]$ and $1/T$, Jander function 3D ($n=2$) was determined to be the mechanism function of the waste cooking oil pyrolysis from the eighteen mechanism functions listed in Table 3.

The differential and integral forms of Jander function 3D ($n=2$) are shown as equations (11) and (12), respectively.

$$f(\alpha) = 6(1 - \alpha)^{2/3} \left[1 - (1 - \alpha)^{1/3} \right]^{1/2} \quad (11)$$

$$G(\alpha) = \left[1 - (1 - \alpha)^{1/3} \right]^2 \quad (12)$$

Using equations (10) and (12), the Coats-Redfern method is expressed as:

$$\ln \left[\frac{\left[1 - (1 - \alpha)^{1/3} \right]^2}{T^2} \right] = \ln \left(\frac{AR}{\beta E} \right) - \frac{E}{RT} \quad (13)$$

The relationship curves of $\ln\{[1-(1-\alpha)^{1/3}]^2\}/T^2$, and $1/T$ at different heating rates are shown in Fig. 3. The activation energy E and the frequency factor A can be calculated through slope and intercept, respectively, were obtained after fitting linear lines by the least square method. The kinetic parameters of waste cooking oil pyrolysis at different heating rates are shown in Table 4.

Table 3. Expressions of some mechanism functions.

No.	Function	$f(\alpha)$	$G(\alpha)$	R^2
1	Mamplé rule, n=1	$1-\alpha$	$-\ln(1-\alpha)$	0.9869
2	Jander 2D, n=0.5	$4(1-\alpha)^{1/2} [1-(1-\alpha)^{1/2}]^{1/2}$	$[1-(1-\alpha)^{1/2}]^{1/2}$	0.9871
3	Jander 3D, n=0.5	$6(1-\alpha)^{2/3} [1-(1-\alpha)^{1/3}]^{1/2}$	$[1-(1-\alpha)^{1/3}]^{1/2}$	0.9918
4	Jander 2D, n=2	$(1-\alpha)^{1/2} [1-(1-\alpha)^{1/2}]^{-1}$	$[1-(1-\alpha)^{1/2}]^2$	0.9946
5	Jander 3D, n=2	$3/2(1-\alpha)^{2/3} [1-(1-\alpha)^{1/3}]^{-1}$	$[1-(1-\alpha)^{1/3}]^2$	0.9953
6	G-B	$3/2[(1-\alpha)^{-1/3}-1]^{-1}$	$1-2/3\alpha-(1-\alpha)^{2/3}$	0.9935
7	Anti Jander 3D	$3/2(1+\alpha)^{2/3} [(1+\alpha)^{1/3}-1]^{-1}$	$[(1+\alpha)^{1/3}-1]^2$	0.9774
8	Z-L-T 3D	$3/2(1-\alpha)^{4/3} \cdot [(1-\alpha)^{-1/3}-1]^{-1}$	$[(1-\alpha)^{-1/3}-1]^2$	0.9660
9	Avrami-Erofeev, n=1/4	$4(1-\alpha)[- \ln(1-\alpha)]^{3/4}$	$[- \ln(1-\alpha)]^{1/4}$	0.9470
10	Avrami-Erofeev, n=1/3	$3(1-\alpha)[- \ln(1-\alpha)]^{2/3}$	$[- \ln(1-\alpha)]^{1/3}$	0.9750
11	Avrami-Erofeev, n=2/5	$5/2(1-\alpha)[- \ln(1-\alpha)]^{3/5}$	$[- \ln(1-\alpha)]^{2/5}$	0.9800
12	Avrami-Erofeev, n=1/2	$2(1-\alpha)[- \ln(1-\alpha)]^{1/2}$	$[- \ln(1-\alpha)]^{1/2}$	0.9832
13	Avrami-Erofeev, n=2/3	$3/2(1-\alpha)[- \ln(1-\alpha)]^{1/3}$	$[- \ln(1-\alpha)]^{2/3}$	0.9854
14	Avrami-Erofeev, n=3/4	$4/3(1-\alpha)[- \ln(1-\alpha)]^{1/4}$	$[- \ln(1-\alpha)]^{3/4}$	0.9859
15	Avrami-Erofeev, n=3/2	$2/3(1-\alpha)[- \ln(1-\alpha)]^{-1/2}$	$[- \ln(1-\alpha)]^{3/2}$	0.9877
16	Avrami-Erofeev, n=2	$1/2(1-\alpha)[- \ln(1-\alpha)]^{-1}$	$[- \ln(1-\alpha)]^2$	0.9880
17	Avrami-Erofeev, n=3	$1/3(1-\alpha)[- \ln(1-\alpha)]^{-2}$	$[- \ln(1-\alpha)]^3$	0.9884
18	Avrami-Erofeev, n=4	$1/4(1-\alpha)[- \ln(1-\alpha)]^{-3}$	$[- \ln(1-\alpha)]^4$	0.9885

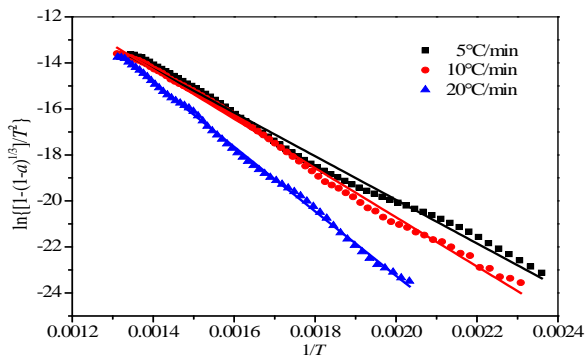


Fig. 3. Relationship curves of $\ln\{[1-(1-\alpha)^{1/3}]^2\}/T^2$ and $1/T$ at different heating rates.

As can be seen, the linear correlation coefficients are over 0.99, which indicated that the model of Jander function 3D ($n=2$) conformed to the process

of waste cooking oil pyrolysis. The activation energy E and the frequency factor A increased with the increase in heating rate, the side chains rupture of aromatic compounds, the C-C bonds cleavage of oxy-compounds in the intermediate products and the decomposition of long-chain hydrocarbons [17, 18].

The bands at $2400-2200\text{ cm}^{-1}$ and $726-586\text{ cm}^{-1}$ indicate the existence of CO_2 resulting from the decarboxylation of fatty acids. The bands in the range of $1880-1650\text{ cm}^{-1}$, due to C=O stretching vibrations, indicated that the generated lipids, aldehydes and ketones contained C=O bonds [16,19]. The characteristic peaks in the range of $1650-1320\text{ cm}^{-1}$ may be caused by the stretching vibrations of aromatic ring C-C and in-plane bending of carboxylic acid COOH, indicated the production of carboxylic acids and hydrocarbons.

Table 4. Kinetic parameters of waste cooking oil pyrolysis.

Heating rate β ($^{\circ}\text{C}\cdot\text{min}^{-1}$)	Temperature range ($^{\circ}\text{C}$)	n	E ($\text{kJ}\cdot\text{mol}^{-1}$)	A (min^{-1})	R^2
5	160-470	2	78.81	1.75×10^4	0.9919
10	180-490	2	88.89	2.09×10^5	0.9963
20	215-507	2	114.61	2.18×10^8	0.9977

The bands at 1300-990 cm^{-1} may be caused by stretching vibrations of C-O-C, linear stretching vibrations of C-C or in-plane bending vibrations of C-H in the aromatic ring, which indicates that ethers, hydrocarbons or phenolic exhalations may be generated in the process of waste cooking oil pyrolysis [20]. From the literature [21], the odd 1-alkenes and n-alkanes are generated by decarboxylation of free radical RCOO cracked from the triglycerides, followed by disproportionation and ethylene elimination. Another free radical RCH₂O transformed to the even alkanes and alkenes by loss a ketene and following disproportion and ethylene elimination. The important production of H₂ mainly results from the crack of hydrocarbons, dehydrogenation of olefins, and the proton extraction from cycloolefins and aromatic hydrocarbons [22] which cannot be detected by FTIR.

The FTIR spectra of waste cooking oil pyrolysis at different temperatures are shown in Fig. 5. The evolution of gas is very weak before 200°C, showing that the primary compounds of waste cooking oil have not pyrolysed at this phase. The characteristic peaks of pyrolysis products become noticeable, indicating waste cooking oil pyrolysis. The primary pyrolysis products contain lipids, hydrocarbons, aldehydes, ketones, acids, etc.

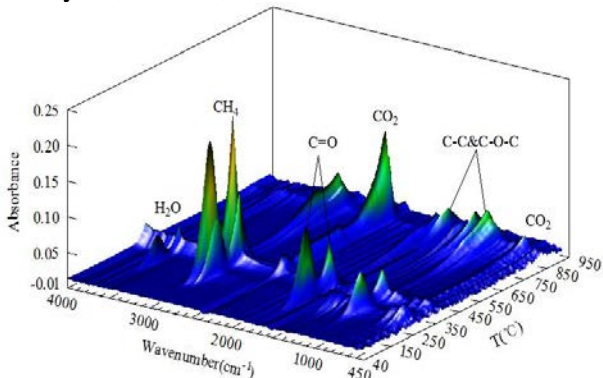
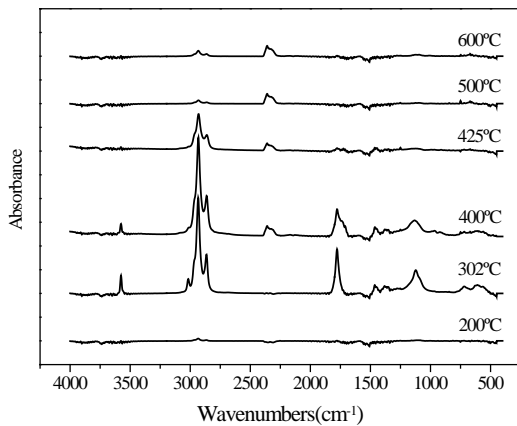


Fig. 4. FTIR spectra of waste cooking oil pyrolysis(20°C).



The pyrolysis products after 450°C are mainly small molecules such as CO₂, CH₄, ketones, aldehydes, ethers, hydrocarbons, etc. The waste cooking oil is mainly derived from vegetable oil and animal fat, which means that the main components of waste cooking oil are all kinds of fatty acid glycerides. However, a part of the fatty acid glycerides would generate acids, aldehydes, ketones, glycerin, hydrocarbons, and bifunctional oxides via oxidation, hydrolysis and pyrolysis in the process of frying and long-term exposure to air and sunshine [23,24]. Although the composition of waste cooking oil is complicated, the studies of fatty acid glycerides pyrolysis made great contribution to reveal the mechanism of waste cooking oil pyrolysis. Chang and Wan provided a complete scheme of triglyceride pyrolysis, which was summarized as two steps [25,26]. Firstly, the triglycerides cracked into fatty acids, acrolein and fatty aldehydes at temperatures lower than 300°C expressed as equation (14). Secondly, the products of the first step cracked into short-chain hydrocarbons at a higher temperature about 400-500°C. The mechanism can be expressed as reactions (14) - (19). The TG-FTIR analysis shows that this theory conforms to the pyrolysis process of waste cooking oil.

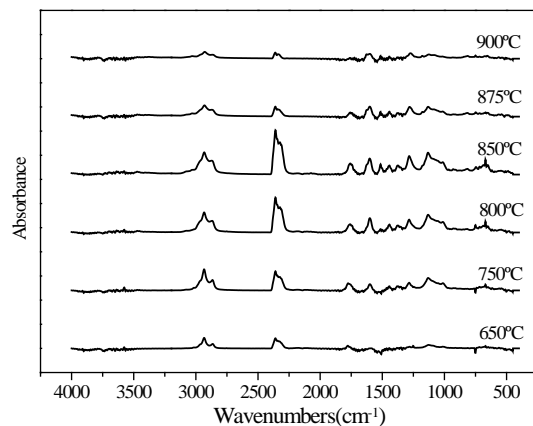
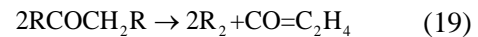
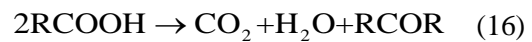
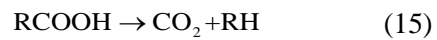
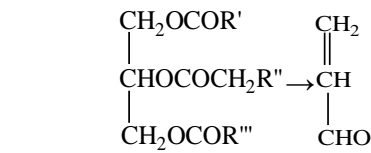


Fig. 5. FTIR spectra of waste cooking oil pyrolysis at different temperatures.

CONCLUSIONS

The pyrolysis of waste cooking oil was investigated. The process of waste cooking oil pyrolysis could be divided into three stages: (i) volatilization of light components from ambient temperature to about 200°C, (ii) pyrolysis of heavy components from about 200°C to 507°C and (iii) crack and condensation of the residue above 507°C. The weight loss rates for these three stages were about 2 wt. %, 95 wt. % and 1wt. %, respectively.

The mechanism function $f(\alpha)$ and the kinetic parameters for the main stage of waste cooking oil pyrolysis were determined by the Coats-Redfern method. The Jander function $3D(n=2)$ was chosen to determine the mechanism of waste cooking oil pyrolysis with the mechanism function $f(\alpha)=6(1-\alpha)^{2/3}[1-(1-\alpha)^{1/3}]^{1/2}$. The activation energies were 78.81kJ/mol at 160-470°C at 5°C/min, 88.89kJ/mol at 180-490°C at 10°C/min and 114.61kJ/mol at 215-507°C and 20°C/min, respectively, which showed that activation energy increased with the increase in heating rate.

There were two steps of the pyrolysis of triglycerides in waste cooking oil. Firstly, the triglycerides cracked into fatty acids, acrolein and fatty aldehyde at temperatures lower than 300°C. Secondly, the products of the first step decomposed into short-chain hydrocarbons, aldehydes, ketones, H₂O, CO, CO₂, H₂, etc., at temperatures about 400-500°C.

Acknowledgements: This project was supported by the National Natural Science Foundation of China (No.U1602272 and 51664039).

REFERENCES

1. M.G. Kulkarni, A.K. Dalai, *J. Eng. Chem. Res.*, **45**, 2901(2006).
2. A.B. Chhetri, K.C. Watts, M.R. Islam, *J. Energies*, **1**, 3 (2008).
3. A.P.S. Chouhan, N. Singh, A.K. Sarma, *J. Fuel Process. Technol.*, **109**, 217 (2013).
4. A.N. Phan, T.M. Phan, *J. Fuel*, **87**, 3490 (2008).
5. A.B. Hassen-Trabelsi, T. Kraiem, S. Naoui, H. Belayouni, *J. Waste Manag.*, **34**, 210 (2014).
6. V.R. Wiggers, A. Wisniewski, L.A.S. Madureira, A.A.C. Barros, H.F. Meier, *J. Fuel*, **88**, 2135 (2009).
7. T. Ito, Y. Sakurai, Y. Kakuta, M. Sugano, K. Hirano, *J. Fuel Process.*, **94**, 47 (2012).
8. S. Xiu, H.K. Rojanala, A. Shahbazi, E.H. Fini, L. Wang, *J. Therm. Anal. Calorim.*, **107**, 823 (2012).
9. M.R. Othman, Y.H. Park, T.A. Ngo, S.S. Kim, J. Kim, *Korean J. Chem. Eng.*, **27**, 163 (2010).
10. S.H. Kim, S.S. Kim, B.H. Chun, J.K. Jeon, *J. Korean J. Chem. Eng.*, **22**, 573 (2005).
11. C. Geng, S. Li, C. Yue, Y. Ma, *J. Energy Inst.*, **89**, 1 (2015).
12. R.Z. Hu, Q.Z. Shi, S.L. Gao, Thermal analysis kinetics, Science Press, Beijing, China, 2008.
13. G. Chen, C. Liu, W. Ma, X. Zhang, Y. Li, B.B. Yan, W.H. Zhou, *J. Bioresource Technol.*, **166**, 500 (2004).
14. Z. Wang, S.Y. Xu, J. Tang, China Light Industry Press, Beijing, China, 2001.
15. X. Gu, X. Ma, L. Li, C. Liu, K. Cheng, Z.Z. Li, *J. Anal. Appl. Pyrolysis*, **102**, 16 (2013).
16. S.F. Weng, Fourier transform infrared spectrum analysis, Chemical Industry Press, Beijing, China, 2010.
17. R.O. Idem, *J. Energ. Fuel*, **10**, 83 (1996).
18. M. Huo, S. Niu, L.U. Chunmei, M. Liu, L.I. Hui, *J. Chem. Ind. Eng. Prog.*, **33**, 1435 (2014).
19. S.R. Wang, Q. Liu, Y. Zheng, L.H. Wen, Z.Y. Luo, K.F. Cen, *J. Eng. Thermophys.*, **27**, 351 (2006).
20. H.P. Yang, R. Yan, T. Chin, *J. Energ. Fuel.*, **18**, 1814 (2004).
21. J.W. Alencar, P.B. Alves, A.A. Craveiro, *J. Agric. Food Chem.*, **31**, 1268 (1983).
22. R.O. Idem, S.P.R. Katikaneni, N.N. Bakhshi, *J. Fuel Process.*, **51**, 101(1997).
23. Y.L. Bi, Z. Guo, T.K. Yang, Oil and fat chemistry, Chemical Industry Press, Beijing, China, 2005.
24. X.H. Lu, Y. Zhang, Y.L. Yu, J.B. Ji, *J. Bioresources*, **5**, 147 (2010).
25. K.D. Maher, D.C. Bressler, *J. Bioresource Technol.*, **98**, 2351 (2007).
26. C.C. Chang, S.W. Wan, *J. Ind. Eng. Chem.*, **39**, 1543 (2002)

Limitations of measurements of supercritical CO₂ sorption isotherms on coals with manometric equipment - an experimental case study

H. Yu*, R. Jiang, L. Chen

School of Chemical and Environmental Engineering, Shandong University of Science and Technology, 266590 Qingdao, China

Received, August 15, 2017; Accepted, December 11, 2017

Accurate measurement of CO₂ adsorption on coals, which is useful for laboratory estimation of CO₂ sequestration potential in coal, has proven to be a complicated matter. A series of potential sources of error in CO₂ sorption measurements is provided here. The paper investigates the effect of experimental parameters, coal swelling and temperature control on the measurement of supercritical CO₂ adsorption isotherms on coals. Accuracy of pressure and temperature sensors will obviously affect the determination of CO₂ adsorption, which is caused by the great value of CO₂ density change with pressure and temperature at a pressure of 8-10 MPa. The influence of pressure- and temperature-sensors accuracy in the reference cell on CO₂ adsorption can be reduced by improving the experimental method, but their effects in the sample cell are difficult to improve. Coal swelling at high pressure leads to an obvious increase in CO₂ adsorption. A high error of supercritical CO₂ adsorption on coal will be caused by the temperature gradient in the sample cell due to the higher Joule-Thomson coefficient of CO₂ and the poor thermal conductivity of coal and CO₂. The errors of pressure and temperature, coal swelling and control of experimental temperature will lead to negative adsorption and change in the shape of the adsorption isotherm, worse reproducibility and repeatability of supercritical CO₂ adsorption.

Key words: CO₂, Sorption, Coal, Error analysis, CO₂ Sequestration.

INTRODUCTION

CO₂ is not only an important synthetic raw material in the chemical industry [1,2], but also one of the greenhouse gases [3]. Underground storage of CO₂ is one of several possible methods to reduce CO₂ emissions to the atmosphere [4]. CO₂ sequestration into deep unminable coal seams is a very attractive option for geologic CO₂ storage [5]. The supercritical CO₂ adsorption on coal is of great interest for estimating the CO₂ sequestration potential of coal beds and enhancing coal bed methane recovery using CO₂ injection into the coal seams [6-7]. The accurate measurement of supercritical CO₂ adsorption has proven to be a complicated matter [8-18]. Limitations of measurements of supercritical CO₂ adsorption on coals with manometric equipment have been studied in part 1 of this series by Jiang *et al.* [8].

In order to better understand the limitations of measurements of supercritical CO₂ sorption isotherms on coals with manometric equipment, this paper investigates the effect of the experimental parameters: accuracy, volume swelling of coal and temperature on CO₂ adsorption. The main purpose of this paper is to provide an interpretation of the high errors of excess adsorption increment and low

repeatability of CO₂ adsorption isotherm measurements.

EXPERIMENTAL

Material

A coal sample was selected to investigate the effect of experimental parameters error and coal swelling on adsorption. The coal sample of particle size less than 0.2 mm was used for adsorption isotherm measurements as well as for analysis of the effect. Proximate analysis, total sulfur and density of the coal sample are given in Table 1.

Experimental apparatus and procedure

Experimental apparatus

Fig. 1 shows a simplified scheme of the experimental set-up for manometric CO₂ adsorption experiments. The set-up for manometric CO₂ adsorption experiments consists of two cells (sample cell and reference cell), two high-precision pressure sensors (max. pressure 25 MPa, precision of 0.25 %) and two micro Pt100 platinum resistances ($\pm 0.1^\circ\text{C}$) to determine the temperature of the two cells. So, a pressure error of 0.05 MPa and temperature error of 0.1K were used to investigate the effect of pressure and temperature on sorption.

To whom all correspondence should be sent:
E-mail: yuhongguan65@163.com

Table 1. Proximate analysis, total sulfur on air-dry basis (wt %) and density of coal sample used in the experiments

Moisture	Ash	Volatile matter	Fixed carbon	Total sulfur	Density (g/cm ³)
3.87	9.40	35.44	51.29	0.57	1.27

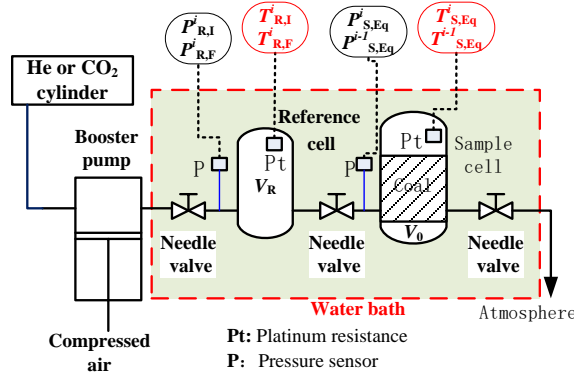


Fig. 1. Simplified scheme of the experimental setup for CO₂ sorption measurement

A booster pump driven with compressed air was used for CO₂ pressurization. The volumes of the empty reference (V_R) and sample cells were obtained by allowing helium to expand from the reference cell into the sample cell. This procedure was performed with both the empty sample cell and the sample cell filled with glass beads of a known volume for calibration. The error of V_R and V_0 is $\pm 0.024 \text{ cm}^3$ and $\pm 0.013 \text{ cm}^3$, respectively. Therefore, the estimated error in the calculation of the reference and sample cell volumes is less than 0.2%.

The standard error is 0.10 mg as quantifying sample with balance, the standard error of coal mass is 0.005 g. Table 2 shows the parameters of the experimental setup and the limits of error for each variable.

Table 2. Parameters of the experimental apparatus and limits of error, Δx , for each experimental variable

Variabile	V_R (cm ³)	V_0 (cm ³)	m (g)	T (°C)	P (MPa)
x	35.4121	40.2345	10.3568	40	Table 3
Δx	0.024	0.013	0.005	0.1	0.05

Experimental procedure

CO₂ excess adsorption experiment on the coal was conducted in a programmed mode at a temperature of 40 °C and pressure up to 20 MPa.

The Gibbs-adsorption increment at the end of the i^{th} step (Δn_i^{ex} in mmol/g) was calculated by Eq. (1).

$$\Delta n_i^{\text{ex}} = V_R (\rho_{R,I}^i - \rho_{R,F}^i) / m - V_0 (\rho_{S,Eq}^i - \rho_{S,Eq}^{i-1}) / m \quad (1)$$

The CO₂ density (ρ) is a function of temperature (T) and pressure (P), which can be calculated with SW-EOS [19]. The pressure includes that in the reference cell before and after CO₂ expansion ($P_{R,I}^i, P_{R,F}^i$) in the i^{th} step, and that in the sample cell at adsorption equilibrium i^{th} and $(i-1)^{\text{th}}$ step ($P_{S,Eq}^i, P_{S,Eq}^{i-1}$). The temperature values include $T_{R,I}^i, T_{R,F}^i, T_{S,Eq}^{i-1}$ and $T_{S,Eq}^i$.

1)th step ($P_{S,Eq}^{i-1}, P_{S,Eq}^i$). The temperature values include $T_{R,I}^i, T_{R,F}^i, T_{S,Eq}^{i-1}$ and $T_{S,Eq}^i$.

$$\rho = f(P, T) \quad (2)$$

Accuracy of supercritical CO₂ adsorption determination

The accuracy of supercritical CO₂ adsorption determination on coal is expressed with accuracy of the sensors (pressure and temperature) and other experimental parameters (volume of two cells and mass of coal sample) of manometric apparatus [8,16-17].

The expected uncertainties or errors of supercritical CO₂ adsorption increment on coal are estimated using error propagation in all the measured variables.

$$\Delta n_i^{\text{ex}} = f(\rho, m, V) \quad (3)$$

$$d\Delta n_i^{\text{ex}} = \sqrt{\left(\frac{\partial \Delta n_i^{\text{ex}}}{\partial \rho} \Delta \rho\right)^2 + \left(\frac{\partial \Delta n_i^{\text{ex}}}{\partial m} \Delta m\right)^2 + \left(\frac{\partial \Delta n_i^{\text{ex}}}{\partial V} \Delta V\right)^2} \quad (4)$$

Errors of experimental parameters

The estimated error of the excess adsorption increment for the i^{th} step caused by the error of $P_{R,I}^i, P_{R,F}^i, P_{S,Eq}^{i-1}$ and $P_{S,Eq}^i$, was calculated with Eqns. (5)-(8) based on Eqns. (1) and (2).

$$\frac{\partial \Delta n_i^{\text{ex}}}{\partial P_{R,I}^i} = \frac{V_R}{m} \left(\frac{\partial \rho_{R,I}^i}{\partial P_{R,I}^i} \right)_T \quad (5)$$

$$\frac{\partial \Delta n_i^{\text{ex}}}{\partial P_{R,F}^i} = -\frac{V_R}{m} \left(\frac{\partial \rho_{R,F}^i}{\partial P_{R,F}^i} \right)_T \quad (6)$$

$$\frac{\partial \Delta n_i^{\text{ex}}}{\partial P_{S,Eq}^{i-1}} = \frac{V_0}{m} \left(\frac{\partial \rho_{S,Eq}^{i-1}}{\partial P_{S,Eq}^{i-1}} \right)_T \quad (7)$$

$$\frac{\partial \Delta n_i^{\text{ex}}}{\partial P_{S,Eq}^i} = -\frac{V_0}{m} \left(\frac{\partial \rho_{S,Eq}^i}{\partial P_{S,Eq}^i} \right)_T \quad (8)$$

The error of the excess adsorption increment caused by the error of volume in the reference cell (V_R) and void-volume in the sample cell (V_0), was calculated with Eqns. (9) and (10) based on Eq. (1).

$$\frac{\partial \Delta n_i^{\text{ex}}}{\partial V_R} = \frac{1}{m} (\rho_{R,I}^i - \rho_{R,F}^i) \quad (9)$$

$$\frac{\partial \Delta n_i^{\text{ex}}}{\partial V_0} = -\frac{1}{m} (\rho_{S,Eq}^i - \rho_{S,Eq}^{i-1}) \quad (10)$$

The increment error caused by the mass of experimental coal sample is,

$$\frac{\partial \Delta n_i^{\text{ex}}}{\partial m} = -\frac{\Delta n_i^{\text{ex}}}{m} \quad (11)$$

The increment errors caused by the error of the experimental temperatures ($T_{R,I}^i, T_{R,F}^i, T_{S,Eq}^{i-1}$ and $T_{S,Eq}^i$) are Eqns. (12)-(15) based on Eqns. (1) and (2).

$$\frac{\partial \Delta n_i^{\text{ex}}}{\partial T_{R,I}^i} = \frac{V_R}{m} \left(\frac{\partial \rho_{R,I}^i}{\partial T_{R,I}^i} \right)_P \quad (12)$$

$$\frac{\partial \Delta n_i^{\text{ex}}}{\partial T_{R,F}^i} = -\frac{V_R}{m} \left(\frac{\partial \rho_{R,F}^i}{\partial T_{R,F}^i} \right)_P \quad (13)$$

$$\frac{\partial \Delta n_i^{\text{ex}}}{\partial T_{S,Eq}^{i-1}} = \frac{V_0}{m} \left(\frac{\partial \rho_{S,Eq}^{i-1}}{\partial T_{S,Eq}^{i-1}} \right)_P \quad (14)$$

$$\frac{\partial \Delta n_i^{\text{ex}}}{\partial T_{S,Eq}^i} = -\frac{V_0}{m} \left(\frac{\partial \rho_{S,Eq}^i}{\partial T_{S,Eq}^i} \right)_P \quad (15)$$

CO₂ density change with pressure at a constant temperature, its change with temperature at a constant pressure, and density can be obtained with the SW-EoS. These relationships can now be used to determine the contribution of each parameter to the increment error.

The errors of sorption increment caused by experimental parameters can be obtained with Eqns. (3)-(13). The error limits of each parameter are obtained with the accuracy of measurement parameters shown in Table 2.

The contribution of each parameter to the expected error of the excess adsorption increment (Δn_{x_j}), were calculated using the viable value, the density changes (Table 3), Eqns. (5)-(15), and the limits of error of each variable, Δx_j (Table 2).

Standard error of excess adsorption

The estimated standard errors of excess adsorption increment caused by pressure, temperature and volume are calculated with Eqns. (16)-(18).

$$\Delta n_p = \sqrt{(\Delta n_{P_{R,I}})^2 + (\Delta n_{P_{R,F}})^2 + (\Delta n_{P_{S,Eq}^i})^2 + (\Delta n_{P_{S,Eq}^{i-1}})^2} \quad (16)$$

$$\Delta n_T = \sqrt{(\Delta n_{T_{R,I}})^2 + (\Delta n_{T_{R,F}})^2 + (\Delta n_{T_{S,Eq}^i})^2 + (\Delta n_{T_{S,Eq}^{i-1}})^2} \quad (17)$$

$$\Delta n_V = \sqrt{(\Delta n_{V_R})^2 + (\Delta n_{V_0})^2} \quad (18)$$

The estimated standard error of the adsorption increment ($d(\Delta n_i^{\text{ex}})$) can be obtained by Eq. (19) and above derivative (Eqns. (5)-(15)). The standard error of total adsorption ($d(n_i^{\text{ex}})$) was calculated by Eq. (20).

$$d(\Delta n_i^{\text{ex}}) = \sqrt{\left(\frac{\partial \Delta n_i^{\text{ex}}}{\partial T_{R,I}^i} \Delta T_{R,I}^i \right)^2 + \left(\frac{\partial \Delta n_i^{\text{ex}}}{\partial T_{R,F}^i} \Delta T_{R,F}^i \right)^2 + \left(\frac{\partial \Delta n_i^{\text{ex}}}{\partial T_{S,Eq}^i} \Delta T_{S,Eq}^i \right)^2 + \left(\frac{\partial \Delta n_i^{\text{ex}}}{\partial T_{S,Eq}^{i-1}} \Delta T_{S,Eq}^{i-1} \right)^2 + \left(\frac{\partial \Delta n_i^{\text{ex}}}{\partial V_R} \Delta V_R \right)^2 + \left(\frac{\partial \Delta n_i^{\text{ex}}}{\partial V_0} \Delta V_0 \right)^2} \quad (19)$$

$$d n_j^{\text{ex}} = \sqrt{(d \Delta n_1^{\text{ex}})^2 + (d \Delta n_2^{\text{ex}})^2 + \dots + (d \Delta n_j^{\text{ex}})^2} \quad (20)$$

RESULTS AND DISCUSSION

CO₂ density change

CO₂ density change at a constant temperature (T) is a partial derivative of the density (ρ) with respect to the pressure (P) variable, i.e. $[\partial \rho / \partial P]_T$, which was investigated in a former paper [17] in detail.

$$\left[\frac{\partial \rho}{\partial P} \right]_T = \frac{1}{RT(1 + 2\delta\phi_\delta^r + \delta^2\phi_{\delta\delta}^r)} \quad (21)$$

CO₂ density change at a constant pressure (P) is a partial derivative of the density (ρ) with respect to the temperature (T) variable, i.e. $[\partial \rho / \partial T]_P$.

$$\frac{P}{RT\rho} = 1 + \frac{\rho}{\rho_c} \phi_\delta^r \quad (22)$$

Rearranging Eq. (22) gives

$$RT\rho + \frac{RT\rho^2}{\rho_c} \phi_\delta^r = P \quad (23)$$

From Eq. (23), the partial derivative of ρ with respect to temperature (T) at a constant pressure (P) is expressed as:

$$R\rho + RT(\partial \rho / \partial T)_P + \frac{R}{\rho_0} \left[\rho^2 \phi_\delta^r + 2\rho T \phi_\delta^r (\partial \rho / \partial T)_P + T \rho^2 \left[(\partial \phi_\delta^r / \partial \rho)_P (\partial \rho / \partial T)_P + (\partial \phi_\delta^r / \partial T)_P \right] \right] = 0 \quad (24)$$

So, the CO₂ density change with temperature at a constant pressure is given by

$$\left[\frac{\partial \rho}{\partial T} \right]_P = -\frac{\rho}{T} \left(\frac{1 + \delta\phi_\delta^r - \tau\delta\phi_{\delta\tau}^r}{1 + 2\delta\phi_\delta^r + \delta^2\phi_{\delta\delta}^r} \right) \quad (25)$$

The description and meanings of the symbols in Eqns. (21) to (25) are detailed in document [19].

The CO₂ density change value ($[\partial \rho / \partial P]_T$ and

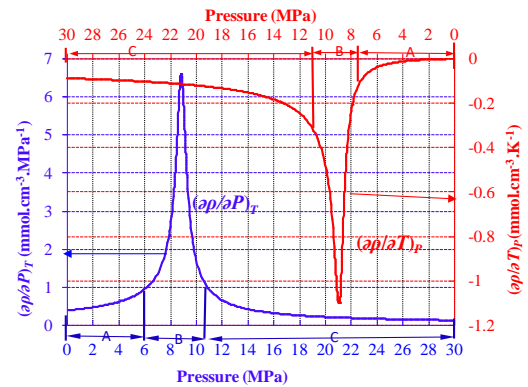


Fig. 2. CO₂ density change ($[\partial \rho / \partial P]_T$) and ($[\partial \rho / \partial T]_P$) at 40 °C, obtained from the SW-EoS.

$\partial \rho / \partial T]_P$) at a temperature of 40 °C and a pressure up to 30 MPa is shown in Fig. 2.

Table 3 shows the experimental results and CO₂ density change.

Table 3. Experimental pressure, density and its change value calculated with SW-EOS, CO₂ adsorption and its increment obtained for the adsorption isotherm of CO₂ at 40°C

i	Pressure (MPa)				Density (mmol/cm ³)				Density change								Adsorption (mmol/g)	
									$(\partial\rho/\partial P)_T$ (mmol·cm ⁻³ ·MPa ⁻¹)				$(\partial\rho/\partial T)_P$ (mmol·cm ⁻³ ·K ⁻¹)					
	$P_{R,I}^i$	$P_{R,F}^i$	$P_{S,Eq}^{i-1}$	$P_{S,Eq}^i$	$\rho_{R,I}^i$	$\rho_{R,F}^i$	$\rho_{S,Eq}^{i-1}$	$\rho_{S,Eq}^i$	$P_{R,I}^i$	$P_{R,F}^i$	$P_{S,Eq}^{i-1}$	$P_{S,Eq}^i$	$T_{R,I}^i$	$T_{R,F}^i$	$T_{S,Eq}^{i-1}$	$T_{S,Eq}^i$	Δn_i^{ex}	n_i^{ex}
(1)	(2)	(3)	(4)	(5)	(6)	(7)	(8)	(9)	(10)	(11)	(12)	(13)	(14)	(15)	(16)	(17)	(18)	(19)
1	6.236	3.873	0.001	2.500	3.670	1.857	0.001	1.108	1.018	0.601	0.384	0.497	-0.046	-0.012	0.000	-0.005	0.170	0.170
2	3.873	3.221	2.5	3.083	1.857	1.483	1.108	1.409	0.601	0.546	0.497	0.535	-0.012	-0.008	-0.005	-0.008	0.003	0.173
3	6.366	4.967	3.083	4.65	3.805	2.581	1.409	2.356	1.063	0.734	0.535	0.689	-0.051	-0.021	-0.008	-0.018	0.027	0.200
4	6.356	5.652	4.65	5.314	3.795	3.125	2.356	2.846	1.059	0.860	0.689	0.792	-0.050	-0.032	-0.018	-0.026	0.027	0.228
5	12.271	10.213	5.314	6.396	16.510	14.691	2.846	3.838	0.598	1.406	0.792	1.074	-0.231	-0.415	-0.026	-0.052	0.223	0.450
6	16.119	9.703	6.396	6.964	18.114	13.809	3.838	4.518	0.306	2.155	1.074	1.346	-0.150	-0.560	-0.052	-0.080	1.259	1.709
7	17.018	11.062	6.964	7.681	18.375	15.634	4.518	5.698	0.276	0.894	1.346	2.050	-0.141	-0.303	-0.080	-0.166	0.474	2.183
8	17.468	10.962	7.681	8.419	18.497	15.542	5.698	7.900	0.264	0.933	2.050	4.473	-0.137	-0.312	-0.166	-0.546	0.102	2.285
9	20.526	12.481	8.419	8.998	19.202	16.632	7.900	11.312	0.203	0.567	4.473	5.672	-0.117	-0.223	-0.546	-1.071	-0.568	1.717
10	19.317	13.531	8.998	9.813	18.945	17.161	11.312	14.034	0.223	0.451	5.672	1.935	-0.124	-0.192	-1.071	-0.519	-0.550	1.167
11	22.344	18.307	9.813	11.222	19.549	18.709	14.034	15.772	0.180	0.243	1.935	0.837	-0.109	-0.131	-0.519	-0.290	-0.459	0.708
12	18.307	16.289	11.222	12.701	18.709	18.166	15.772	16.753	0.243	0.300	0.837	0.537	-0.131	-0.149	-0.290	-0.216	-0.234	0.474
13	22.624	18.777	12.701	15.819	19.599	18.821	16.753	18.021	0.177	0.233	0.537	0.317	-0.108	-0.128	-0.216	-0.154	-0.275	0.198
14	23.903	21.755	15.819	17.548	19.817	19.441	18.021	18.518	0.164	0.187	0.317	0.262	-0.103	-0.112	-0.154	-0.137	-0.082	0.116
15	22.914	21.325	17.548	18.987	19.650	19.360	18.518	18.870	0.174	0.192	0.262	0.229	-0.107	-0.114	-0.137	-0.126	-0.050	0.066

There are $P_{R,I}^i > P_{R,F}^i > P_{S,Eq}^i > P_{S,Eq}^{i-1}$ and they are in the region A (Fig. 2) for pressure points 1 to 4. The final pressures in the reference cell ($P_{R,F}^i$) can also be controlled by regulating the CO₂ quality expanded into the sample cell from the reference cell with a needle valve between the two cells. $P_{R,I}^i$ and $P_{R,F}^i$ may be controlled in the region C (Fig. 2) for pressure points 5 to 15. The equilibrium pressures in the sample cell for the (i-1)th step ($P_{S,Eq}^{i-1}$) and ith step ($P_{S,Eq}^i$) depend on the CO₂ quality expanded from the reference cell, the volumes of the two cells and the sorbed amount on coal. $P_{S,Eq}^{i-1}$ and $P_{S,Eq}^i$ are in the region A for pressure points 5 to 6. For pressure points 7 to 9, $P_{S,Eq}^{i-1}$ and $P_{S,Eq}^i$ are in the region B. $P_{S,Eq}^{i-1}$ and $P_{S,Eq}^i$ are in the region C for the pressure points 10 to 15.

From column (10) of Table 3, the $[\partial\rho/\partial P_{R,I}^i]_T$ values are from 0.164 to 1.063 mmol/(cm³·MPa) at $P_{R,I}^i$. The $[\partial\rho/\partial P_{R,F}^i]_T$ values for the reference cell are from 0.187 to 2.155 mmol/(cm³·MPa) at $P_{R,F}^i$ from column (11) of Table 3. From columns (12) and (13) of Table 3, the maximum $[\partial\rho/\partial P_{S,Eq}^i]_T$ and $[\partial\rho/\partial P_{S,Eq}^{i-1}]_T$ are from 0.229 to 5.672 mmol/(cm³·MPa). The density change of CO₂ with pressure at a constant temperature in the sample cell is obviously greater than that in the reference cell,

especially under medium pressure, which is caused by the operating conditions. The pressure in the reference cell may be controlled in the regions A and C of Fig. 2 by pressurization with the CO₂ booster-pump and the CO₂ quality expanded into the sample cell. However, equilibrium pressure in the sample cell is difficult to be controlled in the regions A and C, and region B is to be avoided, which is caused by CO₂ adsorption on coal and a greater $[\partial\rho/\partial P]_T$ value in the region.

The absolute value of $[\partial\rho/\partial T_{R,I}^i]_P$, $[\partial\rho/\partial T_{R,F}^i]_P$ and $[\partial\rho/\partial T_{S,Eq}^i]_P$ is from 0.012 to 0.231, 0.008 to 0.560 and 0.005 to 1.071 mmol/(cm³·K), respectively. Just like the effect of pressure accuracy, the influence of temperature accuracy in the sample cell on CO₂ adsorption error is greater than that in the reference cell.

As can be seen from Table 3, the value of the adsorption increment is negative as the equilibrium pressure is greater than 8.5 MPa. So, there is a maximum of total adsorption and the adsorption isotherm exhibits an obvious asymmetric parabolic shape.

Error analysis

Based on error propagation, the expected error limit of excess sorption increment at the ith expansion step due to the variable error is calculated with Eqs. (27) and (28) can be used to determine the error limit of excess total sorption at jth step.

$$d\Delta n_i^{\text{ex}} = \Delta n_{P_{R,1}^i} + \Delta n_{P_{R,F}^i} + \Delta n_{P_{S,Eq}^i} + \Delta n_{P_{S,Eq}^{i-1}} + \Delta n_{T_{R,1}^i} + \Delta n_{T_{R,F}^i} + \Delta n_{T_{S,Eq}^i} + \Delta n_{T_{S,Eq}^{i-1}} + \Delta n_{V_R} + \Delta n_{V_0} + \Delta n_m \quad (27)$$

$$dn_j^{\text{ex}} = d\Delta n_1^{\text{ex}} + d\Delta n_2^{\text{ex}} + \dots + d\Delta n_i^{\text{ex}} + \dots + d\Delta n_j^{\text{ex}} \quad (28)$$

The excess CO₂ sorption increment, total sorption isotherms on the coal and their errors at 40°C are shown in Fig. 3 which displays the error limit (calculated with Eqns. (27) and (28)) with filled area plots, standard error (calculated with Eqns. (19) and (20)) with error bars, and sorption increment and total sorption with dotted line. The serial number in Fig. 3 indicates CO₂ expansion step as shown in Table 3.

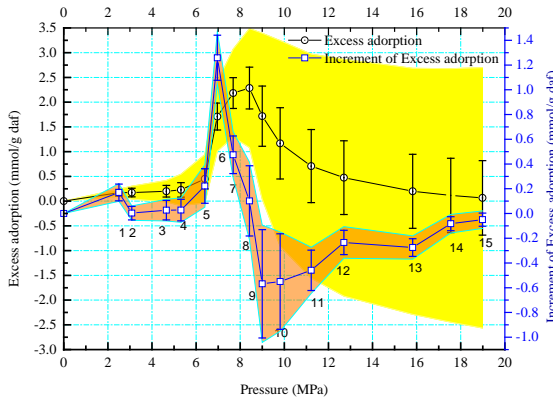


Fig. 3. The excess sorption increment and its isotherms (dotted line), error limit (filled area plot) and standard (error bar) errors of sorption increment and total sorption

The error limit of the adsorption increment calculated with Eq. (27) is greater than the standard error of the increment calculated with Eq. (19), especially at a pressure of 8-10 MPa. With pressure increase, the error limit of the increment increases to a maximum and then decreases. The maximum appears at an equilibrium pressure of 8.998 MPa, being consistent with the maximum $[\partial\rho/\partial P]_T$ of 5.672 mmol/(cm³·MPa) at 40°C. The increment error is very low at a pressure lower than 8 MPa (low pressure) and higher than 10 MPa (high pressure). The maximum error of sorption increment appears at a pressure with negative sorption increment. The negative increment at the i^{th} step indicates the maximum sorption at the $(i-1)^{\text{th}}$ step. The reason why the negative increment or maximum sorption is at the maximum increment-error should be studied in the future.

The error limit of total adsorption calculated with Eqns. (27) and (28) has an extreme value, plotted with filled area in Fig. 3. The error limit is very great, accounting for 54% of the maximum adsorption. The negative adsorption will appear as negative error limit caused by pressure and temperature sensor accuracy, and the shape of the

adsorption isotherm will change as positive error-limit. The error of adsorption caused by the errors of the experimental parameters may result in a lower reproducibility and repeatability of supercritical CO₂ adsorption at high pressure.

Coal swelling effect on the measured adsorption of CO₂

Coal volumetric swelling caused by CO₂ adsorption is a well-known phenomenon [20, 21]. Firstly, the most reported maximum volumetric swelling of coal in CO₂ was within the range of about 1 to 5%, with highest swelling usually associated with lower-rank coals [22-27]. The corrected excess sorption was about 30% greater than the uncorrected value at 15 MPa.

In case of coal density of 1.27 g/cm³ (Table 1), the void volume decreases by 0.003, 0.04 and 0.08 cm³ per gram coal coal swelling of 0.4%, 5.0% and 10.0%, respectively. The error of the void volume in the sample cell is 0.033, 0.408, 0.815 cm³, corresponding to the coal swelling amount above, respectively. The errors caused by coal swelling are obviously greater than the errors in Table 2. The V_0 errors caused by the coal swelling of 0.4%, 5.0% and 10.0% are 2.5, 31.4 and 62.7 times the instrumental error, respectively.

The coal swelling volume of 0.4% has little influence on the accuracy of adsorption measurement. As the coal swelling volume is small in comparison with the void volume error, its effect on CO₂ adsorption is ignorable. So, a great volume of sample cell and a small coal mass (i.e. great specific void volume) may make us ignore coal swelling effect when coal swelling is not too large.

With the increase in the extent of coal swelling, its effect on adsorption measurement becomes greater. At a coal swelling volume of 10%, the influence of the swelling on the adsorption measurement is similar to that of the pressure at medium pressure, and the effect is even greater than that of the pressure at low and high pressure. Coal swelling of 5% or more will obviously increase the CO₂ adsorption, especially at low and high pressure.

Limitation of temperature control

Temperature increases or decreases in the two cells as a result of the Joule-Thompson effect during CO₂ expansion procedure [28]. The temperature of CO₂ in the reference cell will rise with CO₂ pressurization with the CO₂ booster-pump, CO₂ temperature will decrease in the cell when CO₂ is expanded into the sample cell from the cell. The temperature in the sample cell will rise when CO₂ is expanded into the cell from the reference cell.

Therefore, the temperature of the two cells is not always constant during the determination of the adsorption capacity. The CO₂ temperature in the two cells and the temperature of the coal sample in the sample cell depend on the operation process.

The effect of temperature sensor accuracy on the determination of CO₂ adsorption capacity is smaller than that of the pressure sensor, but the temperature of CO₂ gas, cell body, coal sample, valve and pipe connecting the two cells is difficult to be determined because the temperature is not always equal everywhere. The high Joule-Thomson coefficient of CO₂ [19] and the poor thermal conductivity of coal [29-31] can lead to a temperature gradient in the sample cell.

CONCLUSIONS

This study provides an experimental case about the limitation of measurements of supercritical CO₂ adsorption isotherms on coals with manometric equipment at high pressure. The contribution of pressure-sensor accuracy to the uncertainty of incremental adsorption is greater than that of temperature error at equilibrium pressure less than 10 MPa, and the contribution of temperature-sensor accuracy is greater than that of pressure at equilibrium pressure higher than 10MPa. The error of adsorption caused by pressure- and temperature-sensor accuracy may result in lower reproducibility and repeatability of supercritical CO₂ adsorption at high pressure, and negative adsorption and change of the shape of adsorption isotherm. Coal swelling will result in a volume change of the sample cell, and will lead to an obvious increase in CO₂ adsorption in case of large swelling extent of coal. Higher Joule-Thomson coefficient of CO₂ and poor thermal conductivity of coal and CO₂ can lead to a temperature gradient in the sample cell, which will result in a high error of supercritical CO₂ adsorption on coal.

Acknowledgements: This research was supported by the National Natural Science Foundation of China (Grant Nos. 51174127 and 21176145) and Shandong Province Natural Science Foundation (No. ZR2011DM005).

REFERENCES

1. Y. Chen, X. Zhong, Q. Zhang, *Ind. Eng. Chem. Res.*, **51**, 9260 (2012).
2. Y. Chen, Q. Han, Y. Wang, Q. Zhang, X. Qiao, *J. Appl. Polym. Sci.*, **132**, 41723 (2015).
3. S. Sun, C. Liu, Y. Ye, *J. Chem. Thermodyn.*, **57**, 256 (2013).
4. S. Sun, C. Liu, Q. Meng, *J. Chem. Thermodyn.*, **84**, 1 (2015).
5. H. Yu, G. Zhou, W. Fan, J. Ye, *Int. J. Coal Geol.*, **71**, 345 (2007).
6. H. Yu, L. Zhou, W. Guo, J. Cheng, Q. Hu, *Int. J. Coal Geol.*, **73**, 115 (2008).
7. H. Yu, J. Yuan, W. Guo, J. Cheng, Q. Hu, *Int. J. Coal Geol.*, **73**, 156 (2008).
8. R. Jiang, H. Yu, L. Wang, *Bulg. Chem. Commun.*, **49**, 509 (2017).
9. Y. Gensterblum, P. van Hemert, P. Billefont, E. Battistutta, A. Busch, B.M. Krooss, G. De Weireld, K.-H.A.A. Wolf, *Int. J. Coal Geol.*, **84**, 115 (2010).
10. A.L. Goodman, A. Busch, R.M. Bustin, L. Chikatamarla, S. Day, G.J. Duffy, J.E. Fitzgerald, K. A.M. Gasem, Y. Gensterblum, C. Hartman, C. Jing, B.M. Krooss, S. Mohammed, T. Pratt, R.L. Robinson Jr., V. Romanov, R. Sakurovs, K. Schroeder, C.M. White, *Int. J. Coal Geol.*, **72**, 153 (2007).
11. S.J.F. Mohammed, R.L. Robinson Jr., K.A.M. Gasem, *Energy Fuels*, **23**, 2810 (2009).
12. V.N. Romanov, A.L. Goodman, J.W. Larsen, *Energy Fuels*, **20**, 415 (2006).
13. R. Sakurovs, S. Day, S. Weir, *Int. J. Coal Geol.*, **77**, 16 (2009).
14. P. van Hemert, E.S.J. Rudolph, J. Bruining, K.-H.A. A. Wolf, *SPE J.*, **15**, 146 (2010).
15. S. Hol, Y. Gensterblum, C. J. Spiers, *Fuel*, **105**, 192 (2013).
16. H. Yu, W. Guo, J. Cheng, Q. Hu, *Int. J. Coal Geol.*, **74**, 250 (2008).
17. R. Jiang, H. Yu, L. Wang, L. Chen, *Int. J. Smart Sens. Intell. Syst.*, **9**, 468 (2016).
18. D.F. Zhang, L.L. Cu, S.G. Li, P.C. Lian, J. Tao, *Int. J. Global Warming*, **5**, 197 (2013)
19. R. Span, W. Wagner, *J. Phys. Chem. Ref. Data*, **25**, 1509 (1996).
20. S. Day, R. Fry, R. Sakurovs, *Int. J. Coal Geol.*, **93**, 40 (2012).
21. E. Ozdemir, B. I. Morsi, K. Schroeder, *Langmuir*, **19**, 9764 (2003).
22. N. Siemons, A. Busch, *Int. J. Coal Geol.*, **69**, 229 (2007).
23. G. Ceglarska-Stefańska, A. Czapliński, *Fuel*, **72**, 413 (1993).
24. S. Day, R. Fry, R. Sakurovs, S. Weir, *Energy Fuels*, **24**, 2777 (2010).
25. P. Chareonsuppanimit, S. A. Mohammad, R. L. Robinson Jr., K. A. M. Gasem, *Int. J. Coal Geol.*, **121**, 98 (2014).
26. P. J. Reucroft, H. Patel, *Fuel*, **65**, 816 (1986).
27. P. J. Reucroft, A. R. Sethuraman, *Energy Fuels*, **1**, 72 (1987).
28. C.M. Oldenburg, *Energy Convers. Manag.*, **48**, 1808 (2007).
29. B. Tian, Y. Qiao, Y. Tian, Q. Liu, *J. Appl. Pyrol.*, **121**, 376 (2016).
30. Y. Zhang, J. Zhu, X. Wang, X. Zhang, S. Zhou, P. Liang, *Fuel Process. Technol.*, **154**, 227 (2016).
31. X. Qu, P. Liang, Z. Wang, R. Zhang, D. Sun, *Chem. Eng. Technol.*, **34**, 61 (2011)

Relationship between space structure characteristics and site environment of *Pinus Yunnanensis* secondary forests on Mopan Mountain in the middle of Yunnan, Southern China

Y. Zhao^{1,2}, X. Duan^{1,2*}, Sh. Shu^{1,2}

¹Southwest Forestry University, Kunming, Yunnan Province, China

²Yuxi Forest Ecosystem Research Station, China's State Forestry Administration, Kunming, China.

Received August 16, 2017, Accepted December 18, 2017

The influence on forest space structure by the site environment of *Pinus Yunnanensis* secondary forests, which are the main native species at the middle of Yunnan in China is discussed. Based on the analysis of site environment and forest space structure characteristics, the relationships between forest structure and site condition were analyzed using RDA sequencing. Results showed that there are big differences in forest non-space structure at each sample plot, the average diameter and height all displayed significant differences at most sample plots ($P < 0.05$) and different distribution ($P < 0.05$). Otherwise, in forest space structure, the average uniform angle index and neighborhood comparison at each sample plot were near to 0.5, which indicated that most forests had random distribution in the mean state. The interaction between non-spatial structure and spatial structure of forest stands was not equal, and the spatial structure was more influenced by the line length.

Key words: Site conditions; Neighborhood comparison; Uniform angle index; Box-counting dimension; RDA sequence; *Pinus Yunnanensis* secondary forests

INTRODUCTION

Forest structure is an important manifestation of the stand characteristics, and also is a comprehensive reflection of forest growth developmental process and operation [1], which determines the functions of the forest. Therefore, stand structure is a key aspect of controlling forest function [2-4]. The spatial structure of the stand is the spatial arrangement in the forest, which reflects the spatial relationship of the species in the forest community [5]. Spatial structure determines the competitive potentials of trees and their spatial niche, which largely determines the stability of the stand, the possibility of development and the size of the management space [6].

Studies on forest structure characteristics are some of the main contents of forest ecology research in long terms [7]. But most of them focused on the aspects of the stand structure and its habitat factors while the influence of the site conditions on the stand characteristic factors was relatively small [8]. There are only few reports especially on the study of the relationship between spatial structure and site factors of forest stands [9]. At the same time, the studies on stand structure factors were mostly concentrated on a direct one-to-one relationship, and provided no comprehensive summary of the inherent complexity of the forest ecological system, such as the impact of environment on the growth of the

forest nor provided comprehensive information for a systematic study [10,11].

Pinus Yunnanensis is the typical native tree species in Yunnan Province of China, and has a very important role in the forest ecological environment in Yunnan Province, especially the pure forest of the same age [12]. Therefore, this paper chooses the similar age *Pinus Yunnanensis* pure forest as the research object, to explore the effects of different site conditions on stand structure. The relationship between site conditions, stand non-spatial and spatial structure by RDA ordination can provide theoretical basis for the operation and management of *Pinus Yunnanensis*.

STUDY CONDITIONS

The Mopan Mountain National Forest Park is situated in Yunnan Province of China ($101^{\circ}16'06'' \sim 101^{\circ}16'12''$, $23^{\circ}46' \sim 23^{\circ}54'$). The latitude is 1260.0~2614.4 m, which belongs to a subtropical/typical mountain climate region. Annual mean temperature is about 15°C and annual rainfall is about 1050 mm. Extreme maximum temperature is 33°C, extreme minimum temperature is 2.2 °C, the annual sunshine time is 2380 h. The Mopan Mountain soil is upland soil and basalt developed into red soil; the high altitude area is yellow brown soil, soil thickness gives priority to thick soil layer and local thin soil layer with soil thickness of 1 m or so.

To whom all correspondence should be sent:
E-mail: feixue20012360@163.com

METHODS

Data processing and computing

Sample setting and investigation

On the basis of comprehensive reconnaissance, small age difference and different site conditions typical *Pinus Yunnanensis* pure natural secondary forest, 8 fixed sampling spots (50 m×50 m) were set away from the road. The basic situations of the plots are shown in Table 1. Combined with the research objective, in order to meet the needs of the fitting model, in the vicinity of each sample a temporary survey was set, a total of 68 (20 m × 20 m) and in each sample four samples (0.04 hm², 20 m×20 m), that was 32. Hence, 1, 2, 3, 4 samples were in the same location.

The method of mechanical sampling was adopted. In each of the sample plots, the diameter above 3cm and the survival of the *Pinus Yunnanensis* were investigated. Survey indicators including the number of *Pinus Yunnanensis*, diameter, tree height, coordinate and in each sample chose the dominant 2-3 trees, record the number. *Soil sample collection and main physical-chemical indices*

Soil samples were collected at five sampling sites in each fixed plot. Depth was in accordance with the mechanical stratification for 0-20 cm, 20-40 cm and 40-60 cm, using a ring knife (100 cm³) and aluminum box for each layer of collected soil. In each layer of fresh soil the method of four points was applied over a 0.25 mm, 1 mm and 2 mm copper sieve, respectively and put in the soil bag. The chemical indicators were measured in 0.25 mm or 1 mm sieved soil samples, some physical indicators were measured using 2 mm sieved soil sample.

Soil physical properties included soil moisture content (saturated water holding capacity, capillary moisture capacity, and field water holding capacity), bulk density, porosity, mechanical components, and so on.

Site conditions are mainly related to the slope, the slope position, and the physical and chemical factors, in which the slope position and slope direction can be quantified by the method of artificial classification assignment. Stand structure included the stand spatial structure and spatial structure, the latter mainly included stand density, average diameter, tree height; spatial structure mainly included the stand level, tree size differentiation characteristics of distribution and spatial distribution patterns of forest trees; the characteristic indices were: neighborhood comparison (NC), uniform angle index (UAI), box-counting dimension (BCD), etc. [3, 8]. The main factors affecting the stand structure were analyzed according to the order of RDA. In this paper, the correlation analysis, the difference analysis, the multiple comparison and so on used the Spss19.0.

Elevation, terrain and terrain conditions of the sites

According to the law of decreasing temperature with the elevation, the level of the elevation was assessed. For each rise of 100 m, the rank decreased by 1, while the interval from 1600 m to 1700 m was set for grade 4. According to the solar radiation at the different slopes, each unit level was 45°C, and the north as a clockwise starting point. The division results are shown in Table 3. The greater the number, the bigger was the radiation. Treatment of 0.1 units was performed at different angles of the same grade with different changes of 4.5°C. According to interflow, the top-down direction was divided into 2 levels, 2 was for downhill, 1 was uphill. In order to evaluate the site quality, the site factors were classified into two types, macroscopic and microscopic. The macro site factors include: elevation, slope direction, slope position and so on. The micro site factors mainly include soil physical and chemical factors.

Table 1. Sample basic condition of the sample area

Sample	1	2	3	4	5	6	7	8
Slope site	Down	Up	Down	Up	Up	Down	Up	Down
Slope	shady	shady	sunny	sunny	sunny	sunny	shady	shady
Latitude(m)	1823	1874	1958	1929	1993	1945	1823	1856
Small number	14	15	12	12	11	12	12	12
Average diameter (cm)	14.77	13.83	16.80	17.67	13.82	16.91	12.90	13.08
Average height (m)	9.05	7.23	8.73	7.90	9.95	11.44	9.42	11.87
Dominant average tree diameter (cm)	23.48	20.63	28.18	30.20	24.73	24.93	20.05	22.83
Dominant average tree diameter (m)	18.75	20.90	24.43	26.88	24.18	22.63	24.50	23.35
Average density (N/ha)	1038	1288	806	519	1550	431	1644	1122
Age(a)	25	26	27	27	26	25	25	25

RESULTS AND DISCUSSION

Site characteristics of *Pinus Yunnanensis* secondary forest in Mopan Mountain

In the *Pinus yunnanensis* pure forest main distribution area, within the altitude range of 1600 m to 2000 m, 8 samples were set up, covering a series of changes in the south slope to north slope, slope position classification for uphill and downhill. The quantitative results of the topographic elevation are shown in Table 2.

Forest spatial structure angle index features

The smaller the angle index means more uniform trees distribution of the forest structure unit, the opposite means that distribution was assembled. From Figure 2 it is seen that the distribution frequency of the angle index in the first four sample areas of the structure unit was mostly random ($W = 0.5$), the distribution of plot 3 has an obvious trend to be a more evenly distributed structure unit ($W = 0.25$), while plot 2 had more assembled distribution of the structural unit ($W = 0.75$). The characteristics of the last four samples mostly displayed a random distribution of the structural unit; its frequency was around 0.5. The average angle index of each plot was in the order: 0.51, 0.56, 0.48, 0.55, 0.53, 0.52, 0.54, and 0.52. The mean difference was not obvious, so the angle index distribution characteristics of each sample plot difference were tested. The X test was used (Table 3). It can be seen that most of the angle indices of most plots had no significant difference, except for sample plot 1 and plots 2, 7, plots 2 and 3, plots 3 and 4, etc.

Neighborhood comparison characteristics and differences

By the neighborhood comparison, the distribution frequency showed obvious differences in a part of the sample plots. As in the first four sample plots, the plots 1 and 2 had a rather big difference in the neighborhood comparison distribution, there were more reference tree in absolute inferiority in plot 2.

In the last four sample plots, the number of the

Table 2. Basic situation of sample plots

Sample	Latitude	Latitude number	Slope	Slope number	Slope position	Slope quantization
1	1623m	4	NW20°	1.44	Down	2
2	1674m	4	NW30°	1.66	Up	1
3	1958m	1	SE70°	4.44	Down	2
4	1999m	1	SE45°	7.50	Up	1
5	1993m	1	SW60°	6.67	Up	1
6	1945m	1	S	8.00	Down	2
7	1823m	2	NW45°	3.00	Up	1
8	1756m	3	NW45°	3.00	Down	2

reference trees in the middle of the sample plot 5 was significantly lower, and the frequency was 0.1. The advantages and disadvantages in the number of reference trees were greater than the mean, and this was similar to the sample plot 8.

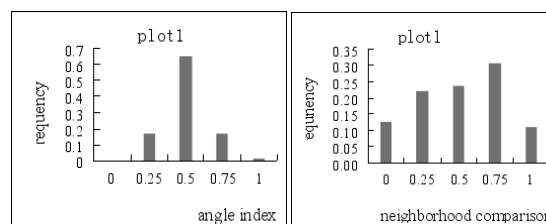


Fig. 1. Angle index and neighborhood comparison for plot 1

In contrast, the distribution of sample plot 6 was more uniform, and the distribution of sample plot 7 was similar to that of 2. Different frequency distribution may be related to forest regeneration, as more young forests favored the neighborhood comparison. In addition, the distribution of the neighborhood comparison was more obvious than that of the angle index. The average number of neighborhood comparison was 0.51, 0.49, 0.53, 0.49, 0.47, 0.48, 0.51, and 0.50, respectively. Because X test distribution can be applied to categorical variables, the distribution of different neighborhoods was also tested. The results are shown in Table 4. It can be seen that the distribution of the neighborhoods in sample plots 1 and 2, 6, 7, 8 showed significant differences, the same was also in plots 5 and 4.

Box-counting dimension characteristics and differences

Level meter box dimension valued generally between 1 to 2, the bigger number pointed to a higher degree of space-occupying, compared with density. This expressed the meaning and the spatial relationship. The inflection point was the demarcation point in different regions of linear of fitting process manifesting the small slope before the inflexion of the linear region. This can be considered as the distribution of individuals in the population state, not having the characteristics of population distribution.

Table 3. Box counting dimensions and turning points for different samples

Plots	Box-counting dimension	Fitted equation	R ²	Turning point
1	1.35	$y=1.35x+4.49$	0.98	3.22
2	1.44	$y=1.44x+4.24$	0.94	2.37
3	1.18	$y=1.18x+4.12$	0.98	4.08
4	1.59	$y=1.59x+5.44$	0.94	1.67
5	1.22	$y=1.22x+4.29$	0.89	3.50
6	1.27	$y=1.27x+4.73$	0.93	2.64
7	1.60	$y=1.60x+5.74$	0.89	1.99
8	1.56	$y=1.56x+5.57$	0.92	1.86

So, this paper lists the fitting equation on the scale of the inflection point, considering the characteristics of population distribution above the inflection point, and the distribution characteristics of the individuals below it. From Table 3 it is seen that there exists a certain difference on the inflection point in different sample plots, and the maximum inflection point is in plot 3, which indicates that the individual polyintegrated population scale unit was loose, and with the increase in density, the population distribution scale showed a trend of decrease. The box-counting dimension fitted well on the population scale, the maximum was 1.60, and the minimum was 1.18. To a certain extent, density changes were closely related, but increased not only with the density increasing box-counting dimension, such as sample plots 6 and 2. At the same time, compared with the angle scale, box dimensions denoted the scatter and gather distribution characteristics of trees on the whole, which belonged to the spatial structure index.

Effect of site conditions on forest structure based on RDA ordination

The relationship between species and environment was analyzed by the method of RDA ordination based on a linear model. RDA based on the analysis of the criteria was the species in advance of the DCA analysis, because the length of the first spindle was less than 3, the choice of RDA analysis was considered more appropriate. In the selection of the function and the role of the indicators, the indicators of significance overlapped and the changes were not big. Soil texture and pH in a variety of places were not significantly different. Factors like angle index, neighborhood comparison, box-counting dimension were considered as species (small arrow) 1, 2, 3; the soil physical and chemical factors: saturation moisture content (%), capillary water holding capacity (%), field water holding capacity

(%), natural moisture content (%), bulk density (g/cm^3), organic matter (g/kg), total N (g/kg), available nitrogen (mg/kg), total phosphorus (g/kg), total potassium (g/kg) and available potassium (mg/kg) for environmental variables (large arrow) 1, 2, 3, 4, 5, 6, 7, 8, 9, 10, 11. At the same time, the terrain factors included: slope, slope position, elevation as the environmental factors 12, 13, 14. The angle index, neighborhood comparison, box-counting dimension were regarded as environmental variables 15, 16 and 17.

After variable selection, on the basis of a significant Monte Carlo permutation test ($P < 0.05$), the optimal RDA ranking results were obtained (shown in Figure 3). In Table 4 the correlation coefficients between each influence factor and the rank axis are shown. RDA first, two ordination axes of the forest spatial structure and the spatial structure of the forest-impact factor variation of the interpretation of the factors were: 99.4% and 99.6%. Therefore, the sorting results had strong explanatory power. Correlated with the absolute value of the first axis were the average diameter, density, etc. The changes of the forest spatial structure were indicated. The second axis (vertical axis) gradient change reflected the change in water and light. It can be seen that the forest density, the average diameter and the box-counting dimension were positively affected. The water and light had negative effects on the neighborhood comparison showing that good moisture and light intensity can greatly ease the competition among individuals, showing a smaller neighborhood comparison.

To sum up, we can make the following judgments: first of all, forest spatial structure and non-spatial structure influenced each other; secondly, soil nutrient factors were easy to affect the forest non-spatial structure and terrain. To bring the water and light changes in the environment was easier to affect the forest spatial structure, including tree size differentiation. However, just clearing the site condition and forest structure of

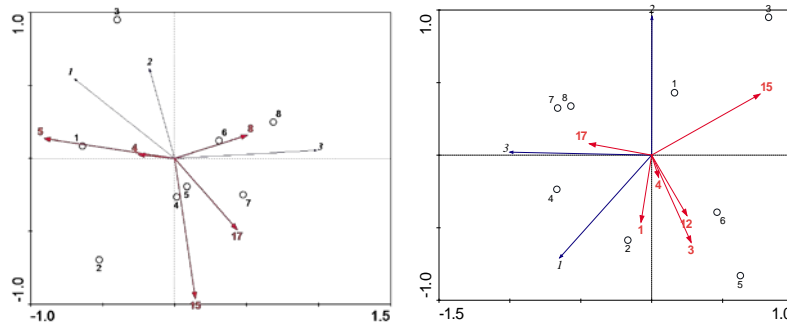


Fig. 2. RDA analysis of non-spatial index, site condition and stand spatial index of stand

Table 4. Correlation coefficients of RDA ordination axis with influencing factors

Variable	4NWC	5BD	8AN	15UAI	17BCD	1SWC	3FWC	4NWC	12Slope	15Average diameter	17Density
First rank axis	-0.250	-0.898	0.499	0.142	0.430	-0.075	0.278	0.049	0.249	0.762	-0.438
Second rank axis	0.025	0.135	0.158	-0.961	-0.489	-0.460	-0.599	-0.151	-0.415	0.419	0.079

Note: SWC-saturation water capacity; FWC- field water capacity; NWC- Natural water content; BD- bulk density; AN- available nitrogen; UAI- Uniform angle index; BCD –Box Counting Dimension

gradient relations cannot point out the relationship within the specific contact, and is unable to determine forest non-spatial structure and spatial structure that are influenced by site conditions. Therefore, it is necessary to work on clarifying and further deepening this relationship.

It should be noted that in the RDA ordination the forest structure factors were not equal, such as angle index as environment variable, which affected the diameter and tree height significantly, and if tree diameter and height were environmental variables, tree height had no effect on angle index (Figure 3).

CONCLUSIONS

This paper studied the relationship between site conditions and forest spatial structure of *Pinus Yunnanensis* on Mopan Mountain in Yunnan Plateau. The following conclusions may be drawn:

Soil moisture was mainly related to forest density, in the middle and low parts, density was high, with more moisture. Some sample plots downhill held more water than the upper slope, soil moisture on sunny slopes was higher than that of shady slopes.

It was found that there was no significant difference in the mean values of the angle index and the neighborhood comparison. But several sample plots in the distribution displayed significant difference. There were significant differences in the angle index distribution, such as plot 1 and 2, 7, plot 2 and 3, plot 3 and 4, and so on. Box counting dimension analysis results showed that the space occupied by forest sample plots was obvious different, box-counting dimension were: 1.35, 1.44, 1.18, 1.59, 1.22, 1.27, 1.60, and 1.56, respectively. The turning point varied, the cluster extent of the sample on the plaque scale was different, and the greater the density, the smaller was the turning point.

There was a mutual influence between the forest spatial structure and the non-spatial structure. The

specific performance was: negative influence of the angle index and the box-counting dimension on the average tree height and the diameter. In turn, the density influence on the angle index was positive. For the forest spatial structure, the slope direction and soil physical properties, such as saturation capacity, natural moisture content, field capacity, and the neighborhood comparison had negative gradient changes. This showed that good water and light were not significant for the individual size of the forest.

Acknowledgements: This research was supported by the Special Fund for National Science Foundation of China (31560233; 31760149), Project of Yunnan Provincial Department of Education (2015Z141); Fund Project to Key Disciplines (Ecology) Project of Yunnan Education Department (05000511311); Fund Project to The forestry science and technology innovation platform project of The State Forestry Administration (2017-LYPT-DW-158);

REFERENCES

- 1.Z.Z. Yu, Forest management (second press). Beijing: China Forestry Publishing house (1993)
- 2.X.G. Kang, Forest resources management. Beijing: China Forestry Publishing house (2001)
- 3.R.L. Bailey, T.R. Dell, *Forest Science*, **19**, 97 (1973)
- 4.M.L. Hanus, D.W. Hann, D.D. Marshall, *Forest Science*, **44**(1), 125 (1998)
- 5.M.P. Tang, SH.Z. Tang, X.D. Lei, G.M. Zhou, ZH.X. Xie, *Forest Resources Management*, **4**, 25-27 (2004)
- 6.W. Su, Y.J. Yue, X.X. Yu, *Journal of Irrigation and Drainage*, **28** (1), 113 (2008)
- 7.U. Berger, M. Adams, V. Grimm, Modelling secondary succession of neotropical mangroves: Causes and consequences of growth reduction in pioneer species. *Perspectives in Plant Ecology Evolution & Systematics*, **7**(4), 243 (2006)
- 8.H.S. Xiao, B. Shao, J.X. Ouyang, *Forest Resources Management*, **4**, 34 (2016)

9. F. Mi, Z.H.D. Tan, Y. Gu, *Scientia Silvae Sinicae*, **51** (7), 107 (2015)
10. S.L. Wang, J.P. Zhou., *Journal of Beijing Forestry University*, **36** (5), 7 (2014)
11. Grace J B. Structural equation modeling and natural systems . Cambridge: Cambridge University Press, 2006.
12. S.X. Liao, Studies on the Landscape Pattern, Stand Structure and Near Nature Management Model of Pinus Yunnanensis in Central Yunnan, China. Beijing: Chinese Academy of Forestry, 2008.

Breaking features of loading key strata based on deep beam structure in shallow coal seam and its limited span-to-depth ratio

F. Wu^{1,2}, X. Sun³, J. Li^{4*}, Ch. Liu^{1,2}, Q. Chang^{1,2}, B. Chen^{1,2}

¹ Key Laboratory of Deep Coal Resource Mining, Ministry of Education of China, China University of Mining and Technology, Xuzhou, China

² School of Mines, China University of Mining and Technology, Xuzhou, China

³ ShanDong Energy Zibo Mining Group CO.,LTD, Zibo, China

⁴ Institute of Mining Engineering, Inner Mongolia University of Science and Technology, Baotou, China

Received September 14, 2017; Accepted December 19, 2017

Based on the occurrence characteristics of loading key strata in a shallow coal seam, we built the mechanical model of the deep beam structure of the loading key strata under different boundary conditions. The features of first breaking and periodic breaking as well as the breaking span of the loading key strata considered as a deep beam structure were analyzed. The analytical solutions of elastic mechanics of stress components and displacement components upon first breaking and periodic breaking of the loading key strata more conformed to the real situations of breaking of overburden rocks of shallow coal seam during the exploitation as compared with analytical solutions of material mechanics and those of elastic mechanics of general long beams. The first and periodic breaking of the loading key strata usually belongs to tensile failure. Limited span-to-thickness ratio ε characterizes the stability of loading key strata, and it is affected by load, strength of rock mass and thickness of the loading key strata.

Key words: Shallow coal seam, loading key strata, deep beam structure, breaking features, limited span-to-thickness ratio.

INTRODUCTION

Shallow coal beams tend to demonstrate unique breaking features and evolution of surface subsidence induced by mining as compared with the ordinary coal seam because of its shallow burial depth, thin bedrock and thick overburden strata [1]. In the mining of shallow coal seams, breaking of the loading key strata directly leads to the overall collapse of the overburden layers and ground surface. As a result, the ground pressure of the working face intensifies with the generation of mining cracks connecting to the ground surface. Therefore, understanding the breaking features and limited span of the loading key strata is of high importance for predicting the roof pressure of working surface in a shallow coal seam and the surface damage caused by mining.

Among various studies on the breaking features of overburden layers and breaking span in shallow coal seams, in [1,2] a theoretical expression of first and periodic breaking spans in the roof under general long-beam structure is presented. In [3,4] the formula of first and periodic weighting steps in the combinational key strata under long beam structure is derived. In [5-7], a key strata theory was applied to the roof control of shallow coal seams, and a roof structure and strata control theory for long-wall mining of shallow coal seams was

established. In [8], particular focus was given to the type and breaking instability of key strata of shallow coal seams. On this basis, it was found that single key strata structure was the fundamental geological cause of mining-induced damage of the shallow coal seams. Most studies on breaking instability of roof or key strata in the mining of shallow coal seams favored the use of mechanical model of long-beam structure, where the thickness-to-span ratio of the rock beam is below 1/5. But in real situations, the loading key strata are generally hard, thick rocks in shallow coal seams. Experimental analysis has shown that the thickness-to-span ratio of the rock beam is generally above 1/5, indicating deep beam structure in the shallow coal seam [9,10]. Therefore, breaking features of loading key strata analyzed by assuming a long-beam structure usually deviate from the real breaking features.

We built a mechanical model of deep beam structure for describing first and periodic breaking of loading key strata in the mining of shallow coal seams based on elastic mechanics. Expressions of stress components and displacement components in deep beam structure were given under different boundary conditions. The breaking features and limited span of the loading key strata were analyzed based on mechanical models.

To whom all correspondence should be sent:
E-mail: ljwcumt@cumt.edu.cn

EXPERIMENTAL

Identifying loading key strata

There may be one or several loading key strata existing in a shallow coal seam [1,2,8]. Instability and breaking of a single loading key stratum will lead to overall collapse of the overburden and ground surface. Moreover, the ground pressure of the working face intensifies. In the presence of several loading key strata, the instability and breaking of non-controlling inferior key strata will lead to increased ground pressure of the working face. As with the situation of a single loading key stratum, the instability and breaking of the main key strata can also lead to the collapse of the overburden and the ground surface with an intensification of the ground pressure in the working face. This is what we call periodic weighting phenomenon.

For shallow coal seams, the loading key stratum is defined as the rock stratum whose failure can lead to overall collapse of the overburden and thick loose layer on the ground surface, resulting in the loss of carrying capacity of the surrounding rock and happening of dynamic disasters [1,3]. Loading key strata are generally hard, thick rock layers that support the overburden and thick loose layer on the ground surface through certain mechanical structures. Breaking of loading key strata may directly lead to mining pressure, rock layer movement and surface subsidence. Loading key strata, single or multiple, can be found in nearly all shallow coal seams. Identifying the loading key strata is crucial for the study of breaking of loading key strata, weighting and safety of the advancing working face.

Fig. 1 shows the overburden distribution of the shallow coal seam with m overlying layers of bedrock. Above the bedrock is the thick loose layer.

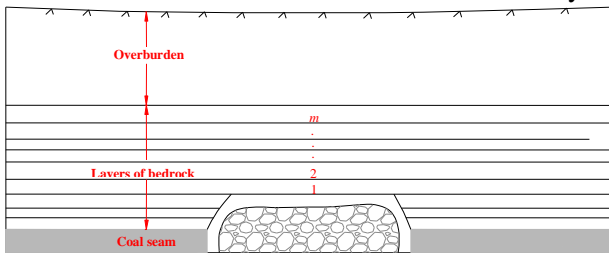


Fig. 1. Overburden distribution of shallow coal seam

Let the thickness of each rock layer be h_i , volume force being γ_i and modulus of elasticity being E_i , where $i=1, 2, 3, \dots, m$. According to the key strata theory [1], the loading key strata must satisfy three conditions:

$$\begin{cases} q_n > q_{n-1} > \dots > q_1 \\ q_n = (q_n)_O, \text{ and } (q_n)_O > (q_n)_{n+1} > \dots > (q_n)_m \\ L_n > L_{n+1} > \dots > L_m \end{cases} \quad (1)$$

where

$$\begin{cases} (q_n)_O = E_n h_n^3 \cdot \left(\sum_{i=n}^{i=m} \gamma_i h_i + \gamma_0 h_0 \right) / \sum_{i=n}^{i=m} E_i h_i^3 \\ (q_n)_m = E_n h_n^3 \cdot \sum_{i=n}^{i=m} \gamma_i h_i / \sum_{i=n}^{i=m} E_i h_i^3 \end{cases}$$

where $(q_n)_O$ is the load imposed by the overburden on the n^{th} rock layer; $(q_n)_m$ is the load imposed by the m^{th} rock layer on the n^{th} rock layer; q_i ($i=1, 2, 3, \dots, n$) is the load acting on the i^{th} rock layer; L_i ($i=n, n+1, \dots, m$) is the breaking step of the i^{th} rock layer.

First breaking mechanical model

As the working face advances, the mined-out area of the loading key strata increases. The stress characteristics of hard, thick loading key strata are different from those of a long-beam structure. Therefore, a mechanical model of clamped deep beam structure under uniform loading was built to analyse first breaking of loading key strata.

Fig. 2 shows the mechanical model of clamped deep beam under uniform loading. The rectangular deep beam with length l and height h is presented with two ends clamped and subjected to uniform loading q .

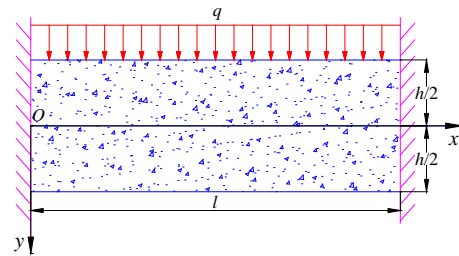


Fig.2. Mechanical model of clamped deep beam under uniform loading

Using the semi-inverse method, the biharmonic stress function is a polynomial with a degree of 5 and 7 variables [11]. Then each stress component of the deep beam structure is given by:

$$\begin{cases} \sigma_x = 2A(2y^3 - 3x^2y) + 6Bxy + 6Cy + 2D \\ \sigma_y = -2Ay^3 + 2Ey + 2G \\ \tau_{xy} = 6Axy^2 - 3By^2 - 2Ex - F \end{cases} \quad (2)$$

From the displacement-stress relationship [12,13] the displacement component is derived:

$$\begin{cases} u = [2A(2+\mu)xy^3 - (2Ax^3 - 3Bx^2 - 6Cx + 2\mu Ex)y + 2Dx \\ \quad - 2\mu Gx] / E' - [B(2+\mu)y^3 + 2(1+\mu)Fy] / E' + \omega y + v_0 \\ v = [-A(1+2\mu)y^4 / 2 - (2\mu Ax^2 - 3\mu Bx - 3\mu Cx + E)y^2 \\ \quad - 2\mu Dy + 2Gy + Ax^4 / 2 - Bx^3 - (2+\mu)Ex^2] / E' - \omega x + v_0 \end{cases} \quad (3)$$

where ω , u_0 and v_0 are arbitrary integral constants, determined by boundary conditions; E' is modulus of elasticity.

If treated as a plane stress problem in elastic mechanics, the boundary conditions for clamped deep beam are usually simplified into displacements $u=0$ and $v=0$ for the fixed end at the mid-point of the end surface in two directions and rotational angle $\partial v/\partial x=0$ or $\partial u/\partial y=0$, as is done in some studies [2,4,12]. Under the above simplified boundary conditions for clamped beam, the analytical solution of the plane stress is more accurate for a shallow beam structure. But great errors may occur for deep beam structure [14-15]. Therefore, simplification of boundary conditions for clamped deep beam should be done carefully and according to the real stress status.

Loading key strata in shallow coal seams bear considerable static load imposed by the overburden layer and the thick loose layer of ground surface. Before first breaking, if the upper surface of the clamped beam undergoes vertical displacement, the entire rock strata will break and lose stability under static load of the overburden. Therefore, for clamped deep beam, changing the boundary condition of rotational angle $\partial v/\partial x=0$ or $\partial u/\partial y=0$ at the central point of the fixed end to vertical displacement $u=0$ at the vertex of the fixed end will better conform to the real situation of shallow coal seam mining [11].

The boundary conditions for the clamped deep structure before the first breaking of the loading key strata are:

$$\begin{cases} y = -h/2, & \sigma_y = -q, \tau_{xy} = 0 \\ y = h/2, & \sigma_y = 0, \tau_{xy} = 0 \\ x = 0, y = 0, & u = 0, v = 0 \\ x = 0, y = -h/2, & u = 0 \\ x = l, y = 0, & u = 0, v = 0 \\ x = l, y = -h/2, & u = 0 \end{cases} \quad (4)$$

Although the loading key strata are thick, the thickness is still smaller than that of the controlling key strata and overburden layer. The loading key strata are under great external load in this sense [1, 16, 17]. By transforming the dead weight of the loading key strata into uniform loading, the calculation can be simplified and better conforms to the real situation.

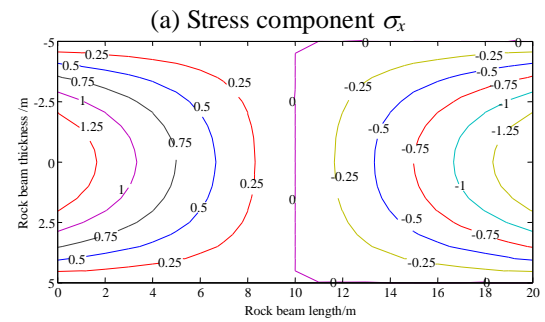
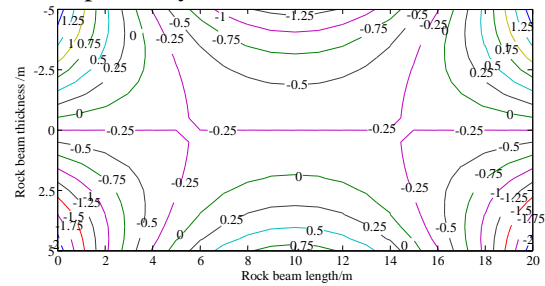
Using the expression of stress component (2), displacement component (3) and boundary conditions (4), the stress component and displacement component before first breaking of the loading key strata are given as follows:

$$\begin{cases} \sigma_x = \frac{4q}{h^3}y^3 - \frac{6q}{h^3}x^2y + \frac{6ql}{h^3}xy - \frac{q(l^2 + h^2 - \mu h^2)}{h^3}y - \frac{\mu q}{2} \\ \sigma_y = \frac{-2q}{h^3}y^3 + \frac{3q}{2h}y - \frac{q}{2} \\ \tau_{xy} = \frac{6q}{h^3}xy^2 - \frac{3ql}{h^3}y^2 - \frac{3q}{2h}x + \frac{3ql}{4h} \end{cases} \quad (5)$$

where q is the sum of loading from the overburden and the dead weight of the loading key strata; μ is the Poisson's ratio of the loading key strata.

$$\begin{cases} u = \left[\frac{2q}{h^3}(2+\mu)xy^3 - \frac{2q}{h^3}x^3 - \frac{3ql}{h^3}x^2 - \frac{q(-l^2 - h^2 + \mu h^2)}{h^3}x + \frac{3\mu q}{2h}xy \right] / E' \\ \quad - \left[\frac{ql(2+\mu)}{h^3}y^3 - \frac{3ql(1+\mu)}{2h}y \right] / E' - \frac{ql(4+5\mu)}{4hE'}y \\ v = \left[-\frac{q(1+2\mu)}{2h^3}y^4 - \frac{2\mu q}{h^3}x^2 - \frac{3\mu ql}{h^3}x - \frac{\mu q(-l^2 - h^2 + \mu h^2)}{2h^3}x + \frac{3q}{4h}y^2 \right. \\ \quad \left. + \frac{\mu^2 q}{2}y - \frac{q}{2}y + \frac{q}{2h^3}x^4 - \frac{ql}{h^3}x^3 - \frac{(2+\mu)3q}{4h}x^2 \right] / E' + \frac{ql(4+5\mu)}{4hE'}x \end{cases} \quad (6)$$

The values were $q=1.0\text{MPa}$, $\mu=0.2$ and $E'=30\text{GPa}$ in this paper. From equations (5) and (6), the distribution curves of stress components σ_x and τ_{xy} and displacement components u and v of the rock beam under the rock beam length $l=20$ m and thickness $h=10$ m were plotted, as shown in Figs. 3 and 4, respectively.



(a) Stress component σ_x
(b) Stress component τ_{xy}
Fig. 3. Stress component distribution of rock beam under clamped conditions

It can be seen that for clamped deep beam under uniform loading, the stress component and displacement component distributions are symmetrical about the central line $x=10$ m of the deep beam, respectively.

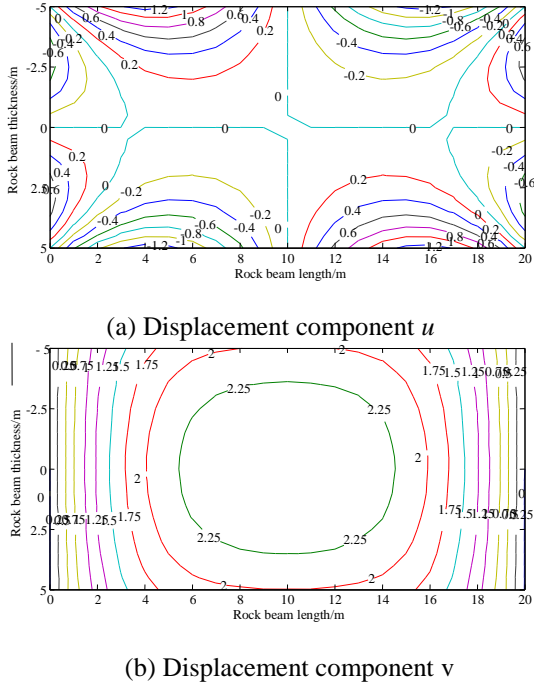


Fig. 4. Displacement component distribution of rock beam under clamped conditions

Periodic breaking mechanical model

After the first breaking, as the working face advances, periodic breaking of the loading key strata will occur. Since the shallow coal seam has higher working thickness, the loading key strata may enter the caving zone and assume a cantilevered beam structure [18]. In light of this, we built a mechanical model of cantilevered deep beam under uniform loading for the analysis of periodic breaking.

Fig. 5 shows the mechanical model of cantilevered deep beam under uniform loading. The rectangular deep beam with length l and height h is presented and subjected to uniform loading q on the upper surface of the beam.

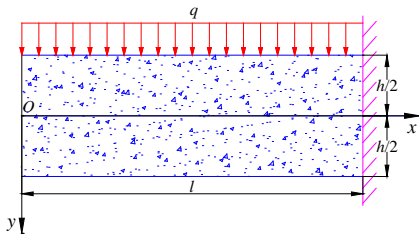


Fig. 5. Mechanical model of cantilevered deep beam under uniform loading

Referring to the method for determining the boundary conditions for clamped deep beam under uniform loading, we considered the shear force and bending moment of the fixed end for the cantilevered conditions before periodic breaking [19]. The boundary conditions for the cantilevered deep beam are:

$$\left\{ \begin{array}{l} y = -h/2, \sigma_y = -q, \tau_{xy} = 0 \\ y = h/2, \sigma_y = 0, \tau_{xy} = 0 \\ x = 0, y = 0, u = 0, v = 0 \\ x = 0, y = -h/2, u = 0 \\ \int_{-h/2}^{h/2} (\tau_{xy})_{x=0} dy = -ql \\ \int_{-h/2}^{h/2} (\sigma_x)_{x=0} y dy = -ql^2/2 \\ \int_{-h/2}^{h/2} (\sigma_x)_{x=0} dy = 0 \end{array} \right. \quad (7)$$

Using the semi-inverse method, the stress components and the displacement components before periodic breaking are given by:

$$\left\{ \begin{array}{l} \sigma_x = \frac{4q}{h^3} y^3 - \frac{6q}{h^3} x^2 y - \frac{12ql}{h^3} xy - \frac{2q(5l^2 - h^2)}{5h^3} y \\ \sigma_y = \frac{-2q}{h^3} y^3 + \frac{3q}{2h} y - \frac{q}{2} \\ \tau_{xy} = \frac{6q}{h^3} xy^2 + \frac{6ql}{h^3} y^2 - \frac{3q}{2h} x - \frac{3ql}{2h} \end{array} \right. \quad (8)$$

where q is the sum of loading from the overburden and dead weight of the loading key strata.

$$\left\{ \begin{array}{l} u = \left[\frac{2q}{h^3} (2 + \mu) xy^3 - \frac{2q}{h^3} x^3 + \frac{6ql}{h^3} x^2 + \frac{2q(5l^2 - h^2)}{5h^3} x + \frac{3\mu q}{2h} x \right] y + \frac{\mu q}{2} x \Bigg/ E' \\ \quad + \left[\frac{2ql(2 + \mu)}{3h^3} y^3 - \frac{3ql}{2h} y \right] / E' + \frac{ql(7 - 5\mu)}{6hE'} y \\ v = \left[-\frac{q(1 + 2\mu)}{2h^3} y^4 - \frac{3\mu q}{h^3} x^2 + \frac{6\mu ql}{h^3} x + \frac{3\mu q(5l^2 - h^2)}{15h^3} x + \frac{3q}{4h} y^2 + \frac{q}{2} y \right. \\ \quad \left. + \frac{q}{2h^2} x^4 + \frac{2ql}{h^3} x^3 + \frac{q(20l^2 + 34h^2 + 30\mu h^2)}{20h^3} x^2 \right] / E' - \frac{ql(7 - 5\mu)}{6hE'} x \end{array} \right. \quad (9)$$

The values were $q=1.0$ MPa, $\mu=0.2$ and $E'=30$ GPa. From equations (8) and (9), the distribution curves of stress components σ_x and τ_{xy} and displacement components u and v of the rock beam under the rock beam length $l=20$ m and thickness $h=10$ m were plotted, as shown in Figs. 6 and 7, respectively.

It can be seen that for cantilevered deep beam under uniform loading, the stress component and displacement component distributions are symmetrical about the central line $x=10$ m of the deep beam, respectively.

RESULTS AND DISCUSSION

In equation (5), let $x=ml$ ($0 \leq m \leq 1$), $y=nh$ ($-0.5 \leq n \leq 0.5$) and $l/h=\varepsilon$. Then the shear stress of the clamped deep beam is:

$$\tau_{xy} = \left| \frac{3\varepsilon q}{4} (2m - 1)(4n^2 - 1) \right| \quad (10)$$

where ε is span-to-thickness ratio of deep beam, i.e., the ratio of span l to thickness h .

From equation (10) and according to the analysis of probable site of breaking for clamped deep beam, when $m=0.5$ and $n=0.5$, $\tau_{xy}=0$. That is, the shear stress of the lower boundary ($l/2, h/2$) of the central

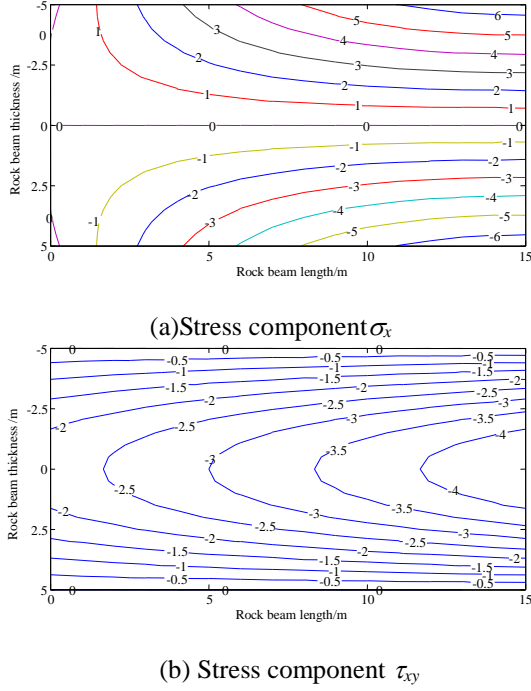


Fig. 6. Stress component distribution of rock beam under cantilevered conditions

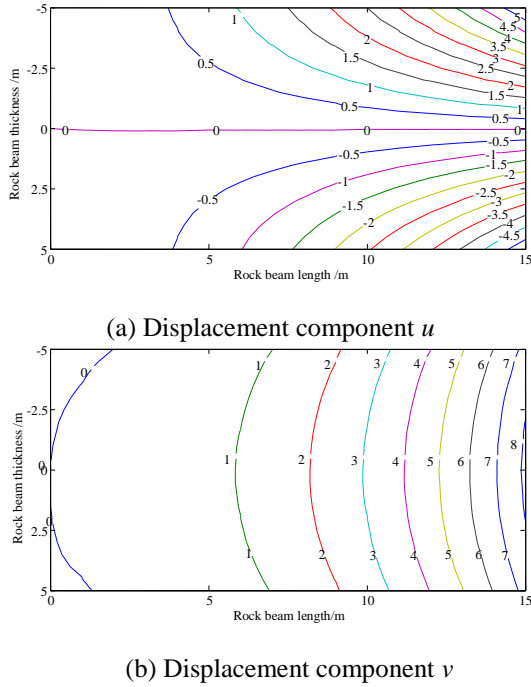


Fig. 7. Displacement component distribution of rock beam under cantilevered conditions

cross-section of the clamped deep beam is 0 (Fig. 3b). At this site, the tensile stress σ_x in the horizontal direction is the maximum principal stress (Fig. 3a). From the above we calculate the tensile stress at this site:

$$\sigma_{x\max} = \sigma_x \Big|_{\left(\frac{l}{2}, \frac{h}{2}\right)} = \frac{ql^2}{2h^2} \quad (11)$$

From equation (10), τ_{xy} reaches the maximum when $m=0$ and $n=0$ or when $m=1$ and $n=0$. That is,

the maximum shear stress is at the fixed end $(0, 0)$ or $(l, 0)$ in the clamped deep beam (Fig. 3b). The shear stress at this site is:

$$|\tau_{\max}| = |(\tau_{xy})_{(0,0)}| = |(\tau_{xy})_{(l,0)}| = \frac{3ql}{4h} \quad (12)$$

When the normal stress at this site reaches the ultimate tensile strength of the rock strata, i.e., when $\sigma_{x\max} = R_T$, the strata will undergo tensile failure. Considering the heterogeneity and brittle fracture of the rock strata, the coefficient η of the rock strata on the verge of failure is used to calculate the limited span upon rupture of the deep beam:

$$L_{iT} = h \cdot \sqrt{\frac{2R_T}{\eta q}} \quad (13)$$

When the shear stress of the clamped deep beam reaches the ultimate tensile strength of the rock strata at this site, i.e., when $\tau_{\max} = R_S$, the rock strata will undergo tensile failure. Then the limited span upon rupture of the deep beam is:

$$L_{iS} = h \cdot \frac{4R_S}{3\eta q} \quad (14)$$

With span-to-thickness ratio $\varepsilon = l/h$ and comparing equations (10) and (11), the limited span-to-thickness ratio upon tensile failure of the deep beam is $\varepsilon_{iT} = \sqrt{2R_T/\eta q}$, and that upon shear failure is $\varepsilon_{iS} = 4R_S/3\eta q$. Thus equations (13) and (14) are respectively changed into:

$$L_{iT} = \varepsilon_{iT} h \quad (15)$$

$$L_{iS} = \varepsilon_{iS} h \quad (16)$$

Similarly, for equation (8), let $x = ml$ ($0 \leq m \leq 1$), $y = nh$ ($-0.5 \leq n \leq 0.5$) and $l/h = \varepsilon$. Then the shear stress of the cantilevered deep beam is calculated by:

$$\tau_{xy} = \left| \frac{3\varepsilon q}{2} (m+1)(4n^2 - 1) \right| \quad (17)$$

From equation (8) and according to the analysis of the probable site of breaking for clamped deep beam, when $m=1$ and $n=-0.5$, $\tau_{xy}=0$. That is, the shear stress of the upper boundary $(l, -h/2)$ of the fixed end of a cantilevered deep beam is 0 (Fig. 6b). At this site, the tensile stress σ_x in horizontal direction is the maximum principal stress (Fig. 6a). From the above the limited span upon tensile failure of the cantilevered deep beam is given by:

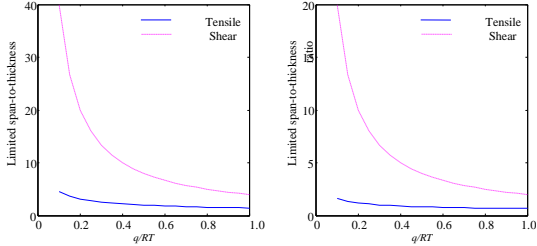
$$L'_{iT} = h \cdot \sqrt{\frac{R_T}{4\eta q} + \frac{7}{40}} \quad (18)$$

The limited span upon shear failure of the cantilevered deep beam is:

$$L'_{iS} = h \cdot \frac{2R_S}{3\eta q} \quad (19)$$

The limited span-to-thickness ratio upon tensile failure is $\varepsilon'_{iT} = \sqrt{R_T/4\eta q + 0.175}$ and that upon shear failure is $\varepsilon'_{iS} = 2R_S/3\eta q$.

Loading key strata in a shallow coal seam are generally sandstone rocks. According to ref. [3], the shear strength of sandstone is 2.22-5.28 times that of the tensile strength (average 3.26 times). With $R_s = 3R_T$ and $\eta=1.0$, we calculate the limited span-to-thickness ratios upon first breaking and periodic breaking of the loading key strata for deep beam structure, as shown in Fig. 8.



(a) First breaking (b) Periodic breaking

Fig. 8. Limited span-to-thickness ratio of deep beam structure of loading key strata in first breaking and periodic breaking ($R_T=3.0\text{MPa}$)

As shown in Fig. 8, the limited span-to-thickness ratio of loading key strata for deep beam structure upon tensile failure will be smaller than that upon shear failure. Thus the limited spans for first breaking and periodic breaking are respectively given by:

$$L_{IT} = h \cdot \sqrt{\frac{2R_T}{\eta q}} \quad (\text{First breaking})$$

$$L'_{IT} = h \cdot \sqrt{\frac{R_T}{4\eta q} + \frac{7}{40}} \quad (\text{Periodic breaking})$$

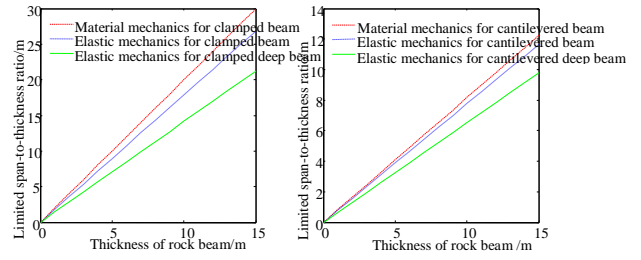
The limited span-to-thickness ratios are $\varepsilon_{IT} = \sqrt{2R_T/\eta q}$ and $\varepsilon'_{IT} = \sqrt{R_T/4\eta q + 0.175}$, respectively.

According to the theory of material mechanics [1, 19], the spans of first and periodic breaking for the clamped deep beam are $L_{IT} = h \cdot \sqrt{2R_T/q}$ and $L'_{IT} = h \cdot \sqrt{R_T/3q}$, respectively. Then using the theory of elastic mechanics [20], the span of first breaking for the clamped deep beam and the span of periodic breaking for the cantilevered beam are respectively given by:

$$L_{IT} = 2h \cdot \sqrt{R_T/\eta q - 0.2} \quad \text{and}$$

$$L'_{IT} = h \cdot \sqrt{R_T/3\eta q + 0.27}.$$

The values were taken as $R_T=3\text{MPa}$ and $q=1.5\text{MPa}$ in this paper. Considering the heterogeneity and brittle fracture of rock strata, the coefficient $\eta=2.0$ was used. Thus the curves of spans of first and periodic breaking vs. thickness of rock beam were plotted using the three calculation methods, as shown in Fig. 9.

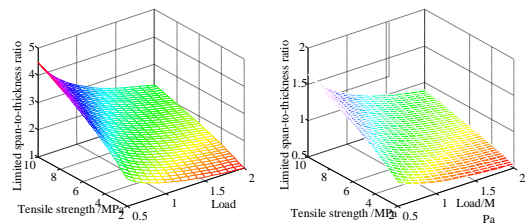


(a) First breaking (b) Periodic breaking

Fig. 9. Comparison of calculation results of three methods

It can be seen from Fig. 9 that as the thickness of the rock beam increases, the breaking span also increases. All three methods achieve small relative errors at a low thickness of the rock beam. But the relative errors increase with the increasing thickness of rock beam. Since the solutions of material mechanics are based on the plane section assumption [19], the calculation does not consider the stress and deformation conditions of the clamped or cantilevered beam boundary. This leads to an overestimation as compared with the other two methods. Solutions of elastic mechanics for general rock beams only consider the stress conditions of the boundary while ignoring the displacement boundary [20]. Consequently, the calculated result will be larger than that based on elastic mechanics for a deep beam. The analytical solutions of elastic mechanics for a deep beam fully consider the stress and displacement boundary conditions as the thickness of rock beam increases. The calculated result better conforms to the real situation of breaking of overburden layer in the mining of shallow coal seam.

Limited span-to-thickness ratio ε of the loading key stratum for clamped deep beam is affected by rock mass strength R_T and load q . Relations of ε to R_T and q under different breaking features are shown in Fig. 10. It can be seen that ε decreases with increasing q and it increases with increasing strength. ε characterizes the stability of the loading key strata.



(a) First breaking ($\eta=2.0$) (b) Periodic breaking ($\eta=2.0$)

Fig.10. Relationship between ε and RT and q

CONCLUSIONS

We built mechanical models for loading key strata in a shallow coal seam based on deep beam structure. The analytical solutions of elastic mechanics for stress components and displacement components upon first and periodic breaking of the loading key strata were calculated.

Both first and periodic breaking can occur as tensile failure or shear failure in the loading key strata. They are affected by limited span-to-thickness ratio and load. For a shallow coal seam, tensile failure is more common upon first and periodic breaking.

By comparing the analytical solutions of material mechanics and elastic mechanics for a general long beam, we found that elastic mechanics more conforms to the real situation of breaking in shallow coal seam as it fully considers the stress and displacement boundary conditions.

The limited span-to-thickness ratio of the loading key strata increases with the increasing strength and thickness of rock mass, but decreases with increasing load. The limited span-to-thickness ratio characterizes the stability of the loading key strata.

Acknowledgments: *Financial support for this research was provided by the National Natural Science Foundation of China (51574220); Fundamental Research Funds for the Central Universities, by China University of Mining and Technology (20142DPY21); the Special Funds of Taishan Scholar Construction Project of China(201309); project funded by the Priority Academic Program Development of Jiangsu Higher Education Institutions (SZBF2011-6-B35).*

REFERENCES

1. M.G. Qian, X.X. Miao, J.L. Xu, X.B. Mao, Key Strata Theory in Strata Control. China University of Mining and Technology Press, Xuzhou, 2003.
2. M.G. Qian, P.W. Shi, Ground Pressure and Strata Control. China University of Mining and Technology Press, Xuzhou, 2003.
3. Z.J. Hou, *J. China Coal Soc.*, **24** (4), 359 (1999).
4. Z.J. Hou, J. Zhang, *J. Liaoning Tech. Univ.*, **23** (5), 577 (2004).
5. Q.X. Huang, *Chin. J. Rock Mech. Eng.*, **21** (8), 1174 (2002).
6. Q.X. Huang: Study on Roof Structure and Ground Control in Shallow Seam Longwall Mining. China University of Mining and Technology Press, Xuzhou, 2000.
7. Q.X. Huang, Roof Structure *J. Coal Sci. Eng.*, **9** (2), 21 (2003).
8. J.L. Xu, W.B. Zhu, X.Z. Wang, M.S. Yin. *J. China Coal Soc.*, **34** (7), 865 (2009).
9. G.F. Wang, *J. Chengdu Uni. Sci. Techno.*, **70**(3), 70 (1997).
10. F.L. Mei, D.S. Zeng. *Mech. Pract.*, **24** (3), 58 (2002).
11. Y. Dai, X. Ji, *J. Tongji Univ. (Nat. Sci. Ed)*, **36** (7), 890 (2008).
12. S.P. Timoshenko, J.N. Goodier, Theory of Elasticity. People's Education Press, Beijing, 1964.
13. H.J. Ding, D.J. Huang, H.M. Wang, *J. Zhejiang Univ.*, **6** (8), 779 (2005).
14. G.F. Wang, Applied Elasticity. Chengdu University of Science and Technology Press, Chengdu, 1995.
15. S.R. Ahmed, A.B.M. Idris, M.W. Uddin, *Comput. Struct.*, **61** (1), 21 (1996).
16. G.F. Wang, *J. Sichuan Univ. (Eng. Sci. Ed.)*, **32** (2), 8 (2000).
17. Q.X. Huang, *J. China U. Min. Technol.*, **34** (3), 289 (2005).
18. J.L. Xu, J.F. Ju, *Chin. J. Rock Mech. Eng.*, **30** (8), 1547 (2011).
19. H.W. Liu, Material Mechanics. Higher Education Press, Beijing, 2004.
20. Z.L. Xu, Elastic Mechanics. Higher Education Press, Beijing, 2006.

Test study on the thickness of the soil layer under the plate affecting the compression failure of the concrete expanded-plate pile

Y. Qian ^{1,2*}, Z. Liu ¹, W. Tian ¹, R. Wang ¹

¹ Jilin Jianzhu University, 130118 Changchun, China

² Jilin Structure and Earthquake Resistance Technology Innovation Center, 130118 Changchun, China

Received, September 8, 2017, Accepted, December 12, 2017

In this paper, the influence of the thickness of soil layer under the plate on the failure behavior of soil surrounding the pile and the bearing capacity of a single pile under vertical compression in the complex soil layer is studied. In the test study, the small model test method of undisturbed soil with a new half-section pile is adopted, which not only solves the question that by the original full-section pile the whole failure behavior of soil surrounding pile cannot be clearly seen, but also solves the deflection that burring soil test cannot ensure soil characteristics according to the actual condition of the construction site. By comparing and analyzing the results of finite element analysis the reliability of the test results was checked. The study results will provide a reliable theoretical basis for the design and application of the concrete expanded-plate pile, promote the popularization and application of the concrete expanded-plate pile and look forward to achieve larger social and economic benefits.

Key words: Concrete expanded-plate pile (CEP pile), Thickness of soil-layer under the plate, Test of undisturbed soil, Finite element analysis, Compression failure.

INTRODUCTION

In recent years, with the rapid development of economy, the construction industry, as the leading industry in the country, which is also changing rapidly, a variety of tall buildings and special-shape buildings were built in everywhere, which put higher and higher requirements to the pile foundation. With the continuous improvement and innovation of the piles, various types of piles gradually appeared, such as multi-section-expanded piles, the bearing capacity of which is increased with the increase in side friction of pile. In the various new types of piles [1,2], concrete expanded-plate piles with high bearing capacity, small settlement, flexible position for design of plate and good benefits of social and environment, have been applied to engineering projects and praised by the society.

Traditionally for the concrete pile with constant section and simple situation of the bearing force, the bearing capacity is provided only by the side of pile and pile end. The innovative concrete expanded-plate piles with higher bearing capacity, lower settlement, good social and environmental benefits, are accepted by more and more people [3]. Although in the concrete expanded-plate pile one or multiple plate bodies are added based on the body of the ordinary concrete pile with constant section, the condition of pile bearing loads has been greatly improved, the loads are commonly afforded through the side of pile, end of pile and end of plate, thus the

bearing capacity of the concrete expanded-plate is greatly increased [4]. The complex bearing characteristics of the concrete expanded-plate pile are not known enough and theoretical research of the concrete expanded-plate pile is far behind the practical engineering project.

In this paper, the effect of the different thickness of the soil layer under the plate on the performance of the concrete expanded-plate, was studied by ANSYS software with finite element analysis [5]. In the study, the test of undisturbed soil was initially adopted, which reduces the difference between laboratory soil and soil in the site, extends the new model test method with half-section pile, and the total process of failure behavior of soil can be observed, making up the disadvantage that only collecting data by the device for analysis and ratiocination in the test study, provides a new method of test study on pile foundation. Through the simulation analysis by ANSYS software to compare and analyze the results obtained by computer simulation analysis, the study on the bearing capacity of a single pile of the concrete extended-plate pile under vertical compression was improved.

EXPERIMENTAL PART

Test of undisturbed soil

Design and manufacture of test device

In this paper, the small model test with half-section pile of the concrete expanded-plate pile under compression was adopted, because traditional testing devices cannot meet the needs of the test, so a multi-functional plat for loading is suitable for the

*To whom all correspondence should be sent:

E-mail: 654675316@qq.com

test demand was specially designed [5] (as shown in Fig.1).



Fig. 1. Multi-functional plat for loading

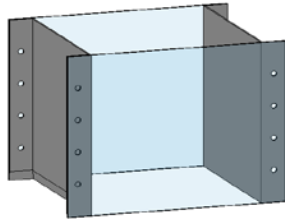


Fig. 2. Model picture of device for getting soil

Design of device for getting soil

Undisturbed soil was selected in the test. In order to get better undisturbed soil, a device for getting soil was designed. In order to keep the device unchangeable, Q235 steel and thickness of the steel plate of 4mm was adopted [5,6], the design model of the device for getting soil is shown in Fig. 2. The dimensions of the device are shown in Table 1.

Table 1. Size of the device for getting soil

	Length (mm)	Width (mm)	Height (mm)	Thickness (mm)
Compression capacity	400	250	130	3

Note: the side of steel plate is length, the side of I-beam is width.

Design of model pile

Due to the small-scale model test selected, and the premise that the soil is destroyed earlier than the pile itself, the material of the specimen has little effect on the test result, so steel Q235 was used as pile material [7], the dimensions of the model piles are shown in Table 2.

Collection of test soil

Undisturbed soil was applied as the test soil, which is a most important difference between this test and previous half-section pile model tests. Combining theories and practices, from aspects of device selection and operation, the way of pressing

Table 2. The size of model pile in the test

Category of Model	Specifications of Different Model Types					
		Name	HDKY1	HDKY2	HDKY3	HDKY4
Hard clay	Compression	L	0	750	1500	2250

the device, the way of taking out the device, etc., were optimized to avoid soil excessive vibration in the process of taking soil, and to ensure characteristics of test soil according to actual condition. The procedure of getting soil for test is as follows: excavation of site, placing and pressing into device, taking out device, cleaning device and soil, packaging and transport.

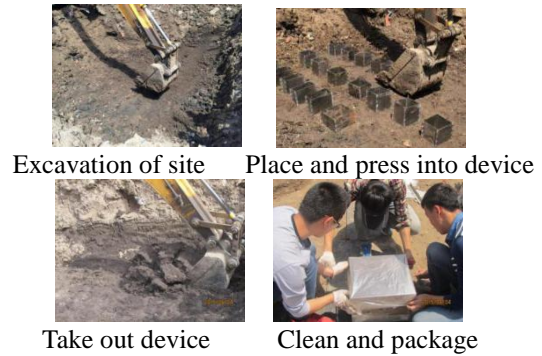


Fig. 3. The process of taking soil

The principle of model test of undisturbed soil

Undisturbed soil was selected as the test soil which is a most important difference between this test and previous half-section pile model tests, it is a premise for a successful test because the natural characteristics of soil are not destroyed as much as possible [4,8]. In addition, due to the multi-functional plat for loading (shown in Fig. 4) adopted, the test process is also different from the past.

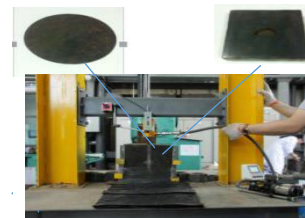


Fig. 4 The loading device of the compression test

Collection of test data

The collection of data in the test is a significant part, because the accuracy of the collection of data is directly related to the results of analysis and comparison of the test data. The collection of data mainly consists of four parts: vertical displacement of model pile, vertical bearing capacity of model pile, photos of soil surrounding the pile at different stages of loading, accuracy of physical properties around test soil.

Table 3. The models established at soil thickness different of reel up and down

Category of Model	Specifications of Different Types Model					
	Name	HDKY1	HDKY2	HDKY3	HDKY4	
Hard clay	Compression	L	0	750	1500	2250

The former three data were recorded at the same time, firstly the model pile was loaded, it underwent vertical displacement, when the displacement reached 1 mm, the magnitude acting on the model pile under the load was recorded [9], every 2 mm of displacement were recorded. The test data on the failure behavior of the soil around the pile were finally recorded until the soil was up to complete failure. After the test, in order to improve the accuracy of the soil data, the test soil should be gauged in time.

RESULTS AND DISCUSSION

Under vertical compression, the thickness of the soil layer under the plate plays a significant role in bearing capacity of the concrete expanded-plate pile, therefore, as the change in the thickness of the soil layer under the plate affects the bearing capacity of the concrete expanded-plates, in the test, the thickness of the soil layer under the plate, in which the plate is embedded, was selected at four conditions as follows: 0 times the cantilever length of plate, 1.5 times, 3 times and 4.5 times (the cantilever length of the plate is the straight distance of the plate protrusion).

Analysis of data about loads-displacement

Based on the above test data, the load-displacement curve of the concrete expanded-plate pile under compression in the test, is shown in Fig. 5.

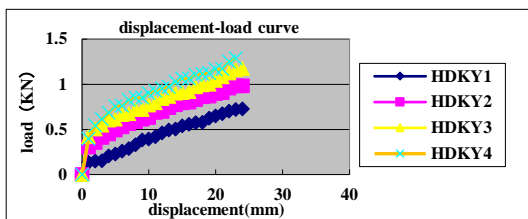


Fig. 5. The load-displacement curve of pile under compression

It can be seen from Fig. 5 that, with the increase in load, the displacement of different concrete expanded-plate pile models in compression gradually increased; for the same load, the displacement, from pile HDKY1 to pile HDYK4, gradually increased with the increase in the thickness of soil under the plate, in the early term (the top of pile displacement in 0~1mm) the load undergoes mutation, under the vertical compression the soil

becomes to a dense situation due to squeezing, which improves the bearing capacity of soil, and the increase in vertical load in unit displacement is very fast, which complies with the result of the gradient of the curve being biggest; in the middle stage (the top of pile displacement in 1~10 mm) with the gradual increase in vertical compression, the trend of vertical load with the displacement increase was gradually flattened, subtle cracks on the soil of plate edge developed, integrity of soil was destroyed and bearing of capacity decreased, the gradient of displacement-load curve slowed down; in the final stage (the top of pile displacement in 10~24 mm) the increased trend of vertical load of the top pile gradually decreased, which means that the soil reaches the failure behavior, while the vertical displacement remains unchanged with the increase in vertical compression.

According to the comparison and analysis of the displacement-load curve of the concrete expanded-plate pile model, it was concluded that:

(1) For the model piles from HDKY1 to HDKY4, the bearing capacity of the concrete expanded-plate pile increased with the increase in load, and the trend of the load-displacement curves remained similar.

(2) The thickness of soil under the plate of model pile HDKY1 was 0 times the cantilever length of the plate, the curve is located at the bottom of the figure. As we can see from Fig. 5 the ultimate bearing capacity of the pile is greater than 0.5KN, when the load reaches 0.5KN, the trend of the load-displacement curve gradually flattened but it was still increasing, the displacement of the pile body reached 24 mm and failure happened due to excessive displacement. The load-displacement curves of the model piles from HDKY2 to HDKY4 were close, the thickness of soil under the plate was 1.5 times, 3 times and 4.5 times the cantilever length of the plate, respectively, the ultimate bearing capacity of the pile was greater than 0.7KN in HDKY2, greater than 0.9KN in HDKY3 and greater than 1.2KN in HDKY4, while the trend of the load-displacement curves of the three types of pile remained unchanged. This indicates that the regulation in the process of soil failure is similar, so the thickness of soil under the plat of the concrete expanded-plate pile is greater than at least 1.5 times the cantilever length of the plate.

(3) When the initial displacement of the model pile reaches 1 mm, the gradient of the load-displacement curve rises in turn, that is, when the displacement of the pile body reaches 1 mm, the load successively increases, but the trend of load does not directly increase with the increase in the thickness of soil under the plat of concrete expanded-plate pile. It can be seen from Fig. 5 that the load of HDKY1 has the smallest increasing range, the loads of HDKY2~HDKY4 have a similar increasing range, which compares with that of HDKY1. This illustrates that when the thickness of soil under the plat of the concrete expanded-plate pile is smaller than 1.5 times the cantilever length of the plate, the effect of the bearing capacity of the pile is not significantly improved; otherwise the effect is very obvious, it also shows that the actual thickness of soil under the plate of the concrete expanded-plate should be greater than 1.5 times the cantilever diameter in order to sufficiently play a role in the bearing capacity of the concrete expanded-plate pile.

Failure behavior of the soil surrounding the pile

The main task of the test was to observe the failure situation of soil surrounding the pile. The behavior before and after the failure of each pile was compared with the failure shapes of soil surrounding the pile and above the plate of four half-sections of the test pile with the increase in the cantilever length of the plate. In the test, half-section pile and test device were specially designed, which provides conditions for observing the failure of pile and soil. The failure process of pile and soil is shown in Fig. 6 (example of pile No.2.)

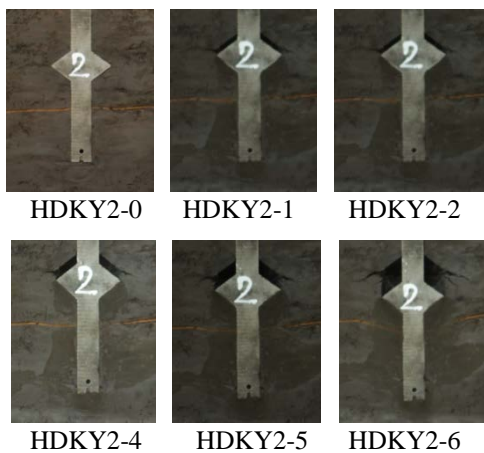


Fig. 6 The failure process of pile and soil with the increasing of vertical compression

Failure behavior and whole process of failure is clearly seen from Fig. 6, which is combined with the above data of load-displacement curve. In the test, the failure process of soil surrounding the half

section expanded-plate under compression is divided in three stages.

First stage - elastic compaction stage. This is the early stage of model test being loaded, load effect is small, the triangular zone compressed under the plate is formed, at this time, the load-displacement curve is linear, with the increasing of load, the soil under the plate and the end of pile are gradually compacted.

Second stage - plastic deformation stage. This is the middle stage of the model test, the load at the top of pile is gradually increased, subtle cracks firstly develop at the soil of plate edge; to compare with the common pile, as the concrete expanded-plate is added to the bearing plate, which increases the interactivity between pile and soil and decreases the vertical displacement of pile body. With the increasing of load, shear failure at the end of the plate is gradually increased, the stress of soil under the plate is gradually increased and settlement displacement of pile also gradually increases, the cracks of the soil surrounding the edge of plate are further extended.

Third stage - failure stage. This is the last stage of the model test, the developing trend of load-displacement curve is gradually flattened, that is, in the situation of larger load increment, the changes of pile displacement are small, the model pile loses the bearing capacity, the failure behavior of the soil surrounding the plate is more serious, the load reaches the ultimate condition. Larger cracks develop at the end of the plate, the compactness of the soil under the plate increases, the sliding failure of soil under the plate finally occurs.

Given all this, as can be seen from the figure of test process under compression, with the increase in vertical compression on the concrete expanded-plate pile, through the watermark under the plate and in the soil surrounding the pile it is obtained that the compactness of the soil under the plate and soil surrounding the pile is increased. In other words, with the increase in vertical compression, the stress under the plate and bottom of pile increases, which is concentrated on the position under the plate. In the undisturbed soil test, the thickness of the soil layer under the plate affects the failure of soil surrounding the concrete plate-expanded pile, as shown in Figs.7 and 8.



Fig. 7. Failure behavior of the soil for different model piles



Fig. 8 Failure behavior after the pile being taken

The summary of the results is as follows:

(1) As the soil itself has a certain degree of elasticity-plasticity, under the initial stage of vertical compression loaded, the soil under the bearing plate of model piles HDKY1 to HDKY4 is compacted; with the increasing of load, in the range of elasticity-plasticity of the ultimate deformation of undisturbed soil, the soil under the the bearing plate is gradually compacted with the increasing of the displacement of pile body. In the process of the soil being compressed, shearing failure firstly develops at the soil of plate edge. As can be seen from Figs. 7 and 8, after the soil is destroyed, the soil in the edge of the bearing plate displays an obvious shearing failure, the effect of degree of shearing failure on the subsoil is decreased on increasing the thickness of the soil under the bearing plate. HDKY1 pile is biggest, HDKY4 pile is the smallest. On the one hand, because of the existence of a bearing plate, the displacement of the test model pile is very small in the early stage. On the other hand, the soil is compacted what is also beneficial to improve the bearing capacity of soil.

(2) For the soil above the plate, at the initial stage of vertical tension loaded for the model pile in the test, the top surface of the plate of the concrete expanded-plate pile does not immediately separate from the soil, and does not destroy the soil above the plate.

(3) For the soil under the plate, in the middle stage of the test, under the effect of vertical compression load, after the soil contacting with the end of plate in the test model pile reaches the soil elastic-plastic limit of deformation, sliding failure develops; a sliding line is first seen at the edge of the plate and along a certain angle θ (the acute angle between the direction of the tangent line and the horizontal line) is developed symmetrically to the outside of the pile. When the vertical compression increases to some degree, the sliding line will be withdrawn.

The following differences were observed:

(1) When there is interaction between pile and soil, the influence of soil thickness under the plate on the bearing capacity of the concrete expanded-plate pile is different. It can be clearly seen from the dividing line of soil in two layers in the figure under

vertical compression that the boundary of HDKY1 is obviously concave, the boundaries of HDKY2 and HDKY3 are not obvious, while the boundary of HDKY4 does not change. This shows that the influence of the soil under the plate of the concrete expanded-plate pile is getting smaller and smaller from HDKY1 to HDKY4, when the thickness of the soil-layer under the bearing plate is greater than 1.5 times the cantilever length of the plate at least. The result is consistent with that of theoretical calculation.

(2) When the soil under the plate of the bearing plate comes to sliding failure, the soil around the edge of the expanded-plate will produce a sliding crack. The angle θ (acute angle) formed along the tangent line of the sliding crack to the horizontal line is known as the sliding angle. It can be seen from the figure that the sliding angle of HDKY1 is small and the sliding curve has the trend of horizontal development, while the development of sliding curves for HDKY2 to HDKY4 is consistent with theory.

Size and specification of model

In this paper, the establishment of a pile model under compression is as follows: length of concrete pile is 5750 mm, diameter of pile is 500 mm, diameter of bearing plate is 1500 mm, height of bearing plate is 750 mm, slope angle of plate is 37° , which is in accordance with the reasonable range found in the previous study [10]. The pile has centrosymmetric structure. In order to directly observe the images such as displacement cloud picture and stress cloud picture of the pile and soil, in the study, the half-section pile model was adopted. The soil layer was silty clay and hard clay, the thickness of both soil layers was 3250 mm.

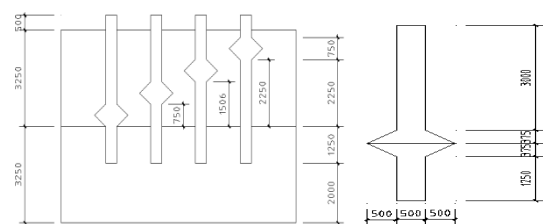


Fig. 9. Diagram of different soil thickness models under the action of vertical compression

Analysis of results by finite element simulation

As can be seen from the curves in Fig.10, when the load is $0 \sim 150\text{KN}$, the displacement of pile is almost not changed; when the load is $200 \sim 450\text{KN}$, the displacement of the pile increases with the increasing of load, which becomes a linear relationship in a certain range; after the load is greater than 450KN , the rate of change of

displacement gradually increases with the increasing of load. At the action of the same load, the displacement of pile gradually decreases. With the increase in the thickness under the plate, the displacement of HDKY4 is the smallest, that of HDKY1 is the largest, and the load-displacement curves of HDKB2 to HDKB4 are basically the same with little change. When the thickness of the soil under plate is less than 1.5 times the cantilever length of the plate, the displacement change is largest in the situation of the same load; when the thickness of the soil under the plate is smaller than 1.5 times the cantilever length of the plate, the displacement gradually decreases in the same load. When the thickness of soil under the plate is 1.5 times, 3 times and 4.5 times the cantilever length of the plate, respectively, the displacement of pile body is not significant. So, it is reasonable that the thickness of the soil under the plate of the concrete expanded-plate pile should be greater than 1.5 times the cantilever diameter.

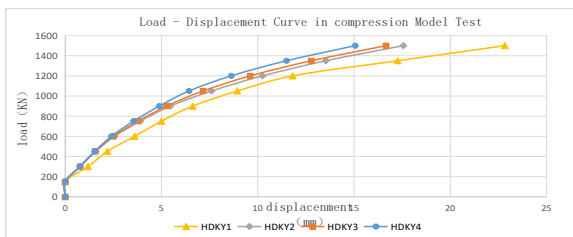


Fig. 10. Load-displacement curves of model pile in the silty clay for finite element analysis

Comparative analysis of model test and simulation result

The following is an example of HDKY2, which shows the trend of the load-displacement curve for model test and simulation test, as shown in Fig. 11.

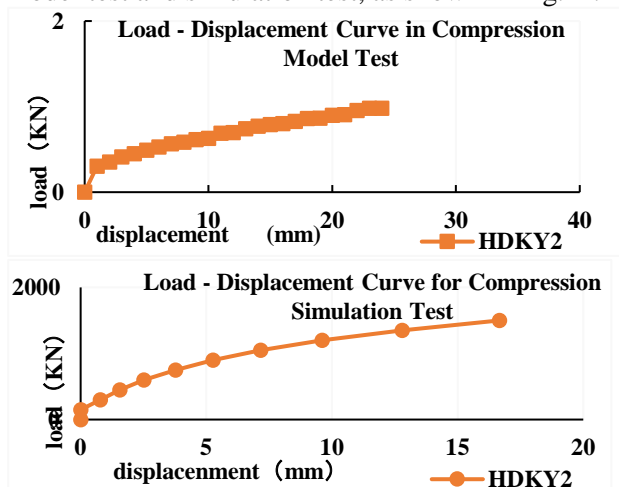


Fig. 11 Test and simulation displacement-load curve contrast

It is known that by comparing the load-displacement curves of the test and simulation

analysis, the load of simulation pile model and test model of HDKY2 under compression are all increased with the increasing of the displacement, the load also exhibits a convex line change with respect to the displacement.

The difference is that the model test at the beginning (displacement 0 ~ 1 mm) the load has mutation, while the simulation analysis, the load has a mutation but little change in the displacement, which is due to the fact that the increasing of displacement is controlled to record the load during the test, while the simulation analysis is to control the increasing of load to derive the displacement, the difference is better able to verify each other. In summary, the study results of model test and simulation analysis are basically the same.

CONCLUSIONS

The study is about the test of undisturbed soil of the concrete expanded-plate pile, of which the innovation point is to break the traditional test laboratory method. The test is carried by taking undisturbed soil from the construction site, and a multi-functional loading platform is designed to ensure the smooth conduct of the test; then, to analyze the initial data and picture the information obtained in the model test. The initial data include collected vertical compression load in the process of loading of test, and corresponding displacement of pile body, picture information is process picture about interactivity of the pile and soil. In the paper, it is adopted that the method of comparison and analysis by the combination of data and picture, and analyze the whole failure behavior of soil surrounding plate in the different stages. The test results obtained from the analysis method are more reliable and persuasive than those obtained from the test data. The important conclusion is as follows: with the increase in vertical compression, the displacement of pile increases, the stress under the plate and bottom of pile also increases, which is focused on the soil under the plate; in order to better improve the bearing capacity of pile, the thickness of the soil under the plate should be at least 1.5 times the cantilever length of the plate.

Acknowledgement: This work was financially supported by the National Natural Science Foundation of China (51278224 and 51678275).

REFERENCES

1. S.Bao-han, H.De-xin, L.Zhen-liang, *J.Ind. Bldg.*, **34** (3), 1 (2004).
2. Q.Yong-mei, *J. JL Archit. Civ. Eng. Inst.*, **21** (2), 14 (2004).
3. Q.Yong-mei, Y.Xin-sheng, W.Ruo-zhu, *J. JL Archit.*

- Civ. Eng. Inst.*, **27** (3), 4 (2010).
4. C.Hai-ming, B.Feng-qi,L.Xiao-wei, *J. HF. Univ. Technol.*, **29** (6), 736 (2006).
 5. Q.Yong-mei, Z.Da-peng, X.Xue-wei, *J. Adv. Mater. Res.*, **578-579**, 232 (2014).
 6. Q.Yong-mei, X.Guang-han, *J. Open Cons. Bldg. Technol.*, **41** (11), 22 (2014).
 7. Z.Yan-qing.Y.Hui, *J. BJ. Univ. Technol.*, **32** (10), 879 (2006).
 8. W. Ruo-zhu, Q.Yong-mei, Y.Xin-sheng, *J. Cons. Bldg. Technol.*, **38** (1), 5 (2011).
 9. Q.De-ling, *J. Geotech. Eng.*, **24** (3), 371 (2002).
 10. X.Xue-wen, *Jilin Jianshu University, Changchun*, 2015.

Research on the environmental protection of magnetron sputtering coating for multi-contour cavity structure products

D. Wang *, B. Hu

School of Mechanical and Electric Engineering, Soochow University, Suzhou 215131, People's Republic of China

Received August 30, 2017; Accepted December 19, 2017

Although chemical coating is mature, with the increasingly serious environmental pollution, limited or prohibited production is inevitable. The common coating method could not be used for the contour cavity structure product as the structure of the product is too complex. Normally, the problem includes: (1) low target utilization rate, (2) not uniform film thickness, and (3) no dead cavity coating. In this paper, some strategies were used to solve the above problems: (1) Multiple rotating cylindrical magnetron sputtering targets were installed to improve the efficiency and uniformity of films; (2) Multiple magnetron sputtering targets and an auxiliary magnetic field were set to improve the plasma density of the vacuum coating chamber and the uniformity of the film on the inner cavity wall; (3) Appropriate magnetron sputtering process parameters were selected to improve the adhesion strength between the film and the substrate interface. Based on the above strategies, a uniform, compact and continuous composite film can be coated on the multi-contour cavity structure product. Magnetron sputtering is a physical vapor deposition method which not only meets the technical requirements of complex surface coating, but also abandons the pollution caused by chemical plating problems. It is an excellent green environmental protection process.

Key words: Multi-contour cavity products; Magnetron sputtering; Green environmental protection process; Film uniformity; Homogenization control.

INTRODUCTION

The common coating method cannot be used for the contour cavity structure product as the structure of the product is too complicated. Normally, the problem is that the film thickness is not uniform and not firm, and in the production process it will cause environmental pollution. In recent years, magnetron sputtering coating has been introduced as a novel coating technology. It is a physical vapor deposition technology which does not produce environmental pollution problems. By applying magnetic field on the surface of the cathode target to form an electron trap, the glow discharge on the target surface forms a plasma region and the atom sputtering target surface coats on the substrate surface [1-3]. Compared with the film produced by the common coating process, the film prepared by magnetron sputtering coating is harder, and the process is highly efficient. Recently, magnetron sputtering coating technology has been widely used in many fields, such as aerospace, engineering, electronic components, precision instruments and so on [4-8]. Current magnetron sputtering coating technology is mainly used for products of simple structure. The use of magnetron coating technology for a contour cavity structure product mainly has the following problems [9]:

1) As magnetron sputtering is planar

sputtering, for the complex cavity of the product, the cathode magnetic field component will cause uneven local sputtering and will lead to target consumption, uneven surface, concave erosion and will influence the quality of the film;

2) For the complex cavity product, the magnetron sputtering coating displays a selective sputtering phenomenon, and at the same time, an antisputtering effect on the film, which causes a large difference between the compositions of the film and the target; the film is uneven and not strong.

Aiming at the above problems based on the character of the contour cavity structure product, some strategies were developed in this paper to improve the magnetron sputtering coating technology.

METHODOLOGY

Basic principle of magnetron sputtering coating

The basic principle of magnetron sputtering is related to the orthogonal electromagnetic field between the substrate and the cathode sputtering target. By passing into the special gas, the glow discharge on the target surface through the orthogonal electromagnetic field forms a plasma region. Under the action of the orthogonal electromagnetic field, the electrons move along the target surface. At the same time, the motion of the electrons is restricted to a certain space to increase the collision probability between electrons and working gas molecules and to improve the ionization

*To whom all correspondence should be sent:
E-mail: wangwangdeshan@163.com

efficiency of the electrons. Electrons and argon atoms collide yielding a positive Ar ion and a new electron. After a number of collisions, the electron loses energy to become 'a final electron' entering into the weak electric field. The argon ion is affected by the electric field to bomb the target surface and sputtering target atoms, by the collision between the target atoms, the atom is sputtered onto the substrate surface by kinetic energy transfer. Finally, the atomic target surface sputtering deposition on the substrate surface forms a thin film [10-12]. Its basic principle is shown in Figure 1.

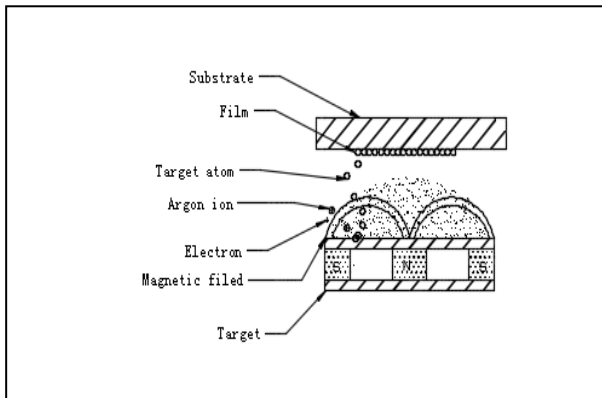


Fig. 1. Basic principle of magnetron sputtering [10]

Internal sputtering coating homogenization control technology for contour cavity structure

Coating the inner cavity of the multicontour cavity structure, the film thickness is uniform and the firm film layer will directly affect the stability and reliability of the coating products.

The key issue of the magnetron sputtering coating technology is how to ensure uniformity and compactness of the film. In this paper, the following strategies are developed to effectively improve and enhance the uniformity and compactness of the films.

1) Use of rotating cylindrical magnetron sputtering target to achieve directional coating

At present, the main target includes a coaxial cylindrical target and a circular planar target, meanwhile, rectangular plane target, rotating cylindrical rectangular target and some special structure targets are also used in the market. The target is mainly composed of a cathode body, a shielding cover, a target and a permanent magnet, a pressing ring, a substrate and other common components. For the multi-edge cavity surface coated multilayer film obtained in this study, the rotating cylindrical magnetron sputtering target is used, and multi-targets are installed at different positions of the coating machine, so that the target can be freely rotated to achieve directional coating.

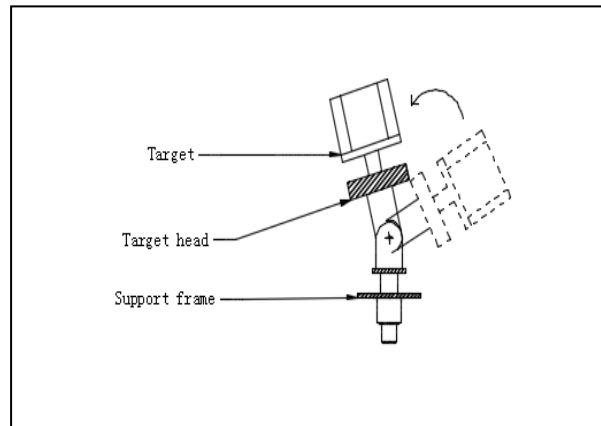


Fig. 2. Rotating cylindrical magnetron sputtering target

2) Set up of a number of magnetron sputtering targets and auxiliary magnetic field to improve the structure of the cathode target

The structure of the unbalanced magnetron sputtering cathode target was improved by using a plurality of magnetron sputtering targets and auxiliary magnetic field, and to improve the density of the vacuum coating plasma chamber, and then to improve the sputtering bias to the deposited coating. At the same time, the reasonable layout of the target permanent magnet ensures the uniformity of the film. Under the requirement of magnetic field strength, the magnetic pole ensures that the distribution of the magnetic field intensity is uniform, thus improving the uniformity of the film and the rate of sputtering. At the same time, the concave target erosion is due to the nonuniformity of the magnetic field component of the planar sputtering cathode target. In this paper, by changing the magnetic field distribution, internal stress of the complex product can be generated in the substrate by sputtering, and a compact continuous and uniform film can be formed.

3) Design of the frame structure of the cathode target rotation and revolution of the cathode target frame structure to improve the uniformity of film thickness

When the substrate and the cathode target are fixed, the uniformity of the film cannot be solved very well. In practice, the contour cavity structure does not move when cathode target rotation and revolution of the cathode target frame takes place. The substrate can be bombarded with the same degree of sputtering particles in different positions. The cathode target frame rotates every week, and a point on the substrate is always in a different position relative to the sputtering target. In this way the film thickness uniformity on the same substrate is guaranteed.

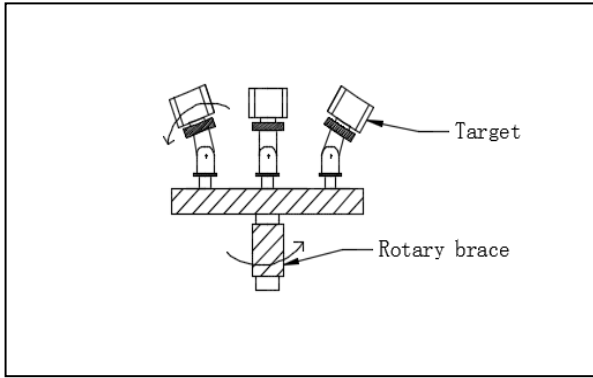


Fig. 3. Cathode rotation and revolution target frame structure

4) Selection of the appropriate parameters of the magnetron sputtering process

The selection of the appropriate magnetron sputtering process parameters, including substrate temperature and gas pressure deposition rate improves the quality of equipment. According to the performance requirements of the film, the sputtering parameters are adjusted to improve the adhesion strength between the film and substrate interface.

EXPERIMENTAL STEPS AND RESULTS

The basic experimental steps are as follows:

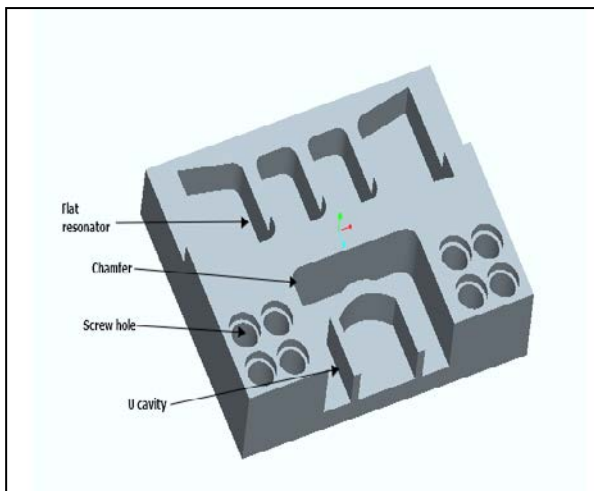


Fig. 4. Structure of the complex cavity

CONCLUSIONS

In this paper, the uniform control method of contour cavity coating was studied. The magnetron sputtering process was improved for contour characteristics of complex cavity structure product through installation of multitargets at different positions in the coating machine, and the target head rotation supports the revolution of the combination model, provides the product surface and complex inner cavity structure with a compact film of uniform thickness. The key technology for complex product cavity magnetron sputtering was optimized.

Table 1. Experimental steps and results

Experimental steps	Contents	Aims
Step 1	According to the requirement of magnetron sputtering cavity structure on the outline of the target, a rotating cylindrical type multi target magnetron sputtering target, sputtering target at different working conditions with a rotating magnetic structure or rotating target structure was used. In the experiment, we used six station magnetron sputtering devices mainly composed of a vacuum detector, vacuum furnace, vacuum system, cathode magnetron, gas input system, and supply, etc.	To improve the utilization rate of the target
Step 2	As the working environment of the contour cavity surface is complex, flexible target head rotation and target head can be used to support effectively sputtering the complex cavity flexible to implement target head rotation and target head can be used to support effectively sputtering the complex cavity	To realize fixed point
Step 3	Setting the auxiliary magnetic field around the cathode target, by improving the shape and distribution of the magnetic field, as well as setting the shield and other measures, the internal stress of the film coating can be produced by the multi contour cavity wall sputtering. The films were continuous and uniform, and the cathode materials were Ti, TiN and TiAlN.	To achieve compactness and uniformity of the film.
Step 4	In the complicated cavity, a plurality of magnetron sputtering targets and auxiliary magnetic fields are used to form a closed magnetic field in the coating chamber, By interaction of the target with the auxiliary magnetic field, the plasma density increases. Thereby, the contour cavity can reach the purpose of depositing the coating.	To improve the target surface plasma density, and the deposition of the film
Step 5	To the different components of the sputtering phenomenon, and the antisputtering rate of the film, select the appropriate process conditions to minimize the antisputtering effect on the film.	Reducing the reflection effect of the substrate and improving the bonding strength of the film.

Results: thin film without cracks; film thickness between 2 μm~8μm; uniformity is better than 6%; hardness up to 2500 HV; with high strength, no peeling; corrosion resistance, heat resistance and abrasion resistance; high utilization rate of the target; controlled deposition rate (2.0~2000) nm/s; film speed (2~13) μm/h.

D. Wang, B. Hu: Research on the environmental protection of magnetron sputtering coating for multi-contour...

Magnetron sputtering is a physical vapor deposition method, which not only meets the technical requirements of complex surface coating, but also abandons the pollution caused by chemical plating problems; it is an excellent green method.

Acknowledgements: *This work was supported by Jiangsu Province basic research project (Natural Science Foundation) of China under Grant No. BK20151220.*

REFERENCES

1. Z. W. Tang. Principle and Application of Thin Films. Second Edition, Beijing: Metallurgical Industry Press, 2003.
2. J. F. Tang, Q. Pei, X. L. Gu. Modern Optical Thin Film Technology. Hangzhou: Zhejiang University Press, 2006.
3. M. B. Tian. Thin Film Technology and Thin Film Materials. Beijing: Tsinghua University Press, 2006.
4. D. G. Xin, *Materials Engineering*, **12**, 72 (2010).
5. Y. H. Di, X. M. Cao, *Development and Application of Metal Materials*, **5** (2004).
6. J. C. Zhang, W. D. Wu, H. Xu, X. H. Tang, *Chinese Journal of Materials Research*, **18**, 4 (2004).
7. J. Jia, *Semiconductor Technology*, **29**, 7 (2004).
8. J. P. Cheng, X. D. Yang, *Special equipment for the electronics industry*, **11**, 27(2009).
9. X. P. Li, Plasma Characteristics of High Power Composite Pulsed Magnetron Sputtering and Preparation of TiN Thin Films. Harbin: Harbin Institute of Technology, 2008.
10. Y. Guo, Measurement of Plasma Ion Energy and Flux Density by Magnetron Sputtering. Shenyang: Northeastern University, 2010.
- X. L. He, *Special equipment for the electronics industry*, **6**, 57(2013).
11. Z. Z. Wu, X. B. Tian, F. Pan, J. Y. Fu, J. H. Zhu *Journal of Metal Research*, **50**, 10(2014).

Study of the influence of Ca²⁺ content in soil on *Brassica Chinensis* L. crop yield under acid rain stress conditions

Ch. Fang, T. Wu, J. Cong, J. Wang*

Environmental Science Department, Jilin University, Changchun 130012, China

Received February 8, 2017, Accepted December 19, 2017

With the rapid development of economy, the frequency and intensity of acid rains is increasing, which is a growing global environmental concern, especially in China. In recent years, techniques to protect the crop yield under acid rain stress conditions have become a focus of attention. In this study, *Brassica Chinensis* L., one of the typical crops in the northeast of China, was selected to examine crop yield under acid rain stress conditions. Based upon two series of simulation experiments, (1) growth and physiological characteristics of *Brassica Chinensis* L. were determined under different acid rain stress conditions, and (2) it was examined whether supplementation with additional Ca²⁺ to soil was able to protect *Brassica Chinensis* L. under these conditions. The results showed that additional Ca²⁺ in soil improved growth and physiological characteristics of *Brassica Chinensis* L. through the increased total and pectic acid Ca²⁺ concentrations in plants. Acid rain stress decreased the yield of *Brassica Chinensis* L., while additional Ca²⁺ administered to soil enhanced the yield. Data suggest that adding Ca²⁺ to soil was effective in preventing the actions of acid rain on *Brassica Chinensis* L. growth.

Keywords: Acid rain; Ca²⁺; *Brassica Chinensis* L.

INTRODUCTION

Acid rain is defined as acidic precipitation with pH below 5.6, in the form of rain, snow, fog, dew and others [1, 2]. Acid rain is a global pollution concern and a continuously growing problem. In recent years, the regions influenced by acid rain have spread from urban centers to outer suburbs and further to rural areas [3, 4]. In the early eighties of the last century, acid rain only appeared in several large cities in China. However, with rapid economic development, the surface area influenced by acid rain increased. At present, China is the major acid rain distributor globally with more than 40% of the region affected by acid rain, especially in the South and East of China. It is worthwhile noting that acid rain in some areas reached even pH levels of 4.5 [5-7]. Acid deposition not only directly affects the growth conditions of plants, but also influences plant growth as a consequence of losing some nutrient elements required for plant growth including calcium (Ca) and magnesium (Mg) in the soil [8]. Previous studies showed that the ecological loss attributed to acid rain reached 45.9 billion Yuan in Jiangsu, Zhejiang and other 11 provinces during the 1990s [9]. Northeast China has relatively good resources for agricultural development and agro-ecological environment, and it is an important commodity grain region. In recent years with the development of industry in Northeast China, annually rising acid rain levels have resulted in a significant negative impact on agricultural production and threaten food security in China [10].

Therefore, the study of the influence of acid rain on typical crops constitutes an important need.

Acid rain may influence crops in different ways such as damage during the seed germination period as evidenced by diminished germination rate of rice and wheat [11]. During the plant growth period, acid rain destroys the leaves of crops such as rice and soybeans by decreasing chlorophyll concentrations in leaves, disturbing cell membrane permeability, increasing impedance stomatal factors, and inhibiting plant photosynthesis [12-14]. When comparing the response of vegetables, grains and other crops to acid rain exposure, Feng (2000) found that vegetables were more sensitive to the effects of acid rain [15].

Ca²⁺ is not only an important and essential element for plants, but it is also needed to increase resilience and act as an important messenger to enable plants to adapt to different environmental changes. In order to ensure the yields of plants, several investigators provided additional Ca²⁺ to soil and thus enhanced plant resistance under acid rain stress [16]. Qiu *et al.* (2002) examining longan found that Ca²⁺ reduced chlorophyll degradation in leaves under acid rain stress, and thus the yield was maintained [17]. Dolatabadian *et al.* (2013) showed that chlorophyll concentrations in wheat leaves were elevated by directly spraying Ca²⁺ on leaves under acid rain stress [18]. Evidence thus indicates that addition of Ca²⁺ reduces the influence of acid rain stress in some plants [19]. However, few investigators examined the effects of acid rain stress on *Brassica Chinensis* L., which is one of the main crops in northeast China. With the increasing

To whom all correspondence should be sent:
E-mail: wangju@jlu.edu.cn

intensity and frequency of acid rain occurrences in northeast China, adverse effects of acid rain on *Brassica Chinensis* L. might rise significantly. In order to maintain *Brassica Chinensis* L. yields, which is essential for food security in China, it is important to diminish the consequences of acid rain. Therefore, the aim of this study was to examine the effects of different Ca^{2+} concentrations on the physiological and nutritional quality changes of *Brassica Chinensis* L. under acid rain stress.

EXPERIMENTAL

Experimental material

The experimental site was a greenhouse in the region of Jilin University, Changchun, Jilin, which is located in the Southern district (43°49'21 "N, 125°16'47" E). Changchun, located in the hinterland of Songliao plain in the Northeast of China, has temperate continental monsoon climate. The annual mean temperature in Changchun is 4.8°C, and average annual precipitation is between 522-615 mm. The greenhouse temperature and other conditions were kept constant and maintained without natural external factors such as wind and precipitation occurring during the experiment. The crop used in this experiment was *Brassica Chinensis* L., which is an important crop sensitive to acid rain stress. The variety was Qingza *Brassica Chinensis* L. hybrids, with thick and hypertrophied leaves growing commonly in northeast China. The experimental soil was black soil which is widely distributed in northeast China [20]. The pH of the experimental soil was 6.5, organic matter content was 23.4 g/kg, available nitrogen content 108.4 mg/kg, available phosphorus 15.3 mg/kg, and potassium 160 mg/kg.

Treatments

The experiment consisted of two factors to be measured, (1) pH and (2) Ca^{2+} concentration of soil. A square wooden box with an approximate area of 0.2m² in each planting area was used with plastic sheeting on the bottom to prevent water loss. A barrier of 0.3 m was placed between the plant districts to avoid interaction. The first series was run during the summer of 2014. The pH was set at two levels, 2.5 or 5.6, Ca^{2+} was added to soil. The total Ca^{2+} concentrations in soil were 240, 1260, 2520, 6300 or 12,600 mg/kg. The 240 mg/kg Ca^{2+} level was considered as soil background concentration [21]. The first series of experiments focused on the influence of different acid rain strength (pH levels) and interaction with different Ca^{2+} concentrations on *Brassica Chinensis* L. growth. The second series of experiments was

conducted in the spring of 2015. The second experiment was set at pH 2.5, 4.5, or 6.89 (CK group) with Ca^{2+} added to soil at concentrations of 110, 440, 770, or 1100 mg/kg and the physiological indices of *Brassica Chinensis* L. were measured. Six indicators were measured (plant height, root length, root fresh weight, root dry weight, fresh weight of eating parts and dry weight of eating parts) which reflect the *Brassica Chinensis* L. growth characteristics.

The amount of solution required for different plots based on soil dry weight was calculated before the experiment and different concentrations of Ca^{2+} solution were added. Before seedling stage, secondary deionized water allocation simulated acid rain was added containing 0.660 mg/L K_2SO_4 , 0.988 mg/L NaSO_4 , 2.613 mg/L CaCl_2 , 0.772 mg/L NH_4NO_3 and 1.442 mg/L $(\text{NH}_4)_2\text{SO}_4$. Acid solutions were prepared at a mole ratio of sulfuric acid and nitric acid [SO_4^{2-}]/[NO_3^-] of 5:1, mixed and adjusted to pH 1. Different amounts of acid solution were added to the simulated acid rain, and desired acidity of the latter was determined with a pH meter. The simulated natural rainfall with no acid solution served as a background. During the seedling stage considered as growth of 6 true leaves, 500 ml of simulated acid rain was sprayed at different concentrations on the leaves of *Brassica Chinensis* L. until water dripped from the leaves at 16:00-17:00 every two days. The spraying was maintained uniform and the intensity of the spray was consistent.

Plant harvesting

Samples were collected at 9:00 on the 7th, 14th, 21st day, by randomly selecting three leaves of *Brassica Chinensis* L. from each group. Different forms of Ca^{2+} concentrations in *Brassica Chinensis* L. were measured according to Ohat *et al.* [22]. The content of soluble sugar was measured by the anthrone method [23]. The chlorophyll meter (SPAD-502 PLUS) was used to measure the chlorophyll content in the leaves [24]. The dry plant weight was obtained after drying in an oven at 105°C. Plant height, petiole length and root length were measured directly by a ruler, 5-10 points with different length were selected for each measurement and the mean values were recorded. In order to more accurately analyze the effect of acid rain and Ca^{2+} on the growth of *Brassica Chinensis* L., three different measuring dates were selected at various growth stages, the results reflect the characteristics during the whole growing process.

Statistical analysis

In this study, Ca^{2+} concentrations in the soil and degree of acid rain stress (pH) were regarded as two factors. All data were analyzed by a two-way analysis of variance (two-way ANOVA: different soil Ca^{2+} concentrations and degree of acid rain stress were regarded as two factors) using SPSS 20.0.

RESULTS AND DISCUSSION

Ca^{2+} concentrations

With the increasing soil Ca^{2+} concentration, the contents of different kinds of Ca^{2+} in *Brassica Chinensis L.* obviously changed, and the results are shown in Figure 1. In the control group (pH=5.6), the contents of different kinds of Ca^{2+} in *Brassica Chinensis L.* increased under low soil Ca^{2+} concentration, then decreased, and finally became stable. When the concentration of Ca^{2+} in the soil was 1260 mg/kg, the contents of most kinds of Ca^{2+} in the plants were higher than those growing with other soil Ca^{2+} concentrations. Especially the concentration of total Ca^{2+} was 49.1mg/kg, which is the highest Ca^{2+} concentration in this experimental group. The concentration of Ca^{2+} in the plants did not gradually increase with the increasing soil Ca^{2+} concentration when the pH of acid rain was 5.6. *Brassica Chinensis L.* absorbed most Ca^{2+} at soil Ca^{2+} concentration of 1260 mg/kg. When the soil Ca^{2+} concentration was higher than 1260 mg/kg, the ability to absorb the Ca^{2+} from the soil may be suppressed, which caused a decrease in the concentration of Ca^{2+} when the soil Ca^{2+} concentration was higher than 1260 mg/kg.

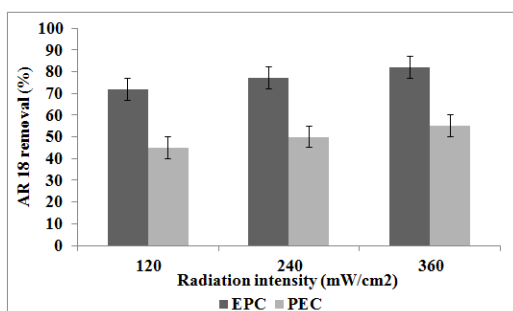


Fig. 1. Influence of Ca^{2+} concentrations treatment on Ca^{2+} concentrations in the *Brassica Chinensis L.* under acid rain stress

Soluble sugar and chlorophyll

Chlorophyll and soluble sugar of *Brassica Chinensis L.* under different pH and soil Ca^{2+} concentrations are illustrated in Figure 2. Compared to the plant grown under normal rain (pH = 5.6), the soluble sugar concentration was considerably higher than that in plants grown under acid rain

stress (pH=2.5). With an increase in soil Ca^{2+} concentration, the levels of soluble sugar rose. When the soil Ca^{2+} concentration was 6300 mg/kg, soluble sugar content was 3.75 mg/kg, the highest value attained. Under different degrees of acid rain stress, chlorophyll concentration increased with increase in soil soluble calcium, and did not maintain a stable concentration in the range of soil soluble Ca^{2+} concentration range designed in this study. In the control group, the chlorophyll concentration of the plant which was not influenced by acid rain increased and tended to stabilize when the soil soluble calcium increased. The chlorophyll concentration of *Brassica Chinensis L.* influenced by light acid rain stress (pH=4.5) was higher than that treated with heavy acid rain stress (pH=2.5).

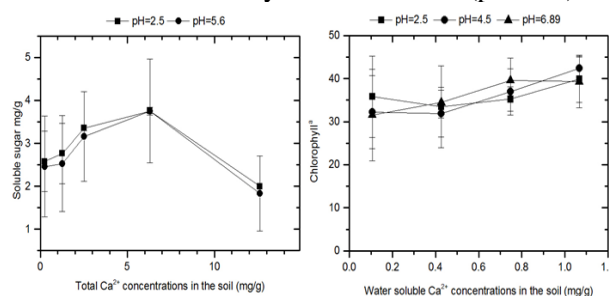


Fig. 2. Influence of Ca^{2+} concentrations treatment on soluble sugar and chlorophyll of *Brassica Chinensis L.* under acid rain stress

Growth characteristics of *Brassica Chinensis L.*

Six growth characteristics were determined and the results are presented in Figure 3. Data show that high concentrations of soil Ca^{2+} significantly increased the height, root fresh weight and root dry weight in a concentration-dependent manner. With the increasing soil Ca^{2+} concentration, the trends of fresh weight and dry weight of root were similar. When *Brassica Chinensis L.* grew without acid rain stress, root dry weight and fresh weight increased with increasing soil Ca^{2+} concentration (from 0.44 to 1.1 g/kg). The fresh weight and dry weight of roots in the control group were highest under the same soil Ca^{2+} concentration. Acid rain stress did not markedly affect plant height. In contrast to plant height, the root lengths were predominantly influenced by pH. In the control group without acid rain, the root lengths increased under low soil Ca^{2+} conditions. However, with the soil Ca^{2+} concentration increasing from 0.44 to 1.1 g/kg, the root lengths manifested a clear decreasing trend from 8.93 ± 0.55 cm to 7.71 ± 0.56 cm and increased to 8.44 ± 0.39 cm when the soil Ca^{2+} concentration was higher than 0.75 g/kg. When the *Brassica Chinensis L.* grew under acid rain stress, the root length gradually increased after the first decrease

(from 0.11 to 0.44 g/kg) with the concentration of soil Ca^{2+} increasing from 0.44 to 1.1 g/kg. With the soil Ca^{2+} concentration increasing, the root length change was not significant and the influence of Ca^{2+} concentration was lower than other degrees (pH = 4.5, 6.89) of acid rain stress.

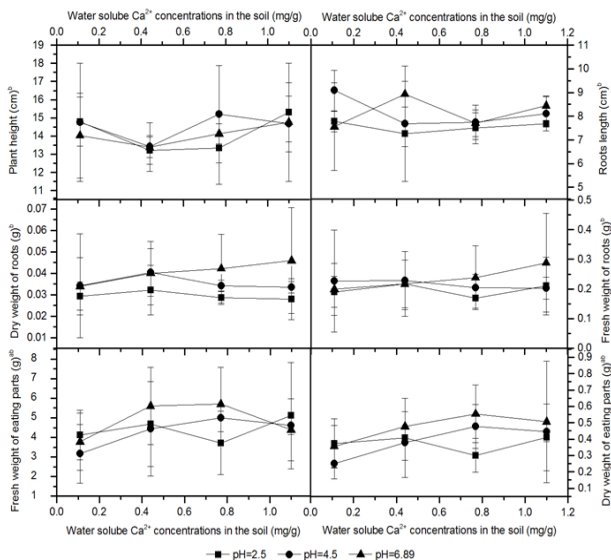


Fig. 3. Influence of Ca^{2+} concentrations treatment on the growth character of *Brassica Chinensis* L. under acid rain stress

Effects of different kinds of Ca^{2+} concentrations

When *Brassica Chinensis* L. grew under acid rain stress, the trend of different kinds of Ca^{2+} concentrations in the plant was different from those growing in a normal (pH=5.6) environment. When the pH of acid rain was 2.5, with the increasing soil Ca^{2+} concentration, the trend of the Ca^{2+} concentrations in the plants could be grouped in two kinds of trends. The trend of inorganic Ca^{2+} and soluble Ca^{2+} concentrations increased with the increasing soil Ca^{2+} concentration while the concentration of other kinds of Ca^{2+} increased after a decreasing trend and finally stabilized. For example, the total Ca^{2+} concentration in the plants was 30200 ± 5100 mg/kg when the soil Ca^{2+} concentration was 240 mg/kg, while, when the concentration of Ca^{2+} in the soil as 1260 mg/kg, the concentration of Ca^{2+} in the plant was the lowest at a value of 26500 ± 2020 mg/kg. When *Brassica Chinensis* L. grew under acid rain stress, the concentration of total Ca^{2+} in the plants was not always increasing with the increasing concentration of Ca^{2+} in the soil. After a short decreasing trend, it could continuously increase when the soil Ca^{2+} concentration was higher than 1260 mg/kg. The trends of pectin acid calcium, tricalcium phosphate and residual calcium concentrations in the plants were similar. Based on the results of the

concentrations of different kinds of Ca^{2+} , we found that the acid rain stress could influence the process of plant absorbing Ca^{2+} from the soil, and it is more obvious for pectin acid calcium and tricalcium phosphate and residual calcium when the soil Ca^{2+} concentration was low. The decrease in these three kinds of Ca^{2+} concentrations leads the total Ca^{2+} concentration in the plants to decrease.

Comparing the contents of different kinds of Ca^{2+} in these two groups, the same soil Ca^{2+} concentrations, the content of Ca^{2+} in the plants was higher than in those growing under serious acid rain stress. When the soil Ca^{2+} concentration was low, the decreasing trend of Ca^{2+} concentrations in the plant was more obvious, which means that the ability of the plant to absorb Ca^{2+} from the soil could be inhibited by the acid rain. When the acid rain stress was strong, the ability to absorb Ca^{2+} might be weakened while with the increase in soil Ca^{2+} concentration, the degree of influence by acid rain on the Ca^{2+} absorption ability of *Brassica Chinensis* L. could be decreased, and the the plant could absorb more Ca^{2+} . When the Ca^{2+} concentration in the soil was high enough, the Ca^{2+} in the plant could be similar to those growing without acid rain.

Effects of soluble sugar and chlorophyll

Chlorophyll and soluble sugar are two important indicators for researchers to know the plant growth condition and are widely used in previous studies [25]. According to Fig. 2, the soluble sugar concentrations in the plant changed significantly when soil Ca^{2+} is different and the pH of acid rain is similar, it is not obvious in turn, so the soluble sugar concentrations in the plant were mainly controlled by soil Ca^{2+} concentration. Some previous studies have focused on the relationship of soluble sugar concentrations of *Brassica Chinensis* L. and acid rain without changing the soil Ca^{2+} concentration [26]. The results showed that the weak acid rain could increase the synthesis rates of soluble sugar of *Brassica Chinensis* L.

Soluble sugar synthesis rate at pH 2.5 was lower than at pH 4.5, and soluble sugar synthesis rates at pH 4.5 was lower than CK. Based on our experimental results, when the soil Ca^{2+} concentration and acid rain were regarded as two control factors, the influence of the acid rain stress on soluble sugar concentration of *Brassica Chinensis* L. was not obvious, and the soluble sugar concentration of the plant was mainly influenced by the soil Ca^{2+} concentration.

Comparing chlorophyll concentration of plants with different degrees of acid rain stress and soil

soluble Ca^{2+} concentrations, high concentrations of soil Ca^{2+} benefit the chlorophyll synthesis of the plant. And with the soil Ca^{2+} concentration increasing, chlorophyll concentration could reach a stable concentration at different degrees of acid rain stress. When *Brassica Chinensis* L. grew under acid rain stress, increased concentration of soil Ca^{2+} could promote the synthesis of chlorophyll and keep the chlorophyll concentration in the plant stable and normal. Although no stable chlorophyll concentration of the plants was reached in this experiment, it was found that high concentration of Ca^{2+} treatment could increase chlorophyll concentrations of *Brassica Chinensis* L. to levels higher than those not influenced by acid rain. These results might mean that the light acid rain stress could increase the chlorophyll concentration of *Brassica Chinensis* L., while with increasing acid rain stress the chlorophyll concentration of the plant could be suppressed. Acid rain could decrease the chlorophyll synthesis rate of *Brassica Chinensis* L. and decrease photosynthetic capacity, which is similar to previous studies through other kinds of plants. High concentrations of Ca^{2+} in the soil could promote the synthesis of chlorophyll, and make the chlorophyll concentrations of plants influenced by acid rain similar with those growing in a normal environment. In previous studies, high concentrations of Ca^{2+} could increase the seeds germination rates of *Medicago sativa* under acid rain stress, and decrease the effect of acid rain stress on the photosynthesis of *Zephyranthes candida* and longan [27]. In our study, high Ca^{2+} concentration also could decrease the effect of acid rain on *Brassica Chinensis* L. and protect the photosynthesis by keeping the chlorophyll concentration, which is similar to previous studies on other kinds of plants.

Effects of growth characteristics

In order to understand the influence of acid rain and soil Ca^{2+} concentration on the growth characteristics, six kinds of indicators (plant height, root length, root fresh weight, root dry weight, fresh weight of eating parts and dry weight of eating parts) were determined, shown in Fig. 3.

With the acid rain stress increasing, the dry weight and fresh weight of roots were both decreasing. When *Brassica Chinensis* L. grew under acid rain stress, with the soil Ca^{2+} concentrations increasing, the dry weight of roots decreased after a short increase trend. High concentration of soil Ca^{2+} could promote the growth of roots when the plant grew without acid rain stress. High concentration of soil Ca^{2+} and strong acid rain stress could inhibit the growth of the roots

and reduce the root dry weight. When *Brassica Chinensis* L. grew without influence by acid rain, the food fresh weight and dry weight decreased after a short peak with soil Ca^{2+} concentration increasing. It can be inferred that the fresh weight could grow well under the suitable soil Ca^{2+} concentration. When it grew under light acid rain stress, this suitable soil Ca^{2+} concentration did not change significantly.

Interaction of acid rain and Ca^{2+} concentration

Based on the two-way ANOVA analysis, the Ca^{2+} concentration in the soil and the degree of acid rain stress were regarded as two factors in the *Brassica Chinensis* L. change while there was no significant influence on the physiological characteristics. Except the height, acid rain stress caused significant differences on the root length, eat fresh weight, dry weight of edible part, root fresh weight and root dry weight of the plant. The analysis results showed that the influence of the interaction between different soil Ca^{2+} concentrations and acid rain stress on the *Brassica Chinensis* L. was not significant. So we can infer that the impacts of Ca^{2+} concentration and acid rain stress on this plant are independent.

For example, when the degree of acid rain increased, the weight of the edible parts of *Brassica Chinensis* L. decreased, while increasing soil Ca^{2+} concentrations could eliminate this influence gradually, and make the yield of *Brassica Chinensis* L. not decrease significantly. So, this reason could explain why the interaction of Ca^{2+} concentration and acid rain on *Brassica Chinensis* L. is not significant.

Two-way ANOVA for growth character, soluble sugar and chlorophyll of *Brassica Chinensis* L. under acid rain stress and Ca^{2+} stress are shown in Table 1.

CONCLUSIONS

Based on all experimental results, it can be inferred that pH and soil Ca^{2+} concentrations influence the physiological characteristics of *Brassica Chinensis* L. Acid rain could influence the key indicators like edible parts weight, root length of plants while, when the soil Ca^{2+} concentration increased, it could reduce the influence caused by acid rain, and keep the yields of the plant, so we can adjust *Brassica Chinensis* L. cultivation methods in the acid rain region according to this study results. For example, an appropriate increase in soil Ca^{2+} concentration could reduce the influence of acid rain stress on the yield in the regions significantly influenced by acid rain.

Table. 1. Two-way ANOVA for growth character, soluble sugar and chlorophyll of Brassica Chinensis L. under acid rain stress and Ca²⁺ stress

	Calcium concentration		pH		Calcium concentration & pH	
	F	P	F	P	F	P
Total calcium	11.861	.000	16.452	.001	23.214	.000
Total calcium	6.433	.002	36.361	.000	16.948	.000
Inorganic calcium	7.390	.001	61.842	.000	4.494	.009
Water soluble calcium	4.983	.006	108.329	.000	4.459	.010
Pectic acid calcium	1.699	.190	16.428	.001	3.662	.021
Tricalcium phosphate	1.836	.162	5.435	.030	2.226	.103
Calcium residue	11.861	.000	16.452	.001	23.214	.000
Plant height	.621	.609	3.185	.062	.219	.966
Roots length	.864	.475	3.507	.049	.686	.663
Fresh weight of eating parts	9.906	.000	14.162	.000	.687	.662
Dry weight of eating parts	3.911	.023	3.669	.043	.473	.820

Acknowledgements: This study is supported by Jilin Provincial Science & Technology Department (No.20130204051SF). The authors thank Changchun Central Environmental Monitoring Station for assistance in the monitoring data and sampling.

REFERENCES

- C. P. Bi, *Environ. Econ.*, **5**, 58(2014).
- P. Liu, F. Xia, J. Y. Pan, Y. P. Chen, H. M. Peng, S. H. Chen. *J. Environ. Sci. Manag.*, **30**, 36 (2011).
- W. X. Wang, G. A. Ding, *J. Res. Environ. Sci.*, **1**, 10 (1997).
- <http://www.mep.gov.cn/gzfw/xzxx/wdxz/>.(2010)
- X. M. Zhang, F. H. Chai, S. L. Wang, S. Z. Sun, M. Han, *J. Res. Environ. Sci.*, **527**, 23 (2010).
- C. P. Bi, *J. Environ. Econ.*, **58**, 5 (2014).
- T. Larssen, G. R. Carmichael, *J. Environ. Pollut.*, **89**, 110 (2000).
- J. E. Zhang, Y. Ouyang, D. J. Ling, *J. Chemosphere*, **2131**, 67 (2007).
- F. Chen, F. H. Chai, *J. Res. Environ. Sci.*, **27**, (1997).
- <http://hbj.jl.gov.cn/hjjc/hjzlx/>.(2010).
- Q. Zhou, Q. L. Zeng, X. H. Huang, G. S. Zhang, C. J. Liang, L. H. Wang, *J. Acta Eco. Sinica*, **2029**, 24(2004).
- Y. M. Zhang, L. Y. Wu, X. X. Wang, J. Zhang, X. P. Gao, M. Y. Xie, H. Hui, P. Wang, H. B. Xu, S. X. Zhao, *J. Agro-environ. Prot.*, **197**, 15 (1996).
- Z. Sun, L. Wang, M. Chen, L. Wang, C. Liang, Q. Zhou, X. Huang, *J. Ecot. Environ. Safety*, **62**, 79 (2012).
- L. Wang, W. Wang, Q. Zhou, X. Huang, *J. Chemosphere*, **355**, 112 (2014).
- Z. W. Feng, *J. Eng. Sci.*, **67**, 46 (2000).
- H. Yang *J. Sichuan Agricultural University*, **43**, 15 (2011).
- D. L. Qiu, X. H. Liu, S. Z. Guo, *J. Chin. J. Appl. Environ. Biol.*, **20**, 8 (2002).
- A. Dolatabadian, S. A. M. M. Sanavy, M. Gholamhoseini, A. K. Joghhan, M. Majdi, A. B. Kashkooli, *J. Phys. Molec. Biol. Plants*, **189**,19 (2013).
- W. J. Hu, J. Chen, T. W. Liu, Q. Wu, W. H. Wang, X. Liu, Z. J. Shen, S. Martin, J. Chen, F. H. Wu, Z. M. Pei, *J. Plant. Soil*, **285**, 380 (2014).
- C. S. Fang, Y. L. She, X. M. Zhao, L. Y. Yan, J. L. Shen, M. L. Guo, J. Wang, *J. Sci. Technol. Eng.*, **158**, 14 (2014).
- L. S. Zhou, *J. Environ. Sci.*, **4**, 4 (1991).
- Y. Ohat, K. Yamamoto, M. J. Deguchi, *J. Sci. Soil Manure*, **19**, 41(1970).
- X. X. Li, J. Z. Li, *J. Storage Process.*, **24**, 13 (2013).
- X. K. Zhu, H. J. Sheng, J. Gu, R. Zhang, C. Y. Li, *J. T. Crop.*, **46**, 25 (2005).
- H. B. Fan, Y. H. Wang, *J. Forest. Ecol. Manag.*, **321**, 126 (2000).
- G. H. Tong, H. L. Liang, J. Chin, *J. Appl. Ecol.*, **1487**, 16 (2005).
- H. Wang, F. Liu, *J. Guizhou Agric. Sci.*, **48**, 38 (2010).
- Z. H. Xu, W. Y. Li, J. H. Lei, Y. Li, G. Y. Ma. *J. Southwest University for Nationalities (Natural Science Edition)*, **48**, 1(2005).

Study on fundamental polishing characteristics in chemical mechanical polishing of gallium arsenide (GaAs) wafer

D. Yi¹, J. Li^{1,2}, J. Cao^{1,2*}

¹. School of Mechanical, Electronic and Control Engineering, Beijing Jiaotong University, Beijing 100044, China;

². Key Laboratory of Vehicle Advanced Manufacturing, Measuring and Control Technology, Ministry of Education, Beijing 100044, China.

Received, September 22, 2017; Accepted December 19, 2017

Chemical mechanical polishing (CMP) experiments were carried out to evaluate the effect of the process parameters on the polishing characteristics of GaAs wafers. CMP of the GaAs wafers was conducted on a commercial polisher; the polishing slurry was freshly prepared from analytical grade materials prior to each experiment. The experimental results indicated that (1) the surface roughness Ra decreases on increasing the rotational speed of the polishing pad and polisher head, and polishing load; (2) the polishing load is one of the main factors that affect the total thickness variation (TTV). With the increase in the polishing load, the TTV of the wafer was reduced accordingly; (3) the material removal rate (MRR) increases on increasing of the rotational speed of the polishing pad, the rotational speed of polisher head, and the polishing load; the change of polishing load has the most obvious effect on the MRR.

Key words: GaAs, Chemical mechanical polishing, Polishing characteristics, Surface roughness.

INTRODUCTION

Gallium arsenide (GaAs) wafer has been widely utilized from macroscale to nanoscale devices for illumination, photoelectric detection, conversion of solar energy. etc., due to its high direct bandgap, saturated electron velocity and electron mobility. For example, GaAs wafer, with its nano-level, smooth, super-flat and damage-free surface, is suitable for metal-organic chemical vapor deposition to produce high-performance flexible solar cells and light emitting diodes (LED) [1, 2]. In machining process, GaAs wafer first encounters a sawing process that introduces defects and/or fracture damage deep into the wafer subsurface, because of its high hardness and brittle nature. Subsequently, lapping and polishing processes are adopted to remove this saw-induced damage and produce a nominally damage-free surface.

At present, chemical mechanical polishing (CMP) is applied as one of the most efficient treatments to produce nano-level smooth surface [3, 4]. In the literature, it is found that various chemical slurries have been used in CMP of GaAs wafers. Matovu *et al.* investigated GaAs removal rates in the presence of H₂O₂ and silica particles and compared them with those obtained in the presence of other oxidizers such as sodium iodate and sodium periodate. Their findings showed that the formation of the oxides of Ga and As is thermodynamically feasible in the aqueous slurries used for polishing of GaAs surfaces; in the absence of mechanical polishing, chemical disslurry of GaAs in aqueous slurries of oxidizers such as NaIO₃, NaIO₄, and H₂O₂ of 3mM concentration is negligible except in slurries of H₂O₂

at pH 10 and pH 12, attributed to the formation of a passivating layer of relatively stable Ga₂O₃ [4]. McGhee *et al.* proposed a three-step mechanism for GaAs removal in aqueous slurry containing H₂O₂ and ammonia [5].

Moreover, some studies also focused on the CMP characteristics of GaAs wafers. Yu *et al.* found that if SiO₂ particles are used in the polishing of the GaAs surface, high polishing speed can bring high rate of tribochemical removal without damage to the surface matrix of GaAs [6]. Wu *et al.* investigated the CMP of GaAs for transmission electron microscope observation and their findings showed that two-step polishing with NH₄OH and H₂SO₄ after conventional ion milling is an effective method to obtain improved surface quality [7]. Ookawa *et al.* found that the material removal rate (MRR) decreases and the surface roughness increases with increase in polishing time if the polishing pad is used for a long time [8].

However, in terms of the CMP of GaAs wafer, there are still many theoretical and technical problems unresolved. In this work, the fundamental polishing characteristics, i.e., the influence of the polishing parameters on the surface roughness, flatness, and MRR, are experimentally studied. Meanwhile, the topographic features of work-surfaces, and the XRD spectrum of the work-surfaces were observed to clarify the material removal mechanism.

MATERIALS AND METHODS

CMP operations of the GaAs wafers were conducted on the commercial polisher (ES36B-4P-4M by Zhejiang Morinaga Co., Ltd., shown in Figure 1) under the processing parameters shown in Table 1 to elucidate the CMP characteristics. The

*To whom all correspondence should be sent:
E-mail: jgcao@bjtu.edu.cn

polishing slurry was composed of oxidizer, dispersant, complexant, pH regulator, and abrasives. In detail, sodium chloride, sodium benzenesulfonate, sodium pyrophosphate, sodium carbonate, and colloidal silica dispersion were used as oxidizer, dispersant, complexant, pH regulator, and abrasives, respectively.

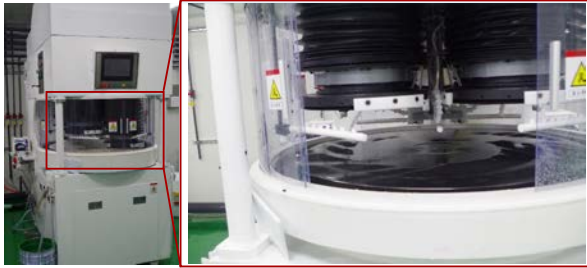


Fig. 1. Experimental setup for CMP of the GaAs wafer
Table 1 Experimental conditions

Polishing head	Rotating speed (r/min)	20, 30, 40, 50
	Load (N)	50, 70, 90, 110
Polishing pad	Rotating speed (r/min)	20, 30, 40, 50
Slurry	Slurry supplying rate (mL/min)	500
	Slurry temperature (°C)	16
Polishing time	10 min	

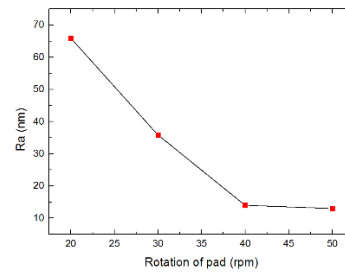
The GaAs wafers used in this work were provided by Jiangxi Deyi Semiconductor Technology Inc. The wafer has a diameter of 4 inch. One of its sides had been lapped and its surface roughness R_a was 110 nm while the other side was not polished. The slurry supplying rate was 500 mL/min, the polishing slurry temperature was 16°C, the rotational speed of the polishing head and polishing pad was changed from 20 r/min to 50 r/min. Load during polishing applied to the wafer varied from 50 to 110N. After CMP, the specimens were ultrasonic rinsed in DI water for 5 min, and then dried off by air spray gun for measurements. The surface roughness and the topography of the polished wafers were evaluated with a surface profiler (Nanovea, MG210). The material removal rate (MRR) was calculated by weighing the wafers before and after CMP. In this study, the total thickness variation (TTV) was used to evaluate the flatness of the GaAs wafers. The thickness at five different points was measured by a micrometer, the difference between maximum thickness and minimum thickness was defined as the TTV.

RESULTS AND DISCUSSION

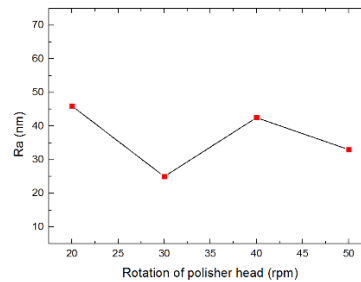
Surface roughness

The effect of CMP process parameters on the roughness is shown in Figure 2. It can be figured out that the surface roughness R_a decreases with the increasing of the rotational speed of polishing pad and polisher head, and polishing load.

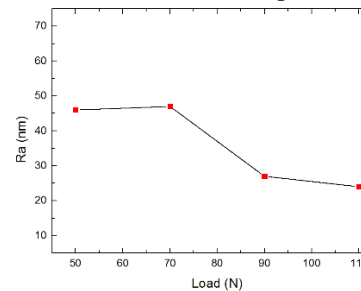
It is particularly interesting to note that the rotational speed of the polishing pad and the polishing load have a great influence on the roughness. Concretely, when the rotational speed of the polishing pad was in the range of 20-40 rpm, the surface roughness was significantly reduced with the increase in rotational speed; when the polishing load was bigger than 70N, the load increase caused an obvious reduction in the surface roughness. However, the rotation of the polisher head had a little influence on the variation of the surface roughness.



(a) Influence of rotation of polishing pad



(b) Influence of rotation of polisher head



(c) Influence of polishing load

Fig. 2. Relations between roughness and process parameters

TTV

Figure 3 shows the effect of CMP process parameters on the TTV. It can be seen that the change in the rotational speed of the polishing pad and polisher head has little influence on the TTV. Meanwhile, the increase in the rotational speed of

the polishing pad and polisher head leads to an increase in TTV, i.e., the TTV becomes worse. The reason why the TTV is getting worse can be ascribed to the severe vibration induced by the rotation of the polishing pad and polisher head at a high speed.

The polishing load is one of the main factors that affect the TTV. With the increase in the polishing load, the TTV of the wafer will be accordingly reduced. This is because at a small polishing load, the GaAs wafer suspends on the polishing pad (Figure 4(a)), resulting in an ineffective contact between the polishing pad and the GaAs wafer. The material removal volumes at different positions of the wafer surface are not equal, therefore, the TTV of the polished wafer is relatively high at low polishing load; as the polishing load rises, the GaAs wafer contacts fully with the polishing pad (Figure 4(b)), improving the TTV of the GaAs wafer.

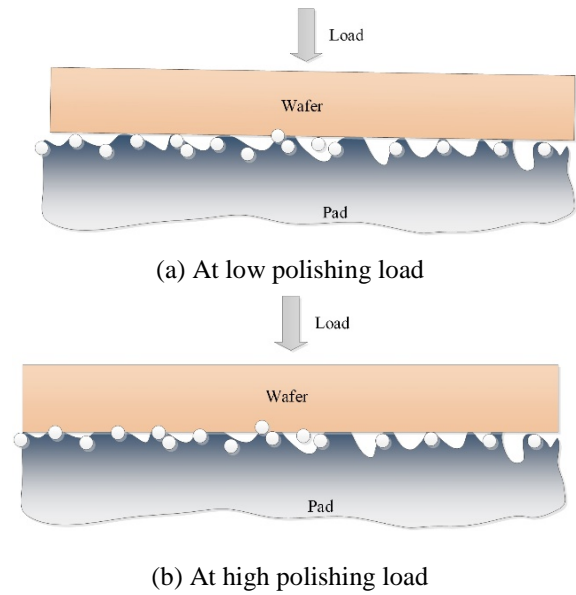
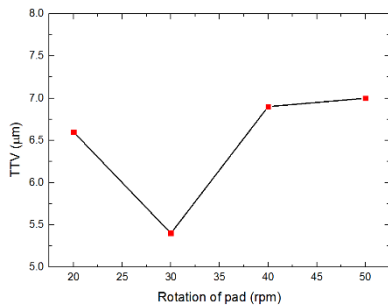
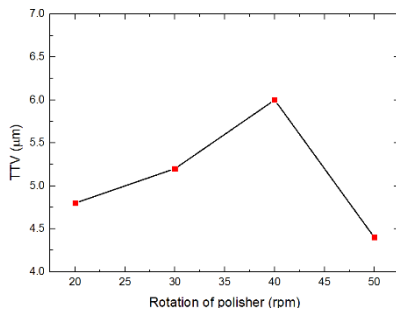


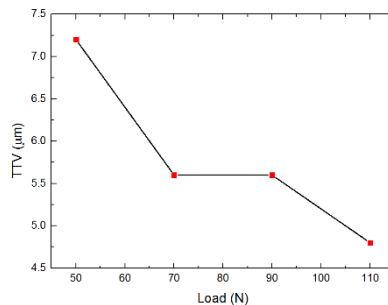
Fig. 4. Contact state between the polishing pad and the wafer



(a) Influence of rotation of polishing pad



(b) Influence of rotation of polisher head



(c) Influence of polishing load

Fig. 3. Relations between TTV and process parameters

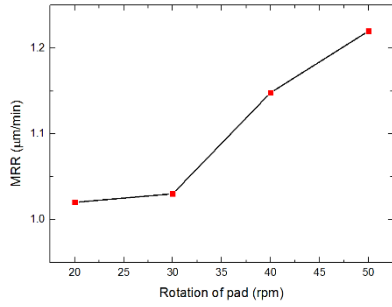
MRR

The effect of process parameters on the MRR in CMP of the GaAs wafer is plotted in Figure 5. It is seen from the graph that the values of MRR increase with the increase in the rotational speed of the polishing pad, the rotational speed of polisher head, and the polishing load. In the CMP process, Preston equation is widely accepted to predict the polishing material removal behavior [8]:

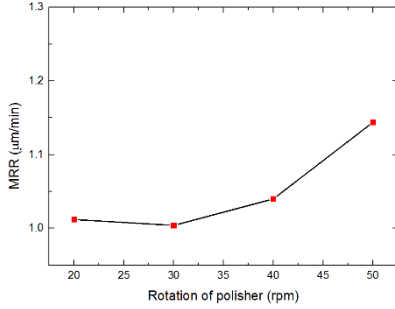
$$MRR = kPv \quad (1)$$

where P is the applied load, V is the velocity at any point on the wafer relative to the pad, and k is the Preston coefficient depending on the processing conditions, such as the slurry, the pad and the process environment.

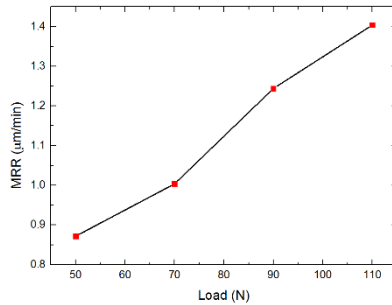
From the Preston equation it is known that MRR is proportional to the relative velocity between the pad and the wafer surface and the applied load. This agrees with the findings in this study. However, the change in the polishing load has the most obvious effect on the MRR, followed by the polishing pad rotational speed, while the influence of the polishing head rotational speed on the MRR is relatively weak. This is possibly so because the increase in the polishing load can increase the friction force between the surface of the substrate and the pad, thus, the MRR increases with the increase in the polishing load. The polishing pad rotational speed has an obvious, while the polishing head rotational speed has a weak influence on the relative velocity of the wafer to the pad. Therefore, the influence of the polishing head rotational speed on the MRR is relatively weak.



(a) Influence of rotation of polishing pad



(b) Influence of rotation of polisher head

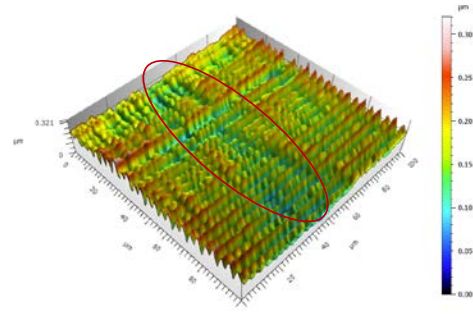


(c) Influence of polishing load

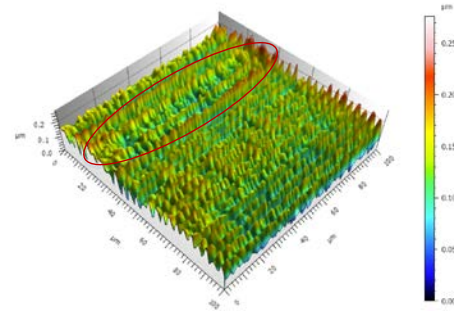
Fig. 5. Relations between MRR and process parameters

Surface topography and material removal mechanism

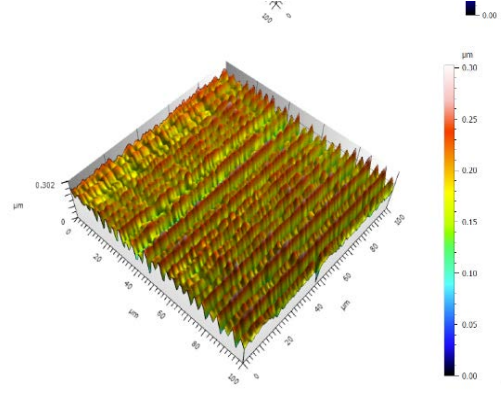
Figure 6 shows the surface topography images of the polished GaAs wafers observed by a surface profiler, when the polishing load is 50N, 70N, 90N, and 110N, and the rotational speeds of the polishing pad and polishing head are 40 r/min and 40 r/min, respectively. From Figure 6(a) it can be seen that there is a local dent on the surface of the workpiece when the polishing load is 50 N, meaning that the MRR is different at the different locations. As shown in Figure 6(b), this phenomenon can be also observed when the polishing load is 70 N. However, the local dents suddenly disappear when the polishing load gets a rise up to 90 N (Figure 6(c)) and 110N (Figure 6(d)), indicating that the MRR is almost the same at different locations. This agrees with the discussed findings



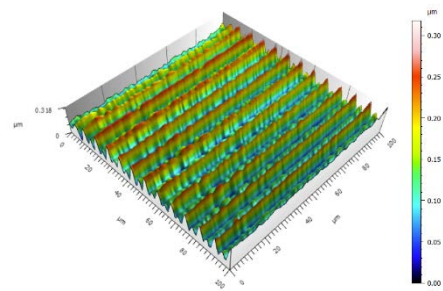
(a) Polishing load is 50N



(b) Polishing load is 70N



Polishing load is 90N



(d) Polishing load is 110N

Fig. 6. Surface topography images of the polished GaAs wafers

In order to elucidate the material removal mechanism in the CMP process, chemical analysis of the GaAs wafer surface before cleaning and after cleaning was performed by XRD, when the polishing load was 50N, and the rotational speeds of the polishing pad and polishing head were 40 r/min and 40 r/min, respectively. Comparing XRD

chemical analysis results of the GaAs wafer surface before cleaning and after cleaning, it is recognized that there are O, Si, Cl, S, Ga, and As elements on the surface before cleaning (Figure 7(a)), while there are only Ga and As elements on the surface after cleaning (Figure 7(b)). Therefore, the material removal process is reckoned as follows: firstly, sodium chloride reacts with GaAs under the circumstances of exceedingly high pressure to form new substances with lower hardness than GaAs and then the resultant softer substances are removed by fused silica abrasive mechanically and plastically.

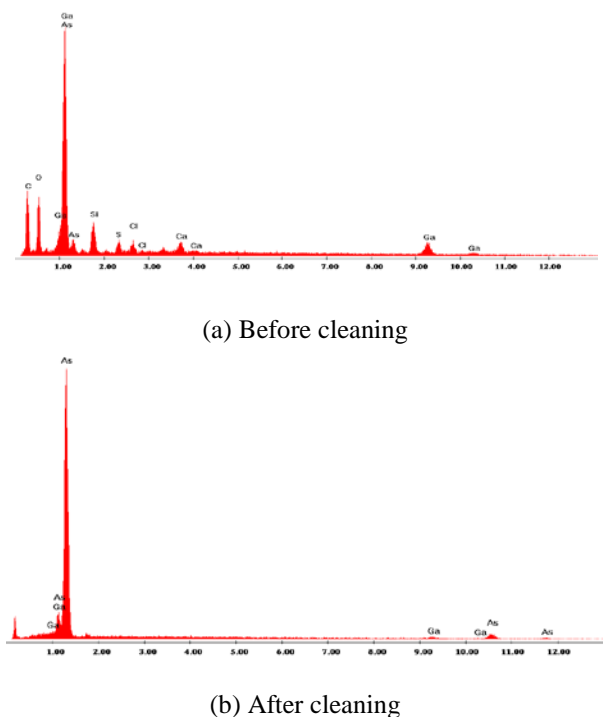


Fig. 7. XRD spectrum of the polished GaAs wafer

CONCLUSIONS

In the present work, the fundamental polishing characteristics, i.e., the influence of the process parameters on the surface roughness, flatness, and MRR, in CMP of a GaAs wafer, were experimentally determined. The material removal mechanism in the CMP process of the GaAs wafer was discussed. The following conclusions can be drawn:

(1) The surface roughness Ra decreases on

increasing the rotational speed of the polishing pad and polisher head, and the polishing load; when the rotational speed of the polishing pad is in the range of 20-40rpm, the surface roughness is significantly reduced with the increase in rotational speed; however, at a polishing load bigger than 70N, the increase in the load causes an obvious reduction in the surface roughness.

(2) The polishing load is one of the main factors that affect the TTV. With the increase in the polishing load, the TTV of the wafer is accordingly reduced.

(3) MRR increases on increasing the rotational speed of the polishing pad, the rotational speed of the polisher head, and the polishing load; the change in polishing load has the most obvious effect on the MRR, followed by the polishing pad rotational speed, while the influence of the polishing head rotational speed on the MRR is relatively weak.

(4) The material removal process in CMP of GaAs wafers is reckoned as follows: firstly, sodium chloride reacts with GaAs under the circumstances of exceedingly high pressure to form new substances with lower hardness than GaAs, and then the resultant softer substances are removed by fused silica abrasive mechanically and plastically.

Acknowledgements: The present work was supported by the Fundamental Research Fund for the Central Universities (M17RC00020).

REFERENCES

1. K. Wasmer, M. Parlinska-Wojtan, S. Graça, J. Michler, *Mater. Chem. Phys.*, **138**, 38 (2013).
2. L.F. Lastras-Martinez, R. Castro-Garcia, R.E. Balderas-Navarro, A. Lastras-Martínez, *Appl. Opt.*, **48**, 5713 (2009).
3. M. Engelhard, C. Klemp, M. Behringer, T. Schroeder, *J. Appl. Phys.*, **120**, 045301 (2016).
4. J.B. Matovu, P. Ong, L.H.A. Leunissen, S. Krishnan, S.V. Bahu, *ECS J. Solid State Sci. Technol.*, **2**, 432 (2013).
5. L. Mcghee, S.G. Mcmeekin, I. Nicol, M.I. Robertson, J.M. Winfield, *J. Mater. Chem.*, **4**, 29 (1994).
6. B. Yu, J. Gao, L. Chen, Z. Zhou, *Wear*, **330**, 59 (2015).
7. Y. Wu, L. Chang, *Micron*, **41**, 20 (2010).
8. T. Ookawa, T. Nishiguchi, *JSME Int. J.*, **47**, 98 (2004).

Influence of kidney tonic formula on the hippocampal neurotrophic factors and proliferation and differentiation of neural stem cells in natural aging rats

J. Yao*, Q. Niu, L. Li, Y. Li, Y. Feng, S. Ma

School of Basic Medicine, University of Henan Chinese Medicine, Zhengzhou, Henan, China

Received, September 28, 2017; Accepted December 19, 2017

The aim of this research was to explore the influence of the quantity of NGF and GDNF in hippocampus on the proliferation and differentiation of hippocampal neural stem cells (NSCs) in natural aging rats and the function of Zuogui pill and Yougui pill. Methods: SD rats were divided into Old group, Zuogui group and Yougui group. Young group (5 months) was set additionally. All rats were fed with common food and free drinking water. Old group was fed to 24 months old. From 20 months old, Zuogui group and Yougui group were fed with food mixing two formulas (0.675g/100g/d) accordingly for 4 months. Western Blot method was utilized to assay the protein expression of NGF, GDNF, nestin and ki-67 in rat hippocampal tissue. Results: compared with Young group, the protein expressions of NGF, GDNF, nestin and ki-67 were all down-regulated in rat hippocampus in Old group, $P < 0.05$; compared with Old group, the protein expression of NGF, GDNF, nestin and ki-67 were all up-regulated in both Zuogui group and Yougui group, $P < 0.05$. Conclusion: the change of protein expression of NGF and GDNF can influence the proliferation and differentiation of NSCs in hippocampus in aged rats, and Zuogui and Yougui pills can ameliorate these trends.

Keywords: Natural aging rats, Hippocampus, NGF and GDNF, Proliferation and differentiation of NSCs, Kidney tonic formula

INTRODUCTION

New neurons continue to be produced in adult mammals. This update focuses on the emerging concept that adult central nervous system (CNS) neurogenesis can be regulated by targeting neurotransmitter receptors, which, in turn, drive expression of crucial neurotrophic and growth factors. Such an approach might enable the development of pharmacological treatments that harness the endogenous potential of the CNS to replace lost cells in neurological disorders such as stroke, Alzheimer's and Huntington's diseases [1]. As the nerve growth factor was found, the neuroscientists believed, there were some kind of nutrients that survival of neurons are depended on. These nutrients come from the target tissue that neurons dominate. With the development of the studies on these nutrients, they have been named as neurotrophic factors (NTFs), which include nerve growth factor (NGF), brain derived growth factor (BDNF), glial derived growth factor (GDNF), etc. NTFs can prevent cell death in degenerative processes, and at the same time NTFs are important for the regulation of proliferation and differentiation of neural stem cells (NSCs) [2], and can induce differentiation of NSCs into different neurons and self proliferation [3]. There is a significant amount of evidence from animal and human studies that links neurodegenerative related cognitive deficits

with changes on brain and peripheral trophic factor levels [4]. NTFs can promote the proliferation and differentiation of NSCs. Here, we aim to explore the influence of the quantity of NGF and GDNF in hippocampus on proliferation and differentiation of hippocampal NSCs in natural aging rats and the function of Zuogui pill and Yougui pill.

EXPERIMENTAL

Materials and analytical methods

Animals: Male Sprague Dawley (SD) rats, SPF grade. Licence number: SCXK(Yu)2010-0002, provided by the Centre of Henan province for experimental animals. Reagents: NGF antibody, GDNF antibody, nestin antibody, ki-67 antibody, Santa Cruz; goat anti-mouse IgG-HRP, Santa Cruz; mouse anti-beta actin, Zhongshan jin qiao. Formula: Zuogui pill and Yougui pill, sixth "Chinese medicine formula" teaching material. Instruments: electrophoresis and electrotransfer instrument, Bio-Rad; refrigerated centrifuge, Thermo; automatic glass homogenate machine, Qilinbeier; electronic analytical balance, Denver Instruments. Method: thirty SD male rats were divided into Old group, Zuogui group and Yougui group. Young group (5 months) was set additionally. All rats were fed with common food and free drinking water. Old group was fed to 24 months old. From 20 months old, Zuogui group and Yougui group were fed with food mixed with two formulas (Zuogui pill and Yougui pill, both 0.675g/100g/d), respectively, for 4 months.

When rats were 24 months old, all rats were anaesthetized from abdomen (urethan, 0.75mg/kg). Bilateral hippocampus were separated from the brain

*To whom all correspondence should be sent:
E-mail: yjp740719@163.com

and kept in a refrigerator at -80°C.

Western Blot method was utilized to assay the protein expressions of NGF, GDNF, nestin and ki-67 in rat hippocampal tissue.

Data were presented as $\bar{x} \pm s$. Statistical software SPSS17.0 was used to analyse all data (one-way ANOVA), $\alpha=0.05$. There was a significant difference at $P<0.05$.

RESULTS AND DISCUSSION

Influence of Zuogui pill and Yougui pill on protein expressions of hippocampal NGF and GDNF in natural aging rats (Table 1)

NGF is a neuro regulating factor, it can nourish neurons and promote synapse development. It was proved that the combined use of NGF/BDNF/bFGF significantly improved the ability of NSCs proliferation and differentiation and the percentage in the multi-factor groups was significantly higher than that in the single-factor groups [5]. Ontogenetic life and stress can have different effects on the NGF in the structures of the limbic system. A significant age-related decrease in NGF and TrkA in the PVN of stressed rats was noted with immunofluorescence staining. However, in the hippocampus, an age-related decrease in NGF-ir or TrkA-ir cells was observed in all rats except in acute forced swim stressed rats. The changes are possibly associated with involuntional aging processes caused by insufficient control of hypothalamic-pituitary-adrenal (HPA) axis functioning in P720 rats and may contribute to disturbances in NGF signaling [6], while the hyperfunction of HPA axis is founded in the process of aging.

GDNF have shown potent neuroprotective effects on different neuronal populations and they are also useful in maintaining the integrity of the corticostriatal pathway. These neurotrophic factors may be suitable for the development of a neuroprotective therapy for neurodegenerative disorders of the basal ganglia [7]. GDNF promotes the survival, growth, and regeneration of dopamine neurons and its tissue distribution is more important than dose for trophic stimulation of dopamine neurons [8]. Clinically relevant and long-lasting regeneration of the dopaminergic system in rhesus macaques lesioned with 1-methyl-4-phenyl-1,2,3,6-tetrahydropyridine 3-6 months before GDNF gene delivery (AAV2-GDNF). The observed progressive amelioration of functional deficits, recovery of dopamine, and regrowth of fibers to the striatal neuropil demonstrate that high GDNF expression in the putamen promotes restoration of the dopaminergic system in a primate model of advanced PD [9]. The aged primate brain challenged

by MPTP administration has the potential to respond to trophic factor delivery and that the degree of neuroprotection depends on GDNF levels [10]. GDNF protects dopamine (DA) neurons from 6-hydroxydopamine (6-OHDA) toxicity [11]. GDNF is essential for regulating dopamine (DA) release in the basal ganglia and for the survival of dopaminergic neurons; GDNF-deficient mice are considered an animal model for aging-related Parkinsonism [12].

It was found in our experiment that compared with Young group, the protein expression of NGF and GDNF were both down-regulated in rat hippocampus in Old group, $P<0.05$. Compared with Old group, the protein expressions of NGF and GDNF were both up-regulated in the Zuogui group and Yougui group, $P<0.05$.

Table 1. Level of protein expression of hippocampal NGF and GDNF in rats of all groups

Groups	n	NGF(OD)	GDNF(OD)
Young Group	8	0.657±0.061 [▲]	0.482±0.015 [▲]
Old Group	8	0.403±0.013	0.275±0.014
Zuogui Group	8	0.624±0.015 [▲]	0.433±0.010 [▲]
Youogui Group	8	0.605±0.009 [▲]	0.395±0.011 [▲]

[▲]Compared with Old Group, $P<0.05$

Influence of Zuogui pill and Yougui pill on protein expressions of hippocampal nestin and ki-67 in natural aging rats (Table 2)

NSCs exist in mammals in life process. But their overall neurogenic potential declines considerably in the early postnatal period. The deficiency of NSCs is related to aging or aging-related diseases.

Hippocampus is an important brain area related to aging. It has been proved that there are NSCs in hippocampal dentate gyrus in aging. Multipotent NSCs also persist in both CA1 and CA3 subfields of the hippocampus in the postnatal period. Such NSCs also retain their ability to give rise to both GABA-ergic and non-GABA-ergic neurons [13]. With aging, Hippocampal neurogenesis diminished and this phenomenon is related to deficiency of NSCs. Nestin and ki-67 are markers of proliferation and differentiation of NSCs.

It was found in our experiment that compared with Young group, the protein expressions of nestin and ki-67 were both down-regulated in rat hippocampus in Old group, $P<0.05$. Compared with Old group, the protein expressions of nestin and ki-67 were both up-regulated in the Zuogui group and the Yougui group, $P<0.05$.

Table 2. Levels of protein expression of hippocampal nestin and ki-67 in rats of all groups

Groups	n	Nestin(OD)	Ki-67(OD)
Young Group	9	0.744±0.101 [▲]	1.017±0.256 [▲]
Old Group	9	0.339±0.097	0.697±0.178
Zuogui Group	9	0.666±0.886 [▲]	0.968±0.303 [▲]
Youogui Group	9	0.568±0.089 [▲]	0.989±0.304 [▲]

[▲]Compared with Old Group, P<0.05

CONCLUSION

The change in protein expression of NGF and GDNF can influence the proliferation and differentiation of NSCs in hippocampus in aged rats, and Zuogui pill and Yougui pill can ameliorate these trends.

REFERENCES

1. T. Hagg, *Neuroscientist*, **1**, 15 (2009).
2. K. Hassanzadeh, M. Nikzaban, M.R. Moloudi, E. Izadpanah, *Iranian Journal of Basic Medical Sciences*, **6**, 18 (2015).
3. G. Gu, W. Zhang, M. Li, J. Ni, P. Wang, *Neuroscience.*, **4**, 291 (2015).
4. C. Campos, N.B.F. Rocha, E. Lattari, F.Paes, A.E. Nardi, S. Machado, *Expert Review of Neurotherapeutics*, **6**, 16 (2016).
5. S.Q. Chen, Q. Cai, Y.Y. Shen, X.Y. Cai, H.Y. Lei, *International Journal of Developmental Neuroscience.*, **11**, 38 (2014).
6. E. Badowska-Szalewska, R. Krawczyk, B. Ludkiewicz, J. Morys, *Neuroscience.*, **4**, 290 (2015).
7. J. Alberch, E. Perez-Navarro, J.M. Canals, *Progress in Brain Research.*, 146 (2004).
8. D.M. Gash, Z.M. Zhang, Y. Ai, R. Grondin, R. Coffey, G.A. Gerhardt, *Annals of Neurology.*, **2**, 58 (2005).
9. A.P. Kells, J. Eberling, X.M. Su, P. Pivrotto, J. Bringas, P. Hadaczek, W.C. Narrow, W.J. Bowers, H.J. Federoff, J. Forsayeth, *Neurosci.*, **28**, 30 (2010).
10. M.E. Emorg, J. Moirano, J. Raschke, V. Bondarenko, R. Zufferey, S. Peng, A.D. Ebert, V. Joers, B. Roitberg, J.E. Holden, *Neurobiol. Dis.*, **2**, 36 (2009).
11. A.D. Cohen, M.J. Zigmond, A.D. Smith, *Brain Res.*, **1**, 1370 (2011).
12. M. Buhusi, K. Olsen, B.Z. Yang, CV. Buhusi, *Frontiers in Behavioral Neuroscience.*, **6**, 10 (2016).
13. A.K. Shetty, B. Hattiangady, *International Journal of Developmental Neuroscience.*, **7**, 31 (2013).

In vitro fluoride release from fluorinated elastic denture material

Zh. Tang^{1,2*}, X. Zhao²

¹ The Second Affiliated Hospital Of Guilin Medical University, Guilin, 541199, China

² The Fourth Military Medical University, Xi'an, 710032, China

Received September 8, 2017; Accepted December 19, 2017

Elastic denture material has been routinely applied to replace missing teeth. Its physical and chemical properties, as well as its flexibility enable its application to cover concave abutment areas, reduce food impaction, and improve the retention of dentures. However, after long-term elastic prosthesis wear, the self-cleaning ability during the chewing process weakens, resulting in a drastically increased chance of local plaque deposition on the abutment and microecological imbalance, which can lead to caries and periodontal diseases. In this study, to effectively prevent and reduce the occurrence of caries around dental restorations such as dentures, different ratios of sodium monofluorophosphate ($\text{Na}_2\text{PO}_3\text{F}$ or MPF) were added to the elastic denture material, and the time-dependent fluoride release process was investigated after soaking in artificial saliva at a temperature maintained at 37°C. The elastic denture materials containing 0%, 3%, 5%, 10%, 15% and 20% (weight ratio) of MPF were soaked in 100 ml and 200 ml of artificial saliva solutions at a constant temperature of 37°C. The solutions were periodically replaced, and a 2 ml sample of each solution was tested just before replacement. The fluoride release rates and patterns were determined using the fluoride selective electrode method. All fluorinated elastic dentures released fluoride at different concentrations, and the higher the added fluoride content, the higher was the fluoride release. The elastic dentures with added MPF demonstrated an effective fluoride slow-release effect. The controlled release of fluoride can effectively prevent and reduce the occurrence of caries around dental restorations such as dentures.

Key words: Caries, Slow-releasing fluoride, Elastic denture material, Release rate

INTRODUCTION

Elastic denture material has been routinely applied to replace missing teeth. Its physical and chemical properties, as well as its flexibility, enable its application to cover concave abutment areas, reduce food impaction, and improve the retention of dentures. In addition, it has excellent biological compatibility and imposes no adverse stimuli on patients' oral mucosa, making it an ideal base material. However, after long-term elastic prosthesis wear, the self-cleaning ability during the chewing process weakens, resulting in a drastically increased chance of local plaque deposition on the abutment and microecological imbalance, which can lead to caries and periodontal diseases. Currently, there is very little literature on the effects of adding fluoride to elastic denture materials; therefore, in this study, different ratios of MPF were added to elastic denture material, and the time-dependent fluoride release process was investigated after soaking in artificial saliva at a temperature maintained at 37°C. The findings of this paper can provide an experimental basis for further clinical application.

EXPERIMENTAL

Materials

Analytical methods

The elastic denture material used in this study was obtained from Changsha Aolun High Tech Co., Ltd; $\text{Na}_2\text{PO}_3\text{F}$ (analytical grade) was obtained from Reagent No.1 Factory of Shanghai Chemical Reagent Co., Ltd; PF-2-01 fluoride selective electrode and saturated calomel electrode (Type 232) were obtained from Shanghai Yue Ci electronic technology Co., Ltd. Six types of elastic denture bases were made with 0%, 3%, 5%, 10%, 15%, and 20% (weight ratio) added $\text{Na}_2\text{PO}_3\text{F}$.

Analytical methods

The base samples were prepared with base wax in dimensions of 9mm × 7mm × 3mm weighing 1 g each. Five samples of each fluoride concentration were prepared, for a total of 30 samples that were divided into six ratio groups. The preparation process was the same as that of removable dentures. The casting wax was shaped in the same way as the samples, and the mold cavity was prepared accordingly with boxing wax. The MPF was dissolved in the self-cure monomer and then either mixed with the elastic denture material particles or sprayed on the surface of the particles. After the solvent volatilized, the MPF was evenly attached to the particles. Next, the conventional compression

*To whom all correspondence should be sent:
E-mail: twzy2007@163.com

molding technique was performed. The samples were soaked in 100 ml and 200 ml artificial saliva solutions, respectively, maintained at a constant temperature of 37°C. The solutions were each replaced on day 1, 2, 3, 6, 9, and 16, and then every 7 days for a length of 65 days. Just before solution replacement on the specified days, 2 ml of solution from each sample was removed and measured using a fluoride ion selective electrode.

Fluoride standard curve

A volumetric pipette was used to transfer 0.05, 0.1, 0.2, 0.4, and 0.6 ml of fluoride standard solution (10 ppm), respectively, to a 50 ml volumetric flask. Then, 20 ml of TISAB solution was added, diluted with distilled water to 50 ml, shaken well and transferred to a 50 ml polyethylene beaker. The latter was placed on a magnetic stirrer with inserted fluoride electrode and saturated calomel electrode. After stirring for about 30 min the reading was stable and the result was recorded. Finally, the fluoride E(mv)-log C F-standard curve was drawn on semi-logarithmic coordinate paper.

Statistical analysis

The rates of fluoride release and the release patterns of the samples of elastic dental materials containing different added fluoride ratios were analyzed by direct chart comparison.

RESULTS AND DISCUSSION

For both the 100 ml and 200 ml artificial saliva solutions, the fluoride release of each fluoride-containing group on days 2 and 3 was not significantly different from that of the fluoride-free group; however, after day 3 the fluoride release rates of the fluoride-containing groups were significantly higher than that of the fluoride-free group.

For the tests in 100 ml artificial saliva solution, the fluoride release of the elastic denture material in the fluoride-containing groups varied significantly in the first 44 days, but stabilized after that. The sample with 20% fluoride had the highest fluoride release, with an average release of 22.87 $\mu\text{g}/(\text{g}\times\text{d})$ and the highest value of 187.6 $\mu\text{g}/(\text{g}\times\text{d})$. The next highest was the sample with 15% fluoride, with an average release of 17.16 $\mu\text{g}/(\text{g}\times\text{d})$; the 10% sample had an average fluoride release of 14.47 $\mu\text{g}/(\text{g}\times\text{d})$. The samples with 5% and 3% fluoride had small amounts of release, with a value of 12.51 $\mu\text{g}/(\text{g}\times\text{d})$ and 11.09 $\mu\text{g}/(\text{g}\times\text{d})$, respectively. The release of the 5% and 10% fluoride groups was not significantly different from day 3 to day 23. The fluoride release

of the 10% fluoride containing group was significantly lower than that of the 15% group in the first 30 days; however, the difference was not significant after day 30. The release of the 3% fluoride containing group was similar to that of the 5% and 10% fluoride groups from day 3 to day 9, but was significantly lower than all groups for the other time points.

For the tests in 200 ml artificial saliva solution, the fluoride release of the fluoride-containing groups varied significantly in the first 37 days and then stabilized between days 38 through 65. Similar to the results of the 100 ml artificial saliva solution test, the sample with 20% fluoride had the highest fluoride release, with an average value of 21.12 $\mu\text{g}/(\text{g}\times\text{d})$ and a highest value of 167.2 $\mu\text{g}/(\text{g}\times\text{d})$, followed by the sample with 15% fluoride, which had an average fluoride release of 17.73 $\mu\text{g}/(\text{g}\times\text{d})$. The 10% group had an average fluoride release of 15.73 $\mu\text{g}/(\text{g}\times\text{d})$, and the 5% group had an average fluoride release of 13.95 $\mu\text{g}/(\text{g}\times\text{d})$. The 3% group had the lowest average fluoride release of 12.08 $\mu\text{g}/(\text{g}\times\text{d})$. The fluoride release of the 10% and 15% fluoride groups was not significantly different from day 2 to day 16, but after that the release of the latter group was significantly higher than of the former group. The fluoride release of the 3% fluoride group was similar to that of the other fluoride containing groups for the first three days, and was significantly lower after that. After day 37, the fluoride release of all groups stabilized.

The addition of fluoride to the denture material is thought to protect abutments from caries by increasing local fluoride concentrations. The fluoride released to the saliva forms fluoride ions, which bond to the calcium ions dissolved in the saliva from enamel to form calcium fluoride and then attach to the enamel plaque interface. Moreover, calcium fluoride can elevate the enamel pH by neutralizing acidic substances, and fluoride in its free state may also bind to calcium and phosphorus in the saliva, forming fluoro-apatite on the enamel surface and promoting enamel remineralization [1-4]. Studies have shown that fluoride released at low concentrations inhibits acid production by affecting the metabolism of bacteria; at high concentrations, the infiltration depth of fluoride into newly-demineralized enamel is significantly increased, which hardens enamel softened by caries and inhibits the continuation of demineralization [5-7]. Removable dentures have been widely applied clinically to replace missing teeth. The physical and chemical characteristics of the base material have a direct impact on the health of the close contacting abutment. By adding

fluoride to the denture material, fluoride ions can infiltrate the material surface or pass through internal pores to spread to the saliva and tooth surface [8], slowly releasing fluoride near the enamel and maintaining a low concentration of fluoride at the surrounding tissues to prevent caries. Due to the special structural features of the attachment of elastic dentures and the large extension range of the base, the self-cleaning ability of the abutment during the chewing process weakens after long-term wear, and the chance of dental plaque deposition increases, resulting in local microecological imbalance, which is a cause of dental caries and periodontal disease. Because the elastic denture material maintains long-term close contact with the abutment surface, it is necessary to add fluoride in the denture material to prevent caries.

MPF is a white powder that is water-soluble at room temperature (0-25°C) and is internationally recognized as an excellent third-generation anti-caries agent. Moreover, it has tooth desensitization, water fluoridation, and antibacterial effects, and is widely used as a fluoride toothpaste additive, preservative, and fungicide [9,10]. Currently, it is mainly used as an anti-caries fluoride agent in toothpaste. The fluoride in MPF exists in a complex ion state (FPO₃) with a neutral pH; therefore, it is more stable than free fluoride. In addition, it is highly compatible with other materials. These advantages make it an ideal fluoride additive [11,12]. The results of this study demonstrated that the addition of MPF to the elastic denture material led to a slow-release of fluoride.

The fluoride release curves shown in Figures 1 and 2 illustrate how each group of fluorinated elastic denture samples reached a peak on the first day, declined sharply on days 2 and 3, and increased again on day 4.

In the 100 ml artificial saliva, the fluoride release increased irregularly in the first 44 days, and stabilized after that. In the 200 ml artificial saliva, the fluoride release increased irregularly in the first 37 days and stabilized after that. This may have been due to the fact that at the beginning of the soaking, the MPF on the surface of the fluoride-containing elastomeric denture material began to dissolve, which formed a release peak. Later, the release of the MPF deep inside the denture material slowed down because of limited diffusion channels. However, after further soaking, the material absorbed water and expanded in various degrees, forming many tiny gaps on the surface of the material, which resulted in an uneven release of deep MPF. At the end of the experiment,

after soaking for a period of time (44 days in 100 ml solution and 37 days in 200 ml solution), the swelling rates of the material were basically uniform, which meant that the fluoride release was stable.

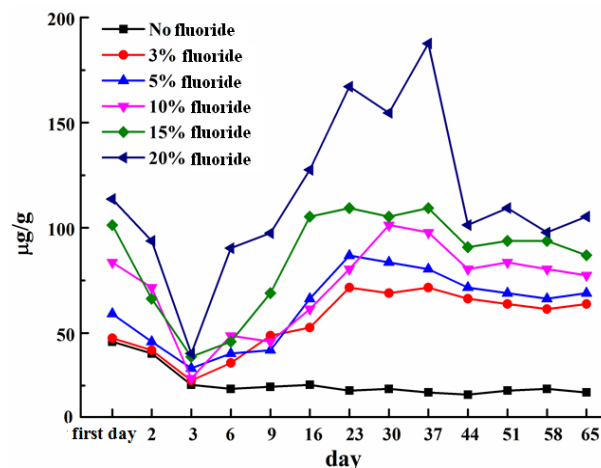


Fig. 1. Relationship between fluoride release (100 ml solution) and fluoride ratio in elastic denture material

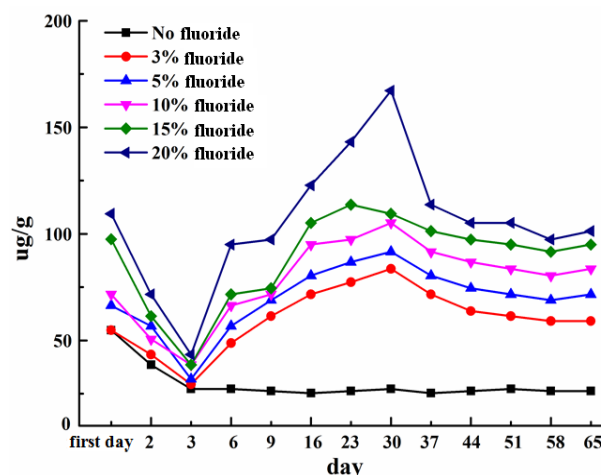


Fig. 2. Relationship between fluoride release (200 ml solution) and fluoride ratio in elastic denture material

Elastic denture material is an active polymer plastic composed of polycarbonate nylon composites. It has excellent flexibility, toughness, bending performance, corrosion resistance, and pressure forming ability. Moreover, it is resistant to high temperatures; it holds a stable volume without deformation at temperatures of 260-290°C. In addition, it is non-toxic, tasteless, biologically safe, and inexpensive. It displays progressive osmosis and good water absorption. Although the fluoride itself has no slow-release capability, added *in gitto* to elastic denture material at low concentrations to form complexes in the form of “fluoride libraries”, it demonstrated sustained release action to the surface of the material. Foreign and domestic

studies have added fluoride to thermo-coagulation materials, self-curing resins, and a variety of filling materials in anti-caries experiments; however, there have been no experiments or tests performed with fluoride added to elastic dentures. For the first time, in this study fluoride was added to elastic denture material for anti-caries protection and improved the denture preparation process. For a more realistic simulation of the oral environment, to reduce interference factors, and increase the accuracy of the experiments, in this study samples were innovatively soaked in 100 ml and 200 ml of artificial saliva at a constant temperature of 37°C and then fluoride release tests were performed. The scientific nature of the experiment was also enhanced by analyzing the release rates at different time points. As shown in the fluoride release curves, the higher the fluoride content of the elastic denture material, the higher are the fluoride release levels. The amount of fluoride in the material also affected the physical properties, color, and appearance of the material [13]. Therefore, the determination of the optimal ratio of fluoride requires more comprehensive consideration and should be further clinically validated. There is a wide range of oral fluoride doses that can cause acute poisoning; an oral dose of 6-9 mg/kg body weight can cause acute poisoning symptoms, and a one-time dose of 50mg/kg body weight is lethal [14-18]. The MPF doses added to the material in this study's experiments were much lower than the toxic dosage levels. Furthermore, exogenous fluoride is quickly diluted in saliva. Some of the fluoride in the saliva forms compounds and deposits in the enamel, some is deposited in the plaque, and some is excreted by oral self-cleaning. Most of the fluoride absorbed in the blood is excreted from the body with other body fluids. Clinically, it is highly safe.

CONCLUSION

The results of this study revealed that the addition of sodium monofluorophosphate into elastic denture material effectively released a certain concentration of fluoride when maintained at a constant temperature of 37°C in artificial saliva over a long period of time. The controlled release of fluoride can effectively prevent and reduce the occurrence of caries around dental restorations such as dentures. These findings provide experimental and theoretical basis for further clinical research. However, due to limited experimental conditions and time, the fluoride release in this study was only observed for 65 days, and longer-term fluoride

release experiments should be conducted for a more in-depth understanding.

Acknowledgements: *This study was supported by the Scientific Research and Technology Development Plan of Guangxi Province (grant No. 14124004-1-10) and the Scientific Research Plan Project of Guilin City (grants No. 20140120-8-1, 2016012709). The funders had no role in study design, data collection and analysis, decision to publish, or preparation of the manuscript.*

REFERENCES

1. W. Xin, K.C. Leung, E.C. Lo, M.Y. Mok, M.H. Leung, *BMC Oral Health*, **17**, 63 (2017).
2. S. Savas, E. Kucukyilmaz, E.U. Celik, *Pediatr. Dent.*, **38**, 511 (2016).
3. A. Akkus, D. Karasik, R. Roperto, *J. Clin. Exp. Dent.*, **9**, e569 (2017).
4. A.B. Paula, A.R. Fernandes, A.S. Coelho, C.M. Marto, M.M. Ferreira, F. Caramelo, *J. Evid. Based Dent. Pract.*, **17**, 23 (2017).
5. N. Agrawal, N.D. Shashikiran, S. Singla, K.S. Ravi, V.K. Kulkarni, *J. Dent. Child. (Chic.)*, **81**, 117 (2014).
6. M.M. Manarelli, A.C.B. Delbem, L.C. Báez-Quintero, F.R.N. de Moraes, R.F. Cunha, J.P. Pessan, *Acta Odontol. Scand.*, **75**, 376 (2017).
7. A. Vicente, A.J. Ortiz Ruiz, B.M. González Paz, J. García López, L.A. Bravo-González. *PLoS One.*, **12**, e0176389 (2017).
8. N. Patil, B. Jawale, R. Redasani, L. Chaudhari, J.B. Garde, V.S. Chauhan, *J. Contemp. Dent. Pract.*, **13**, 452 (2012).
9. S. Young, F. Sufi, M. Siddiqi, R. Maclure, J. Holt, *J. Clin. Dent.*, **27**, 97 (2016).
10. A. Jose, J. Ward, L. Shneyer, J. Skinner, N. Jeal, M. Cronin, M.L. Bosma, *J. Clin. Dent.*, **27**, 1 (2016).
11. C.R. Parkinson, M. Siddiqi, S. Mason, F. Lippert, A.T. Hara, D.T. Zero, *Caries Res.*, **51**, 170 (2017).
12. N.X. West, T. He, E.L. Macdonald, J. Seong, N. Hellin, M.L. Barker, *Clin. Oral Investig.*, **21**, 533 (2017).
13. J. Guo, H. Zhu, *Chinese Journal of Prosthodontics*, **10**, 73 (2009).
14. F. Goodarzi, A.H. Mahvi, M. Hosseini, S. Nedjat, R. Nabizadeh Nodehi, M.J. Kharazifard, *J. Dent. Res. Dent. Clin. Dent. Prospects*, **10**, 127 (2016).
15. M. Norman, S. Twetman, A. Hultgren Talvilahti, E. Granström, C. Stecksén-Blicks, *Community Dent. Health*, **34**, 27 (2017).
16. R.I. Garcia, S.E. Gregorich, F. Ramos-Gomez, P.A. Braun, A. Wilson, J. Albino, *Prev. Chronic Dis.*, **14**, E17 (2017).
17. A.M. Cavalli, A.G. Rebouças, L. Zanin, F.M. Flório, *J. Contemp. Dent. Pract.*, **17**, 451 (2016).
18. D.M. O'Mullane, R.J. Baez, S. Jones, M.A. Lennon, P.E. Petersen, A.J. Rugg-Gunn, *Community Dent. Health*, **33**, 69 (2016).

Controlling the abnormal state in the Rb-E2F pathway involving microRNAs

L.L. Li¹, J.W. Shen^{2*}, Z.R. Liu³

¹ Department of Basic Course, Guangdong Institute of Technology, Guangdong, China

² School of Mathematics and Statistics, Xuchang University, Xuchang, China

³ School of Mathematics and Statistics, Yunnan Normal University, Yunnan, China

Received August 29, 2017, Accepted December 19, 2017

Experiments have shown that microRNAs play an important role in regulating gene networks. They can orchestrate whole cellular programs by simultaneously regulating the expression of a group of genes. Restoring microRNAs to normal levels in cancer cells can reverse the aberrant cell growth. So understanding how to control the normal levels of microRNAs in the cancer cells is a critical step in controlling cancer. In this paper, a method to control microRNAs levels is presented by investigating the gene regulative network involving the Rb-E2F pathway and microRNAs (miR449); also, the influence of noises on the dynamical behaviour of the Rb-E2F pathway is studied by using a mathematical model. The results show that there is a relationship between noise density and system response. Through finding and defining the phenomenon of stochastic resonance it was found that the stochastic resonance can be controlled through the optimal noise intensity, and the microRNA levels can be controlled. These findings are propitious in providing a novel way to heal cancer.

Keywords: MicroRNAs, Noise, Stochastic resonance.

INTRODUCTION

Maintenance of normal cell function and tissue homeostasis is dependent on the precise regulation of multiple signaling pathways [1]. Once the balance is destroyed, genetic diseases such as cancer arise. Rb and E2F proteins play important roles in the regulation of cell division, cell growth, and programmed cell death by controlling the expression of genes involved in these processes; they are best known for their regulation of the cell cycle at the G1/S transition [2]. The Rb gene was the first identified tumor suppressor gene [3], and it now is recognized as playing a fundamental role in a signaling pathway that controls cell proliferation [1]. Rb regulates the transcription of genes that are essential for DNA replication and cell cycle progression by binding and inhibiting E2F transcription factors [4]. In recent years, a large number of studies have focused on the mechanisms controlling cellular proliferation associated with human cancer experimentally regulated by the Rb-E2F pathway [5-8]. As we all know, microRNAs (miRNAs) are an abundant class of tiny RNAs that regulate the expression of protein-coding genes in plants and animals [9]. They are thought to have the capacity for serving as diagnostic and prognostic biomarkers in human cancers [10]. This paper mainly focuses on miR-449, which can induce cell senescence and apoptosis and act as a tumor suppressor through regulating Rb/E2F activity [11,

12]. MiR-449 provides a twofold safety mechanism to avoid excessive E2F-induced proliferation by cell cycle arrest and apoptosis [13]. Mathematical models have been established to explain the nonlinear dynamical behavior of the Rb-E2F pathway [13-15], which mainly concentrate on the stability and bifurcation. However, these models do not take into account the effects of noise.

Noise is ubiquitous in the real world, and always be deemed to play a destructive role in natural synthetic systems [16], but the response of a nonlinear system to a weak signal is optimized by the presence of a particular level of noise. This phenomenon is called stochastic resonance (SR) [17]. The concept of SR was firstly proposed by Benzi [18]. In the past several decades, a lot of research about SR has been performed experimentally in different fields, including biological systems [19-21], physical systems [22, 23] and so on. Moreover, theories of SR have been developed for multistable systems, monostable systems, excitable systems, as well as threshold crossing detectors [17]. Because of the coherence effect of SR on nonlinear systems, SR has been used to control harmful behavior of biological systems. In recent months, researchers at the Mayo Clinic Comprehensive Cancer Center of USA [24] discovered a way to potentially reprogram cancer cells back to normalcy and showed that restoring the normal miRNA levels in cancer cells can reverse the aberrant cell growth in laboratory experiments.

In the cell, substantial cell-to-cell variation (or

To whom all correspondence should be sent:
E-mail: xcjwshen@yahoo.com

"noise") may be observed [25], therefore, controlling the normal expression of microRNAs by using the noises and related theory becomes the primary work of this article. Firstly, the Rb-E2F pathway network involving miR449 modeled by a stochastic differential equation and their biological significance will be introduced. Secondly, by simulating and inducing the measure of stochastic resonance, how the additive noise influences the stabilities of gene network, and how to control the irregular expression of miR449 and others will be discussed. Thirdly, a mechanism to explain the biological significance of these dynamical behaviors will also be given.

EXPERIMENTAL

Stochastic differential equation model of Rb-E2F pathway mediated by miR449

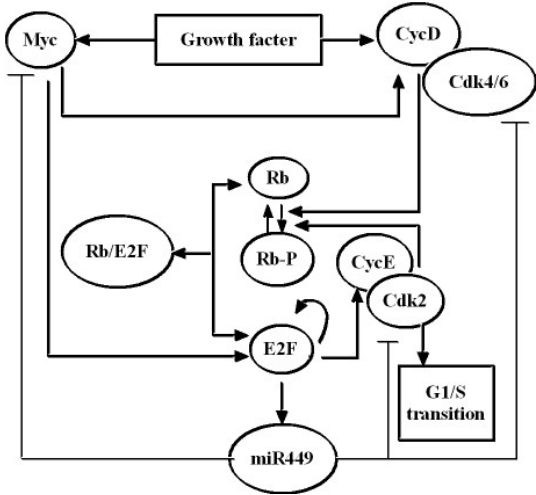


Fig. 1. Rb-E2F pathway mediated by miR449

Based on the works of Yan *et al.* [13] and Yao *et al.* [15], the simplified model considered in this paper is shown in Figure 1. Yao *et al.* [15] provided a mathematical model in the absence of miR449 and indicated that the Rb-E2F pathway acts as a bistable switch to convert signal inputs into all-or-none E2F responses. Yan *et al.* [13] developed another mathematical model and further investigated the stability and bifurcations of E2F, CycE and miR449 in the presence of miR449. The main task in this paper is to consider the effects of noises on the dynamic behavior of the models with miR449, when noises are taken into account. The stochastic differential equation model of the network including miR449 is described by the following system:

$$\begin{cases} \frac{dx_1}{dt} = k_{11} \frac{x_3}{k_{12} + x_3} \frac{x_1}{k_{13} + x_1} + k_{14} \frac{x_3}{k_{15} + x_3} + k_{16} x_4 \frac{x_8}{k_{17} + x_8} + \\ k_{18} x_5 \frac{x_8}{k_{19} + x_8} - k_{110} x_1 - k_{111} x_6 x_1 \\ \frac{dx_2}{dt} = k_{21} \frac{x_1}{k_{22} + x_1} - k_{23} x_2 - k_{24} x_2 \frac{x_3}{k_{25} + x_3} - k_{26} x_2 \frac{x_4}{k_{27} + x_4} - \\ k_{28} x_2 \frac{x_5}{k_{29} + x_5} \\ \frac{dx_3}{dt} = k_{31} \frac{S}{k_{32} + S} - k_{33} x_3 - k_{34} x_2 \frac{x_3}{k_{35} + x_3} \\ \frac{dx_4}{dt} = k_{41} \frac{S}{k_{42} + S} + k_{43} \frac{x_3}{k_{44} + x_3} - k_{45} x_4 - k_{46} x_2 \frac{x_4}{k_{47} + x_4} + \sqrt{D} \xi(t) \\ \frac{dx_5}{dt} = k_{51} \frac{x_1}{k_{52} + x_1} - k_{53} x_5 - k_{54} x_2 \frac{x_5}{k_{55} + x_5} \\ \frac{dx_6}{dt} = k_{61} + k_{62} \frac{x_7}{k_{63} + x_7} - k_{64} x_6 x_1 - k_{65} x_4 \frac{x_8}{k_{66} + x_8} - \\ k_{67} x_5 \frac{x_6}{k_{68} + x_6} - k_{69} x_6 \\ \frac{dx_7}{dt} = k_{71} x_4 \frac{x_6}{k_{72} + x_6} + k_{73} x_5 \frac{x_6}{k_{74} + x_6} + k_{75} x_4 \frac{x_8}{k_{76} + x_8} + \\ k_{77} x_5 \frac{x_8}{k_{78} + x_8} - k_{79} \frac{x_7}{k_{710} + x_7} - k_{711} x_7 \\ \frac{dx_8}{dt} = k_{81} x_6 x_1 - k_{82} x_4 \frac{x_8}{k_{83} + x_8} - k_{84} x_5 \frac{x_8}{k_{85} + x_8} - k_{86} x_8 \end{cases} \quad (1)$$

where $x_1, x_2, x_3, x_4, x_5, x_6, x_7, x_8$ represent the concentrations of E2F, miR449, Myc, CycDCdk4/6 complex, CycE-Cdk2 complex, Rb, phosphorylated Rb and Rb/E2F complex, respectively, and S is the intensity of the growth factor; the noise $\xi(t)$ is assumed as a Gaussian noise with zero mean and $\langle \xi(t) \xi(t') \rangle = \delta(t - t')$, and D is the noise intensity. In the following simulations, all parameter values are shown in Table 1 unless specified elsewhere.

RESULTS AND DISCUSSION

Oscillation induced by noise

Deterministic model corresponding to the stochastic differential equation model can induce oscillation in specific parameter interval oscillation. The growth factor S was chosen as a governing parameter because it is the key parameter responsible for controlling the G1/S transition in both mammalian and plant cell cycle. Fang *et al.* [13] provided us with the following results: As the change of S , two Hopf bifurcations appear at $S \approx 1.119$ and $S \approx 3.854$ for the deterministic system. Meanwhile, when S is smaller than 0.9312 or larger than 3.854, E2F and CycE are both monostable, bistability occurs in the range starting from $S \approx 0.9312$ and $S \approx 1.117$, and sustained oscillations can be seen within the limits of $S \approx 1.119$ and $S \approx 3.854$, more details are presented in the

original article [13]. The results of numerically integrating system (1) using stochastic simulation methods, are shown in Figures 2 and 3.

Figure 2 demonstrates that noise can influence the steady states of E2F, miR449 and CycE. In Figure 2(a), the noise intensity is $D=0$, and E2F, miR449 and CycE are all stable. Oscillation appears when the noise intensity is $D=0.1$ (Figure 2(b)). In order to give a better description of the effects of noise on the genes, the results in Figure 3 show how the amplitudes of E2F, miR449 and CycE vary with the change in noise intensity under the condition of $D=0, 0.001, 0.05, 0.1$. It is clear that the amplitudes of E2F, miR449 and CycE are gradually increasing with the increase in D within a certain range of noise intensity.

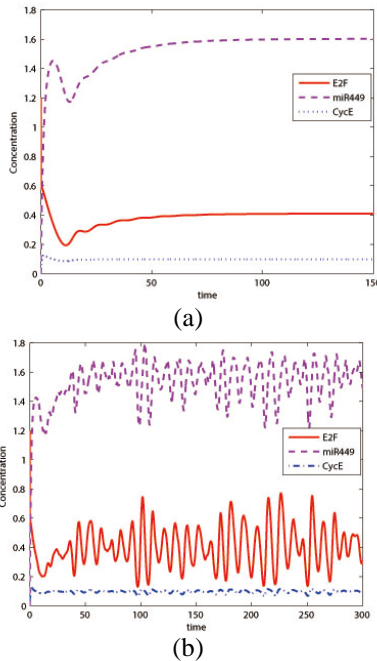


Fig. 2. Time courses of E2F, miR449 and CycE at $S=5$, the other parameters are shown in Table 1. Initial values are $x_{10}=1.2, x_{20}=0, x_{30}=0, x_{40}=0, x_{50}=0, x_{60}=0.55, x_{70}=0, x_{80}=0$, (a) $D=0$; (b) $D=0.1$.

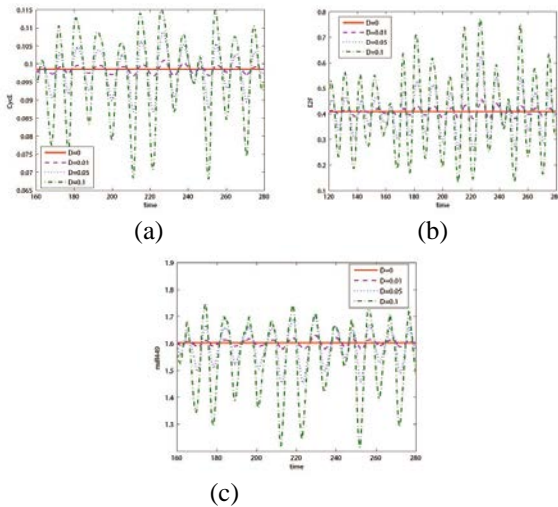


Fig. 3. Time courses of E2F, miR449 and CycE at $S=5$ under the condition of $D=0, 0.001, 0.05, 0.1$. The other parameters are shown in Table 1. The initial values is as follows: $x_{10}=1.2, x_{20}=0, x_{30}=0, x_{40}=0, x_{50}=0, x_{60}=0.55, x_{70}=0, x_{80}=0$,

Stochastic resonance induced by noise

Here, the main task is to determine what is the most appropriate noise intensity for the responses of E2F, miR449 and CycE, i.e. SR. In order to effectively characterize the phenomenon of SR, the notion of the characteristic correlation time /cct is introduced as follows [26]:

$$cct = \int_0^{\infty} C^2(t)dt$$

$$\text{where } C(t) = \overline{y(t)y(t+\tau)},$$

$$\overline{y(t)} = y(t) - \langle y(t) \rangle$$

Figure 4 shows that the variation of cct depends on noise intensity, in Figure 4(a) it can be seen that cct reaches a maximum value at the noise amplitude $D=0.15$, i.e., SR occurs at $D=0.15$. According to the notion of SR above, signal responses are in the optimal state when the noise amplitude is $D=0.15$. Figure 4(b) shows the cct for different S (4, 4.5, 5): as the growth factor S increases, the maximal value of cct decreases, and the corresponding noise amplitude D increases.

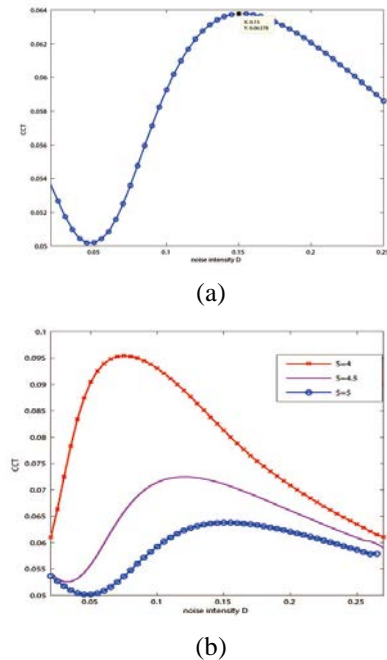


Fig.4. Correlation time vs noise amplitude D : (a) $S=5$, (b) $S=4, 4.5, 5$, the other parameters are shown in Table 1.

The resonance phenomenon characterizes cancer progression [27]. Virtually, all human cancers are induced when the control of the

normal gene regulatory network is disrupted [8]. In the Rb-2F pathway, CycE and its associated kinases, cdk2 regulate the passage through the G1-phase, which together form active complexes required for entry into the S-phase [28]. Rb is the principal substrate during the G1-phase for activating cyclin/cdk complexes [29], and E2F can promote the expression of genes and entry into S-phase [30]. The numerical results suggest that E2F, CycE and miR-449 can suddenly burst even with small amplitude noise from the viewpoint of nonlinear dynamics. This small noise can cause energy to reach the energy barrier and make E2F, CycE and miR-449 away from the steady state, leading them to enter an abnormal state, resulting in the formation of a cancer cell [31].

CONCLUSIONS

Previous experimental results [25] have shown that abnormal expression of microRNAs can induce abnormal expression of its target gene, which can lead to irregular vibration of the cell and cause the cancer to happen. In the above investigation it is shown that the miR449 and its target genes (E2F, CycE, etc.) suddenly burst and oscillate irregularly when noises arise. However, when noise intensity reaches an optimal state, the oscillation of miR449 becomes increasingly regular (Figure 3), and tends to irregularity as noise intensity exceeds the optimal state. In order to explain these phenomena, a mechanism of SR is proposed, and it is found that the expression of miR449 which plays an important role in the Rb - E2F pathway can be controlled. Ref. [32] shows that the Rb/E2F pathway is critical in regulating the initiation of DNA replication and the control of this pathway is disrupted in virtually all human cancers. Also, Feng *et al.* [11,33] have shown that miR-449 regulates the Rb/E2F pathway through an auto-regulatory feedback circuit. In these complex gene networks, controlling noise intensity is a critical point in controlling cancer. According to the idea from reference [24], this paper presents a possible method to make the tumor cells to move back to normal cells through the mechanism of SR.

Table 1. Parameters for the model

Rate constant	Value	Rate constant	Value	Rate constant	Value
k_{11}	0.4	k_{32}	0.5	k_{66}	0.92
k_{12}	0.15	k_{33}	0.7	k_{67}	18
k_{13}	0.15	k_{34}	0.6	k_{68}	0.92
k_{14}	0.003	k_{35}	0.15	k_{69}	0.06
k_{15}	0.15	k_{41}	0.45	k_{71}	18
k_{16}	18	k_{42}	0.5	k_{72}	0.92
k_{17}	0.92	k_{43}	0.03	k_{73}	18
k_{18}	18	k_{44}	0.15	k_{74}	0.92

k_{19}	0.92	k_{45}	1.5	k_{75}	18
k_{110}	0.25	k_{46}	1	k_{76}	0.92
k_{111}	180	k_{47}	0.92	k_{77}	18
k_{21}	1.4	k_{51}	0.35	k_{78}	0.92
k_{22}	0.15	k_{52}	0.15	k_{79}	3.6
k_{23}	0.02	k_{53}	1.5	k_{710}	0.01
k_{24}	0.6	k_{54}	0.7	k_{711}	0.06
k_{25}	0.15	k_{55}	0.92	k_{81}	180
k_{26}	1	k_{61}	0.18	k_{82}	18
k_{27}	0.92	k_{62}	3.6	k_{83}	0.92
k_{28}	0.7	k_{63}	0.01	k_{84}	18
k_{29}	0.92	k_{64}	180	k_{85}	0.92
k_{31}	1	k_{65}	18	k_{86}	0.03

Note: the descriptions of the parameters in Table 1 are given in [13,15].

Acknowledgements: This work is supported by the National Natural Science Foundation of China (11772291,11572278) and Innovation Scientists and Technicians Troop Construction Projects of Henan Province (2017JR0013).

REFERENCES

- 1.R.C. Sears, J.R. Nevins, *J. Biol Chem*, **277**, 11617 (2002).
- 2.H. Lee, PhD Thesis, RU, Rutgers,2011.
- 3.D. Hanahan, R.A. Weinberg, *Cell*, **100**(1), 57(2000).
- 4.N. Ghanem, M.G. Andrusiak, D. Svoboda, S.M. Al Lafi, L.M. Julian, K.A. McClellan, Y. De Repentigny, R. Kothary, M. Ekker, A. Blais, D.S. Park, R.S. Slack, *J. Neurosci.*, **32**(24), 8219 (2012).
- 5.E. Khav, B.S. Thesis, U.A., Tucson, 2013.
- 6.J. White, E. Stead, R. Faast, S. Conn, P. Cartwright, S. Dalton, *Mol. Biol. Cell*, **16**(4), 2018 (2005).
- 7.J.R. Nevins, G. Leone, J. DeGregori, L. Jakoi, *J. Cell Physiol.*, **173**(2), 233 (1997).
- 8.J.R. Nevins, *Hum. Mol. Genet.*, **10**(7), 699 (2001).
- 9.L.P. Lim, N.C. Lau, E.G. Weinstein, A. Abdelhakim, S. Yekta, M.W. Rhoades, C.B. Burge, D.P. Bartel, *Genes Dev.*, **17**(8), 991 (2003).
- 10.H.W. Kang, M. Crawford, M. Fabbri, G. Nuovo, M. Garofalo, S.P. Nana-Sinkam, A. Friedman, *PLoS One*, **8**(1), e53663 (2013).
- 11.X. Yang, M. Feng, X. Jiang, Z. Wu, Z. Li, A. Meiyee, Q. Yu, *Genes Dev.*, **23**(20), 2388 (2009).
- 12.T.B. Kheir, E. Futoma - Kazmierczak, A. Jacobsen, A. Krogh, L. Bardram, C. Hother, K. Grønbaek, B. Federspiel, A.H. Lund, L. Friis-Hansen, *Mol. Cancer*, **10**(1), 29 (2011).
- 13.F. Yan, H. Liu, J. Hao, Z.Liu, *PLoS One*, **7**(9), e43908 (2012).
- 14.M.N. Obeyesekere, S.O. Zimmerman, E.S. Tecarro, G. Auchmuty, *Bull. Math. Biol.*, **61**(5), 917 (1999).
- 15.G. Yao, T.J. Lee, S. Mori, J.R. Nevins, L. You, *Nature Cell Biology*, **10**, 476 (2008).
- 16.Z. Sun, X. Yang, W. Xu, *Phys. Rev. E. Stat. Nonlin. Soft Matter Phys.*, **85**, 061125 (2012).

17. J.J. Collins, C.C. Chow, C.C. Ann, T.I. Thomas, *Phys. Rev. E*, **54**(5), 5575 (1996).
18. R. Benzi, A. Sutera, A. Vulpiani, *J. Phys. A: Math. Gen.*, **14**, L453 (1981).
19. A. Longtin, A. Bulsara, F. Moss, *Phys. Rev. Lett.*, **67**, 656 (1991).
20. J.K. Douglass, L. Wilkens, E. Pantazelou, F. Moss, *Nature*, **365** (6444), 337 (1993).
21. S.M. Bezrukov, I. Vodyanoy, *Nature*, **378**, 362 (1995).
22. P. Jung, K. Wiesenfeld, *Nature*, **385**(6614), 291 (1997).
23. M.M. Alibegov, *Phys. Rev. E*, **59**(5), 4841 (1999).
24. A. Kourtidis, S.P. Ngok, P. Pulimeno, R.W. Feathers, L.R. Carpio, T.R. Baker, J.M. Carr, I.K. Yan, S. Borges, E.A. Perez, P. Storz, J.A. Copland, T. Patel, E.A. Thompson, S. Citi, P.Z. Anastasiadis, *Nature Biology*, **17**, 1145 (2015).
25. Y. Pilpel, *Methods Mol. Biol.*, **759**(2011), 407 (2001).
26. S.P. Arkady, K. Jdoturgen, *Phys. Rev. Lett.*, **78**(5), 775(1997).
27. Z. Agur, *Croat. Med. J.*, **55** (2), 93 (2014).
28. T. Hunter, J. Pines, *Cell*, **79**(4), 573 (1994).
29. R.A. Weinberg, *Cell*, **81**(3), 323 (1995).
30. J.R. Nevins, *Science*, **258**, 424 (1992).
31. J. Shen, L. Chen, K. Aihara, *Lecture Notes in Operations Research*, **13**, 251 (2010).
32. J. Revins, *Hum. Mol. Genet.*, **10**(7), 699 (2001).
33. M.Feng, Q.Yu, *Cell Cycle*, **9**(2), 213 (2010).

Research progress in oil-field scale prevention techniques

J. Dong, X. Sui*, B. Wang*, Y. Liu, Ch. Yan, L. Zhu, D. Yuan, L. Li

Provincial Key Laboratory of Oil & Gas Chemical Technology, College of Chemistry & Chemical Engineering,
Northeast Petroleum University, Daqing 163318, China

Received September 14, 2017, Accepted December 19, 2017

The presence of scaling poses significant issues in the production and recovery benefits of oil fields. This article reviews the causes of oilfield scales and elaborates on common scale prevention methods, including chemical technique, ultrasonic technique, electromagnetic technique, and metal coating technique. The paper describes the existing techniques in detail, lists their respective advantages and disadvantages, and proposes a technology variation that can reduce the formation of scales. This work is expected to contribute guidance in normal oil field production.

Key words: Scaling causes; Scale prevention technique, Scale prevention mechanism

INTRODUCTION

Over recent years, various flooding techniques, including water flooding, polymer flooding [1,2], and three-component combination flooding [3-7], have been widely employed to enhance oil recovery in oil fields, which has caused increasingly serious scaling problems [8-10]. Scaling in formation can lead to formation plugging, which prevents water injection from reaching the injection allocation amount. Thus, oil well productivity is greatly reduced. Scaling in wellbores can increase the burden of underground maintenance operations. In addition, it can cause scrapping of water injection wells and oil wells. Scaling can also lead to blockage in pipelines, delivery pumps, and heat exchangers, which can affect the normal operation of crude oil treatment systems and sewage treatment systems, thereby increasing the costs associated with cleaning and replacing the equipment and pipelines. The deposition of scales can also result in local corrosion of the equipment and pipelines, leading to perforation in a short time and shortening of service life. Various scaling prevention measures have been proposed to solve these different scaling problems in oil fields. However, the complex and variable situations in oilfield production have produced higher demands for scale prevention and have also promoted the development of scale prevention techniques [11-14].

CAUSES OF OILFIELD SCALING

Incompatible chemical mixture

Mixtures between two liquids with incompatible chemical properties promote the interaction between scale-forming ions. Examples of this type

of mixtures include the formation water with incompatible ions at different layers, formation water with surface water, clean water with waste water, and mixtures of different high-salinity liquids. Variations in formation pressure, temperature, flow velocity, and pH value can break the original chemical equilibrium; reduce the water's capacity in mineral dissolution, cause oversaturation, and lead to depositions, thereby generating salt scales. Non-crystalline silicon dioxide and quartz are formed by the dehydration condensation reaction of silicic acid gels.

Defective pipelines

The flow line, flow velocity, pressure and density of the oil gas may change suddenly in some defective pipelines or at the turnings of pipelines, which readily leads to the aggregation of scales and subsequent passageway blockages.

Free sediments

The formation on the bottom of wells always contains a relatively high proportion of unstable and free sediments. These sediments can be carried to the well holes and pipelines during oil and gas production under certain conditions, which may result in scale formation and sand plugging.

Flooding agents

The flooding agents also corrode pipeline materials to a certain degree. Many dissolved gases, such as oxygen and carbon dioxide, are included in the pipeline fluids. These pipeline materials can undergo ionization, resulting in the formation of ferric hydroxide, ferric oxide, ferrous carbonate, ferrous sulfate and other corrosive materials. These can corrode the pipeline and also provide conditions for adhesion of other dirty materials, which promote scaling.

To whom all correspondence should be sent:

E-mail: suixin@nepu.edu.cn

wangbh@nepu.edu.cn

External conditions variation

During the crude oil transport process in the pipelines, variations in external conditions, such as environment, temperature and pressure, can lead to the crystallization or decomposition of macromolecular hydrocarbons in the crude oil, such as coking materials, paraffins, and pitch. These materials adhere to the pipelines and combine with inorganic scales, such as sediments, leading to the formation of scale samples that are difficult to remove. Even crystals can be separated out from the high-solubility materials under certain external conditions, and they are then mixed with other scale samples.

Organic scale formation

Organic matter and bacteria contained in the crude oil are attached to the solid particles that are scattered in the crude oil or on the pipeline walls, and they react with the excretions from the microorganisms in the water to form slimes. The organic scales can adhere to the pipeline inwalls in a flocculent pattern. The existence of the organic scale can provide the conditions for the subsequent reproduction of dirt, resulting in thick dirt layers. In addition, defects in the pipeline inwalls or corruptions along the pipelines can also provide conditions for the formation of organic scales.

COMMON SCALE PREVENTION TECHNIQUES IN OIL FIELDS

Chemical scale prevention methods

Adding chemical anti-scaling agents is the most widely used method for inhibiting and slowing the formation of scales in both domestic and foreign oil fields. The chemical method involves the addition of anti-scaling agents to prevent or reduce the production of inorganic salt scales. The most popular chemical scale prevention mechanisms are described in detail below:

Solubilization

After being dissolved in water, the anti-scaling agent reacts with the scale-forming cations in the water to form stable soluble complexes. These complexes stabilize the scale-forming cations and thereby inhibit the deposition of salt scales. The anti-scaling agent added in small amounts, can react with many scale-forming ions to form chelates [16].

Crystal distortion and threshold effects

The anti-scaling agent is adsorbed onto the active growing points on the crystal and then reacts

with the scale-forming cations to form chelates, which can inhibit the regular growth of the crystal lattice and can cause crystal distortion. Accordingly, the stress inside the large crystals increases, which makes the crystal more likely to rupture. However, it is not easy to inhibit the crystallization of scales. According to the spiral dislocation theory, during crystallization, crystal growth around the growing point is restricted when the finite active growing points are covered by molecules of the anti-scaling agent, which leads to inhibition of the crystallization and scale growth [17,18].

Electrostatic repulsion

The chain structure of the anti-scaling agent adsorbs several micro-crystals that have the same charge, and the electrostatic repulsion generated can hinder the collisions between the crystals, thereby hindering their growth. Meanwhile, polymers adsorb and wrap around the scale-forming micro-crystals, which allows the crystalline grains to achieve a favorable dispersion. The scale-forming micro-crystals can then be washed away by water [19].

Chemical anti-scaling agents

Dating back to the 1930s, anti-scaling has experienced a long development history, ranging from inorganic to organic matter, and from micromolecular to macromolecular polymers. Some anti-scaling agents have also been used for the preparation of nano-emulsions to improve scale prevention effects. Currently, the most commonly used anti-scaling agents in oil fields are organic phosphonate, low-molecular polymers, including homopolymers and copolymers, and modified polymers. Organic phosphonates are generally used for the prevention of calcium carbonate scale formation, while low-molecular polymers are used for the prevention of sulfate scale formation. Thus, these two types of anti-scaling agents can be combined for the prevention of mixed scale formation.

Organic phosphonate

Organic phosphonate anti-scaling agents in oil fields mainly include amino trimethylene phosphonic acid (ATMP), ethylenediamine tetra methylenephosphonic acid (EDTMP), diethylenetriamine pentamethylene phosphonic acid (DTPMP), hydroxyethylidene diphosphonic acid (HEDP), butane phosphate 1,2,4-tricarboxylic acid (PBTCA), 2-hydroxyphosphonoacetic acid (HPA), polyamino polyether methylene phosphonic acid (PAPEMP) and 3-hydroxy-3-phosphonobutyric

acid (HPBA).

ATMP and HEDP were both developed in the 1960s and are still widely used in water treatment. In the 1980s, the organic phosphonic carboxylic acid was developed, in which PBTCA exhibited outstanding scale prevention performances under severe conditions, such as high temperatures, high hardness, and high pH values. Macromolecular organic phosphonic acid PAPEMP was prepared in the 1990s with a molecular mass of up to approximately 600 g/mol. Ether bonds were introduced into PAPEMP to increase calcium tolerance, scale-prevention ability, and dispersion performance.

Polymer-type

The most popular polymer-type anti-scaling agents used in oil fields include polyacrylic acid (PAA), polymethacrylic acid (PMA), hydrolyzed polymaleic acid (HPMA), maleic acid/acrylic acid (MA/AA), acrylic acid/hydroxypropyl acrylate (AA/HPA), sulfonated styrene/maleic acid (SS/MA), maleic acid/methyl acrylate/vinyl esters, acrylic acid/2-acrylamide-2-methyl propyl sulfonic acid (AA/AMPS), PPMA, phosphono-carboxylic acid (POCA), and polyaspartic acid (PASP). Among these polymer-type anti-scaling agents, PASP has the most favorable corrosion characteristics and scale inhibition effects and can replace phosphorous water treatment agents; PAA can disperse sediments and micro-crystals in salts, such as calcium carbonate and calcium sulfate without depositing them in the water, which allows the material to boast excellent scale inhibition performance; HPMA combines lattice distortion and threshold effects to effectively disperse calcium phosphate micro-crystals and to achieve favorable heat stability, which is useful for scale and corrosion inhibitions under high-temperature conditions; POCA can inhibit both scaling and corrosion and also has fairly high calcium tolerance, which allows this material to be referred to as a real multi-function agent.

Nano-emulsion-type

In low-water-content formation, soluble flooding agents can lead to slow oil production and can cause harms to reservoirs. The use of nano-emulsion to transport soluble flooding agents can effectively solve these problems. This method exhibits the following advantages: the emulsion droplets can be easily deformed and therefore do not readily block pore throats; the emulsion droplets can increase the sweep area and cannot lead to water coning; the emulsion droplets can be

retained in the porous media and slow down demulsification and release with a long scale-prevention period; the anti-scaling agents cannot be released in great amounts before the oil well resumes production, and there is no waste, which is not comparable by the other squeeze methods; after the flooding operation is finished, the emulsion cannot retard oil production, which offers high operational benefits [20].

Physical scale prevention methods

Physical methods include the prevention of inorganic salts from depositing on the system walls through certain actions, during which inorganic salts can form crystal nuclei and even crystals in the solution. These crystals should be suspended in the solution without adhering to the system walls. Common physical scale prevention methods include ultrasonic scale prevention technique, magnetic scale prevention technique, and metal coating scale prevention technique, which are described in detail below.

Ultrasonic technique

Ultrasonic scale removal and prevention equipment is mainly composed of an ultrasonic generator, an ultrasonic energy converter, and pipeline assemblies for the installation of the ultrasonic energy converter. The equipment can be classified into three types according to installation method, including external equipment, embedded equipment, and built-in equipment. Ultrasonic scale removal and prevention equipment mainly uses a high-intensity acoustic field for the treatment of fluid by utilizing the ultrasonic wave's cavitation effect, activation effect, shear effect, and inhibition effect. Therefore, the scale-forming materials in the fluid can exhibit a series of changes in physical configurations and chemical properties, as a result of which these scale-forming materials are dispersed, smashed, loosened, and ultimately not easily attached to the pipe walls to form scales. The various ultrasonic effects are described below:

(1) Cavitation effect. The energy of an ultrasonic wave can directly produce a large number of cavities and bubbles in the fluid medium. The rupturing of these cavities and bubbles generates a strong pressure peak within a certain range. Even some local pressure peaks can reach up to thousands of psi atmospheric pressure. These pressure peaks can smash the scale-forming materials and suspend them in water. Moreover, the scale layer that has already been formed will easily come off. The ultrasonic wave capitation effect is now widely applied in cleaning [21].

(2) Activation effect. Ultrasonic waves can enhance the activities of both flowing fluids and scale-forming materials, destroy scales' formation conditions, and diminish deposition conditions on the walls of the energy converter. Accordingly, the scale forming materials can form scattered sedimentary bodies rather than hard scales on the pipe walls.

(3) Shear effect. When the scale layer, pipe walls, and water are exposed to the radiation of ultrasonic waves, these three components can generate unsynchronized vibrations as a result of differing responses to the frequency of the ultrasonic wave. This generates relative movement at a high velocity. Differences in velocity result in a relative shear force between the scale layer and the interface of the pipe wall of the energy converter, leading to fatigue and loosening in the scale layer.

Inhibition effect of ultrasonic waves. The application of the ultrasonic waves results in changes in the fluid's physical and chemical properties, which effectively inhibits nucleation and growth of the ions in water on the pipe walls. Consequently, the number of scale-forming ions attached on the surface of the heat exchanger is reduced. Experimental results have shown that increasing the duration of the application of the ultrasonic wave results in increased scale prevention performance. When the ultrasonic wave is applied on the water, a sufficiently large ultrasonic energy can produce a transient, local, great, high-temperature, high-pressure, high-electric-field-intensity, and extreme physical environment in the transmission medium under normal-temperature and normal-pressure environmental conditions. The fluid can then produce the so-called acoustic cavitation effect and induce a series of mechanical, physical, chemical and biological effects. Accordingly, the goals of preventing and removing the scales in the fluids can be achieved.

The ultrasonic scale prevention technique exhibits several advantages, such as environmental protection, desirable performance, low costs, no corrosion, high quality, simple equipment, and ability to be easily controlled or remotely automated. These advantages have caused ultrasonic scale prevention to become a new high-efficiency technique in scale prevention applications. The equipment for ultrasonic scale prevention has the following characteristics:

(1) Synchronization of scale removal and prevention. The equipment can achieve the goals of scale removal and prevention simultaneously. It will remove the pre-existing scale and continuously

prevent scale formation over a long period of time;

(2) Lower power consumption and low operating costs. A single device consumes only 1 KW/day at most. The output peak power of the power supply is continuously adjustable, and the device is maintenance-free;

(3) Triple automatic protection with favorable safety and reliability. The equipment combines intelligent function control with triple automatic protection, including overcurrent protection, overvoltage protection, and over-temperature protection;

(4) Humanization design and automatic control. The control instrument can automatically track frequency and monitor both the working conditions of the heat exchanger and the load conditions of the equipment in order to follow the responses in real time. When the equipment operates with no load, it can send an acoustic-optic alert and power off to protect the equipment's operation;

(5) Environmental protection. No chemical agents are used during the whole scale removal and prevention processes, with no corrosion, no interference, no pollution, no radiation, and no harm to operation staff and heat exchange devices;

(6) Energy conservation and consumption reduction. The average energy saving ratio exceeds 30%, excluding the benefits induced by prolonging the service life of the heat exchange devices and by halting the work and production associated with using other scale removal methods.

Electromagnetic technique

The electromagnetic scale prevention technique also has a series of advantages, such as small investment, easy operation, no toxicity, and no pollution. Moreover, this technique can combine many functions, such as scale prevention, scale removal, and sterilization. It is one of the most promising scale prevention methods. Although the electromagnetic scale prevention technique has been now widely applied in production practices, it still lacks the determination of a uniform theory regarding the phenomena observed experimentally. The existing proposed mechanisms can be classified into the following four types listed below:

(1) Intraatomic effect. Eliassen *et al.* stated that ion electron transfer required a considerable input of magnetic energy [22]. However, Ellingsen and Vik pointed out that this variation was quite transient and could not explain the magnetic memory effects [23].

(2) Effects of pollutants. Magnetism can enhance corrosion and dissolution, and it can

produce trace amounts of Fe^{2+} ions in the system. Fe^{2+} can inhibit the formation of hard scales and produce soft muds, which can be discharged with the pollutants to achieve scale removal and prevention. However, this mechanism cannot explain the experimental results in non-invasive magnetic processors and high-purity solutions.

(3) Molecule/ion interaction effect. According to the hydrogen bond rupture and deformation theory, magnetic treatment can strengthen the water's permeability, destroy the binding force between scales and walls, thereby causing peeling of limescales. Nevertheless, such explanations are typically qualitative. Srehrenik *et al.* [24] proposed a quantum mechanism based on magnetic fluid dynamics. This theory can explain the magnetic memory effect, but does not explain the behavior of cations in water besides Ca^{2+} .

(4) Interface effect. The double-electric-layer deformation theory assumes that the diffuse layers induced by the Lorentz force are isotropic. The Lorentz force can cause a substitution between synergistic ions and opposite ions, which can change the distribution of charges in double electric layers. Accordingly, the charges at the boundary of the stern layer and the potential can change transiently. This mechanism explains the flocculation and crystallization behaviors and also provides a quantitative performance parameter, potential. However, it cannot explain the flocculation under static conditions, as reported by Higashitani *et al.* [25].

Metal coating technique

In this technique, thermal spraying, electroplating, electroless plating, coating, or magnetron sputtering is used to coat the metal surface with hydrophobic substances [26]. The surface coating scale prevention technique exhibits certain characteristics, such as low surface energy, and a low and stable friction coefficient, which prevents the formed scales from becoming easily attached from the pipe walls to prevent scaling.

Technologies designed for scale prevention

Technologies have been put forward to either destroy or reduce scale-forming opportunities by varying the properties of flooding solutions, the equipment shapes, and some parameter ratios [13]. The specific scale prevention measures are described below:

(1) Small-interference screw pump, long-plunger, and short-pump-barrel pumping unit can be adopted to reduce friction between the produced liquid and the equipment.

(2) Underground choke can be adopted to form water-in-oil emulsions to reduce the flow velocity of oil wells and the production pressure difference.

Insoluble products can be deposited in the mixtures with incompatible water, leading to the formation of scales. Therefore, necessary chemical tests should be conducted on the formation water, the related property data should be mastered, and appropriate injection water should be selected in order to guarantee a favorable compatibility. The water exit layer and interlayer can be selectively blocked, and equipment and pipe columns with cover layers can be used to avoid mixing with the incompatible water.

CONCLUSIONS

Scale prevention in oil fields is a long-term, difficult task, and it is highly significant in practical production settings. The main development direction of chemical scale prevention agents is to develop novel low cost agents with excellent scale prevention performance, and high compounding stability. Moreover, these agents should be capable of both scale prevention and corrosion inhibition. Physical scale prevention exhibits a series of advantages, such as low cost, easy operation, and little environmental pollution. Physical methods can work quickly and have direct effects, which is desirable for scale prevention in severe scaling sites, such as oil wells and pipelines in the ground. Physical and chemical methods should be combined for scale prevention, while chemical methods alone are preferable for scale removal.

REFERENCES

- 1.H. Saboorian-Jooybari, M. Dejam, Zh.X. Chen, *Journal of Petroleum Science and Engineering*, **142** (6), 85 (2016).
- 2.A.M. AISofi, M. J. Blunt, *Journal of Petroleum Science and Engineering*, **124**, 46 (2014).
- 3.K. Panthi, H. Sharma, K. K. Mohanty, *Fuel*, **164** (2), 18 (2016).
- 4.F.L. Zhao, Y.F. Ma, J. Hou, J.X. Tang, D.H. Xie. *Journal of Petroleum Science and Engineering*, **135** (11), 88 (2015).
- 5.K. M. Ko, B. H. Chon, S. B. Jang, H. Y. Jang, *Journal of Industrial and Engineering Chemistry*, **20** (1), 228 (2014).
6. A. Abass, Olajire, *Energy*, **77**, 963 (2014).
7. Y. Y. Zhu, Q.F. Hou, G.Q. Jian, D. S. Ma, Z. Wang, *Petroleum Exploration and Development*, **40** (1), 96 (2013).
8. X. Sui, H.M. Wu, B.H. Wang, J. D., H.J. Wu, L. Li, D.D. Yuan, *Advanced Materials Research*, **850-851**, 221 (2014).
9. X. Sui, B.H. Wang, Q.X. Dong, H.M. Wu, J. Dong,

- H.J. Wu, L. Li, D.D. Yuan, *Energy Education Science and Technology*, **31** (4), 2321 (2013).
10. Q. Wang, J.H. Liu, L. Han, J. Q. Ma, *Journal of Changchun University of Science and Technology (Natural Science Edition)*, **39** (1), 129 (2016)
 11. A. Hiratsuka, D. R. Pathak, *Journal of Water Resource and Protection*, **5** (6), 604 (2013).
 12. S. Muryanto, A. P. Bayuseno, H. Ma'mun, M. Usamah, Jotho, *Procedia Chemistry*, **9**, 69-76 (2014).
 13. J.B. Chen, Z.J. Ma, D.M. Liu, L. H. Wang, *Industrial Water Treatment*, **31** (5), 13 (2011).
 14. H. Sun, Y. Chen, H.J. Qian, *Chemical Reagents*, **34** (11), 991 (2012),
 15. A.B. Cai, J.J. Wu, D.X. Hou, H. X. Liu, *Corrosion & Protection in Petrochemical Industry*, **21**(2), 62 (2004).
 16. R. Wang, Q. Zhang, J. Ding, et al, *Chemical Industry and Engineering*, **18** (2), 79 (2001).
 17. B.Q. Zheng, Q.Q. Zhu, *Oilfield Chemistry*, **2**, 181 (1984).
 18. J. W. Suito, W. J. Marnfr, R. B. Rittfr, *Can. J. Chem. Eng.* **55**, 374 (1977).
 19. J.L. Zuo, Sh.R. Ren, H.M. Yu, *Petroleum Engineering Construction*, **34** (4), 7 (2008).
 20. P. Chen, O Vikane, T Asheim, T Hagen, R Boreng, *SPE 100466*, 130, 2006.
 21. E. Maisonhaute, C. Prado, P. C. White, R. G. Compton, *Ultrasonics Sonochemistry*, **9** (6), 297 (2002).
 22. R. Eliassen, R. T. Skrinde, W. B. Davis, *Journal American Water works Association*, **50** (10), 1371 (1958).
 23. F. T. Ellingsen, E. A. Vik, *Zurich SS8*, 12 (1982).
 24. S. Srehrenik, S. Nadiv, I. J. Lin, *Magnetic and Electrical Separation*, **5** (2), 71 (1993).
 25. K. Higashitani, A. Kage, K. Imai, *Journal of Colloid and Interface Science*, **156**, 90 (1993).
 26. W.J. Han, Q.W. Meng, L.SH. Liu, *China Coatings*, **23** (2), 54 (2008).

Bavachin antioxidant effects on the cardiac myocytes of mice in exhaustive exercise

W.Y. Zhu¹, X. Yue², X. Lv², Ch. Yi^{1*}, J. Liu^{2*}

¹ Division of Abdominal Tumor, Cancer Center of West China Hospital, Sichuan University, No. 37, Guoxue Road, Chengdu, Sichuan, 610041, PR China

² Traditional Chinese Medicine Research and Development Laboratory, Southwest University, No. 160, Xueyuan Road, Rongchang, Chongqing, 402460, PR China

Received September 28, 2017, Accepted December 19, 2017

Bavachin is the main substance extracted from *Psoralea corylifolia* which is a widely used traditional Chinese medical herb. Studies have shown that bavachin may have a vital antioxidant role in exercise-induced myocardial mitochondrion injury, but the specific antioxidation effect of this herb still remains unexplored. Our study is dedicated to evaluate the antioxidant effect of bavachin in mice with one-off exhaustive swimming, and explore the underlying mechanisms. Bavachin (16 mg·kg⁻¹) was orally administered to mice for 13 days before the forced swimming to exhaustion test. The average swimming time to exhaustion of bavachin-treated mice was prolonged by 56.5% (71.86±28.88 min) compared with that of the control group (45.86 ±12.09 min). Structural analysis showed that myofibrils in the experimental group were lined up in register, the number of mitochondria increased, the membrane structure was clear and kept intact. Malondialdehyde (MDA) contents of the experimental groups significantly decreased ($p < 0.05$) compared with the control group. The activity of H⁺-K⁺ ATPase, respiratory chain complex I (RCC I), cytochrome c oxidase (COX) and the levels of superoxide dismutase (SOD) of the experimental groups significantly increased ($p < 0.05$) compared with the control group. Therefore, this study provides a new idea about the protective mechanism of cardiac muscle mitochondria by using bavachin as a natural adjuvant antioxidant to improve the antioxidative levels in mice with one-off exhaustive swimming. These results provide scientific evidence that bavachin has a potential as an antioxidant agent for human beings such as athletes and elderly persons.

Key words: bavachin; one-off exhaustive swimming, mitochondria, energy metabolic enzymes.

INTRODUCTION

Exercise-induced oxidative stress (EIOS) is an imbalance favouring pro-oxidants over antioxidants induced by exhaustive exercise, which may result in the damage of biological components, and has been associated with many pathologic conditions, especially the myocardial mitochondrion injury. The EIOS has been well documented [3,15,23,24]. So far, more than three kinds of mechanisms about EIOS have been studied, but researchers still remains divided about what triggers the oxygen free radicals (OFR) booming in EIOS [17]. However, it seems to be obviously summarized that, in the exhaustive exercise, the animal cells produce increased amounts of free radicals [18] and ample reactive oxygen species (ROS), and most OFR are produced by electronic leakage [7] in a series of cytochrome-based enzymes formed in the respiratory chain in the mitochondrial inner membrane, where the mitochondria *in vivo* generate most of the cellular energy supply as adenosine triphosphate (ATP) by ATPase [13]. Under the condition of exhaustive exercise, the OFR cannot

be well eliminated by SOD; when the level of OFR exceeds the antioxidant defences, oxidative stress occurs. The surplus OFR disturb the synthesis of ATP in mitochondria and the catalytic activity of H⁺-K⁺ ATPase, RCC I and COX. Furthermore, the OFR elevated membrane lipid peroxidation [5] could disturb the protein structure, lead to the structural and functional modification of mitochondria, accelerate the energy metabolism disorder and myocardial cellular damage, and the physiological disturbance of the cardiac muscle. Mitochondrial functional disorders have been implicated in the etiology of several human diseases. In addition, malondialdehyde (MDA) is the main metabolic product of lipid peroxides; the level of MDA reflects the level of OFR and lipid peroxidation, and MDA is commonly used as an indicator of lipid peroxidation [2].

There is a lot of research proving that some natural antioxidants which include many kinds of botanical medicines and medicinal foods, could improve the anti-oxidative level *in vivo*. There are several herbs [9] reported to decrease oxidative stress. Recently, it was indicated that one of the herbs, *psoralea corylifolia*, has more than six pharmacological effects, including antioxidant effect [12]. And there are more than 23 kinds of active

To whom all correspondence should be sent:

E-mail: Yicheng6824@outlook.com;

liujuanb@163.com.

These authors contributed equally to the work.

ingredients in *psoralea* [26]. Previous research [19,26] has suggested that bavachin could elevate the activity of SOD in hepatocyte, eliminate OFR, but this has not been studied in EIOS yet.

The objective of the present study is to investigate whether bavachin could attenuate the OFR damage during exhaustive exercise, and explore the underlining antioxidation mechanism. Our study reveals the antioxidant action of bavachin by using exhaustive swimming mice model for the first time. Based on the morphological changes of cardiac myocyte after exhaustive swimming with or without pretreatment of bavachin, our study further verified the antioxidant effect of bavachin.

EXPERIMENTAL

Materials

Plant and reagents

Bavachin was extracted by the Traditional Chinese Medicine Research and Development Laboratories, RongChang Campus, Southwest University (China). The structure of bavachin is shown in Fig 1. Superoxide dismutase (SOD) activity assay kit, malondialdehyde (MDA) assay kit, H⁺-K⁺ ATPase activity determination kit and Coomassie Plus (Bradford) assay kit were provided by the Nanjing Jiancheng Bio-engineering Institute (China). TRIZOL® Reagent was purchased from Shanghai Bio-engineering Co., Ltd (China). PrimeScript RT reagent kit with gDNA eraser and SYBR® Premix Ex Taq™ were purchased from Takara Biotechnology Co., Ltd (Japan). 2×Taq PCR master mix kit was purchased from Tiangen Biological Technology Co., Ltd (China). NADH, cytochrome C and Janus green B were purchased from Sigma (USA).

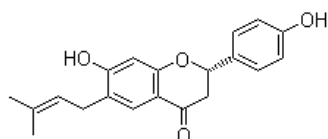


Fig. 1. Molecular formula of bavachin, molecular weight: 324.38, chemical formula C₂₀H₂₀O₄, purity of bavachin 97%.

Animals grouping

Male Kunming mice weighing 20-22 g were purchased from the Experimental Animal Center of Sichuan University, used in accordance with the Guidelines on the Care and Use of Laboratory Animals issued by the Chinese Council on Animal Research. The study was approved by the ethical committee of Sichuan University. The mice were randomized into the following 5 groups of 10 mice each: control group without any treatment and

exercise; untreated group (exhaustive exercise group) which received 16 mg·kg⁻¹ body mass of distilled water by gastric perfusion; three treated groups (bavachin-treatment and exercise group) administered with bavachin by gastric perfusion at doses of 24 mg·kg⁻¹ body mass, 16mg·kg⁻¹ body mass and 12 mg·kg⁻¹ body mass, respectively, according to the toxicologic and pharmacologic pretests. In the present study the 16 mg · kg⁻¹ body mass group was chosen as the best dose group in the following tests.

Modeling preparation

Swimming was performed in a glass flume that was 50 cm long, 40 cm wide and 30 cm high; water temperature was maintained at 32±0.5 °C. Mice in the treated groups were subjected to exhaustive swimming with a load of 5% of their bodyweight attached to the tail of each mouse at 9 a. m., 30 min after giving the drug. The swimming duration until the mouse was exhausted and remained below the water surface for 10 s, without turning over when lying on its back, was recorded. Mice were sacrificed, the heart tissue was removed and divided into two parts: one was used to isolate the mitochondria, the other was used in the study of gene expression.

Myocardial mitochondria isolation and identification

The heart tissue was washed with precooled normal saline three times before it was put into the homogenate medium. The tissue was cut up in the ice bath and homogenized. The heart homogenate was centrifuged for 10 min at 1500 rpm at 4°C, the supernatant was recentrifuged for 10 min at 10,000 rpm at 4 °C, then was discarded. The deposit was resuspended and centrifuged for 10 min at 10,000 rpm at 4 °C. The deposit was resuspended and supplied with 1% Janus green B, the mitochondria particles were dyed in blue-green. Mitochondrial protein content was determined with the Coomassie brilliant blue method. The concentration of mitochondrial protein was adjusted to be 1.5 mg/ml.

Electron microscope observation

The heart tissues in each group were sectioned and repaired into blocks (1mm×1mm×1mm) for preparing to make paraffin sections after the exhausting swimming. Those sections were fixed and dehydrated according to the methods [27,20,22], then the operator used epoxy resin 821 as the entrapment agent to imbed tissue using UC7 RT ultramicrotome, uranyl acetate and citromalic acid lead double stainings and TECNAI 10 electron

microscope to observe the changes in cellular morphology and ultrastructure.

Measurement of enzyme indexes

The activity of SOD, H⁺-K⁺ATPase of mitochondria and the MDA level was measured according to the respective kit instruction.

The activity of COX was measured according to Sciamanna [18] in a 3 ml reaction mixture containing 0.1 ml of 1.5 mg/ml heart mitochondria, 1.5 ml of 0.1 mM phosphate buffer, pH 7.0, and 1.3 ml of distilled water. 0.1 ml of 0.07% reduced cytochrome c was added after 5 min at 36 °C in the water bath. A550 (absorbance at 550 nm) was recorded every 30 s. The activity of COX was represented by the decreasing rate of A550, and it was estimated using the formula: COX (n mol • min⁻¹ • mg⁻¹) = 54.6 × the change of A 550/min.

According to the method described by Veitch *et al.* [27], the activity of RCC I was measured as given below. Briefly, 0.03 ml of mitochondrial suspension was added to 0.2M phosphate buffer solution, pH 7.4, 0.3 ml of 10 mM potassium ferricyanide, the volume was adjusted to 2.97 ml. Then, 30 µl of 0.1M NADH (prepared with 10 mM Tris) was added as the initiator. The absorbance was monitored at 420 nm. Activity was measured spectrophotometrically by determining the decrease in absorbance at 420 nm. A molar extinction coefficient of E420 = 1.03 mmol•L⁻¹/cm was used in the calculations. Activity was given in µmol of substrate consumed per min per mg of mitochondrial protein.

Measurement of ATPase 6 gene expression level

Total RNA extraction was performed using a TRIzol reagent kit. RNA integrity was verified electrophoretically and spectrophotometrically by OD 260/OD 280 nm, absorption ratio > 1.95. Total RNA was reverse transcribed into cDNA using a PrimeScript RT reagent kit with gDNA eraser (Takara) according to the manufacturer's instructions. Real-time PCR was used to determine mRNA levels using a SYBR Premix Ex Taq™ II kit (Takara). Real-time PCR was performed in a Mini Opticon Real PCR Detector (BIO-RAD, USA). β-actin was used as internal control. The PCR primers were designed as follows: the forward primers of β-actin and ATPase 6 are 5'-TCACCCACACTGTGCCCATCTATGA-3' and 5'-ACACCAAAGGACGAACCTG-3', respectively. The reverse primers of β-actin and ATPase 6 are 5'-CATCGGAACCGCTCATTGCCGATAG-3' and 5'-CGGTGAGAAGTGGGCTAAAG-3', respectively. The PCR products were a 295 bp

fragment of β-actin and a 207 bp fragment of ATPase 6. PCR cycles included 94 °C for 30 s, followed by 39 cycles consisting of 95 °C for 5 s, 59 °C for 30 s and 65 °C for 5 s. Measure the fluorescence signal generated during each amplification cycle. The standard curve, the dissolution curve, amplification curve and the cycle threshold (Ct) value were analysed by the Bio-Rad CFX Manager software. Semiquantification of ATPase 6 was calculated using the 2^{-ΔΔCT} method [16].

Statistical analysis

The statistical analyses were performed using the SPSS for Windows version 20.0. All results were expressed as means ± standard error. Statistical comparisons of mean values were analyzed by one-way ANOVA. P<0.05 was considered as the significant level of difference.

RESULTS AND DISCUSSION

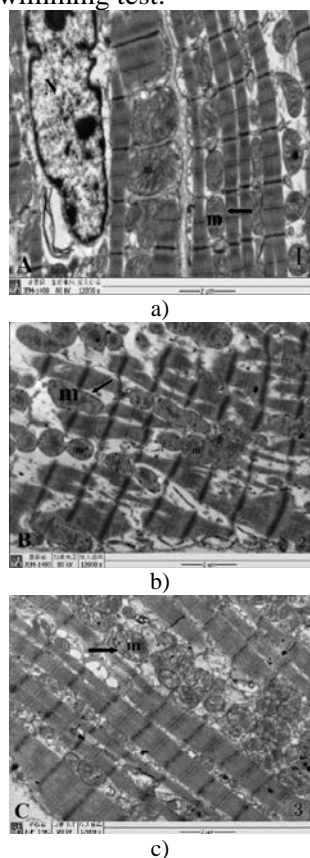
The direct appearance of the anti-fatigue ability of bavachin is the elevated tolerance to exhaustive exercise. Weight-loaded exhaustive swimming duration was used to evaluate the tolerance. The mean duration of exhaustive swimming of the untreated group and mice receiving bavachin in the treated group was 45.86 ± 12.09 and 71.86 ± 28.88 min, respectively. Bavachin given at a dose of 16 mg kg⁻¹ significantly lengthened the swimming duration (p<0.01). The result of one-off exhaustive swimming time of mice ($\bar{x} \pm s$, n=10) are shown in Table 1.

Table 1. One-off exhaustive swimming time of mice ($\bar{x} \pm s$, n=10). Data of swimming time are mean ± standard deviation (SD). The control group used as the vacuity contrast.

Groups	Concentration (mg•kg ⁻¹)	Swimming time (min)
Control group	—	—
Untreated group	—	45.86±12.09
Treated groups	24	75.21±22.16
	16	71.86±28.88
	12	56.22±16.32

Structure alteration is the base of the function alteration, the ultrastructure undergoes the earliest variation. As shown in Fig 2, cardiac muscles were damaged after exhaustive exercise in each group. In the muscle tissue of exhaustive exercised mice, mitochondria showed characteristic vacuolation and varying sizes, cristae disappeared or were deformed, myomeres were incomplete, myofibrils were disarrayed and disassociated when compared with those of the control group. By contrast, bavachin administration in the 16 mg•kg⁻¹ dose

group correlated with lesser cardiac myocytes damage. There is no obvious pathology change of myofibrils in the treated groups, but some mitochondria in the treated groups seemed vacuolated and swollen. The obvious pathological changes observed in the untreated group (exhaustive group) revealed that exhaustive exercise may damage the structure of mitochondria and myofibrils, while bavachin can protect against damage in cardiac muscles effectively during the exhaustive swimming test.



□HV □ mag □ — 2 μm —
□80 kV □ 12000 × JEM -1400

Fig. 2. Ultrastructure of mice myocardial cells. A: blank group. B: untreated group (one-off exhaustive swimming group). C: treated group (bavachin group) (A-C, magn., 12000×). M, mitochondrion; N, nucleus; C, chromatin; Scale bar, 2 μm; HV, 80kV.

Compared with those of the control group (A), the myocardial mitochondrial cristae in the untreated group (B) were not clear, vacuolization appeared and mitochondrial morphological multiple myofibrils (M) were incomplete and appeared dissociated. In the 16mg·kg⁻¹ bavachin treated group (B), the myofibrils were complete, and the sarcomeres were well arranged, but vacuolization of the mitochondria appeared and the size was irregular.

As shown in Table 2, cardiac myocytes of mice in saline control group had higher MDA levels but

lower SOD levels than those of the control group, while MDA and SOD levels of mice in the treated group (16 mg·kg⁻¹) showed significant minimal changes.

MDA and SOD in the control group were obviously higher than those in the control group, which signifies that the one-off exhaustive swimming caused EIOS in mice. Bavachin significantly minimized the concentration variation of MDA and SOD which indicated that bavachin can protect the cardiac mitochondria from the EIOS damage.

Tab 2. Effect on the content of mice myocardial mitochondria MDA and the activity of SOD in exhaustive mice ($\bar{x} \pm s$, n=10).

Groups	MDA (n mol·mgprot ⁻¹)	SOD (U·mgprot ⁻¹)
Control group	0.97±0.14	43.51±3.71
Untreated group	2.28±0.390**	33.05±2.63**
Treated group	1.47±0.421 ^Δ	36.06±2.10 ^Δ

Note: Data are mean ± SD. * represents the significant difference compared with the control group (P<0.05), ** represents the extremely significant difference compared with the control group (P<0.01), ΔΔ represents the very significant difference compared with the untreated group (P<0.01), Δ represents the significant differences compared with the untreated group (P<0.05). This note is also applied in fig 3.

As shown in Fig 3, the activity of H⁺-K⁺-ATPase, RCC I and COX decreased in the control group. Bavachin (16 mg·kg⁻¹) could protect the cell from exhaustive exercise induced oxidative damage by increasing the activity of H⁺-K⁺-ATPase, respiratory chain complex and COX.

For the first time this study revealed that bavachin increased the expression of ATPase 6 in cardiac myocytes by RT-PCR. As shown in Figure 6, cardiac myocytes of mice in the untreated group (exhaustive exercise group) had lower ATPase 6 mRNA expression than the control group. The bavachin treatment could significantly up-regulate the expression of ATPase 6 mRNA.

Exhaustive exercise can produce increased ROS which disturbs the oxidant/antioxidant balance, thus elicits oxidative damage. Oxidative stress always followed cardiac damage [8] and other diseases. So there is a necessary and sufficient reason to protect the cardiac muscle from the oxidative damage by using a new antioxidant. This study provides a new idea about using bavachin as a potential natural adjuvant antioxidant to improve the antioxidative levels and anti-fatigue in mice.

In this study, the oxidative stress in mice was caused by one-off exhausted swimming in order to assess the exercise ability and anti-fatigue at the same time. The results shown in Table 1 suggested that after intragastric administration of bavachin,

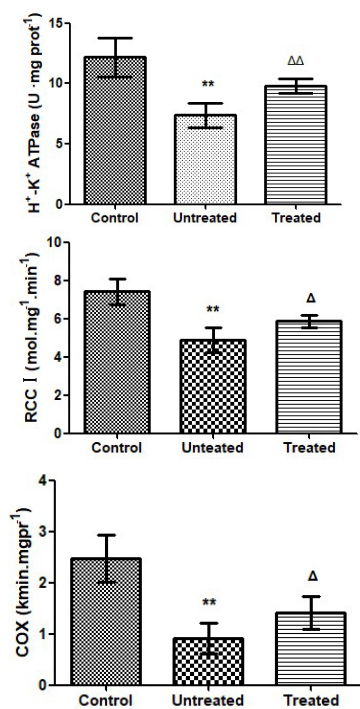


Fig. 3. Effect on the activity of H⁺-K⁺ATPase, RCC I and COX in myocardial mitochondria in mice (n=10), (COX, cytochrome c oxidase.)

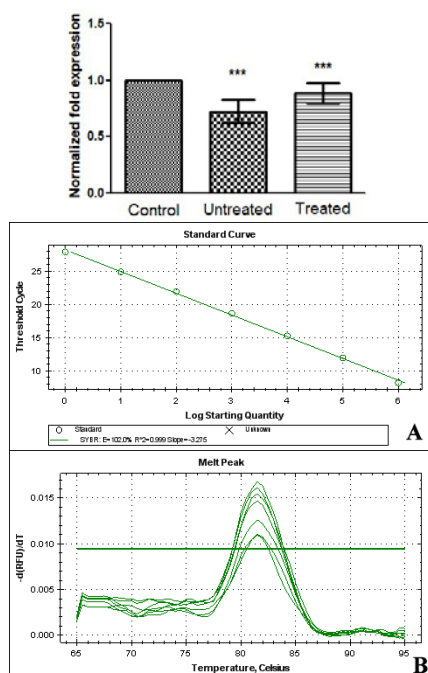


Fig. 4. ATPase6 gene expression in the mice myocardial tissue and standard curve and dissociation curve of fluorescence quantified PCR. A: Standard curve of ATPase subunit 6 gene. B: Dissociation curve of ATPase subunit 6 gene. Data are mean \pm SD. ***P<0.01, treated (n=6) and untreated (n=6) vs. control (n=6). Untreated: ATPase6 gene expression after one-off exhaustive training treated without bavachin; and treated: ATPase6 gene expression after one-off exhaustive swimming treated with bavachin.

the time of exhausted swimming was lengthened, and bavachin improved the anti-fatigue ability in mice.

After observing the myocardial mitochondrial ultrastructural organization in one-off exhausted swimming mice by electron microscope, the myocardial mitochondrial cristae were not clear, vacuolization appeared, mitochondrial morphology was abnormal, the size was irregular, multiple myofibrils were broken and dissociation appeared. This indicated that exhausted exercise could damage the structure of mitochondria and myofibrils, and these results were similar to those in ref. [6]. In the bavachin group, the myofibrils were complete and the sarcomeres were well arranged, but vacuolization appeared in the mitochondria and the size was irregular, the degree of injury was lower than that in the one-off exhausted swimming group. This observation revealed that, after giving bavachin, the structure of mitochondria concerned with aerobic metabolism was quickly recovered, in order to accelerate the body recovery.

Mitochondria are the main site where energy and ROS are released [4]. O₂ as the terminal electron acceptor in the respiration chain generates a superoxide anion (O₂^{•-}) after obtaining an electron from complex I, II or III. In the normal exercise, O₂^{•-} can be detoxicated by the mitochondrial oxidase SOD. Oxidative stress only occurs while excess ROS cannot be fully cleaned up by antioxidant system. Mitochondrial dysfunction and secondary increase in ROS induce cell death and apoptosis [11]. One important manifestation of muscle fatigue is ATP decrease, energy metabolism abnormality and ROS increase, which can initiate a chain reaction and damage biomacromolecules, then repeatedly damage mitochondria. Muscle fatigue and damaged mitochondria can form an aggravating vicious circle. The results exhibited that bavachin reduced malondialdehyde (MDA) and significantly increased superoxide dismutase levels in myocardial mitochondria.

During exhausted exercise, the body needs to consume massive energy. The energy metabolism gets fast and multiple ROS are produced. If the ROS are not cleared in time, they could attack the cell membrane; lipid peroxides might produce more ROS, attack its double bond, and cause a chain reaction of ROS, causing ion and energy metabolism disturbance. SOD was the primary antioxidative enzyme in the free radicals release clearance mechanism and oxidation-antioxidation mechanism.

There are two main parts of mitochondria participating in the energy transformation process,

one is ATPase and the other is respiration chain. Research shows that the energy of cell comes from the process of oxidative phosphorylation. Several enzymes are involved in this process. H⁺-K⁺ ATPase is on the intima of mitochondria which is the key enzyme in ATP synthesis. Enzymatic activity of H⁺-K⁺ ATPase was measured in this research. Enzymatic activity of H⁺-K⁺ ATPase decreased leading to a decrease in ATP, imbalance of oxidative phosphorylation, dysfunction of energy synthesis and influence on the physiological process. The results show that the enzymatic activity of H⁺-K⁺ ATPase in the exhausting exercise group decreased. After gastric perfusion of bavachin for two weeks, the enzymatic activity of H⁺-K⁺ ATPase in mice myocardium increased.

Mitochondrial complex I is the biggest enzyme complex in the initiating terminal respiration chain. It is also the sensitive site in ROS damage [10]. The change of complex I is a representative mark for the mitochondrial oxidative phosphorylation. Exhausting exercise can lead to superoxide formation and occurrence of cell death, which can decrease the amount of mitochondria, the mitochondrial membrane potential energy (ATP), the activity of respiratory chain complexes I and IV. The results show that the activity of respiratory chain complexes I in the untreated group obviously decreased; by gastric perfusion of bavachin flavonoid, the enzymatic activity of respiratory chain complexes I increased. So the operator inferred that bavachin provides anti-oxidation protection by respiratory chain complexes I.

COX marks the process of oxidative phosphorylation in the mitochondrial complex, and it is the only cytochrome that can pass electrons to the oxygen molecule. It is the junction between respiratory metabolism and oxygen. COX and succinate dehydrogenase are the key enzyme among mitochondrial respiratory enzymes, the decrease of enzymatic activity of COX and succinate dehydrogenase can affect the process of mitochondrial oxidative phosphorylation. The results show that the enzymatic activity of COX decreases in the exhausting exercise group, which can cause an inhibition of the function in the oxidative phosphorylation electron transport chain. ATP decreases while ROS increases, it can cause energy metabolic disturbance too [1, 25]. By gastric perfusion of bavachin flavonoid, the enzymatic activity of COX increases, so we can concluded that bavachin provides anti-oxidation protection by enzymatic activity of COX.

Compared with other relevant studies, this study ignored some secondary factors, such as ischaemia,

oedema, NOS and etc., but it still demonstrates the antioxidant effect of bavachin in a constructive way.

CONCLUSION

In this experiment, the data demonstrate that bavachin could prolong the time of exhaustive swimming, increase the activities of H⁺-K⁺ ATPase, COX and RCC I, decrease the oxidative stress reaction in cells, and prevent the myocardial cells from oxidative damage. Through real-time fluorescence quantitative PCR (RTFQ-PCR) it was found that the exhaustive swimming could down-regulate the expression of ATPase 6 mRNA, but after giving bavachin, the expression of ATPase subunit 6 in mice myocardium increased, which suggested that bavachin might up-regulate the expression of ATPase subunit 6.

Acknowledgements: The authors thank the Natural Science Foundation Project of CQ-CSTC (NO.7042) and Science & Technology Projects of China (2013FY110600) for financial and instrumental supports.

REFERENCES

1. A. Sarniak, J. Lipińska, K. Tytman, S. Lipińska, , *Postepy Hig. Med. Dosw.*, **70**, 1150 (2016).
2. A.A.M. Adly, *Res. J. Immunol.*, **3**(2), 129 (2010).
3. R.W. Dal Negro, M. Visconti, *Pulmonary Pharmacology & Therapeutics*, **41**, 48 (2016).
4. D.W. Busija, I. Rutkai, S. Dutta, P.V. Katakam, *Compr. Physiol.*, **6**(3), 1529 (2016).
5. E. Altinoz, T. Ozmen, Z. Oner, H. Elbe, M.E. Erdemli, H.G. Bag, *Bratisl. Med. J.*, **117**(7), 381 (2016).
6. W. Wu, S. Chang, Q. Wu, Zh. Xu, P. Wanf, Y. Li, P. Yu, G. Gao, Zh. Shi, X. Duan, Y.-Zh. Chang, *Cell Death & Disease*, **7**(11), e2475 (2016).
7. C.M. Deaton, D.J. Marlin, *Clin. Tech. Equine. Pract.* **2**(3), 278 (2003).
8. S. Zainalabidin, SNFSN Shahidin, S.B. Budin, *Sains Malaysiana*, **45**(2), 207 (2016).
9. I. Paur, M.H. Carlsen, B.L. Halvorsen, R. Blomhoff, *J. Industrial & Engineering Chemistry Fundamentals*, **25**(2), 244 (2011).
10. V. Martínez-Cisuelo, J. Gómez, I. García-Junceda, A. Naudí, R. Cabré, N. Mota-Martorell, M. López-Torres, M. González-Sánchez, R. Pamplona, G. Barja, *Exp. Gerontol.*, **83**, 130 (2016).
11. G. Barrera, F. Gentile, S. Pizzimenti, R.A. Canuto, M. Daga, A. Arcaro, G.P. Cetrangolo, A. Lepore, C. Ferretti, C. Dianzani, G. Muzio, *Antioxidants*, **5** (1), 7 (2016).
12. C.J. Sang, R. Tulasi, S.R. Koyyalamudi, *Cancers*, **8** (3), 33 (2016).
13. H. Tsutsui, S. Kinugawa, S. Matsushima, *Am. J. Physiol. Heart Circ. Physiol.*, **310** (6), 2181 (2011).

14. Y.S. Keum, K.K. Park, J.M. Lee, K.-S. Chun, J. H. Park, S. K. Lee, H. Kwon, Y.-J. Surh, *Cancer Lett.*, **150** (1), 41 (2000).
15. E.N. Chirico, C. Faës, P. Connes, E. Canet-Soulas, C. Martin, V. Pialoux, *Sports Med.*, **46** (5), 629 (2016).
16. M. Yamagishi, *Mol. Breeding*, **36** (1), 3 (2016).
17. N.B.J. Vollaard, J.P. Shearman, C.E. Cooper, *Sports Med.*, **35**(12), 1045 (2005).
18. N. Okudan, S. Revan, S.S. Balci, M. Belviranlı, H. Pepe, H. Gökbek, *Bratisl. Lek. Listy*, **113** (7), 393 (2012).
19. Y.L. Qiu, J. Liu, *Chin. J. Vet. Sci.*, **46** (3), 55 (2010).
20. E.F. Rosa, R.F. Ribeiro, F.M. Pereira. E. Freymüller, J. Aboulafia, V.L. Nouailhetas, *J. Appl. Physiol.*, **107** (5), 1532 (2009).
21. J. Sastre, M. Asensi, E. Gascó, F.V. Pallardó, J.A. Ferrero, T. Furukawa, J. Viña, *J. Am. J. physiol.*, **263** (5 Pt 2), R992 (1992).
22. M.A. Sciamanna, J. Zinkel, A.Y. Fabi, C.P. Lee, *Biochimica et Biophysica Acta*, **1134** (3), 223 (1992).
23. S.K. Powers, Z. Radak, L.J. Li, *J. Physiol.*, **594** (18), 15 (2016).
24. M. Wiecek, M. Maciejczyk, J. Szymura, S. Wiecha, M. Kantorowicz, Z. Szygula, *J. Sports Med. Phys. Fitness*, **57** (7-8), 942 (2016).
25. S. Rahman, J.A. Mayr. Disorders of Oxidative Phosphorylation, Inborn Metabolic Diseases. Springer, Berlin Heidelberg, (2016).
26. H. Haraguchi, J. Inoue, Y. Tamura, K. Mizutan, *Phytotherapy Res. Ptr.*, **16** (6), 539 (2002).
27. K. Veitch, A. Hombroeckx, D. Caucheteux, H. Pouleur, L. Hue *Biochem. J.*, **281** (3), 709 (1992).

Study of the influence of karst water runoff on mining based on fuzzy mathematics

A.J. Shao, L.Y. Zhao*, S.W. Wang

Hebei GEO University, Shijiazhuang, Hebei, China

Received September 4, 2017, Accepted December 19, 2017

Taking Fengfeng coal field as an example, the paper applies the fuzzy mathematics principle to the strength of karst runoff zone of Minmetals field partition. The frequency statistics method is adopted to define the membership degree, elevation, single well water inflow, karst rate, and hydration group classification. At the same time, considering the influence of the ionic concentration of karst water runoff intensity, the fuzzy comprehensive evaluation method is used for the calculation, and the results show that the strength of the karst runoff zone will affect the safety of mining. Karst water runoff intensity is proportional to the concentration of the ions. The relationship between runoff intensity and single well water inflow is most obvious. The biggest water inflow of the single well is in a strong runoff zone, and in a weak runoff zone it is very small, which provides decision basis for mine safety production planning. Minmetals is located in the Ordovician limestone strong runoff belt of Gushan east side, thus constituting a serious threat for deep coal seam mining. The research in this paper provides a theoretical basis for Minmetals deep seam mining from the weakest runoff.

Key words: Fuzzy mathematics, Karst water, Runoff belts, Mining.

INTRODUCTION

Fengfeng coal field is located at the border area of Shanxi, Hebei and Henan provinces. On the west side there is a mountain area, and on the east side sloping plains. The coal reserves are large, and it is a typical karst water filling deposit. Fengfeng mine field, which is within the scope of the formation of the Ordovician and Permian lime, is located in the runoff karst belt of Gushan east, and karst water is a serious threat to the safety mining of ore deposit. There is Ordovician limestone karst run-off zone (hereinafter referred to as the gray) and the big blue limestone also has the characteristics of runoff belt according to coal mining practice, but the Ordovician limestone runoff belt is much bigger than the large blue limestone runoff belt. On the other hand, there are strong and weak points of runoff, the strong belt is a great threat to safe mining. Therefore, the research on the strength of the runoff has a practical significance for the mining of the coal seam at a 100 m level below the horizontal [1,2].

Fuzzy mathematics (Fuzzy for short) is proposed by L.A. Zadeh in 1965 in the "Fuzzy sets". With the development of computer science, it can solve many problems which cannot be solved by the "deterministic mathematics" and "random mathematics". It has great advantages for description and handling of fuzzy events. Fuzzy comprehensive evaluation is a kind of method of comprehensive evaluation of phenomena which are influenced by various factors. In recent decades, fuzzy mathematics has been widely applied in many fields such as geology, environment, agriculture, medicine, meteorology, etc. [3]. Fuzzy mathematics is applied to the study of groundwater, mainly for the

evaluation of groundwater quality [4-7] and of groundwater pollution [8-10] in two aspects. Fuzzy mathematics was applied to the research of groundwater runoff belt by Liu [11], Zhang [12], Liu [13], Tian [14], Xu [15], Zheng [16], Zhao [17]. In this paper, the fuzzy comprehensive evaluation method was used to study the strength of karst runoff zone, the "frequency statistics method" was used to determine the membership degree, and good results were achieved.

THEORY OF FUZZY COMPREHENSIVE JUDGMENT

Comprehensive Evaluation Principle

Given two finite fields [3]:

$$\mathbf{U} = \{u_1, u_2, \dots, u_n\}$$

$$\mathbf{V} = \{v_1, v_2, \dots, v_m\}$$

where \mathbf{U} is a collection of factors of comprehensive evaluation, a total of N factors; \mathbf{V} is a collection of reviews, a total of M levels.

Set the factor $\mathbf{R}_i = (r_{i1}, \dots, r_{ij}, \dots, r_{im})$ is the single factor evaluation for i , which can be seen as a subset of the Fuzzy on the \mathbf{U} , r_{ij} indicates the evaluation of the i factor for the degree of membership of j to v_j , thus the total evaluation matrix of n factors is obtained.

To whom all correspondence should be sent:
E-mail: zhaoliya0503@126.com;

$$\mathbf{R} = \begin{pmatrix} \mathbf{R}_1 \\ \vdots \\ \mathbf{R}_i \\ \vdots \\ \mathbf{R}_n \end{pmatrix} = \begin{pmatrix} r_{11} & \cdots & r_{1j} & \cdots & r_{1m} \\ \cdots & \cdots & \cdots & \cdots & \cdots \\ r_{i1} & \cdots & r_{ij} & \cdots & r_{im} \\ \cdots & \cdots & \cdots & \cdots & \cdots \\ r_{n1} & \cdots & r_{nj} & \cdots & r_{nm} \end{pmatrix} \quad (1)$$

In the process of evaluation, because of the different proportion of each factor, the method of statistical test or expert evaluation can be used to establish the weight distribution between the factors, denoted by:

$$\mathbf{A} = (a_1, a_2, \dots, a_n) \quad (2)$$

where $a_i \in [0,1]$, $i=1,2,\dots,n$ and $\sum_{i=1}^n a_i = 1$, \mathbf{A} is the right coefficient row vector. In the assessment of groundwater pollution, the formula for weight calculation is:

$$a_i = \frac{c_i}{c_{0i}} \quad (3)$$

where: a_i is the weight; c_i are the measured values of the i pollutant; c_{0i} is the concentration allowable value of the i kind of water for a certain purpose. If the standard value of a single factor is divided into several grades, for example, three grades, c_{0i} represents the average of the three levels: $c_{0i} = (\text{first-class water standard} + \text{second-class water standard} + \text{third-class water standard})/3$. Fuzzy mathematical operations only allow the weights to be taken in the $[0,1]$ interval, so the weight value of each factor must be normalized and the normalized formula is:

$$a_i = \frac{\frac{c_i}{c_{0i}}}{\sum_{i=1}^n \frac{c_i}{c_{0i}}} \quad (\sum_{i=1}^n a_i = 1) \quad (4)$$

The model of comprehensive evaluation can be obtained by using the compound operation of the fuzzy matrix:

$$\mathbf{B} = \mathbf{A} \circ \mathbf{R} \quad (5)$$

that is,

$$(b_1, b_2, \dots, b_j, \dots, b_m) = (a_1, a_2, \dots, a_n) \circ \begin{pmatrix} r_{11} & \cdots & r_{1j} & \cdots & r_{1m} \\ \cdots & \cdots & \cdots & \cdots & \cdots \\ r_{i1} & \cdots & r_{ij} & \cdots & r_{im} \\ \cdots & \cdots & \cdots & \cdots & \cdots \\ r_{n1} & \cdots & r_{nj} & \cdots & r_{nm} \end{pmatrix} \quad (6)$$

In the formula: $\mathbf{B} = \mathbf{A} \circ \mathbf{R}$ is the fuzzy transformation of $U \rightarrow V$; \mathbf{R} is the fuzzy

transformation matrix; \circ is multiplication of fuzzy matrix, setting $\circ = M(\wedge, \vee)$, $b_j = \vee(a_i \wedge r_{ij})$ ($j=1,2,\dots,m$), \wedge represents small, \vee represents large, namely, when a matrix operation is performed, weight coefficient of each element of the row vector \mathbf{A} is multiplied by the corresponding element of \mathbf{R} column vector, taking the minimum value of the two elements.

For b_j ($j=1,2,\dots,m$), according to the principle of maximum membership degree, taking $b_k = \max\{b_1, \dots, b_j, \dots, b_m\}$, so v_k which is the corresponding comment of b_k is the conclusion of the comprehensive evaluation.

Determination of membership degree

In fuzzy mathematics, the fuzzy boundaries of things are etched by the degree of membership. There are two methods for determining the degree of membership, one is the membership function method, and the other one is the frequency statistics method.

Membership function method

In most of the literature, the membership function is used to determine the membership degree r_{ij} , such as groundwater quality evaluation, groundwater pollution assessment and so on.

Frequency statistics method

According to the actual observation data, making the scatter diagram, the membership degree is equal to the number of samples s_j divided through the total number of s_n in a certain range of samples:

$$r_{ij} = \frac{s_j}{s_n} \quad (7)$$

Frequency statistics method is applied to the case of a large number of samples, such as the higher degree of hydrogeological exploration in the mining area, especially some of the old mining sites with rich observation data and exploration holes.

KARST RUN-OFF ZONE PARTITION

This paper applies the fuzzy comprehensive evaluation method to distinguish the strength of karst runoff zone of Minmetals field partition, providing decision basis for a mining plan. The membership degree is determined by the frequency statistics method, and the results are obtained by the composite operation of the fuzzy matrix.

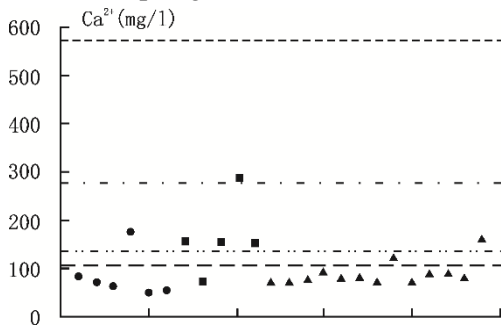
Determination of evaluation factors

There are many factors that affect the strength of the karst runoff zone, such as elevation, water outflow from a single well, karst rate and water chemical group classification. According to the measuring point of the actual data of Minmetals, the paper

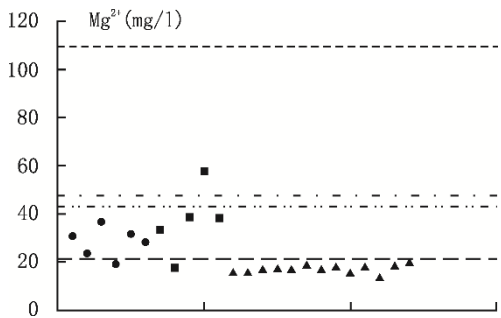
chooses the karst groundwater's five factors C_a^{2+} , M_g^{2+} , SO_4^{2-} , HCO_3^- and single well water gushing amount as the evaluation factors. The concentration of each ion in the groundwater of different runoff intensity is also different, the average runoff intensity is small, and the runoff is weak, the concentration is large. The relationship between the single well water flow and the strength of the runoff is most obvious, single well water outflow of the strong runoff zone drilling is very large, and weak runoff with single well water inflow is very small.

Determination of evaluation set

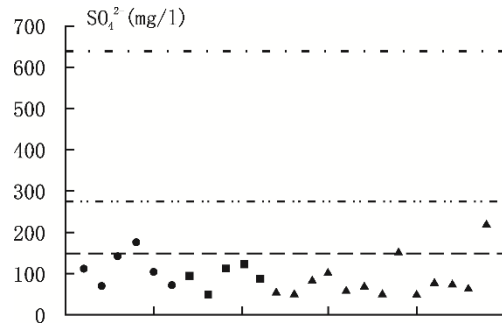
The paper takes the data of Minmetals mining field drilling for samples, a total of 24 samples in three areas, 13 samples of Daqing limestone, 5 samples of the central area of Ordovician limestone, 6 samples of the east wing area of Daqing. Factor set $U = (C_a^{2+}, M_g^{2+}, SO_4^{2-}, HCO_3^-, \text{water inflow of single well } q)$, comments collection is $V = (\text{strong, medium, weak, extremely weak})$, each factor on the four grade evaluation of the partition is shown in Table 1. According to the actual observation data of each well, the observation data of the well bore are determined in the planar rectangular coordinate system (Figure 1), the sample is the horizontal axis, the factor value is the vertical axis. The ratio of the number of samples and the total number of samples in this interval determines the membership degree of a certain factor to a comment (interval), that is, the use of frequency statistics method determines the membership degree.



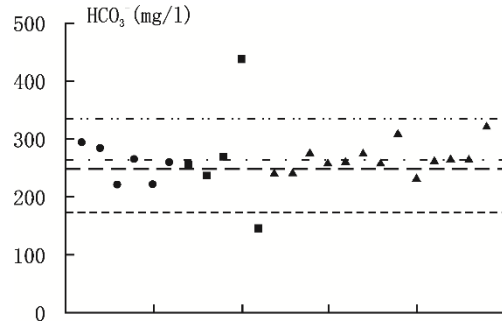
a. Corresponding diagram of the sample points and C_a^{2+}



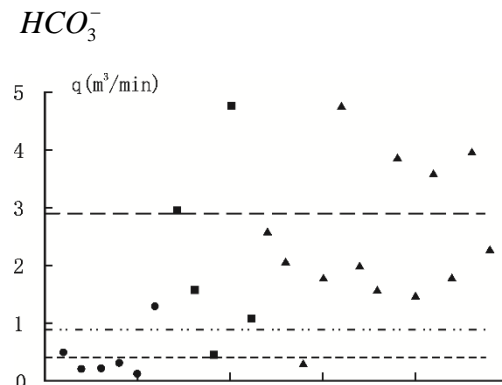
b. Corresponding diagram of the sample points and M_g^{2+}



c. Corresponding diagram of the sample points and SO_4^{2-}



d. Corresponding diagram of the sample points and



e. Corresponding diagram of the sample points and the single well of the water inflow

- Eastern Region Daqing
- Central Region Ordovician limestone
- ▲ Central Region Daqing
- Strong runoff division line
- · - · - Medium runoff division line
- · - - Weak runoff division line
- Extremely weak runoff division line

Fig. 1 Scatter diagram of each factor

The fuzzy evaluation matrix R (Table 1) can be obtained by the scatter diagram. The activity of SOD, H⁺-K⁺ATPase of mitochondria and the MDA level was measured according to the respective kit instruction.

Table 1. Fuzzy evaluation matrix R

	Central Daqing limestone				Central area of Ordovician limestone				East wing area of Daqing limestone			
R ₁	0.846	0.077	0.077	0	0.2	0	0.6	0.2	0.833	0.167	0	0
R ₂	1	0	0	0	0.2	0.6	0	0.2	0.167	0.833	0	0
R ₃	0.846	0.154	0	0	1	0	0	0	0.833	0.167	0	0
R ₄	0.231	0.615	0.154	0	0.2	0.4	0.2	0.2	0.333	0.5	0.167	0
R ₅	0.308	0.615	0	0.077	0.6	0.2	0.2	0	0	0.167	0.167	0.666

Determination of weight

In the limestone region, the content of M_g^{2+} is very small, so its weight should be set smaller. The effects of the three factors of C_a^{2+} , SO_4^{2-} and HCO_3^- in the karst runoff zone are almost the same, so they have equal weights. The water inflow of the single well q has the most obvious effect on the strength of the karst runoff, and its weight is also the largest, so the determined weight A = (0.17, 0.09, 0.17, 0.17, 0.4).

Comprehensive evaluation

The fuzzy output B of central Daqing limestone is:

$$B = A \circ R = (0.17, 0.09, 0.17, 0.17, 0.4) \times$$

$$\begin{pmatrix} 0.846 & 0.077 & 0.077 & 0 \\ 1 & 0 & 0 & 0 \\ 0.846 & 0.154 & 0 & 0 \\ 0.231 & 0.615 & 0.154 & 0 \\ 0.308 & 0.615 & 0 & 0.077 \end{pmatrix}$$

$$b_1=(0.17 \wedge 0.846) \vee (0.09 \wedge 1) \vee (0.17 \wedge 0.846) \vee (0.17 \wedge 0.231) \vee (0.4 \wedge 0.308)=0.308$$

In the same way: $b_2=0.4$, $b_3=0.154$, $b_4=0.077$
Therefore: B=(0.308, 0.4, 0.154, 0.077)

From the above results we can see that the membership degree of b_2 is the biggest, therefore, we can judge the central Daqing limestone as a moderate runoff zone. In the same way:

Fuzzy output of the central Ordovician limestone B=(0.4, 0.2, 0.2, 0.17), so it is a strong runoff zone;

Fuzzy output of the Daqing east wing area B=(0.17, 0.17, 0.167, 0.4), so it belongs to a very weak runoff zone.

From the above evaluation results, the central and east wing area belong to two different runoff zones, central Daqing limestone is a moderate runoff zone (compared with Ordovician limestone), the east wing area Daqing limestone is a very weak runoff zone and the central region of the Ordovician limestone is a strong runoff zone.

CONCLUSIONS

Through the above analysis and calculations, it is shown that the east wing area of Daqing limestone is an extremely weak runoff zone; the central area of the Ordovician limestone is a strong runoff zone, the central Daqing limestone is a medium runoff area (compared with the Ordovician limestone). These results are in line

with the actual situation of the mine drilling, and the vast majority of holes is consistent with the results according to the minmetal actual observation data. Minmetals is located in the Ordovician limestone strong runoff belt of Gushan east side, the Daqing limestone moderate runoff belt is added to the central area, forming two sets of runoff belt systems, which is a strong runoff zone, posing a serious threat to the mining of deep coal seams. East wing area is extremely weak, which is favorable for the exploitation of mines, so the exploitation of the deep coal seam can be started from the east wing area.

REFERENCES

1. A.J. Shao, Coal mine and groundwater inrush, Beijing: Earthquake Press, 2001.
2. A.J. Shao, Mine groundwater. Beijing: Geological Publishing House, 2005.
3. J. Xie, Ch. Liu, Fuzzy mathematics method and its application (4th ed.). Wuhan: Huazhong University of Science and Technology Press, 2013.
4. X.Y. Tu, X.P. Gao, *Journal of Hydraulics*, **8**, 64 (2003).
5. Sh. Chen, X. Yu, *Journal of Liaoning Technical University*, **5**, 691 (2003).
6. Zh. Liu, L. Ye, *Journal of applied foundation and engineering science*, **3**, 286 (2007).
7. Yu Qiao, X. Liang, Yu. Wang, B.Zh. Yan, H.Zh. Liu, J. Liu, *Water energy science*, **6**, 27 (2015).
8. Yu. Feng, *Progress in Environmental Science*, **2**, 56 (1995).
9. J. Liang, G.X. Xie, G.M. Zeng, Sh.L. Guo, X.D. Li, L. Shi, Ch.Y. Du, Q. Cai, *Journal of Hunan University* (Natural science edition), **6**, 54 (2009).
10. R. Ma, J.X. Shi, J.Ch. Liu, *Journal of Jilin University* (Earth Science Edition), **4**, 1130 (2012).
11. G.Y. Liu, *Journal of Hebei Institute of Geology*, **3-4**, 305 (1985).
12. W. Zhang, G. Wang, *Advances in Water Science*, **2**,180 (2000).
13. J. Liu, *Survey science and technology*, **1**, 48 (2004).
14. Q. Tian, D. Yao, *Coal Technology*, **5**, 82 (2008).
15. M. Xu, Effect of limestone water on the safety of 10 coal seam in Liudian coal mine of taiyuan group and the discrimination of Water Inrush Source. Anhui University of Science and Technology, Master thesis, 2008.
16. G. Zheng, *Yangtze River*, **44**(18), 53 (2013).
17. Zh. Zhao, J. I. Baolin, X. Song, Ke Xu. *Yellow River*, **37**(6), 67 (2015).

Impact of quadric surface carrier on gas flow radial dispersion pattern in a vehicle catalytic converter

B. Ding

School of Traffic, Northeast Forestry University, Harbin, Heilongjiang, China

Received September 28, 2017; Accepted December 19, 2017

In a conventional vehicle catalytic converter with flat-end carrier and common diffusion header, most of engine exhaust passes through a small-radius tubular part of the centre of the honeycomb carrier where the catalyst is rapidly deteriorated with high load and the honeycomb is easily fragmented on thermal stress. To improve the radial distribution of the exhaust gas by optimizing the structure of the converter is valuable in theory and practice for enhancing the conversion, service life, and reducing the cost. In this study, numerical simulation and experiment verification of the gas flow in an automotive catalyst converter with several quadric surface-shaped honeycomb carriers were performed based on ANSYS-CFD code and test, and the influence of the carrier fore-end types matching of diffusion headers on flow radial uniformity was studied. The effects show that cone-headed and sphere-headed honeycomb carriers improved the flow radial distribution especially in a cone-headed honeycomb carrier matching an enhanced diffusion header (EDH), thus the uniformity evaluation index can be increased by 29.4%–33.9%. The cone apex angle should be controlled between 60° and 90° so as to get comprehensive advantages of better flow distributional uniformity along desired radial reliability and small size of converter.

Key words: Vehicle catalyst converter, Quadric surface honeycomb carrier, Diffusion header, Numerical simulation, Gas flow radial dispersion, Uniformity evaluation index.

INTRODUCTION

Catalyst converters are currently widely used as the most effective way to reduce the harmful exhaust from the vehicle engine, and are extended to the field of large marine and mining engines [1-3]. With research in depth, the gas flow radial distribution, which has great influence on conversion efficiency and service life, has become one of the primary valuations for designing automotive catalyst converters [4-5]. Normally, the structure of a conventional diffuser matching with a planar fore-end honeycomb carrier hardly permits satisfying diffusion, so that the gas flow radial distribution is clearly not uniform, which leads to low conversion efficiency, faster local deterioration, higher radial thermal stress and shorter service life of the catalyst converter [6]. This problem exists not only in a under-body catalytic converter but also in others such as exhaust manifold converter, close coupled converter, supercharger coupled converter, which is caused by internal structure of the converter [7-8]. To improve the internal gas diametral distribution, a number of unconventional fore-end shaped honeycomb carriers including quadric surface and diffusions were designed. The flow fields of these new types of catalyst converters were simulated based on ANSYS-CFD. In the experiment, the effects of gas flow radial distribution on some fore-end shaped honeycomb

carriers coupled with different types of diffusers were discussed, and the internal structure of the catalyst converter was optimized.

SIMULATION OF GAS FLOW PATTERN IN THE CONVERTER

Considering the structure of the honeycomb ceramic carrier catalyst and the flow condition of the engine exhaust, the numerical simulation adopted the mathematical model based on Newton fluid dynamics theory.

Gas flow control equation

For a steady gas flow, the mass and momentum conservation equations are as follows [9]:

$$\frac{\partial}{\partial x_j}(\rho V_j) = 0 \quad (1)$$

$$\frac{\partial}{\partial x_j}(\rho V_j V_i + \tau_{ij}) = -\frac{\partial p}{\partial x_i} + s_i \quad (2)$$

where: V_i, V_j - velocity in the direction of i, j ; x_i, x_j - displacement in the direction of i, j ; p - fluid pressure; ρ - fluid density; s_i - source referring to the resistance of the honeycomb carrier; τ_{ij} - viscous stress for Newtonian fluids;

$$\tau_{ij} = 2\mu s_{ij} - \frac{2}{3}\mu\delta_{ij}\frac{\partial V_k}{\partial x_k} + \tau_{ij}^{(T)} \quad (3)$$

where: μ - viscosity coefficient; δ_{ij} - Kroneker function; $\tau_{ij}^{(T)}$ - Reynolds stress tensor due to

To whom all correspondence should be sent:
E-mail: ding_bq@163.com;

turbulent pulsation, $\tau_{ij}^{(T)} = -\overline{\rho V_i V_j'}$; s_{ij} - strain rate tensor given with the following equation:

$$s_{ij} = \frac{1}{2} \left(\frac{\partial V_i}{\partial x_j} + \frac{\partial V_j}{\partial x_i} \right) \quad (4)$$

Turbulence model

Reynolds stress can be calculated with a typical k - ε model to self-contain the above gas flow control equation:

$$\tau_{ij}^{(T)} = 2\mu_T s_{ij} - \frac{2}{3}\rho k \delta_{ij} \quad (5)$$

where: μ_T refers to the turbulence viscosity coefficient given with:

$$\mu_T = \rho C_\mu \frac{k^2}{\varepsilon} \quad (6)$$

k —turbulent kinetic energy, $k = \frac{1}{2} \overline{V_i V_i'}$, meeting the

following equation:

$$\rho \frac{\partial k}{\partial t} + \rho V_j \frac{\partial k}{\partial x_j} = \frac{\partial}{\partial x_j} \left[\left(\mu + \frac{\mu_T}{\sigma_k} \right) \frac{\partial k}{\partial x_j} \right] + S_k \quad (7)$$

where: $S_k = P_k - D_k$, $P_k = \tau_{ij}^{(T)} \frac{\partial V_i}{\partial x_j}$, is the originative

term, $D_k = \rho \varepsilon$, is the dissipative term; ε —turbulent dissipation rate, $\varepsilon = \nu \frac{\partial^2 V_i'}{\partial x_k^2} \frac{\partial V_i'}{\partial x_k}$, meeting the

following equation:

$$\rho \frac{\partial \varepsilon}{\partial t} + \rho V_j \frac{\partial \varepsilon}{\partial x_j} = \frac{\partial}{\partial x_j} \left[\left(\mu + \frac{\mu_T}{\sigma_\varepsilon} \right) \frac{\partial \varepsilon}{\partial x_j} \right] + S_\varepsilon \quad (8)$$

where: $S_\varepsilon = P_\varepsilon - D_\varepsilon$, $P_\varepsilon = C_{\varepsilon 1} \frac{\varepsilon}{k} \tau_{ij}^{(T)} \frac{\partial V_i}{\partial x_j}$, is the

originative term, $D_\varepsilon = C_{\varepsilon 2} \rho \frac{\varepsilon^2}{k}$, is the dissipative term.

Gas flow model in a honeycomb carrier

As a kind of porous medium, the honeycomb ceramic carrier is composed of many same-sized tiny rectangular tubes parallel with the axis of the converter. It can be simulated by the equivalent continuous method [10]. If the resistance is very high, the convection term and the diffusion term will be neglected. Then the momentum equation can be simplified as:

$$\frac{\partial p}{\partial x_i} = -K_i V_i \quad (9)$$

$$K_i = \alpha_i |\vec{V}| + \beta_i \quad (10)$$

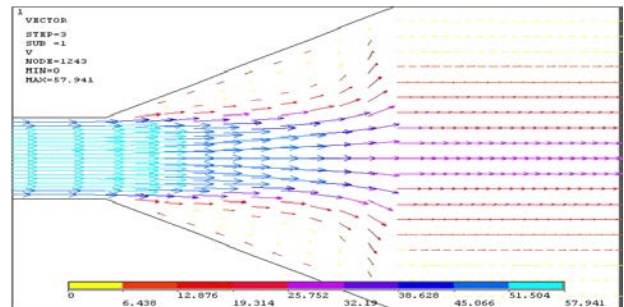
where: K_i —permeability, which is proportional to the velocity at the relevant position; α_i , β_i —empirical constants, which take the value of 1×10^5

both in the radial and circumferential directions of the honeycomb carrier, in the case of considering the gas flow just along the axial direction and no mass exchange in the radial and circumferential directions.

Simulative boundary conditions

With the above model, simulation was based on the module FLOTTRAN CFD. Normally, being an axisymmetric automotive analyst converter, the gas flow is treated as a planar flow passing by the symmetry axis. Numerous parallel tubes are distributed in a unit cross-sectional area of the honeycomb carrier and the equivalent diameter of the tubes is very small. Thus, in the range of displacement of automotive engine, the gas flow in the carrier can be regarded as a steady laminar flow. During the simulation, the axial velocity of the gas flow through the intake of the converter was assumed to be uniform in diameter, and the range adopted was 17–53 m/s, circumferential and radial velocity was zero. Meanwhile, the gas flow inlet pressure was made 1MPa, inlet temperature was made 293.0K. At the exit side of the converter, a well-developed laminar flow was made, the pressure could be assumed as atmospheric pressure, and the boundary was no-slip.

One of the gas flow field diagrams simulated inside the catalytic converter is shown in Fig. 1.



Conventional plane fore-end carrier, 30° semi-angle diffuser

Fig. 1. Gas flow field diagram simulated inside the converter

EXPERIMENTS

In order to verify the reliability of the flow field numerical model, a testing system was set up and the velocity of the gas flow in the catalyst converter was measured. One of the test devices is schematically shown in Fig. 2. Using air as the gas flow supply and cordierite honeycomb carrier as the uncovered fore-end shaped carrier, the radial distribution of the axial velocity of the gas through the carrier was tested with Y-style Pitot tube on the steady flow test bed.

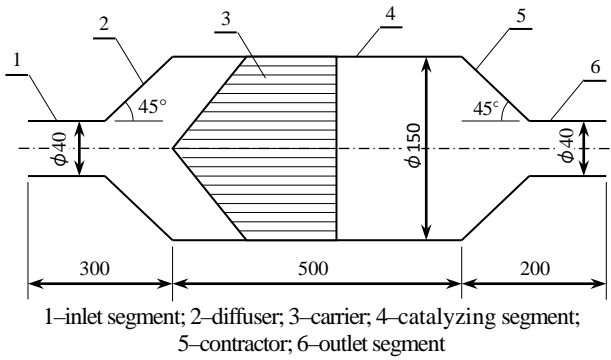


Fig. 2. Structure of the experimental converter

Some of the results are shown in Fig. 3, indicating the comparison between the test and calculated results. With a series of experiments, the test data were well able to match the calculated results, which was satisfying for discussing the character of gas flow in different types of converter and analyzing the diametral distribution of the gas flow.

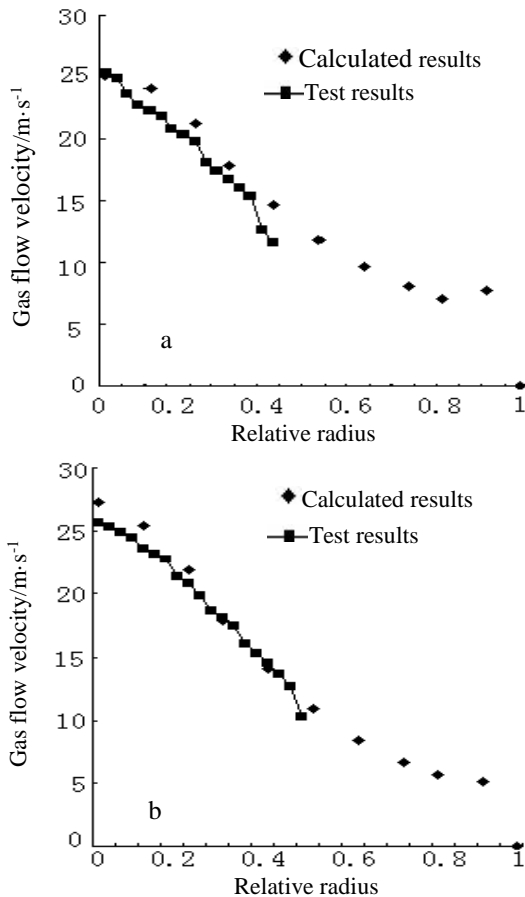


Fig. 3. Testing results and calculating results of gas flow velocity. a) 90° Fore-end shaped cone carrier, 30° semi-angle diffuser; b) 120° Fore-end shaped cone carrier, 30° semi-angle diffuser

OPTIMIZING THE STRUCTURE

Uniformity evaluation index of gas flow radial distribution

Neglecting the on-way resistance, the difference between the diameter of the inlet segment and the catalyzing segment is the cause of the non-uniform gas flow radial distribution in the catalyst converter. Considering the radial difference, in order to test the effects on different fore-end shaped carriers matching with different diffusers under the same condition, the ratio $\gamma_{0.3}$ of mean gas flow velocity in the whole carrier cross section to mean flow velocity in the cross-sectional area of relative radius of 0.3 around the converter axes was defined as the index for evaluating the uniformity of gas flow radial distribution:

$$\gamma_{0.3} = \frac{\bar{v}}{v_{0.3}} \quad (11)$$

where: \bar{v} - mean flow velocity of the gas flow at the whole carrier cross section along the converter axes, m/s; $v_{0.3}$ - mean flow velocity in the cross-sectional area of a relative radius of 0.3, m/s.

The definition is related to the diameter ratio of the catalyzing segment to the inlet segment. It satisfies the conformity of the experimental conditions and is able to testify the internal gas flow distributional uniformity in diameter. It also can be extended to automotive analyst converters with different inlet segments and catalyzing segment diameters based on its essence.

Fore-end shape of the carrier

With the maintained numerical model and boundary conditions, the internal gas flow field with different fore-end shaped carriers was simulated. The radial distribution curves of the axial gas flow velocity through the cross section of the carriers are shown in Fig. 4. In Table 1, the flow uniformity index is presented.

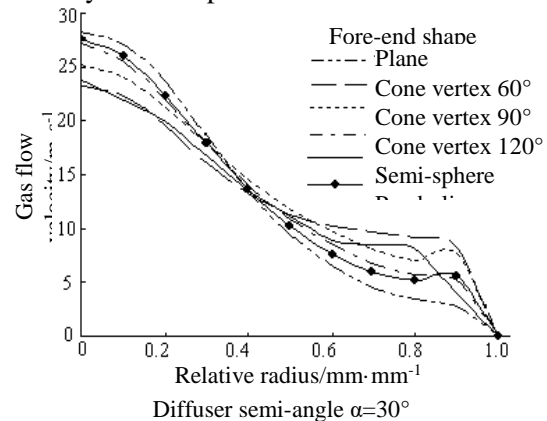


Fig. 4. Radial distribution of gas flow velocity with different fore-end shaped carriers

Table 1 Flow uniformity index with different fore-end shaped carriers¹

Fore-end shape of carrier		$\gamma_{0.3}$
Conventional plane		0.5645
Parabolic	Vertex 120°	0.6318
Sphere		0.6636
Cone	Vertex 120°	0.6504
	Vertex 90°	0.6944
	Vertex 60°	0.7056

Note: ¹Catalyst converter diffuser semi-angle $\alpha=30^\circ$

When using the fore-end shaped cone carrier, the gas flow radial distribution uniformity was clearly improved and the gas flow uniformity increased with the decrease in the vertex angle. With the same vertex angle, the uniformity index of the parabolic fore-end was smaller than that of the cone-shaped fore-end. Consequently, shaped fore-end structure is in a way working as a baffle. The smaller the vertex angle, the better are the effects of gas flow radial diffusion. However, undersized vertex angle will unbalance the honeycomb carrier, which is unfavorable for fixing and sealing carrier and will increase the volume of the catalyst converter. Considering the technologic processing of production, it is inadvisable to make the vertex angle over 60°.

Diffuser structure matching with carrier

Effects of different diffusers matching with different honeycomb carriers on the gas flow radial distribution were simulated, where the diffusers included four types such as 30°, 45°, 60°-semi-angle and enhanced diffusion header (EDH); the honeycomb carriers included five types such as planar fore-end, 90° vertex angle fore-end, 120° vertex angle fore-end, semisphere fore-end and parabolic fore-end. In some cases of different inlet gas flow velocity, Fig. 5 indicates the difference of gas flow radial distribution between 30°-semi-angle diffuser matching with a conventional planar fore-end carrier and EDH matching with 90° vertex angle fore-end carrier. Detailed uniformity indices with different matching are shown in Table 2.

From the simulation results it can be seen that matching with different diffusers, planar and

Table 2 Radial diffusion with different matchings¹

Diffuser	Fore-end shape of carrier	$\gamma_{0.3}$	Diffuser	Fore-end shape of carrier	$\gamma_{0.3}$
30° Semi-angle	Plane	0.5645	60° Semi-angle	Plane	0.5225
	Parabolic	0.6318		Parabolic	0.5201
	Sphere	0.6636		Sphere	0.5230
	Vertex 120°	0.6504		Vertex 120°	0.5235
	Vertex 90°	0.6944		Vertex 90°	0.5464
45° Semi-angle	Plane	0.5407	EDH	Plane	0.6576
	Parabolic	0.5522		Parabolic	0.6528
	Sphere	0.5968		Sphere	0.6854
	Vertex 120°	0.5921		Vertex 120°	0.6646
	Vertex 90°	0.6210		Vertex 90°	0.6998

Note: ¹Inlet gas flow velocity: 53m/s

parabolic fore-end carriers normally led to poorer diffusion. Matching with a 60° or 45° semi-angle diffuser led to the lowest uniformity index, where the parabolic fore-end shape made a better improvement than planar fore-end when the diffuser semi angle was less than 45°. The reverse was observed when the diffuser semi-angle was over 45°. Sphere- and cone-shaped carriers both improved the radial diffusion, and the uniformity index $\gamma_{0.3}$ considerably increased. EDH matching with 90° cone carrier led to the best improvement of distribution, and the uniformity index increased by 29.4%–33.9% compared to the conventional structure.

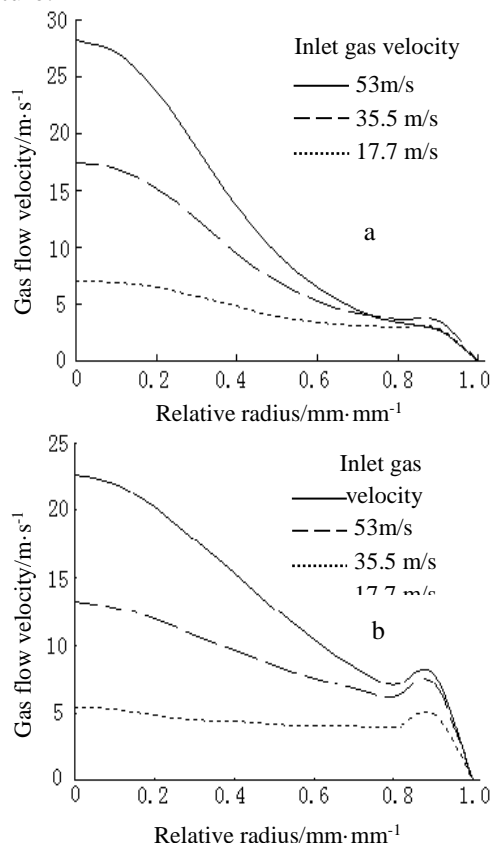


Fig. 5. Gas flow radial distribution with two different matchings; a) 30° semi-angle diffuser, conventional fore-end shaped planar carrier; b) EDH, 90° fore-end shaped cone carrier

CONCLUSIONS

(1) A new uniformity index was defined more distinctly and logically than traditionally to evaluate gas flow radial distribution in automobile catalytic converters.

(2) Compared to the fore-end shaped planar carrier, the cone or sphere carrier lead to better gas flow radial distribution in the automotive catalyst converter. The improvement is prominent when using the cone carrier, especially when the vertex is under 90°. In the simulation and experiment, smaller vertex is able to increase the uniformity index. Comprehensively considering the technologic processing of production, reliability and tight structure, a vertex angle within the range of 60°-90° was suggested.

(3) Fore-end shaped cone carrier matching with EDH makes the best improvement of the gas flow diametral distribution. Especially when a 90° vertex carrier matches with EDH, the uniformity index can be increased by 29.4%–33.9%.

REFERENCES

1. A. Mukherjee, K. Roy, J. Bagchi, K. Mondal, *Journal for Research*, **2**, 29 (2016).
2. D. Bernečić, R. Radonja, *Scientific Journal of Maritime Research*, **25**, 15 (2011).
3. D.H. Wang, M.Q. Zou, *Coal Mine Machinery*, **37**, 55 (2016).
4. B. Liu, Y. Liang, L.Y. Zhou, J. Wang, *Journal of Hunan University (Natural Sciences)*, **31**, 17 (2004).
5. S.P. Harshil, J.P. Dipak, *International Journal for Scientific Research & Development*, **3**, 74 (2015).
6. S.J. Jeong, W.S. Kim, *Chemical Engineering Communications*, **189**, 1314 (2002).
7. B.Q. Ding, M.Y. Li, *Vehicle Engine*, **3**, 20 (2011).
8. C.P. Om Ariara Guhan, G. Arthanareeswaran, K.N. Varadarajan, S. Krishnan, *Journal of Computational Design and Engineering*, **3**, 198 (2016).
9. D.Q. Mei, Z.X. Liu, Y. Miao, Sh. Zhang, *Vehicle Engine*, **3**, 10 (2013).
10. X.L. Chen, W.G. Zhang, Z. Huang, *Journal of Shanghai Jiaotong University*, **38**, 1205 (2004)

Influence of freezing and thawing cycles on bamboowood's surface properties

X. Liu^{1,2}, X. Guan^{2*}, M. Guo¹, X. Wang¹, J. Lin²

¹Material Science and Engineering College, Northeast Forestry University, Heilongjiang, Harbin 150040, China

²College of Materials Engineering, Fujian Agriculture and Forestry University, Fujian, Fuzhou 350002, China

Received September 22, 2017; Accepted December 19, 2017

“Replacing wood by bamboo” is a research hotspot in the current field of wood science. Performing freezing and thawing cycles on moso bamboo chips and bamboo surface feature analysis before and after freezing and thawing cycles, results indicated that at freezing temperature of -16—20°C, freezing time of 6 h, thawing time of 1.5 h, ice melting temperature of the bamboo chips of 60 °C, and 4 cycles, the surface glue absorption of moso bamboo could reach up to 11.01% with an increasing rate up to 92.41%. Plan B could be used to increase bamboo wood's specific surface area by 267.06%. Pore volume was increased by 37.65%. Mean pore size was reduced by 62.87%. In cross section, the interval between primary tissues and vascular bundle was slightly enlarged, so that adhesive distribution would be evener. Relevant height of diffraction peaks in cellulose crystalline region was reduced by 106 cps and relevant crystallinity was lowered by 1.4%.

Keywords: Bamboo wood; Freezing and thawing disposal; Permeability; Surface performance

INTRODUCTION

Bamboo is an environmentally friendly natural renewable material, with fast growth rate, excellent tenacity and abrasive resistance. Within 3-5 years, it may find broad utilization. There are abundant bamboo woods in China, which are excellent materials to replace woods to manufacture artificial boards [1,2]. At present, bamboo-based artificial boards mainly include bamboo plywood, reconsolidated bamboo and glued laminated bamboo, etc., which are composed of bamboo materials, glued by phenolic resin and produced by assembling and hot-pressing [3-5]. Bamboo wood has lots of lipids and saccharides, resulting in poor permeability of bamboo surface [6]. As a result, how to improve permeability of bamboo surface and make close-grained bamboo wood become a porous material to improve bonding performance and enhance internal bonding strength of bamboo-based artificial boards has been the research hotspot in recent years.

Freezing and thawing cycles form ice crystals to expand cellular structure of bamboo wood, increase specific surface area, so as to expand its pores, loosen cytoderm, promote moisture movement in the drying process, improve diffusion rate, enhance surface performance of bamboo wood, and improve dipping effects of adhesives [7-9]. In the paper, the authors discussed the optimal process of bamboo wood freezing and thawing cycle through parallel experiments, used modern analysis to study the changes of bamboo wood's surface features before and after freezing and thawing cycle, and provided theoretical basis that freezing and thawing cycle can

improve bamboo wood's surface permeability.

EXPERIMENTAL

Experimental Materials

Bamboo chip: 5 year-old crude moso bamboo, string bamboo chip with removed tabasheer and bamboo green; thickness 2±0.2 mm, moisture content 30%; bamboo comes from Sanming Yong'an Forest Farm in Fujian, lifting 1.5-2 m.

Adhesive: phenolic resin, viscosity 36 mPa.s, pH value 10-12, solid content 25%.

Test Facilities

Refrigerator (BCD-257SL, Qingdao Haier), electrically heated thermostatic water bath (DK-98-1, Tianjin Tester), specific surface area and aperture tester (ASAP2020HD88, American Micromeritics), scanning electron microscope (S-3400N, Japan Hitachi), X-ray diffraction analyzer (DX270, Japan Hitachi)

Test Methods

Bamboo wood's freezing and thawing cycle: on the basis of previous studies [10-11], the freezing temperature was set up as -16—20 °C, ice melting time 1.5 h, ice melting temperature 60 °C, cycle index 4 times, freezing time 3 h, 6 h and 9 h; glue-absorbing quantity of phenolic resin was measured according to GB/TF14074-2006 Detection Methods of Wood Adhesive and Resin. The test was repeated 5 times. The result was the mean of all tests.

To find out the effect of freezing and thawing cycle on bamboo wood's permeability, the influence of freezing and thawing cycle on bamboo wood's surface performance was analyzed as follows:

(1) Specific surface area and aperture were tested. Nitrogen was used as absorbing medium. BET method was applied to calculate the specific surface

*To whom all correspondence should be sent:

E-mail: liuxueshen412@163.com

area of the samples. With integrals, the pore volume between pore size distribution intervals was calculated. Mean pore size was calculated as $4V/A$ (V is the pore volume, A is the specific surface area in m^2/g). Changes in cellular structure before and after freezing and thawing cycle were followed. The influence of freezing and thawing cycle on bamboo wood's specific surface area, aperture, pore volume, etc., was studied.

(2) Scanning electron microscope was used to analyze the main microstructural features of bamboo wood surface before and after freezing and thawing cycle. Microcosmic structure chart in all directions for bamboo wood was observed, photographed and recorded.

(3) X-ray diffraction analysis was used to study bamboo wood's microcrystalline structure features before and after freezing and thawing cycle. By continuous scanning, X-ray diffraction peak chart of the samples was obtained. According to the empirical formula, cellulosic crystallinity was calculated to determine changes of crystallinity [12-13].

$$X_c = \frac{I_{002} - I_{am}}{I_{002}} \times 100\%$$

X_c : crystallinity, I_{002} : diffraction intensity of crystal face I_{am} : diffraction intensity in amorphous region. Scanning range: $10^\circ-80^\circ$; step length: 0.02° ; scanning speed: $5^\circ/min$; tube flow and pressure: $40mA, 40kV$.

RESULTS AND DISCUSSION

Glue-absorbing test of freezing and thawing cycle

As shown in Table 1, with the extension of the freezing time, bamboo wood's glue-absorbing capacity increased. When freezing time was 6 h, the glue-absorbing capacity reached the maximum. By comparing with bamboo wood's glue-absorbing capacity with unfreezing treatment, it was improved by a factor of nearly two. However, after a freezing time of 9 h, the glue-absorbing capacity was reduced and its stability was also reduced. Nevertheless, by comparing with the control group,

Table 1. Test results of glue-absorbing capacity before and after freezing and thawing cycle

Freezing time/h	Glue-absorbing capacity/%						Increasing rate
	Specimen 1	Specimen 2	Specimen 3	Specimen 4	Specimen 5	Mean	
Untreated	6.12	5.88	5.07	5.52	6.01	5.72±0.46	-
3 (Scheme A)	6.45	6.73	6.42	6.67	6.71	6.60±0.16	15.31
6 (Scheme B)	10.81	11.23	10.51	11.12	11.36	11.01±0.32	92.41
9 (Scheme C)	8.71	9.24	10.11	8.98	9.89	9.39±0.61	61.09

Tab. 2 Testing results of samples' specific surface area before and after freezing and thawing cycle

Indicators	Blank group	Freezing and thawing group	Changing rate
Specific surface area/ $\times 10^{-2}m^2/g$	0.85	3.12	267.06%
Pore volume / $\times 10^{-4}cm^3/g$	1.62	2.23	37.65%
Mean pore size/nm	73.14	27.16	-62.87%

the glue-absorbing capacity was still improved by 61.09%, because with the extension of the freezing time, the internal structure of bamboo wood retained the micromechanical force generated by freezing and thawing cycle, so that bamboo wood's organizational structure was occupied by moisture. Therefore, it caused adverse effects on phenolic resin glue.

The above-mentioned test indicated that the optimal treatment procedure of bamboo wood's freezing and thawing cycle was 1.5 h, ice melting temperature of $60^\circ C$, 4 cycles, frozen time of 6 h, (Table 1, scheme B).

Bamboo wood's surface feature analysis before and after freezing and thawing cycle

Bamboo wood's specific surface area

As shown in Table 2, bamboo wood's specific surface area after freezing and thawing cycle in scheme B significantly increased by 267.06%.

Bamboo wood's pore volume after freezing and thawing cycle increased to $2.23 \times 10^{-4} cm^3/g$ from the untreated $1.62 \times 10^{-4} cm^3/g$ (an increase by 37.65%). However, pore size decreased by 62.87% after freezing and thawing cycle, indicating that freezing and thawing cycle may have an important influence on the changes in bamboo wood's specific surface area, pore volume and mean pore size. After a freezing and thawing cycle, bamboo wood's specific surface and pore volume were obviously improved. With a freezing and thawing cycle, a circular hole with a smaller diameter was obtained, so that the micropore number was increased. To sum up, the freezing and thawing cycle contributes to expanding bamboo wood's microcellular structure, so as to improve bamboo wood's surface permeability.

Scanning Electron Microscope Analysis of Bamboo Wood's Fiber Structure

As shown in Figure 1, the internal pore diameter of bamboo wood was smaller after a freezing and thawing cycle of scheme B and the overall interspace was expanded. Bamboo wall's vascular

Table 3 Test results of relative crystallinity before and after freezing and thawing cycle

Categories	Diffraction angle/ $2\theta^\circ$	Relative strength/cps	Relative crystallinity/%
Blank group	22.62	1071	39.7
	16.74	640	
Freezing and thawing (Scheme B)	22.50	965	38.3
	16.47	588	

bundle distribution without a freezing and thawing cycle was loose, presenting an irregular shape. Moreover, there were a few elementary tissues. The cross section was close to an oval. Bamboo wood's cross section after freezing and thawing cycle was slightly expanded between elementary tissues and vascular bundle. Most of parenchyma cells were encircled around vascular bundle. Moreover, cells were large. The arrangement was compact and well-aligned and the cross section was close to roundness.

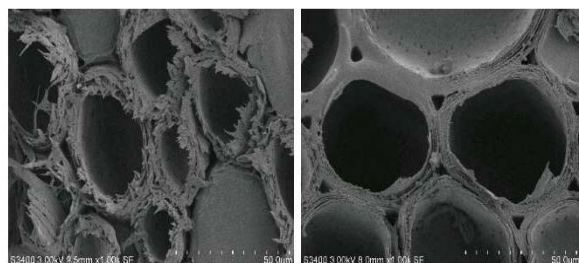


Fig. 1 Scanning electron microscope comparison of the cross section before and after bamboo wood's freezing and thawing cycle

As shown in Figure 2, the pores of bamboo wood cells without freezing and thawing cycle were small and closely arranged. Bamboo wood after a freezing and thawing cycle was evenly distributed with some glue solution between elementary tissues and cells. There were obvious cell intervals between parenchyma cells. Some phenolic resin glue adhesive could enter into the cell cavity of the parenchyma cells through the cell pores, so as to fill in parenchyma cells.

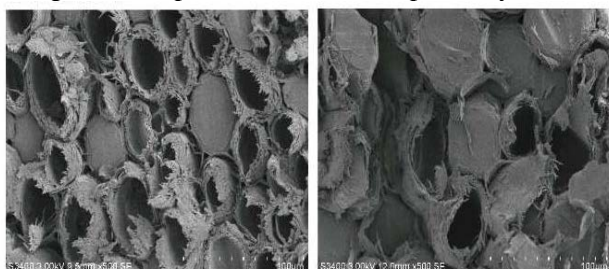


Fig. 2 Scanning electron microscope comparison of the glue-absorbing cross section before and after bamboo wood's freezing and thawing cycle

XRD diffraction analysis of bamboo wood's microstructure

As shown in Figure 3, after a freezing and thawing cycle of scheme B, the relative strength of the diffraction peak in the cellulosic crystalline region changes, because cellulose underwent

hydrolysis and pyrolysis during the freezing and thawing cycle, so that cellulosic crystalline region was destroyed to some extent. As for freezing and thawing cycle, there was a prominent crystal diffraction peak around 22.50° for the diffraction angle 2θ . There was a weaker crystal diffraction peak around diffraction angles 16.47° and 35.05° .

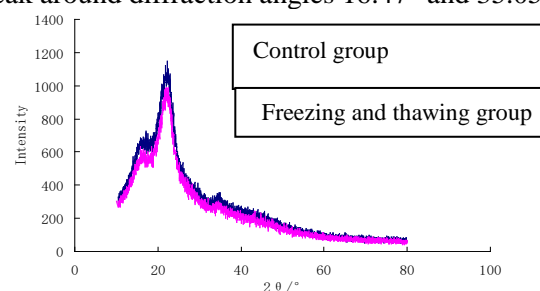


Fig. 3 XRD diffraction pattern before and after bamboo wood's freezing and thawing cycle

As shown in Table 3, after freezing and thawing cycle of scheme B, the relative crystallinity of cellulose was reduced to some extent. This was greatly beneficial to improve bamboo wood's glue-absorbing capacity. Due to the freezing and thawing cycle, bamboo wood's structure was looser and more scattered. The scattered bamboo wood's structure was good for permeation of adhesive, so as to improve glue-absorbing properties of bamboo wood.

CONCLUSIONS AND PROSPECTS

(1) Freezing and thawing cycle could improve the permeability of bamboo wood. With 4 cycles at ice melting time of 1.5 h and thawing temperature of 60°C the optimal frozen time was 6 h. When the frozen time exceeded 8 h, both the permeability and stability of bamboo wood decreased. Moreover, long time was not good for cost control.

(2) Freezing and thawing cycle made bamboo wood's surface features to change as follows: specific surface area increased by 267.06%; pore volume increased by 37.65%, and the mean pore size decreased by 62.87%. The interval between cross section's elementary tissues and vascular bundle was slightly enlarged, so that the adhesive was evenly distributed in bamboo's elementary tissues and cellular intervals. The relative height of the diffraction peak in the cellulosic crystalline region decreased by 106 cps and the relative crystallinity decreased by 1.4%.

(3) In the future, consideration should be given

to age and terrain clearance of bamboo wood. Response surface analysis and orthogonal test should be used to further refine the permeability of bamboo wood.

Acknowledgements: *The national natural fund(31600455); 2014 Forestry Science and Technology of Fujian Province; Teaching and research project of young and middle-aged teachers in Fujian Province(JB13046); Youth Fund Program of Fujian Agriculture of Forestry University (2011xjj17).*

REFERENCES

1. W. Zhang, T. Chen, X. Sun, *Hunan Forestry Science and Technology*, **37**(5), 53 (2010).
2. M. Ren, W. Song, *Forestry Economy*, **6**, 33 (2008).
3. X. Zhang, Y. Guo, *World Bamboo and Rattan*, **2**, 35 (2009).
4. J. Han, *Wood Industry*, **20**(2), 52 (2006).
5. Results of the 8th National Forest Resources Inventory, *Forestry Resource Administration*, **1**, 1, (2014).
6. J. Han, *Forestry Industrialization*, **34**(1), 12 (2007).
7. W. Xiao, D. Li, Zh. Wu, *Plastic Industry*, **38**(7), 50 (2010).
8. J. Feng, Q. Shi, X. Huang, J. Chen, Y. Chen, Y. Ouyang, *Plastic Industry*, **41** (6), 83 (2013).
9. L. Duan, *Water Conservancy of Inner Mongolia*, **5**, 20 (2013).
10. Q. He, D. Li, Ch. Wu, *Guizhou Chemical Engineering*, **35**(1), 16 (2010).
11. T. Chen, Study on Bamboo-based Container Soleplate Based on Freezing and Thawing Cycle, Fuzhou: Fujian Agriculture and Forestry University, 2016.
12. B. Hou, W. Liu, X. Fan, *Physical and Chemical Inspection (Physical Fascicule)*, **9**, 452 (2007).
13. X. Ma, L. Huang, L. Chen, *Paper Science and Technology*, **2**, 75 (2012)

Synthesis and structure-activity relationships of a new highly selective rodenticide - brominated *n*-piperidine dibenzocycloheptoid

F. Chen, Ch. Qu, J. Wang, L. Liu, Sh. Ning

Department of Chemistry, College of science ,Northeastern University, Shenyang City, People's Republic of China

Received August 15, 2017; Accepted December 19, 2017

With the widespread use of anticoagulant rodenticides, drug-resistant rats appeared, thus new types of rodenticides being needed. N-piperidine-10,11-dihydro dibenzo[a,d]cyclohepten (R) is a highly selective rodenticide but because of its low toxicity, it is not widely used. By adding bromine to the rodenticide molecule, the toxicity dramatically improves by keeping its high selectivity. Five different new brominated N-piperidine dibenzocycloheptoid rodenticides were synthesized in the present work. Toxicology experiments showed that the new rodenticides have excellent palatability and selectivity. Death time and death number relation graphs show that the distribution is moderate and is concentrated in 1 to 2.5 h. Brominated N-piperidine dibenzocycloheptoid is an excellent rodenticide.

Key words: Highly selective rodenticide, N-piperidine dibenzocycloheptanone, Bromo-substitution, *Rattus norvegicus*, Toxicity

INTRODUCTION

Rodents are widely distributed, endangering agriculture and spreading diseases [1-3]. The efficient control of the rodents has been a major subject [4-8]. Rodenticides have already become an important part of pesticides [9]. With the widespread use of first- and second-generation anticoagulant rodenticides, drug-resistant mouse populations emerged [10-12]. N-piperidine-10,11-dihydro-5H-dibenzo [a, d] cyclohepten is the most selective known rodenticide. But the toxicity of this compound is relatively lower in comparison with other rodenticides, which limits its use. Bromine is an effective toxic agent [13-15]. Connecting bromine atoms to this rodenticide could enhance the toxicity. The molecular formulas of the rodenticides R,R₁,R₂,R₃,R₄ are shown in Fig. 1. Synthesis routes of these substances are shown in Fig. 2.

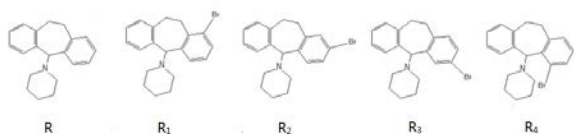


Fig. 1. Structural formulas of compounds R₁,R₂,R₃,R₄

EXPERIMENTAL

Materials and analytical methods

Equipment and reagents

The main reagents required are: phthalic anhydride, phenylacetic acid, sodium acetate, sodium borohydride, bromine water, thionyl chloride, piperidine, sodium sulfite, aluminum chloride.

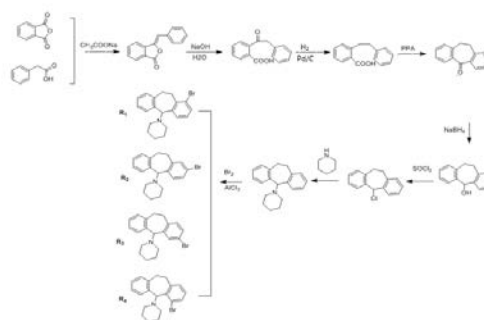


Fig. 2. Synthesis road of compound R

The IR spectra were recorded by FT-IR spectroscopy on a Spectrum One spectrometer. The solid samples were analyzed by the KBr tableting method. The NMR data were acquired on an ARX 300 nuclear magnetic resonance (1H-NMR) spectrometer using TMS as internal standard, CDCl₃ and DMSO as solvents.

Synthesis of dibenzosuberone

10.00 g (67.56 mmol) of phthalic anhydride, 8.70 g (63.95 mmol) of phenylacetic acid and 0.43 g (5.24 mmol) of anhydrous sodium acetate were added into a three-neck flask and the mixture was heated at 120-130°C for 6 h, cooled and filtered. Recrystallization gave 9.94 g product.

10 g of synthetic benzylidenephthalide, 6 ml of water and 16 ml of 30% sodium hydroxide solution were added into a the three-neck flask and the mixture was heated at 38°C and stirred for 8.5 h. The pH was adjusted to 7.0 by hydrochloric acid. The reaction gave 2-phenylacetylbenzoic acid. The product was not separated and the next reaction directly followed.

*To whom all correspondence should be sent:
E-mail: E-mail:1600209@stu.neu.edu.cn

1.00 g of 5% Pd/C was added to the above system and the reaction was carried out at 95°C and 2 MPa under nitrogen for 8 h. After the end of the reaction, hydrochloric acid was added to the solution to adjust the pH at 3. Filtration and recrystallization gave 9.15 g of 2-phenylethyl benzoic acid.

20.00 g (88.40 mmol) of 2-phenethylbenzoic acid and 20.00 g (59.20 mmol) of polyphosphoric acid were added to a 250 mL three-neck flask. The mixture was heated at 120°C under stirring and refluxed for 5 h. The organic phase was extracted and evaporated to dryness to give 16.36 g of a pale yellow solid.

Synthesis of R_1 , R_2 , R_3 and R_4

25.01 g (120.00 mmol) of dibenzocycloheptanone were added into a 250 mL three-neck flask. Sodium borohydride was added slowly. The mixture was stirred at room temperature for 4 h and allowed to stay overnight. Then concentrated hydrochloric acid was added to adjust to pH 3. The product after filtration was 22.58 g.

To 20.02 g (95 mmol) of the prepared dibenzoheptol in a 250 mL three-neck flask, 50.00 mL of thionyl chloride was added dropwise at 80°C and reacted for 4 h. After completion of the reaction, unreacted sodium sulfoxide was removed at 50°C under a vacuum of 0.035 MP. The obtained product was reddish brown.

90.00 mL of piperidine were added to a 250 mL three-neck flask and were stirred at 0°C. Then 5-chloro-10,11-dihydro-5H-dibenzo[*a,d*] [7] annulene was slowly added. The mixture was stirred at room temperature till no gas was produced. 70 ml of water were added to the organic phase. The solvent was evaporated to dryness giving 18.86 g of a light brown solid.

The conditions of the chromatographic separation were as follows: stationary phase silica gel 75 ~ 45 μ m; column height 20 cm (wet packing); eluent - a mixture of n-hexane and ethyl acetate (30 : 1, M / M).

R₁: 2.05 g, recovery 11.76%, melting point 163.2°C, ¹H NMR (CDCl₃, 300Hz, δ) 5.19 (s, 1H, -CR₁R₂N-H), 7.19 (m, 1H, Ph-H), 2.87~2.90 (m, 4H, CH₂), 2.25 (m, 4H, CH₂), 1.59 (m, 6H, CH₂), 7.10~7.20 (m, 3H, Ph-H), 7.09~7.12 (s, 1H, Ph-H).

R₂: 3.56 g, recovery 20.35%, melting point 175.4 °C, ¹H NMR (CDCl₃, 300Hz, δ) 5.18 (s, 1H, -CR₁R₂N-H), 7.17 (s, 1H, Ph-H), 7.13 (m, 1H, Ph-H), 2.87~2.91 (m, 4H, CH₂), 2.25 (m, 4H, CH₂), 1.59 (m, 6H, CH₂), 7.10~7.21 (m, 3H, Ph-H), 7.09~7.12 (s, 2H, Ph-H).

R₃: 0.95 g, recovery 5.38%, melting point 178.1 °C; ¹H NMR (CDCl₃, 300Hz, δ) 5.18 (s, 1H, CR₁R₂N-H), 7.73 (d, 1H, Ph-H), 7.33 (m, 1H, Ph-H), 2.87~2.91 (m, 4H, CH₂), 2.25 (m, 4H, CH₂), 1.59 (m, 6H, CH₂), 7.05~7.21 (m, 3H, Ph-H), 7.09~7.12 (m, 2H, Ph-H).

R₄: 0.25 g, recovery 1.46%, melting point 185.7 °C, ¹H NMR (CDCl₃, 300Hz, δ) 5.19 (s, 1H, CR₁R₂N-H) 7.13 (d, 1H, Ph-H), 2.87~2.91 (m, 4H, CH₂), 2.23~2.25 (m, 4H, CH₂), 1.59 (m, 6H, CH₂), 7.04~7.21 (d, 3H, Ph-H), 7.06~7.12 (m, 3H, Ph-H).

R₅: 16.23 g, recovery 72.56%, melting point 175.2 °C, ¹H NMR (CDCl₃, 300Hz, δ) 5.18 (s, 2H, CR₁R₂N-H), 7.44 (s, 2H, Ph-H), 7.79 (d, 2H, Ph-H), 7.12 (d, 2H, CH₂), 2.45 (m, 4H, CH₂), 1.39~1.50 (m, 6H, CH₂), 2.86~2.90 (m, 4H, Ph-H).

Determination of feeding coefficient

Feeding coefficient is an index that shows the palatability of rodenticides [31-32]. The captured experimental rats were of the kind *rattus norvegicus* in Shenyang and were reared in the laboratory. The rats were 150 ~ 300 d old, weighing 150 ~ 200 g, half male and female (females not pregnant).

Determination of LD₅₀

Experimental animals were mice (*mus musculus*) belonging to Kunming closed group, aged 28 ~ 30 d, weight 18 ~ 22 g, half male and female (female not pregnant). Experimental animals *rattus norvegicus* were caught in Shenyang and were reared in the laboratory, age 150 ~ 300 d, weight 150 ~ 200 g, half male and female (females not pregnant).

RESULTS AND DISCUSSION

The experimental results for R_1 , R_2 , R_3 , R_4 , R_5 selectivity are 0.9, 0.87, 0.71 and 0.68, respectively.

The LD₅₀ of R , R_1 , R_2 , R_3 , R_4 and R_5 of *rattus norvegicus* and the mice were calculated by the Karber method [16-17].

The results are shown in Table 1. Table 2 shows that the reduction ratio of LD₅₀ percentage for *rattus norvegicus* is larger than that for mice for all R_1 , R_2 , R_3 , R_4 and R_5 , which means that the rate of increase in the toxicity of such rodenticides against *rattus norvegicus* is greater than against mice. The newly synthesized rodenticide enhances the selectivity. The toxicity of brominated compounds has been strengthened while retaining the high selectivity of the original drug.

Table 1 Toxicity comparison of each rodenticide against *rattus norvegicus*

Product	Rodenticide				
	R	R ₁	R ₂	R ₃	R ₄
LD50 (mg/kg)	8.85	6.79	5.65	7.55	9.16
LD50 reduction (mg/kg)	-	2.06	3.20	1.30	-0.31
LD50 reduction percentage (%)	-	23.28	36.16	14.69	-3.15

Table 2 Toxicity comparison of each rodenticide against *mus musculus*

Project	Rodenticide				
	R	R ₁	R ₂	R ₃	R ₄
LD50 (mg/kg)	939.72	882.67	855.07	883.08	970.05
LD50 reduction (mg/kg)	-	57.05	84.65	56.64	-30.33
LD50 reduction percentage (%)	-	6.07	9.01	6.03	-3.23

The toxicity of the rodenticides changes with the substitution position of bromine on the benzene ring. R₄ was the most toxic, and R₂ was the least toxic. The toxicity mechanism of the rodenticides is related to the biological activity of the nitrogen atom which contained in there. In the body of *rattus norvegicus*, the nitrogen-containing organics first combine with the substance and then exert toxic effects. It is a bimolecular process [18]. The reason for the difference in toxicity of the newly synthesized drugs is related to the extent of steric hindrance. Because bromine in R₄ is closer to the nitrogen, it hinders the contact between the nitrogen atom in the compound and the biological active group of the organism, which affects the toxicity. Thus the toxicity of R₄ is small. On the contrary, the bromine atom in the R₁ and R₂ molecules is far

away from the nitrogen atom. So the steric hindrance is small and the toxicity is strong.

It can be seen from the experimental data that brominated N-piperidine dibenzocycloheptoid, especially the 2-brominated compound, is the best rodenticide in the examined group. It has strong toxicity and good selectivity.

REFERENCES

1. L. D. Singla, N. Singla, V. R. Parshad, P. D. Juyal, N. K. Sood, *Integrative Zoology*, **3**(1), 21 (2008).
2. N. Pakdel, S. Naem, F. Rezaei, *Vet. Res. Forum*, **4**(2), 105 (2013).
3. J. Saki, S. Khademvatan, *Biomed Research International*, **2014**(5), 383859 (2013).
4. D. L. Peardon, *Pest Control*, **42**(9), 14 (1974).
5. S. Thomas, Rodent control, US: 6194007, 2001-2-27.
6. Zh. Feng, X. Huang, *Guangzhou Agricultural Sciences*, **5**, 44 (2001).
7. F. D. Hector, K. S. Heinrich, W. S. John, Rodenticide, US: 4035493, 1977-7-12.
8. F. D. Hector, M. S. Connie, Method of exterminating rodents and other vertebrate pests, US: 5151416, 1992-9-29.
9. H. Choi, D. Conole, D. J. Atkinson, *Chemistry & Biodiversity*, **13**(6), 762 (2016).
10. M. Tian, *Liaoning chemical industry*, **28**(1), 27 (1999).
11. Ch. Wang, Techniques and Strategies of deratization, Beijing: Science and technology of China press, 83, 1990.
12. C. David, D. Gary, G. Erica, *TPesticide Science*, **43**(1), 83 (1995).
13. L. Huang, Preparation of organic intermediates, Beijing: Chemical Industry Press, 75, 1997
14. N. Fan, Organic Synthesis, Beijing: Beijing Institute of Technology Press, 53, 1993.
15. B. C. Saunders, G. J. Stacey, G. E. Wilding, *Chemical Society Reviews*, **6**, 773 (1949).
16. Z. Zhang, The principle of determining the toxicity of insecticides: methods and applications, Beijing: Beijing publishing house, 27, 1988.
17. A. Li, A. Lidi, O. Meifeng, *Chinese Journal of Vector Biology and Control*, **11**(1), 43 (2000).
18. S.M. Jay, E.C. Murphy, L. Shapiro, *Tetrahedron*, **72**(35), 5331 (2016).

Experimental study on dynamic shear modulus and damping ratio of CAS-1 lunar regolith simulant

F. Yu*, Sh.X. Chen, Y. Zhang, J. Li, Zh.J. Dai

State Key Laboratory of Geomechanics and Geotechnical Engineering, Institute of Rock and Soil Mechanics, Chinese Academy of Sciences, Wuhan, Hubei, 430071, China

Received September 1, 2017; Accepted December 19 2017

In the paper an experimental study of the dynamic parameters of CAS-1 lunar regolith stimulant is carried out, and the law by which different void ratios and confining pressures influence the dynamic shear modulus G and the damping ratio λ is analyzed. The test results show that, in the case of real lunar surface under very low stress levels and large void ratio, the dynamic shear modulus G is smaller, and the damping ratio λ is larger; the dynamic shear modulus diminishes quickly and the damping ratio increases sharply along with the increase of dynamic shear strain γ . Using the Hardin-Drnevich Model, the paper comes to the average fitted curve of the normalized dynamic shear modulus G/G_{\max} and the normalized damping ratio λ/λ_{\max} changing with γ on the conditions of different void ratios and confining pressures. The correlative equation between the maximum dynamic shear modulus G_{\max} , the maximum damping ratio λ_{\max} , the dynamic parameters such as the reference shear strain γ_r and the stress levels σ are discussed. Based on this, the range intervals of G_{\max} , λ_{\max} and γ_r within the coring and sampling depth (0~3m) of lunar regolith, as well as the recommended values of G/G_{\max} and λ corresponding to various shear strain are presented.

Key words: CAS-1 lunar regolith simulant, Dynamic shear modulus, Damping ratio, Dynamic shear modulus ratio

INTRODUCTION

As the key to the Lunar Exploration Phase 3 Program, “Lunar soil sampling” aims to obtain lunar regolith samples of stratification quality. However, in the process of sampling, a key problem may be the dynamic response resulting from interactions between the coring device and lunar regolith under particular environmental conditions of the lunar surface. Lunar regolith samples are so precious that even the United States, which already have 381 kg of lunar regolith samples, are very strict and prudent in using them. It is for this reason that the paper carefully chooses a “lunar regolith simulant” [1] with similar mechanical properties to real lunar soil in order to carry out this basic mechanical experimental study.

Scholars at home and abroad [1-12] have conducted relevant research on the physical and mechanical properties of different lunar regolith simulants. Zheng *et al.* [2] mainly studied the microwave dielectric property of CAS-1 lunar regolith simulant; Li *et al.* [7-8] discussed the basic physical and mechanical properties of the lunar regolith simulant made of volcanic ash in Jilin Province of China; Jiang *et al.* [9,10] explored the effects of grain grading and moisture content on the mechanical property of TJ-1 lunar regolith simulant, and carried out a relevant experimental study on the bearing characteristics of TJ-1 lunar regolith simulant. Haydar *et al.* [11] conducted experiments on the tensile property of JSC-1 lunar regolith

simulant and discussed how the weight and thickness of the lunar regolith simulant influence the tensile strength. Robert *et al.* [12] observed and analyzed the micro structure of lunar regolith simulant and performed studies on the improvement of mechanical properties of lunar regolith simulant.

All studies mentioned above are oriented to statics of lunar regolith simulant and focus mainly on its basic physical and mechanical properties. In contrast, few studies are about the dynamic properties or are relevant to lunar regolith coring. Therefore, the present paper will carry out a relevant basic dynamic experimental study by using the CAS-1 lunar regolith simulant (national standard sample) which is jointly developed by the Institute of Geochemistry and the National Astronomical Observatories, Chinese Academy of Sciences in replace of real lunar soil. The dynamic shear modulus and damping ratio are two primary parameters of the dynamic properties of soil and indispensable dynamic parameters for studying the dynamic properties of the soil layer. Consequently, carrying out a dynamic property analysis of dynamic shear modulus and damping ratio of lunar regolith simulant serves as a significant basis for studying the mutual effects between lunar regolith and sampling device.

The lunar surface features a special environment of waterless dryness and weightlessness (1/6 g), and the compactness looseness of lunar soil is differently distributed in breadth and depth. Based on the facts, the paper will use GDS resonant column apparatus to carry out dynamic property tests of lunar regolith simulant with different void

*To whom all correspondence should be sent:
E-mail: yufei8720@163.com

ratios in a series of different low confining pressures and regular confining pressure of the ground. It tries to find out the varying pattern of dynamic shear modulus and damping ratio of lunar regolith simulant subjected to dynamic load, and then uses theoretical analysis to work out the average varying curves of $G/G_{\max} - \gamma$ and $\lambda / \lambda_{\max} - \gamma$ and relevant dynamic parameter values. Furthermore, the paper quantitatively analyzes the law by which the confining pressure affects different test results, and finally, it presents the reference values of dynamic modulus and damping ratio within the strain range, resulting from change of confining pressure of lunar regolith simulant with different void ratios.

TEST SCHEME

Experimental equipment

The experimental apparatus to be used in the study is the Stokoe-type resonant column apparatus (RCA) produced by the British GDS Instruments Company. Its principle is elaborated in Bai's studies [13,14].

Experimental material

The experimental material is CAS-1 lunar regolith simulant (national standard sample) [2] successfully developed by the Institute of Geochemistry and the National Astronomical Observatories, Chinese Academy of Sciences. The particles of CAS-1 lunar regolith simulant are typical grinded particles in angular shape [2], similar to the particle morphology of the world famous JSC-1 lunar regolith simulant [3] which also has conspicuous grinding vestiges.

Through the specific gravity bottle test, the relative density G_s is worked out to be 2.66, which falls into the category of relative density (2.3~3.2) [15] of real soil particles. The gradation of particles of CAS-1 lunar regolith simulant is between the upper and lower limits of parts of real lunar soil.

Test method

In advance of the experiment, the test samples of lunar regolith simulant were oven-dried and cooled to room temperature. By controlling the void ratio of lunar regolith simulant, the void ratio e of lunar regolith simulant in two different degrees of looseness was set to be 1.0 and 0.8, respectively. According to the specific gravity, their corresponding initial dry density ρ_d was 1.33 g/cm³ and 1.48 g/cm³.

During the test, the confining pressure was set at two stress levels: low confining pressure (25, 50, 75, 100 kPa) and regular confining pressure (150, 200, 250, 300 kPa). The excitation voltage applies to CAS-1 lunar regolith simulant. Prior to the

confining pressure test at each level, stabilize for 30 minutes and do not conduct the tests until the LVDT sensor placed on the rotary plate detects the stability of axial settlement amount of the test samples.

TEST RESULTS

Under different stable confining pressures, the relation curves between dynamic shear modulus G and shear strain γ of lunar regolith simulant of different compactness are presented in Figure 1. As can be seen, G gradually diminishes with the increase of γ . When the shear strain is smaller, G diminishes more slowly, and when shear strain increases to a certain extent, the dynamic shear modulus begins to diminish quickly. The change of dynamic shear modulus along with shear strain reflects the non-linear and hysteretic law of the dynamic stress-strain relationship of the soil [16].

By comparing the test results under different confining pressures, it can be seen that G decreases with the decrease of confining pressure. On the condition of the same excitation voltage, the shear strain is larger and the trend of dynamic shear modulus diminishing with the increase of shear strain is even more conspicuous.

By comparing the test curves of different void ratios it can be seen that the larger the void ratio, the smaller is the dynamic shear modulus G . On the condition of the same excitation voltage, the shear strain is larger, and the dynamic shear modulus-shear strain curve is steeper. This means that G diminishes rapidly with the increase of shear strain and there is no obvious flatness.

Figure 2 shows the relation curves between damping ratio λ and shear strain γ of lunar regolith simulant with different compactness under the condition of different confining pressures. It can be seen from the diagram that the damping ratio increases with the increase of shear strain, and when shear strain increases to a certain extent, the damping ratio increases sharply. By comparing Figure 1 with Figure 2, it is seen that the stage during which the dynamic shear modulus diminishes quickly is exactly the stage where the damping ratio increases rapidly. By comparing the test results of different confining pressures, it can be seen that the smaller the confining pressure, the larger is the damping ratio. On the condition of a small shear strain, the effect of confining pressure on damping ratio is small, but with the increase of shear strain, the effect of confining pressure on damping ratio is dramatically enlarged.

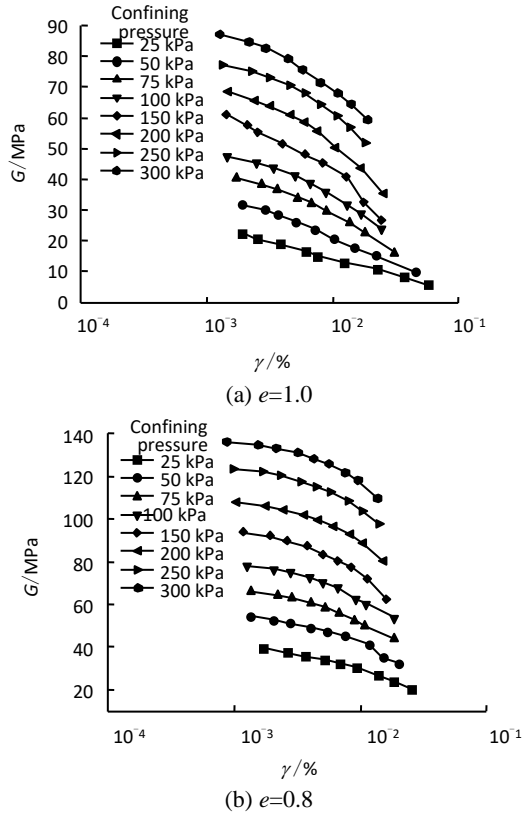


Fig. 1. Relationships between dynamic modulus G and shear strain γ of lunar regolith simulant.

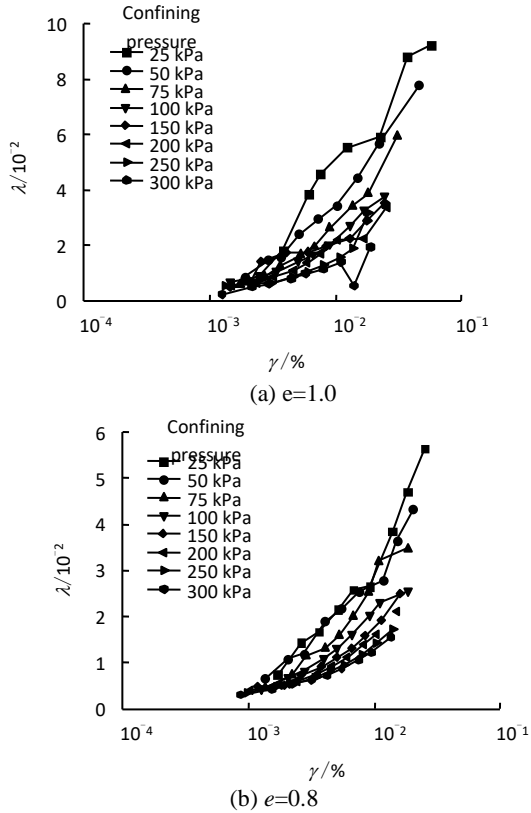


Fig. 2. Relationships between damping ratio λ and shear strain γ of lunar regolith simulant.

By comparing the test results of different void ratios, it can be seen that the larger the void ratio, the larger is the damping ratio, and the steeper is the

damping ratio-shear strain curve.

The above test results show that: the stress levels and compactness exert a significant influence on the dynamic shear modulus G and the damping ratio λ of lunar regolith simulant; under circumstances of real lunar surface, when the stress level is very low and the void ratio is large, the touch points between lunar soil particles are few, resulting in slow transmission of tress wave in lunar soil and are represented by a smaller G and a larger λ ; and with the increase of shear strain, the dynamic shear modulus diminishes rapidly whereas the damping ratio sharply increases. Such a property has significant effects on the lunar soil coring rate and completeness of the sample.

ANALYSIS OF TEST RESULTS

Analysis of test data

As is shown by the test results, the test curves are of good regularity. By using the famous Hardin-Drnevich [17] Hyperbolic Model, the dynamic stress-strain relationships can be described as follows:

$$G = \frac{\tau}{\gamma} = \frac{G_{\max}}{1 + \gamma/\gamma_r} \quad (1)$$

$$\lambda = \lambda_{\max} (1 - G/G_{\max}) \quad (2)$$

$$\gamma_r = \frac{\tau_{\max}}{G_{\max}} \quad (3)$$

Therefore,

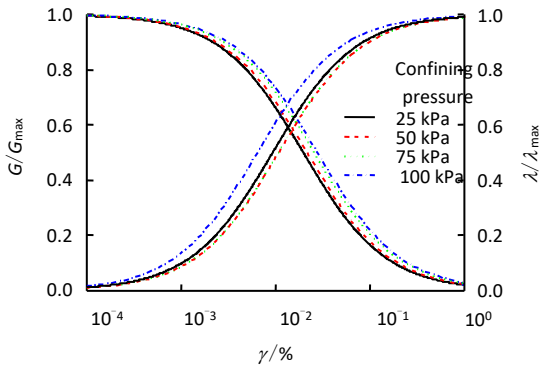
$$G/G_{\max} = \frac{1}{1 + \gamma/\gamma_r} \quad (4)$$

$$\lambda/\lambda_{\max} = \left(\frac{\gamma/\gamma_r}{1 + \gamma/\gamma_r} \right) \quad (5)$$

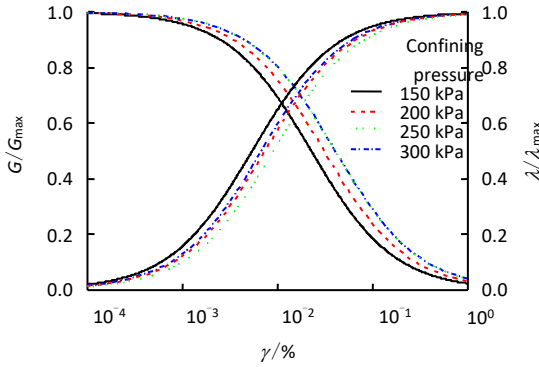
In the equation, τ and γ_r are dynamic shear stress and reference shear strain respectively; G_{\max} , λ_{\max} and τ_{\max} are the maximum dynamic shear modulus, the maximum damping ratio and the maximum dynamic shear stress, respectively. G_{\max} and λ_{\max} can be measured by the resonant column test, with the results shown in Table 2.

The relationships between dynamic shear modulus, damping ratio and shear strain were experimentally measured. Conduct regression analysis of them by using (1) ~ (5) and the least square method, and make equalization [18,19] of the results from different test regressions. The results are presented in Figure 4.

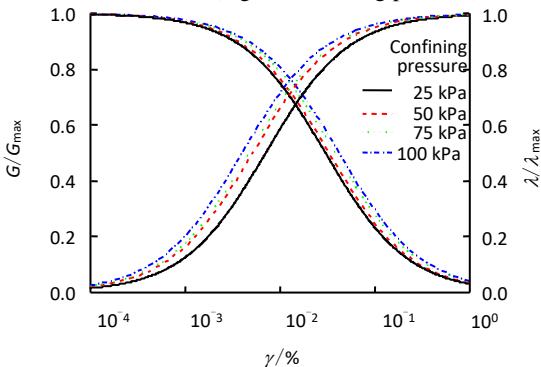
It follows from Figure 4 that the Hardin-Drnevich Hyperbolic Model is suitable for describing the dynamic constitutive relationship of lunar regolith simulant.



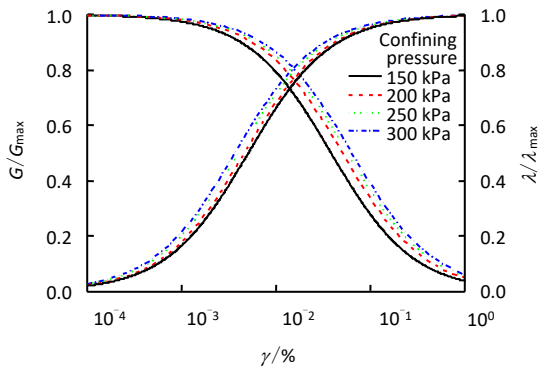
(a) $e=1.0$ (low confining pressure)



(b) $e=1.0$ (regular confining pressure)



(c) $e=0.8$ (low confining pressure)



(d) $e=0.8$ (regular confining pressure)

Fig. 4. G/G_{max} - γ and λ/λ_{max} - γ experimental curves of different pore ratios of lunar regolith simulant under different confining pressures.

Varying pattern of G_{max}

Figure 5 shows that G_{max} is in a good linear relationship with the confining pressure σ (25 ~

300kPa) and increases with the increase of confining pressure σ . The expression is as follows:

$$G_{max} = A_1 + B_1\sigma \quad (6)$$

In the equation, A_1 is the intercept of the straight lines; and B_1 is the slope of the straight lines. The values of A_1 and B_1 are listed in Table 3.

Therefore, in combination with Equation (6) and parameter values in Table 3, when the confining pressure ranges between 0~25 kPa, the values of G_{max} of the test samples with void ratios of 1.0 and 0.8 are derived reversely to be 21.908~27.583MPa and 38.518~47.006MPa, respectively.

Table 3. Fitting results of G_{max} and confining pressure σ .

Void ratio e	A_1	B_1
1.0	0.227	21.908
0.8	0.340	38.518

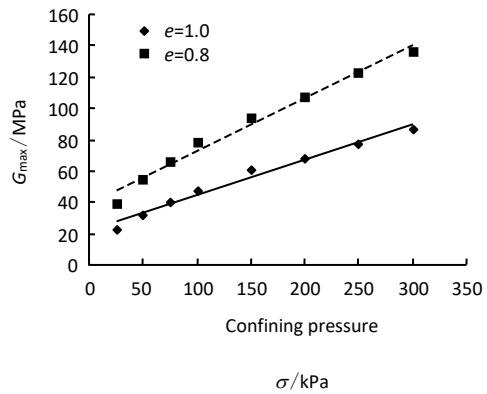


Fig. 5. Relationships between G_{max} and confining pressure σ .

Varying pattern of λ_{max}

Figure 6 shows the relationship between λ_{max} and confining pressure σ of CAS-1 lunar regolith simulant. Within the range of lower confining pressures (0~25kPa), λ_{max} diminishes rapidly with the increase of σ . Furthermore, it can be seen from the diagram that the two are in a linear relationship and λ_{max} diminishes faster in a linear way when the void ratio e of the test samples is 1.0; within the range of regular confining pressures (100 ~ 300kPa), the relationship between the maximum equivalent hysteretic viscoelastic damping ratio λ_{max} and σ of CAS-1 lunar regolith simulant undergoes obvious transitions. That is, λ_{max} shows a pattern of slow decrease with the increase of σ . Describe the pattern of how λ_{max} at these two stages varies with σ in a linear relationship, and the uniform expression is:

$$\lambda_{max} = A_2 + B_2\sigma \quad (7)$$

The values of A_2 and B_2 under low and regular confining pressures are listed in Table 4. In combination with Equation (7) and parameter values in Table 4, when the confining pressure

ranges between 0~25 kPa, the values of λ_{max} of the test samples with void ratio of 1.0 and 0.8 are derived reversely to be $11.240 \times 10^{-2} \sim 9.415 \times 10^{-2}$ and $6.530 \times 10^{-2} \sim 5.520 \times 10^{-2}$, respectively.

Table 4. Fitting results of λ_{max} and confining pressure σ .

Void ratio e	Low confining pressure (25~100 kPa)		Regular confining pressure (100~300 kPa)	
	A_2	B_2	A_2	B_2
	1.0	-0.073	11.240	-0.008
0.8	-0.040	6.530	-0.006	3.197

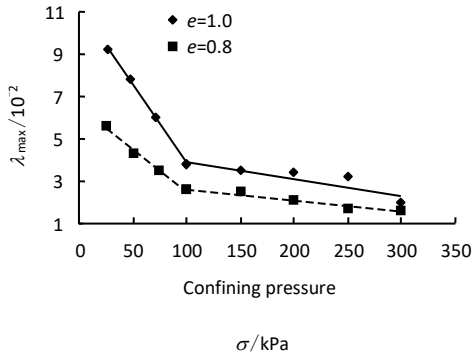


Fig. 6. Relationships between λ_{max} and confining pressure σ .

Varying pattern of the reference shear strain γ_r

Figure 7 shows that the reference shear strain γ_r (fitting parameter) is in good linear relationship with the confining pressure σ and increases with the increase of confining pressure σ . The uniform expression is as follows:

$$\gamma_r = A_3 + B_3\sigma \quad (8)$$

The values of A_3 and B_3 are listed in Table 5.

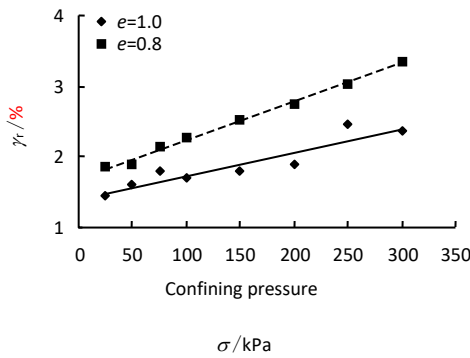


Fig. 7. Relationships between γ_r and confining pressure σ .

Table 5. Fitting results of γ_r and confining pressure σ .

Void ratio e	A_3	B_3
1.0	0.003	1.407
0.8	0.006	1.685

When the confining pressure ranges between 0~25 kPa, the values of γ_r of the test samples with void ratio of 1.0 and 0.8 are derived reversely to be 1.407% ~ 1.489% and 1.685% ~ 1.822%, respectively.

Recommended values of G/G_{max} and λ of lunar regolith simulant

In the process of sampling, with the gradual increase of the depth of lunar soil layer, the surrounding stress levels will be higher and higher. In this sense, the range values of confining pressure, to some extent reflect the sampling depth of lunar soil. In combination with the test results and fitting curves, in Table 6 relevant test results of test samples with void ratio being 1.0 and 0.8 respectively are listed as recommended values. Such test results are within the range of strain and are obtained from the change of confining pressure. This is of certain reference value for lunar soil sampling.

Table 6. Recommended values of G/G_{max} , λ and γ of the lunar regolith simulant (0-100 kPa).

Shear strain γ / %	$e=1.0$		$e=0.8$	
	G/G_{max}	$\lambda/10^{-2}$	G/G_{max}	$\lambda/10^{-2}$
0.001	1.000	0.710	1.000	0.570
0.003	0.917	1.220	0.954	1.100
0.005	0.818	2.310	0.886	1.770
0.007	0.758	2.770	0.829	2.200
0.01	0.679	3.400	0.727	3.140
0.02	0.547	4.750	0.617	4.000
0.04	0.369	6.680	0.508	6.130

CONCLUSIONS

(1) By conducting a comparative study of CAS-1 lunar regolith simulant and real lunar soil it was found out that the particle morphology and composition of CAS-1 lunar regolith simulant fall into the category of the particles of real lunar soil and is applicable to dynamic experimental research; by carrying out GDS resonant column experiments, the law by which different void ratios and confining pressures influence the dynamic shear modulus G and damping ratio γ is found out.

(2) The stress level and the compactness exert a significant effect on the dynamic G and λ . Under the conditions of real lunar surface, lower stress levels and larger void ratio, there will be smaller G and larger λ , and with the increase of shear strain, the dynamic shear modulus decreases rapidly whereas the damping ratio increases sharply. This property significantly affects the coring rate of lunar regolith and the completeness of the sample.

(3) By analyzing the test data using the Hardin-Drnevich Hyperbolic Model, the paper works out, for CAS-1 lunar regolith simulant with void ratios of 1.0 and 0.8 respectively, the average fitting curves between G/G_{\max} and λ/λ_{\max} with the change of γ under low and regular confining pressures, and relevant dynamic parameters.

(4) The paper quantitatively analyzes the correlative equation between the maximum dynamic shear modulus G_{\max} , maximum damping ratio λ_{\max} , reference shear strain γ_r and the confining pressure σ when the void ratio is 1.0 and 0.8, respectively, and accordingly, the values of G_{\max} , λ_{\max} and γ_r when the lunar regolith sampling depth ranges between 3~5m and the stress level is between 0 ~ 25kPa. To be specific, G_{\max} is 21.908 ~ 27.583MPa and 38.518 ~ 47.006MPa, respectively; λ_{\max} is $11.240 \times 10^{-2} \sim 9.415 \times 10^{-2}$ and $6.530 \times 10^{-2} \sim 5.520 \times 10^{-2}$, respectively; and γ_r is 1.407% ~ 1.489% and 1.685% ~ 1.822%, respectively.

The reference values of the dynamic parameters related to CAS-1 lunar regolith simulant given in the above research are of great reference for the ground model test and numerical simulation research in the process of lunar soil sampling.

REFERENCES

- 1.H. Kirkici, M.F. Rose, T. Chaloupka, *IEEE Transactions on Dielectrics and Electrical Insulation*, **3**(1), 119 (1996).
- 2.Y.C. Zheng, S.J. Wang, J.M. Feng, *Acta Mineralogica Sinica*, **27**(3/4), 571 (2007).
- 3.S.D. McKay, L.J. Carter, W.W. Woless, *Engineering, Construction, and Operations in Space IV*, New York, 857 (1994).
- 4.B.M. Willmann, W.W. Boles, S. McKay, *Aerospace Engineering*, **8**(2), 77 (1994).
- 5.J.L. Klosky, S. Sture, H.Y. Ko, *Proceedings of the Fifth International Conference on Space 96 Albuquerque*, New York, 680 (1996).
- 6.S.W. Perkins, C.R. Madson, *Journal of Aerospace Engineering*, **9**(1), 1 (1996).
- 7.J.Q. Li, M. Zou, Y. Jia, *Rock and Soil Mechanics*, **29**(6), 1557(2008).
- 8.M. Zou, J.Q. Li, G.M. Liu, *Rock and Soil Mechanics*, **32**(4), 1057 (2011).
- 9.M.J. Jiang, L.Q. Li, F. Liu, *Rock and Soil Mechanics*, **32**(7), 1924 (2011).
10. M.J. Jiang, Y.S. Dai, H. Zhang, *Rock and Soil Mechanics*, **34**(6), 1529 (2013).
11. A. Haydar, S. Stein, B. Susan, *Materials Science and Engineering*, **478**(1), 201 (2008).
12. J.G. Robert, A.G. Marty, A.F. Raymond, *American Institute of Aeronautics and Astronautics*, San Jose:[s. n.], (2006).
13. L.D. Bai, *Chinese Journal of Rock Mechanics and Engineering*, **30**(11), 2366 (2011).
14. L.D. Bai, *Berlin: School of Planning Building Environment*, Technical University of Berlin, 2011.
15. Y.C. Zheng, Z.Y. Ouyang, S.J. Wang, *Journal of Mineralogy and Petrology*, **24**(4), 14 (2004).
16. S.M. Wu, *Soil dynamics*, China Architecture and Building Press, 2000.
17. B.O. Hardin, V.P. Drnevich, *Journal of the Soil Mechanics and Foundations Division, ASCE*, **98**(6), 603 (1972).
18. X.M. Yuan, R. Sun, J. Sun, *Earthquake Engineering and Engineering Vibration*, **20**(4), 133 (2000).
19. H.T. Cai, Y.M. Li, B.S. Ou, *Rock and Soil Mechanics*, **31**(2), 361(2010)

Experimental study on the soil-water characteristic curve of the unsaturated loess in East Gansu province

T. Wang^{1,2}, Y.M Ding^{1,2*}, X.W Zhao^{1,2}, B.G Liu², Y. Song^{1,2,3}

¹ Architectural and Civil Engineering Institute, Weifang University of Science and Technology, Weifang 262700, China;

² Key laboratory of university facilities horticulture in shandong province, Weifang 262700, China;

³ Western Engineering Research Center of Disaster Mitigation in Civil Engineering of Ministry of Education, Lanzhou University of Technology, Lanzhou, 730050 PR China;

⁴ Key Laboratory of Disaster Prevention and Mitigation in Civil Engineering of Gansu Province, Lanzhou University of Technology, 730050, Lanzhou, China

Received September 8, 2017; Accepted December 19, 2017

In order to study the soil-water characteristic curve (SWCC) of unsaturated loess in East Gansu province, the effects of initial dry density and net mean stress on the SWCC of unsaturated loess were studied by a unsaturated soil triaxial apparatus. The results showed that when the matrix suction was the same, the moisture content of samples decreased with the increase in net mean stress. The larger the initial dry density, the smaller was the moisture reduction rate, and the higher was the final moisture content. Through the Van Genuchten model it was found that the residual moisture content θ_r decreases with the increase in net mean stress; the numerical values of the fitting parameters α and n do not change significantly as the net mean stress increases. The initial dry density mainly has an effect on the parameters θ_r and α of SWCC while the parameter n is not much affected.

Key words: Unsaturated loess; Soil-water characteristic curve; Matrix suction; Initial dry density; Net mean stress; VG model parameters

INTRODUCTION

As important as the research on consolidation curves in saturated soil mechanics, SWCC research is considered significant for explaining the character of unsaturated soils, subject to which the characteristics of permeability, deformation and strength and many mechanical model parameters of unsaturated soils are determined [1]. According to modern soil mechanics, the SWCC and its mathematical model are some of the constitutive relations of unsaturated soils [2-4]. Therefore, many scholars have made a large number of studies on the SWCC of unsaturated soils with the concept, theory and method based on which the constitutive relation is studied, and explained some characteristics of unsaturated soils in depth using SWCC. From a broad point of view, a SWCC refers to a curve that considers the effect of stress path and state [5].

In the research on the SWCC of unsaturated soils, many scholars have paid attention to the factors that influence the SWCC of unsaturated soils and made related research, obtaining many valuable achievements. Vanapalli *et al.* [6] made experiments on SWCC under different confining pressures of sandy soils of different water contents; by summarizing the results of the research made by the scholars including Black, Mitchell, Fleureau and Avalue, Zhang [7] discovered the rule of change in

air-entry value, residual volumetric water content and water holding capacity in relation to soils; through experiments under conditions of one-dimensional lateral confinement, Ng *et al.* [8] found that the SWCC hysteresis loop was reduced with the increase in initial compactness of soil. With two kinds of unsaturated loess of different initial dry density, Xu *et al.* [8] analyzed the effect of stress state on SWCC under conditions of non-pressure, pressure equalization, bias, loading and unloading stress.

For economic reasons, previous research was mainly made on the loess of the northwest regions including Lanzhou and Xi'an, but rarely on East Gansu [9-13]. With the further implementation of the national strategy of developing the western region and the Belt and Road incentive, since Qingyang is a pilot sponge city, Eastern Gansu is making efforts to boost the construction of infrastructures, in which case there undoubtedly will be many engineering problems, such as slope stability, landslide, design of bearing capacity of shallow foundations and subgrade filling. However, research is rarely made on the unsaturated loess of East Gansu, and many designs in terms of geotechnical engineering are mainly based on the research on those of Xi'an and Lanzhou as well as the actual experience in engineering, which does not fully conform to the actual situation of Eastern Gansu and will undoubtedly cause many potential

To whom all correspondence should be sent:
E-mail: wangteng2035@163.com.

safety hazards or wastes for local construction. That's why it is necessary to make systematic and in-depth research on the unsaturated loess of Eastern Gansu so as to provide experimental data and theoretical basis for local constructions [14-16].

To deeply reveal the SWCC of the unsaturated loess of Huangtuyuan in Eastern Gansu, in the present paper a test was made on the SWCC, from a broad point of view, of the unsaturated loess of Huangtuyuan with an unsaturated soil triaxial apparatus.

Test samples, instrument and method

Basic nature of soil samples

The soil samples for the test are taken from a construction site of Qingyang 7~9 m below the ground. As silty clays, the samples have a natural water content of 13.22% and an average natural density of 1.64 g/cm³, with a plastic limit WP of 17.50% and a liquid limit WL of 29.52%. Refer to Table 1 for the basic physical indicators of the undisturbed samples on the site.

Table.1 Physical indicators of Q3 loess

W (%)	P (g/cm ³)	ρ_d (g/cm ³)	G _s	e	W _L	W _p
13.22	1.64	1.43	2.71	0.895	17.5	29.52

Test instrument

Since the effect of the uniformity of triaxial samples is non-negligible [17], in the paper, special equipment (shown in Figure 1) was used to prepare triaxial samples by the static pressure method to ensure uniform dry density and water content. When the dry density conforms to the design, the test data are more representative.



Fig. 1. Triaxial test apparatus for unsaturated soils and sampling devices

Measuring matric suction is important for SWCC research, but most authors have not considered the stress state and volume deformation

Table 2. Test scheme of soil-water characteristic curves

No.	ρ_{sd} / g/cm ³	net mean stress/kPa	matrix suction /kPa
1	1.70	50	0,10,25,50,75,100,150,200,250,300,350,400,450
2	1.70	100	0,10,25,50,75,100,150,200,250,300,350,400
3	1.70	150	0,10,25,50,75,100,150,200,250,300,350
4	1.60	150	0,10,25,50,75,100,150,200,250,300,350
5	1.50	150	0,10,25,50,75,100,150,200,250,300,350

of samples in the testing process [18]. The proposed FLSY10-1 stress-strain unsaturated soil triaxial apparatus may be used to study the effect of net mean stress on SWCC, in which the change in volume is considered.

Test method

From a broad point of view, a SWCC refers to a curve that considers the effect of stress path and state [19]. In the paper, the unsaturated soil triaxial apparatus was used to study the effect of net mean stress and initial dry density on SWCC. When the initial dry density was 1.70 g/cm³, the net mean stress was 50 kPa, 100 kPa and 150 kPa respectively; when the net mean stress was 150 kPa, the initial dry density was 1.50 g/cm³, 1.60 g/cm³ and 1.70 g/cm³, respectively. The test was made on saturated triaxial samples. The detailed method is listed in Table 2.

As both pore air and pore water exist in unsaturated soils and move slowly, it will take a long time to make the pressure of pore air and pore water become stable in the testing process. Considering the weak permeability of unsaturated soils, it is important to establish a standard for sample deformation and drainage stability under the matric suction at each level. According to related studies, the stability is subject to the following standard: the volume of change and water discharge is less than 0.01 cm³ within 2 h, and it takes no less than 48 h to make the test on matric suction at each level, and such SWCC lasts about one month (the specific period is subject to the final matric suction designed in the test).

Test results and analysis

Effect of net mean stress on SWCC

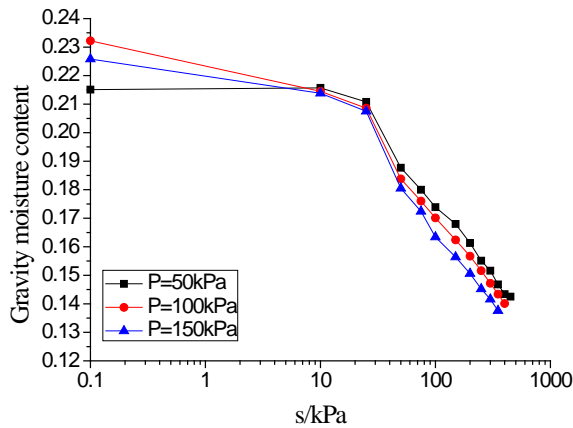
Since the volume of samples in the SWCC test is variable, the gravitational water content of the samples is not fully linear to the volumetric water content under the matric suction at each level. Particularly, according to ref. [20], if no consideration is given to the change in the volume of soil samples in the test, the volumetric water content obtained using the mass-based water content through the equation of $\theta = (\rho_d / \rho_w)w$ is lower than the actual content, thus increasing the matric suction by about 100 kPa.

The unsaturated soil triaxial apparatus proposed may be used to directly obtain the variation in the volume of the samples at any time, thus avoiding any error arising from the change in the volume in the testing process. The gravitational water content w_i and the volumetric water content θ_i of the samples under the matric suction at the i^{th} level were calculated as:

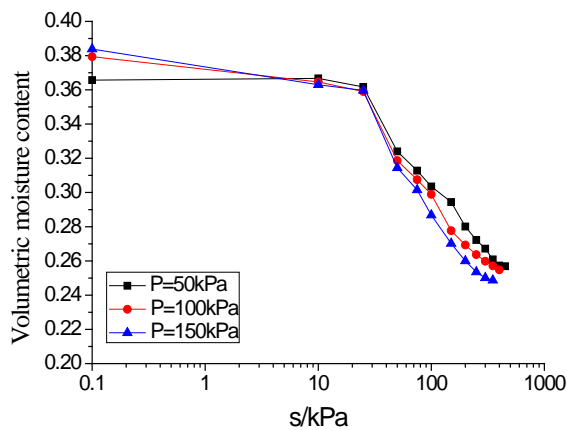
$$w_i = \frac{m_{wi}}{m_s} = \frac{m_{wo} - \Delta m_i}{m_s} = \frac{\rho_d V_o w_o - \Delta m_i}{\rho_d V_o} \quad (1)$$

$$\theta_i = \frac{V_{wi}}{V_i} = \frac{\rho_d V_o w_o - \Delta m_i}{(V_o - \Delta V_i) \rho_w} \quad (2)$$

wherein, V_o and m_{wo} refer to the initial volume and initial water content of the samples, respectively; ΔV and Δm_i refer to the volume of change in and water discharged from the samples under the matric suction at the i^{th} level, respectively.



(a) Presentation with gravity moisture content



(b) Presentation with volumetric moisture content

Fig. 2. SWCC under different net stress

As it takes a long time to make the SWCC test, inevitably, there is a difference between the water discharge measured with the data collection system and the actual discharge. According to the actual

water discharge (difference between the initial mass and the mass after the test), a correction was made to the measured value under the matric suction at each level. Considering the error in measuring the water discharge arising out of the environmental factors including temperature next to the drain pipe of the unsaturated soil triaxial apparatus, a drain pipe of the same specification as the pipe was provided to correct for the evaporation of water in the drain pipe in the testing process.

In the test, the gravitational water content w and the volumetric water content θ were used to express SWCCs under different net mean stresses. The test result is expressed in a semilog coordinate system as shown in Figure 2.

According to Figure 2, there are some differences between the SWCCs expressed with volumetric water content and gravitational water content, but both present roughly the same form. A SWCC under each net mean stress is divided into 2 different sections based on the demarcation point of the matric suction s which equals 25 kPa. In the first section, the water content slightly changes with the increase in matric suction. This is because the initial water content in the samples is nearly saturated, and the imposed pore pressure u_a is small, making the gas phase in soils suspended in water as closed bubbles and flow with water, in which case the soils are nearly saturated. In the second section, when the matric suction reaches a value (air-entry value of soils), the water content approximately linearly decreases with the increase in matric suction. This is because when air enters the soil and occupies a large pore channel in the soil due to the increase in pore pressure, more water is discharged from the soil with the further increase in air pressure and the water content rapidly decreases, in which case the gas phases in the soil are connected partly and internally. In relation to typical soil-water characteristics, the test result is mainly presented in the first and second sections of the typical SWCC. Due to the limit of the test instrument, the air-entry value of the terracotta panel is 500 kPa, leaving it impossible to measure the residual water content and present the third section of the typical SWCC.

Through comparison between the three SWCCs under different net mean stresses, the initial water contents of the three samples are slightly different due to an error in the process of sample saturation, which is a secondary factor compared with the net mean stress and is negligible. According to further analyses, when the matric suction is less than 25 kPa, the three are slightly different, which might arise from the low matric suction; when the matric suction exceeds 25 kPa, the three become

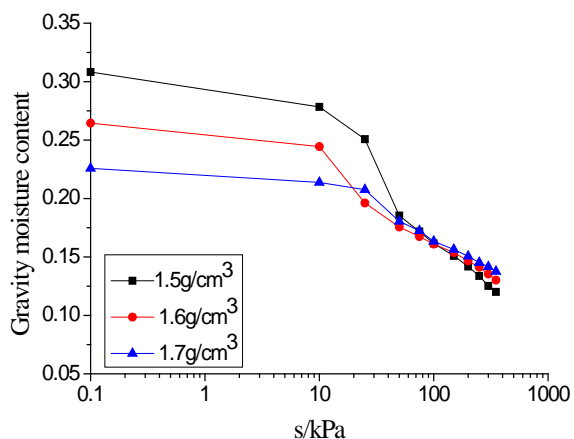
increasingly different, and move to the bottom left with the increase of net mean stress, that is, in the event of same matric suction, the water content decreases with the increase in net mean stress.

Particularly, the demarcation point of 25 kPa is not necessarily the air-entry value of soils, which needs to be obtained through further reduction of the imposed air pressure or fitting with a proper mathematical model of SWCC.

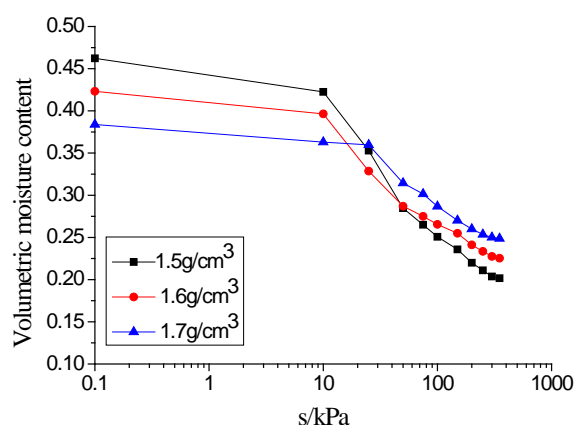
Effect of initial dry density on SWCC

The SWCCs at different initial dry densities are shown in Figure 3.

Through comparison between Figures 3(a) and 3(b), there are some differences between the SWCCs expressed with gravitational water content and volumetric water content in the test points in the upper part and the points of intersection, which arise from the difference in initial dry density and the continuous change in sample volume in the testing process.



(a) Presentation with gravity moisture content



(b) Presentation with volumetric moisture content

Fig. 3. SWCC under different dry density

However, the two figures present roughly the same form, so an analysis is mainly made on the effect of initial dry density on the SWCC expressed with volumetric water content.

According to Figure 3, similar to the SWCCs under different mean stresses, each of the SWCCs at different initial dry densities is divided into 2 different sections based on a demarcation point. When the initial dry density $\rho_d=1.5 \text{ g/cm}^3$ and $\rho_d=1.6 \text{ g/cm}^3$, the demarcation point $s=10 \text{ kPa}$; when $\rho_d=1.7 \text{ g/cm}^3$, $s=25 \text{ kPa}$. In the first section, with the increase in matric suction, the water content slightly changes; in the second section, when the matric suction reaches a certain value (air-entry value of soils), the water content approximately linearly decreases with the increase in matric suction. The mechanism of the interaction between matric suction and water content is the same as that for net mean stress.

According to Figure 3, there are large differences between the SWCCs at different initial dry densities. When the initial dry density $\rho_d=1.5 \text{ g/cm}^3$, the initial water content is maximum, followed by that when $\rho_d=1.6 \text{ g/cm}^3$; when $\rho_d=1.7 \text{ g/cm}^3$, the initial water content is minimum. This is because the water contents in saturated samples are different due to the difference in soil compactness and the more compact the soils, the lower becomes the water content. When the matric suction is large, the water content in the soils of the initial dry density ρ_d of 1.7 g/cm^3 is maximum, showing that the soils of high dry density have a strong ability to hold water. From qualitative point of view, although no air-entry value has been measured through the test, we may infer that the value is maximum when $\rho_d=1.7 \text{ g/cm}^3$ based on the demarcation points and forms of the SWCCs at different initial dry densities. Moreover, following the maximum slope in the second section when $\rho_d=1.5 \text{ g/cm}^3$, the slope when $\rho_d=1.6 \text{ g/cm}^3$ is greater than that when $\rho_d=1.7 \text{ g/cm}^3$, and the SWCC slope (dehumidification rate) is maximum in the event of low dry density, that is, with the increase in matric suction, the less the dry density, the higher becomes the dehumidification rate (dewatering rate). There are large differences between the samples of same volumetric water content and different dry densities in matric suction.

Accordingly, in relation to remolded loess, dry density has a great effect on SWCC, for the reason that the change in density leads to a change in the pore size of soils and the radius of curvature of the meniscus in soils. With the increase in dry density, the void ratio is reduced, thus leaving it more difficult for air to enter and depart from soils and for water to discharge from soils. Therefore, the air-entry value is large for samples of high dry density. In addition, the dehumidification rate is low when the degree of saturation of the samples of high

initial dry density decreases, so the water content in the samples of high initial dry density is high in case of large matric suction.

Results of fitting with Van Genuchten model and its analysis

Through analysis of the results of the SWCC test in the event of different net mean stresses and initial dry densities, it is highly nonlinear. In the process of fitting data with different mathematical models, the authors found that some indicators which could not be obtained through tests may be obtained through fitting of the test results (volumetric water contents under different matric suctions) with the Van Genuchten model, thus comprehensively analyzing the effect of net mean stress and initial dry density on SWCC.

Introduction to Van Genuchten model

Through research on SWCC, in 1980 Van Genuchten *et al.* proposed an expression between volumetric water content and matric suction, which is called Van Genuchten (hereinafter called “VG”) model. The model is a mathematical equation in the form of power function. Due to its definite parameters and wide applicability, it is widely used in the fields of geotechnical engineering and soil research [21]. The expression is as follows:

$$\theta = \theta_r + \frac{\theta_s - \theta_r}{[1 + (\alpha\psi)^n]^{(1-m)}} \quad (3)$$

wherein, θ —volumetric moisture content; θ_r —residual moisture content; θ_s —saturated water content; ψ —the matrix suction of soil; α , m , n —fitting parameters; α relates to the air-entry value and is expressed in kPa^{-1} ; m and n relate to the curve form.

Afterwards, Van Genuchten *et al.* found the correlation between m and n (i.e. $m=1-1/n$). Through simplification of the above equation into equation (4), the VG model becomes more applicable.

$$\theta = \theta_r + \frac{\theta_s - \theta_r}{[1 + (\alpha\psi)^n]^{(1-1/n)}} \quad (4)$$

Fitting result in the event of different net mean stresses

In combination with RETC, with the user-defined function module of the software of Origin, the VG model is defined to fit the data obtained from the test. To ensure the fitting accuracy, evaluation is made on the fitting effect based on $\text{Adj.}R^2$ (adjust R square).

According to Figure 4, the curve fitted with the VG model approximately conforms to the measured data. In Table 3, $\text{Adj.}R^2$ is over 0.93, showing that the test data may be well fitted and SWCC may be

described with the VG model.

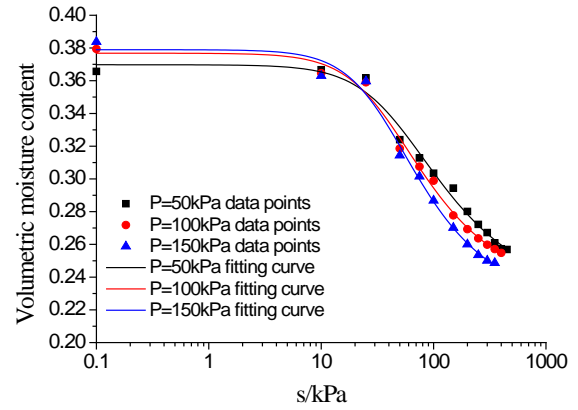


Fig. 4. Fitting curves of samples under different net stress

Table. 3 Fitting parameters of test data under different net stress

Sample status	θ_s	θ_r	α	n	Adj. R^2
$P' = 50\text{kPa}$	0.3829	0.2302	0.0272	1.7520	0.9664
$P' = 100\text{kPa}$	0.3812	0.2271	0.0321	1.8310	0.9312
$P' = 150\text{kPa}$	0.3790	0.2231	0.0283	1.8093	0.9875

SWCC form may be reflected by fitting parameters. According to the fitting parameters in Table 3, with the increase in net mean stress, the residual volumetric water content θ_r gradually decreases but slightly changes, and the fitting parameters α and n slightly change, making it impossible to reflect an obvious rule of change. This might be because net mean stress has no great effect on SWCC and there is a small number of test objects and a certain error in fitting.

Fitting results in the event of different initial dry densities

With the user-defined function module of the Origin software, the test data in the event of different initial dry densities were fitted by the least square method, yielding the result shown in Figure 5. The parameters fitted with the VG model are listed in Table 4.

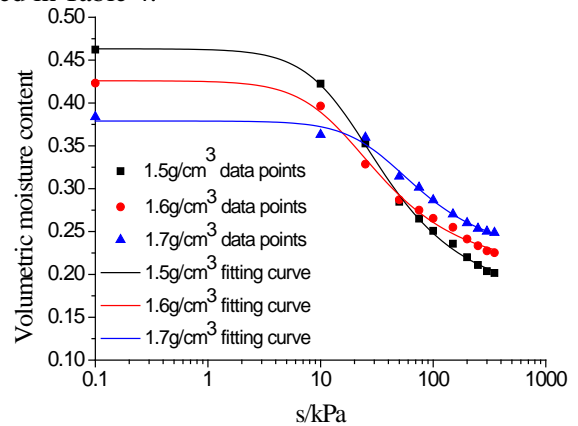


Fig. 5. Fitting curves of samples with different initial dry density

Table 4 Fitting parameters of test data under different initial dry density

Sample status	θ_s	θ_r	α	n	Adj.R ²
$\rho_d=1.5\text{g/cm}^3$	0.4632	0.1723	0.0632	1.7217	0.9976
$\rho_d=1.6\text{g/cm}^3$	0.4259	0.2057	0.0607	1.7316	0.9924
$\rho_d=1.7\text{g/cm}^3$	0.3790	0.2231	0.0283	1.8093	0.9875

According to Figure 5, in relation to the three curves, the fitting effect is good and the Adj.R² is high, being over 0.98.

Different sample states are subject to the fitting parameters and SWCC form. According to Table 4, when the initial dry density is high, the saturated volumetric water content θ_s is low. This is because the pore volume of the samples of high dry density is low and the water content in the samples is accordingly low; the larger the initial dry density, the higher becomes the residual volumetric water content θ_r ; with the increase in initial dry density, the fitting parameter α which relates to the air-entry value of soils decreases, but the fitting parameter n which relates to the curve form slightly changes, which is consistent with the result of the research made by Wang *et al.* [22]. Accordingly, the effect of initial dry density on SWCC is mainly subject to the parameters of θ_r (residual volumetric water content) and α (relevant to air-entry value), but slightly depends on n . In other words, the larger the initial dry density, the lower become the pore size and the radius of curvature of the capillary meniscus, making larger pressure become necessary for air to enter soil pores and thus leaving the air-entry value become greater. Similarly, when the matric suction is high and the volumetric water content keeps the same, the higher the initial dry density, the larger becomes the matric suction. Furthermore, the soils of high initial dry density are of low permeability, so the residual volumetric water content is high.

CONCLUSIONS

(1) Measuring matrix suction is important for SWCC research, but most authors have not considered the stress state and volume deformation of samples in the testing process. The proposed FLSY10-1 stress-strain unsaturated soil triaxial apparatus may be used to study the effect of net mean stress on SWCC by considering the change in volume.

(2) From a broad point of view, each of the SWCCs which consider the effect of mean stress and density is divided into 2 sections based on a demarcation point, of which the one that considers net mean stress shows that when the matric suction is low, there is little difference between curves, and when the matric suction exceeds the air-entry value

to a definite extent, the water content decreases with the increase in net mean stress. The one that considers density shows that the greater the initial dry density, the lower becomes the dehumidification rate (dewatering rate) and the higher becomes the water content accordingly; through comparison between the SWCCs at different initial dry densities in form and demarcation point, the air-entry value is maximum when $\rho_d=1.7\text{g/cm}^3$.

(3) Through fitting of the test data with the Van Genuchten model as a 4-parameter equation, based on the evaluation made on the fitting effect with Adj.R², we found that this model may be used to fit the SWCC of unsaturated loess in Eastern Gansu. From a broad point of view, the fitting result in relation to the SWCC which considers the effect of net mean stress shows that with the increase in net mean stress, the residual volumetric water content θ_r reduces but slightly changes, and the fitting parameters α and n slightly change; the fitting result in relation to the SWCC which considers the effect of density is mainly subject to the parameters of θ_r (residual volumetric water content) and α (relevant to air-entry value), but slightly depends on n .

REFERENCES

1. Z.H. Zhang, C.G. Zhao, M. Deng, *Rock and Soil Mechanics*, **4**(26), 667 (2005).
2. T. Wang, M.G. Zhou, G.K. Zhou, X. Yang. *Journal of Residuals Science & Technology*, **6**(13), 371 (2016)
3. J. Cote, J. M. Konrad, *Proceedings of the 3rd International Conference on Unsaturated Soils, Recife, Brazil*, 255 (2002).
4. M.R. Zhou, J.W. Wang, T. Wang, X. Yang. *Journal of Architecture and Civil Engineering*, **1**(34), 99 (2017).
5. T. Sugii, K. Yamada, T. Kondou, *Proceedings of the 3rd International Conference on Unsaturated Soils, Recife, Brazil*, 10 (2002).
6. X.D. Zhang, *Bei Jing, Beijing Jiaotong University*, 2010.
7. C. W. W. Ng, Y. W. Pang, *Journal of Geotechnical and Geoenvironmental Engineering*, **2**(126), 157 (2000).
8. M. Xu, F.Y. Liu, D.Y. Xie, *Journal of Shaanxi Water Power*, **3**(12), 8 (1996).
9. X.D. Zhang, C.G. Zhao, G.Q. Cai, Y. Liu, *Rock and Soil Mechanics*, **5**(31), 1463 (2010).
10. H. Chen, C.F. Wei, F.F. Chen, J.F. Zeng, *Rock and Soil Mechanics*, **1**(34), 128 (2013).
11. J.H. Zhang, Z.H. Chen, *Chinese Journal of Rock Mechanics and Engineering*, **Z2**(32), 3987 (2013).
12. Z.H. Chen, D.Y. Xie, Y.Sh. Wang, *Yantu Gongcheng Xuebao*, **3**(15), **9** (1993).
13. H., Z.H. Chen, G. Li. *Rock and Soil Mechanics*, **4**(21), 316 (2000).

14. C.G. Bao, B.W. Gong, L.T. Zhan. In: *Proceedings of 2nd International Conference on Unsaturated soils*. Beijing: International Academic Publishers, 71 (1998).
15. ZH. J. Shen. *Chinese Journal of Geotechnical Engineering*, **1**(18), 1 (1996).
16. M. Aubertin, M. Mbonimpa, B. Bussière, *Canadian Geotechnical Journal*, **6**(40), 1104 (2003).
17. L. Zhang, ZH.H. Chen, F.X. Zhou, SH.G. Sun, SH.X. Hu, ZH. H. Yao. *Chinese Journal of Geotechnical Engineering*, **39**(5), 906 (2017).
18. S. K. Vanapalli, D. G. Fredlund, D. E. Pufahl, *Geotechnical Testing Journal*, **3**(19), 259 (1996).
19. Terzaghi K. *New York: Wiley*, 1943.
20. F. Chu, SH.J. Shao, C.L. Chen. *Chinese Journal of Rock Mechanics and Engineering*, **2**(33), 413 (2014).
21. R. Sommer, C. Stoeckle, *Journal of Irrigation and Drainage Engineering*, **8**(136), 559 (2010)
22. T.Y. Zhao, J.F. Wang. *Journal of Central South University (Science and Technology)*, **6**(43), 2445 (2012).

Temperature and wear characteristics of TBR tread rubber and its constitutive characterization

L. Ma^{1*}, H. Yin^{1,2}, Z. Wang^{1*}, J. Wu², Z. Wang², Sh. Hu¹, Zh. Miao¹

¹ School of Electromechanical Engineering, Qingdao University of Science and Technology, Qingdao 26606, China

² Hangzhou Zhongce Rubber Company Limited, Zhejiang Hangzhou 310018, China

Received, March 8, 2017; Accepted December 19, 2017

An auxiliary heating device for rubber wheels is developed based on the Akron wear testing machine. The temperature dependence of the rubber wear is analyzed. The results demonstrate that the relationship between the wear and temperature can be described by a quadratic polynomial function. The wear resistance at high temperature is related to the glass transition temperature of the rubber. At high temperature, butadiene rubber (BR) exhibits higher wear resistance than natural rubber (NR) and styrene butadiene rubber (SBR), due to its higher glass transition temperature. In addition, the friction energy of the LAT100 wear is calculated by the finite element method. A power function relationship between the wear and the friction energy is obtained by fitting the test data. Finally, a comprehensive expression of the rubber wear as a function of temperature is set up based on the relationship between temperature, wear volume, and frictional energy. This work improves the thermo-mechanical coupling model of rubber wear, and provides a new theoretical basis for more accurate analysis of rubber wear.

Keywords: Wear, Rubber, Temperature, Thermo-mechanical coupling model

OBJECTIVES AND BACKGROUND

Rubber products such as tires take advantage of their viscoelasticity and large nonlinear deformation capability. The investigation of tire wear was originally initiated by studying the mechanism of rubber wear. Grosch and Schallamach [1], Savkoor [2], Schallamach [3, 4] and a few other scholars first conducted a systematic research on rubber wear. Grosch and Schallamach studied the relationship between the temperature and velocity of rubber friction, and analyzed the surface pattern of sliding rubber wear (Schallamach wear pattern). Savkoor and later Persson *et al.* [5, 6] performed comprehensive research on the bond friction theory of rubber. In recent years, scholars worldwide focus on the aspects of material improvement and material aging properties [7-13]. These studies provide guidelines and detailed understanding of rubber wear mechanisms. Nevertheless, due to the complexity of the rubber wear process, it is necessary to study the thermodynamic behavior of rubber wear. Scholars all over the world have done a lot of research on this topic. The tire is usually working at much higher temperature than the ambient temperature, and the wear performance is lowered at high temperature. Thus, it is very important to study the effect of temperature on the wear properties. This paper chose truck bus radial (TBR) tire tread rubber as the test subject, and used a newly-developed temperature abrasion test device

to test the temperature of rubber abrasion wear. The wear model of rubber can be characterized as a function of friction energy and temperature.

MODELING OF THE RELATIONSHIP BETWEEN RUBBER ABRASION AND TEMPERATURE

Data regression analysis was conducted based on a variable temperature wear experiment of the rubber. A quadratic polynomial mathematical model describing the relationship between rubber wear and temperature was established.

Experiment

Testing equipment

Based on the Akron wear testing machine, an auxiliary equipment and experimental method of variable temperature wear were developed (shown in Figure 1). The experimental method was different from the traditional rubber wear testing method which performs the experiment at high temperature through changing the ambient temperature. In this test, the way of heating the rubber wheel was closer to the actual working conditions of the tires. In addition to the functions of the traditional Akron wear machine, the main new features are as below:

(i) A heating wire was used to heat the rubber wheel. A thermocouple was used to measure the temperature of the rubber wheel. The temperature was controlled by the temperature control instrument. The temperature of the rubber wheels ranges from room temperature to 100°C. The ambient temperature for the experiment was 25°C.

To whom all correspondence should be sent:
E-mail: wzp_ww1@163.com

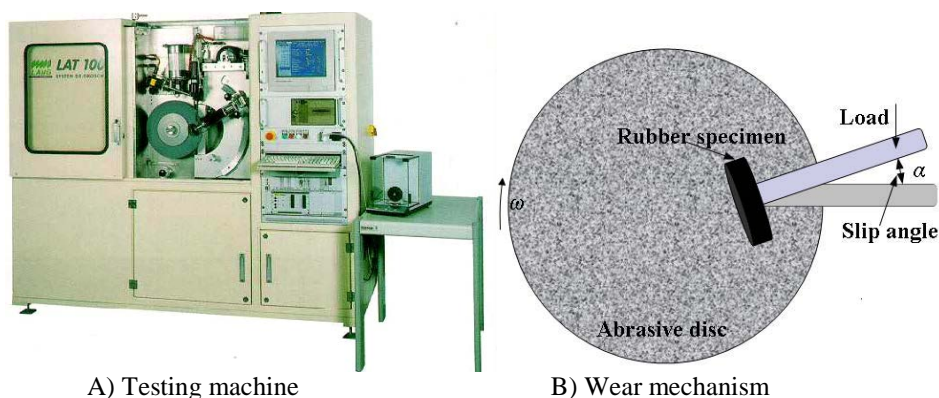


Fig. 1. LAT100 wear test machine and schematic

(ii) A sand dispersing device was added, and the type of sand was properly chosen to solve the problem of surface adhesion of rubber wheel crumbles which may affect the precision of the test.

(iii) The wear rubber sample and the rubber wheel were pasted together by low temperature sulfide curing to prevent slippage of the rubber sample from the rubber wheel at high temperature.

Experimental material

Four TBR tread rubbers were tested: A011 (NR+N234+SiO₂), A019 (NR+N234), A015 (NR+N134), A017(NR+BR+N234).

RESULTS AND DISCUSSION

The variable temperature wear testing device was used for the rubber wear test under different temperatures. The test results are analyzed and discussed below.

The Akron standard rotation distance was 1.61 km. We took half the distance for the grinding test, which is 1709 rotations. Each test was performed two times to get an average of the wear data. The experimental data are shown in Table 1.

Because the Akron wear takes place at low speed and moderate temperature, the surface temperature cannot reach above 40°C. In order to eliminate the effect of friction heat between the rubber wheel and grinding wheel in the experiments, the experimental temperature was set above 40°C when the relationship between the temperature and wear was analyzed. Figure 2 shows the relationship between the wear and temperature. The dependence of the wear on temperature can be described by a quadratic polynomial function which has a decent fitting accuracy. The four types of TBR tread rubber have different using purposes. A011, A015, A019, A017 are intended for low rolling resistance, integrated pavement, high-speed road, and rough road, respectively. Through the analysis of the data (Table 1 and Figure 2), we concluded that at low heat tread temperature, A011 was the most sensitive while A017 used for the rough road was the least sensitive to the temperature.

Due to the use of NR and BR in the A017 tread rubber and the higher glass transition temperature of BR, its high temperature wear resistance is reasonable. It can be predicted that the high

Table 1. The wear performance of different TBR tread rubbers at different temperatures (load of 26.7N, angle of 15°)

Distance, m	Temperature, °C	A011, g	A015, g	A017, g	A019, g	A015-1, g	A017-1, g	A019-1, g
1000	40	0.12854	0.11464	0.09779	0.11046	0.07737	0.06225	0.07118
1000	60	0.15220	0.13597	0.15559	0.13454	0.10019	0.08323	0.08738
1000	70	0.19589	0.17366	0.16259	0.16510	0.13096	0.10803	0.13263
1000	80	0.23709	0.21136	0.17829	0.19319	0.15428	0.12911	0.17415

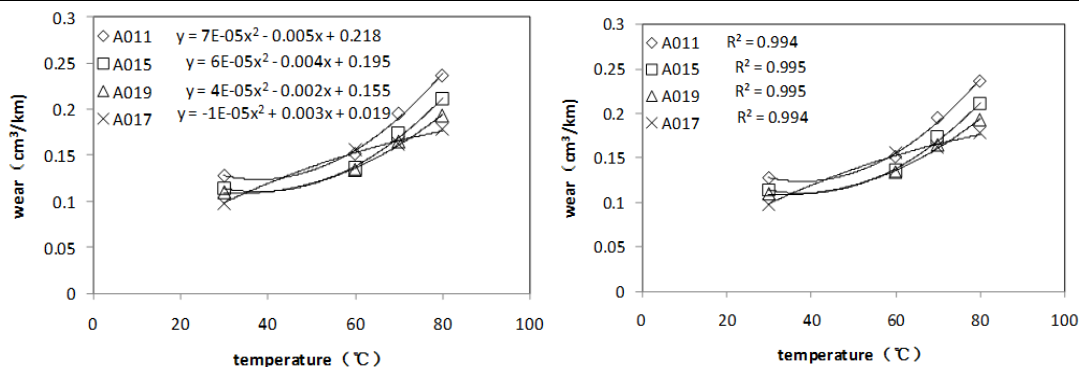


Fig. 2. Four types of tread rubber wear as a function of temperature under 26.7N, 15°, 76 r/min

temperature wear resistance of SBR will be poor, because its glass transition temperature is lower than that of NR. Nevertheless, things can be different in the actual use of the tires. By comparing the wear resistances at the same temperature, BR will cause the tire to roll at a higher temperature in the actual use due to the higher heat generation. The wear resistance also needs to be reevaluated.

Meanwhile, the wear resistance is only one of the important parameters of the tire performance. High temperature will lead to more quality-related problems of the tire, which is perhaps the reason that very few BR are applied to high-speed and long-distance tires for truck and passenger cars.

The experimental results show that there is a quadratic polynomial relationship between the rubber wear and the temperature:

$$A_T = a \cdot T^2 + b \cdot T + c \quad (1)$$

where A_T is wear quality (g), T is rubber wheel temperature (°C), a , b are care fitting coefficients. The sensitivity analysis of the temperature can be performed by a simple first-order and second-order derivative. Smaller a and b correspond to better wear resistance at high temperature.

LAT100 WEAR TEST OF RUBBER MATERIAL AND CALCULATION OF FRICTION ENERGY

LAT100 wear test

(1) Test device: we used a LAT100 abrasion rubber wear testing machine made by VMI company, Holland, which is widely used in rubber industry (Figure 3).

(2) Test principle: the contact surface of the LAT100 abrasion machine is a rotary disc. A certain angle and load is set for the rubber wheel, the rotary disc drives the rubber wheel to rotate at the set speed. Infrared scanning and force sensor are used to

measure the longitudinal force, lateral force, and the surface temperature. The amount of the rubber wear is determined by weighing the debris that the rubber wheel was ground out during the test (Figure 3).



Fig. 3. Finite element modeling of the test

(3) Test conditions: load (N): 30. speed (km/h): 5, 10, 15, 20. deflection (°): 0°, 15, 30°, 40°. Rubber wheel: Φ 80 mm \times δ 17 mm. Three types of samples were prepared for each experimental condition. The total data points were 48. Ambient temperature: 25°C.

EXPERIMENTAL RESULTS

The experimental results are shown in Table 2.

Finite element analysis of the mechanical properties of rubber LAT100

Finite element modeling

The finite element model of tire wear was established based on ABAQUS and is shown in Figure 4. The linear elastic model was adopted to describe the constitutive relation of the rubber. Element type of CAX4R was adopted to describe the rubber property. The number of elements per section was 829. The number of sections was 74 and the total number of elements was 61346. The contact surface of the grinding wheel was set as rigid body. The friction coefficient was 0.40. Wear disc rotated with the angular velocity ω . The load was exerted on the center of the rubber wheel.

Table 2 Wear results of LAT100 and friction energy simulation data

Slip angle, °	Velocity, km/h	Distance, m	Weight loss, g	Surface temperature, °C	Frictional energy density, J/m ²
0	5	1000	0.0006	22.6	1076.9
0	10	1000	0.0007	24.6	1915.9
0	15	1000	0.0020	25.1	3314.9
0	20	1000	0.0028	25.4	4421.5
15	5	1000	0.0444	32.3	284268.9
15	10	1000	0.0746	37.4	568557.3
15	15	1000	0.0679	43.9	852838.4
15	20	1000	0.0817	48.3	926282
30	5	1000	0.1634	41.0	623953.3
30	10	1000	0.1731	41.7	1017191
30	15	1000	0.2778	51.0	1525796
30	20	1000	0.4078	44.4	2034337
40	5	1000	0.1448	27.7	898665.4
40	10	1000	0.2096	30.3	1822607
40	15	1000	0.4108	32.4	2228761
40	20	1000	0.7877	32.5	2971692

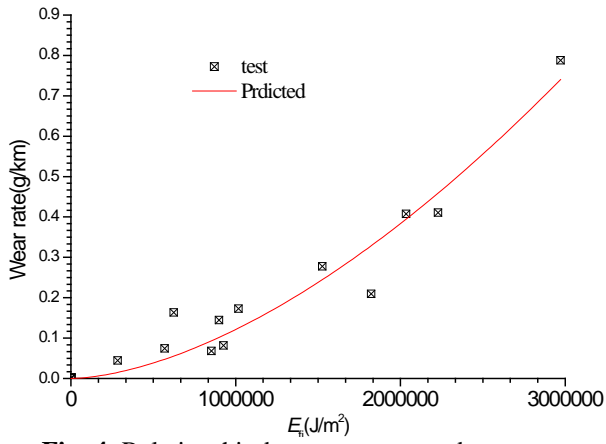


Fig. 4. Relationship between measured wear rate and friction energy

RESULTS AND DISCUSSION

The simulation conditions were the same as the LAT 100 experimental conditions: load (N): 30; speed (km/h): 5, 10, 15, 20; deflection (°): 0, 15, 30, 40. Figures 5 to 7 show the results of the contact pressure, transverse and longitudinal shear stress, and slip under the condition of load 30 N, speed 20 km/h, degrees 0° and 30°.

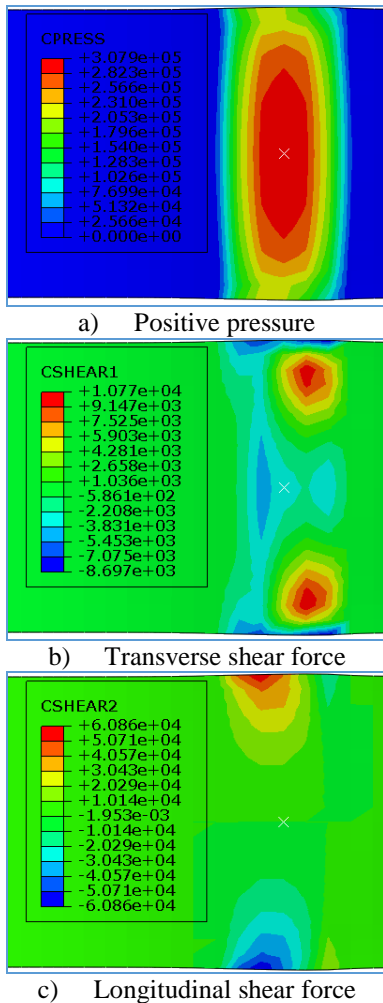


Fig. 5. Positive pressure, transverse and longitudinal shear stress distribution under 0° (unit: N/m²)

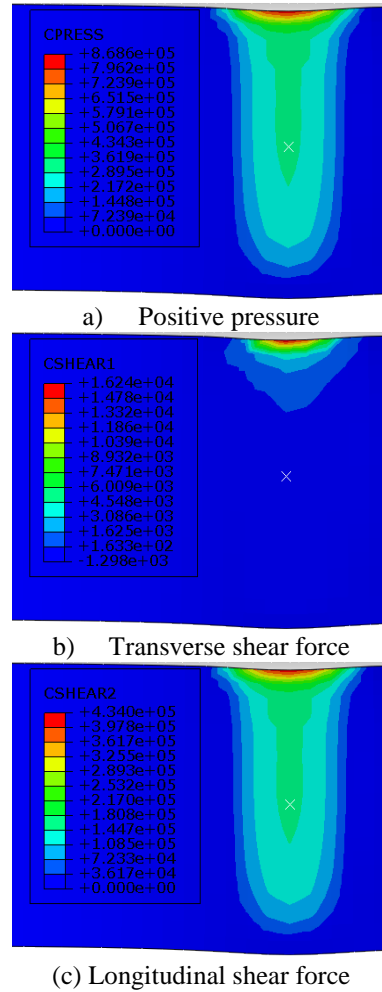


Fig. 6. Positive pressure, transverse, and longitudinal shear stress distribution under 30° (unit: N/m²)

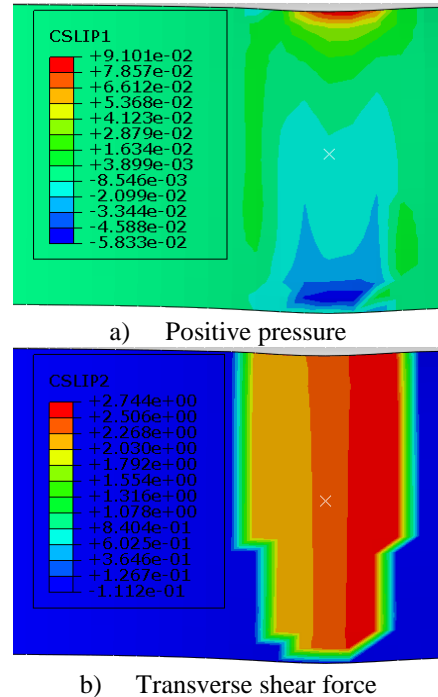


Fig. 7. Vertical and horizontal sliding distance under 30° (unit: mm)

Friction energy calculation and experimental fitting

Here we calculate the longitudinal and transverse shear forces of each contact element in the contact surface between the rubber wheel and the wear disc. The two shear forces are expressed

$$\text{as: } \tau_i = \tau_{eq} \frac{\dot{\gamma}_i}{\dot{\gamma}_{eq}} \quad (i=1,2) \quad (2)$$

where $\tau_{eq} = \mu P$, τ_{eq} is the frictional stress. μ is the friction coefficient. P is the normal contact force. $\dot{\gamma}_{eq} = \sqrt{(\dot{\gamma}_1)^2 + (\dot{\gamma}_2)^2}$. $\dot{\gamma}_i$ is the tangential slip velocity. The subscript 1 represents longitudinal, 2 represents horizontal.

The formula for calculating the frictional energy of each element is:

$$W_{elem} = \tau_{eq} \dot{\gamma}_{eq} \quad (3)$$

The formula for calculating the total friction energy density per round of rubber wheel is

$$E = \left(\int_0^L \sum_{i=1}^n w_i \right) / S \quad (4)$$

where w_i is the frictional energy of each element in the ground. L is rubber perimeter, n is the total number of elements that rubber wheel is in contact with the ground at a given time. $S = 0.5\pi\phi^2\delta$. Φ , δ and S are the diameter, thickness and grounding area of the rubber wheel, respectively.

Table 2 shows the experimental results of the LAT100 wear test. The friction energy density was obtained from the simulation result. The wear and surface temperature of the rubber wheel rise with the increase of the speed and angle.

The wear prediction model can be obtained from the above results:

$$A_E = C_E E^m \quad (5)$$

In the formula, $C_E = 1.3129E-11$, which is the material constant. $m=1.66$, which is the relational index.

Figure 7 shows that there is a power function relationship between the measured wear rate and the simulated friction energy. The measured results are in good agreement with the simulation results.

WEAR ENERGY MODEL CONSIDERING TEMPERATURE EFFECT

The relationship between temperature, friction energy, and wear can be summed up as follows:

(1) Rubber heat originates from the rubber friction energy dissipation and the hysteresis heat due to viscoelastic deformation. The effect of speed and temperature on wear can be characterized by a single temperature variable according to the Williams-Landel-Ferry equation. So it is more

reasonable to focus on the influence of temperature, because the effect of speed on wear is mainly from the rise of temperature. There is a quadratic polynomial relation between the wear and the temperature.

(2) The effect of load and slip on wear can be expressed by the friction energy. There is a power function relationship between the rubber wear and friction energy. Finite element analysis was used to fit the power function relationship between the rubber wear and friction energy to obtain the power exponent and relation constant.

Assuming that under normal temperature T_0 and constant speed V_0 , wear capacity is A_0 . E_0 is its corresponding friction energy. The relative expression of the relationship between wear and friction is:

$$A_{rel} = C_E \bullet \left(\frac{E}{E_0} \right)^m \quad (6)$$

Similarly, the relative expression of the relationship between wear volume and temperature is:

$$K_{rel} = \frac{A_T}{A_{T_0}} = (aT^2 + bT + c) / A_0 \quad (7)$$

The expression of rubber wear model considering temperature influence is:

$$A = A_{rel} \bullet K_{rel} = C_m E^m \bullet (a_1 T^2 + a_2 T + a_3) \quad (8)$$

The wear thermal coupling model for tire finite element analysis can be expressed as:

$$A_{ij} = C_m E_{ij}^m \bullet (a_1 T_{ij}^2 + a_2 T_{ij} + a_3) \quad (9)$$

where A_{ij} , E_{ij} , T_{ij} are for each unit node wear, friction energy and temperature, respectively. The i , j for the node number: $i, j=1,2,3,\dots, M$ is the power exponent, C_m , a_1 , a_2 , a_3 are constants, and their values are related to the formulation and working conditions of the rubber.

CONCLUSIONS

In this paper, the relationship between temperature, friction energy, and rubber wear was studied. In particular, the influence of temperature on wear was investigated, which further improved the thermal-mechanical coupling model.

(1) There is a quadratic polynomial relation between the wear and temperature. The wear of rubber has a significant temperature dependence. The relationship between rubber wear and temperature can be described by quadratic polynomials. The wear resistance at high temperature is related to the glass transition temperature of the material itself. The glass transition temperature of BR is higher than that of NR and SBR, which shows better characteristics of wear resistance at high temperature.

(2) There is a power function relation between the wear and friction energy. Based on the LAT100 wear test machine, wear experiments were carried out under various conditions, which can be calculated using finite element simulation, fitting wear on friction power function relation expression, and power index and relation constants.

(3) Temperature model of tire wear. The comprehensive wear model of rubber can be represented by two variables: friction energy and temperature. The thermal coupling model of tire wear for finite element analysis can be expressed as:

$$A_{ij} = C_m E_{ij}^m \bullet (a_1 T_{ij}^2 + a_2 T_{ij} + a_3)$$

The friction heat generation and accumulation of the tire due to extreme working conditions need further research because it is difficult to be measured and moreover, it is accompanied by the complex process of thermal degradation and chemical changes.

Acknowledgements: This research is funded by the National Natural Science Foundation of China (51576102) and the University scientific research project of Shandong (J16LB09)

REFERENCES

1. K.A. Grosch, A. Schallamach, *Rubber Chemistry and Technology*, **39**(2), 287 (1966).
2. A.R. Savkoor, *Wear*, **8**(3), 222 (1965).
3. A. Schallamach, *Proc. Phys. Soc. B.* **66**, 386-392 (1953).
4. A. Schallamach, *Rubber Chemistry and Technology*, **41**(1), 209 (1968).
5. B.N.J. Persson, *Physical Review Letters*, **87** (11), 116101 (2001).
6. B.N.J. Persson, F. Bucher, B. Chiaia, *Physical Review B*, **65**, 184106 (2002).
7. G.A. Schwartz, S. Cervený, *Polymer*. **44**(23), 7229 (2003).
8. Q. Fu, X. Wu, M. Wen, *Silicone Material*, **7**(1), 28 (2003).
9. K. Zhang, Y. Huang, Y. Ma, D. Zhou, *Chemical propellants and polymer materials*, **2**(6),44 (2004).
10. X. Wei, Sh. Yu, M. Xu, J. He, *Rubber Industry*, **7**, 441 (2008).
11. K.T. Gillen, M. Celina, R. Bernstein, *Polymer Degradation and Stability*, **82**, 25 (2003).
12. A.U. Paeglis, A. Simple, *Rubber Chemistry and Technology*, **77**(2), 242 (2004).
13. R. Bernstein, K.T. Gillen, Fluorosilicone and Silicone O-ring Aging Study. *Office of Scientific & Technical Information Technical Reports*, 2007.

Impact of electrical environment on wireless sensor communication

B. An*, W. Zhang

State Key Laboratory of Alternate Electrical Power System with Renewable Energy Sources (North China Electric Power University), Beijing 102206, China

Received September 22, 2017; Accepted, December 19, 2017

In order to ensure security and reliability of Internet of Things, electromagnetic disturbance issue in electrical environment is studied, where a wireless sensor is applied. Research on characteristics of electromagnetic disturbance in substations of different voltage levels and of different insulation types is carried out through field measurements. Simulation and field experiment of electromagnetic disturbance and communication obstruction produced by electrical equipment is performed to reveal impact on communication quality of wireless sensor.

Keywords: Wireless sensor, Electromagnetic disturbance, Communication obstruction, Electrical environment

INTRODUCTION

State Grid Co., Ltd. proposes an “Internet of Things” program which is featured by “Sense, Transmission, Awareness” in order to increase the management level in Smart Grid. Smart monitoring system using the Internet of Things in electrical environment is a vital part of Smart Grid and secures grid electrical operation [1].

Through field experiment in a 400kV GIS substation carried out by the British power system Co., Ltd, original data with electromagnetic disturbance which contain impulse signal were acquired [2, 3]. Impulse signal was produced by switch operation, partial discharge and periodic process of power electronics. Research also illustrates that SF₆ gap breakdown and vacuum gap breakdown result in negative impact on wireless communications [4, 5]. Research indicates that rise time of current impulse produced by partial discharge in strong dielectrics such as SF₆ reaches to 50ps, which means that the impulse includes frequency components up to 3GHz and may generate electromagnetic disturbance to impact communication quality of wireless sensors [6, 7, 3]. Scotland power system Co., Ltd. in UK studied the impact to wireless sensors produced by electromagnetic disturbance of partial discharge and obtained some results [4, 8].

This paper mainly focuses on the impact on communication of a wireless sensor in electrical environment. Wireless sensors employ ZigBee techniques and communicate in the band of 2.4GHz~2.5GHz, which is easy to be impacted by electromagnetic disturbance [9, 10]. When electromagnetic disturbance is severe, the wireless sensor may lose information packet or even stop working. This paper studies the characteristics of electromagnetic disturbance by field measurement, which may impact on the communication of a

wireless sensor. Electromagnetic disturbance was generated by electrical field and magnetic field at power frequency, corona discharge, partial discharge and gap breakdown in substations of different voltage levels and of different insulation types. Measurement data of electromagnetic disturbance in complex electrical environment were acquired by wide-band antenna, digital oscilloscope and receiver. Simulation was performed to reveal the impact on communication of a wireless sensor under electromagnetic disturbance and obstruction of electrical equipment [11].

MEASUREMENT AND STATISTICAL ANALYSIS OF ELECTROMAGNETIC DISTURBANCE

Electromagnetic disturbance on a wireless sensor caused by a complex electromagnetic disturbance cannot be negligible, with wide application of the Internet of Things in electrical environment. Through field measurement, the electromagnetic disturbance characteristics in substations of different voltage levels and different insulation types were obtained. Statistic properties of electromagnetic disturbance were analyzed.

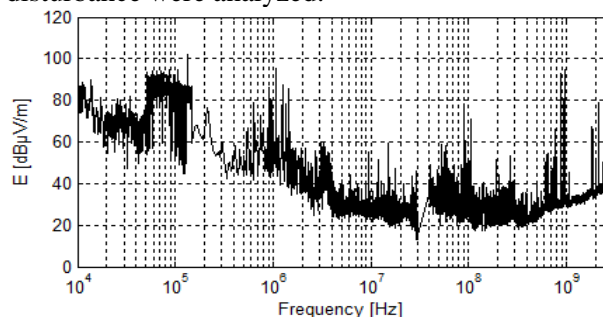


Fig. 1. Spectrum of electromagnetic disturbance around a circuit breaker in a 500kV GIS substation

The spectrum of electromagnetic disturbance around a circuit breaker in a 500kV GIS substation measured by a receiver is shown in Fig. 1. The dominant frequencies are around 100kHz, 1MHz,

To whom all correspondence should be sent:
E-mail: bo_an_cnbd@sina.com

3MHz, 110MHz, 936MHz, 1.84GHz and 2.43GHz, which cover the communication frequency band of a wireless sensor, i.e. 2.4GHz. In this GIS substation, packet loss rate of wireless sensor was about 5.6% in a performance test.

Since the disturbance spectrum of each single measurement is different, data of a single measurement are not representative for the overall level of disturbance. Fig. 2 shows spectrum envelope diagrams of 100%, 80% and 50% measured at 4 measurement points in 500kV open air and GIS substations. The 100% spectrum envelope diagram denotes the maximum value at each frequency in the spectra of all measurement data. The 80% spectrum envelope diagram means 80% of the maximum value at each frequency in the spectra of all measurement data. The 50% spectrum envelope diagram represents half of the maximum value at each frequency in the spectra of all measurement data. The dominant frequencies are around 0.1MHz, 1MHz, 110MHz, 960MHz, and 2GHz, which may impact communication quality of a wireless sensor [12].

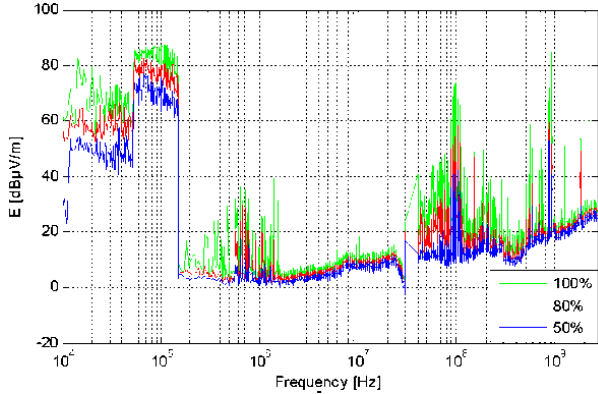


Fig. 2. Spectrum envelope diagrams of 100%, 80% and 50% at 4 measurement points in open air and GIS substations at the voltage level of 500kV

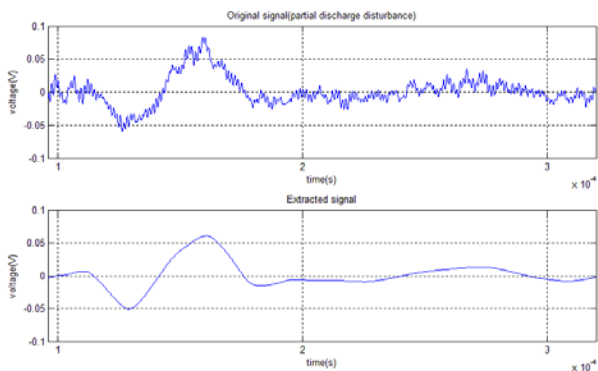


Fig. 3. Impulsive signal extraction

Electromagnetic disturbance in substations of different voltage levels and different insulation types was acquired by field measurement. Statistic features of electromagnetic disturbance were obtained. Using wavelet packet transform as demonstrated in Fig. 3, impulsive signal was

extracted from these electromagnetic disturbance data. In order to acquire approximate and detail coefficients, symlet-6 wavelet was employed for 12-layer wavelet transformation. By applying Stein's unbiased risk estimate (SURE), the best tree was obtained. According to these coefficients of each layer, the impulsive signal was reconstructed.

Pulse characteristic parameters such as peak to peak value, duration, etc., were collected from the extracted impulsive signal and distribution fitting of these parameters was statistically analyzed. Probability density function (PDF) was calculated for the extracted impulsive signal features. According to numerous mathematical probability distribution functions, best fitting distribution of pulse characteristic parameters was acquired [13]. PDF of peak to peak value, which obeys normal distribution, is shown in Fig. 4. PDF of duration that obeys log-logistic distribution is illustrated in Fig. 5.

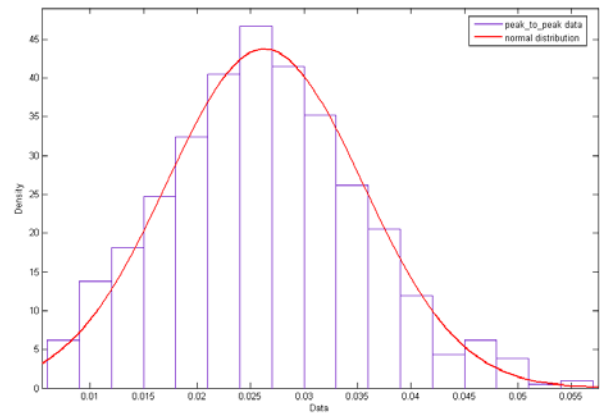


Fig. 4. PDF of peak to peak value

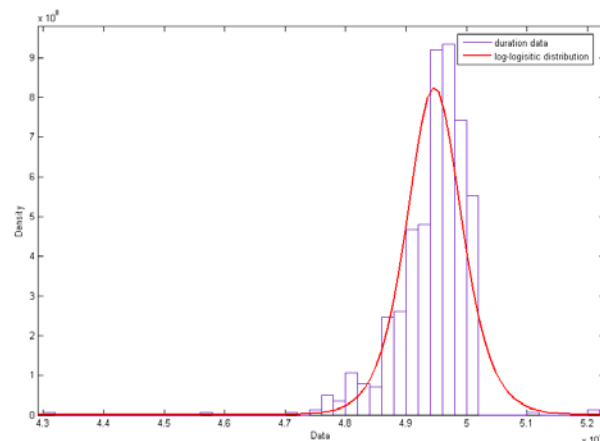


Fig. 5. PDF of duration

SIMULATION AND EXPERIMENT

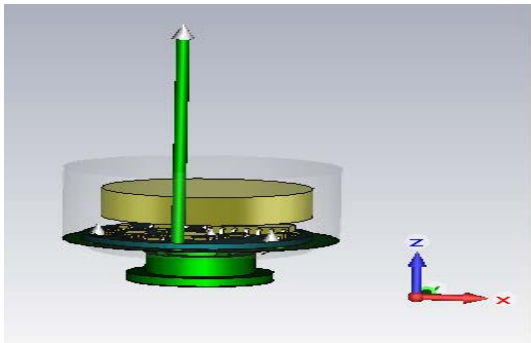
Simulation and Experiment of Electromagnetic Disturbance to Wireless Sensor

The electromagnetic disturbance from the electrical equipment was studied in order to reveal the immunity of the wireless sensor, when the latter is applied in electrical environment. Field measurement and experiment indicated that the

communication quality of the wireless sensor is impacted by electromagnetic disturbance. Analysis of the measurement data indicated that the frequency range of electromagnetic disturbance includes the communication frequency of the wireless sensor, i.e. 2.4GHz. The model of the wireless sensor was established in order to reveal the distribution of induced voltage inside the wireless sensor.



(a) A photo of a wireless sensor



(b) Model of a wireless sensor

Fig. 6. Photo and model of a wireless sensor

The photo and model of the wireless sensor are shown in Fig. 6 (a) and (b), respectively. Set plane wave as an excitation source and assign electrical field strength 10V/m according to the IEC Standard 61000-4-3 definition for the third class test level. A disturbance signal in simulation, taking a partial discharge signal as an example, was set as an excitation source, shown in Fig. 3. Fig. 7 shows the spectrum of induced voltage on the antenna, the dominant frequencies of which are 1.2GHz and 2.3GHz. The maximum value of induced voltage is 1.04V, which is high enough to lead to communication packet loss of the wireless sensor. After all, the 1.2GHz signal component can easily generate 2.4GHz signal by frequency multiplication, which is the communication band of the wireless sensor, and leads to the same frequency interference. The 2.3GHz signal component causes neighboring interference. The frequency components at 1.2GHz and 2.3GHz impact on the communication quality of the wireless sensor.

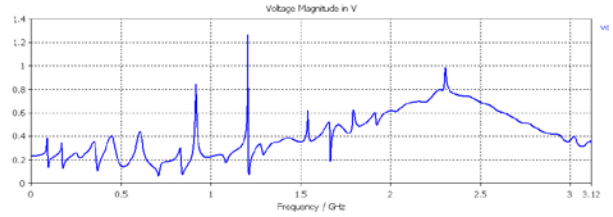


Fig. 7. Spectrum of induced voltage signal on the antenna

Field experiment testified that electromagnetic disturbance of electrical equipment influences the communication quality of the wireless sensor. The representative photo of the field experiment is shown in Fig. 8.



Fig. 8. A photo of the field experiment on the electromagnetic disturbance of a wireless sensor

Immunity test on the wireless sensor was performed at an open area test site, as shown in Fig. 9, in order to obtain communication performance of the wireless sensor under electromagnetic disturbance and to indicate the variation in work state with variation of electrical field strength of the electromagnetic disturbance. A wireless sensor acts as a transmitter and receiver under electromagnetic disturbance generated by signal generator, power amplifier and transmitting antenna.



Fig. 9. Photo of immunity test on the wireless sensor performed at an open area test site

Electromagnetic disturbance varies in the frequency band range of 100MHz to 2.5GHz. Critical electrical field strength of normal-operation/packet-loss work state and of packet-loss/halt work state was acquired by test at a frequency around 2.4GHz and 1.2GHz, which is the most sensitive frequency, as shown in Figs. 10 and 11.

“Critical electrical field strength of normal-operation/packet-loss work state” means that during communication under this electrical field strength, the work state of the wireless sensor changes from normal operation to packet loss. “Critical electrical field strength of packet-loss/halt work state” means that during communication under this electrical field strength, the work state of wireless sensor changes from packet loss to halt [14].

At electrical field strength of 0.80V/m that is almost at the noise level at the frequency of 2.405GHz that is the current communication frequency of the wireless sensor, the latter stops working, as illustrated in Fig. 10. At frequencies that are lower or higher than 2.405GHz in the frequency range of 2.4GHz~2.409GHz, the critical electrical field strength is higher than 0.80V/m. The same frequency interference area is around 2.405GHz, and the impact of electromagnetic disturbance at this frequency is outstanding. Taking as an example the frequency of 2.409GHz, the electrical field strength that makes the wireless sensor start losing packet during communication is 9.6V/m and the wireless sensor stops working when it rises to 11.6V/m. With the increase in electrical field strength at each frequency, the wireless sensor experiences a process from normal operation to packet loss, and then to halt, its packet loss rate rising from 0 to 100% during communication, as illustrated in Fig. 12 at the frequency of 2.409GHz.

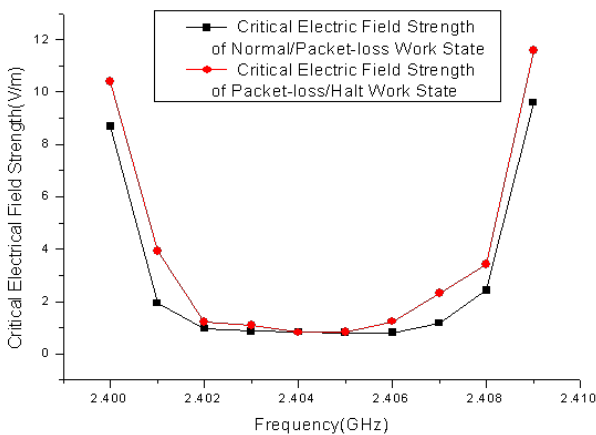


Fig. 10. Critical electric field strength at 2.4GHz

There is also a distinguished sensitive area as shown in Fig. 11 in the frequency range from 1.2GHz to 1.2035GHz. The most sensitive frequency in this range is 1.203GHz that is about half of the communication frequency of a wireless

sensor, i.e., 2.405GHz. However, the whole electrical field strength level is much higher than that in the frequency range of 2.4GHz. Wireless sensor halted working at 1.203GHz at an electrical field strength of 2.45V/m, but changed the work state from normal operation directly to halt at electrical field strength of 36.93V/m at 1.2035GHz, while it did not halt working at 1.2GHz even at the maximum value of electrical field strength during communication in this open field test site.

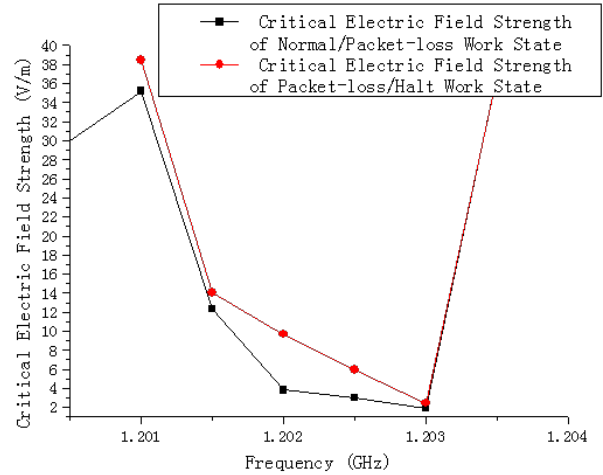


Fig. 11. Critical electric field strength at 1.2GHz

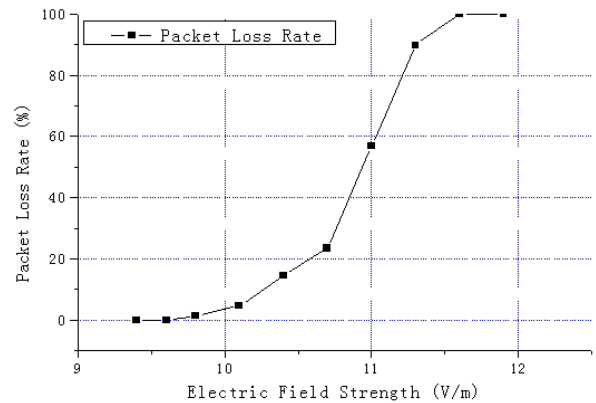


Fig. 12. Packet loss rate variation at the frequency of 2.409GHz

The immunity test indicates that the wireless sensor may be impacted and lose packet at 2.4GHz and 1.2GHz during communication. Detailed curves in Figs. 10, 11 and 12 illustrate the communication sensitivity of the wireless sensor at specific frequency and electrical field strength of disturbance.

Simulation and Experiment of Communication Obstruction of a Wireless Sensor in Electrical Environment

Simulation model which employs the uniform theory of diffraction at a high frequency range (i.e. 2.4GHz) to solve large size problem, was studied to obtain the magnitude of electrical field when electromagnetic disturbance exists in the electrical environment. Different placement locations of the wireless sensor resulted in different effects of

electromagnetic disturbance, because of the distance of disturbance source and obstruction layout.

A transformer model was established in order to reveal the communication obstruction of wireless sensors, as demonstrated in Fig. 13. Through simulation, it was illustrated that when a wireless sensor modeled as a dipole transmitting antenna, is placed around the transformer, the wireless sensor at different locations produces different electrical field distributions, due to distance and obstruction. According to the electrical field distribution, the induced voltage inside the receiving wireless sensor and the effective wireless sensor communication range was estimated and thus, wireless sensor communication obstruction of electrical equipment was evaluated [15].

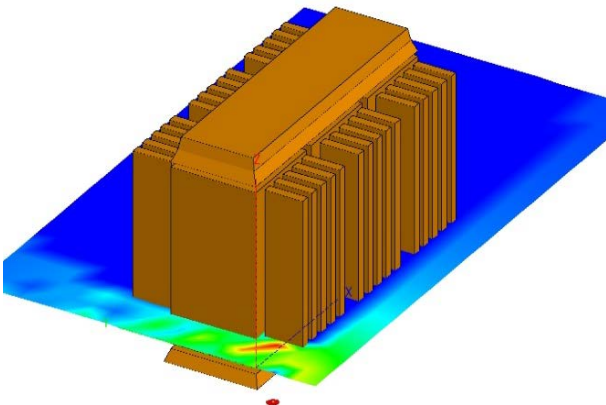


Fig. 13. A transformer model

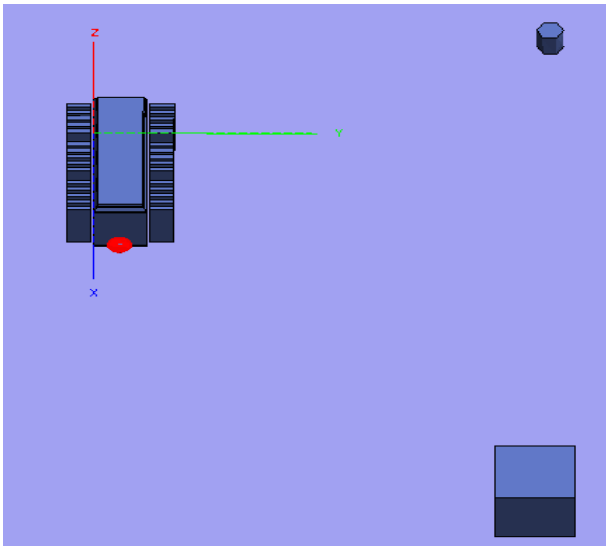


Fig. 14. Location of electrical equipment

Protection room and capacitor were located at the right side of the transformer as demonstrated in Figure 14. When the wireless sensor is placed on the left of transformer at a height of 1 m, 2 m and 3 m, the electrical field distribution is illustrated in Fig. 15 (a), (b) and (c), respectively. The red part in this figure denotes the maximum value of the electrical field strength (i.e. 3.6V/m), while the blue part represents the minimum value. This simulation shows that the transformer obstructs the

communication of wireless sensors, since the electrical field distribution is obviously impacted by the transformer. Different placement heights of the wireless sensor, as demonstrated in Fig. 15, result in different electrical field distribution, and therefore lead to different communication ranges of the wireless sensor in the same electrical environment. The communication quality is impacted by the height of wireless sensor around the electrical equipment.

When the wireless sensor is placed on the right of the transformer at a height of 1 m, 2 m and 3 m, the electrical field distribution is demonstrated in Fig. 16 (a), (b) and (c). Obviously, the electrical field distribution is mostly focused in the area of the transformer, capacitor and protection room. Different placement heights of the wireless sensor, as shown in Fig. 16, produce different electrical field distribution and different communication range of wireless sensor.

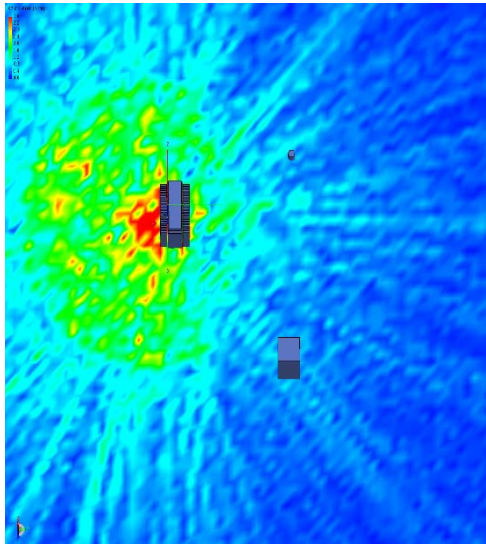
Fig. 17 (a), (b), (c) and (d) shows that the electrical field distribution is distinctively different when the wireless sensor is placed at a height of 0 m above, below, on the left and on the right of the transformer. This simulation presents that a different placement of the wireless sensor around the transformer at the same height yields different electrical field distribution, because the large-size electrical equipment, i.e., the transformer, blocks the communication of the wireless sensor. The communication quality of the wireless sensor at the same height around the electrical equipment varies when wireless sensor changes position.

By simulation, it was illustrated that the communication obstruction of the wireless sensor produced by electrical equipment is a vital factor having an impact on the communication quality. Different positions and different heights of the wireless sensors result in different communication ranges around the transformer, protection room and capacitor. Therefore, the communication quality of the wireless sensor is impacted by obstruction of electrical equipment.

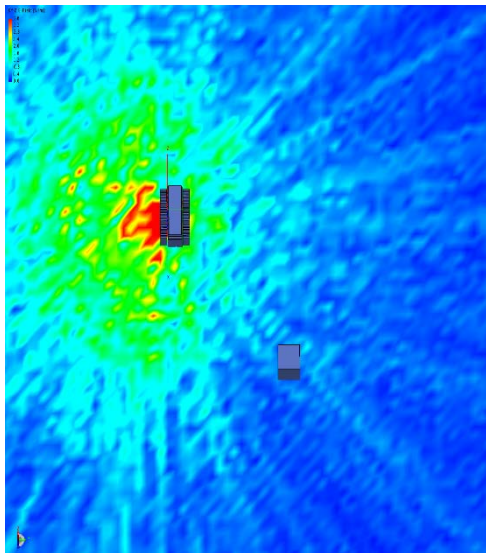
Field experiment verified this conclusion and Fig. 18 is a representative photo.

CONCLUSION

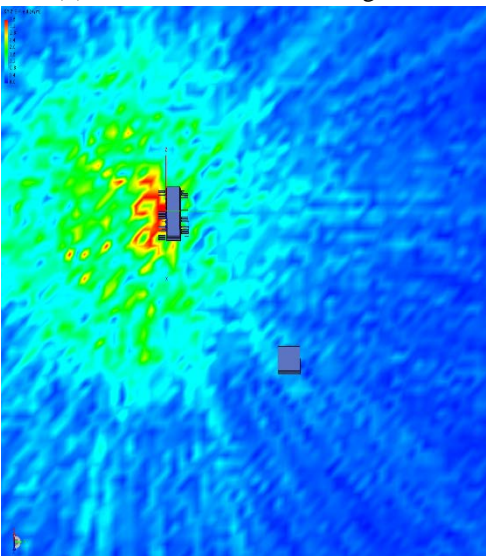
The measurement data in substations of different voltage levels and of different insulation types were studied and statistically analyzed. Experiment and simulation indicated that the communication quality of the wireless sensor is impacted by electromagnetic disturbance and the location of electrical equipment, such as transformer, protection room and capacitor in the electrical environment. Communication obstruction produced by the electrical equipment influences the communication quality of the wireless sensor at different locations.



(a) Wireless sensor at the height of 1m

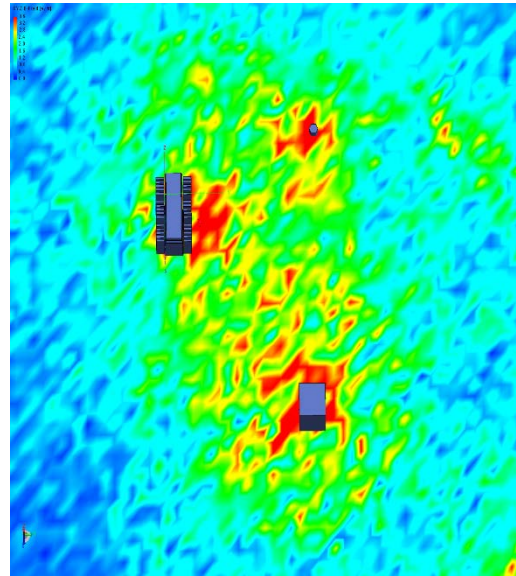


(b) Wireless sensor at the height of 2m

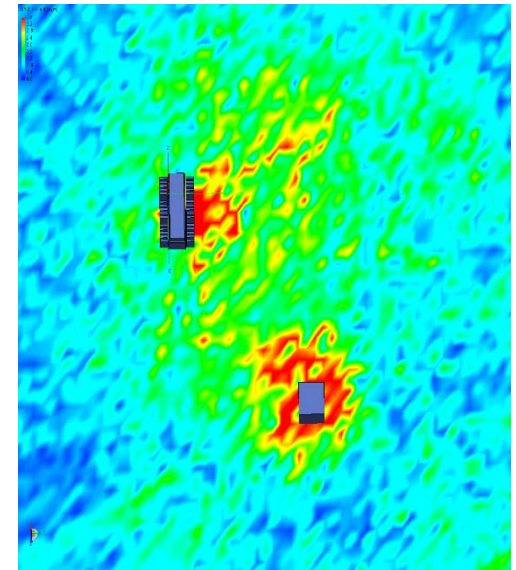


(c) Wireless sensor at the height of 3m

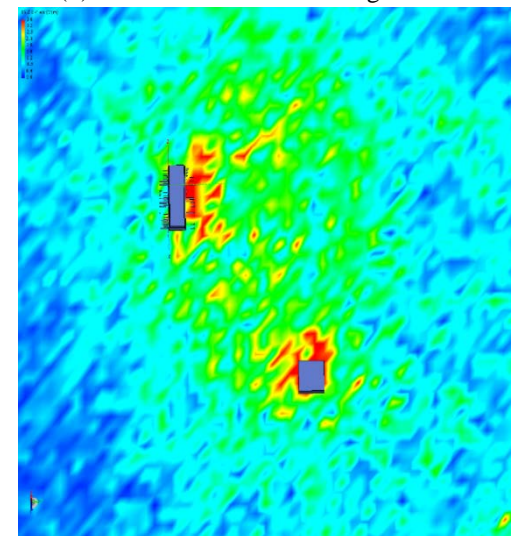
Fig. 15. Electrical field distribution when the wireless sensor is placed at a height of 1m, 2m and 3m on the left of the transformer



(a) Wireless sensor at the height of 1m

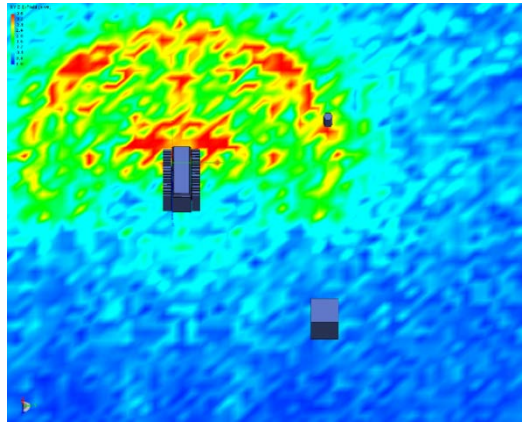


(b) Wireless sensor at the height of 2m

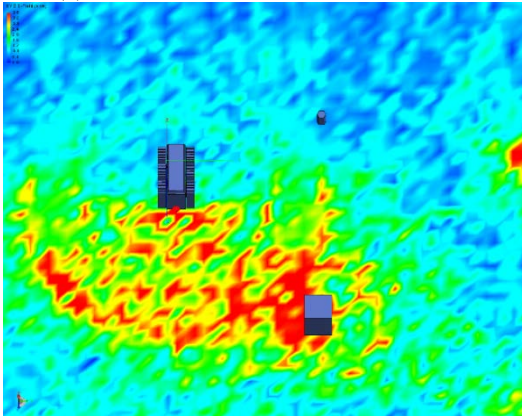


(c) Wireless sensor at the height of 3m

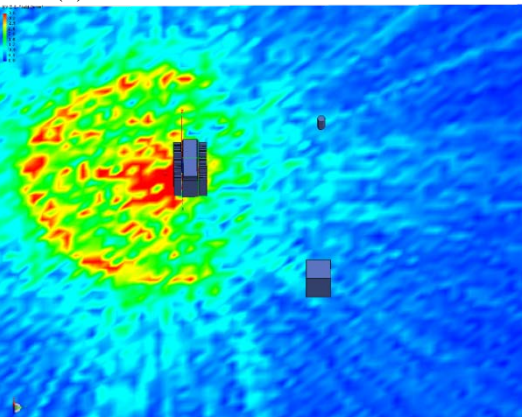
Fig. 16. Electrical field distribution when wireless sensor is placed at the height of 1m, 2m and 3m on the right of the transformer



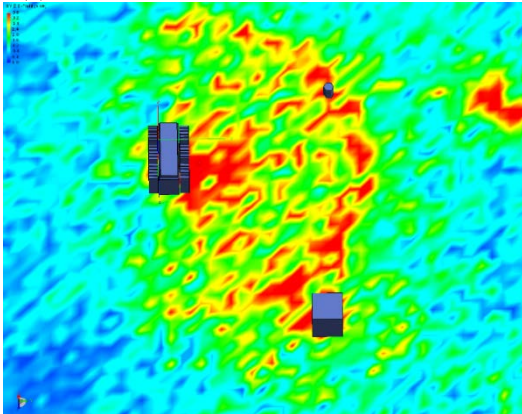
(a) Wireless sensor above the transformer



(b) Wireless sensor below the transformer



(c) Wireless sensor on the left of the transformer



(d) Wireless sensor on the right of the transformer

Fig. 17. Electrical field distribution when the wireless sensor is placed at the height of 0 m around the

transformer



Fig. 18. A photo of the field experiment on communication obstruction of a wireless sensor

Acknowledgements: This paper is supported by the Fundamental Research Funds for the Central Universities 2014MS85 of China.

REFERENCES

1. F. Cleveland, Use of Wireless Data Communications in Power System Operations, *2006 IEEE PES Power Systems Conference and Exposition*, 631-640, 2006.
2. Q. Shan, I. A. Glover, R. C. Atkinson, S. A. Bhatti, I. E. Portugues, P. J. Moore, R. Rutherford, M. Fatima, Q. Vieira, A. Marcus, N. Lima, B. A. de Souza, *Transactions on Electromagnetic Compatibility*, **53**(3), 653, (2011).
3. Q. Shan, I. A. Glover, R. Rutherford, S. Bhatti, R. Atkinson, I. E. Portugues, P. J. Moore, Detection of ultra-wide-band impulsive noise in a 400kV air insulated electricity substation, *20th International Conference on Electricity Distribution*, Paper 0174, Prague, June 2009.
4. Z.X Liu, Y.L Huang, L.Z Yao, Y.J Gong, M. Han, Rong Zeng, Zhiqiu Li, "Experiment on the application of Bluetooth in vacuum switch cabinet", *Electric Utility Deregulation and Restructuring and Power Technologies, 2008. DRPT 2008. Third International Conference on*, Nanjing, China, April 2008.
5. W.H Siew (MIEEE), YC Liu, B Musa, F Mir, Y Wang, "Basis for a Wireless Network for EMC Measurements in Electric Substations", *2007 International Symposium on Electromagnetic Compatibility, EMC 2007*, pp. 2638 - 2642, 2007.
6. M.D Judd, O. Farish, J.S Pearson, B.F Hampton, "Dielectric windows for UHF partial discharge detection", *Dielectrics and Electrical Insulation, IEEE Transactions on [see also Electrical Insulation, IEEE Transactions on]*, vol. 8, pp. 953 - 958, 2001.
7. H. Lu, L. Zhan, Y. Liu, W. Gao, "A Microgrid Monitoring System Over Mobile Platforms", *Smart Grid, IEEE Transactions on*, vol. PP, pp. 1 - 10, 2016.
8. C. Chang, C. S. Chang, J. Jin, T. Hoshino, M. Hanai, and N. Kobayashi, "Source classification of partial

- discharge for gas insulated substation using waveshape pattern recognition", *Dielectrics and Electrical Insulation, IEEE Transactions on [see also Electrical Insulation, IEEE Transactions on]*, vol. 12, pp. 374 - 386, 2005.
9. Q.S Shan, I.A Glover, P J Moore, I E Portugues, R J Watson, R Rutherford, R Atkinson, Shahzad Bhatti, "Laboratory Assessment of WLAN Performance Degradation in the Presence of Impulsive Noise", *Wireless Communications and Mobile Computing Conference, 2008. IWCMC '08. International*, pp. 859 - 863, 2008.
 10. Axel Sikora, "Coexistence of IEEE802.15.4 (ZigBee) with IEEE802.11 (WLAN), Bluetooth, and Microwave Ovens in 2.4GHz ISM Band", Revised Version V0.3: 12th September 2004.
 11. D. Dardari, P. Closas, P.M. Djuric, "Indoor Tracking: Theory, Methods, and Technologies", *Vehicular Technology, IEEE Transactions on*, vol. 64, pp. 1263 - 1278, April 2015.
 12. W.D Zhang, B. An, X. Cui, J.K Li, Y.B Shi, S.Y Liu, "A Study on Electromagnetic Disturbance in Substation to Wireless Sensor Unit", *2012 International Symposium on Electromagnetic Compatibility (EMC EUROPE 2012)*, p 6 pp., 2012.
 13. B. An, W. Zhang, Z. Wang, "Study on Influence of Electromagnetic Disturbance on Wireless Sensor Unit in Substation", *Antennas and Propagation in Wireless Communications (APWC), 2015 IEEE-APS Topical Conference on*, pp. 654 - 657, 2015.
 14. B. An, W.D Zhang, X. Cui, J.K Li, Y.B Zhi, S.Y Liu, "A Study on Immunity of Wireless Sensor Unit in Substation", *2012 International Symposium on Electromagnetic Compatibility (EMC EUROPE 2012)*, p 5 pp., 2012.
 15. B. An, W.D Zhang, H.J Ma, X. Cui, Y. Jin, F.B Meng, "A Study on Electromagnetic disturbance and Immunity of Wireless Sensor Unit in Substation", *2014 XXXIth URSI General Assembly and Scientific Symposium (URSI GASS)*, p 4 pp., 2014.

An empirical analysis of the economic development, energy structure and energy consumption in Zhejiang Province

S. Zhang*, Y. Fang, Y. Han

School of Economics and Management, Zhejiang University of Science and Technology, Hangzhou, 310023, P.R. China

Received September 27, 2017, Revised December 19, 2017

4Since the 21st century, the economy of stable, healthy and rapid development brought a rapid increase in energy consumption. The correct understanding and the analysis of energy consumption in the economic development help to more rationally grasping of the situation of economy and provides a reference for the healthy development of economy and a model for the development of other regions. Based on the data of Zhejiang Province from 1990 to 2016, this paper studies the relationship between energy consumption, energy structure and economic development through empirical analysis, unit root test, Granger causality test. At the same time, it puts forward a series of policy recommendations about how to improve the utilization of energy and accelerate the development of Zhejiang economy.

Key words: Energy consumption, Energy structure, Economic development, Empirical analysis

INTRODUCTION

Energy is the strategic basis for the survival and development of human resources; there are more people and less land, as well as less energy in Zhejiang province; its coal reserves are less than one ten-thousandth of the country proven coal reserves. "No oil, lack of coal, less electricity" means lack of energy, and more than 95% of the energy consumption has to rely on provincial transfer. But it is an "energy consumption province." In 2015, for example, the total energy consumption was 196.1 million tons standard coal which was by about 4.2% over 2014. Among them, the coal consumption was 13.799 million tons standard coal, basically flat with 2014; oil and products consumption was 29.09 million tons, by about 5.3% over the previous year; natural gas consumption was 7.8 billion cubic meters, by about 2.0% over the previous year; consumed electricity from water, nuclear, wind and other sources was 49.6 billion kw·h, about 19.9% over the previous year. The province energy consumption significantly increased, while the economic development showed sudden leaps and bounds in Zhejiang province. From 1990 to 2016, its GDP increased from 90.469 billion yuan to 468.4 billion yuan. The data show that economic development and energy consumption follow the same trend of growth. This paper will start from the above issues, the economic development and the structure of energy consumption, basing on the analysis of energy consumption structure to find better solutions.

CURRENT SITUATION IN ZHEJIANG

The change in total energy consumption

The region lacks energy and has low self-sufficiency rate, although the energy consumption depends on import, it is higher than the national level. The charts can be seen in Fig.1. While the energy consumption continues to grow, the rate of growth declines from the highest rate of 16.07% to the lowest level of 3.86%. At the beginning of the 21st century, owing to the rapid development of economy, some high-energy-consumption basic industries appeared in the overall high-speed growth "Eleventh Five-Year Plan" period and the rate of total energy consumption growth was 6.96%. During the "Twelfth Five-Year Plan" 4 years ago, the average annual increase was 13.8% - higher than during the "Eleventh Five-Year Plan" (6%). This growth momentum prompted the self-sufficiency rate to decrease by 0.68% over the previous year, and 96.5% of the energy depend on external supply, thus energy security being fragile. During the "Thirteenth Five-Year Plan" period, the local government continued to attach great importance to energy conservation work to improve energy efficiency, and conscientiously implement energy saving policies and measures, making the total energy consumption growth momentum significantly inhibited. Although the growth rate of energy consumption has come down, the expansion of the total amount is obvious. From the total energy consumption point of view, the energy consumption appeared a "rapid growth, moderate growth, rapid rise, steady growth" evolution trend.

*To whom all correspondence should be sent:
E-mail: syzh201@163.com

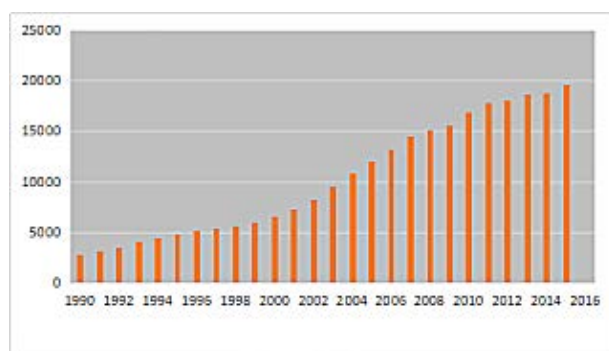


Fig.1. 1990-2016 total amount of energy consumption in Zhejiang (unit: 10,000 tons of standard coal)

Structure of energy consumption analysis

The current energy consumption is mainly coal consumption, oil consumption, natural gas consumption and electricity consumption.

The structure of energy consumption is still dominated by coal, but its proportion shows a declining trend. While the production of coal was declining, self-sufficiency rate is less than 1%, the coal supply basically relies on the transfer from foreign provinces and import. So, the government will take some measures to curb this phenomenon, reducing the use of coal and inhibiting its growth. In the "Eleventh Five-Year Plan" period the use of coal fell by 4.8%, but in the first three years of the "Twelfth Five-Year Plan", the locals introduced a large number of coal-fired power generation stations, making the proportion of coal to decrease by only 1.6%, the average annual decline being 0.5% and slowing down.

So far, the land field has not found yet oil and gas resource, and all oil resources basically rely on external supply. In recent years, refined oil consumption maintained an average annual growth rate of 17.26%. Refined oil consumption reached 25.271 million tons in 2016, by 13.68% over the previous year. Among them are 12.4683 million tons of gasoline, and 7.5649 million tons of diesel. Ratio of diesel to gasoline is 1.64: 1.

Since the beginning of using natural gas from the west to east in 2004, the natural gas market has developed rapidly. In 2016, natural gas consumption reached 8.8 billion cubic meters, by about 12.8% over the previous year. However, the consumption of natural gas is still subject to great restrictions. It also lacks the necessary natural gas spiked facilities and urban reserves of gas sources, affecting natural gas transfer.

Electric power as the most important secondary energy in production and life, the total energy consumption has expanded year by year. Although the intensity of national economic energy

consumption has declined year by year, the decline slowed down year by year, and the power consumption intensity increased year by year. Overall, the energy consumption structure is still dominated by the polluting coal. This poor energy consumption structure has caused serious environmental pollution, high energy cost of products, weak competitiveness and many other issues. In recent years, natural gas, other high-quality energy sources such as solar energy, geothermal energy and other new energy developments continue to increase, improving the proportion of natural gas. Other high-energy and new energy sources will be the future of a long period of energy consumption structure adjustment.

The basic situation of economic development

Over the past 20 years, with the steady growth of total energy consumption, the GDP also showed a good upward trend. GDP reached 428.846 trillion yuan in 2015, which is a 6.70% increase over the previous year. From 1990 to 2015, the GDP of Zhejiang Province increased from 90.469 billion yuan to 42886.49 billion yuan, with an average increase about 13%. By contrasting the GDP of different years, it is clear that from the early nineties to the middle of the twentieth century, the GDP growth rate was relatively fast, nearly four times over a short period of six or seven years. In the late 1990s, the GDP growth rate gradually flattened. After 2000, the GDP growth rate was gradually accelerated in a short period of 15 years it rose from 6,141,303 million yuan to 42886.49 billion yuan, which also reflects the good momentum of development of the economy in the "Eleventh Five-Year Plan" period, "Twelfth Five-Year Plan" period and "Thirteenth Five-Year Plan".

EMPIRICAL ANALYSIS

Data selection and description

In this paper, the energy consumption was assessed from the total energy consumption and energy structure of the data from 1990 to 2015. Economic development was expressed as gross domestic product(Y) obtained by the growing consumption of electricity, and the total amount of energy consumption (E). The proportion of electricity consumption to total consumption represents the energy structure (S).

Unit root test

Since the Granger causality test is sensitive to the smoothness of the sequence, the ADF method was used to test the unit root of each variable. The unit root test is also very sensitive to different lag orders.

Table 1. Results of the Johansen co-integration test

Number of CEs assumed	Eigen values	Eigen value test		Extreme Eigen value test	
		Trend statistics	5% of the critical value	Extreme Eigen value statistics	5% of the critical value
None	0.583482	34.04793	29.79707	21.01979	21.13162
At most 1	0.272240	13.02814	15.49471	7.626803	14.26460
At most 2	0.201528	5.401337	3.841466	5.401337	3.841466

When the ADF test was carried out, the AIC information criterion was used to determine the lag order. The results show that all lnY, lnS, and lnE have unit roots and unstable sequences. They are single-homogeneous and second-order single whole, so the co-integration test requirements are met.

Co-integration test

On the basis of the above tests, we used the Johansen maximum likelihood method to test the covariance of the three variables. Table 1 lists the Johansen test results.

The maximal Eigen value test gave the same conclusion: it rejects the null hypothesis that there is no covariant vector at the 5% significance level, and accepts the hypothesis of covariate vector in the system. The whole test uses the co-integration equation:

$$\ln Y = 0.66933 \ln S + 0.30887 \ln E \quad (1)$$

There is a long-term stable relationship in the model, the elasticity coefficient of lnS to lnY is 0.66933, and the elastic coefficient of lnE is 0.30887, indicating that GDP will grow by 0.66933% if energy structure increases. GDP will grow by 0.30887% for every 1% of energy consumption increase. It can be seen that in the long run, the change of energy structure has more impact on GDP than the impact of energy consumption, which also shows the importance of adjusting and optimizing the energy structure for economic development for a long time.

Granger causality test

In order to verify the direction of the causal relationship of the three variables, this paper used Granger causality to test lnY, lnS and lnE. According to the criteria of determining the lag order, the latter was determined to be 2. We can conclude that it accepted the existence of lnY and lnE two-way causal relationship at the 10% significance level, and lnS is lnY Granger reason. It can be concluded that economic development, energy structure and energy consumption are in a causal relationship indicating that the economic development will also promote the increase in energy consumption. At the same time, the increase in energy consumption changes energy structure, and will also affect economic development.

CONCLUSIONS AND RECOMMENDATIONS

Through the above empirical analysis, the following conclusions may be drawn:

Between Zhejiang economic development, energy structure and energy consumption there exists a causal relationship. Energy structure and energy consumption have a strong impact on the economic development; in turn, the latter can affect energy consumption while the energy structure has a weak impact. Through the co-integration test it was found that the effect of energy structure on GDP is higher than that of economic consumption. Based on the above conclusions, while other conditions remain unchanged, the full supply of energy can be protected if an appropriate speed of sustainable development is maintained. In the long run, it is of great significance to adjust and optimize the energy structure for economic development.

The empirical analysis shows that the sustained growth of Zhejiang economy strongly depends on energy consumption. Energy as a necessary factor of production and strategic material has a significant impact on the development of Zhejiang economy, while coal consumption in energy consumption structure is difficult to change in a long time. Through the above analysis, we give the relevant policy recommendations:

1) To ensure coordinated development of energy and economy, and actively develop a variety of new energy sources we are vigorously transforming the traditional energy industry and actively developing new energy sources, improving the energy industry technological content. As Zhejiang is located in the southeast coastal areas, it has tidal and wind energy reserves. At the same time, it should deal with the sustainable development of the energy industry and resolutely stop all kinds of short-term behaviors.

2) To optimize the energy consumption structure and strive to "clean" direction adjustment, Zhejiang province should actively develop hydropower, optimize the development of coal, focus on the development of nuclear power and vigorously develop natural gas power generation, solar energy, biomass and other renewable energy sources and try to reduce coal in energy consumption. Specific measures can be divided into the following three aspects: coal, oil, and natural gas. Zhejiang province

should jointly promote the development of these resources from the aspects of science, technological development and policy support.

3) To speed up the upgrading of industrial structure, and promote the transformation of economic development because the energy efficiency of different industries is very different. Zhejiang province proportion of secondary industry is as high as 53%, and energy efficiency is better than in the country. This shows that industrial energy utilization is high; on the other hand, it shows that energy-saving potential is very large. If the proportion of the third industry rises while the proportion of the secondary industry is relatively low, it is necessary to control the total energy consumption and improve energy efficiency.

4) To improve the energy reserve system and the ability to deal with emergencies. As Zhejiang has a big economy, energy construction must be able to resist risks, there must be certain strategic material reserves, including both physical and channel aspects. Material reserves are setting up for price factors such as climate change, climate change, boom, social turmoil and so on. According to the prevailing situation, there is a guaranteed bottom line. Channels are mainly reflected in the source and transport, ensuring long-term supply base, railway

safety, and maritime transport. The stability of the province and the overall situation of the country has a very big significance in this aspect.

Acknowledgements: This research was financially supported by the National Natural Science Foundation of China (Grant NO. 11771399) and the 2015 cross Pre-research project of Zhejiang University of Science and Technology (Grant NO. 2015JC09Y).

REFERENCES

1. E. Sh. Yu, J.Y. Choi, *Journal of Energy and Development*, **10**, 249 (1985).
2. J.W. Liang L. Zhou, Energy Consumption and Economic Growth: Co-integration and Granger Causality Test , 2012 IEEE 19th International Conference on Industrial Engineering and Engineering Management (IE&EM 2012).
3. Q. Zhu, Zh.H. Luo, *Eco-Economy*, **4**, 34 (2015).
4. Ch.X. Zhang, *Special Economic Zone*, **3**, 53 (2009).
5. X.Z. Luo, *Assets and Industries*, **4**, 23 (2007).
6. Q.W. Zhu, *Depth Study*, **8**, 15 (2009).
7. L. Li, G.H. Zhou, Ch.H. Wang, *Economist*, **6**, 50 (2015).
8. Y.X. Ma, *Journal of Northwestern University*, (2009).
9. L.B. Zhang, *Journal of Nanjing University*, (2015).

Analysis of pharmacological adverse reactions of western medicines

Fang Qi

The First Affiliated Hospital of Soochow University, Suzhou, China

Received October 13, 2017; Accepted December 20, 2017

Objective: To analyze the pharmacological adverse reactions from clinical western medicines applications, providing guidance to strengthen the western medication safety. **Method:** A retrospective analysis was conducted to study the case data of 58 patients who had adverse reactions during the western medicines treatment from September 2015 to March 2016 in our hospital. **Results:** The results showed that the most common medication route of adverse reactions was intravenous drip and infusion. The incidence of adverse reactions was mainly in skin and accessories, and the main adverse reactions were scalp rash, swelling, scaling, etc. The main western medicines which could lead to adverse reactions were antibiotics, digestives, endocrines, etc. **Conclusion:** There are many kinds of western medicines and the combination of different pharmacological drugs can produce adverse reactions. Therefore, clinicians should strengthen the mastery of the pharmacological properties of western medicines and rationally use the drug according to the actual situation of patients, improve the safety of medication and reduce the occurrence of adverse reactions.

Key words: Western medicines; Pharmacology; Adverse reactions; Clinical manifestations

INTRODUCTION

Pharmacology itself is a high-degree summarization of the core and fundamentals of medicine, its content is specific, and in-depth application and research can be carried out only with clear category and content of the western medicines. The application of western medicines is relatively common in daily life, at present, many patients will choose western medicines in disease treatment, but western medicines might endanger the human body, even causing other diseases or accelerating the aging of human body. In the treatment of human diseases, western medicines themselves have limitations such as possible adverse reactions. The common administration mode of western doctors is using clinical prescription drugs, with a wide range of drugs and combined utilization to enhance the treatment effect [1]. But there are taboos in the application methods and pharmacological properties of different drugs, if the physician lacks adequate understanding of the physical and chemical properties of the prescription drug, it is easy to lead to irrational medication, resulting in the occurrence of adverse reactions in patients [2]. Therefore, the analysis of patients adverse reactions in using western medicines and promotion of the rationality of clinical medication of western medicines have become the focus of attention at this stage of clinical medication. In this paper, the reports and clinical data of 58 patients who had adverse reactions during the western medicines treatment in our hospital were reviewed and summarized in order to provide experience

guidance for rational clinical application.

MATERIALS AND METHODS

General information

The case data and adverse reaction reports of 58 patients who had adverse reactions during the western medicines treatment from September 2015 to March 2016 in our hospital were selected as the study object, including 32 males and 26 females, aged 8 to 72 years old, mean age of 46.2 ± 5.4 years old.

Methods

A retrospective analysis including the patients' age, gender, adverse reaction symptoms, the type of drug used, the causes and treatment of adverse reactions, etc. [3] of the selected patients was conducted, and statistical analysis of the results obtained was made by using Excel.

RESULTS

Analysis of the routes of administration of western medicines causing adverse reactions

At present, the common clinical western medicines administration routes include intravenous drip, intravenous injection, intramuscular injection, oral administration, etc. The main routes of administration and incidence of adverse reactions in this group were: 2 cases of intramuscular injection, accounting for 3.45%; 8 cases of intravenous injection, accounting for 13.79%; 42 cases of intravenous drip, accounting for 72.41%, 6 cases of oral administration, accounting for 10.35% (Table 1). It was concluded that intravenous drip was the most effective way to induce adverse reactions of western medicines, and intramuscular injection,

To whom all correspondence should be sent:
E-mail: bo_an_cnbd@sina.com

intravenous injection and oral administration can also lead to adverse reactions.

Table 1. Administration routes of patients with adverse reactions

Administration route	Number of cases (%)
Intramuscular injection	2 (3.45)
Intravenous injection	8 (13.79)
Intravenous drip	42 (72.41)
Oral administration	6 (10.35)

Main occurring parts and clinical manifestations of patients with adverse reactions

Through the analysis of clinical data of this group of patients, we can learn that patients have varying degrees of clinical symptoms. As shown in Table 2, the main parts of patients with adverse reactions of western medicines were skin and accessories, accounting for 56.89%, mainly skin ulceration, rash, scaling, swelling, itching, etc., followed by nervous system and digestive system, accounting for 15.52% and 13.79%, respectively, with main clinical manifestations of headache, insomnia, confusion, loss of appetite, vomiting, diarrhea, abdominal distension, etc. Other adverse reactions occurred in the respiratory system (6.90%), cardiovascular system (5.17%) and urinary system (1.73%). There are also some patients having adverse reactions in different parts concurrently. The reasons for adverse reactions include combined application of western medicines, improper use, improper dose, repeated drug use, pharmacological antagonism, etc.

Main medication types of patients with adverse reactions of western medicines

Table 2. Main occurring parts and clinical manifestations of patients with adverse reactions (%)

Parts	Number of cases and percentage	Clinical manifestations
Skin and accessories	33 (56.89)	Skin necrosis, mucosal ulceration, rash, suppurative blisters, scaling, swelling, itching, etc.
Nervous system	9 (15.52)	Excessive excitement, lethargy, limb twitching, insomnia, confusion, hand tremor, fatigue, chills, dizziness, headache, body temperature rise, etc.
Digestive system	8 (13.79)	Loss of appetite, nausea, vomiting, abdominal distension, diarrhea, abdominal pain, etc.
Respiratory system	4 (6.90)	Cough, dry throat, breathing difficulties, shortness of breath, voice crack, etc.
Cardiovascular system	3 (5.17)	Palpitation, chest tightness, arrhythmia, tachycardia, etc.
Urinary system	1 (1.73)	Dysuria, oliguria, hematuria, etc.

Table 3. Main medication types of patients with adverse reactions of western medicines

Types of medication	Number of cases (%)
Antibiotics	16 (27.59)
Digestive system drugs	11 (18.97)
Nervous system drugs	9 (15.52)
Cancer drugs	7 (12.07)
Respiratory system drugs	6 (10.34)
Immune system drugs	4 (6.89)
Blood system drugs	3 (5.17)
Other types of drug	2 (3.45)

The study showed that, in this group of patients, there were 16 cases where adverse reactions occurred due to the use of antibiotics, accounting for 27.59%; 11 cases and 9 cases due to the use of digestive system drugs and nervous system drugs, accounting for 18.97% and 15.52%; there were also 7 cases of cancer drugs, 6 cases of respiratory drugs, 4 cases of immune system drugs, 3 cases of blood system drugs and 2 cases of other types of drug, see Table 3 below.

Treatment of patients with adverse reactions of western medicines

58 patients in this group with adverse drug reactions were basically cured after effective symptomatic treatment, in which 2 patients with severe adverse reactions improved after treatment, the overall cure rate was 96.55%. Antibiotics have the highest incidence of adverse reactions, so hospitals should make strict regulations on the use of antibiotics to reduce the incidence of adverse reactions, and intravenous drip can also lead to a higher incidence of adverse reactions, so this type of administration should be attached with enough attention! In addition, by observing the clinical symptoms of patients with adverse reactions, allergic reactions are related to the patient's physical condition, drugs and other factors, so the various types of adverse reactions in patients disappeared or decreased after drug withdrawal, sufficient attention should also be paid in re-medication, so as to avoid serious consequences resulting from individual differences.

DISCUSSION

Drugs are one of the commonly used methods of clinical disease treatment. The scientificity of medication, prognosis and the rationality of treatment effect directly affect the prognosis and treatment effect of patients. In order to effectively reduce the patient's clinical treatment time while effectively ensuring the treatment effect, clinicians will also take a combination of western medicines for the treatment of the disease. From the perspective of clinical treatment, it is the main purpose to carry out combined therapy through the mechanisms of different western medicines to achieve an improvement of curative effect [4]. However, due to the wide variety of western medicines, the pharmacological response between different drugs is uncertain, and with the increasing incidence of adverse reactions of western medicines in recent years, how to ensure the rationality of drug use is still the focus of medical science.

Theoretical system and connotation of western medicines

The main idea of the medical profession at the present stage is to understand that though there are some hidden adverse reactions in western medicines, they have obvious disease treatment effect and short cure time. On the contrary, although Chinese herbal medicines have less adverse reactions, the treatment time is long. Therefore, there have been produced compound Chinese and Western medicines with short cure time and less adverse reactions, so as to achieve disease treatment effect. Whether with Chinese and Western compound medicines, Chinese herbal medicines or western medicines, healthy and scientific and treatment can only be achieved after analysis and research of the theoretical connotation of pharmacy.

Contents of western medicine pharmacological system

The contents of western medicine pharmacological system are based on the modern scientific chemistry, biology and physics, for example, the relevant parts of the body are examined by a microscope, and the functional status of the organism is expounded through biochemical changes, physiological functions and pathomorphology. It is an important basis for the selection of appropriate prevention and treatment methods, also a key criterion for diagnosis of disease. The main worry of choosing drugs for disease treatment is the impact on body pathology, physiological and biochemical index changes, so appropriate drugs that can play a role in disease prevention and treatment are chosen. Doctors

usually give little consideration of the impact of internal factors during treatment, emphasizing the pertinency of external factors on patients' functional indices, which is the key to Western pharmacology theory.

Connotation of western medicines concept

Fundamentally, western medicine itself is similar to relevant contents of the pharmacological system of Western medicine, for example, the drug is acidic or alkaline, liquid or solid, but no matter what, the key is the physical properties or chemical properties of the drug. For example, lowering blood pressure, increasing blood sugar or inhibiting bacteria should be expressed in the drug efficacy of the corresponding pathological, physiological and biochemical indices and terms, the difference of the drug functions should be the key consideration in the aspect of biological activity, avoiding the use of different drugs and regarding the efficacy as a whole. In other words, western medicines must strictly follow the western pharmaceutical theory in the application process of drugs.

Major impact of western medicines on human health

Direct impact of western medicines on body

Western medicines are used by many patients due to their quick effect, however, improper application would directly damage the body organs. For example, many antibiotics will directly harm the patient's liver and kidney functions, and radiation therapy will directly hurt the body parts of patients, chemotherapy will destroy the bone marrow hematopoietic function and gastric mucosa, etc.

Destruction or inhibition of viscera function, resulting in a permanent imbalance of human endocrine

Long-term use of western medicines will leave a large amount of drug residues in the patient's body, some drugs will remain in the human tissues after drug absorption, and are difficult to discharge, causing direct impact on human health. Many clinical hormone drugs will largely inhibit liver function, resulting in endocrine disorders in patients, etc., and even life-long dependence on the drug.

Hindering of the body's own recovery and disease rehabilitation functions

Fundamentally, human beings resemble other living beings on earth. They have the function of self-protection, for example, they have very strong ability to resist viral and bacterial infection, and also have some self-healing functions on body diseases, automatically repairing and reconstructing

illness-related or injury-related injuries. Therefore, the uncontrolled abuse of drugs will lead to a gradual replacement of the inherent functions of the human body to survive, even hindering the rehabilitation function and slowly losing the body resistance ability. Even some of the functional planning may also be passed on to future generations, so that it will weaken the body of future generations, and ultimately lead to the degradation of virus recovery functions of human species.

Viral and bacterial evolution endangering human health

The development of antibiotics indeed cured many infectious diseases caused by viral infection, also greatly contributed to the cause of human health. However, the large application of antibiotics, combined with exaggerated condition of patients in clinical treatment, resulting in patients' superstition of drug treatment efficacy, formed the current abuse of antibiotics in the medical field. The large application of antibiotics on the one hand will lead to patients' severe clinical adverse reactions, on the other hand also accelerated the evolution of many cell viruses to have stronger drug resistance, and then upgrade to a new strain with larger toxicity, and the study cycle of drug is significantly slower than the evolution of the viruses and bacteria. Since western medicines can not distinguish, so beneficial bacteria will be killed while killing viral microbes, resulting in flora imbalance.

In this paper, the clinical data of 58 patients who had adverse reactions in our hospital were reviewed and summarized, the results showed that the most common route of administration was intravenous drip, accounting for 72.41%, and the most common route of administration for patients who had adverse reactions of western medicines was intravenous drip, accounting for 72.41%, intravenous injection, intramuscular injection and oral administration also led to adverse reactions. The main parts of patients with adverse reactions were skin and accessories, accounting for 56.89%, followed by nervous system and digestive system, accounting for 15.52% and 13.79%, respectively, with the main clinical manifestations of rash, swelling, fever, vomiting, dizziness, insomnia, abdominal distension, diarrhea, etc. After analysis of the patients' adverse reactions of western medicines, irrational medication is the main cause, and due to the different mechanisms of action of the drugs, and the individual differences of patients, it is easy to cause the occurrence of adverse reactions. In the survey, there was 1 patient with gastric bleeding by taking indomethacin and aspirin at the same time, the main reason is that

indomethacin has a strong stimulating effect; aspirin hydrolysis will generate salicylic acid to stimulate the gastrointestinal tract mucosa. Therefore, the combined use of both will bring more serious adverse reactions.

In order to effectively reduce the incidence of adverse reactions, and effectively improve the treatment effect, we can do the following: firstly, we should strengthen the understanding of the relevant adverse reactions, master the pharmacodynamics and contraindications of different western medicines, and conduct medication in strict accordance with the instructions and specific conditions of patients. Prescription of drugs shall be made after fully understanding the patient's condition and the pathological effects of different drugs, developing scientific drug medication. Secondly, the relevant medical staff should actively strengthen the drug use knowledge training, make clear the pharmacological effects and use knowledge of western medicines. In response to the occurrence of patients with adverse reactions, nurses should also closely observe and diagnose the patient's condition, make timely and effective treatment to avoid aggravation of the disease. In addition, pharmacists also need to strengthen the intervention of western medication, carry out a rigorous review of western medicine prescription [5]. Hospitals also need to strengthen the dynamic management of the use of western medicines, and ensure drug safety.

In conclusion, there are many kinds of western medicines and the combination of different pharmacological drugs can produce adverse reactions. Therefore, clinicians should strengthen the mastery of the pharmacological properties of western medicines and rationally use the drug according to the actual situation of patients, improve the safety of medication and reduce the occurrence of adverse reactions.

REFERENCES

1. X.L. Zhang, *China Continuing Medical Education*, **07**, 246 (2015).
2. C.H. Nan, *Contemporary Medical Symposium*, **15**, 154 (2014).
3. S.Y. Che, C.A. Zhang, Y.B. Yang, *Health for All (Academic Edition)*, **11**, 81 (2015).
4. H. Chen, J.Q. Wang, *Journal of Clinical Medical Literature*, **12**, 2283 (2015).
5. H. Chang, *World Latest Medicine*, **16**, 145 (2016).
6. D.B. Guan, *Economic and Technical Cooperative Information*, **17**, 41 (2014).
7. W.J. Xu, Y. Guo, *Health for All (Periodical)*, **10**, 24 (2014).
8. M.H. Ma, *World Latest Medicine*, **16**, 147 (2016)

Discriminating geochemical anomalies by geological-geochemical method: A case study on Nagan section of E'dong area in Wuxu ore field in Guangxi Province, China

R.Ch. Zhou ^{1,2}, J. Wu ^{2,3*}

¹*School of Geosciences and Info-Physics, Central South University, Changsha, Hunan, China*

²*College of Resource and Metallurgy, Guangxi University, Nanning, Guangxi, China*

³*Guangxi Zhongke Geological Exploration Co.Ltd, Nanning, Guangxi, China*

Received April 15, 2017, Accepted December 29, 2017

The Edong Pb-Zn-Sb ore district is an important mineralized anomaly area in the Wuxu ore field, Guangxi province China. The secondary halo method was used to locate blind Pb-Zn-Sb ore bodies in the Edong district. A strong single Zn secondary anomaly was found across the F3 fault zone in the Edong ore district. Alteration features and trace element concentration of country rock along the F3 fault and the ore veins in the Edong mineralized district were compared to discriminate if the Zn secondary anomaly was caused by mineralization or not. The F3 fault zone did not undergo alteration as those associated with Pb-Zn-Sb ore veins. The country rocks across the F3 fault zone is characterized by strong Zn anomaly without Pb anomaly and the country rocks surrounding ore veins, on the other hand, have anomalies of Pb and Zn. Based on the above difference between the F3 fault zone and Pb-Zn-Sb veins in alteration features and geochemical anomaly of element association, together with the geochemical characteristics of galena, sphalerite, and stibnite during weathering, it is concluded that the strong single Zn anomaly around the F3 fault zone does not caused by mineralization, but rather by the absorption of zinc sulfate by clay mineral in the F3 fault zone. Our conclusion has been testified by drill hole. This work provides a clue for discriminating if a geochemical anomaly is caused by mineralization or not and is therefore very important for supervising ore exploration.

Key words: Geochemical anomaly detection; geochemical features of ore forming elements; Wuxu ore field; Guangxi

INTRODUCTION

Geochemical prospecting is an effective and widely used method for precious metals and nonferrous metals prospecting, it features economical, fast and simple and so on[1]. The results of the geochemical analysis are usually massive amounts of analytical data and a variety of geochemical anomalies. Anomaly recognition is the basis of anomaly evaluation[2][3]. How to find the anomalies corresponding to the ore body among the large amount of geochemical anomalies is the key to geochemical exploration[4]. For decades, geotechnical prospecting engineers have been working to solve this problem, and have proposed a geological prospecting method; cross section method at the anomaly center[5]; multi-method comprehensive study[6]; determine whether the mine is caused by anomaly by analyzing the relevant ore-forming elements ratio and zoning[7][8]; estimate the geochemical anomaly from geology, structure, terrain, mineral elements and other aspects[9]; some researchers analyze geochemical anomalies through elemental geochemical migration behavior, but are mainly limited to volatile elements such as mercury[10]. In this paper, the geological significance of geochemical anomalies in the E'dong Pb-Zn-Sb ore district, Wuxu ore field is analyzed by means of

mineralization element anomaly combination, mineralization element endogenous and supergene geochemical behavior and anomaly area alteration. This work provides a new method and idea for the effective identification of anomaly.

GEOLOGICAL CHARACTERISTICS OF WUXU OREFIELD AND E'DONG DEPOSIT

Wuxu orefield is located in the southern section of the Dumeng polymetallic metallogenic belt (Fig. 1 a) in Guangxi China, which is an important ore deposit area of Danchi metallogenic belt. There are Devonian Naxing Formation, Luo Fu Formation, Durian River Group, Wuzhishan Formation, and some Carboniferous and Middle Triassic in the exposed strata of this region. The ore-hosting rock bodies are mainly standard group of mudstone and malm sandstone of the Middle Devonian, followed by Luofu group of mud limestone and charcoal limestone. The deposits are mainly in the form of veins in the stratigraphic fracture zone, which is a medium-low temperature hydrothermal deposit [11]. The composition of mineral elements is complex, mainly Pb, Zn, Sb, Ag, mineralization alteration is weak, mainly sericite, silicification, pyrite mineralization and carbonation. The main deposits of Wuxu orefield are located in the west of the anticline, and the eastern mineralization is weak. The mineralization element combination of Wuxu orefield has obvious zoning (Fig. 1b), that is, the central part on the plane has a combination of Pb, Zn, Sb, Ag, the surrounding of Hg and As.

To whom all correspondence should be sent:
E-mail: 78300928@qq.com

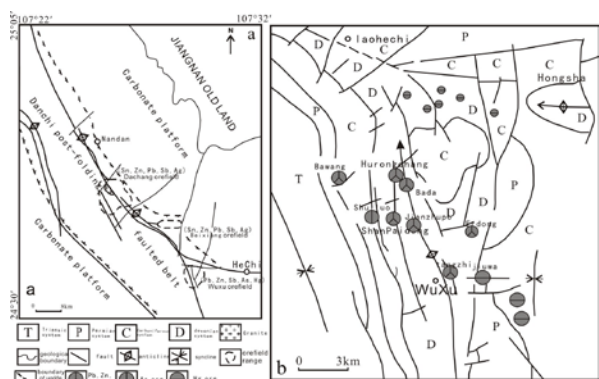


Fig.1. Simplified geological map of the Danchi ore belt (a) and the Wuxu ore field (b)

E'dong Pb, Zn, Sb mineralization anomalies are located at the east of Wuxu orefield (Fig. 1b), with Pb and Zn mineralized small veins, two 20 to 40 cm thick Pb and Zn veins at depths of more than 180 meters of drill hole (ZK02) are found, veins move towards SN, tend to west. The Nagan ore block is located in the north of the E'dong mineralized anomaly area, and the exposed strata are mainly the mudstone and malm sandstone of the Middle Devonian Donggangling Formation (D2d) and the Late Devonian Liujiang group (D3l). A near-SN F3 fracture (Fig. 2a) is developed along Nagan ore block, sporadic gossan are seen along the F3 fault which is considered to be an important potential area for ore prospecting.

SAMPLES AND ANALYTICAL METHODS

Sporadic exposed gossan are seen along F3 fault, with possible development of mineralization deep down, Hechi Yuanhe Mining Co., Ltd. made a

secondary halo scouring on the F3 fault zone surface to analyze the deep prospect of F3 fracture prospecting. The sampling profile of the geochemical scanning surface is perpendicular to the F3 fracture (Fig. 2a), the distance between the sampling lines is about 100 meters, about 20 meters between the samples, main collecting B layer soil. The original halo samples are located in the F3 fault zone and are collected along the vertical F3 fault. The trace element composition of the sample was completed at the analysis and test centre of Guilin Institute of Mineral Geology. Ag and Sn were analyzed by WSP-1 spectroscopy, the analysis error is less than 2%; Cu, Pb, Zn, As, W and Sb were analyzed by ICP-MS, and the analysis error is less than 3% (Table 1).

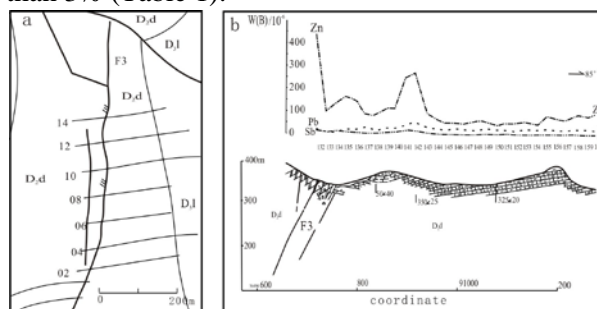


Fig.2. Simplified geological map of the Nagan mineralized spot (a) and ore forming anomalies along the profile number 8 line (b) (1. F3 Fault; 2. Fault; 3. Middle Devonian; 4. Late Devonian; 5. Geochemical scanning line; 6. Zinc anomaly line; 7. Lead anomaly line; 8. Antimony anomaly line; 9. Geochemical sampling number)

Table 1. Trace element contents of primary and secondary halos across the F3 fault

No.\Sec-halos	Pb	Zn	Sb	Cu	As	No.\Sec-halos	Pb	Zn	Sb	Cu	As
132	20.1	439	14.9			147	20.1	45.9	4.98		
133	8.12	91.4	8.21			148	16.9	60.4	4.12		
134	9.43	136	13.4			149	25.8	60.3	7.46		
135	20.1	165	8.98			150	20.9	41.2	4.23		
136	20.4	150	7.41			151	19.7	53.2	8.99		
137	31.2	81.3	3.46			152	14.9	49.2	5.34		
138	14.1	86.2	5.12			153	24.8	57.4	4.98		
139	27.1	116	6.12			154	19.7	37.2	5.11		
140	25.4	115	9.98			155	25.1	84.1	6.22		
141	35.2	260	15.8			156	19.2	69.4	7.41		
142	53.3	273	17.2			157	20.4	66.3	4.87		
143	30.1	96	9.21			158	25.3	89.2	5.96		
144	24.4	68.1	6.41			159	24.2	79.9	3.97		
145	20.3	51.2	5.41			160	20.1	95.8	4.97		
146	24.9	50.1	6.13								
No.\Pri-halos	Pb	Zn	Sb	Cu	As	No.\Pri-halos	Pb	Zn	Sb	Cu	As
GP3	26.7	84.7	5.92	78.7	58.9	Ng-06	11.6	670	13.7	323	80.7
GP4	25.6	131	8.31	131	19.5	Ng-05	17.4	3600	27.0	206	156
GP7	16.3	716	4.98	114	127	Ng-04	17.8	277	7.82	281	31.2
GP10	13.2	678	26	42.1	155	Ng-03	21.1	1100	4.6	111	228
GP11	9.5	1900	5.25	928	87.5	Ng-01	21.2	3500	8.8	201	308
Ng03-01	10.7	880	14.4	166	88.3						

CHARACTERISTICS OF GEOCHEMICAL ANOMALY IN NAGAN MINERALIZED BLOCK

The microelement analysis results of the secondary halo and primary halo are shown in Fig. 1 and Fig. 2b. From Fig. 2b, it is known that there is a high Zn anomaly near F3 fault zone in the Nagan ore block (Fig. 2b). Primary halo analysis showed that zinc content in the primary halo in F3 fault zone is particularly high, up to 3600ppm, almost reached the industrial grade of zinc ore; Pb and Sb content is not high, even lower than the average of this area (mean: Pb: 44.9ppm, Sb: 5.5ppm, 638 sample mean values). The main mineralization elements are Zn, Pb, Sb, Ag in Wuxu orefield, while only Zn anomaly in F3 fault, with a lack of Pb and Sb. So, is the Nagan ore Zn anomaly in the F3 fault zone of Nagan ore block an ore-caused anomaly? Has deep mineralization occurred in F3 fault zone?

Geochemical anomaly plays a key role in ore prospecting [4], in the evaluation of geochemical anomaly, it is necessary to consider the anomaly intensity changes, but not be limited to high intensity anomaly. This is mainly because there are many complex factors that affect the intensity of anomaly, including the impact of mineralization, and the role of post-epigenetic effects. Therefore, geochemical anomaly evaluation should not only consider the intensity, but also the mineralization characteristics, the element combination of mineralization of the mining area or the mineralization point, the geochemical behavior of the element under hydrothermal action, and the geochemical behavior of the element under hypergenesis.

Hydrothermal deposit is the formation of deposits from the hydrothermal large-scale precipitation of ore-forming elements due to materialized environment changes[12-16]. After the precipitation of ore-forming elements, the residual ore-forming fluids will continue to migrate upward, and chemical reactions with rocks occurs while rising, forming an ore-forming element anomaly and alteration belt much larger than the orebody at the top[16-20]. If the F3 fault is formed by mineralization (zinc has almost reached the boundary grade), the relevant mineralization alteration and the relevant element combination should be seen. Therefore, through the alteration feature analysis of F3 fault zone, comparison of ore-forming elements combination anomaly in the vertical F3 fault and at the mineralized anomaly point, we can identify whether it is an ore-generated anomaly.

(1) Characteristics of anomaly belt alteration and its geological significance

The deposit in this area is a low-temperature hydrothermal deposit, with major alteration of carbonate, sericite, silicification and pyrite [21].

Therefore, if mineralization occurs at deep F3 fault, the top should develop some low-temperature alteration combination.

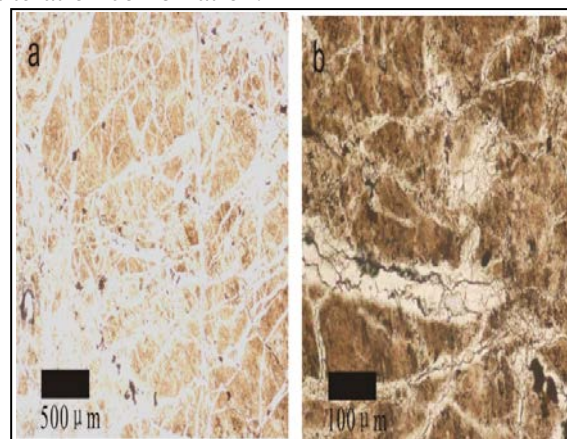


Fig.3. Microscopic photos showing the alteration characteristics of the argillaceous siltstone in the F3 fault zone

We performed a microscopic observation of the F3 fault zone samples, and found non-directional arrangement (Fig. 3a) in argillaceous siltstone and directional aligned veins of quartz and limonite (Fig. 3b), with no low-temperature alteration mineral combinations. The veins of quartz are very clean with no sulfide, with limonite formed by leaching. The veins of quartz and the mineralization alteration are completely different, hence it is reasonable to conclude that the quartz are not related to mineralization and are more likely to be side secreted products. The alteration mineral characteristics of argillaceous siltstone in F3 fault zone do not support that mineralization occurred deep in F3 fault zone.

(2) Characteristics of Ore-forming Primary Halo Elements Combination in E'dong Mineralized Area

The deposits with the same ore-forming role also have a similar ore-forming elements combination [13]. The mineralization of Pb and Zn in the E'dong mineralized anomaly zone has the development of Pb and Zn mineralization in ZK02 drill hole at about 2 km south of Nagan ore block. The geochemical behavior of Pb and Zn in hydrothermal fluids is similar and migrates mainly in the form of chlorine complexes in hydrothermal fluids [22,23]. Thus, if F3 anomaly is an ore-caused anomaly, theoretically the primary halo should form Pb-Zn anomaly instead of single-zinc anomaly. In order to analyze the characteristics of E'dong mineralization halo anomaly, we analyzed the composition of 21 core-like trace elements in the upper and lower plate rocks of Nagan ore block drill hole ZK02 lead-zinc mineralization (Table 2). The results show that the contents of Pb and Zn in the rocks of the upper and lower plates of the mineralization veins are relatively high, which is consistent with the theoretical analysis.

Table 2. Trace element content of roof and floor rocks surrounding ore vein in the Edong mineralized area

Nb.	Pb	Zn	Ag	W	Sn	As	Sb
ZK02-1	64.4	380	0.03	1.2	2.9	262	14.6
ZK02-2	50.3	138	0.03	1.1	2.6	31.9	13.3
ZK02-3	69.2	62.1	0.07	1.0	1.9	23.6	3.62
ZK02-4	11.6	23.8	0.09	1.2	1.1	72.9	1.01
ZK02-5	99.3	155	0.07	1.3	3.7	45.8	1.63
ZK02-6	25.9	41.1	0.07	1.0	1.0	1.8	0.42
ZK02-7	219	479	0.04	1.3	2.9	11.2	0.73
ZK02-8	240	329	0.06	1.0	3.1	58.3	3.01
ZK02-9	28.3	32.6	0.06	1.2	2.5	126	5.21
ZK02-10	52.2	72	0.04	1.0	2.3	9.9	1.44
H1	24.3	125	0.05		4.0	46.4	7.33
H2	2000	1100	2.28		4.1	89.5	13.7
H3	44.5	124	0.09		4.1	130	10.9
H4	32.3	65.1	0.10		4.3	32.2	10.6
H5	130	199	0.26		3.6	34.9	103
H6	40.6	144	0.11		4.4	51.9	9.23
H7	49.6	110	0.08		4.3	32.5	42.6
H8	576	257	0.19		4.3	42.3	257
H9	2000	872	0.76		3.5	58.7	1865
H10	433	501	1.10		3.9	60.5	236

(Analysis unit: test report of Guilin Analysis and Test Center of Nonferrous Metals. Test results: ωB/10-6)

To compare the anomaly combination characteristics of the primary halo elements in drill hole ZK02 and F3 fault in the E'dong mineralized area, we used SPSS software to study and compare the two groups of ore-forming elements model (Fig. 4), and found that the correlation between lead and zinc in F3 fault zone was very poor, almost 0 (0.0454).



Fig. 4. Cluster diagrams of the rock samples from the F3 fault zone (a) and drill hole surrounding the ore veins in the E'dong mineralized area (b)

The correlation analysis of ore-forming elements in the primary halo of drill hole shows that the mineralization of the Nagan orefield will form Pb-Zn anomaly instead of single-Zn anomaly. Wuxu orefield has mainly Pb-Zn-Sb-Ag mineralization, with no single Zn mineralization. The analysis of massive geological data (analysis report of ore field reserves) of Wuxu orefield shows a combination of Pb, Zn and As. Only single-Zn anomalies are

around F3, and lack of anomalies formed by Pb, As or other elements, hence it is not an ore-caused anomaly.

(3) Analysis of single zinc and high anomaly formation in F3 fault zone

The obvious difference among the alteration characteristics of F3 fault zone, single-Zn anomaly in the secondary and primary halo and ore-forming primary halo elements combination in Wuxu orefield and E'dong mineralized area indicates that the single-Zn anomaly in Nagan ore block is not an ore-induced anomaly, so how did it form?

E'dong area is an old mine with a certain history of mining, and in the past there had been indigenous refinery near the F3 fault zone. During the process of indigenous mineralization, the above elements will be polluted on the surrounding surface. The elements of Zn, Pb, Sb and other elements are different in the geochemical environment under the geochemical environment (Liu Yingjun et al., 1980). Zn, Pb, Sb mineralization in the mining area are mainly in the forms of galena, sphalerite and refractory antimony ore. To understand why there is such a high single-zinc anomaly along the F3 fault zone, firstwe need to understand the main ore minerals: the geochemical behavior of sphalerite, galena and stibnite under supergene conditions.

Galena is stable in the surface conditions than the sphalerite, and it will form PbSO₄ that is insoluble in water in oxidation. PbSO₄ has poor activity and is difficult to migrate, when encountered carbonate rock, it further forms lead carbonate (cerusite), and cerusite is more stable and easy to dissolve in water. Therefore, lead is not easy to migrate in the surface conditions. Sphalerite has very low oxidation potential and is very susceptible to weathering, especially when there are

other sulfides. Sphalerite is more easily oxidized and the oxidation reaction is as follows: $ZnS+2O_2 \rightarrow ZnSO_4$ [24]. Zinc is highly active in the geochemical environment of the earth and is susceptible to oxidation and migration with surface water. Clay minerals have a certain adsorption of zinc sulfate [24], broken rocks in the crushed zone are more easily weathered to form clay mineral zone. When the zinc sulfate-containing fluid goes through the broken zone, it is easy to be adsorbed by clay minerals, and zinc enrichment can occur in the crushing zone. Stibnite forms valentinite when being oxidized, stibnite and other valentinite-containing complex sulfur minerals have very low solubility in the surface fluid, and are not easy to migrate under supergene conditions [24].

It can be seen from the above analysis that the activity of Zn under supergene conditions is strong, Pb and Sb are inert, while clay minerals have strong adsorption effect on zinc sulfate. F3 fault zone is relatively broken, easier to occur leaching and weathering at the surface conditions, forming clay mineral enrichment zone. Since this area is a Zn, Pb and Sb mineralization area, and the indigenous soil refining near F3 fault zone in the past will pollute the surrounding strata. The Zn, Pb, Sb and other elements in the polluted surrounding surface will undergo differential migration at the late supergene conditions, enriching Zn in the relative development of clay mineral fissure zone and forming high single-Zn anomaly.

To sum up, we think that the single-Zn anomaly in F3 fault is not an ore-caused anomaly, but formed in the late supergene conditions from absorption, and the deep F3 fault zone does not have great mineralization potential.

Although we carried out a comprehensive analysis, it is suggested that the Zn anomaly in F3 is not an ore-caused anomaly and the potential of deep prospecting is not great, but the technical staff of the production unit think it necessary to carry out engineering verification considering such a high zinc anomaly developed in the tectonic broken zone of mining area. Hechi Yuanhe Mining Co., Ltd worked on F3 in November 2013 to verify the hole depth of 345.5 m, penetrated the F3 fault zone and found no mineralization alteration, which further confirmed that our anomaly evaluation is correct. This further shows that in-depth understanding of the geology and geochemical characteristics of deposits can be more effective in identifying geochemical anomalies, providing a successful example for future identification of anomalies.

CONCLUSION

(1) The high-zinc anomaly in the F3 fault zone of Nagan ore block, E'dong mineralized area, Wuxu orefield is not an ore-caused anomaly, but

formed through when the contaminated zinc in the surface is melted and migrated under supergene conditions in indigenous smelting or by being adsorbed by clay or limonite in the F3 fault zone.

(2) Geochemical anomalies are not necessarily ore-caused anomalies, in the analysis of geochemical significance of geochemical exploration, it is necessary to understand the combination and alteration characteristics of ore-forming elements, but also to understand the geochemical behavior of different mineral elements in the supergene environment.

(3) An in-depth understanding of the geology and geochemical characteristics of deposits can be more effective in identifying geochemical anomalies, providing guidance for ore prospecting.

Our conclusion is based on the special area along the F3 fault zone in which clay minerals are well developed. More attention should be paid to geochemical behavior of sulfide minerals such as galena, sphalerite, pyrite, stibnite etc. during weathering in the future work. To comprehensively realize the role of clay minerals in the formation of secondary halo anomaly, the absorption of clay mineral for Pb, Zn, Sb, Ag and Au should be detailed studied in the future.

Acknowledgements: This work was supported by National Key R&D Program of China (2016YFC0600407) and Chinese NSFC (41372084).

REFERENCES

1. Ch. B. Wu, Y. W. Qiu, *Geology and Exploration*, **3**, 49 (1985).
2. P. Gong, Zh. D. Ma, *Earth Science-Journal of China University of Geosciences*, **38**, S1, 113 (2013).
3. S.G. Zhou, K.F. Zhou, Y. Cui, J.L. Wang, J.L. Ding, *Journal of Geochemical Exploration*, **154**, 171 (2015).
4. A.M. Gonbadi, S.H. Tabatabaei, E.J.M. Carranza, *Journal of Geochemical Exploration*, **157**, 81 (2015).
5. X.Ch. Zhu, *Geology and Exploration*, **8**, 58(1980).
6. Y.J. Wang, F. Chen, *Geology and Exploration*, **6**, 22 (1965).
7. H. Li, G.Y. Zhang, B. Yu, D.L. Li, *Earth Science Frontiers*, **17**(1), 287 (2010).
8. D.L. Wan, *Geology and Exploration*, **1**, 45 (1990).
9. G.A. Lyu, Q.Q. Liu, *Geology and Exploration*, **9**, 53 (1987).
10. G.K. Hu, J.J. Tian, W.M. Lai, *Geology and Exploration*, **12**, 55(1980).
11. J.M. Cai, X.H. Xu, B.H. Li, *Journal of Chengdu Institute of Technology*, **22**(1), 69 (1995).
12. J.W. Hedenquist, J.B. Lowenstern, *Nature*, **370**, 519 (1994).
13. H. Y. Liang, P. Xia, X. Z. Wang, J. P. Cheng, Z. H. Zhao, C.Q. Liu, *Ore Geology Reviews*, **31**, 304 (2007).

14. T. Baker, E. V. Achterberg, C.G. Ryan, *Geology*, **32**, 117 (2004).
15. W.C. Su, C.A. Heinrich, T. Pettke, X.C. Zhang, R Z. Hu, B. Xia, *Economic Geology*, **104**, 73 (2009).
16. Y.J. Chen, *Earth Science Frontiers*, **17**(2), 27 (2010).
17. H.Y. Liang, W.D. Sun, W.C. Sun, *Economic Geology*, **104**, 587 (2009).
18. W.D. Sun, H.Y. Liang, M.X. Ling, *Geochimica et Cosmochimica Acta*, **103**, 263 (2013).
19. M.J. Kalczynski, A.E. Gates, *Ore Geology Reviews*, **61**, 226 (2014).
20. J. Mick, R.M. Tosdal, T. Bissig, CM. Chamberlain, K.A. Simpson, *Economic Geology*, **109**, 891 (2014).
21. L. Chen, W.T. Huang, J. Wu, J. Zhang, H.Y. Liang; Sh.P. Lin, Y.Q. Zou, *Geochimica*, **11**, 546 (2015).
22. Z. Zajacz, W.E. Halter, T. Pettke, M. Guillong, *Geochimica et Cosmochimica Acta*, **72**(8), 2169 (2008).
23. X. Chen, J.J. Liu, D.H. Zhang, Y.L. Tao, *Geological Journal of China Universities*, **20**(3), 388 (2014).
24. Y.J. Liu, L.M. Cao, Zh.L. Li, H.N. Wang, T.Q. Chu, J.R. Zhang, *Geochemistry of element [M]*. Beijing: Science Press, 1984: 518.

Removal of *p*-chlorophenol in wastewater through catalytic ozonation using $\text{MnO}_x/\text{Al}_2\text{O}_3$

Y.S. Wan*, D.W. Li

Department of Environmental & Safety Engineering, Changzhou University, Changzhou, Jiangsu, 213164, China

Received August 30, 2017, Accepted, December 27, 2017

In order to study the effect of catalytic ozonation with $\text{MnO}_x/\text{Al}_2\text{O}_3$ in wastewater purification, the effect of the catalyst $\text{MnO}_x/\text{Al}_2\text{O}_3$ on the removal of *p*-chlorophenol from water samples was simulated. The results showed that the addition of catalyst for 10 min of reaction could improve the removal efficiency by 20.15% in comparison with ozone alone. The catalyst was prepared by the impregnation method with a $1.5 \text{ mol}\cdot\text{L}^{-1}$ precursor solution of manganese nitrate. The removal efficiency was good at a calcination temperature of 500°C , and the removal rate reached 81.75% after 20 min of reaction. The catalyst was stable, and the removal rate of the catalyst after repeated use was 70.12% after 20 min of reaction. The characterization results show that the surface of the catalyst $\text{MnO}_x/\text{Al}_2\text{O}_3$ has a more active reaction platform than the carrier Al_2O_3 , which is helpful to improve the catalytic activity.

Keywords: Catalytic ozonation; $\text{MnO}_x/\text{Al}_2\text{O}_3$; *p*-chlorophenol

INTRODUCTION

With the increasingly serious industrial wastewater pollution, the toxicity, bioaccumulation and other characteristics of organic pollutants in wastewater can harm human health [1]. The organic pollutants in the organic wastewater include aromatic compounds, phenols and heterocyclic compounds, and their damage to the water environment gradually increases. The removal of organic pollutants in wastewater generally includes: adsorption, coagulating sedimentation, advanced oxidation, etc. [2,3]. The catalytic ozonation technology has the characteristics of rapid response, low cost and no secondary pollution. It has a wide application prospect for the deep treatment of industrial wastewater.

The mechanism of catalytic ozonation consists in producing $\cdot\text{OH}$ with strong oxidizing property through the decomposition of the ozone attached to the catalyst surface hydroxyl groups. $\cdot\text{OH}$ can promote free radical chain reactions in the solution and on the catalyst surface [4]. The use of catalyst in the reaction can effectively promote the formation and utilization of active substances such as $\cdot\text{OH}$. Under mild experimental conditions, the organic pollutants in wastewater can be removed quickly [5,6]. The commonly used catalytic materials are activated carbon [7], honeycomb ceramics and porous metal oxides [8,9], which can load active components or directly serve as a catalyst in ozone degradation reaction, enhance ozone oxidation effect, and effectively remove organic pollutants from wastewater [10]. The

catalyst with metal oxides as stable active components determines the removal efficiency of ozone oxidation, high efficiency, long life, etc., and is widely used in the catalytic ozonation research [11,12]. In this paper, the catalyst $\text{MnO}_x/\text{Al}_2\text{O}_3$ was used to remove the target pollutant *p*-chlorophenol in wastewater, and the catalyst was added to the single ozone system to enhance the oxidation efficiency of ozone and increase the production and utilization rate of $\cdot\text{OH}$.

EXPERIMENTAL

Materials

Main instruments and reagents

Instruments: ozone generator (Taixing Environmental Protection Equipment Co., Ltd., model QHW-15), constant temperature water bath, pH meter, UV-visible spectrophotometer, tube furnace, drying oven, high performance liquid chromatograph (HPLC, LC-10T), fully automatic specific surface area analyzer (V-Sorb 2800P).

Reagents: methyl alcohol, chromatographically pure, *p*-chlorophenol, calcium carbonate, manganese nitrate, indigo disodium sulfonate, sodium thiosulfate and potassium iodide, all analytically pure. In the preparation of aqueous solutions ultrapure deionized water was used, in which *p*-chlorophenol was not detected.

Test apparatus

As shown in Fig.1, the apparatus is made of ordinary glass and polyethylene plastic, the connecting part is rubber tube, the reaction column is placed in a water bath and the bottom part has an aerating apparatus. Prior to the start of the test, the reaction column was washed with ultrapure water three times and treated by pre-ozonation for 5 min

*To whom all correspondence should be sent:
E-mail: wanyushan@126.com

to remove impurities remaining in the reaction column. All solutions used in the test were prepared using ultrapure water. The apparatus was placed and conducted in a fume hood.

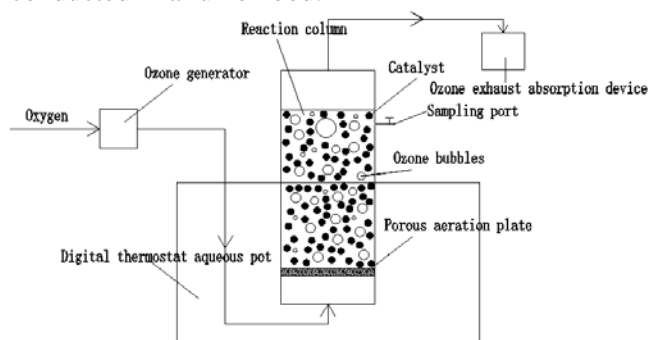


Fig. 1. Test apparatus

In the test, the appropriate amount of sample solution was taken at different time points, sodium thiosulfate solution (0.5 mL , $0.01\text{ mol}\cdot\text{L}^{-1}$) was added to stop the reaction, the sample solution was analyzed by HPLC (High Performance Liquid Chromatography), the test exhaust was introduced into a KI solution (2%) for absorption. Simulated industrial wastewater ($50.0\text{ mg}\cdot\text{L}^{-1}$ *p*-chlorophenol) was used.

Pretreatment of catalyst

Catalyst carrier is an important factor affecting the catalyst performance. The carrier should have unique structure (specific surface area, pore structure) to ensure the thermal stability and mechanical strength of the catalyst, and is the active center of the reaction. In the catalytic ozonation system, the commonly used carriers are Al_2O_3 , TiO_2 , honeycomb ceramics, activated carbon, etc. The reaction conditions of catalytic ozonation are mild, the reaction solution contains no strong acid and alkali, and will not cause great damage to the catalyst structure. Al_2O_3 , honeycomb ceramics and activated carbon have porous structure and large effective specific surface area, which are suitable to a catalyst carrier. In the catalytic ozonation system, ozone adsorption ability of the catalyst surface and the ability to generate $\cdot OH$ determines the catalytic capacity. Metal oxides MnO_x , TiO_2 and other materials are widely used in catalytic ozonation to improve the production and utilization rate of $\cdot OH$. Al_2O_3 has a large specific surface area and high mechanical strength, this test loads MnO_x by taking Al_2O_3 as the carrier to study its effect in ozonation reaction.

Carrier Al_2O_3 ($\Phi 5\text{ mm}$, YiPu Catalyst Co., Ltd.) was grinded, passed through a 60 mesh nylon sieve, baked for 15 h at 95°C in the drying oven after being washed, and then roasted for 5 h at 500°C in the tube furnace to remove surface impurities, then, after natural cooling the carrier Al_2O_3 was preserved. The treated Al_2O_3 was impregnated in a $1.5\text{ mol}\cdot\text{L}^{-1}$

solution of manganese nitrate, stirred continuously for 24 h, aged at 105°C for 24 hours, washed with ultrapure water, dried at 105°C for 10 h, and roasted at 500°C for 5 h to obtain the catalyst MnO_x/Al_2O_3 .

Analysis method

Determination of *p*-chlorophenol in water samples: *p*-chlorophenol was determined by HPLC with the chromatographic column ($4.6\text{ mm}\times 250\text{ mm}$, $5\mu\text{m}$, C-18-AR-II). Detection wavelength was 280 nm , mobile phase consisted of methanol and water (volume ratio of 7:3), flow rate $=1.0\text{ mL}\cdot\text{min}^{-1}$. The samples analyzed by liquid chromatography were compared with standard samples by qualitative and quantitative analysis.

Determination of ozone concentration in water samples using the indigo disodium sulfonate method was used with a UV-visible spectrophotometer at a wavelength of 610 nm . Catalyst characterization: the specific surface area and pore volume of the catalyst samples were determined using a fully automated specific surface area and porosity analyzer.

RESULTS AND DISCUSSION

Effect of load mode

Impregnation method takes manganese nitrate as the precursor, adding the treated Al_2O_3 ; precipitation method adds the solution of calcium carbonate to the manganese nitrate solution by drops; formed precipitate loads to the surface of Al_2O_3 , the concentration of each solution was $1.5\text{ mol}\cdot\text{L}^{-1}$. MnO_x was loaded onto Al_2O_3 to remove *p*-chlorophenol in wastewater by impregnation method and precipitation method, the results are shown in Fig. 2. Test conditions: $C_{O_3}=2.0\text{ mg}\cdot\text{L}^{-1}$, $C_{p\text{-chlorophenol}}=50.0\text{ mg}\cdot\text{L}^{-1}$, $C_{MnO_x/Al_2O_3}=2.0\text{ g}\cdot\text{L}^{-1}$, $\text{pH}=6.5$, $t=20^\circ\text{C}$, the follow-up test will adopt the same reaction conditions if not specified.

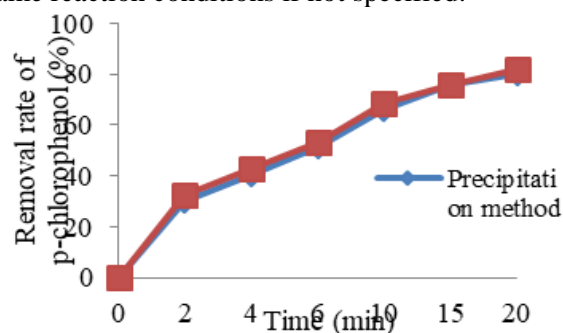


Fig. 2. Effect of load mode

As can be seen from Fig. 2, the removal rate of *p*-chlorophenol reached 80.27% and 82.09% , respectively, after 20 min of reaction using the catalyst. This indicates that the dispersion effect of MnO_x on the carrier surface is good, the precipitation method does not significantly improve

the load effect, and there is no obvious removal performance difference of *p*-chlorophenol after calcination of the catalyst.

Effect of impregnation liquid concentration

Fig. 3 shows the comparison of the removal efficiency of *p*-chlorophenol by the catalyst prepared with different concentrations of manganese nitrate precursor solution.

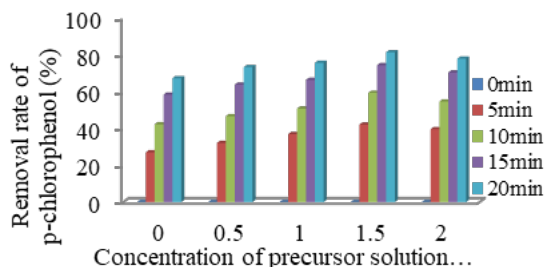


Fig. 3. Effect of precursor solution on MnO_x/Al_2O_3

It is observed that the removal efficiency of *p*-chlorophenol in the solution is enhanced with the increase in precursor solution concentration. When the concentration of precursor solution reached $1.5 \text{ mol}\cdot\text{L}^{-1}$, the removal efficiency of *p*-chlorophenol was significant, reaching 74.28% in 15 min and 81.31% in 20 min. When the concentration of manganese nitrate precursor solution was increased, the removal rate of *p*-chlorophenol decreased, and when manganese nitrate solution was $2.0 \text{ mol}\cdot\text{L}^{-1}$, the removal rate of *p*-chlorophenol was 70.31% after 15 min of reaction and 77.81% after 20 min. This was so because at a low concentration of precursor solution the loading of MnO_x on the carrier surface was low. After high-temperature calcination, some active sites of the carrier Al_2O_3 were inactivated, so the removal rate of *p*-chlorophenol decreased. When the concentration of the precursor solution was increased, the MnO_x loading on Al_2O_3 surface increases. After high-temperature calcination, a large amount of MnO_x adhered to the surface of the carrier, which blocked the pore structure of Al_2O_3 , resulting in reduction of the effective surface area of the carrier, leading to a decrease in the number of active sites on the catalyst surface and in removal efficiency.

Effect of calcination temperature

The calcination temperature in preparing the catalyst MnO_x/Al_2O_3 by the impregnation method affects the catalytic activity. The mechanical strength of MnO_x/Al_2O_3 can be increased by calcination, and the active component can be retained. At the same time, the surface impurities of MnO_x/Al_2O_3 can be removed, so that the catalyst MnO_x/Al_2O_3 has a more effective surface area and a richer pore structure. This requires a suitable calcination temperature. The high calcination

temperature not only damages the surface pore structure of the catalyst, but also affects the formation of MnO_x/Al_2O_3 surface active components and crystal structure, leading to the reduction of MnO_x/Al_2O_3 specific surface area.

Fig. 4 shows the comparison of the removal efficiency of *p*-chlorophenol by the catalyst (concentration of precursor solution $1.5 \text{ mol}\cdot\text{L}^{-1}$) after 5 h of calcination at temperatures of 300 °C, 400 °C, 500 °C, 600 °C.

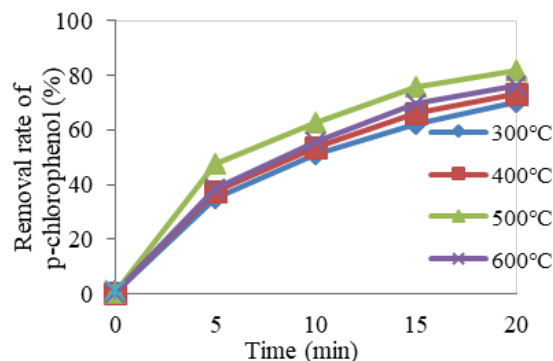


Fig. 4. Effect of calcination temperature on MnO_x/Al_2O_3

The results show that the calcination temperature has a significant effect on the removal of *p*-chlorophenol by the catalyst MnO_x/Al_2O_3 . When the calcination temperature gradually increased, the removal rate of *p*-chlorophenol first increased and then decreased, and catalytic ozonation was better at a calcination temperature of 500 °C. When the temperature was raised from 300 °C to 500 °C, the removal rate of *p*-chlorophenol increased from 70.20% to 81.75% after 20 min of reaction, and the removal rate of *p*-chlorophenol was reduced to 76.36% at 600 °C. Because the temperature gradually increased in the catalyst crystal formation process, the catalyst surface generated more active sites and increased catalytic activity. When the catalyst MnO_x/Al_2O_3 calcination temperature reached 500 °C, the active sites were evenly distributed on the surface of MnO_x/Al_2O_3 after calcination, achieving a balance. The temperature increase will change the surface crystal structure of MnO_x/Al_2O_3 , decrease the active sites and reduce the catalytic activity, and the removal rate will decrease. The preparation conditions of MnO_x/Al_2O_3 in the follow-up test are as follows: concentration of precursor solution: $1.5 \text{ mol}\cdot\text{L}^{-1}$, calcination temperature: 500 °C.

Effect of reaction temperature

In the case of ozone, the reaction temperature has two effects: as the temperature increases, the reaction rate increases, and the number of activated molecules increases; while the solubility of ozone in water is negatively correlated with temperature, the temperature increases, the ozone in solution

decreases, and the utilization rate decreases. Fig. 5 shows the removal rate of *p*-chlorophenol and the volatilization of *p*-chlorophenol at temperatures t of 10, 20, 30, 40, 50, 60 °C under the conditions of O_3+MnO_x/Al_2O_3 and O_3 alone. The reaction conditions only changed the reaction temperature, other conditions remained unchanged.

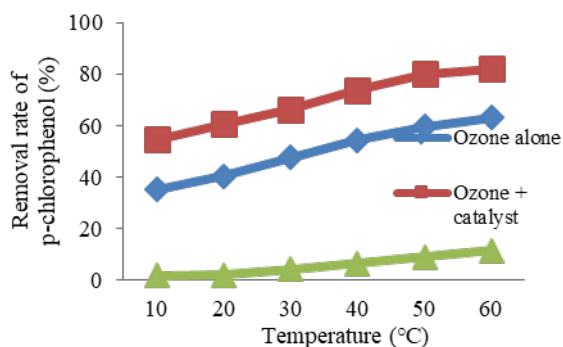


Fig. 5. Effect of reaction temperature on the removal of *p*-chlorophenol

It can be seen from Fig. 5 that the volatilization of *p*-chlorophenol increases with the increase in reaction temperature, the volatilization rate is 1.65% at 10 °C and 11.37% at 60 °C. The removal rate of *p*-chlorophenol by O_3+MnO_x/Al_2O_3 and O_3 system alone gradually increased with the increase of reaction temperature. When the temperature rose from 10°C to 60°C, the removal rate of *p*-chlorophenol by $O_3+ MnO_x/Al_2O_3$ increased from 54.67% to 82.13% after 10 min of reaction, and the removal rate of ozone alone increased from 35.26% to 63.17%. The removal rate was by 20.15% higher than that of ozone alone after 10 min of reaction at a normal temperature of 20 °C, and the removal efficiency by using O_3+MnO_x/Al_2O_3 was significantly increased. The catalyst promoted the formation of $\cdot OH$ by ozone decomposition over the experimental temperature range, the removal of organic pollutants from wastewater by catalytic ozonation is significant.

Stability of MnO_x/Al_2O_3

The catalyst (MnO_x/Al_2O_3) was used repeatedly (1, 2, 5, 8 and 10 times), each time during 10 h. Fig. 6 shows the results of the repeated removal of *p*-chlorophenol by MnO_x/Al_2O_3 . It can be seen that repeated use of MnO_x/Al_2O_3 has a certain effect on the removal efficiency. The increase in the time of use and the decrease in removal efficiency are due to the presence of certain substances in the removal process that are attached to the surface and pore structure of the catalyst and cover some active centers, leading to inactivation of some active sites on the MnO_x/Al_2O_3 surface, even causing some MnO_x/Al_2O_3 to completely lose activity.

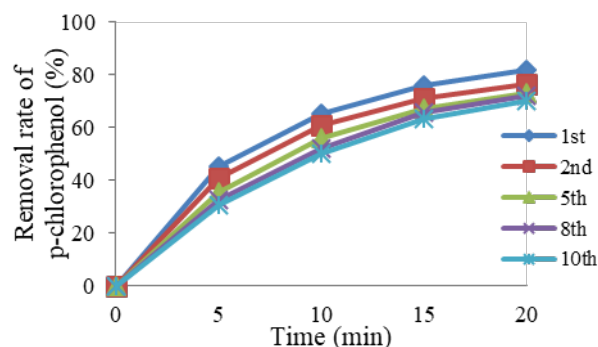


Fig. 6. Effect of repeated use of the catalyst on the removal of *p*-chlorophenol

The repeated use of the catalyst can decrease the activity of the catalyst, but the decrease degree is small. After 100 h of use, the removal rate of *p*-chlorophenol was still above 70.12% after 20 min of reaction.

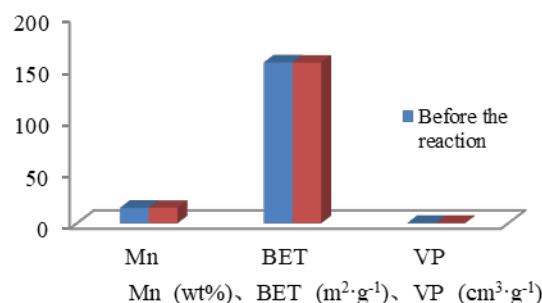


Fig. 7. Measurement results of MnO_x/Al_2O_3 specific surface area

Fig. 7 shows the results of specific surface area measurement of the catalyst MnO_x/Al_2O_3 , Mn content, specific surface area and pore volume of MnO_x/Al_2O_3 before and after the reaction (not used and used 10 times). It was found that MnO_x/Al_2O_3 had a slight decrease in specific surface area and a 0.1 wt% decrease in Mn content, MnO_x/Al_2O_3 pore volume slightly increased, but the change was very small, so after the catalyst MnO_x/Al_2O_3 has been used 10 times and for a total of 100 h, the specific surface area and surface morphology only had minor changes.

Characterization analysis of MnO_x/Al_2O_3

The active sites and the adsorption sites on the catalyst surface are determined by their specific surface area, pore volume, pore size, etc. The catalyst plays an important role in catalytic ozonation. Catalytic ozone reaction occurs on the surface of the catalyst. The unsaturated oxygen atoms and metal ions on the catalyst surface correspond to Lewis bases and acids, while Brønsted acid, Lewis base and acid sites are the active centres of the catalyst. The test measured the specific surface area of the catalyst MnO_x/Al_2O_3 and the carrier Al_2O_3 , the results are shown in Table 1.

Table 1. Specific surface area measurement results of Al₂O₃ and MnO_x/Al₂O₃

	Mn, (wt%)	BET, (m ² ·g ⁻¹)	VP, (cm ³ ·g ⁻¹)
Al ₂ O ₃	0	182.6281	0.58595
MnO _x /Al ₂ O ₃	15.02	155.7832	0.57987

As shown in Table 1, the specific surface area and pore volume of the carrier Al₂O₃ are larger than that of the catalyst surface because MnO_x is loaded on the carrier surface at high temperature. The Mn content in the catalyst is 15.02 wt%. According to preliminary test results, the removal efficiency of *p*-chlorophenol by the ozonation using the catalyst MnO_x/Al₂O₃ can improve the catalytic activity of the reaction system.

Although the effective specific surface area and pore volume of MnO_x/Al₂O₃ decreased, the catalytic activity of MnO_x/Al₂O₃ was still good, indicating that the number of active sites on the catalyst surface did not decrease. It can be seen that the catalyst MnO_x/Al₂O₃ surface can provide a more favorable reaction platform, promote the adsorption of organic compounds in the solution and the decomposition of ozone, effectively removing the organic pollutants in the wastewater.

CONCLUSIONS

(1) The preparation conditions of the catalyst MnO_x/Al₂O₃ were screened out by using *p*-chlorophenol (50 mg·L⁻¹) as the target pollutant, comparing with the removal efficiency using different loading methods, concentrations of precursor and calcination temperatures. The effects of different preparation methods (impregnation method and precipitation method) on the catalytic activity were not obvious. The catalytic activity of the catalyst MnO_x/Al₂O₃ was influenced by the calcination temperature – as the calcination temperature increased, both MnO_x/Al₂O₃ surface activity and the catalytic activity of the catalyst increased. However, the catalytic activity of MnO_x/Al₂O₃ will be weakened when the calcination temperature is too high. The favorable calcination temperature is 500°C. MnO_x/Al₂O₃ was prepared at the calcination temperature of 500°C and with a 1.5 mol·L⁻¹ manganese nitrate precursor solution the removal rate of *p*-chlorophenol was 81.75% after 20 min of reaction.

(2) After the catalyst MnO_x/Al₂O₃ has been used 10 times for a total of 100 h, the catalytic effect was still good, and the removal rate of *p*-chlorophenol was above 70.12% after 20 min of reaction and repeated use. When the temperature rose from 10 °C to 60 °C, the volatilization rate of *p*-chlorophenol increased, the removal efficiency by O₃+MnO_x/Al₂O₃ and O₃ system alone gradually increased with the increase in temperature. O₃+MnO_x/Al₂O₃ catalyst system can effectively remove *p*-chlorophenol in wastewater in the mentioned temperature range.

(3) The analysis of carrier Al₂O₃ and catalyst MnO_x/Al₂O₃ showed that the Mn content in the catalyst was 15.02 wt%. Compared with carrier Al₂O₃, the specific surface area and pore volume of the catalyst MnO_x/Al₂O₃ were reduced, but MnO_x/Al₂O₃ surface can provide more active reaction platforms, thus creating a place for the generation and reaction of ·OH and helping to improve the catalytic performance.

REFERENCES

1. Z.P. Min, Q. Chen, D.C. Liang, *J. Anhui Agric. Sci.*, **44**(29), 51 (2016).
2. M.Y. Qu, *Tech. Development of Enterprise*, **35**(5), 89 (2016).
3. H.L. Lvand, D.Q. Liu, *Environ. Prot. Petrochem. Ind.*, **29**(4), 15 (2006).
4. A. Ikhlaiq, D.R. Brown, B. Kasprzyk-Hordern, *Appl. Catal. B-Environ.* **129**(7432), 437 (2013).
5. Y.H. Chen, D.C. Hsieh, N.C. Shang, *J. Hazard. Mater.* **192**(3), 1017 (2011).
6. B. Liu, A.M. Li, M.F. Xia, Z.L. Zhu, *Adv. Mater. Res.* **538-541**, 2285 (2012).
7. H.F. Hong, Z.C. Pan, G. Xu, C.M. Xiao, Z.G. Wei, S.Y. Xu, *Ind. Water & Waste*, **41**(3), 29 (2010).
8. F. Delanoë, B. Acedo, N.K.V Leitner, B. Legube, *Appl. Catal. B-Environ.*, **29**(4), 315 (2001).
9. J.E. Lee, B.S. Jin, S.H. Cho, S.H. Han, O.S. Joo, K.D. Jung, *Korean J. Chem. Eng.*, **22**(4), 536 (2005).
10. Y.Y. You, X.Q. Lu, D.Y. Xu, T. Zhang, Y. Shi, A. Yang, *Environ. Eng.*, **32**(1), 37 (2014).
11. Q.S. Zhu, J.F. Chen, H.Y. Jiang, S.H. Guo, H.D. Liu, *Chem. Ind. Eng. Prog.*, **33**(4), 1010 (2014).
12. A.S. Fajardo, R.C. Martins, F.R.M. Quinta, *Environ. Technol.*, **34**(3), 301 (2013).

Coordinated development of environment and tourism in China using grey relational analysis

J. Zhao^{1,2*}, Sh.M. Li¹

¹ School of Economic & Management, Northwest University, 710127, Xi'an, Shaanxi, China.

² School of History, Culture and Tourism, Huaiyin Normal University, 223300, Huai'an, Jiangsu, China.

Received September 15 2017, Revised September 21 2017

Coordinated development of tourism and environment is of great significance to the development of human society. The assessment of current development of tourism and environment in China using the theory of grey system established a relationship model for the coordinated development of tourism and environment. Based on the statistics of the development indicators of tourism and environment in China from 2007 to 2015, this paper analyzes the coordinated development of the relationship between them. The analysis results show that the correlation coefficient of tourism and environmental development indicators in China is 0.530, which has the same direction and positive correlation in general. Tourism receipts, domestic tourist arrivals and domestic tourism receipts are the strong correlation tourism development indicators of environmental development. International tourism receipts and international tourist arrivals account for 50% of moderate correlation tourism development indicators of environmental development. Total amount of the wastewater discharge and total number of nature reserve are the strong correlation environmental development indicators of tourism development. This shows that tourism development has an important influence on the environment.

Key words: Environment, Tourism, Coordinated development, Grey relational analysis, China

INTRODUCTION

Tourism has become the world's largest industry. The number of international tourists exceeded 1.2 billion in 2016. Such a large-scale tourism activity may have a substantial impact on the environment. In China, the total tourism revenue in 2016 was 469 trillion yuan, soared by 13.6% compared with the former year. According to the World Tourism Organization (WTO), in 2016, the overall contribution rate of China's tourism industry to the national economy was 11%, and the overall contribution to social employment exceeded 10.26%, which was basically the same as the world average. China has already become an important force in the global tourism economy. Tourism is regarded as environmental protection industry, but in its development process, there are also a series of problems. Tourism development has both positive and negative impacts on the ecological environment of the destination. According to the report of UNWTO, in climate changes caused by human activity, the responsibility of the global tourism industry is expected to reach 7% by the year 2050, tourist transportation, accommodation and other related activities caused by carbon dioxide emissions 1%-3% of total emissions, and accounts for about 5%-14% percent of man-made global warming [1]. In order to expand tourist reception, some cities in China sacrifice their ecological environment and promote the development of Tourism. The impacts of tourism activities on the ecological environment

are mainly reflected in the atmosphere, water, soil, geological features, plants, animals, microbes, landscapes, etc.

RESEARCH DESIGN

Literature review

In recent years, the rapid development of tourism industry has brought about a lot of negative impacts on environmental development as well as a rapid economic growth. Therefore, many researchers began to study the relationship between tourism and environment, such as tourism and greenhouse gas [2], sustainable tourism and climate change [3-6]. Different cases are selected to study the sustainable development of tourism and environment such as Amazon [7], sub-Saharan Africa [8], and Turkey [9]. With the development of tourism, the negative impact on the environment is constantly emerging, and many scholars focus on the barriers of the coordinated development of them [9,10].

Theoretical analysis

Grey system theory

Grey system theory uses a specific concept of information. It defines situations with no information as "black", those with perfect information as "white", and the situations between these extremes are described as being "grey". It can be used to deal with situations lacking sufficient information or sample data. Grey system theory has been applied in industry, agriculture, physical control, economics, energy and communication areas [11,12]. Grey relational analysis (GRA) is a

*To whom all correspondence should be sent:

E-mail: sylvan_zj@foxmail.com

theoretical method of grey system theory that is one of the most widely adapted models of Grey system theory. It was developed by Julong Deng in 1982 [12].

System theory

According to the viewpoint of system theory, there is a material cycle and interactive restriction between tourism and environment. The two subsystems form a high-level system through the coupling of elements [13]. Tourism activities obtain the necessary resources from the environmental system, and tourism revenue provides financial support for the transformation of environmental system resource elements [14].

Coordinated development theory

The purpose and substance of coordination is to promote the system or organization from unbalanced development to equilibrium, and then to a new imbalance, so as to achieve a new balance. It is a cycle of continuous upgrading processes. In the process of development, we should deal with all kinds of relationships properly, effectively utilize various resources, and establish the active cooperative relationship to achieve the common goals. Coordination of interconnected subsystems or system elements through mutual aid and cooperation optimizes the whole system development to achieve the overall optimization of the system. It is a benign condition to coordinate decision makers' actions consistent with each other, in order to achieve maximum utility.

Grey relational model for the coordinated development of environment and tourism

Tourism development has both positive and negative impacts on the ecological environment of the destination. Combined with the development of tourism and environment, the development of tourism industry increases the economic income, promotes environmental protection work, at the same time bringing a series of negative effects on the environment. The development of tourism and the environment is a unified interaction system. In this system, the tourism and environment interact and associate with each other. The complexity of the relationship between tourism and environment depends not only on their own complexity, but also depends on measuring the efficiency of multi factors, theory incompleteness, different reference systems, quantitative calculation model considering the irrationality of defects as well as data, etc. The relationship between tourism development and environment has the characteristics of incomplete information, diversity of standards and uncertainty, which conforms to the basic characteristics of a grey relational system. Therefore, a grey association

model of tourism and environment coordinated development can be established.

Assuming that X is a sequence set, when it has numerical proximity, quantity comparability, and nonnegative properties, the sequence set is called grey incidence sequence set:

$$X = \left\{ \begin{array}{l} x | i \in N, N = \{0, 1, 2, \dots, m\}, m \geq 2, x_i = (x_i(1), x_i(2), x_i(3), \dots, x_i(n)), \\ x_i(k) \in X, k \in K, K = \{1, 2, \dots, n\}, n \geq 3 \end{array} \right\}$$

where $\gamma(x_0(k), x_i(k))$ are the Grey correlation coefficients of X_i to X_0 ; $\gamma(x_0, x_i)$ are the Grey correlation coefficients of X_i to X_0 .

Based on the relationship between tourism and environmental development, the following empirical analysis model was established:

The natural sequence $X(t), Y(t)$, that is:

$$X_i(t_k) = \{X_i(t_1), X_i(t_2), \dots, X_i(t_k)\}$$

$$Y_j(t_k) = \{Y_j(t_1), Y_j(t_2), \dots, Y_j(t_k)\}$$

$$i, j, t = \{1, 2, \dots, n\}$$

Then there is the correlation coefficient $\gamma_{ij}(t)$ of $X(t)$ and $Y(t)$ at time t .

$$\gamma_{ij} = \frac{1}{1 + \left| \frac{\Delta x(t)}{\partial_{x_i}} - \frac{\Delta y(t)}{\partial_{y_j}} \right|} \text{ p.s.: } t \in T$$

$$\Delta x(t) = x(t+1) - x(t)$$

$$\Delta y(t) = y(t+1) - y(t)$$

$\partial_{x_i}, \partial_{y_j}$ are the standard deviations of x_i and y_j .

Indicators and model selection

Basis for the index selection

Based on the research results of domestic and foreign scholars, combining the basic characteristics of China's environment and tourism, and considering the availability of data, the following ten environmental and tourism development indicators are selected. The values of x_i and y_j are derived from the corresponding index values of each year in Table 1.

Data selection

For this study, researchers evaluated data from the China tourism statistics bulletin and National Environmental Statistics Bulletin (China). As the impact of tourism on the environment has an obvious lag which, according to expert estimations, is 3-4 years, the index of tourism development selected the period from 2007 to 2011, the environment development index selected the period from 2011 to 2015, which is a lag of four years. The specific indicators and data as shown in Table 2 and 3.

Table 1. Grey correlation index of tourism and environment in China

Tourism development indicators	Variables	Environmental development indicators	Variables
Tourism receipts (trillion RMB)	$x_1(t)$	Total amount of the wastewater discharge (100 million tons)	$y_1(t)$
Domestic tourist arrivals (billion people)	$x_2(t)$	Total amount of SO ₂ in the exhaust emission (10 thousand tons)	$y_2(t)$
Domestic tourism receipts(trillion RMB)	$x_3(t)$	Industrial solid waste production (100 million tons)	$y_3(t)$
International tourism receipts (billion USD)	$x_4(t)$	Total number of nature reserves (number)	$y_4(t)$
International tourist arrivals (100 million people)	$x_5(t)$	Total investment in environmental pollution control (100 million RMB)	$y_5(t)$

Table 2. Tourism development indicators data table (2007-2011)

Tourism development indicators	Variables	2007	2008	2009	2010	2011
Tourism receipts (trillion RMB)	$x_1(t)$	1.096	1.160	1.290	1.570	2.250
Domestic tourist arrivals (billion people)	$x_2(t)$	1.610	1.712	1.902	2.103	2.641
Domestic tourism receipts(trillion RMB)	$x_3(t)$	0.777	0.875	1.018	1.258	1.931
International tourism receipts (billion USD)	$x_4(t)$	41.919	40.843	39.675	45.814	48.464
International tourist arrivals (100 million people)	$x_5(t)$	1.319	1.300	1.260	1.340	1.350

Table 3. Environmental development indicators data table (2011-2015)

Environmental development indicators	Variables	2011	2012	2013	2014	2015
Total amount of the wastewater discharge (billion tons)	$y_1(t)$	65.92	68.48	69.54	71.62	73.53
Total amount of SO ₂ in the exhaust emission(million tons)	$y_2(t)$	22.18	21.18	20.44	19.74	18.59
Industrial solid waste production (billion tons)	$y_3(t)$	3.23	3.29	3.28	3.26	3.27
Total number of nature reserves (number)	$y_4(t)$	2640	2669	2697	2729	2740
Total investment in environmental pollution control (billion RMB)	$y_5(t)$	602.62	825.36	903.72	957.55	880.63

According to the model of the empirical analysis of the coordinated development of tourism and environment, set at $T = 1, T = 2, T = 3, T = 4, T = 5$ time series, using the formula listed in front. Calculate the grey relational degree of the environmental development index to tourism development index as shown in Table 4.

Table 4. Grey relational degree of environmental development index $y_1(t) \sim y_5(t)$ to tourism development index $x_1(t) \sim x_5(t)$.

r_{ij}	$y_1(t)$	$y_2(t)$	$y_3(t)$	$y_4(t)$	$y_5(t)$
$x_1(t)$	0.718	0.440	0.348	0.643	0.563
$x_2(t)$	0.715	0.428	0.418	0.668	0.628
$x_3(t)$	0.717	0.436	0.419	0.642	0.587
$x_4(t)$	0.604	0.531	0.454	0.527	0.411
$x_5(t)$	0.460	0.526	0.466	0.529	0.371
AVG	0.643	0.472	0.421	0.602	0.512

Correlation strength with $0 < r \leq 0.35$ is a weak correlation, with $0.35 < r \leq 0.65$ is a moderate correlation, and with $0.65 < r \leq 1.0$ is a strong correlation. The established correlation between tourism and environment development is shown in Table 5, 6 and 7.

Table 5. Strong correlation between environmental development indicators and tourism development indicators.

Environmental development indicators	Strong correlation
$y_1(t)$	$x_1(t), x_2(t), x_3(t)$
$y_2(t)$	
$y_3(t)$	
$y_4(t)$	$x_2(t)$
$y_5(t)$	

Table 6. Moderate correlation between environmental development indicators and tourism development indicators.

Environmental development indicators	Moderate correlation
$y_1(t)$	$x_4(t), x_5(t)$
$y_2(t)$	$x_1(t), x_2(t), x_3(t), x_4(t), x_5(t)$
$y_3(t)$	$x_2(t), x_3(t), x_4(t), x_5(t)$
$y_4(t)$	$x_1(t), x_3(t), x_4(t), x_5(t)$
$y_5(t)$	$x_1(t), x_2(t), x_3(t), x_4(t), x_5(t)$

Table 7. Weak correlation between environmental development indicators and tourism development indicators

Environmental development indicators	Weak correlation
$y_1(t)$	
$y_2(t)$	
$y_3(t)$	$x_1(t)$
$y_4(t)$	
$y_5(t)$	

RESULTS AND DISCUSSION

According to table 4, it can be calculated the average (R) of Grey relational degree of environmental development index to tourism development index in China from 2007 to 2015 is 0.530(R=0.530), showing a moderate correlation. The percentages of strong correlation, moderate correlation, and weak correlation respectively is 16%, 80% and 4%. The domestic tourist arrivals ($x_2(t)$) appear twice in strong correlation index of environmental development, accounting for 50% in the strong correlation factors. That is, the domestic tourist arrivals are the main factor affecting the development of China's environment, to attach importance to it.

From the analysis of the relationships between tourism development indicators and environmental development indicators in China, the following three conclusions can be drawn:

(1) Tourism receipts ($x_1(t)$), number of domestic tourist arrivals ($x_2(t)$) and domestic tourism receipts ($x_3(t)$) are the strong correlation indicators of environmental development. Tourism receipts ($x_1(t)$) positive impact on the environment development is to provide more financial support for environmental protection and development; at the same time, long tourists staying time, diverse tourism demands, may have a negative impact on the environment. Number of domestic tourist arrivals ($x_2(t)$) is the majority of the number of tourist arrivals. The concept and behavior of domestic tourists have a great impact on the environment. Domestic tourism receipts ($x_3(t)$) is a major component of tourism receipts. Tourism revenue can be used to improve and upgrade the local environment.

(2) Moderate correlation indicators of environmental development contain tourism receipts ($x_1(t)$), number of domestic tourist arrivals ($x_2(t)$), domestic tourism receipts ($x_3(t)$), international tourism receipts ($x_4(t)$) and international tourist arrivals ($x_5(t)$). International tourism receipts ($x_4(t)$) and international tourist arrivals ($x_5(t)$) occupy 50%, and the rest indicators share the other half. The Tibetan people in Bitahai Nature Reserve in Yunnan Province (China) use to stop some foreign tourists from damaging the

environment and telling them the importance of environmental protection.

(3) Total amount of wastewater discharge ($y_1(t)$) and total number of nature reserves ($y_4(t)$) are the strong correlation environmental development indicators of tourism development. Air pollution is one of the three main factors that influences British tourists coming to China. Animal food safety is also an important factor for international tourists. Reduction of the discharge of wastewater and increase in the number of natural reserves will greatly promote the development of tourism.

CONCLUSION

The results of the research show that tourism receipts, domestic tourist arrivals and domestic tourism receipts are the strong correlation indicators of environmental development. Tourists with different environmental awareness have different impact on the environmental. Raise tourist awareness of conservation. Elevate the cultural qualities of domestic tourists. When tourism activities have a negative impact on the environment, the number of tourists can be controlled by raising the ticket price, although tourism revenue will temporarily decline, but in the long run, the local environmental protection can promote the tourism industry. The amount of tourism revenue will be used for environmental protection and ecological improvement, and the environmental protection fund shall be no less than 10% of the income from scenic spot. It was significant to promote the coordination of tourism and environment in China.

Acknowledgements: This research was supported by the key project of National Social Science Foundation: Research on the tourism cooperation basis and path of The Silk Road Economic Belt(No. 14AJY025), Major bidding project of key research base of Humanities and social sciences of Ministry of Education: Research on the coordinated development of the cultural heritage protection and heritage sites in the western region (No.12JJD790018),and support program for young outstanding talent of Huaiyin Normal University: Research on the development and design of water culture tourism products in Huai'an (No.13HSQNS15). The authors also wish to thank the editor and the reviewer for their valuable comments.

REFERENCES:

- 1.UNWTO, and UNEP (prepared by D. Scott, B. Amelung, S. Becken, J P. Ceron, G. Dubois, S. Gossling, P. Peeters and M C. Simpson). Climate Change and Tourism: Responding to Global Challenges [M]. Madrid: 2008.13-16.

- 2.D. Scott, P. Peeters, S. Gössling. *J. Sustainable Tourism*, **18**(3), 393 (2010).
- 3.D. Scott, *J. Sustainable Tourism*, **19**(1), 17 (2011).
- 4.D. Weaver, *J. Sustainable Tourism*, **19**(3), 5 (2011).
- 5.P. Peeters, G. Dubois. *J. Transp. Geogr.*, **18**(3), 447 (2010).
- 6.A. Budeanu, G. Miller, G. Moscardo, C. S. Ooi, *J. Clean. Prod.*, **111**(5), 285 (2016).
- 7.A. Cama, F.G. Montoya, J. Gómez, J.L.D.L. Cruz, F. Manzano-Agugliaro, *J. Clean. Prod.*, **59**(3), 32 (2013).
- 8.J.W. Lee, T. Brahmasrene, *International Journal of Sustainable Development and World Ecology*, **23**(3), 221 (2016).
- 9.B. Hatipoglu, M.D. Alvarez, B. Ertuna, *J. Clean. Prod.*, **111**, 306 (2016).
- 10.J. Hultman, F. Säwe, *J. Clean. Prod.*, **111**, 327 (2016).
- 11.A. Bezuglov, G. Comert, *Expert Systems with Applications*, **62**(11), 284 (2016).
- 12.J.-L. Deng, *Systems & Control Letters*, **1**(5), 288 (1982).
- 13.G. Munda, *Environment Development and Sustainability*, **7**(1), 117 (2005).
- 14.M.P. van Dijk, M. Zhang, *Environmental Impact Assessment Review*, **25**(6), 667 (2005).

Monitoring of distribution of mineral elements during cultivation of *Auricularia auricula* in northeastern China

J. Ch. Zhang^{1,2}, X. H. Kong^{1,2*}, Y. P. Ma¹, X. Y. Wang¹, H. Chen¹, P. Q. Zhang^{1,2}, D. Sh. Yu¹,
X. D. Dai^{1,2}, Q. F. Ma^{1,2}, Z. H. Han^{1,2}

¹Institute of Microbiology, Heilongjiang Academy of Sciences, Harbin 150010, China

²Institute of Advanced Technology, Heilongjiang Academy of Sciences, Harbin 150020, China

Received, September 1, 2017; Accepted December 20, 2017

The aim of this study was to establish differences in mineral element levels in the mycelium substrate, fungal residues and different tidal fruiting bodies of *Auricularia auricula*. The distribution of mineral elements in the mycelium matrix and fruiting body was determined during the cultivation process, which would enable the determination of the physiological characteristics of *A. auricula* mineral nutrition status. Inductive coupled plasma optical emission spectrometry (ICP-OES) was used to measure 14 mineral element levels in the hypha matrix of fungal residues grown in three cultivation pilot areas. Data showed that the amounts of 3 mineral elements, such as potassium, boron and iron decreased while those of 6 elements including calcium, magnesium, and manganese increased. There were differences depending upon the experimental scenario. Evidence indicates that the growing fruiting bodies of *A. auricula* exhibit varying concentrations of mineral elements, which may be important for use as medicines to treat various diseases.

Key words: *Auricularia auricula* cultivation, Mineral element content distribution

INTRODUCTION

Auricularia auricula, also known as black fungus, is utilized as an edible and medicinal fungus [1]. A variety of mineral elements are required in addition to carbon nutrition and nitrogen nutrition for cultivation of *A. auricula*. Some studies reported the metal ion content in black fungus and other mushrooms. Li *et al.* [2] identified the presence of Ca, Cu, Fe, K, Mg, Mn, Na, and Zn in fruiting bodies of the highly-prized matsutake mushroom (*Tricholoma matsutake*) from 12 separate sites in Southwest China. Wang and Wang [3] demonstrated that the amounts of Fe and Mn in the black fungus of Qinba mountain areas were higher, while the amounts of Ca and Mg in the Northeast were higher. Shi and Luo [4] found that the concentrations of Ca and Zn in wild black fungi in the Chayu region were significantly higher than in the Yadong and Lulang regions. Feng *et al.* [5] determined that *A. auricula* from northeast regions contained higher amounts of Ca, Co, Fe, P, Zn and Cr while *A. auricula* from Fengqing country of Yunnan contained higher amounts of Cu, K and Se. Li [6] and Wang [3] studied the content of inorganic nutrients in *A. auricula*.

In addition, there are many studies on the accumulation of heavy metals (Pb, Hg, Cd, As) in edible fungi, and the different kinds of edible fungi having different enrichment ability to metal ion were found out [7, 8].

The aim of this study was to measure the contents of 14 mineral elements in mycelia matrix, fungus bran and fruiting bodies of *A. auricula* in 3 cultivated areas at different harvest times. The contents of mineral elements were determined by ICP-OES.

EXPERIMENTAL

Materials and methods

Test strains

The strains of *A. auricula* used in the study were “Hei 29” and “Heiwei 10”, which were preserved and provided by the Institute of Microbiology, Heilongjiang Academy of Sciences.

Culture medium

The medium used for Shangzhi was: sawdust 88%, fine bran 8%, soybean meal 3%, lime 0.5%, gypsum 0.5%; cultivated strain: Hei 29.

The medium used for Mudanjiang was: sawdust 83%, rice husk 10%, soybean meal 2%, wheat bran 2%, corn flour 2%, gypsum 1%; cultivated strain: Heiwei 10.

The medium used for Baishan was: sawdust 80%, rice husk 16%, soybean meal 3%, lime 0.5%, gypsum 0.5%; cultivated strain: Hei 29.

Cultivation method

The configured medium was installed in a polyethylene plastic bag, then steam-sterilized and inoculated. The inoculated medium bags were cultivated at 25 °C. After about 45 days, 180-220

*To whom all correspondence should be sent:
E-mail: kxh29@126.com

round holes were punched on the outside of the bag, then water was sprayed on them. The fruiting bodies grew out of the bags after 10-15 days. When growing to a diameter of 4-5 cm, these fruiting bodies were cut from the bags and denoted as Flush-1; on keeping watering, other fruiting bodies were cut from the bags after about 7-10 days, denoted as Flush-2, and so on.

100 bags were in each plot, random sampling of 30 bags, 3 replicates in each plot.

Sample collection method

Medium filled with hyphae (mycelial matrix), harvested culture medium (fungus bran) and *A. auricula* fruiting bodies were harvested at the 1st, 3rd and 6th flushes, respectively, dried in sun light, weighed and the average value was calculated and recorded as dry weight (DW).

Sample digestion

Mycelial matrix, fungus bran and fruiting bodies were ground into powder with a whirlwind. 0.2g samples were put in PTFE crucibles in which 10 mL nitric acid and 0.50 mL perchloric acid were added. The crucibles were covered overnight and then placed in a controlled constant temperature electric heating plate at 120 °C to dissolve completely. The solution was concentrated to about 1.00 ml, then cooled, diluted with distilled water to 25.00 mL and shaken up before determination. A blank test was carried out by the same method.

Determination of the content of mineral elements

7000DV type ICP-OES analyzer of Perkin Elmer Company was used to determine the content of mineral elements (detection limit ≤ 1ppb). Test conditions: delay time: 20 s; radio-frequency power: 1300 w; plasma flow: 15 L/min; sample flow: 1.5 L/min.

Table 1. Results of the consumption of substrate and the yield of fruiting body

Test area	Shangzhi		Baishan			Mudanjiang					
	1	1	2	3	1	2	3	4	5	6	
Harvesting flushes											
DW of fruiting bodies A (g/bag)	37.0	4.8	4.6	20.7	5.9	6.4	4.8	6.2	26.0	6.2	
DW of fungus bran B (g/bag)	240		280				290				
DW of mycelial matrix C (g/bag)	295		325				365				
Conversion rate of the substrate (%) A/(C-B)	67.6		67.4				74.0				

Table 2. Contents of mineral elements in the mycelial matrix and the fungus bran (I) compared with the substrate mycelium in one group (by t-test), *P<0.05, **P<0.01 (n=3).

Element (mg/g)	Ca	Mg	Mn	Na	Al	P
Shangzhi mycelial matrix	15.8	1.71	0.126	0.242	0.884	0.766
Shangzhi fungus bran	20.5**	2.14**	0.192*	0.252	0.933	0.747
Mudanjiang mycelial matrix	14.7	2.02	0.159	0.254	0.805	0.771
Mudanjiang fungus bran	18.9**	2.07	0.182	0.263	0.851	1.11**
Baishan mycelial matrix	20.3	1.382	0.172	0.267	0.729	0.695
Baishan fungus bran	25.1**	1.51	0.229	0.341*	0.819	0.763

Data processing

On the basis of three replicates for each sample, mean values and standard errors were calculated. By EXCEL column diagram and broken line chart, the results were shown, and the significance of the difference between the two groups was analyzed by a t-test. P>0.05 indicates that the difference was not significant; P<0.05 shows a significant difference; P<0.01 shows an extremely significant difference.

RESULTS

Substrate consumption and fruiting body yield

Similar substrates and formula were selected for the cultivation test in three plots. Different cultivated varieties and harvesting methods of single flush (Shangzhi), three flushes (Baishan), and six flushes (Mudanjiang) were used. The harvest flushes, yield and substrate consumption are shown in Table 1. The results showed that the cultivation process of *A. auricula* was consistent with the utilization of substrate.

Contents of mineral elements in the mycelial matrix and the fungus bran

After determining the content of 14 mineral elements (K, Na, Ca, Mg, P, Cu, Fe, Mn, Al, B, Zn, Pb, As and Hg) which are common in *A. auricula*, it was found that the content of elements such as Ca, Mg, Mn, Na, Al, P in the fungus bran was higher than that in the mycelial matrix, among which the increasing range of Ca was the largest, up to more than 25%, as shown in Table 2. The content of elements such as K, B and Fe in the fungus bran was less than that in the original mycelial matrix, as shown in Table 3. The decrease of K was the largest, up to around 30%, which showed that much more quantity is demanded in the growth and development.

Table 3. Contents of mineral elements in the mycelial matrix and the fungus bran (II) compared with the substrate mycelium in one group (by t-test), *P<0.05, **P<0.01 (n=3).

Element (mg/g)	K	B	Fe
Shangzhi mycelial matrix	0.314	0.143	1.91
Shangzhi fungus bran	0.209**	0.081**	1.42**
Mudanjiang mycelial matrix	0.313	0.065	1.32
Mudanjiang fungus bran	0.195**	0.057	1.11*
Baishan mycelial matrix	0.358	0.035	1.26
Baishan fungus bran	0.291**	0.029	1.09

Table 4. Comparison of the contents of mineral elements between the mycelial matrix and the fungus bran (III)

Element(mg/g)	Cu	Zn	Pb	As
Shangzhi mycelial matrix	0.041	0.00303	0.00133	0.000233
Shangzhi fungus bran	0.039	0.00322	0.00114	0.000213
Mudanjiang mycelial matrix	0.041	0.00319	0.00131	0.000126
Mudanjiang fungus bran	0.039	0.00296	0.00128	0.000134
Baishan mycelial matrix	0.037	0.00298	0.00112	0.000106
Baishan fungus bran	0.038	0.00296	0.00121	0.000111

Table 5. Comparison of mineral element contents in fruiting bodies in Baishan area

Element (mg/g)	K	Na	Ca	Mg	Fe	Mn	Al	B	Zn	P
Flush-1	9.49	0.81	5.53	2.31	0.54	0.07	0.37	0.03	0.001	3.49
Flush-2	10.80	0.61	5.68	2.12	0.83	0.08	0.50	0.02	0.002	3.87
Flush-3	4.71	0.302	3.73	1.18	0.18	0.04	0.10	0.01	0.001	2.13

Table 6. Comparison of mineral element contents in fruiting bodies in Mudanjiang area

Element(mg/g)	K	Ca	P	Mg	Na	Fe	Mn	Al	B	Zn
Flush-1	10.41	8.08	4.82	2.16	0.64	0.47	0.03	0.12	0.02	0.005
Flush-2	10.73	8.17	5.61	2.66	0.61	0.31	0.03	0.16	0.02	0.006
Flush-3	10.42	6.48	5.13	2.48	0.56	0.22	0.04	0.14	0.03	0.005
Flush-4	10.00	9.89	5.56	2.37	0.34	0.19	0.02	0.13	0.02	0.005
Flush-5	8.58	6.63	5.64	2.47	0.31	0.42	0.05	0.31	0.04	0.004
Flush-6	10.15	2.48	2.79	1.74	0.32	0.19	0.04	0.12	0.04	0.004

Mineral element contents in fruiting bodies

In the tests of Baishan and Mudanjiang, the fruiting bodies of *A. auricula* were collected in 3 flushes and 6 flushes, respectively. The content change of mineral elements in the fruiting bodies shows that most of mineral element contents decreased with the increase of flush, as shown in Tables 5 and 6.

Before the 3rd flush of Baishan and the 5th flush of Mudanjiang, the fruiting body yield obviously increased, while the content of mineral elements in the corresponding fruiting bodies significantly decreased. The results showed that the transfer efficiency of mineral elements was different from other nutrients.

In plants, researchers have laid a theoretical foundation for the regulation of plant resistance to mineral nutrients [9]. Meng *et al.* [10] studied the distribution of mineral elements in tobacco leaves of Guangxi base and analyzed the relationship between the supply of soil and the mineral composition of tobacco in different regions. Guo *et al.* [11] found that brown rice protein content

significantly correlated with P, K, Cu, Mn and other mineral elements. Liu *et al.* [12] studied the content change of main mineral elements to explore the factors influencing the leaf senescence of raspberry fruit maturity. Yu *et al.* [13] studied the correlation between wild *Radix Salviae Miltiorrhizae* and its inorganic elements in different habitats. In the study of mineral elements in edible fungi, researchers sampled *Tricholoma matsutake* from 12 districts at different faraway distances in the Southwest of China to determine the contents of mineral elements such as Ca, Cu, Fe, K, Mg, Mn, Na and Zn by atomic absorption spectrometry [2]. Koyyalamudi *et al.* [14] determined the content of trace minerals in the fruiting bodies of *Agaricus bisporus*. Mleczek *et al.* [15] compared the content of six kinds of wild edible fungi such as *Boletus edulis*, *Cantharellus cibarius* collected in Poland and other six kinds of nutrient elements (Ca, Fe, K, Mg, Mn, Na), and respectively studied the biological concentration factor (BCF). Gramss and Voigt [16] determined the mineral content of matrix and fruiting body, and studied fungal mineral absorption rules from non-embedded beech wood

substrate. So far, there is no report on the migration of mineral elements in the cultivation of *A. auricula*.

In this study, although there were some differences in the matrix, cultivated varieties and management methods, the content changes of mineral elements were consistent. The results showed that the growth process of *A. auricula* was selective to mineral elements. Analysis of utilization of substrate showed that the selectivity of mineral elements is closely related to the physiological characteristics of *A. auricula*, the concentration of mineral elements in the substrate and the management methods of cultivation. The experimental data showed that the utilization of mineral elements (K, B and Fe) was higher than that of the whole nutrients. Therefore, it was suggested that the addition of these elements might improve the transformation efficiency.

The analysis showed that K, Ca, P, Mg and other elements have a higher content in fruiting bodies. It can be concluded that these four elements were important to the growth of *A. Auricula*, which was similar to the elements K and P in the growth of plants.

The change of mineral elements content in different flushes showed that, with the growth rate increasing and the growth time extension, the synthetic ability of proteins and carbohydrates of *A.auricula* gradually decreased, leading to a decrease in the content of relevant mineral elements, and this trend will decrease the yield till stoppage. It can be inferred that those mineral elements are the same as other nutrients whose transfer efficiency will affect the growth quality and yield of *A. auricula*.

CONCLUSION

In different experiments, 3 elements (K, B and Fe) and 6 elements (Ca, Mg, Mn, etc.) showed a consistent declining and rising tendency. The element content in the fruiting body gradually decreased along with the harvesting flushes. The results showed that the growth of *A. auricula* had different selectivity and transfer efficiency to mineral elements.

Acknowledgements: This work was supported by grants from Excellent Youth Foundation of Heilongjiang Province of China (No.: JC201316) and China Agriculture Research System (CARS20).

REFERENCES

1. Y.C. Dai, L.W. Zhou, Z.L. Yang, *Mycosystema*, **29**, 1 (2010).
2. T. Li, J. Zhang, T. Shen, Y.D. Shi, S.B. Yang, T. Zhang, J.Q. Li, Y.Z. Wang, H.G. Liu, *Chemical Papers*, **67**(6), 672 (2013).
3. X.A. Wang, M. Wang, *Food Research And Development*, **37**(19), 128 (2016).
4. S. Shi, Z. Luo, *Food Research And Development*, **38**(2), 33 (2017).
5. X.F. Feng, N. Zhao, S.Z. Ze, B. Yang, *Guizhou Agricultural Sciences*, **8**(4), 35 (2016).
6. Y.H. Li, *Chemical Engineer.*, **26**(5), 42 (2014).
7. C.Y. Huang, J.X. Zhang, *Edible Fungi of China*, **23**(4), 7 (2004).
8. Q.E. Liu, *Modern Agricultural Science & Technology*, **9**, 109 (2012).
9. X. Li, The physiological, biochemical and molecular mechanism of mineral elements regulating tobacco resistant to PVY^N. Shenyang Agricultural University, Doctor Degree paper (2009).
10. D.L. Meng, Y. Deng, D.F. Zeng, W.G. Wang, *Guangxi Tobacco*, **22**(6), 32 (2008).
11. Y.M. Guo, H.H. Li, S.M. Li, Y.B. Duan, P. Huang, J. Tu, *Journal of Plant Genetic Resources*, **14**(1), 173 (2012).
12. H.P. Liu, F. Guo, B.G. Li, X.M. Zhang, G.H. Qi, Y.C. Li, *Northern Horticulture*, **40**(24), 5 (2016).
13. Y.G. Yu, X.D. Zhang, Z.N. Hou, Y. Li, C. Shen, Z.C. Qi, S.R. Liang, *Journal of Zhejiang Sci-Tech University (Natural Sciences)*, **47**(1), 1 (2017).
14. S.R. Koyyalamudi, S.C. Jeong, S. Manavalan, *Journal of Food Composition and Analysis*, **31**(1), 109 (2013).
15. M. Mleczek, M. Siwulski, K. Stuper-Szablewska, K. Sobieralski, Z. Magdziak, P. Golinski, *Journal of Environmental Science and Health, Part B: Pesticides, Food Contaminants, and Agricultural Wastes*, **48**(4), 308 (2013).
16. G. Gramss and K.D. Voigt, *Biological trace element research*, **154**(1), 140 (2013).

Experimental insights into a novel over-saturated brine cement slurry used in anhydrite formation

L. Xu¹, H. Gao², J. Xu³, M. Xu^{4*}, X. Wang⁴, F. You⁴, Y. Long¹

¹ College of Petrochemical and Energetic Engineering, Zhejiang Ocean University, Zhoushan, China

² Engineering Technology Research Institute of PetroChina Xinjiang Oilfield Company, Karamay, China

³ Institute of exploration techniques, CAGS, Langfang, China

⁴ Hubei Cooperative Innovation Center of Unconventional Oil and Gas, Yangtze University, Wuhan, China

Received, September 22, 2017; Accepted December 20, 2017

Well cementing properties of anhydrite formation are always challenging, due to the negative impact of anhydrite on the stability of cement slurry. Design and development of certain cement slurry appropriate in anhydrite formation is always essential. In combination to anhydrite properties of Missan Oilfields, herein, systematic experiments were made to develop a special kind of weighted over-saturated brine cement slurry. The density of cement slurry was designed up to 2.36 g/cm³ to mitigate the plastic deformation of anhydrite formation. Dosages of key additives were optimized by evaluating performance of cement slurry. The results showed that the developed cement slurry had favorable properties such as appropriate rheology, good fluid loss control, short thickening time, right angle consistency, and rapid development of compressive strength. This work not only provides instructive information on a kind of novel weighted over-saturated cement slurry of anhydrite formation, but also extends an important category of cement slurries.

Keywords: Over-saturated brine; Cement slurry; Anhydrite formation; Performance evaluation.

INTRODUCTION

In well cementing operations, an appropriate type of cement slurry is always fundamental, which enables the sustainable, safe and economic production of oil & gas. However, the anhydrite cementing remains a large obstacle to the efficient well operation because of the negative properties of anhydrite rock: (1) cramping behavior caused by the horizontal stress, (2) mirabilite and gypsum swelling, (3) instable rock structure, and (4) abnormal pressures. The common cement slurries appear to be very limited in salt resistance, and some cannot work in the anhydrite formation. It is thus not surprising that various accidents linked with the wellbore shrinkage, pear-shaped profile, casing deformation, or even well collapse, have been encountered in the cementing operation of anhydrite formation.

In recent years, a new kind of cement slurries based on saturated brine (e.g., NaCl and KCl) has been widely reported, which exhibits excellent applicability in anhydrite cementing [1-5]. In 2000, Liu *et al.* [6] proposed a semi-saturated and a saturated brine cementing system to improve the salt resistance of cement slurries. Subsequently, Tao *et al.* [7] further analyzed accidents of anhydrite cementing in Tuha Oilfield, and developed a

investigated the effect of NaCl and KCl concentration on the properties of the cement slurry, and pointed out that the type and content of salts were the key to the saturated brine cement slurry. In addition to the salt-resistance, the density of the cement slurry is another factor to retard cramping behavior of anhydrite. Recently, Xu *et al.* [9] have developed weighted saturated brine cement slurry. The density of such slurry can be consciously controlled using specific spherical weighting materials.

Despite a wide range of investigations on saturated brine cement slurries, the common results appear to be very limited to the unique anhydrite formation. When the formation environments are varying, the intrinsic characteristics of rock would change. Thus, the cement slurry of anhydrite formation needs to be explored in combination with certain environments, for the purpose of effective implement of cementing operation. In Missan Oilfields, a huge thickness (500 m) of anhydrite formation was detected at 2,000 m, which would readily cause various cementing accidents. According to the in-field cementing project, a double stage cementing technology was designed: at the first stage, the densities of lead and tail slurry were proposed to be 2.36 g/ml and 2.33 g/ml, respectively; at the second stage, the densities of both the lead and tail slurries were proposed to be 2.36 g/ml. To ensure quality of double stage cementing, the thickening times of lead and tail slurry were proposed in the range of 360~480min and 150~180 min, respectively.

*To whom all correspondence should be sent:
E-mail: xuhu_11@yeah.net

saturated brine cement slurry which can entirely avoid cementing failure. Simao *et al.* [8]

Previous studies focused mainly on semi-saturated and saturated cement slurries. In contrast, less attention has been paid to over-saturated systems. In the present work, extensive laboratory tests were carried out to develop a novel kind of over-saturated brine cement slurry well appropriate to the anhydrite formation. As a continuous study on the high performance of cement slurry, this work cannot only provide instructive information on the over-saturated brine cement slurry, but also extend the category of cement slurry system.

METHODOLOGY

Experimental materials

The over-saturated brine cement slurry was constructed with nine functional additives, including weighting agent, filtrate loss reducer, expanding agent, strength stabilizer, dispersant, defoamer, and retarder (see Table 1). Here, several key additives that can significantly affect the performance of cement slurry such as the weighting phase, filtrate loss reducer, proppant, strength stabilizer, and the retarder were typically taken into account.

Testing performance

As for the over-saturated brine cement slurry, several primary performances like those of rheology, filtrate loss, compressive strength, and thickening were examined. Rheological data of the designed cement slurry were measured at six specific shear rates 600, 300, 200, 100, 6 and 3 rpm with the Fann 35 viscometer. Filtration tests were

performed at 6.9 MPa and the considered temperature by the fluid-loss cell. The thickening performance was measured at 120oC/110MPa using the HTHP consistometer. The gel strength was examined by a static gel strength analyzer. Using the compressive strength tester, the compressive strength of cement stone was measured at 120oC after 24 h of curing.

Experimental design

With the selected functional additives, the over-saturated brine cement slurry available in Missan Oilfields can be constructed by optimizing the additive dosage. Herein, dosages of key additives such as saturated salt, filtrate loss reducer, strength stabilizer, retarder, and proppant were optimized by a set of one-factor experiments, as shown in Fig. 1. As a consequence, the optimized formula of over-saturated brine cement slurry can be defined.

RESULTS AND DISCUSSION

Content of filtrate loss reducer

As one kind of liquid filtration loss reducer, LATEX contains about 50 wt.% of colloidal particles with a size of 0.05~0.5μm, which can fill the filter cake to reduce its permeability. To optimize the content of LATEX, the performance of cement slurry concerning thickening, compressive strength, filtration, and rheology, was tested in the range of 0~7.5wt.%. The relations between LATEX contents and fluid loss, compressive strength, and thickening time are presented in Fig. 2.

Table 1. Components of the over-saturated brine cement slurry designed here

Additives	Ingredients	Terms
Continuous phase weighting material	Over saturated NaCl solution	NaCl
Filtrate loss reducer-A(FLR-A)	AMPS-polymer	AMPS-P
Filtrate loss reducer-B(FLR-B)	Styrene-butadiene latex	LATEX
Proppant	Silicone fluid	MX
Solid phase weighting material	Hematite	---
Expanding agent(EX)	Metal oxide	EX
High temperature(HT) strength stabilizer	Silica flour	SP
Dispersant	Formaldehyde condensation polymer	CF44L
Defoamer	Anionic surfactant	CX66L
Retarder	Phosphonate	H63L

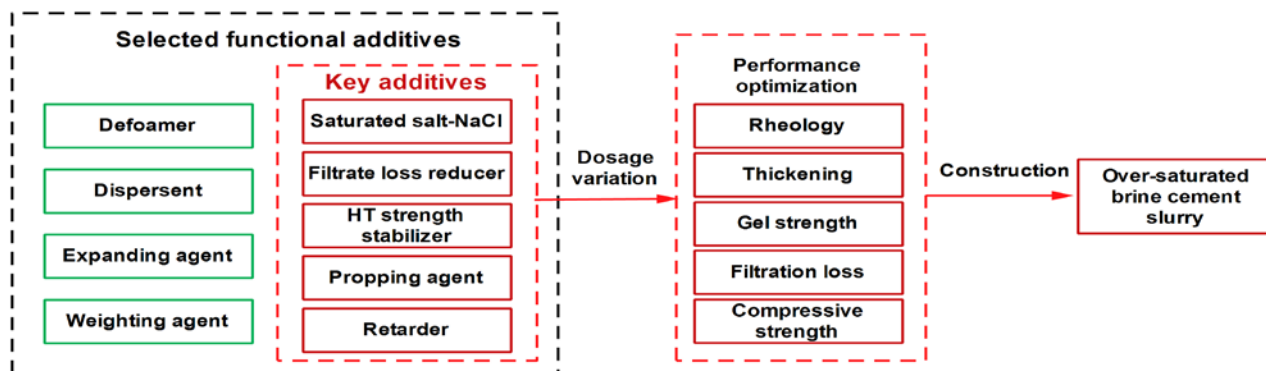


Fig. 1. Experimental design of constructing over-saturated brine cement slurry.

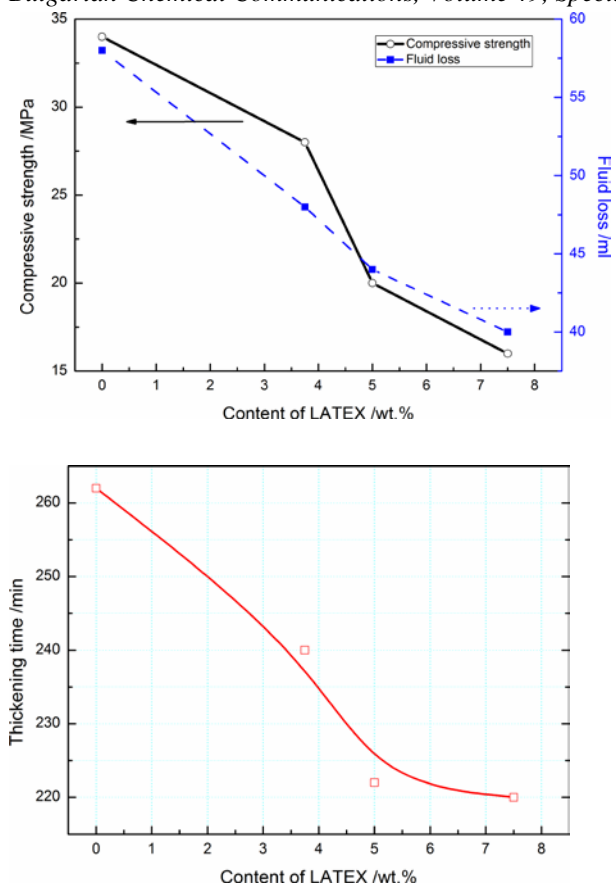


Fig. 2. upper: relation between content of LATEX and compressive strength and fluid loss; lower: curve of content of LATEX vs. thickening time.

In Fig. 2, all of the tested data involving the compressive strength, fluid loss, and thickening time declined with a rise of the LATEX content, wherein the fluid loss exhibited a larger decrease than others. For example, the fluid loss was reduced by 31% when LATEX content increased to 7.5wt%. This result disclosed that LATEX performed well as filtrate reducer in the slurry. Due to the special liquid state, LATEX can penetrate the deep formation and form an effective block to prevent fluid loss. Note that the LATEX content should be controlled because this additive can lower the compressive strength of slurry.

Further, Table 2 lists the rheological parameters for the slurry with the considered LATEX content. One can find that for the investigated contents, all rheological readings slightly increased, suggesting that LATEX had a little impact on the slurry rheology. On the basis of the results obtained above, the LATEX content was proposed to be 5 wt.%.

To optimize the content of NaCl, the performance of cement slurry was tested in the content range of 0~60wt.%. Note that, the NaCl content was calculated with respect to fresh water.

Table 2. Rheological readings of the cement slurry at different LATEX contents

Latex content (wt.%)	Rheological readings		
	$\theta_{600}/\theta_{300}$	$\theta_{200}/\theta_{100}$	θ_6/θ_3
0	190/101	72/39	5/3
3.75	225/129	92/50	5/3
5	245/140	101/56	5/3
7.5	255/147	107/60	6/4

Content of NaCl

In Fig. 3, one can observe that with increasing NaCl content, both compressive strength and fluid loss value decreased, but a reverse trend was found for the thickening property. The larger the NaCl content, the longer was the thickening time.

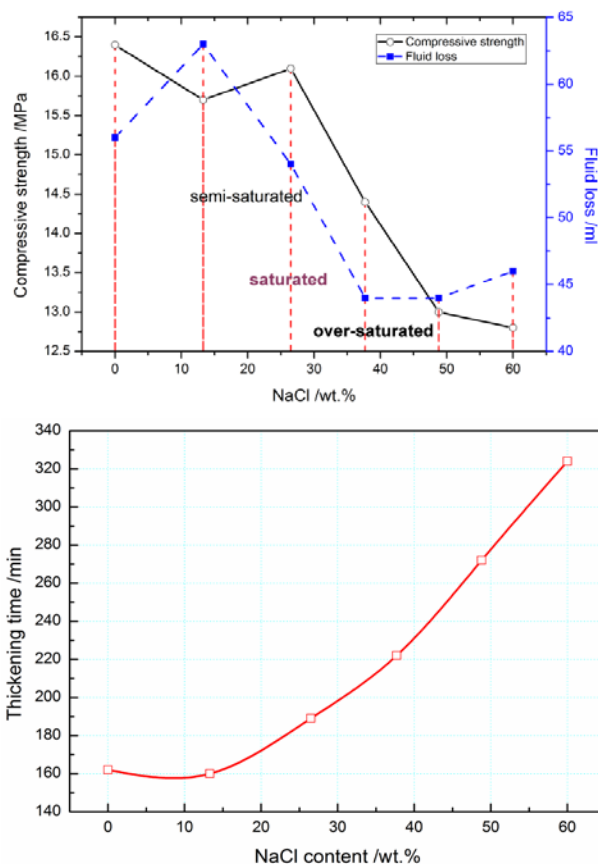


Fig. 3. Upper: relation between content of NaCl and compressive strength and fluid loss; lower: curve of content of LATEX vs. thickening time

In particular, thickening time rapidly increased while the NaCl content exceeded 50wt.%, displaying a strong retard property at the high NaCl contents. This phenomenon should be mainly attributed to weak hydration of cement caused by the high NaCl content. In general, the thickening property is closely associated with the compressive strength of cement slurry. The longer the thickening time, the weaker becomes the compressive strength. Here, the compressive strength decreased with an increment of NaCl content.

Table 3. Rheological readings of the cement slurry at different NaCl contents

NaCl content (wt.%)	Rheological characteristic readings		
	$\theta_{600}/\theta_{300}$	$\theta_{200}/\theta_{100}$	θ_6/θ_3
0	—/—	246/150	16/12
13	—/200	149/84	9/5
26	242/138	99/54	5/3
38	245/140	101/56	5/3
49	225/126	91/50	5/3
61	230/129	92/50	5/3

Rheological characteristic readings obtained by a six-speed viscometer are listed in Table 2. The rheological readings decreased with increasing NaCl content, which reflected that NaCl can dilute the cement slurry to some degree. When the NaCl content was 0wt.%, for instance, the θ_{600} and θ_{300} readings exceeded the measurement range of viscometer; when the NaCl content was 49wt.%, the values of high shear rates (i.e., θ_{600} and θ_{300}) were 225 and 126, respectively. Meanwhile, the θ_6 and θ_3 readings tested at 49wt.% NaCl content were separately reduced by 69% and 75%, when compared to those tested at 0wt.% NaCl content. These results showed that in the over-saturated brine system, NaCl should be important to improve the comprehensive performance of the slurry. The NaCl content was determined to be 49wt.% in the over-saturated system.

Content of HT strength stabilizer

The influence of the SP content on the properties is illustrated in Fig. 4. To elucidate the strength of the cement slurry, thickening tests were carried out at 130°C/110MPa and compressive strength tests were performed at 150°C.

As can be seen in Fig. 4, the thickening time decreased and the compressive strength ascended with increasing SP contents. In particular, thickening time had a dramatic decrease when the SP content was larger than 35wt.%, suggesting that the compressive strength is significantly reinforced. This result was well consistent with the change trend of compressive strength with increasing SP contents. Such reinforcing behavior can be rationalized by the theory of particle size distribution. The size of SP particles was in the range of about 300 mesh, which can cooperatively work with cement particles to significantly improve compressive strength of cement stone. As a result, the filtration of the slurry can also be effectively reduced. Herein, the SP content was proposed to be 49wt.% on the basis of analyses of the compressive strength and thickening.

Also, Fig. 4 displays the stability of HT compressive strength with exposure time at different SP contents. Two main changes can be observed in the considered time: (1) the

compressive strength increased with SP content, and (2) the compressive strength was improved with increasing time. While the SP content was 20wt.%, for instance, the compressive strengths obtained at 3d and 7d were 9.4MPa and 1.4MPa, respectively, and the former was lower by 5MPa than the latter. SP was excellent in enhancing HT strength stabilization, which would be suitable for the over-saturated brine slurry.

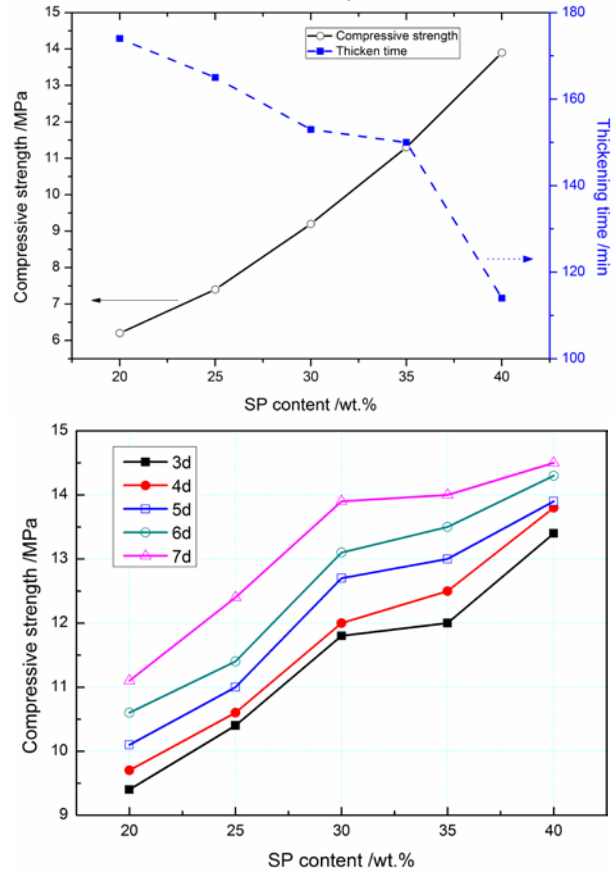


Fig. 4. Upper: relation between SP content and compressive strength and thickening time; lower: relation of SP content and compressive strength after a long-term high temperature.

Content of retarder

Effect of the H63L content on thickening time was investigated and is presented in Fig. 5.

The thickening time dramatically decreased with an increment of the H63L content, which revealed strong retardation capability. The thickening times of the slurry at the considered H63L content spanned over a large range from 186 to 315 min, and the latter was nearly two times larger than the former. It is worth mentioning that the retardation effect of H63L should be attributed to its chemical reaction with Ca^{2+} and OH^- in the cement slurry. The final product can precipitate on the surface of slurry hydration and hinder further cementing action. According to the operation requirements on-site, the thickening time of the slurry was designed

in the time range of 180~300 min. According to testing data and cementing standard, H63L content of 1.5wt.% was enough for the cement slurry.

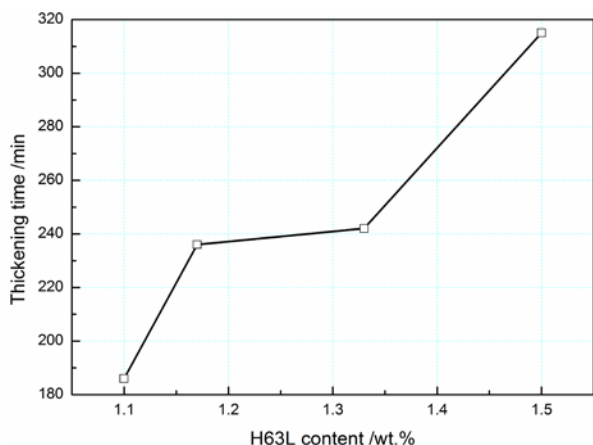


Fig. 5. Relation between H63L content and thickening time.

As follows from the data presented in Figs. 2~5, the major retard contribution to the designed slurry thickening property emerged from the retarder, H63L. In spite of partial retardation caused by brine, its effect appeared to be quite limited. Given the thickening time of 160~320 min, for example, variations of H63L and NaCl contents separately were 1.5wt.% and 61wt.%, and the H63L content was by one order of magnitude lower than that of NaCl, disclosing the dominant retardation by H63L.

Content of proppant

MX was employed as the proppant in the over-saturated brine slurry, and its main component is silicone fluid. Effect of MX on properties is presented in Fig. 6.

One can readily observe that with increasing MX content, the compressive strength was reinforced and the fluid loss declined. As the MX content raised up to 12wt.%, for instance, the compressive strength increased by about 100%, while the fluid loss decreased by almost 45%. These findings showed that MX had an excellent propping capability in the over-saturated slurry. On the other hand, an increment of the MX content can, as expected, greatly decrease the thickening time, which was reverse to the variation of compressive strength. In fact, the propping action of MX should be mainly attributed to its size cooperativity. MX is a particular kind of ultra-fine active nano-particles, which can entirely full the pores (or little fractures) in the cement stone. As a consequence of propping behavior, the stability and strength of the final cement stone can be improved and the gas channels can be effectively removed upon solidification.

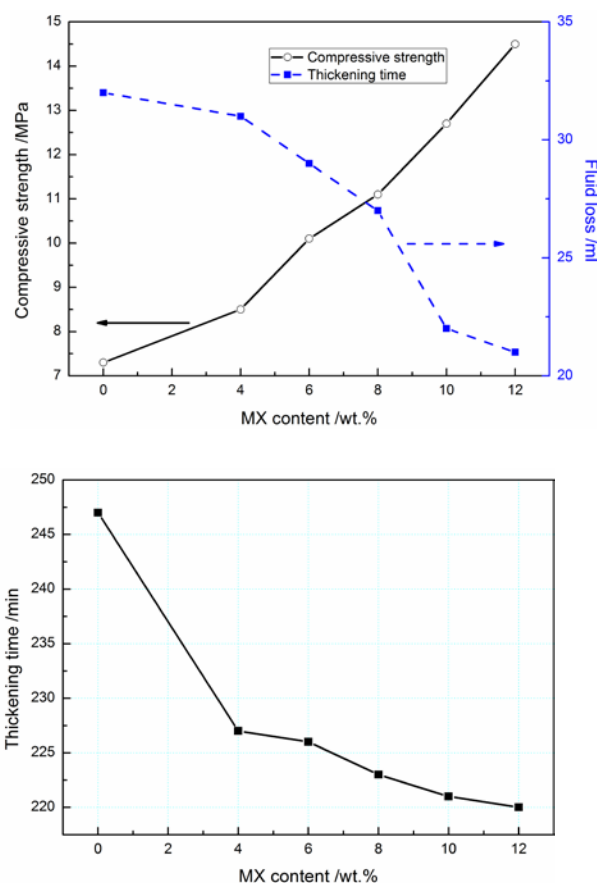


Fig. 6. upper: relation between MX content and compressive strength and fluid loss; lower: relation of MX content vs. thickening time.

Evaluation of over-saturated brine cement slurry

On the basis of the results obtained above, the formula of over-saturated brine cement slurry was proposed as:

G class cement + 60wt.% fresh water + 30wt.% NaCl + 10wt.% HT strength stabilizer + 112.5% weighting agent + 5wt.% FLR-B + 10wt.% FLR-A + 2wt.% dispersant + 10wt.% proppant + 0.8wt.% retarder + 1wt.% defoamer + 1.5wt.% EX.

It should be referred that the density of the designed slurry can be controlled by reasonably varying the dosage of weighting agent. Herein, 112.5wt.% of weighting agent was added and the density of the over-saturated brine cement slurry was as high as 2.36 g/ml.

Curves of gel strength and consistency vs. time that indicate real-time variation of characters for over-saturated cement slurry are given in Fig. 7. The gel strength increased from 48 Pa to 240 Pa in 30 min, as marked with red lines, which disclosed the strong capability of anti-gas channeling for the designed slurry. In the consistency curve, on one hand, the initial consistency was lower than 20 BC, displaying robust rheology during the course of cement cycle; on the other hand, the consistency

quickly increased up to 100 BC in 20 min and, in this regard, a certain right angle consistency occurred, which should be extremely essential to ensure the cementing quality for the double stage cement slurry.

Acknowledgements: This work was supported by grants from Excellent Youth Foundation of Heilongjiang Province of China (No.: JC201316) and China Agriculture Research System (CARS20).

REFERENCES

1. Y.C. Dai, L.W. Zhou, Z.L. Yang, *Mycosystema*, **29**, 1 (2010).
2. T. Li, J. Zhang, T. Shen, Y.D. Shi, S.B. Yang, T. Zhang, J.Q. Li, Y.Z. Wang, H.G. Liu, *Chemical Papers*, **67**(6), 672 (2013).
3. X.A. Wang, M. Wang, *Food Research And Development*, **37**(19), 128 (2016).
4. S. Shi, Z. Luo, *Food Research And Development*, **38**(2), 33 (2017).
5. X.F. Feng, N. Zhao, S.Z. Ze, B. Yang, *Guizhou Agricultural Sciences*, **8**(4), 35 (2016).
6. Y.H. Li, *Chemical Engineer.*, **26**(5), 42 (2014).
7. C.Y. Huang, J.X. Zhang, *Edible Fungi of China*, **23**(4), 7 (2004).
8. Q.E. Liu, *Modern Agricultural Science & Technology*, **9**, 109 (2012).
9. X. Li, The physiological, biochemical and molecular mechanism of mineral elements regulating tobacco resistant to PVY^N. Shenyang Agricultural University, Doctor Degree paper (2009).
10. D.L. Meng, Y. Deng, D.F. Zeng, W.G. Wang, *Guangxi Tobacco*, **22**(6), 32 (2008).
11. Y.M. Guo, H.H. Li, S.M. Li, Y.B. Duan, P. Huang, J. Tu, *Journal of Plant Genetic Resources*, **14**(1), 173 (2012).
12. H.P. Liu, F. Guo, B.G. Li, X.M. Zhang, G.H. Qi, Y.C. Li, *Northern Horticulture*, **40**(24), 5 (2016).
13. Y.G. Yu, X.D. Zhang, Z.N. Hou, Y. Li, C. Shen, Z.C. Qi, S.R. Liang, *Journal of Zhejiang Sci-Tech University (Natural Sciences)*, **47**(1), 1 (2017).
14. S.R. Koyyalamudi, S.C. Jeong, S. Manavalan, *Journal of Food Composition and Analysis*, **31**(1), 109 (2013).
15. M. Mleczek, M. Siwulski, K. Stuper-Szablewska, K. Sobieralski, Z. Magdziak, P. Golinski, *Journal of Environmental Science and Health, Part B: Pesticides, Food Contaminants, and Agricultural Wastes*, **48**(4), 308 (2013).
16. G. Gramss and K.D. Voigt, *Biological trace element research*, **154**(1), 140 (2013).

Study on polystyrene conformational changes in supercritical fluid anti-solvent process by small angle X-ray scattering

Q. Huo^{1*}, D. Li², Zh. Wu³

¹Biochemical Engineering College of Beijing Union University, Beijing, China

²Institute of Chemistry, Chinese Academy of Sciences, Beijing, China

³Institute of High Energy Physics, Chinese Academy of Sciences, Beijing, China

Received August 17, 2017; Accepted December 20, 2017

A preliminary study of the polymer conformation in supercritical fluid anti-solvent process was carried out by the method of grazing-incidence small angle X-ray scattering at the station of Beijing Synchrotron Radiation Facility (BSRF). The experiments showed that in the continuous process of adding an anti-solvent, polymer chain stretching occurred from random coil to a curled sphere.

Key words: Supercritical fluid CO₂; Anti-solvent process; Polystyrene; Small angle X-ray scattering

INTRODUCTION

In recent years, more and more emphasis is put on supercritical fluid technology. There are two main reasons: first, supercritical fluids have many unique properties; second, this technique causes little or no pollution [1-3]. Supercritical fluids (SCFs) have many unique properties near the critical point; the fluid physical and chemical properties such as viscosity, density, diffusion coefficient, solvation capability, dielectric constant are sensitive to changes in temperature and pressure. Viscosity and diffusion coefficients are close to those of gases, the density and the solvation ability are close to those of liquids. So far, supercritical fluid technology has been applied in many areas such as extraction and separation technology [4], petrochemistry [5], analytical techniques [6], chemical reaction engineering, materials science, biotechnology, etc. [7, 8], and has broad prospect.

Preparation of particles is an important part of the chemical industry. Particles which have different properties can be used as stationary phases, adsorbents, catalyst carriers, etc., supercritical fluid anti-solvent process technology applications have attracted attention in this regard [9, 10]. The principle of the anti-solvent process (SAS) is: Many substances are soluble in organic solvents, but insoluble in a certain gas or a supercritical fluid. Meanwhile, under high pressure, the solubility of CO₂ and other gases in many organic solvents is high, resulting in volume expansion of the solvent, therefore, when the gas or supercritical fluid is dissolved in the solvent, the solvent capacity for dissolving the solute decreases,

and under appropriate conditions part or all of the solute can be precipitated which is called anti-solvent process (SAS). In the anti-solvent process, the nature of the precipitate (particle size, crystal type, etc.) can be adjusted by pressure, temperature and speed of the gas dissolution. SAS techniques have applications in many areas such as natural products isolation, explosive fragmentation [11], preparation of drug particles [12], recrystallization of inorganic substances [11], etc.

Small angle X-ray scattering (SAXS) originates from spatial fluctuations of the electronic density within a material. It is ideally suitable for investigating the geometric structure of inhomogeneous materials containing regions in which fluctuation or variation in electron density extends over distances of about 0.4 nm to 200 nm (e. g., nanomaterials or porous materials). The X-ray intensity emitted from a common X-ray source is always very low, so that the application of SAXS is limited. By using synchrotron radiation with high intensity as X-ray source, SAXS measurement can be well improved [13, 14].

Our work is to make use of small angle x-ray scattering (SAXS) study of polystyrene conformational changes in the supercritical fluid anti-solvent process. X-ray scattering like other light scattering is caused by the unevenness of the system. For example, there are particles of dust and water vapor in the atmosphere, the electron densities of the atmospheric dust and water vapor are different. When the light illuminates the subject, they produce scattered light. If the size of the particles (as the polymer solution) dispersed in uniform media is a few microns, because the X-ray waves are much smaller than visible light, only a small range of angles ($\theta < 2^\circ$) of the scattered light can be observed [15]. The intensity of the scattered

*To whom all correspondence should be sent:
E-mail: huo_q2002@aliyun.com

light, intensity angular dependence are concerned with the particle size, morphology and distribution. So you can use small angle x-ray scattering to study the size and morphology of the polymer in a supercritical fluid anti-solvent process [16].

Small-angle x-ray scattering (SAXS) experimental station equipped with an SAXS camera was used for the on-line control and data acquisition. SAXS has an accuracy of 1 μm slit system, ionization chamber for monitoring the light intensity, it has a plane perpendicular to the beam which can be both horizontally and vertically adjusted to the direction of the sample, low vacuum pipe which can adjust length, sealed with 25 μm thick Kapton film at both ends, detector is a scintillation counter. Angular resolution of the device is better than 0.16 m rad. Synchrotron light source has a small source size, collimation, high brightness advantage (higher than ordinary light by at least 2 to 3 orders of magnitude), which can greatly improve the resolution and sensitivity, shorten the time of the experiment, simplify complicated data rectification work, carry out studies on the structure which cannot be carried out with a conventional X-ray source [17].

30 years ago, using Flory's mean-field theory, Stockmayer first proposed that if the solvent becomes poor solvent from a good solvent, flexible polymer chain can curl into uniform density sphere from random coil stretch. Theory and practice of this prophecy have fostered extensive research. Research on the polymer chains transition in supercritical fluid anti-solvent process, not only has important theoretical significance, but it is relevant to many biological processes; it also makes sense for promoting the development of supercritical fluid technology.

In this paper, using small-angle X-ray scattering (SAXS), preliminary studies on the polymer conformational changes within supercritical fluid anti-solvent (SAS) process were performed. These changes are characterized by sharing radius of gyration R_g , which verify the feasibility study using SAXS. In the future, we will carry out more in-depth and meticulous research in this area.

EXPERIMENTAL

Materials

CO_2 , purity 99.995% (Beijing Analytical Instrument Factory), polystyrene (PS), $M_w = 7.8 \times 10^6$, $M_w / M_n = 1.1$ (Institute of Chemistry), toluene (Beijing Chemical Plant), in SAXS experiments, the concentration of PS/toluene solution was 3.2×10^{-3} g/mL.

Methods

Small-angle x-ray scattering (SAXS) experiment was carried out in the Beijing synchrotron radiation beam line within 4B9A small angle X-ray scattering experimental station. Put the sample cell which contains PS solution into the scattering chamber, add anti-solvent to the solution and measure the parameters P_c under continued pressure until the cloud point pressure in the scattering device. Fluid pressure was controlled by gauges (IC Sensor Co., Model 193), pressure measurement error is less than $\pm 0.105\text{MPa}$, the temperature of scattering pool was controlled by a platinum resistance thermometer, the temperature measurement error is less than $\pm 0.1\text{K}$.

RESULTS AND DISCUSSION

Scattered light intensity changes with pressure

Synchrotron radiation SAXS experiment was performed at 35°C and concentration of 3.2×10^{-3} g/mL of the polystyrene/toluene solution. The latter was continuously pressurized, after equilibrium, the scattering intensity $I(h)$ measured under each pressure value with an angle (h) changed. In this experiment, six different pressures were used: 1, 21.6, 32.8, 41.6, 49.6, 55.2 ($\times 10^5\text{Pa}$), shown in Fig.1. From the scatter diagram can be seen that at a lower pressure, the scattering intensity $I(h)$ is monotonously decreasing, which indicates that the PS chain stretching presented random coil conformation. At $49.66 \times 10^5\text{Pa}$ pressure, the scatter graph shows oscillations, which indicate that PS random coil curling happens and becomes spherical. Our equilibrium experiments also proved that the solution cloud point pressure was $P_c 48.3 \times 10^5\text{Pa}$, when the pressure is greater than P_c , phase separation and precipitation occurs

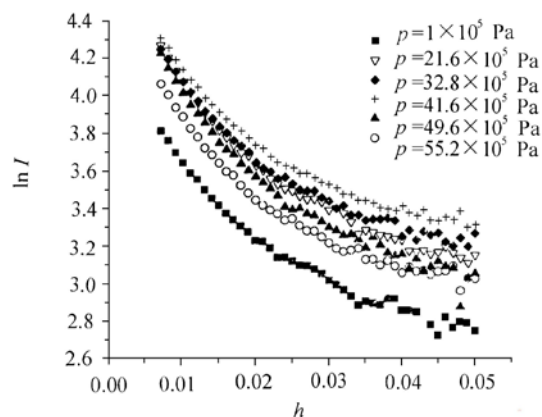


Fig.1. Scattering intensity $I(h)$ with an angle (h) changes when PS/toluene solution is continuously pressurized.

In the scatter plot we also see that when $P < P_c$, the scatter plot of the six different pressures substantially coincides which indicates that $I(h)$ is independent of pressure. From the theory, for the same molecular weight and concentration conditions, the scattering intensity should be a constant; when $P > P_c$, the scattering intensity decreases with increasing pressure. For this light intensity decrease there may be two reasons: one reason may be due to the curled sphere when PS chain density is increased, so that the center of the sphere segment of the scattered light may be blocked on the surface of the segment and second scattering occurs, so that the scattered light intensity decreases; another factor may be due to the curling process, causing a change in the long chain of solvated polymer, resulting in a decrease in scattered light.

Sharing radius of gyration (R_g) changes with pressure

With $\ln(h)$ as the vertical axis and h^2 as the horizontal axis, the slope of the line is $-R_g^2/3$, a function of chain size (R_g) which describes PS can be obtained. Scattering vector $h = (4\pi/\lambda)\sin\theta$, scattering intensity $I(h)$ according to the following formula, deducing absorption of substrate and scattering of the substrate, the parameters of sample thickness and light intensity P_0 derived normalize [18].

$$I(h) = \frac{[I_m(h) - I_d(h)] - [I_s(h) - I_d(h)] \exp(-\mu_f t_f)}{P_0 \mu_f t_f \exp(-\mu_f t_f - \mu_s t_s)}$$

In the above formula, $I_d(h)$ is the background noise, $I_m(h)$ and $I_s(h)$, respectively the actual measured scattering intensity and the substrate measured scattering intensity, μ_f , t_f , and μ_s , t_s are the absorption coefficient and the thickness respectively film (f) and the substrate (t). We summarize the sharing rotation radius (R_g) changes with pressure in Fig. 2.

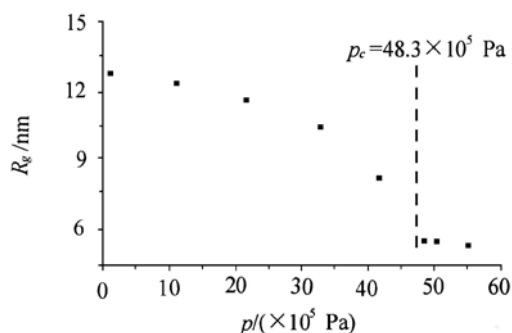


Fig.2. Effect of pressure on PS chain size (R_g)

As the pressure increases, the central portion of each polymer chain shrinks, R_g makes steep drop, in the area I, $p < p_c$, R_g becomes small with increasing pressure, which shows that strong contraction occurred in the molecular chain. In the area II, $p > p_c$, R_g is linearly decreasing, which shows only a slight molecular chain of PS shrinkage.

According to PS chain size (R_g) dependence on the pressure, we propose a mechanism: in the continuous process of adding an anti-solvent, polymer chain stretching occurred from random coil to a curled sphere, and this process can be divided into two sub-processes: rapid contraction of non-entangled chains and entanglement and slow contraction of the chain.

CONCLUSION

Using small angle X-ray scattering, we studied the polymer conformational changes in the supercritical fluid anti-solvent process. From the analysis of the experimental parameters it can be concluded that: the more CO_2 is added to the polymer solution, the more easily molecules are separated, and the conformational change with which the polymer chain stretches from random coil to curl the ball is also easily found.

Acknowledgement: This work was financially supported by National Natural Science Foundation of China (Grant No. 11475020, 8151114029), Chaoyang District collaborative innovation project (Grant No. XC1608).

REFERENCES

- 1.S.F. Li, X.W. Wu, C.X. Hou, Y. Zhang, *Modern Chemical Industry*, **27**, 1 (2007).
- 2.J. Jung, M. Pemit, *Journal of Supercritical Fluids*, **20**, 179 (2001).
- 3.C. Quan, S.F. Li, S.J. Tian, *Journal of supercritical fluids*, **31**, 149 (2004).
- 4.Y.Y. Gao, H. You, C. Chen, X.L. He, C.S. Chen, *Food Sci.* **23**, 154 (2002).
- 5.T.J. Liu, Z.G. Du, Y. Guo, X.H. Yang, Y.G. Zhang, *Chem. Ind. & Eng. Pro.(China)*, **30**, 1676 (2011).
- 6.Y.P. Wang, *Chinese Traditional Patent Medicine*, **33**, 1070 (2011).
- 7.J.M Levy. *J. Chromatographic Science*, **27**, 341 (1989).
- 8.M.J. Burk, S. Feng, M.F. Gross, W. Tumas, *Am. Chem. Soc.*, **117**, 8277(1995).
- 9.L.Y. Lee, L.K. Lim, J. Hua, C.H. Wang, *Chem. Eng. Sci.*, **63**, 3366 (2008).
- 10.K. Byrappa, S. Ohara, T. Adschiri, *Adv. Drug Deliv. Rev.*, **60**, 299 (2008).

11. M.A. McHug, V.J. Krukoniš, *Supercritical Fluid Extraction, Principles and Practice*, 2nd ed., Boston, Butterworth-Heinemann, 1994.
12. W.J. Schmitt, M.C. Salada, G.G. Shook, S.M. Speaker, *AIChE J.*, **41**, 2476 (1995).
13. W.H. Wang, H.Y. Han, Y.C. Yu, L. Li, X.H. Guo, *Journal of East China University of Science and Technology (Natural Science Edition)*, **41**, 277 (2015).
14. C.Z. Yang, J. M. Newsarn, *Progress in Physics*, **12**, 130 (1992).
15. W.H. Wang, L. Li, X. J. Yu, H. Han, X. Guo, *Journal of Polymer Science: Part B. Polymer Physics*, **52**, 1681 (2014).
16. Q. De Robillard, X. Guo, M. Ballauff, T. Narayanan, *Macromolecules*, **33**, 9109 (2000).
17. B.Z. Dong, W.J. Sheng, *High Energy Physics and Nuclear Physics*, **19**, 284 (1995).
18. X.X. Guo, M.F. Guo, *Beijing Synchrotron Radiation Facility Annual Report*, **1**, 70 (1997).

Dynamic analysis of aluminum flows in production stage in mainland China: 1996-2014

Sh. Liu

College of Management Science, Chengdu University of Technology, Chengdu 610051, P. R. China

Received August 30, 2017; Accepted December 20, 2017

This paper applies substance flow analysis (SFA) and stocks and flows framework (STAF) to conduct dynamic analysis of aluminum flows in the production stage in mainland China from 1996 to 2014. Key findings include: (1) aluminum production industry of China developed rapidly from 1996 to 2010, larger and larger scrap was recycled and reused, while almost all flows declined at various degrees from 2011 to 2014; (2) in bauxite mining process, resource efficiency indices did not rise but dropped slowly, and net import dependence indices increased little by little, from 0.019 in 1996 to 0.413 in 2014; (3) in alumina production and primary aluminum electrolysis processes, resource efficiency indices were both large and stable, basically above 0.9, and net import dependence indices declined generally and gradually; (4) although secondary aluminum increased sharply from 1996 to 2011, its proportion grew slowly, reached the maximum of 0.198 in 2010 and decreased after 2011. Therefore, ore dressing-Bayer method, tailing reelection technologies, intelligent use of scrap and Go-Out Strategy must be promoted at a large scale as soon as possible.

Key words: Substance flow analysis; Production stage of aluminum industry; Resource efficiency and net import dependence.

INTRODUCTION

Aluminum is the second most abundant metallic element in the earth's crust after silicon, accounting for 8% of the earth's crust [1], yet it is a comparatively new industrial metal that has been produced in commercial quantities for just over 100 years. However, more aluminum is produced today than all other nonferrous metals combined [2]. Great growth in demand and consumption of aluminum containing products (aluminum used in transportation (automobiles, airplanes, trucks, railcars, marine vessels, etc.), buildings and constructions (windows, doors, siding, etc.), consumer durables (appliances, cooking utensils, etc.), machinery and equipment (manufacturing, construction, agricultural equipment, etc.), electrical engineering (wires and cables, transformers, generation equipment, etc.), containers and packaging (cans, foil, etc.), and other products)) [3] in recent decades owns to its wonderful properties: (1) light weight. It weighs about one-third as much as steel or copper; (2) it has low density and it is malleable, ductile, and easily machined and cast; (3) it has excellent corrosion resistance and durability; (4) it has high thermal conductivity, electrical conductivity and reflectivity, no low temperature brittleness and magnetism. So, measured either in quantity or value, the usage of aluminum exceeds that of any other metal except iron, or it is important in virtually all segments of the world economy.

Modern society and recent decades have

witnessed a significant increase in aluminum use [4], particularly in China. China, an extraordinarily populous, fast developing, but still underdeveloped country, has the potential to influence the entire world's use of materials. From 1991 to 2007, the average increasing rates of aluminum production and consumption in China were about 4 times the global level. However, the production of aluminum requires much more energy than of many other metals and causes large amounts of greenhouse gas (GHG) emissions [5], especially in the primary aluminum electrolysis process. Production of primary aluminum is highly energy-intensive and with heavy environmental burdens associated with resources extraction and pollutant emissions [6]. The environmental impacts of primary aluminum industry are much higher than that of aluminum recycling industry and aluminum semi-production industry. Although the energy required for producing secondary aluminum (separation and remelting of aluminum scrap) might be only 5-10% of that needed for primary aluminum [7], China as a developing country has been lacking scrap for domestic secondary aluminum production in recent years [8]. In addition, China's static depletion time of bauxite was less than 15 years since 2009. Given the potential to increase its in-use stock, a secure supply of bauxite may become a challenge for China in the near future.

So, in consideration of the large energy consumption of primary aluminum production and the lack of scrap and bauxite in mainland China, this paper applies substance flow analysis (SFA) and stocks and flows framework (STAF) to analyze aluminum element stocks and flows and its whole

*To whom all correspondence should be sent:
E-mail: liusl0223@sina.com

life cycle in the Production stage in mainland China from 1996 to 2014. The object of this paper is to explore the segments of higher net import dependence index and lower resource efficiency index to finally realize environment-friendly metallurgy in the Production stage. Conducting the detailed aluminum substance flow analysis of Production stage helps to understand the overall condition of aluminum production industry in China in recent years, and contributes to providing quantitative and scientific policy evidence to implement cleaner production, develop circular economy and realize sustainable development.

EXPERIMENTAL

Fig. 1 depicts the stocks and flows system boundary of aluminum, and the entire life cycle and sub-processes of aluminum in China is distinct. In Production stage, there are three sub-processes: mine/mill, smelter and refinery. Then comes the Fabrication and Manufacture stage, aluminum alloys and pure aluminum are fabricated to foundry casting, rolling, extrusion, rod and wire, and other semi-products; next, final aluminum-containing products are manufactured combined with other raw materials. As for consumption structure, aluminum-containing products in the Use stage are sorted into 7 categories: building and construction (B&C), transportation (T), consumer durables (CD), machinery and equipment (M&E), electrical engineering (EE), containers and packaging (C&P), and others. In the Waste Management and Recycling stage, end-of-life products and scrap are collected, separated and treated.

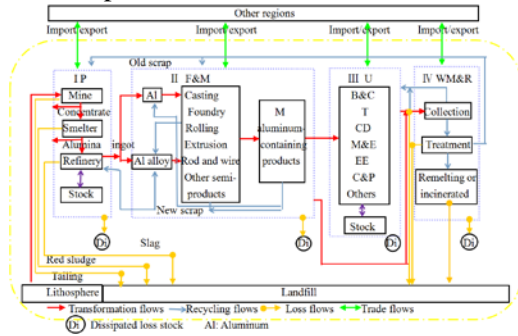


Fig. 1. System boundary of the stocks and flows framework for anthropogenic aluminum cycle (refer to Chen)

Some products are remelted to produce secondary aluminum, but others that have no economic values are incinerated. Trade or exchange with other regions occurs in every stage sub-processes. At the same time, resources and energy consumption, dissipated loss and pollutant emissions to the environment happen at every stage too.

The system boundaries include spatial boundary,

temporal boundary and scope. The spatial boundary of this paper is the geographical border of mainland China, and the temporal boundary is the period of 1996-2014. The scope means 3 sub-processes (bauxite mining, alumina production and primary aluminum electrolysis) of the entire life cycle only in the Production stage, not all four stages. Actually, aluminum, either bauxite, alumina or primary aluminum, exists in its chemical compound form in the nature. But all values of aluminum stocks and flows in this study are in terms of aluminum content, therefore the aluminum content was calculated using atomic weights and some transfer coefficients estimated from the literature and experts (Fig. 2).

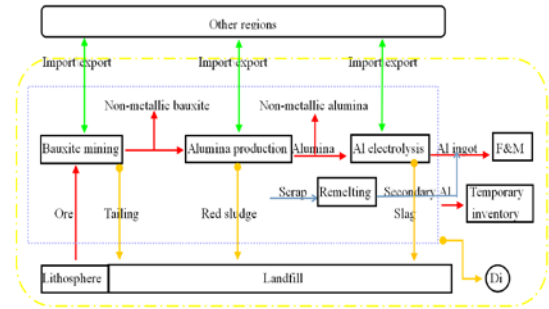


Fig. 2. System boundary of the Production stage of aluminum

For the calculation of stocks and flows with respect to sub-processes in the Production stage, the basic relationship given in Eq. (1) adheres to the mass conservation principle:

$$\Delta Stocks = \sum F_{input}^i - \sum F_{output}^i \quad (1)$$

$\Delta Stocks$ means net accumulation, loss to environment or depletion of aluminum, and F designates the whole flows into or out of process i . However, change in stock is so small that can be negligible [9] in theoretical and real world, and Eq. (1) becomes

$$\sum F_{input}^i = \sum F_{output}^i \quad (2)$$

This corresponds to the substance flows diagram of Production stage, and the input and output include domestic and net imported production, respectively.

The index of resource efficiency measures the ratio of qualified products or output (namely excluding waste flows), and R_{re} is defined as follows:

$$R_{re}^i = (\sum F_{output}^i - \sum F_{waste}^i) / \sum F_{input}^i \quad (3)$$

The larger value of resource efficiency implies that the production of process i is efficient within the Production stage of aluminum industry. And the lower value of it implies the contrary.

The index of net import dependence measures

the degree of domestic aluminum production industry dependence upon foreign aluminum production or foreign raw materials supply, and R_{id} is defined as follows:

$$R_{id}^i = \sum F_{netimport}^i / \sum F^i \quad (4)$$

In this equation, F^i can represent not only output flows, but also input flows, and $F_{netimport}^i$ means net imported aluminum-containing products or raw materials in process i . Obviously, one country or region can master the lifeline of aluminum production industry regardless of foreign aluminum production status, raw materials supply or aluminum market demand if its value is small. On the contrary, the aluminum industry of one country or region is threatened by international market, like walking on the thin ice.

This index is a criterion used to measure the ratio of secondary aluminum remelted from scrap occupying the total output of Production stage (excluding trade volume) to weigh the recycling situation of scrap.

$$R_s = \sum F_{secondary} / (\sum F_{primary} + \sum F_{secondary}) \quad (5)$$

A larger value of this index indicates that secondary aluminum occupies a large proportion and is essential to the aluminum production industry, of course, and the lower value indicates that scrap is not used wisely, which produces huge waste and pollution to the whole ecosystem due to the absence of waste management and recycling.

RESULTS AND DISCUSSION

Fig. 3 illustrates the trends of some indices: resource efficiency and net import dependence in bauxite mining process, alumina production process and primary aluminum electrolysis process respectively, as well as the proportion of secondary aluminum of the entire Production stage from 1996 to 2014.

Although secondary aluminum increased sharply from 1996 to 2011, its proportion only reached a maximum of 0.198 in 2010. The values of this index grew slowly on the whole, rising in some years and dropping in other years. After 2011, secondary aluminum was too much reduced. Along with gradually decreasing bauxite output, drastically decreasing alumina and primary aluminum production in 2014, this index went up after dropping. China's in-use stock of aluminum is still too "young" and small to generate high quantities of aluminum scrap for domestic secondary aluminum production [8]. On the other hand, the fare damage rate of secondary aluminum in remelting process is relatively high in China because of participation of many individual workshops and the low melting technologies level.

In bauxite mining process, resource efficiency index did not rise but dropped slowly, while the net import dependence index continuously rose on the whole from 1996 to 2014, especially from 2005 to 2006. The abnormal phenomenon of resource efficiency index implies that there exists more and more serious waste in bauxite mining process on the one hand, and on the other hand, it further exposes the current situation of more low-grade ore and less high-grade ore in China. China is a net importer of bauxite, and there is no doubt that China is relying more on foreign countries or regions due to the sustaining rise of the net import dependence index. The average growth rate (49.4%) of the net imported amount from other regions is much larger than that (6.8%) of domestic mining amount on account of globalization and more and more global corporation. In the condition of global market of fierce competition and constant change, this status must be paid more attention to in order to guard resource security.

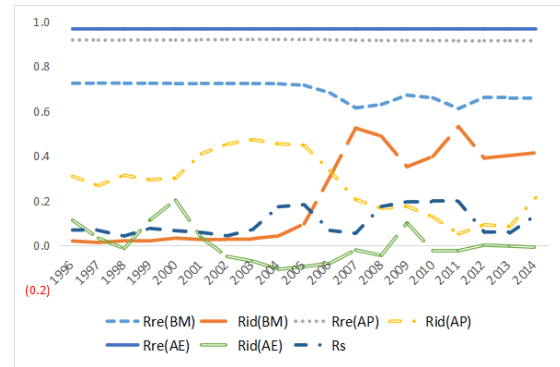


Fig. 3. The tendency of indices in three sub-processes of Production stage from 1996 to 2014. (BM: bauxite mining; AP: alumina production; AE: aluminum electrolysis)

In alumina production process, the values of resource efficiency index are relatively high without too big fluctuations, and it is more effective than bauxite mining process. What is more optimistic is that the net import dependence index had the tendency of decline in this process, although it rose slightly in 2014. This appearance can be explained mainly from the following two aspects: the amount of net import was gradually reduced since 2006, lessened sharply in 2011 and increased a little from 2012 to 2014; domestic alumina output augmented at a high speed for the period of 1996-2013 except 2014. These two conditions jointly determined the change of net import dependence index in this process.

In primary aluminum electrolysis process, the values of resource efficiency index are the highest in these three sub-processes of the Production stage. This means that primary aluminum electrolysis process is the most effective process and unit of

resource consumption is minimum in Production stage. Like the variation of the net import dependence index in alumina production process, its values had the tendency of decline as a whole in this process. However, unlike the values of net import dependence index in alumina production process, there are mainly negative values in this process and China is basically a net exporter of primary aluminum. The decreasing amount of net import and increasing amount of domestic primary aluminum production can account for the declining tendency of the net import dependence index. The amount of primary aluminum import less than that of export can account for the negative values of the net import dependence index. What is noteworthy is that the values of net import dependence index reached up to 0.1 in 2009. Under the influence of financial crisis, there are some unusual points in 2009 other than for the rest of years: decrease in output of domestic primary aluminum and export, dramatic increase in import. From 2011 to 2014, the values of the net import dependence index were extremely close to 0, so China will be a country of balance between import and export for primary aluminum in the future.

CONCLUSION

Based on the input-output model and mass conservation principle, this paper applies the resource management method of SFA and STAF framework to illustrate the whole life cycle of aluminum in Production stage in China for the period of 1996-2014. The positive average growth rates of various flows for the period of 1996-2010 revealed that China is a net importer of bauxite and alumina, aluminum production industry of China developed rapidly, and large scrap was recycled and reused because of advancing concept of waste management and recycling. However, the condition of these flows and average growth rates is another image for the period of 2011-2014. Negative average growth rates show a decreasing tendency of various flows. It is a good time of optimization and integration of domestic aluminum market, and implementation of Go-Out Strategy to overseas merger and acquisition.

Resource efficiency index and net import dependence index of three basic sub-processes of Production stage, as well as the proportion of secondary aluminum of the entire Production stage from 1996 to 2014 were calculated in this way. Although secondary aluminum increased sharply from 1996 to 2011, the index of proportion of secondary aluminum grew slowly and reached only a maximum of 0.198 in 2010. After 2011, the amount of secondary aluminum was reduced too much. Participation of some large enterprises can improve utilization of aluminum scrap and reduce the fare damage rate in remelting process by higher technology level and standard management. Resource efficiency indices in alumina production and primary aluminum electrolysis processes are large and stable, while that in bauxite mining process does not rise but drops slowly. Net import dependence indices in alumina production and primary aluminum electrolysis processes decline generally and gradually, nevertheless that bauxite mining process goes up little by little.

From the perspective of environment-friendly metallurgy and resource security, bauxite mining process needs to be paid more and more attention to. Ore dressing-Bayer method must be promoted at a large scale as soon as possible and tailing reelection technologies must be advanced to realize comprehensive utilization of tailing.

REFERENCES

1. A. Sverdlin, Introduction to aluminum. In: G.E. Totten, D.S. MacKenzie, eds. Handbook of aluminum, New York: Marcel Dekker, Inc. 1, 1, 2003
2. K. Halvor, *J. Occup. Environ. Med.*, **56**(55), S2 (2014)
3. C. Luca, *Resour. Conserv. Recycl.*, **72**, 1 (2013)
4. L. Gang, B. Daniel Müller, *J. Clean Prod.*, **35**, 108 (2012)
5. T.E. Norgate, *J. Clean Prod.*, **15**(8-9), 838 (2007)
6. W.Q. Chen, *Resour. Conserv. Recycl.*, **54**, 557 (2010)
7. M. Melo, *Resour. Conserv. Recycl.*, **26**, 81 (1999)
8. W.Q. Chen, L. Shi, *Resour. Conserv. Recycl.*, **65**, 18 (2012)
9. L. Zhang, J.M. Yang, *Sci. Total. Environ.*, **478**, 80 (2014)

Double motor intelligent control system for industrial agitation based on Kingview and single chip microcomputer

Y.J. Wang^{1*}, K.Y. Wei, H.H. Liu

Department of Electronics Information Engineering, School of Electronics and Information Engineering, Liaoning University of Technology, Jinzhou, China

Received September 7, 2017, Accepted December 20, 2017

To overcome the uneven stirring problem of a conventional single motor and meet the high stability requirements in pulping process of semi-solid alloy slurry, a double motor intelligent control system based on Kingview and single chip microcomputer (SCM) is designed. The system mainly includes the motor and its driving circuit, the power circuit, speed and voltage current detection circuit, Kingview and SCM control system. The double motor operation can be controlled effectively so as to achieve precise control of the agitating speed. The proposed method is illustrated through the preparation of a semi-solid alloy slurry in the laboratory. The experimental results show that the system can precisely match the double-motor speed and achieve better results than a single motor stirring system.

Key words: Intelligent double motor control system, Pulping process of semi-solid alloy slurry, Kingview, Single chip microcomputer.

INTRODUCTION

The metal semi-solid processing technology in industrial stirring is to directly shape the solid-liquid slurry where the spherical primary solid phase is uniformly suspended in the liquid metal mother liquor. As an advanced metal processing technology in the 21st century, it is provided with the advantages of high efficiency, high energy saving and high molding performance. Extensive research has been conducted on the effects of external factors such as microgravity fields, electromagnetic fields, and ultrasonic fields on the microstructures during solidification [1-4]. Although the kind of agitation affects the microstructure and its rheological properties, these methods cannot make an ideal cracking effort on the dendrite fracture mechanism in fact. Some industrial agitation preparation technologies cannot meet the needs of industrial production in automation control system, stability and reliability. Considering the important role of intelligent control in industrialization and semi-solid processes, a double motor intelligent control compound agitation method is proposed. The method can greatly improve the stability, reliability and operability of automatic control in industrial production. The mixed slurry can be fully stirred to achieve an accurate control.

Based on the motor parameter detection, a double motor control system combining the Kingview interface with SCM is designed. The

three-phase phase shift voltage regulator circuit is used to drive the rotation of a three-phase motor and a three-phase stator magnetic field. The lift control is realized by a DC motor [5-7]. The motor parameter detection and control system mainly includes computer configuration control, SCM control system, signal acquisition circuit and motor drive circuit. The motor drive circuit adopts H-bridge structure to control the steering, speed and other functions of the motor by receiving control commands given by the control system. The SCM control system uses STM32F103ZET as core microprocessor so as to realize the closed-loop control of the motor combining with PI algorithm. By connecting with the configuration software interface of the computer, the control of the motor parameters is achieved.

OVERALL DESIGN OF THE SYSTEM

The control system consists of a motor and its driving circuit, a power circuit, speed and voltage current detection circuit, Kingview and SCM control system. Since the controlled object in the agitation system usually has large inertia and hysteresis characteristics, the proportional plus derivative controller is used to improve the dynamic characteristics of the system in the process of adjustment. The speed of the motor can be measured by the infrared laser receiving module, the working voltage and current can be measured by the pressure flow detection module, and the measured physical quantity is fed back to the control module. The overall design scheme is shown in Figure 1.

*To whom all correspondence should be sent:
E-mail: wyj_lg@163.com

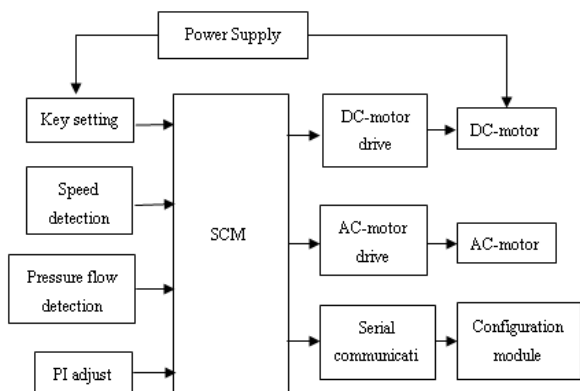


Fig. 1. Overall design block diagram.

HARDWARE DESIGN

Single-chip microcomputer system

Figure 2 shows the minimum system of a single chip microcomputer, in which the two capacitors connected to the 8 MHz crystal oscillator are ceramic capacitors, which is convenient for the oscillation of the crystal oscillator. Considering the noise problem, the SCM STM32F103ZET is contrary to the traditional C51 SCM [8-9], hence the low level reset is used.

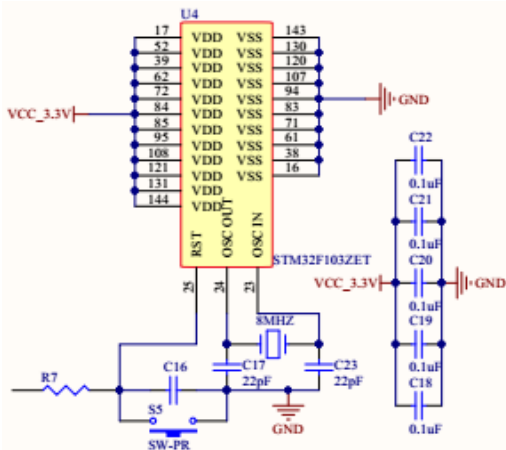


Fig. 2. SCM minimum system.

Three-phase AC voltage regulator principle

Three-phase AC voltage regulating circuit adopts wireless star connection mode, and the load is pure resistive load. Each phase must be connected with another phase in the conduction time. Hence, it is same as the three-phase bridge full-control rectifier circuit, there are two thyristors in the current flow path. Therefore, double pulse or wide pulse trigger should be used. The three-phase trigger pulse should be followed by a difference of 120 degrees in turn, and the trigger pulse of two

anti-parallel thyristors in the same phase should be a difference of 180 degrees.

The phase shift angle is controlled by the potentiometer output voltage. Potentiometer output voltage is 0~5V. The corresponding three-phase voltage regulator circuit output voltage is 0~380V. Meanwhile, it is used to control the three-phase stator at the bottom of the agitator so that alternating magnetic field is generated with it, and by the corresponding control, the stirred object is in the opposite direction of the magnetic field generated by the three-phase stator at the bottom, so that it is fully stirred.

Figure 3 is a waveform diagram of the trigger pulse when the conduction angle of the upper and lower anti-parallel thyristors in the same phase is 60 degrees in the three-phase phase shift voltage regulator circuit, where the abscissa is time (sec), and the ordinate is signal output, high level is 1. Each thyristor turns on 120 degrees, and the two thyristors trigger pulses differ by 180 degrees.

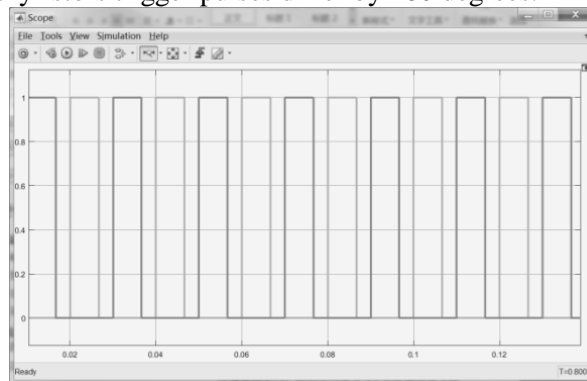


Fig. 3. Trigger pulse waveform.

The DC motor driving circuit

The control signal outputted by SCM is transmitted to the NOR gate through the high-speed optical coupler so as to control direction signal and PWM output signal to produce a certain logic output through the hardware. The logic signal is used to control the direction of the motor by controlling diodes D2, D6, and D3, D5, as shown in Figure 4.

The corresponding logic output signal timing diagram is presented in Figure 5. When DIR is low level, the corresponding waveform can be monitored at point A, while point B is low level. When DIR is high level, point B outputs the PWM waveform.

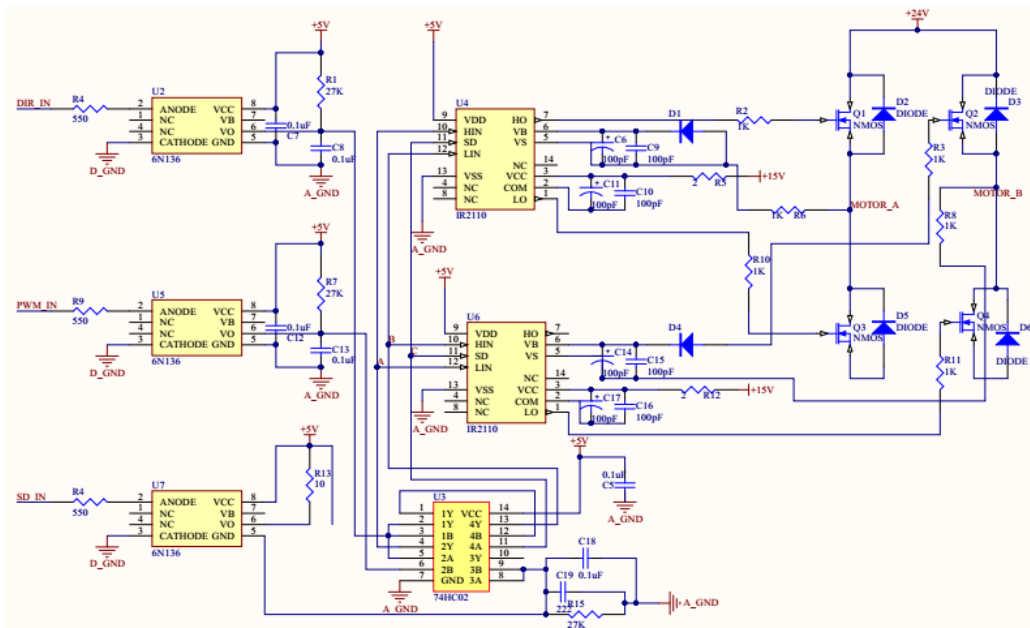


Fig. 4. DC motor driving circuit.

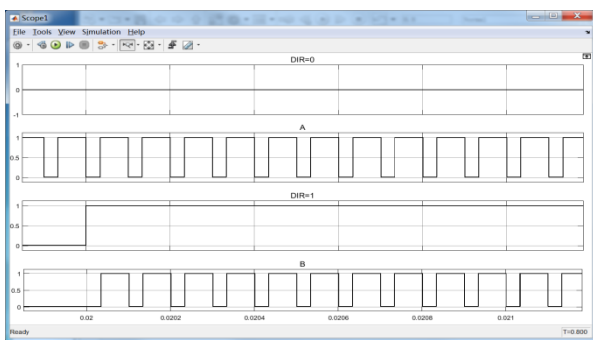


Fig. 5. Timing diagram.

Speed and pressure flow detection principle

The speed detection is measured by the reflective photoelectric sensor KM15/16. In the case of accurate positioning, the symmetrical installation of multiple reflective pieces or reflective stickers on the measured parts will acquire better measurement results. When the reflective sticker on the rotating part passes through the photoelectric sensor, the output of the photoelectric sensor output will change once, and the speed can be got by measuring the change frequency. The pressure flow detection uses the bidirectional and high-precision current sensor ACS712 in which there is a high precision linear hall sensor circuit. The current is linear with its output voltage, and the response is extremely fast. The pressure flow detection circuit is shown in Figure 6. The current is sent to pin 3 and 4 of the ACS712. The sine wave outputting from the seventh pin is filtered through the half-wave rectifier filter which can output the DC voltage

signal. Since the input impedance of the A/D detection side of STM32F103ZET is low, the voltage signal after rectifying and filtering will have a large fluctuation, which has a great influence on the detection accuracy, hence, the voltage follower is added at the A/D input terminal.

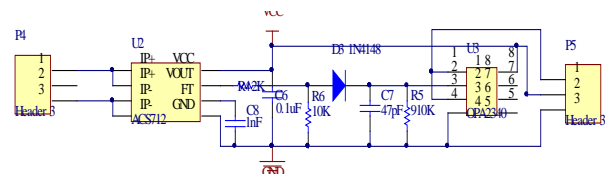


Fig. 6. Pressure flow detection circuit.

SOFTWARE DESIGN

Programmable controller (PC) design

Production control ability can be improved by using Kingview software monitoring system. The communication parameters of Kingview should be consistent with the SCM [10]. The monitoring interface is shown in Figure 7, the corresponding control information can be outputted through the button on the interface, and the serial port transmits the information to SCM. The actual operation of each part is controlled through the processing. The parameter settings of Kingview and SCM must be matched. The PC on the read and write operations sends different instructions to the SCM by using serial port communication. The lower-computer receives the instructions and returns to the PC according to the corresponding read and write command format.

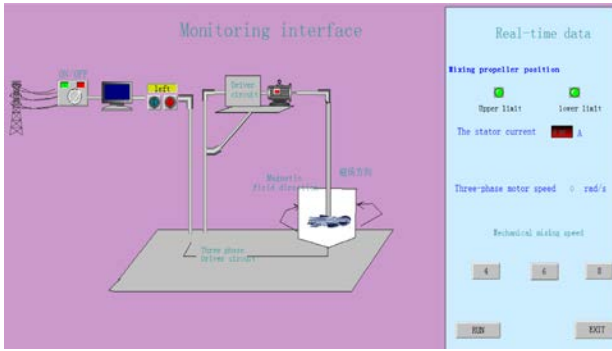


Fig. 7. Monitoring interface.

If the operation is abnormal, the lower-computer should send corresponding instructions, hence it is clear that the operation of the whole system can be observed through the PC.

SCM system software design

First, each module is initialized. According to the initial speed and direction, determine whether the speed reaches the predetermined value, and use the PI algorithm to achieve a constant speed. Then call the subroutines to determine whether the current exceeds the rated value so as to protect the motor and the circuit. The main program flow diagram is shown in Figure 8(a). Figure 8 (b) shows the speed flow diagram. I/O interface initialization and module configuration are implemented. The main program will call the speed detection subroutine at regular intervals. In order to achieve high accuracy, the multi-measurement average method can be used.

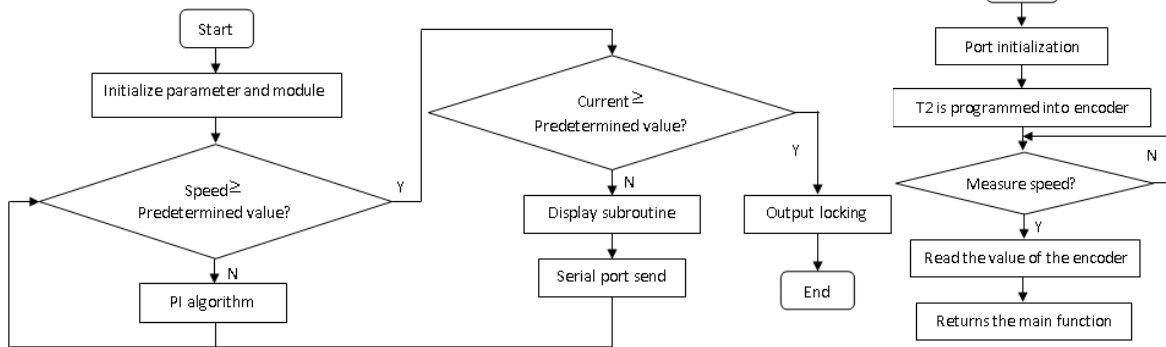
PI algorithm

Using the digital PI control, the expression is:

$$u(k) = K_p \times \left\{ e(k) + \frac{T}{T_i} \times \sum_0^k e(j) + \frac{T_d}{T} \times [e(k) - e(k-1)] \right\} \quad (1)$$

With the increment PI, the output value at the (k-1) sampling time is:

$$u(k) = K_p \times \left\{ e(k-1) + \frac{T}{T_i} \times \sum_0^{k-1} e(j) + \frac{T_d}{T} \times [e(k-1) - e(k-2)] \right\} \quad (2)$$



(a) Main program flow diagram

(b) Speed flow diagram

Fig. 8. Software flow diagram.

Equation (3) is obtained by subtracting equation (1) from equation (2).

$$\Delta uk = K_p \times [e(k) - e(k-1)] + \frac{T}{T_i} \times e(k) + \frac{T_d}{T} \times [e(k) - 2e(k-1) + e(k-2)] \quad (3)$$

The equation (3) is simplified

$$\Delta uk = A \times e(k) + B \times e(k-1) + C \times e(k-2) \quad (4)$$

From the equations listed above, if the sampling period is given, once A, B, and C are determined, the amount of control can be obtained as long as the deviation value of the three measurements. Since A, B and C are determined by the load, their values are determined by the specific conditions in different load conditions.

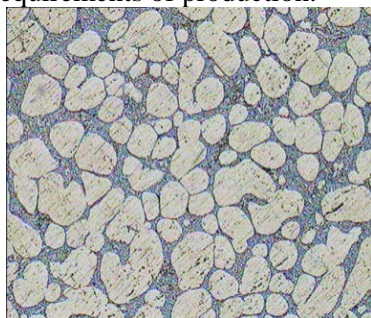
EXPERIMENTAL RESULTS

The DC motor driving circuit requires that the output voltage should be always stable at 24V. In actual measurement, the power supply circuit can output 24V stably no matter whether the output is connected to the load, and the design requirements are satisfied. Meanwhile, the drain-source voltage of MOSFET is measured. The bus voltage is 350V, the reset voltage is 120V, the peak voltage is 120V, and the peak voltage of drain-source is 584V, all of which are within the voltage range of the MOSFET, it meets the design requirements.

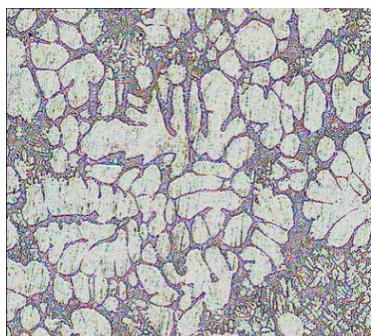
The control system is used in the preparation of A356 semi-solid alloy slurry in the laboratory. Motor speed test results: when the current is 2-3A, the speed can reach 180-300 rpm; when the current is 3-4A, the speed can reach 300-700 rpm, which meets the design requirements of 300-500 rpm in preparation.

The A356 alloy melt with temperature of 650°C is poured into the pulp chamber with a temperature of 400 °C .The direction of rotating magnetic field produced by electromagnetic stirrer is opposite to that of homogeneous stirring rod.

The input power of the electromagnetic stirrer is 2.5 Kw, the frequency is 20Hz, and the rotation speed of the homogeneous stirring rod is 400 r/min. When preparing the slurry, the stirring direction of electromagnetic stirrer and homogeneous stirring rod is changed periodically at 5-15 sec intervals. The semi-solid slurry of A356 alloy is obtained until the alloy melt temperature reached 600 °C, and the preparation time is 5 min. Finally, the semi-solid A356 alloy ingot is used as the raw material of the thixotropic shape. The prepared slurry water quenching microstructure is shown in Figure 9(a), qualified grain microstructure is obtained, which can be directly put into the die casting machine, extruder machine or forging machine for direct forming, and can also be cooled to get the semi-solid A356 alloy ingot as a thixotropic forming raw material. The slurry water quenching organization by using a single mechanical stirring is shown in Figure 9(b), which is composed of a large irregular near spherical primary phase and scattered but still directional dendritic crystal. In practice, it does not meet the requirements of production.



(a) Water quenching microstructure of double motor agitated slurry.



(b) Water quenching microstructure of single mechanical agitated slurry.

Fig. 9. Water quenching microstructure of slurry.

CONCLUSIONS

The double motor intelligent control system can realize strong and uniform agitation, and the monitoring interface can display the agitating speed, working current and commutation conditions in real time. The PC monitoring interface, SCM control system and motor driving circuit can effectively coordinate the operation, and can realize the accurate control of motor rotation speed and the accurate matching of speed between the two motors.

The agitation control system is suitable for the preparation of aluminum-based alloy and its composite semi-solid slurry or ingot. It is also suitable for the preparation of other non-ferrous metals and their composite materials, as well as ferrous metals and their composite semi-solid slurries or ingots.

Acknowledgements: This work was supported by National Natural Science Foundation of China (No.61503169) and the Natural Science Foundation of Liaoning province (No. 2015020102).

REFERENCES

1. B. Yucel, *Mater. Sci. Engin. A*, **528**, 5636 (2011).
2. J.E. Felix, U. Joachim, *Chem. Engin. Technol.*, **39** (7), 1251, (2016).
3. R. Ortega, A. Van Der Schaft, F. Castanos, A., Astolf, *IEEE Trans. Automat. Contr.*, **53** (11), 2527 (2008).
4. A.J. Hugo, *Agitation and Fluid Mixing Technology. Chemical Reactor Modeling*, Springer International Publishing Switzerland, Springer, Cham, 2014.
5. D. Casadei, M. Mengoni, G. Serra, A. Tani, L. Zarri, *IEEE Trans. Ind. Appl.*, **46** (4), 1436, (2010).
6. A.A.E. Abdulrahman, B.M. Rosbi, *Procedia Engin.*, **41**, 420, (2012).
7. M. Rahul, K. Tejbeer, *Int. J. Advan. Engin. Sci. Technol.*, **8** (2), 291, (2011).
8. M. Liu, J. Yu, H. Liang, *Instrum. Techn. Sens.*, **5**, 95, (2010).
9. G. Peng, Z.Q. Qin, *Application practice of embedded microcontroller based on ARM Cortex-M3 STM32 series*. Beijing: Electronic Industry Press, China, 2011.
10. L.F. Yang, J. Yuan, W. Liu., X.M. Nie, X.L. Pei, *Appl. Mech. Mater.*, **121**, 3195, (2012).

Use of artificial neural networks for modeling the fabric temperature in heat setting processes

M. Gu¹, X. Xu¹, W. Xiong¹, H. Pan¹, W. Dai^{2*}

¹ Institute of Automation, Faculty of Mechanical Engineering and Automation, Zhejiang Sci-Tech University, Hangzhou, China

² School of Information & Electronic Engineering, Zhejiang Gongshang University, Hangzhou 310019, China

Received September 19, 2017, Accepted December 20 2017

The objective of this paper is to investigate the temperature of fabric while doing heat setting, because the key parameters were hard to confirm using a physical model. Therefore artificial neural network (ANN) with four layers was adopted. The oven temperature, the size of fabric, the weight of fabric and time were selected as input variables as they have significant influence on the temperature of the fabric during heat setting process. Adam algorithm was adopted to optimize the efficiency and the speed of ANN training. The predicted and experimental values agree well, indicating that the ANN models yield a good prediction in heat setting process

Key words: Heat-setting, Prediction model, Neural network, Fabric temperature.

INTRODUCTION

Fabric produces a lot of creases in the process of winding, weaving, tufting and knitting, which have adverse effects on its performance and need to be eliminated by the process of heat-setting [1]. Heat setting is a thermal and mechanical process to achieve certain desired results. The effects of heat setting process bring fabrics in dimensional stability, temperature resistance and other desirable attributes like higher volume, wrinkle resistance, etc.

Heat-setting in the stenter is one of the most important processes in the textile industry, which is also one of the most energy-intensive and expensive processes. The most important parameters in the heat setting are temperature, dwell time and overfeed[2]. In order to get better qualitative results and reduce energy consumption, lots of experiments were done to find the influence of different parameters in heat setting process [3-5]. "One factor at a time" principle was usually chosen to design experiments and analyze how the textile characteristics (average weight, mesh density, thickness and tensile strength) changed depending on the heat setting parameters. Those studies focused on the qualitative analysis and lacked a precise mathematical model. How do these factors affect the energy consumption of the heat setting process needs further to be quantified.

Mathematical modelling of the dry fabric heat setting process is important because it enables suitable process parameters setting, reducing of the costs due to quality constraints. It is difficult to build a mathematic model which can be used in different processing situations during the various fabric processes in the stenter machine. There are a few

references found to discuss the mathematic model of the heat setting process, most of these references were discussing the fabric drying behaviour using the theory of mass and heat transfer in porous media [7,8], not mentioning the model of fabric temperature. Based on the principle of energy balance, Zhang *et al.* [9] proposed a mathematical model, the dynamic relationships between hot air temperature, flux and temperature of heat transfer oil were analyzed, and the influence of ambient conditions on the performance of the stenter machine was also investigated. The model is complex, the parameters change in different situations. Based on the mechanism of hot air jet heating, a new simple model was proposed [10], it has produced good effect in the actual processing application when using the same fabric. While the property of the fabric changes, the model parameters need to be reacquired.

Accurate modelling of the heat-setting behaviour of the fabric at different situations is very difficult with conventional analytical solutions since it is very sensitive to parameters. From a textile point of view, to know the effect of some production parameters in various textile applications, neural network models are used since they have proved to be useful tools for many prediction-related problems. For instance, to identify the relationship between fabric drape, low stress mechanical properties and finishing, an artificial neural network model was set up based on various process parameters [11]. To identify the thermal resistance of textile fabrics, two different back-propagation artificial neural network architectures were compared in [12]. In those studies, results showed that the Artificial Neural

To whom all correspondence should be sent:
E-mail: dwz@zjgsu.edu.cn

Network (ANN) algorithms provided more accurate predictions.

Due to this fact, in this research the application of the artificial neural network approach for modelling the fabric temperature in the dry heat-setting processes, was explored. The processing of fabrics was carried out on a hot air drying furnace instead of stenter. The temperature of the furnace, the weight of fabric, the area of the fabric and the time were used as input parameters of the ANN models, which were then analysed and compared to predict the temperature of the fabrics. With this research it was shown that the prediction of an ANN for the fabric temperature of different fabrics subjected to different furnace temperature processes is possible. This result has good reference to the optimization of the temperature setting value.

PHYSICAL MODEL DESCRIPTION

The hot air jets through the overhanging textile sample at a certain temperature. In order to obtain the model, the following two assumptions were made:

- the fabric is dry without water evaporation;
- the fabric is uniformly heated.

From the heat transfer law and energy balance, the increment of internal enthalpy of the fabric is equal to that of hot air carried by the heat transfer to the fabric [13]:

$$\Phi(\tau) = h(\tau)\Delta S[T_w(\tau) - T(\tau)] = \rho c_p \Delta V \frac{dT}{d\tau} \quad (1)$$

Here, $\Phi(\tau)$ is heat transfer through a certain area in a unit time, $h(\tau)$ is coefficient of heat transmission, ΔS is the area of fabric, $T_w(\tau)$ is the boundary temperature of fabric at time τ , $T(\tau)$ is the temperature of the fabric. ρ is density of the fabric, c_p is specific heat capacity, ΔV is the unit fabric heat exchange volume, let $\Delta V/\Delta S = \delta$, here δ is the thickness of fabric.

The temperature of the fabric can be written as follows form equation (1) by mathematical transformation:

$$T(\tau) = T_w(\tau) - \exp\left[-\frac{h(\tau)}{\rho c_p \delta} \tau\right](T_0 - T_{w0}) \quad (2)$$

where the boundary temperature $T_w(\tau)$ can be written as:

$$T_w(\tau) \approx \left[\frac{T_{air}(\tau) + T(\tau)}{2}\right] \quad (3)$$

The temperature of the fabric can also be written as follows:

$$T(\tau) = T_{air}(\tau) - \exp\left[-\frac{h(\tau)}{\rho c_p \delta} \tau\right](T_{air(0)} - T_0) \quad (4)$$

Equation (4) shows that the temperature of the fabric is changed with an exponential function when heated. The speed of temperature change is related to the physical property parameters of the fabrics, surface heat transfer conditions and coefficient of heat transmission. When doing heat-setting in the textile industry, different types of fabrics which have different sizes, weight and thickness will be processed in the same machine. But the material will always be the same, which means that c_p will not change. The difficulty is that when a new fabric comes, it is hard to calculate the temperature.

ANN METHODOLOGY

Artificial Neural Network (ANN) is an information processing system that roughly replicates the behavior of a human brain by emulating the operations and connectivity of biological neurons.

In order to predict the fabric temperature, this paper adopted the model of the network as shown in figure 1. The number of hidden layers and nodes will affect the network accuracy and the length of the training process. This paper adopted the back-propagation neural network model of 4-12-12-1.

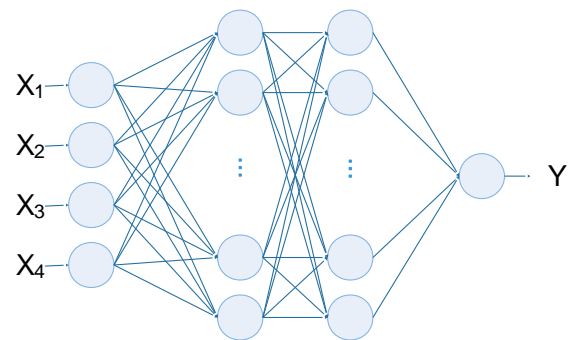


Fig. 1. Schematic of the topology of the network includes of hidden and output layer

The input variables were: temperature of the oven, weight of the fabric, size of the fabric and the time. The output was the temperature of the fabric.

For all data-sets, the hyperbolic tangent sigmoid transfer function (Equation (5)) in the hidden layer and a logarithmic sigmoid (Equation (6)) transfer function in the output node were employed.

$$\tanh x = \frac{e^x - e^{-x}}{e^x + e^{-x}} \quad (5)$$

$$f(x) = \frac{1}{1 + e^{-x}} \quad (6)$$

The optimal architecture of the ANN model and its parameter variation were determined based on the minimum value of the mean square error (MSE) of the training and testing sets. MSE measures the performance of the network according to Equation (7).

$$\text{MSE} = \frac{1}{N} \sum_{i=1}^N (y_{\text{exp}(i)} - y_{\text{ANN}(i)})^2 \quad (7)$$

where N is the number of data points, $y_{\text{ANN}(i)}$ is the ANN prediction, $y_{\text{exp}(i)}$ is the experimental data. i is an index of data.

The back propagation of the error, using the minimum variance learning method of gradient descent, will reverse the error, and constantly adjust the connection weight between the neurons in the network, so that the error eventually reached the minimum. However, when the fastest direction of the gradient decreases and the direction of the minimum point of the error surface deviates greatly, the path to the minimum point will be lengthened, so that the network learning efficiency is low and the speed is slow.

In order to overcome this deficiency, this paper uses Adaptive Moment Estimation (Adam) algorithm [14] to optimize, which calculates the historical gradient attenuation method similar to the momentum. The adjustment formula is:

$$g_t = \nabla_{\theta} f_t(\theta_{t-1}) \quad (8)$$

$$m_t = \beta_1 * m_{t-1} + (1 - \beta_1) * g_t \quad (9)$$

$$v_t = \beta_2 * v_{t-1} + (1 - \beta_2) * g_t^2 \quad (10)$$

m_t and v_t are the weighted average of the gradient and the weighted square error, initially 0 vector. When the attenuation factors β_1 and β_2 are close to 1, m_t and v_t are tend to 0 vector. So m_t and v_t deviation correction:

$$\hat{m}_t = m_t / (1 - \beta_1^t) \quad (11)$$

$$\hat{v}_t = v_t / (1 - \beta_2^t) \quad (12)$$

Finally, Adam's update equation is:

$$\theta_t = \theta_{t-1} - \alpha * \hat{m}_t / (\sqrt{\hat{v}_t} + \epsilon) \quad (13)$$

In this paper, $\alpha = 0.001$, $\beta_1 = 0.9$, $\beta_2 = 0.999$ and $\epsilon = 10^{-8}$.

EXPERIMENTS

The heat setting process was carried out using an experimental apparatus as shown in Figure 2. This apparatus is a well-insulated oven and has vents at the top. It controls the air with controlled velocity by an electric blower and controls temperature by electrical resistance with the aid of an intelligent controller. Additional two temperature sensors with $\pm 1^\circ\text{C}$ accuracy were placed to measure the hot air temperature in the oven.

Figure 3 shows the schematic of heat setting process taken in the experimental apparatus.

The oven was run without the sample for a certain time to set the desired conditions before each heat setting experiment. Heat setting process started when the temperature of the oven was stable. The fabric sample fitted with a thermocouple was placed into

the oven quickly and measurement started at this point. Fabric temperature, oven temperature and heat setting time were recorded and saved in PC with the aid of a data recorder at 500 ms intervals. The heat setting time of the sample was determined until the product reached the fixed temperature and kept stable.



Fig. 2. The experimental apparatus used for heat setting.

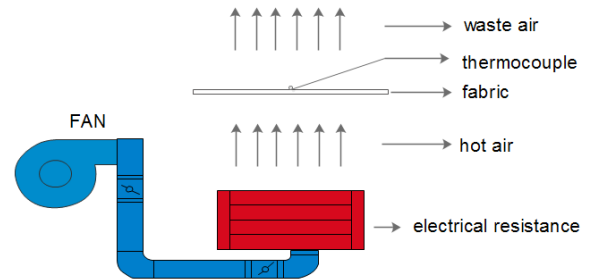


Fig. 3. The schematic of the experimental apparatus.

The sample weights and the size of the fabric were measured and recorded before the heat setting process.

18 types of fabrics with different weight and composition were selected. The fabric samples were heat set at different time and temperatures. Over 40 sets of data were recorded for each type of fabric.

RESULTS AND DISCUSSION

Experimental data from this study were used to train and test an ANN model proposed above for prediction of fabric temperature during the heat setting process. This data were divided into two groups of training and test with 50% and 50% samples.

The model has good learning ability, after 400 cycles training, the mean square error (MSE) reached 0.000153, and the training convergence curve is shown in Figure 4.

In order to verify the accuracy of the model, two fabrics were randomly chosen at different oven temperatures.

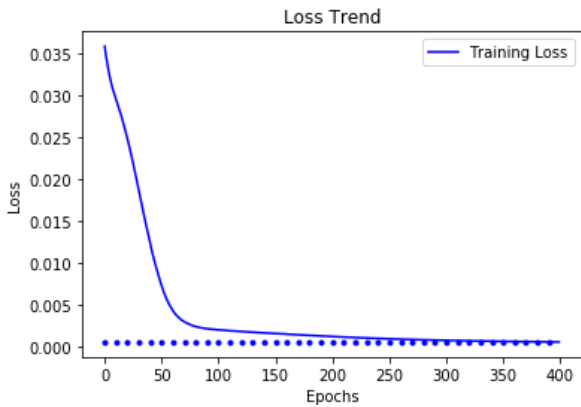
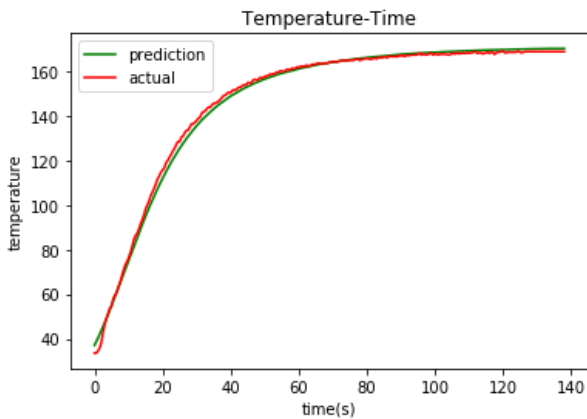
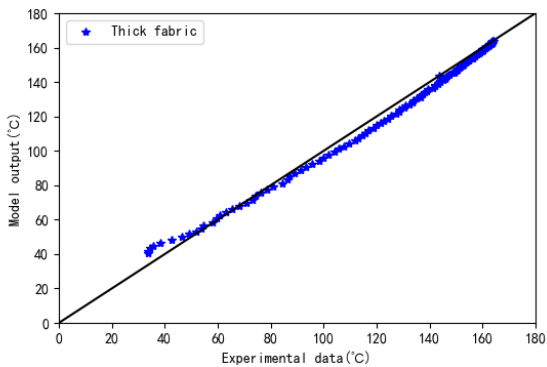


Fig. 4. Training convergence curve

Figure 5 shows a comparison between experimental results and predicted values using the neural network model when using thin fabric. Figure 5(b) depicts the agreement between experimental data and model results (for the thin fabric) and shows good correlation. This trend is also depicted in Figure 6(b) using a thick fabric.



(a) Experimental and predicted value



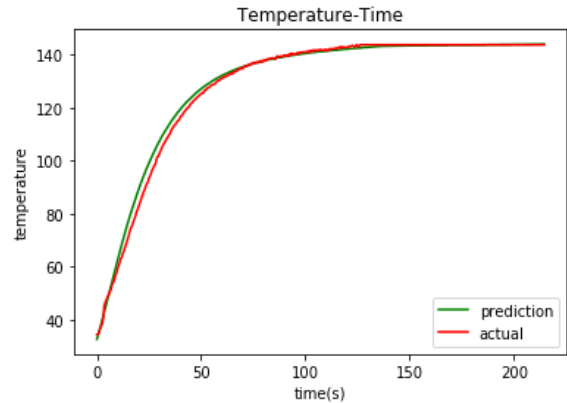
(b) Correlation analysis of model predicting results

Fig. 5. Comparison between ANN method and actual results using a thick fabric.

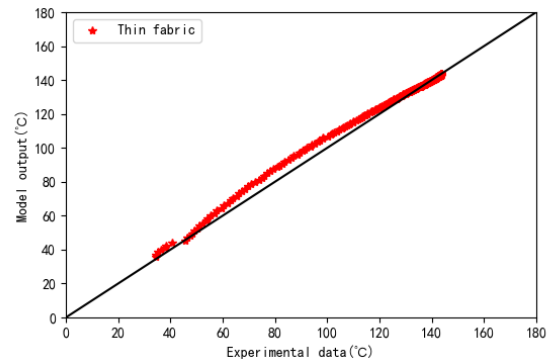
The statistical results such as MSE and r^2 are shown in Table 1.

Table 1. Statistical results of 2 samples

	R^2	MSE
Thick fabric	0.997882	0.000200
Thin fabric	0.997154	0.000167



(a) Experimental and predicted value



(b) Correlation analysis of model predicting results

Fig. 6. Comparison between ANN method and actual results using thin fabric.

The statistical results indicate that the model shows a good fit with experimental data. ANN models show a good relationship between the experimental and predicted response values in different heat setting processes using different samples.

CONCLUSION

The ANN has a potential to model complex and nonlinear processes in the textile industry. The back-propagation network model can be used to predict the fabric temperature when the relative importance of inputs is known. Using a combination of basic parameters: oven temperature, weight and size of the fabric and time, the model was built. The Adam algorithm was adopted, the efficiency and the speed of training were also improved. Experimental results testify to the fact that the network is capable of prediction with high accuracy in heat setting process.

Acknowledgements: This work is partially supported by The National Natural Science Foundation of China (No. 61503341), the Natural Science Foundation of Zhejiang Province (No. LQ14F030013).

REFERENCES

1. M.B. Quadri. *Drying Technology*, **33**(1), 18 (2014).
2. L.Q. Zeng. *Textile Dyeing & Finishing Journal*, **33** (12), 1 (2011).
3. D.N. Marvin. *Coloration Technology*, **70** (1), 16 (2008).
4. R.H. Yang, C.W. Kan. *Fibers & Polymers*, **14**(8), 1347 (2013).
5. S. Sardag, O. Ozdemir, I. Kara, *Fibres & Textiles in Eastern Europe*, **15**(4), 50 (2007).
6. N. Besler, Y.S. Gloy, T. Gries, 48th Conference of the International Federation of Knitting Technologists (IFKT), **141**(1), 1 (2016).
7. A. Cay, I. Tarakçioğlu, A. Hepbasli, *Drying Technology*, **28**(12), 1359 (2010).
8. U. Akyol, A.E. Akan, A. Durak, *The Journal of the Textile Institute*, **106**(3), 260 (2014).
9. Y.B. Zhang, R. Ren, H.P. Pan, *CIESC Journal*, **62**(6), 2360 (2011).
10. M.M. Gu, *3rd International Conference on Advances in Energy, Environment and Chemical Engineering*, Chengdu, China, **69**,1 (2017)
11. S. K. Bahadir, F. Kalaoglu, S. Jevsnik, S.H. Eryuruk, C. Saricam. *Fibres & Textiles in Eastern Europe*, **23**(2), 90,(2015).
12. D. Bhattacharjee, V.K. Kothari, *Textile Research Journal*, **77**(1), 4 (2007).
13. L. Fu, L.L. Tang, L. Li, *Modern Manufacturing Engineering*, **27**(1), 66 (2013).
14. D.P. Kingma, J. Ba, *3rd International Conference for Learning Representations*, San Diego, United States of America, (2015)

Effect of sorbent concentration on Pb(II) sorption on Mg-Al-EDTA layered double hydroxides

X.T. Wang^{1,&}, L.X. Zhao^{2,*,&}, L. Li¹, Q.F. Chen², Q. Li², J. Zhang²

¹ Huadian Electric Power Research Institute, Shandong Branch, Jinan, P. R. China

² Analysis and Test Center, Shandong Academy of Sciences, Jinan 250014, P. R. China

Received September 22, 2017, Accepted December 20, 2017

The sorption of Pb(II) on a Mg-Al-EDTA layered double hydroxide (LDH) sample was investigated at different sorbent concentrations and the sorbent concentration effect (C_s -effect) was observed. The sorption isotherm and kinetic process at a given C_s value can be adequately described by the classic Freundlich model and a pseudo-second-order kinetic equation. However, the classic Freundlich model cannot describe the C_s -effect observed in the studied sorption system. We believe that the C_s -effect can be attributed to the deviation of the real sorption system from an ideal one. It was confirmed that the surface component activity (SCA) model can adequately describe the C_s -effect observed in sorption experiments.

Key words: Pb(II), LDH, Sorbent concentration effect, Surface component activity model.

INTRODUCTION

Pb(II) is a common heavy metal pollutant resulting from both natural and anthropogenic sources. Sorption is the primary technology considered for the treatment of wastewater containing Pb(II) because of its simplicity, low cost, high efficiency and wide adaptability. The layered double hydroxides (LDHs) are a kind of potential sewage treatment agent. From both theoretical and practical aspects, it is essential to understand the sorption process behavior of Pb(II) on LDHs.

The sorbent concentration (C_s) used in the sorption treatment process of wastewater is an important factor influencing the removal efficiency of pollutants from aqueous solutions [1–4]. It has been observed that the pollutant-removal efficiency increases with increasing C_s for a given initial pollutant concentration; however, the sorption capacity of the sorbent decreases [1–4]. This phenomenon is known as the C_s -effect [5–7] and has been observed in numerous laboratories in various solid-liquid systems during sorption equilibrium studies [7–12].

Recently, we developed a surface component activity (SCA) model [13–15] in which the activity coefficient of the solid surface component sorption sites was assumed to be a function of C_s rather than unity because of the deviations in the behavior of a real sorption system from that of an ideal one.

In this study, Mg₂Al-EDTA-LDH was synthesized and the sorption of Pb(II) on this LDH

in aqueous solutions was examined at various C_s values. The C_s -effect was studied. Special emphasis was placed on the applicability of the SCA model in describing sorption equilibria and kinetics with the C_s -effect.

MATERIALS AND METHODS

Materials

All chemicals used in this work were of analytical grade. Ultra-pure water was used in all cases.

Mg₂Al-EDTA LDH with a Mg²⁺/Al³⁺ molar ratio of 2:1 was prepared by co-precipitation. An aqueous solution containing 0.1 mol Mg(NO₃)₂·6H₂O and 0.1 mol Al(NO₃)₃·9H₂O was dropwise added to distilled water while the solution was stirred. During the synthesis, the temperature was maintained at 65°C and pH at 11–12 by the simultaneous addition of EDTA-Na₂ ammonia solution with EDTA-Na₂/Al molar ratio equal to 1. The reaction mixture was aged in the mother solution at room temperature and then filtered, washed with deionized water until the pH was neutral. The filter cake was further hydrothermally treated at 80°C for 24 h. The sol was dried, triturated and sieved to collect the particles of <74 μm in diameter. Mg₂Al-EDTA LDH was characterized by XRD (Fig. 1).

Sorption experiments

Kinetic experiments of the sorption of Pb(II) on Mg₂Al-EDTA LDH sample were carried out by the following steps. A known mass of Mg₂Al-EDTA LDH sample was dispersed in 250 mL of Pb(NO₃)₂ solution. The suspension was stirred at a constant

To whom all correspondence should be sent:

E-mail: lingxi0716@163.com

[&] These authors contributed equally to this work and should be considered co-first authors.

speed and maintained at 25±0.2 °C. Aliquots (5 mL) of the suspension were withdrawn at predetermined time intervals (*t*) and filtered through a 0.45 μm syringe filter. The remaining Pb(II) concentration of the filtrate was determined by atomic absorption spectrometry (TAS-990, Beijing Purkinje General Instrument Co., Ltd.). The sorbed amount Γ_t was calculated by the following equation:

$$\Gamma_t = \frac{(C_0 - C_t)V}{m} \quad (1)$$

where C_0 (mg/L) and C_t (mg/L) are the initial and the remaining concentration, respectively, V (mL) is the volume of the suspension and m (g) is the mass of the LDH sample.

Sorption isotherms of Pb(II) on Mg₂Al-EDTA LDH sample were obtained by the batch equilibration technique [16-18]. Solutions Pb(II) with various concentrations (0-1000 mg/L) of were prepared in 0.01 mol/L NaNO₃ with Pb(NO₃)₂, and the pH values of the solutions were adjusted to 5.0. Known masses of LDH samples were mixed with Pb(II) solutions of various initial concentrations in polyethylene centrifugal tubes. The centrifugal tubes were put into a thermostated water bath shaker at 25±0.2°C for 24 h. Then the suspensions were centrifuged at a speed of 4000 r/min. The Pb(II) equilibrium concentrations in the supernatants were determined by flame atomic absorption spectrometry. The equilibrium sorbed amounts were calculated using the following equation:

$$\Gamma_e = \frac{(C_0 - C_e)V}{m} \quad (2)$$

where C_e (mg/L) is the remaining (equilibrium) concentration.

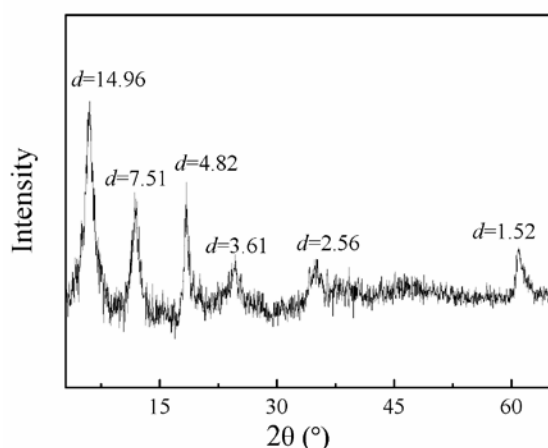


Fig. 1. XRD pattern of the Mg₂Al-EDTA LDH sample

RESULTS AND DISCUSSION

Sorption isotherms

Fig. 2(a) shows the sorption isotherms of Pb(II) on Mg₂Al-EDTA LDH at different LDH concentrations. As can be seen, the sorption isotherms decline

significantly as the sorbent concentrations increase. This phenomenon accords with the law which is described by a C_s -effect.

Classical Freundlich equation is represented as:

$$\Gamma_e = K_F C_e^{n_F} \quad (3)$$

where Γ_e is equilibrium sorption amount, C_e is equilibrium concentration, K_F and n_F are Freundlich constants [19].

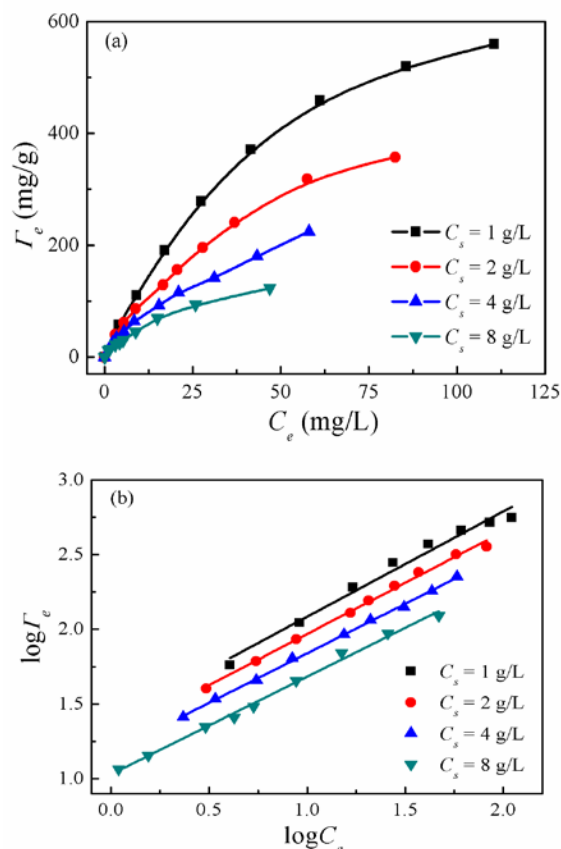


Fig.2. Sorption isotherms (a) and linear correlation plots for the classical Freundlich equation (b) at different sorbent concentrations

Table 1. Parameters of the classical Freundlich equation at different sorbent concentrations

C_s (g/L)	n_F	K_F	R^2
1.0	0.704	24.02	0.980
2.0	0.685	19.24	0.996
4.0	0.663	15.03	0.999
8.0	0.651	10.71	0.995

The sorption data of Pb(II) on Mg₂Al-EDTA LDH were fitted with the Freundlich equation (see Fig.2(b)). It was found that the Freundlich equation can adequately describe the sorption equilibrium for a given C_s value, and all correlation coefficients (R^2) were greater than 0.98. The fitted Freundlich parameters, K_F and n_F , for various C_s values are presented in Table 1. The dependence of the Freundlich parameters on C_s showed that the classical Freundlich model cannot predict the C_s -effect.

Considering the deviation of a real sorption system from an ideal one, we proposed an alternative model, SCA model [13-15]. It suggests that (1) the surface of the sorbent is uniform, that is, all sorption sites are equivalent; (2) all sorption occurs through the same mechanism; (3) at the maximum sorption, only a monolayer is formed; (4) the molecular sizes of solute and solvent are similar; (5) surface component (sorption site or adsorbed solute) activity coefficient is not equal to unity because of the deviation of the real sorption system from an ideal one. A Freundlich-SCA equation can be derived as follows:

$$\Gamma_e = K_S \cdot f_{H_2O}^s \cdot C_e^{n_S} \quad (4)$$

The coefficients, n_S and K_S , of a given system are independent of sorbent concentration.

The C_s -dependent function of $f_{H_2O}^s$ is in exponential form:

$$f_{H_2O}^s = \exp(-\gamma C_s^\alpha) \quad (5)$$

where γ and α are empirical constants. Then,

$$K_F = K_S \exp(-\gamma C_s^\alpha) \quad (6)$$

Thus, the C_s -dependent function of $f_{H_2O}^s$ can be estimated from the relationship between the experimentally measured K_F values and C_s values.

The change of K_F with C_s for the sorption system was fitted to Eq. (6) using a non-linear least-squares method (Excel Solver) (see Fig. 3), and the best-fit values of the empirical constants, γ and α , are 0.563 and 0.452.

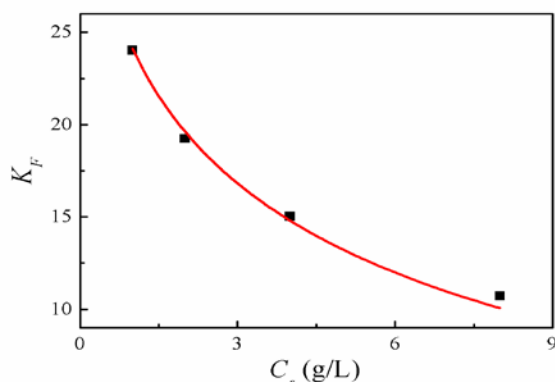


Fig.3. Relationship between K_F and C_s

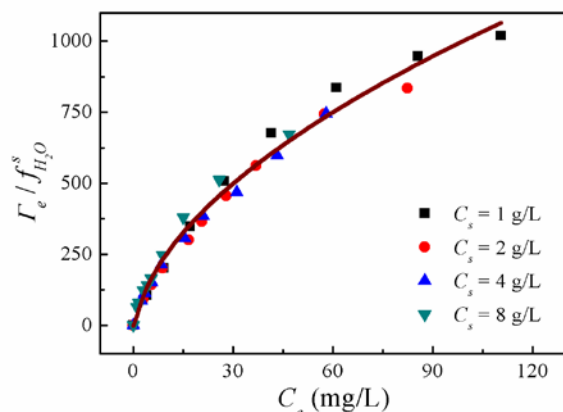


Fig.4. Isotherm plot of the Freundlich-SCA model

Using the simulated γ and α values, the normalized non-linear plot of $(\Gamma_e / f_{H_2O}^s)$ vs. C_e for the studied system was obtained (see Fig. 4). As can be seen, a unique line for various C_s values was obtained. The K_S and n_S values are 52.87 and 0.651. The correlation coefficients (R^2) of the non-linear plot were higher than 0.98, indicating that the Freundlich-SCA equation can adequately describe the C_s -effect observed in the studied system.

Sorption kinetics

Fig. 5 shows the sorption kinetics of Pb(II) on Mg₂Al-EDTA LDH at different LDH concentrations. It is seen that the sorption processes are rapid.

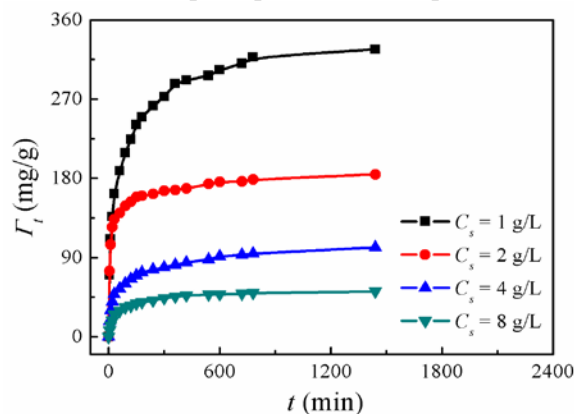


Fig. 5. Sorption kinetics at various sorbent concentrations

The first step involved fast sorption of almost the whole amount of Pb(II) in the solution within a few hours, followed by slower sorption. Pseudo-second-order model can fit the kinetic data for a given C_s value (Fig. 6).

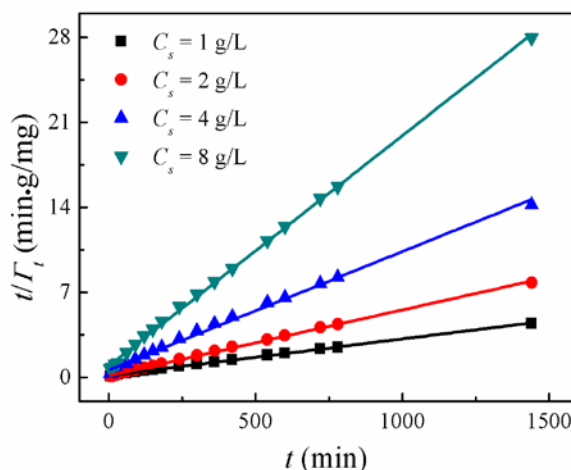


Fig. 6. Pseudo-second-order sorption kinetics

The parameters are listed in Table 2. Pseudo-second-order kinetic model [20] is expressed as:

$$\frac{t}{\Gamma_t} = \frac{t}{\Gamma_e} + \frac{1}{\Gamma_e^2 k_2} \quad (7)$$

where k_2 (g/mg·min) is the rate constant of pseudo-second-order sorption. The fitted parameters for

various C_s values are presented in Table 2. The values of k_2 changed with C_s . This phenomenon indicates that the C_s -effect also exists in the sorption kinetics.

Table 2. Parameters of the pseudo-second-order kinetic equation at different sorbent concentrations

C_s (g/L)	Γ_e (mg/g)	k_2 (g·mg ⁻¹ ·min ⁻¹)	R^2
1.0	357.1	5.47×10^{-5}	0.996
2.0	181.5	1.99×10^{-4}	0.998
4.0	102.4	1.60×10^{-4}	0.995
8.0	52.66	3.86×10^{-4}	0.999

The equilibrium partition coefficient of Pb (II) between solid and liquid phase can be obtained by sorption kinetics data. The partition coefficient (K_p) is the ratio of the solid-phase and dissolved concentrations of chemicals at equilibrium. It can be expressed as:

$$K_p = \frac{\Gamma_e}{C_e} \quad (8)$$

The partition coefficient-SCA equation can be derived as follows:

$$K_p = \exp(-\gamma C_s^\alpha) K_p^0 \quad (9)$$

where K_p^0 is the intrinsic partition coefficient of a given system, which is independent of sorbent concentration. The change of K_p with C_s for the sorption system was fitted to Eq. (9) using a non-linear least-squares method (Excel Solver) (see Fig. 7), and the best-fit values of the empirical constants, γ , α and K_p^0 , are 0.559, 0.455 and 3.239. The values of γ and α are similar to those obtained by the Freundlich-SCA equation for the sorption isotherm.

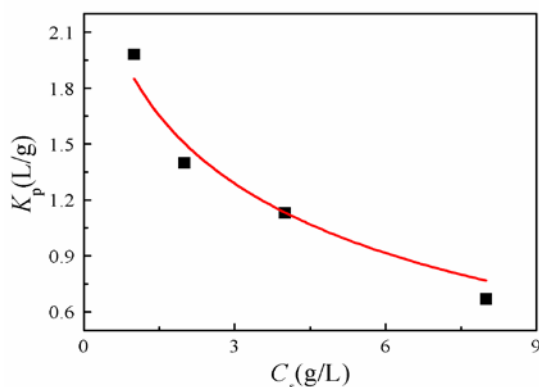


Fig. 7. Simulated variation curve of the partition coefficient with sorbent concentration

CONCLUSION

A significant C_s -effect was observed in the sorption of Pb(II) on Mg-Al-EDTA LDH. The classic Freundlich model and the pseudo-second-order kinetic equation sorption can well describe the sorption isotherm and kinetic process at a given C_s value but cannot describe the C_s -effect observed. The C_s -effect data can be described using the Freundlich-SCA

equation and partition coefficient-SCA equation. We believe that the C_s -effect can be attributed to the deviation of the real sorption system from an ideal one. This study confirms the applicability of the SCA model for describing the sorption process with the C_s -effect.

Acknowledgements: This work was supported by the Shandong Provincial National Natural Science Foundation of China (ZR2015YL014), the National Nature Science Foundation of China (21703125) and the Major Science and Technology Program for Water Pollution Control and Treatment (2015ZX07203007 and 2015ZX07203005).

REFERENCES

1. N.N. Das, J. Konar, M.K. Mohanta, S. C. Srivastava, *J. Colloid Interface Sci.*, **270**, 1 (2004).
2. G. Crini, P. M. Badot, *Prog. Polym. Sci.*, **33**, 399 (2008).
3. L. Lv, P. Sun, Z. Gu, H. Du, X. Pang, X. Tao, R. Xu, L. Xu, *J. Hazard. Mater.*, **161**, 1444 (2009).
4. Y. Yang, N. Gao, W. Chu, Zhang, Y. Ma, *J. Hazard. Mater.*, **209–210**, 318 (2012).
5. D.J. O'Connor, J.P. Connolly, *Water Res.*, **14**, 1517 (1980).
6. T.C. Voice, C.P. Rice, W.J. Weber, *Environ. Sci. Technol.*, **17**, 513 (1983).
7. T.C. Voice, W. Weber, *J. Environ. Sci. Technol.*, **19**, 789 (1985).
8. D. M. DiToro, J.D. Mahony, P. R. Kirchgraber, A. L. O'Byrne, L. R. Pasquale, D. C. Piccirilli, *Environ. Sci. Technol.*, **20**, 55 (1986).
9. G. Pan, P.S. Liss, *J. Colloid Interface Sci.*, **201**, 71 (1998).
10. A.K. Helmy, E.A. Ferreiro, S.G. Bussetti, *J. Colloid Interf. Sci.*, **225**, 398 (2000).
11. T.W. Chang, M.K. Wang, *Chemosphere.*, **48**, 419 (2002).
12. X.F. Wu, Y.L. Hu, F. Zhao, Z.Z. Huang, D. Lei, *J. Environ. Sci.*, **18**, 1167 (2006).
13. L.X. Zhao, W.G. Hou, *Colloids Surf. A*, **396**, 29 (2012).
14. L.X. Zhao, S.E. Song, N. Du, W.G. Hou, *Acta Physico-Chimica Sinica*, **28**, 2905 (2012).
15. L.X. Zhao, S.E. Song, N. Du, W.G. Hou, *Colloid Polymer Sci.*, **291**, 541-550 (2013).
16. M. C. Hermosin, L. Pavlovic, M. A. Ulibarri, J. Cornejo, *Water Res.*, **30**, 171 (1995).
17. L. Ma, R.K. Xu, J. Jiang, *J. Environ. Sci.*, **22**, 689 (2010).
18. P. Ding, K.L. Huang, H. Yang, G.Y. Li, Y.F. Liu, *J. Cent. South Univ. Technol.*, **17**, 277 (2010).
19. C. H. Sheindorf, M. Rebhun, M. Sheintuch, *J. Colloid Interf. Sci.*, **79**, 136 (1981).
20. Y. S. Ho, *J. Hazard. Mater.*, **136** (3), 681 (2006).

Theoretical research on the moisture content of fine silty sand affecting the failure behavior of soil of the MEEP pile under vertical tension

Y. Qian^{1,2*}, S. Liang¹, R. Wang¹, X. Su³

¹Jilin Jianzhu University, Changchun, China

²Jilin Structure and Earthquake Resistance Technology Innovation Center, Changchun, China

³Northeast Electric Power Design Institute Co. LTD of China Power Engineering Consulting Group, Changchun, China

Received August 18, 2016; Accepted December 20, 2017

Due to its moisture content, fine silty sand has a certain influence on the failure behavior and bearing capacity of soil surrounding the MEEP pile. In this paper, using ANSYS software, an analytical model of the MEEP pile is built with the bearing plate embedded in the fine silty sand. By analyzing different models, the results for the moisture content affecting the failure behavior of soil surrounding the pile are compared in order to provide a reliable theoretical basis for the uplift bearing capacity calculation of the MEEP pile in the fine silty sand.

Keywords: Vertical tension, Fine silty sand, Moisture content, Failure behavior, Multi-Extruded-Expanded-Plates pile (MEEP pile)

INTRODUCTION

Moisture content is an important physical and mechanical index and its changes are linked to cohesive strength, internal friction angle, density and other important indices [1]. The study of the moisture content affecting the bearing capacity of the MEEP pile and the failure mechanism of soil surrounding the pile has a far-reaching significance, because the moisture content can directly affect the failure behavior and bearing capacity of soil [2]. As one of the main soils of pile foundation, the fine silty sand is different from clay and silty clay, because in dry condition and saturation, the shear strength is very small, and the cohesive force, internal friction angle and other parameters of fine silty sand are almost inexistent [3]. So, the most suitable moisture content should be studied, because the force mechanism of moisture content in extremely low and high condition is of significance. This paper selects the common moisture content under normal conditions. It is assumed that the moisture content of the analysis model can be 10%, 15%, 20%, 22.5%, 25%, 27.5%, 30%, 35%, respectively. The moisture content affects the failure behavior of the soil surrounding the MEEP pile under vertical tension.

ANALYSIS MODEL ESTABLISHED BY ANSYS SOFTWARE

Determination of material properties

In order to make the analysis results more practical, in this paper, material parameters are based on the physical and mechanical performance index of the fine silty sand from actual engineering survey reports [4]. The indices of physical and mechanical properties of fine silty sand and concrete in ANSYS model are shown in Table 1.

Determination of model dimensions

As the main research is about the effect of different moisture content on the interaction between pile and soil, and the failure mechanism of soil surrounding the MEEP pile, the analysis model of pile body must be completely placed in the same soil layer in order to reduce the influence of other factors. The vertical loads, the location of the plate of pile and the scope of surrounding soil must be considered when the model is established [5, 6]. In this paper, the model pile is completely set in the fine silty sand and its thickness is 10800 mm, including the length of pile body (6800 mm) and of the soil beneath (4000 mm).

Table 1. Indices of physical and mechanical performance of various materials

Soil layer	Density (g/cm ³)	Elasticity modulus (Mpa)	Poisson's ratio	Cohesive force (Kpa)	Internal friction (°)	Dilatation angle (°)	Friction coefficient
Fine silty sand	1.95E-009	3.0E4	0.25	8	25	25	0.30
Concrete	25.0	2.5e7	0.20	-	-	-	-

* To whom all correspondence should be sent:

E-mail: 654675316@qq.com

The diameter of reserve soil surrounding the pile is 4000 mm, to ensure that the pile and the bearing plate under vertical tension influencing the soil are enough. According to the change in moisture content, this paper uses 8 models, each having its own number and moisture content [7] (see Table 2). The dimensions of the model built by finite elements can be seen in Figure 1. The model diagram of piles and soil, and the model grid diagram established by ANSYS are shown in Figures 2 and 3, respectively.

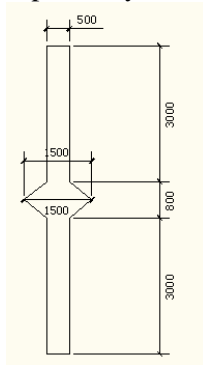


Fig. 1. Diagram of model dimension

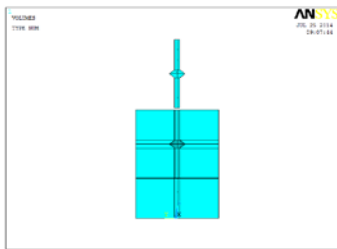


Fig. 2. Model diagram built by ANSYS

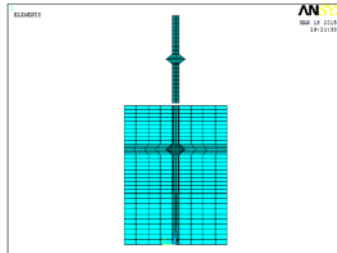


Fig. 3. Grid diagram of model

Analysis of results calculated by finite element simulation

Through the analysis of models by the above method, each of the models is loaded step by step [8, 9]. The load is divided by the area and is uniformly put on the top of the pile with half-circle section. The loading starts from 200KN (converted

to load divided by area 1000 KN/m²) and increases step by step with 200KN. All of these analyses form the nephogram and curve for parameters such as displacement, stress, strain, etc. The typical calculation results are analyzed as follows.

Analysis of displacement results

From the results of finite element analysis by ANSYS, a displacement nephogram of step 8 (loading of 1600KN) was selected for all models (moisture content from 10% to 35%). The vertical direction (Z direction) displacement nephograms of piles and soil of model TSMP1-TSMP8 are shown in Figure 4.

The analysis of the nephograms in Figure 4 shows that the vertical displacement of piles and soil of models TSMP1-TSMP3 is basically the same and its change along with the moisture content is not big [10], but for the model TSMP4-TSMP7, the vertical displacement gradually increases with the increase in moisture content and the bearing capacity is gradually reduced. The maximum change of displacement of piles and soil was for TSMP7. The model TSMP8 was up to failure behavior at the third step (loading of 600KN), for the moisture content was too high, so it could not be further loaded. From the analysis results of the ANSYS model it follows that the vertical displacement value of one fixed point of pile under different loads is as shown in Table 3, and a load-displacement curve can be formed (shown in Figure 5) from the data of the table, in order to analyze the rule of vertical displacement of pile under vertical force action with the change in loads.

It can be seen from Figure 5 that with the increase in moisture content, the pile displacement of TSMP1-TSMP6 has the same change and the growth of the displacement is more stable. The pile displacement change of TSMP7-TSMP8 is bigger and suddenly undergoes an obvious change. The model TSMP8 was destroyed at a very low load.

From the analysis of the nephogram and load-displacement curve above it can be concluded that when the moisture content of fine silty sand is between 10% and 20%, the failure behavior of the soil is relatively stable and has a smaller effect on the bearing capacity.

Table 2. Name of model and moisture content

Moisture content (%)	10	15	20	22.5	25	27.5	30	35
Name of the model	TSMP1	TSMP2	TSMP3	TSMP4	TSMP5	TSMP6	TSMP7	TSMP8

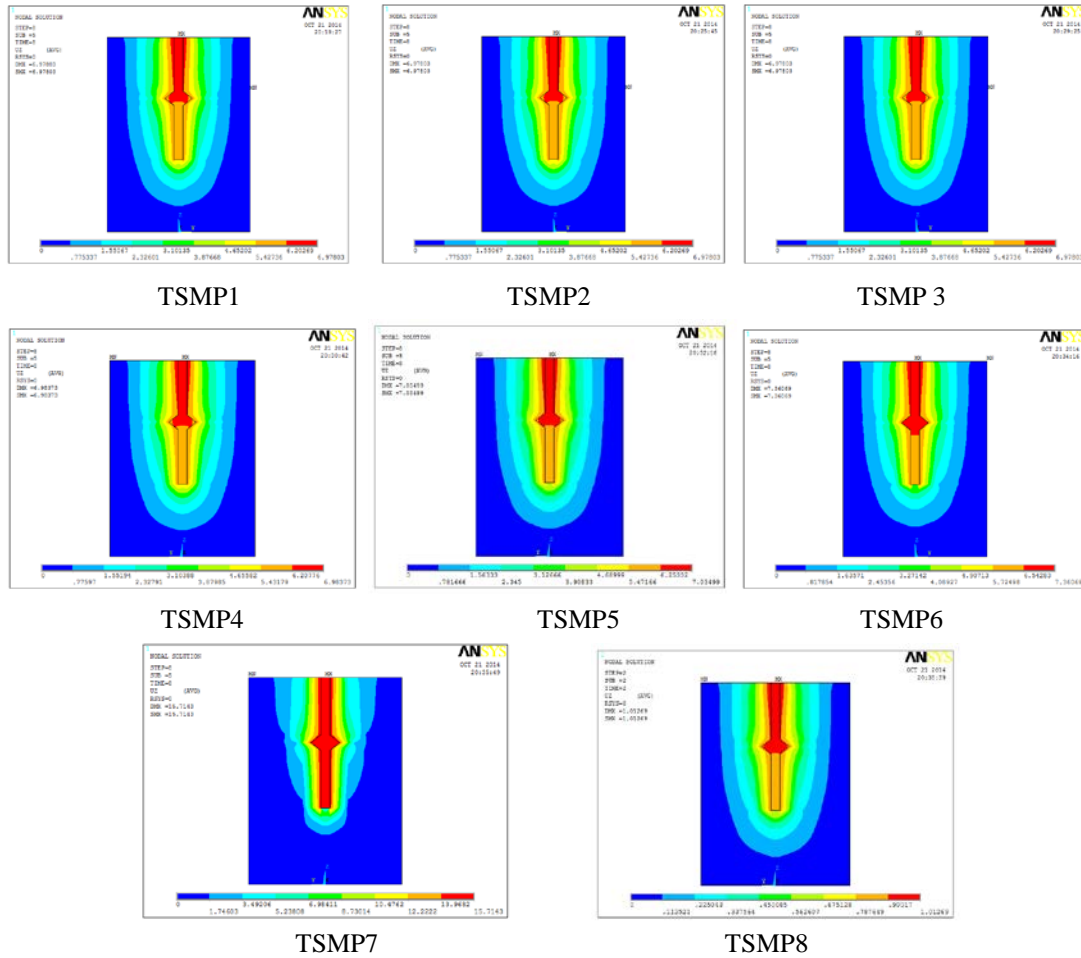


Fig. 4. Z direction displacements of piles and soil of different models in fine silty sand

Table 3. Data of vertical displacement at one fixed point of the pile under different loads

	200KN	400KN	600KN	800KN	1000KN	1200KN	1400KN	1600KN
TSMP1	-0.83E-29	0.99571	1.9914	2.9872	3.9830	4.9788	5.9747	6.9705
TSMP2	-0.83E-29	0.99571	1.9914	2.9872	3.9830	4.9788	5.9747	6.9705
TSMP3	-8.30E-30	0.99571	1.9914	2.9872	3.983	4.9788	5.9747	6.9705
TSMP4	3.88E-30	0.99578	1.9916	2.9874	3.9833	4.9792	5.9751	6.9762
TSMP5	4.18E-30	0.99578	1.9916	2.9874	3.9833	4.9792	5.98	7.0274
TSMP6	2.39E-29	0.99578	1.9916	2.9875	4.0074	5.0562	6.1652	7.3529
TSMP7	3.72E-30	0.99578	1.9916	3.0153	4.0933	5.3457	8.6161	15.706
TSMP8	0.37E-29	1.0116	19.53	-	-	-	-	-

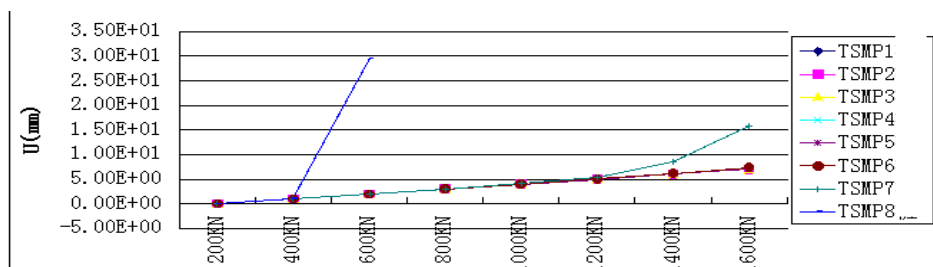
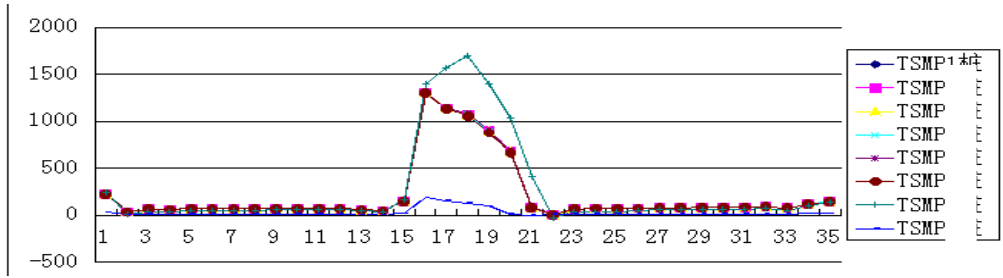
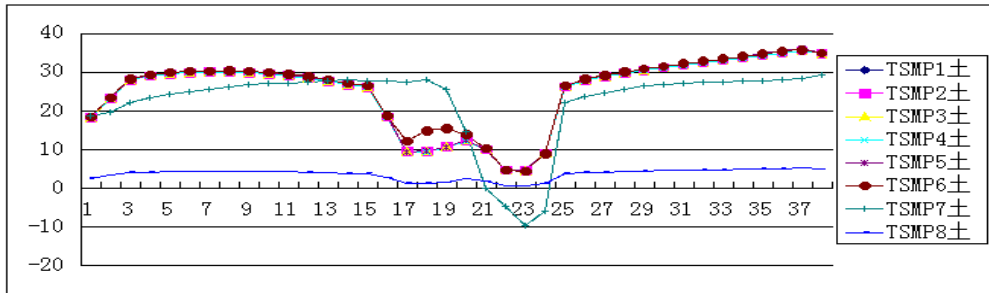


Fig. 5. Displacement-load curve of different model piles with different moisture content in the fine silty sand



Note: the location of change is at the location of the bearing plate in the curve shape

Fig. 6. Shear stress curve of pile body under the same load for different models



Note: the location of 16-20-24 is the location of the bearing plate

Fig. 7. Shear stress curve of soil surrounding pile under the same load for different models

When it is between 20% and 30%, the failure behavior of the soil changes, and the displacement increases stably, showing that the bearing capacity gradually decreases to a lower extent. When it is between 30% and 35%, the displacement suddenly changes at a larger load, showing that the bearing capacity decreases more; when it is above 35%, the model is destroyed under a lower load, showing that the bearing capacity is extremely low.

Analysis of stress and strain results

From the results calculated by ANSYS, it can be extracted that the shear stress data of variety of model pile body and soil surrounding the pile under the same load action, from which the curves are formed as shown in Figure 6 and Figure 7.

It can be seen from Figure 6 that the shear stress of different model pile bodies has a maximum value at the location of the bearing plate. From TSMP1 to TSMP6, the shear stress in the bearing plate has the same change with the increase of moisture content. The maximum change rate of shear stress can reach the top point for TSMP7-TSMP8, so the model TSMP8 is destroyed at a smaller load when the moisture content is 35% and the shear stress of the pile body is small. Therefore, the stress condition of the pile body is more stable when the moisture content is between 10% and 27.5%.

It can be seen from Figure 7 that the shear stress of the soil surrounding the pile in the different models has the minimum value at the location of the bearing plate, and the model TSMP8 is destroyed

under a smaller load when the moisture content is 35% and the shear stress of the pile body is extremely small. The shear stress of the soil surrounding the pile of TSMP1-TSMP6 has the same increase rate at the location of the bearing plate, and the shear stress of the model TSMP7 is bigger than that of the others. In general, the shear stress at the location of plate is bigger than under the plate. The shear stress of model TSMP7 is smaller than that of the others, and the shear stress under the bearing plate is bigger than that of the soil surrounding the bearing plate. The shear stress surrounding the pile of TSMP8 is extremely small.

The following conclusions can be drawn from the stress-strain nephogram and respective curve:

From the Z direction stress figure it follows that the stress can reach the maximum value at the top of the pile of model TSMP1-TSMP8, and decreases gradually from the top to the end of the pile body. The stress of the pile body obviously changes at the location of the bearing plate, but it is basically the same under the plate. The Z direction stress of TSMP1-TSMP6 pile is mostly the same, but the change for model TSMP7 is obvious, especially for the stress of the soil surrounding the pile. The stress of TSMP8 is only in the Z direction under the second step load, and it is destroyed with increasing load.

From the first main stress figure it can be concluded that from TSMP1 to TSMP6 the change of the first main stress is the same with increasing moisture content, and it decreases from top to end of the pile body. It strongly changes above the bearing

plate, but not under the bearing plate. The maximum of the first main stress from TSMP1-TSMP6 is mostly the same. The nephogram of TSMP8 is at the second step load and has a lower capacity.

From the total strain figure of Z direction it can be concluded that the maximum total strain in Z direction is mostly the same from TSMP1 to TSMP3 with the increase in moisture content and is slightly larger for TSMP1 than for TSMP2 and TSMP3. The maximum total strain in Z direction gradually increases with the same rate for TSMP4 to TSMP7; the maximum for TSMP7 is higher than for TSMP6; TSMP8 is destroyed at the third step load, and from the figure it can be seen that the moisture content is not higher than 27.5%, but less than 20% is most appropriate.

From the elastic strain diagram of Z direction it can be gained that the maximum value of all models appears near the location under the plate, and it gradually decreases from TSMP1 to TSMP7 and distributes symmetrically along the pile axis. The maxima of models TSMP1-TSMP3 are mostly the same, but their decrease rate increases from TSMP4 to TSMP7. The model TSMP8 is destroyed at the third step.

CONCLUSION

It is concluded that the moisture content in the fine silty sand has a certain effect on the failure behavior of soil surrounding the pile when the MEEP pile is under vertical load. Through the analysis of various parameters it is shown that for a moisture content of the fine silty sand between 10% and 20%, the failure behavior of the soil is relatively stable and has a lower impact on the bearing capacity; when it is between 20% and 30%, the failure behavior of soil changes, and the displacement stably increases, showing that the

bearing capacity gradually decreases, but the extent is not high; when it is between 30% and 35%, the displacement suddenly changes at a larger load, showing that the bearing capacity further decreases; when it is above 35%, the model is destroyed under a lower load, showing that the bearing capacity is extremely low. Therefore, the effect of moisture content on the bearing capacity should be considered and properly modified in the process of design and capacity calculation of the MEEP pile ad.

Acknowledgement: This work is financially supported by the National Natural Science Foundation of China (51278224 and 51678275). This work is financially supported by The Education Department of Jilin Province of China ([2016]151).

REFERENCES

1. Q. Mu, Ch. Ma, T. Miao, *The Academic Journal of Geotechnical Engineering*, **26**, 674 (2004).
2. H. Chen, F. Ban, X. Liu, *The Academic Journal of Hefei University of Industry (Natural Science Version)*, **29**(6), 736 (2006).
3. H. Ling, Z. Yin, Z. Cai, *The Geotechnical Mechanic*, **29**(3), 651 (2008).
4. C. Shen, X. Fang, H. Wang, S.G. Sun, J.F. Guo, *The Geotechnical Mechanic*, **30**(5), 1347 (2009).
5. X. Xie, The failure state and bearing capacity study of the Multi-Extruded- Expanded- Plates pile influenced by soil properties. (2015).
6. Y. Qian, X. Yin, R. Wang, *Geotechnical Engineering World*, **12**(9), 67 (2009):
7. D. Qian, *Journal of geotechnical engineering*, Vol. **24**(3), 371 (2002).
8. X. Gao, Bearing characteristics test and numerical simulation analysis of the squeezed branch and plate pile. (2007).
9. C. Lu, *Journal of engineering survey*, **6**, 12 (2001).
10. Y. Zhang, H. Yuan, *Journal of Beijing university of technology*, **32**(10), 879 (2006).

Study on the influence of the abrasion angle on the rubber abrasion performance at different scales

Z. Wang*, Sh. Hu, F. Zhang, L. Ma*

School of Electromechanical Engineering, Qingdao University of Science and Technology, Qingdao, Shandong, China

Received September 28, 2017; Accepted December 19, 2017

Rubber abrasion experiments under different temperatures and angles were carried out using a high temperature rubber abrasion tester to study the influence of temperatures and angles on the rubber abrasion performance. Surface morphology images of rubber samples were obtained using a 3D measuring laser microscope and their corresponding surface characteristic parameters were then obtained including the arithmetic mean deviation of outline (Ra), the root mean square deviation of outline (Rq), the 3D arithmetic mean deviation (Sa) and the 3D root mean square deviation (Sq). The scale effect on roughness measurements of the rubber abrasion surface was also investigated and an optimal magnification multiple in the microscope was recommended based on the variation data of the line roughness and the surface roughness at various magnifications.

Key words: Rubber composites, Rubber abrasion, Surface morphology, Scale effect

AIMS AND BACKGROUND

As an important industrial raw material, rubber has many advantageous performance characteristics. Improving abrasion performance of rubber products can not only bring considerable economic and social benefits but also enhance products' safety and working life.

In abrasion tests, a series of abrasion patterns on the rubber surface, called Schallamach abrasion patterns [1,2], would be produced with parallel ridges perpendicular to the sliding direction. After numerous experiments, an abrasion model based on the failure mechanism was proposed by some researchers [3-9]. Most of the previous abrasion experiments were carried out at room temperature. Many surface characteristics in the abrasion process and the temperature effect on the abrasion performance were rarely investigated, and it is necessary to identify and investigate the scale range and the optimal scale in the study of the self-affinity fractal characteristics and to determine the upper and lower boundaries of the scale range of self-affinity fractal [10-12].

In this paper, a high-temperature abrasion test was conducted to measure the rubber abrasion volume under different angles and the corresponding surface morphology and microstructure characteristic parameters were obtained using a 3D measuring laser microscope. The relationship between the rubber abrasion performance and the surface morphology characteristics was identified and analyzed.

EXPERIMENTAL

Experimental materials and instruments

Tread rubber from an all-steel radial tire was investigated. The equipment used in the experiment included a rubber mixer (XSM-500), a roll mill (BL-6175-BL), a plate vulcanizing apparatus (HS-100T-FTMO-2PT), a rotorless curemeter (GT-M2000-A), a densimeter (GT-XS-365M), a double- end grinding machine (MZ-4101), a 3D measuring laser microscope (LEXT OLS4100) and a new type of abrasion tester intentionally designed for more realistic abrasion studies.

Experimental procedures

Step 1. Prepare rubber samples and paste them to a heatable wheel. Then place the wheel in a vulkometer and bake at 115°C for 2.5 h. After that, cool the wheel at room temperature for 24 h.

Step 2. Install the cooled rubber wheel on a rubber abrasion tester and heat it by a heating system to a desired temperature based on the experimental matrix.

Step 3. Start and operate the rubber abrasion tester for 500 revolutions as a pre-grinding. Then, weigh the rubber wheel and rubber strips after taking it off from the tester and cleaning it up and mark the total mass as m_1 .

Step 4. Install the rubber wheel on the tester again and operate the tester for 1709 revolutions (500 meters). Then, the total mass of the wheel and rubber strips m_2 is obtained, after taking off and cleaning up.

Step 5. Calculate the abrasion volume using the following equation according to GB/T533:

$$V=(m_1-m_2)/\rho \quad (1)$$

To whom all correspondence should be sent:
E-mail: wzp_ww1@163.com

V - abrasion volume of the sample, cm^3 .

m_1 - mass of the sample after pre-grinding, g.

m_2 - mass of the sample after test, g.

ρ - density of the sample, g/cm^3 .

RESULTS AND DISCUSSION

Abrasion tests under different angles and temperatures were carried out under a load of 26.70N on the high temperature rubber abrasion tester with a 40# abrasion wheel. The tests were replicated several times for a given angle and temperature and the average values were adopted as the experimental data. Table 1 shows the experimental results at various combinations of temperatures and angles. It is seen from the table that the abrasion volume increases as the angle and temperature increase. Namely, the abrasion volume is the greatest at 21° angle and the smallest at 9° angle and in between for other angles. Similarly, the abrasion volume is the greatest at 80 °C and the smallest at 25 °C and in between at 60 °C.

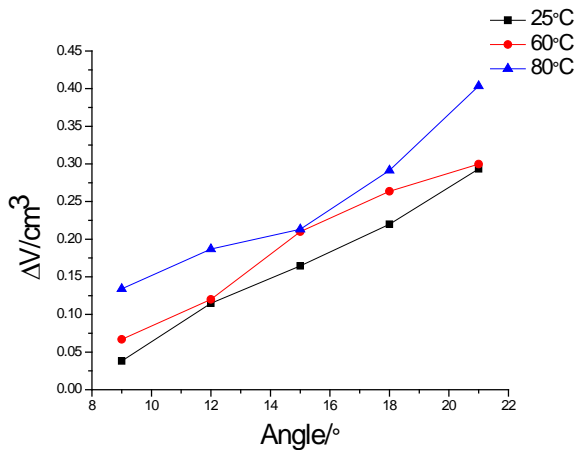


Fig. 1. Relation between the abrasion volume and the angle

Table 1. Experimental results for the abrasion of rubber strips

Temperature / °C	Angle / °	ρ / (g/cm^3)	m_1 / g	m_2 / g	Δm / g	ΔV / cm^3
25	9	1.131	69.975	69.932	0.043	0.0380
25	12	1.106	69.002	68.875	0.127	0.1148
25	15	1.101	65.616	65.435	0.181	0.1644
25	18	1.105	67.241	66.998	0.243	0.2199
25	21	1.101	68.325	68.002	0.323	0.2934
60	9	1.105	67.757	67.683	0.074	0.0670
60	12	1.074	66.821	66.692	0.129	0.1201
60	15	1.105	65.446	65.214	0.232	0.2100
60	18	1.096	68.023	67.734	0.289	0.2637
60	21	1.104	76.262	75.931	0.331	0.2998
80	9	1.096	68.177	68.030	0.147	0.1341
80	12	1.081	76.429	76.227	0.202	0.1869
80	15	1.104	67.329	67.094	0.235	0.2131
80	18	1.115	67.612	67.287	0.325	0.2915
80	21	1.105	67.556	67.110	0.446	0.4036

Analysis of the abrasion value

According to the experimental results in Table 1, the relation between the abrasion volume and the angle is plotted in Fig. 1. It is also observed from the above experimental results that the abrasion volume increases with the increase in temperature. Due to its viscoelasticity and large deformation under cyclic loading, rubber usually shows a strong time lag behavior in the dynamic changing process accompanied with a large quantity of heat generation, which leads to a sharp temperature rise in the rubber sample over time. Under heating, the physicochemical properties of rubber are significantly different from those at room temperature. At high temperature, the molecular thermal motion energy in rubber composites increases and its kinematic component becomes more active, which leads to thermal decomposition of the rubber material and results in changes in the rubber surface microstructure, the molecular chain form, the chain conformation and mesh structure inside the rubber, the degree of pyrolysis of the materials and the surface structure. Meanwhile, the viscosity within rubber would drop, which further affects material properties like strength, elasticity modulus and dynamic behavior, and deteriorates the abrasion resistance. Furthermore, the abrasion performance becomes unstable at high temperature. That is why the relation between the abrasion volume and the angle shows great fluctuations.

Abrasion surface analysis

Both 2D and 3D images of rubber abrasion surface morphologies at different angles were obtained at 25 °C using load of 26.70N for the 40# abrasion wheel, as shown in Fig. 2.

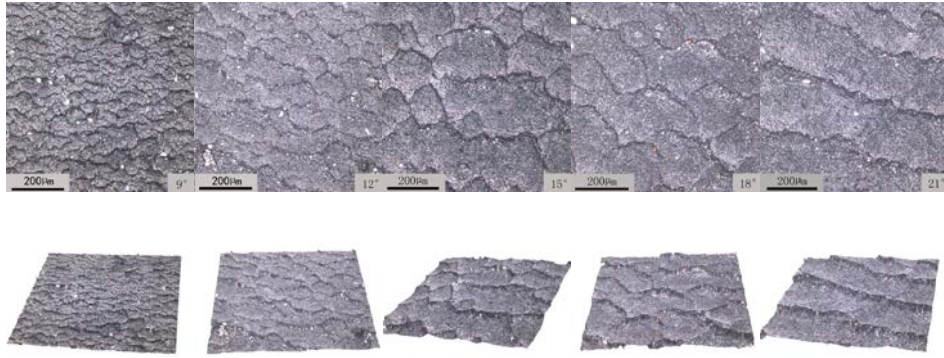


Fig. 2. 2D and 3D microscope images of abrasion surface under different angles

It can be seen from Fig. 2 that the abrasion surface evolves from a tiny scaly abrasion pattern to a strip mill grain as the angle increases and the grinding grain spacing and depth gradually increase. It is indicated that the friction stress between the rubber surface and the grinding wheel is lower under a smaller angle and thus the shear force in the rubber chain is also lower at small angles, which increases its ability to tear. As the angle continuously increases, the friction stress between the rubber surface and the grinding wheel gradually increases and the shear stress in the rubber molecular chain also increases, which deteriorate the rubber’s ability to resist tear. At larger angles, abrasion is severe as the grains continue to grow and the tear formation pit contour continues to expand. In the meantime, the flaky grinding pattern becomes a ladder-shape grinding pattern and the surface becomes rougher. Therefore, the greater the angle, the higher is the friction stress and the more severe is the abrasion. As the grinding pattern spacing and height increase, the abrasion surface becomes more complicated too.

To further explore the characteristics of the abrasion surface morphology, its variation with the angle can be described with R_a , R_q , S_a and S_q , where R_a represents the arithmetic mean of the distance between the points on the outline and the datum line in the sampling length; R_q represents the root mean square height of the outline in the sampling length; S_a is an index to characterize the surface roughness in the microscopic field scale and S_q is the standard deviation of the surface height distribution.

Those characteristic parameters describing the rubber abrasion surfaces, as shown in equations (1) to (4), were obtained for angles 9°, 12°, 15°, 18° and 21° using the 3D measuring laser microscope under load of 26.70N and temperature of 25 °C for the 40# abrasion wheel, as shown in Table 2.

The experimental data in Table 2 can also be illustrated in the line chart shown in Fig. 3.

Table 2. Characteristic parameters of the surface under different angles

Angle / °	$R_a / \mu\text{m}$	$R_q / \mu\text{m}$	$S_a / \mu\text{m}$	$S_q / \mu\text{m}$
9	0.915	1.150	1.124	1.537
12	0.935	1.177	1.145	1.528
15	1.110	1.435	1.347	1.894
18	1.348	1.772	1.611	2.316
21	1.476	1.934	1.684	2.589

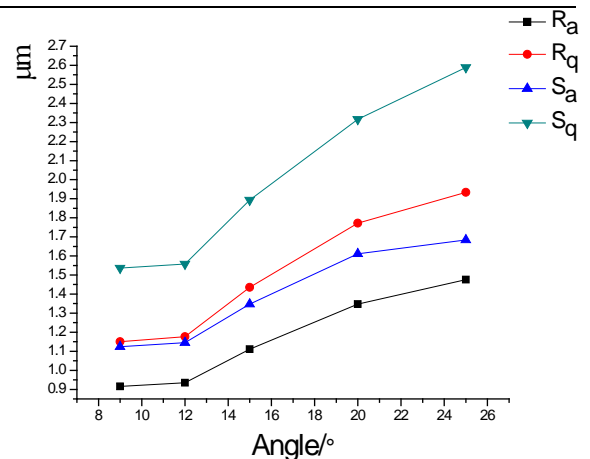


Fig. 3. Line chart of R_a , R_q , S_a and S_q and angle

It is seen from Fig. 3 that the characteristic parameters R_a , R_q , S_a and S_q continuously increase with angle increase. Their increase is almost neglectable for angles less than 12°. As defined, R_a and R_q are related to the height of contour convex peaks, their greater values at higher angles indicate that the abrasion marks have gradually changed from an abrupt morphology to a gentle one. In addition, the height of contour convex peaks increases with more fluctuation and the abrasion surface becomes rougher. S_a and S_q can be used to describe the abrasion surface height and its distribution, respectively. The higher values of S_a and S_q at greater angles shown in Table 2 and Fig. 3 indicate a more dispersive surface height and a more severe and complex abrasion surface

morphology. These results are consistent with the results depicted in Fig. 2.

Scale effect in roughness measurements

The contours of the curve images from the abrasion surface morphology of the rubber sample tested under the condition of 15° angle, 80 °C temperature, 26.70N load and 40# wheel were collected by a 3D measuring laser microscope using different observation scales. The microstructure of the abrasion surface outline shows some self-similarities and the abrasion surfaces display similar microscopic features as hierarchy nesting of infinite levels under different observation scales. The line roughness parameters on rubber abrasion surfaces at different observation scales were obtained under the test conditions of 15° angle, 80 °C temperature, 26.70N load and 40# wheel using the 3D measuring laser microscope, as shown in Table 3.

Table 3. Line roughness parameters under different observation scales

Magnification multiples	R _a / μm	R _q / μm	R _{sk}
108	1.111	1.343	0.057
216	1.168	1.467	0.098
324	1.292	1.636	0.195
427	1.315	1.649	0.208
555	1.375	1.726	0.239
640	1.296	1.590	0.173
769	0.319	0.396	0.075
854	0.144	0.175	0.031

The experimental data in Table 3 are also replotted in Fig. 4.

Characteristic parameters *R_a*, *R_q* and *R_{sk}* initially increase with an increased magnification multiples, then start to decrease after magnification multiples greater than 550 and finally rapidly drop when the magnification multiple reaches 769. This suggests that a finer surface profile structure would

be collected at miniature observation scales, which results in slightly increased line roughness parameters. However, the further identification and characterization of the microstructural level is limited by the resolution of the measuring instrument (resolution limits) and the rubber surface structure itself (physical limits).

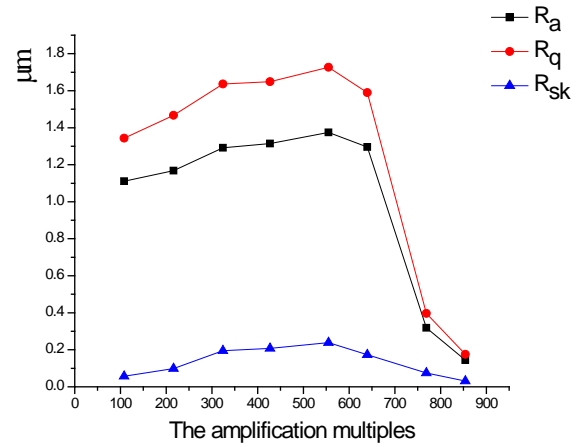


Fig. 4. Values of *R_a*, *R_q* and *R_{sk}* at different amplification multiples

When the magnification multiple is greater than 769, only two or three abrasion patterns can be observed within observation area and thus the associated surface characteristic parameters would not reflect the true structural characteristics of the rough surface. Therefore, the magnification should be controlled at 324-640 during the measurement of the characteristic parameters of the surface roughness.

The 2D images of the abrasion surface morphologies at different observation scales were also collected using the 3D measuring laser microscope for the rubber sample tested under the conditions of 15° angle, 80 °C temperature and 26.70N load and 40# wheel. The images are shown in Fig. 5.

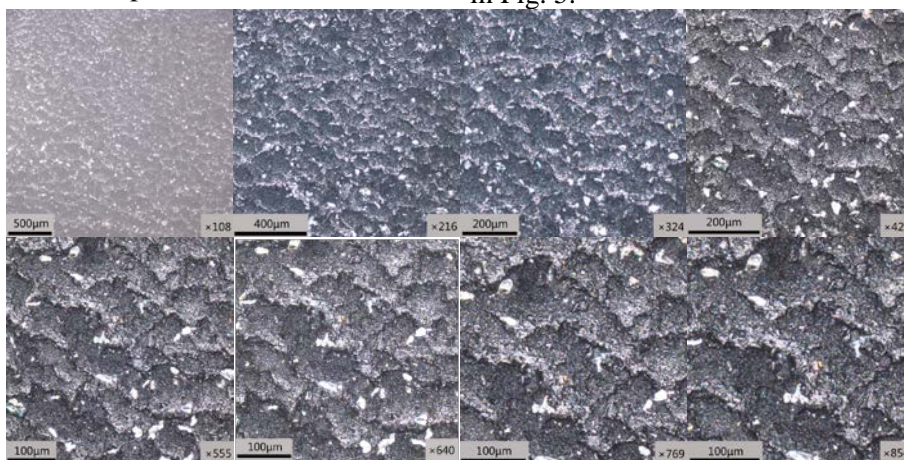


Fig. 5. 2D images of abrasion surface under different magnifications

The corresponding surface roughness parameters of rubber abrasion surfaces at different observation scales are given in Table 4.

Table 4. Surface roughness parameters under different observation scales

Magnification multiples	$S_a / \mu\text{m}$	$S_q / \mu\text{m}$	S_{ku}
108	1.782	2.403	6.792
216	1.767	2.385	6.566
324	1.708	2.311	6.564
427	1.680	2.298	6.358
555	1.658	2.238	6.272
640	1.629	2.189	5.911
769	1.606	2.146	5.662
854	1.583	2.101	5.157

The experimental data in Table 4 can be displayed in graphical form, as shown in Fig. 6.

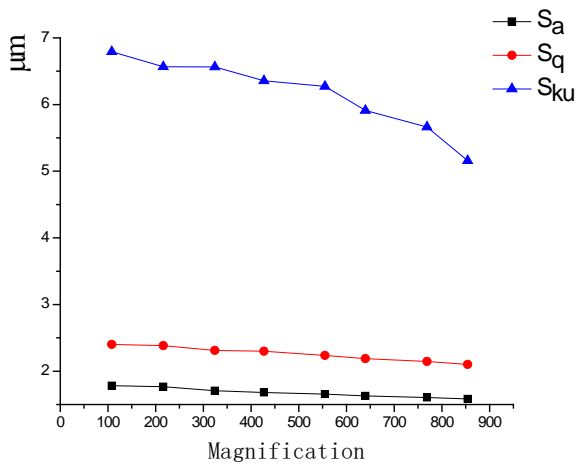


Fig. 6. Variation image of S_a , S_q and S_{ku} with magnification

It is seen from Fig. 6 that the characteristic parameters S_a , S_q and S_{ku} gradually decrease as magnification multiples increase, as expected since the surface roughness parameters were calculated based on the entire image range at a given magnification multiple. The abrasion surface would be reduced in the viewable region of the microscope with a small observation scale and thus the observed abrasion patterns would be enlarged and refined. In addition, the observation area would contain less information on the changes in the abrasion pattern and the corresponding measurements may miss some of the asperity structures that contribute to the rough surface, which would result in a reduced value of surface roughness.

Based on the above results and data analysis of the line roughness and surface roughness from rubber abrasion surface morphology, it is recommended that the best observation magnification is within 324-640.

CONCLUSIONS

The rubber abrasion performance and surface morphology characteristics at various angles were investigated from the perspectives of the abrasion volume and the characteristic parameters of abrasion surfaces under different scales. Based on the above studies, some conclusions can be made:

(1) The angle has a significant influence on the rubber abrasion performance. The abrasion volume increased proportionally with the increase in angle. At higher temperatures, the dependence of the rubber abrasion performance on the angle becomes more uncertain and shows a great fluctuation in data.

(2) The characteristic parameters of the abrasion surface increase with the increase in angle. The larger angle could lead to more severe abrasion and result in a more complex abrasion surface morphology.

(3) The microstructure of the abrasion surface morphology shows a self-similarity structure and its roughness measurement depends upon the scales used in the measurement. The magnification multiple should be kept within 324-640 in the study of rubber abrasion surface morphology.

Acknowledgements: This research was funded by the National Natural Science Foundation of China (51576102), the Science and Technology Program of Shandong Higher Education (J16LB09), the Green Tire and Rubber Collaborative Innovation Project (2015GTR0018).

REFERENCES

1. J. Chen, J. A. Donovan, *Xiangjiao Cankaoziliao*, **25**(7), 50 (1995).
2. P. Thavamani, A. K. Bhowmick, *J. Mater. Sci.*, **28**(5), 1351(1993).
3. B. Lorenz, B.N.J. Persson, S. Dieluweit, T. Tada, *J. Eur. Phys. E*, **34**, 129 (2011).
4. A. Shojaei, M. Arjmand, A. Saffar, *J. Mater. Sci.*, **46**, 1890 (2011).
5. M. Arjmand, A. Shojaei, *Tribol. Lett.*, **41**, 325 (2011).
6. B.N.J. Persson, *Phys. Rev. Lett.*, **87**(11), 116101 (2001).
7. B.N.J. Persson, *Phys. Rev. Lett.*, **89**(24), 245502 (2002).
8. B.N.J. Persson, F. Bucher, B. Chiaia, *Phys. Rev. B*, **65**(18), 184106 (2002).
9. Z. Li, Experimental Study and Numerical Analysis of Tire Tread Wear Behavior. Hefei: University of Science and Technology of China, 2013.
10. J. N. Wang, H. P. Xie, X. Y. Tian, K. Marek, *Chinese J. Rock Mech. & Eng.*, **19**(1), 11(2000).
11. H. P. Xie, Introduction to Fractal-rock Mechanics. Beijing: Science Press, 1997.
12. P. Cao, L. Luo, T. Y. Liu, K. Zhang, *Sci. Tech. Rev.*, **29**(24), 57 (2011).

Instructions about Preparation of Manuscripts

General remarks: Manuscripts are submitted in English by e-mail. The text must be typed on A4 format paper using Times New Roman font size 11, normal character spacing. The manuscript should not exceed 15 pages (about 3500 words), including photographs, tables, drawings, formulae, etc. Authors are requested to use margins of 2 cm on all sides.

Manuscripts should be subdivided into labelled sections, e.g. **Introduction, Experimental, Results and Discussion**, etc. **The title page** comprises headline, author's names and affiliations, abstract and key words. Attention is drawn to the following:

a) **The title** of the manuscript should reflect concisely the purpose and findings of the work. Abbreviations, symbols, chemical formulas, references and footnotes should be avoided. If indispensable, abbreviations and formulas should be given in parentheses immediately after the respective full form.

b) **The author's** first and middle name initials and family name in full should be given, followed by the address (or addresses) of the contributing laboratory (laboratories). **The affiliation** of the author(s) should be listed in detail by numbers (no abbreviations!). The author to whom correspondence and/or inquiries should be sent should be indicated by asterisk (*) with e-mail address.

The abstract should be self-explanatory and intelligible without any references to the text and containing not more than 250 words. It should be followed by key words (not more than six).

References should be numbered sequentially in the order, in which they are cited in the text. The numbers in the text should be enclosed in brackets [2], [5, 6], [9–12], etc., set on the text line. References are to be listed in numerical order on a separate sheet. All references are to be given in Latin letters. The names of the authors are given without inversion. Titles of journals must be abbreviated according to Chemical Abstracts and given in italics, the volume is typed in bold, the initial page is given and the year in parentheses. Attention is drawn to the following conventions: a) The names of all authors of a certain publication should be given. The use of "et al." in the list of references is not acceptable. b) Only the initials of the first and middle names should be given. In the manuscripts, the reference to author(s) of cited works should be made without giving initials, e.g. "Bush and Smith [7] pioneered...". If the reference carries the names of three or more authors it should

be quoted as "Bush *et al.* [7]", if Bush is the first author, or as "Bush and co-workers [7]", if Bush is the senior author.

Footnotes should be reduced to a minimum. Each footnote should be typed double-spaced at the bottom of the page, on which its subject is first mentioned. **Tables** are numbered with Arabic numerals on the left-hand top. Each table should be referred to in the text. Column headings should be as short as possible but they must define units unambiguously. The units are to be separated from the preceding symbols by a comma or brackets. Note: The following format should be used when figures, equations, etc. are referred to the text (followed by the respective numbers): Fig., Eqns., Table, Scheme.

Schemes and figures. Each manuscript should contain or be accompanied by the respective illustrative material as well as by the respective figure captions in a separate file (sheet). As far as presentation of units is concerned, SI units are to be used. However, some non-SI units are also acceptable, such as °C, ml, l, etc. The author(s) name(s), the title of the manuscript, the number of drawings, photographs, diagrams, etc., should be written in black pencil on the back of the illustrative material (hard copies) in accordance with the list enclosed. Avoid using more than 6 (12 for reviews, respectively) figures in the manuscript. Since most of the illustrative materials are to be presented as 8-cm wide pictures, attention should be paid that all axis titles, numerals, legend(s) and texts are legible.

The authors are required to submit the text with a list of three individuals and their e-mail addresses that can be considered by the Editors as potential reviewers. Please, note that the reviewers should be outside the authors' own institution or organization. The Editorial Board of the journal is not obliged to accept these proposals. The authors are asked to submit **the final text** (after the manuscript has been accepted for publication) in electronic form by e-mail. The main text, list of references, tables and figure captions should be saved in separate files (as *.rtf or *.doc) with clearly identifiable file names. It is essential that the name and version of the word-processing program and the format of the text files is clearly indicated. It is recommended that the pictures are presented in *.tif, *.jpg, *.cdr or *.bmp format.

The equations are written using "Equation Editor" and chemical reaction schemes are written using ISIS Draw or ChemDraw programme.

EXAMPLES FOR PRESENTATION OF REFERENCES

REFERENCES

1. D. S. Newsome, *Catal. Rev.–Sci. Eng.*, **21**, 275 (1980).
2. C.-H. Lin, C.-Y. Hsu, *J. Chem. Soc. Chem. Commun.*, 1479 (1992).
3. R. G. Parr, W. Yang, *Density Functional Theory of Atoms and Molecules*, Oxford Univ. Press, New York, 1989.
4. V. Ponec, G. C. Bond, *Catalysis by Metals and Alloys (Stud. Surf. Sci. Catal., vol. 95)*, Elsevier, Amsterdam, 1995.
5. G. Kadinov, S. Todorova, A. Palazov, in: *New Frontiers in Catalysis (Proc. 10th Int. Congr. Catal., Budapest,(1992)*, L. Guzzi, F. Solymosi, P. Tetenyi (eds.), Akademiai Kiado, Budapest, 1993, Part C, p. 2817.
6. G. L. C. Maire, F. Garin, in: *Catalysis. Science and Technology*, J. R. Anderson, M. Boudart (eds), vol. 6, SpringerVerlag, Berlin, 1984, p. 161.
7. D. Pocknell, *GB Patent 2 207 355* (1949).
8. G. Angelov, PhD Thesis, UCTM, Sofia, 2001, pp. 121-126.
- 9 JCPDS International Center for Diffraction Data, *Power Diffraction File*, Swarthmore, PA, 1991.
10. CA **127**, 184 762q (1998).
11. P. Hou, H. Wise, *J. Catal.*, in press.
12. M. Sinev, private communication.
13. <http://www.chemweb.com/alchem/articles/1051611477211.html>.

Texts with references which do not match these requirements will not be considered for publication!!!

CONTENTS

Zh. Wang, Zh. Yu, X. Sun, Y. Wang, L. Xu, Chirality- and size-dependent elastic properties of a single-layered graphene sheet	5
M. Zhao, J. Zhang, Zh. Lei, Q. Kang, Application of a MEE-rock debris separation technique in deep hole bench blasting	9
X. Li, X. Wang, Evaluation of motor function based on self-correction analytical hierarchy process	15
B. Yang, Q. Wang, X. Zhao, Ch. Wang, J. Liu, H. Yang, Sh. Liu, F. Yin, W. Zhang, Biological conversion of H ₂ and CO ₂ into CH ₄ at room temperature and atmospheric pressure: a promising approach for reducing CO ₂ emissions and increasing biomethane production	20
J. Dong, L. Zhu, D. Gu, H. Sheng, Ch. Yan, B. Wang, Theoretical and experimental study on the safety chemistry of separation of oil/water transition layer by oxidation of chlorine dioxide	24
D. Wang, B. Hu, Study of the mechanism of magnetron sputtering of hybrid bonded diamond as carbon film coating for the surface of cavity structures	29
Y. Qian, D. Teng, T. Lu, R. Wang, Research on the moisture content of adjacent soil layer affecting the failure behavior of soil and the uplift bearing capacity of the MEEP pile	33
C. Gao, X. Zhang, N. Xu, X. Tang, Photo-induced toxicity in the rotifer <i>Branchionus plicatilis</i> by anthracene (ANT) in absence and presence of UV irradiation and mechanisms underlying observed effects	39
P. Huang, Y. Zhang, Analysis of seepage characteristics of mine fractures based on geothermal utilization	44
H. Yu, R. Jiang, L. Chen, Supercritical CO ₂ extraction of organic matter from coal based on CO ₂ sequestration in deep coal seams	49
H. Wang, L. An, X. Zhang, Evaluation of regional innovation ability based on green and low-carbon perspective .	55
Y. Liu, H. Pang, X. Li, T. Gao, W. Zhao, Nitrogen transformation and biodiversity characteristics of fluvo-aquic soil from Hebei plain, China	59
Ch. Li, X.-K. Sun, J.-H. Xu, Q.-L. Chang, Slicing filling principle and repeated mining key technology for extra-thick coal seams in small coal pit destroyed areas	65
B. Li, J. Li, H. Zhou, Y. Wei, H. Wang, J. Hu, Pyrolysis characteristics and kinetic analysis of waste cooking oil .	71
H. Yu, R. Jiang, L. Chen, Limitations of measurements of supercritical CO ₂ sorption isotherms on coals with manometric equipment - an experimental case study	77
Y. Zhao, X. Duan, Sh. Shu, Relationship between space structure characteristics and site environment of <i>Pinus Yunnanensis</i> secondary forests on Mopan Mountain in the middle of Yunnan, Southern China	83
F. Wu, X. Sun, J. Li, Ch. Liu, Q. Chang, B. Chen, Breaking features of loading key strata based on deep beam structure in shallow coal seam and its limited span-to-depth ratio	89
Y. Qian, Z. Liu, W. Tian, R. Wang, Test study on the thickness of the soil layer under the plate affecting the compression failure of the concrete expanded-plate pile	96
D. Wang, B. Hu, Research on the environmental protection of magnetron sputtering coating for multi-contour cavity structure products	103
Ch. Fang, T. Wu, J. Cong, J. Wang, Study of the influence of Ca ²⁺ content in soil on <i>Brassica Chinensis</i> L. crop yield under acid rain stress conditions	107
D. Yi, J. Li, J. Cao, Study on fundamental polishing characteristics in chemical mechanical polishing of gallium arsenide (GaAs) wafer	113
J. Yao, Q. Niu, L. Li, Y. Li, Y. Feng, S. Ma, Influence of kidney tonic formula on the hippocampal neurotrophic factors and proliferation and differentiation of neural stem cells in natural aging rats	118
Zh. Tang, X. Zhao, <i>In vitro</i> fluoride release from fluorinated elastic denture material	121
L.L. Li, J.W. Shen, Z.R. Liu, Controlling the abnormal state in the Rb-E2F pathway involving microRNAs	125
J. Dong, X. Sui, B. Wang, Y. Liu, Ch. Yan, L. Zhu, D. Yuan, L. Li, Research progress in oil-field scale prevention techniques	130
W.Y. Zhu, X. Yue, X. Lv, Ch. Yi, J. Liu, Bavachin antioxidant effects on the cardiac myocytes of mice in exhaustive exerciseteta	136
A.J. Shao, L.Y. Zhao, S.W. Wang, Study of the influence of karst water runoff on mining based on fuzzy mathematics	143
B. Ding, Impact of quadric surface carrier on gas flow radial dispersion pattern in a vehicle catalytic converter ...	147
X. Liu, X. Guan, M. Guo, X. Wang, J. Lin, Influence of freezing and thawing cycles on bamboowood's surface properties.....	152
F. Chen, Ch. Qu, J. Wang, L. Liu, Sh. Ning, Synthesis and structure-activity relationships of a new highly selective rodenticide - brominated <i>n</i> -piperidine dibenzocycloheptoid	156
F. Yu, Sh.X. Chen, Y. Zhang, J. Li, Zh.J. Dai, Experimental study on dynamic shear modulus and damping ratio of CAS-1 lunar regolith simulant	159
T. Wang, Y.M Ding, X.W Zhao, B.G Li, Y. Song, Experimental study on the soil-water characteristic curve of the unsaturated loess in East Gansu province	165

L. Ma, H. Yin, Z. Wang, J. Wu, Z. Wang, Sh. Hu, Zh. Miao, Temperature and wear characteristics of TBR tread rubber and its constitutive characterization	172
B. An, W. Zhang, Impact of electrical environment on wireless sensor communication	178
S. Zhang, Y. Fang, Y. Han, An empirical analysis of the economic development, energy structure and energy consumption in Zhejiang Province	186
Fang Qi, Analysis of pharmacological adverse reactions of western medicines	190
R.Ch. Zhou, J. Wu, Discriminating geochemical anomalies by geological-geochemical method: A case study on Nagan section of E'dong area in Wuxu ore field in Guangxi Province, China	194
Y.S. Wan, D.W. Li, Removal of <i>p</i> -chlorophenol in wastewater through catalytic ozonation using MnO _x /Al ₂ O ₃	200
J. Zhao, Sh.M. Li, Coordinated development of environment and tourism in China using grey relational analysis.	205
J. Ch. Zhang, X. H. Kong, Y. P. Ma, X. Y. Wang, H. Chen, P. Q. Zhang, D. Sh. Yu, X. D. Dai, Q. F. Ma, Z. H. Han, Monitoring of distribution of mineral elements during cultivation of <i>Auricularia auricula</i> in northeastern China	210
L. Xu, H. Gao, J. Xu, M. Xu, X. Wang, F. You, Y. Long, Experimental insights into a novel over-saturated brine cement slurry used in anhydrite formation	214
Q. Huo, D. Li, Zh. Wu, Study on polystyrene conformational changes in supercritical fluid anti-solvent process by small angle X-ray scattering	220
Sh. Liu, Dynamic analysis of aluminum flows in production stage in mainland China: 1996-2014	224
Y.J. Wang, K.Y. Wei, H.H. Liu, Double motor intelligent control system for industrial agitation based on Kingview and single chip microcomputer	228
M. Gu, X. Xu, W. Xiong, H. Pan, W. Dai, Use of artificial neural networks for modeling the fabric temperature in heat setting processes	233
X.T. Wang, L.X. Zhao, L. Li, Q.F. Chen, Q. Li, J. Zhang, Effect of sorbent concentration on Pb(II) sorption on Mg-Al-EDTA layered double hydroxides	238
Y. Qian, S. Liang, R. Wang, X. Su, Theoretical research on the moisture content of fine silty sand affecting the failure behavior of soil of the MEEP pile under vertical tension	242
Z. Wang, Sh. Hu, F. Zhang, L. Ma, Study on the influence of the abrasion angle on the rubber abrasion performance at different scales	247
INSTRUCTIONS TO THE AUTHORS	252